Investigating strong gravitational lensing with infrared space missions : AKARA, Spitzer and Herschel

Thesis

Investigating strong gravitational lensing with infrared space missions: *AKARI*, *Spitzer* and *Herschel*

The Open University

Rosalind Hopwood

Department of Physics and Astronomy

The Open University

A thesis submitted for the degree of

Doctor of Philosophy

December 2010

For my Husband

Acknowledgements

I am eternally grateful to my supervisor Stephen Serjeant for giving me the opportunity to change the direction of my path in life, in order follow a new and far more interesting academic career. I also thank my parents for their continued support over the long route my education journey has taken. I thank Mattia Negrello for his guidance and support, and our mutual love of useless stuff. In particular I thank my husband for his support and understanding and belief, especially during the many evenings he spent alone over the past three years.

The Open University

EX12 Revised 27 January 2010

RESEARCH SCHOOL

Library Authorisation Form

Please return this form to the Research School with the two bound copies of your thesis to be deposited with the University Library. All candidates should complete parts one and two of the form. Part three only applies to PhD candidates.

Part One: Candidates Details

Name: ROSALIND Hopwood PI: R7279754

Degree: Doctor of PHILOSOPHY

Thesis title: INVESTIGATING STRONG GRAVITATIONAL LENSING WITH INFRARED SPACE MISSIONS: AKARI, SPITZER AND HERSCHEL

Part Two: Open University Library Authorisation

I confirm that I am willing for my thesis to be made available to readers by The Open University Library, and that it may be photocopied, subject to the discretion of the Librarian.

Signed: Ros Hopwood Date: 14.02.11

Part Three: British Library Authorisation [PhD candidates only]

If you want like a copy of your PhD thesis to be available on loan to the British Library Thesis Service as and when it is requested, please tick Section A of this form.

The University has agreed that your participation in the British Library Thesis Service should be voluntary. Please tick either (a) or (b) to indicate your intentions.

(a) ☑ I am willing for The Open University to loan the British Library a copy of my thesis.

(b) ☐ I do not wish The Open University to loan the British Library a copy of my thesis.

Signed: Ros Hopwood Date: 14.02.11

Abstract

This thesis addresses the use of strong gravitational lensing to facilitate deep mid-infrared observations of star-forming galaxies and to study highly dust obscured sub-millimetre galaxies (SMG). 15 μm extragalactic number counts were taken from ultra deep AKARI mapping of the gravitational lensing cluster Abell 2218, which is the deepest image taken by any facility at this wavelength. Via strong gravitational lensing these data probe beyond the AKARI blank field confusion limit. By de-magnifying the extracted source catalogue and performing careful photometric de-blending, using multi-wavelength positional priors, galaxy number counts down to $\sim$ 0.01 mJy were achieved. These counts are $\sim$3$\times$ deeper than previous results and resolve 70-100% of the cosmic infrared background at 15 μm, giving a new stronger lower limit of $2.0\pm0.3\,\mathrm{nW\,m^{-2}\,Hz^{-1}}$. These data are sampling the normal star forming population that dominates the peak epoch of star formation. Stacking analysis of the AKARI 15 μm source positions at *Herschel*/SPIRE wavelengths, show that a deep 15 μm galaxy population resolves around 40% of the 250 μm cosmic infrared background, but is less representative of galaxy populations sampled at longer wavelengths, where the background is dominated by sub-mm galaxies. This thesis also focuses on strong galaxy-galaxy lensing events and the decoupling of the lens and source photometry in order to estimate redshifts and constrain physical characteristics. The first sample of bright sub-mm gravitational lenses, selected at SPIRE 500 μm by the *Herschel* Astrophysical Terahertz Large Area Survey, are investigated with light profile and SED fitting, to derive physical characteristics. For two of the five lenses, it was possible to disentangle the lens and background galaxy components in highly photometrically blended *Spitzer* data, after observations by the Submillimeter Array revealed the lensed structure. The lensed background galaxies are highly dust obscured SMG with intrinsic infrared luminosities < ultra luminous infrared galaxies (ULIRGs), and constrain the number density of un-lensed ULIRGs and hyper luminous infrared galaxies to $< 3.2\,\mathrm{deg^{-2}}$.

Contents

Chapter 1

Introduction

1.1 The extragalactic background light

The Universe is filled with photons associated with extragalactic stellar nucleosynthesis and active galactic nuclei (AGN) accretion, which when integrated over the age of the Universe define the extragalactic background light (EBL). The EBL is therefore a fossil record of galaxies and of black hole accretion over cosmic time, and thus provides a useful diagnostic for models of galaxy formation and evolution. The EBL can be further divided by wavelength range into 'cosmic backgrounds', e.g. the cosmic microwave background (CMB) is the radiation remnant of the Big Bang and is described by a thermal blackbody spectrum with a temperature of 2.73 K. The CMB dominates the total energy of the EBL, but its distinct signal can be easily subtracted from the cosmic backgrounds at other wavebands. Plotting the energy of the EBL as a function of wavelength, i.e. the spectral energy distribution (SED; figure 1.1), highlights a significant feature – the cosmic optical background (COB; $\sim 0.01 - 5\,\mu$m) and the cosmic infrared background (CIRB[1]; $\sim 5 - 1000\,\mu$m) have roughly equal energy budgets. The discovery of the CMB [Penzias & Wilson, 1965] supported theories predicting the existence of the CIRB, a background light distinct from the CMB due to the markedly different physical processes responsible for producing the constituent photons, which would trace the cosmic star-formation history. A prediction by [Low & Tucker, 1968] that the CIRB would peak at far-infrared (FIR) wavelengths at around 1-10% of the intensity of the CMB, was proved to be correct by the first detection of the CIRB, by the Diffuse Infrared Background Experiment (DIRB) aboard the COsmic Back-

[1]Note that the near-infrared (NIR) is included within in the COB, as it represents unobscured emission from stars and galaxies

ground Explorer (COBE) [Fixsen et al., 1998; Hauser et al., 1998; Lagache et al., 1999; Puget et al., 1996]. The equality of the CIRB and COB energy peaks was one of several significant discoveries made at the advent of Infrared (IR) space missions that had profound consequences for the development of observational astronomy, historically dominated by the optical and radio wavelength regimes. The energy contribution to the COB is dominated by an unobscured stellar component from galaxies, with a minor contribution from optically bright AGN. These sources of radiation are also the underlying source of the CIRB, where the UV and optical radiation is absorbed and reprocessed by dust grains and re-radiated as lower energy photons. Dust is intimately linked with the mechanisms that drive the formation and evolution of galaxies, and characterises the IR SED with strong broad spectral features, such as polycyclic aromatic hydrocarbon (PAH) emission over $3 - 12\mu$m and silicate absorption 9.7μm and a cool grey body components at FIR/sub-millimetre (sub-mm). These features provide strong diagnostics for star-formation activity and the AGN fraction of dust obscured galaxies.

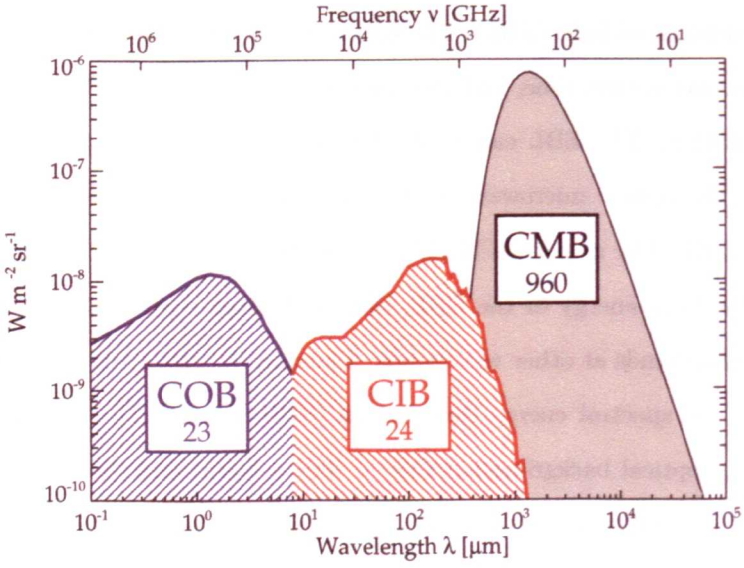

Figure 1.1: The relative total energies of cosmic backgrounds. The cosmic microwave background (CMB) dominates the background light and is a fossil remnant of the big bang. The cosmic optical background (COB) is due to unobscured emission of galaxies and AGN, and the cosmic infrared background (CIB; CIRB in the main text) is due to dust obscured galaxies and AGN. The numbers given on the plot correspond to the brightness of each background. (Figure credit: H. Dole et al./IAS).

The equivalent total energies measured for the COB and CIRB, indicate that for every

two UV/optical photons in the Universe one was absorbed and reradiated by dust. Thus optical surveys miss a large fraction of dust obscured star-formation. If the UV and optically dominated galactic emission locally ($z \lesssim 0.2$) were consistent throughout the Universe then observing at these wavebands alone would reveal the co-moving star-formation rate as a function of redshift, however there is a rapid increase observed in the infrared volume emissivity up to redshifts $z \sim 1$ [Rodighiero et al., 2010]. This is reflected in the star-formation rates estimated from purely UV and optical observations, e.g. the original Madau diagram [a plot of the cosmic star-formation history expressed as the star-formation rate per co-moving volume as a function of redshift; Madau et al., 1996], which incorporated no correction for optical extinction by dust of star forming galaxies and, therefore, significantly underestimated the star-formation rates at higher redshifts $z \gtrsim 1.5$. The energy contained in the CIRB implies that the integrated star-formation rate at redshifts $z \sim 1.5$ must be a factor of 2 or more higher than these UV/optically based estimates [e.g. Franceschini et al., 2001]. UV/optical surveys alone do not provide a fully representative galaxy sample at higher redshifts, and therefore the study of distant evolution should be investigated at longer wavelengths. However observing longwards of the NIR presents certain challenges over the optical regime – not all of which can be conquered with improved technology. Atmospheric extinction is significant at mid-infrared (MIR) to sub-mm wavebands (see figure 1.2), with minimal to no atmospheric window between 15μm and 400μm, therefore infrared space missions are essential. Now with the advent of the *Herschel* Space Observatory the full infrared spectrum has seen dedicated space experiments. Degradation of angular resolution and increasing 'confusion noise' seen with increasing wavelength are more difficult to overcome. Gravitational lensing offers a way to study galaxies beyond these intrinsic limits.

1.2 Observational noise

Noise associated with astronomical observations can be assigned to two main classes: systematic and random. Sources of systematic noise come from the intrinsic properties of a detector (instrumental noise), the statistical fluctuations of random photon counts (Poisson noise or background noise) and cosmic ray events. Instrumental noise includes dark current and readout noise. Dark current originates from thermally excited electrons within the detector, which cannot be distinguished from electrons liberated by a photon event. Dark current is subtracted as dark frames,

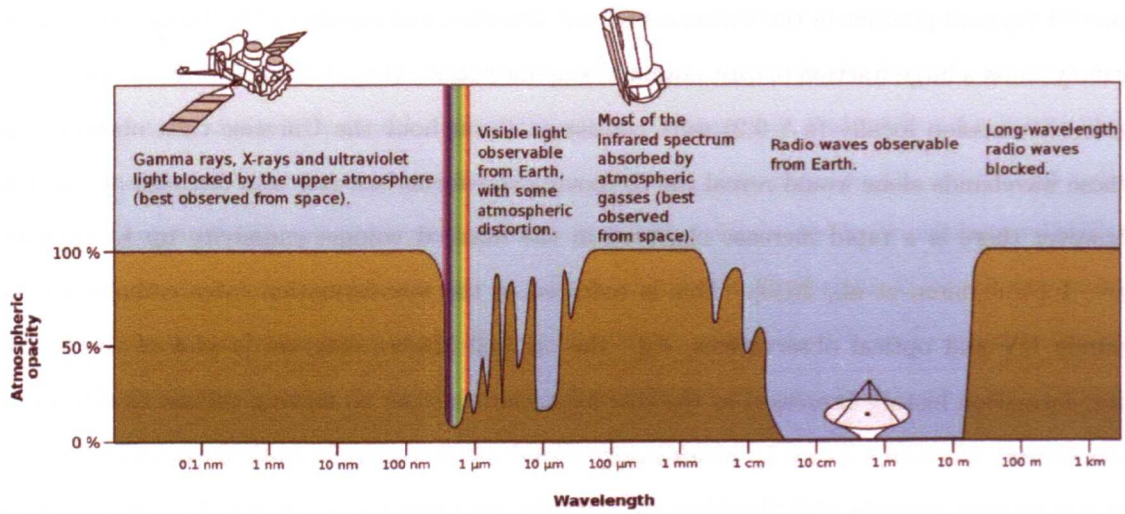

Figure 1.2: The atmospheric absorption at the MIR to sub-mm wavelengths is almost comprehensive, thus infrared facilities are at high altitude. Observing from space is the ideal situation to avoid this issue. Picture credit: NASA

which are exposures taken with no illumination. Readout noise (as the name suggests) originates from the analogue to digital conversion during the read out of the electrons generated during an exposure. Readout noise is not dependent on exposure time, and the resulting systematic offset can be subtracted using a 'bias frame', taken with a zero exposure time. There is also variation seen between the sensitivity of the pixels, which is multiplicative noise, that can be corrected on dividing the data by a flat field, obtained by exposure to a uniform light source to gauge the true pixel response. The flat field also corrects for contaminants on the lens and vignetting. Instrumental noise is dealt with during the pipeline stage of data reduction where the additive noise is corrected before the multiplicative, so the flat fielding should be performed as the final instrumental noise correction step. Due to the random nature of electron based noise each correction frame should ideally be the combination of several separate exposures. The signal-to-noise of aperture photometry of an object observed with a CCD can be calculated using the 'CCD equation' [Howell, 1989], which is commonly written as

$$\frac{S}{N} = \frac{N_*}{\sqrt{N_* + n_{pix}(N_{sky} + N_{dc} + N_{rn}^2)}} \tag{1.1}$$

where N_* are the total number of sky subtracted photons within the aperture, n_{pix} is the number of pixels within the aperture and N_{sky}, N_{dc} and N_{rn} are the total number of sky photons, dark current photons and read noise photons (all per pixel in units of e^-), respectively. Note that the term for readnoise is squared as it does not obey Poisson statistics. The CCD equation can be written in its extended form [Merline & Howell, 1995] as

$$\frac{S}{N} = \frac{N_*}{\sqrt{N_* + n_{pix}\left(1 + \frac{n_{pix}}{n_B}\right)(N_{sky} + N_{dc} + N_{rn}^2 + G^2\sigma_f^2)}} \tag{1.2}$$

where the additional terms account for the noise from the analogue to digital conversion of the data, σ_f is the 1σ fractional pixel counts loss due to digitisation (ADU) and G is the gain.

Noise due to real signal, known as confusion noise, tends to be the limiting noise source for MIR, FIR and sub-mm data. There are two reasons why this is the case. Firstly, the angular resolution of an image is proportional to the wavelength of the observations and inversely proportional to the diameter of the telescope mirror, therefore observations at infrared wavelengths require unfeasibly large mirror diameters to achieve the equivalent resolution that can be achieved at optical or NIR. For example, in order for the infrared space telescope *AKARI* [Murakami et al., 2007] to achieve the resolution the *Hubble* Space Telescope (*HST*) Advanced Camera for Surveys (ACS) F450W data (taken using the *HST* 2.5m mirror) at 15μm, it would require a mirror size of approximately 44 meters in diameter. Secondly, there is a limit to the depth of any astronomical observation that is set by the confusion noise, beyond which individual objects cannot be separated [Condon, 1974]. Images may become confusion limited when unresolved faint sources dominate the RMS fluctuations of the image within the resolution beam (over the noise in the image). The confusion noise σ_c due to point sources below a flux density limit $S_{\rm lim}$ can be expressed in terms of the sky variance as

$$\sigma(S)^2 = \int_0^{S_{\rm limx}} S^2 \Omega (dN/dS)\, dS \tag{1.3}$$

where dN/dS are the differential source counts of the underlying galaxy population and Ω is the resolution beam area [e.g. Negrello et al., 2004].

The combination of these two issues results in data with a limiting background noise of numerous faint objects that are beyond the resolving power of the detector and a high fraction of photometrically blended objects that lie above the background confusion. A consequence of this noise source is that once data approaches the confusion limit, the sensitivity will not see the $\sqrt{N}$ improvement expected for N additional pointings. Confusion noise also leads to greater photometric and positional errors [e.g. Coppin et al., 2006; Hogg, 2001] for an extracted source catalogue. Gravitational lensing is the only way to observe individual galaxies beyond the confusion noise.

1.3 Observing the dusty Universe

1.3.1 Infrared galaxy populations

Although the CIRB was predicted, massive galaxies emitting most of their energy at infrared wavelengths, with infrared luminosities (L_{IR}) $\geq 10^{12}\,L\odot$ were not, and at the time, the origin of this extreme luminosity was unknown [Houck et al., 1985]. The discovery of these infrared-luminous galaxies, in the mid 1980s, was among the notable achievements of the first infrared space mission, the Infrared Astronomy Satellite (IRAS), and led to the classification of luminous infrared galaxies (LIRG;$10^{11} \leq L_{IR}/L_{\odot} < 10^{12}$), ultra luminous infrared galaxies (ULIRG; $10^{12} \leq L_{IR}/L_{\odot} < 10^{13}$) and hyper luminous galaxies (HLIRG; $L_{IR} \geq 10^{13}\,L_{\odot}$). IRAS was unable to probe much beyond the low redshift regime $z < 0.2$, with the exception of a few examples of ULIRGs and HLIRGs [e.g. Rowan-Robinson et al., 1991]. The Infrared Space Observatory (ISO) was launched in the mid-90s and had the capability to observe in the MIR to FIR to higher redshifts, extending out to around a blank field redshifts of $z\sim1$, followed by the *Spitzer* space telescope in 2003 and *AKARI* in 2006 (see section 1.3.2 and chapter 2 for a more detailed description of the *AKARI* mission), both of which extended this redshift range further. ISO, *Spitzer* and *AKARI* identified significant numbers of LIRG and ULIRG showing that although these galaxies are rare locally, the number density of LIRG increases steeply with redshift as $(1+z)^4$ out to redshifts of $z\sim1$, beyond which the numbers of ULIRG also increase [Lonsdale et al., 2006]. With the commissioning of SCUBA in 1997, observing at 450 μm and 850 μm, the sub-mm was probed for the first time. SCUBA observations revealed high redshift ($z > 2$), highly dust obscured galaxies with high infrared luminosities ($>$ LIRG) and bright 850 μm

flux densities at the mJy level, which could not be accounted for by galaxy evolution models of the time. These galaxies are usually referred to as SMG. Observations at sub-mm wavelengths benefit from a negative K-correction, allowing SMG to be sampled over a wide redshift range $1 < z < 10$. Follow-up observations of SMG are hampered by the large beam size of sub-mm instruments, which results in poor positional accuracy. Also, as other wavelengths do not benefit from a negative K-correction, identifying the correct counterpart to a SMG is challenging (although radio data is able to provide a more precise position). The recently launched *Herschel* Space Observatory addresses some of these issues at sub-mm wavelengths, however gravitational lensing effects are still necessary to study SMG over a wide range of redshift and luminosity.

1.3.2 The infrared space telescope: AKARI

The Japanese infrared space telescope *AKARI* was developed by the Institute of Space and Astronautical Science (ISAS), which is part of the Japan Aerospace Exploration Agency (JAXA). Launched in 2006, *AKARI* observed in the mid and near-infrared, until the beginning of 2010. *AKARI* data offers greater sensitivity than ISO and coverage at 15 μm, filling a gap in the *Spitzer* filter coverage. Observing at 15 μm allows the sampling of redshifted PAH emissions of star-forming galaxies, around redshifts of 0.5 - 1.5 and therefore offers a means to study the Universe at the peak epoch of star-formation.

1.3.3 The *Herschel* Space Observatory

The deeply ambitious plan to launch a far infrared and sub-mm space mission with a 3.5 m telescope – the largest telescope of any space mission (figure 1.3) – began almost three decades ago in 1982, when the Far Infrared and sub-millimetre space telescope FIRST was proposed. FIRST was accepted as one of the European Space agency (ESA) cornerstone projects in 1997 and renamed the *Herschel* Space Observatory [*Herschel* Pilbratt et al., 2010] in 2000. The name *Herschel* was chosen to pay respect to the founder of infrared Astronomy, William Herschel, who was first to identify the infrared spectrum. *Herschel* was conceived to provide unprecedented sub-mm imaging and spectroscopy, without the limitations of atmospheric absorption (see figure 1.2), which were still pertinent goals when *Herschel* launched in May 2009. Sub-mm observations offer a unique view of the hidden Universe, as these wavelengths are sensitive to the most

dust obscured processes and high redshift objects such as massive highly optically extinct star burst galaxies [i.e. SMG; Smail et al., 1997] and Compton thick AGN [e.g. Georgantopoulos et al., 2009].

Before *Herschel*, sub-mm observations were tempered by high levels of confusion noise, small fields of view and slow scan times (leading to long integration times and, therefore, limited area surveys), plus technical difficulties due to the inherent challenge presented when observing at these wavelengths [e.g. Kovács et al., 2006; Mortier et al., 2005; Weiß et al., 2009]. The sub-mm has, therefore, yet to be explored to the same extent as NIR and MIR, although there have been recent advances made by the Balloon-borne Large Aperture Submillimeter Telescope [BLAST; Marsden et al., 2009] and the South Pole Telescope [SPT; Vieira et al., 2010], and in the near future with the Submillimetre Common-User Bolometer Array 2 [SCUBA2 Holland et al., 2003].

Herschel successfully arrived at the second Lagrangian point (L2) to begin observations at FIR and sub-mm wavelengths, 930,000 miles from the Earth. At this position in space there is a relatively constant *Herschel* to Earth to Sun alignment, which helps to minimise the effects of unwanted radiation from the Earth, Moon and Sun (see figure 1.4). *Herschel*'s 3.5m telescope, which is the largest for a space mission to date, allows unprecedented angular resolution for the associated wavelength range. To achieve the predicted sensitivities the mirror needs to be passively cool to $\sim$ 85K, while the focal plane instruments are housed in a liquid helium cooled cryostat, and operate at a few Kelvin. *Herschel* houses two focal plane imaging photometers, which cover the FIR to sub-mm wavebands. The Photodetector Array Camera & Spectrometer [PACS Poglitsch et al., 2010] is the shorter wavelength instrument, covering the FIR over 55-210 μm, with three channels - 'Blue' at 70μm, 'Green' at 100μm and 'Red' at 160μm. The bolometer array of the Red channel has two subarrays of 16 x 16 pixels, whereas for the Blue and Green there are 4 by 2, 16 x 16 subarrays (see Appendix B for an in-depth review of de-glitching the OU PACS data reduction in IDL and the conversion to Jython and implementation within HIPE). Observing at longer wavelengths is *Herschel*'s Spectral and Photometric Imaging REceiver [SPIRE Griffin et al., 2010], which covers three sub-mm wavebands; 250μm, 350μm and 500μm. *Herschel* offers the chance to observe the optically obscured Universe in new detail, and to examine the cool emissions from massive star-forming galaxies and AGN over a wide range of

redshifts. Figure 1.5 shows the PACS and SPIRE filter response curves plotted in comparison to an Arp220 SED (taken from the SWIRE template library [Polletta et al., 2007]), which has been shifted to several different redshifts, in order to highlight that PACS and SPIRE are sampling around the peak emission from dust. The available wavelength range and lower confusion levels (relative to previous FIR/sub-mm missions), coupled with the fast scan capabilities of *Herschel*, will provide information towards answering outstanding questions in terms of galaxy evolution, star-formation, AGN accretion, feedback, among other areas where dust obscuration has limited progress. Initial results from the Science Demonstration Phase (SDP; see A&A special issue: '*Herschel*: the first science highlights', July-August 2010, Vol. 518) illustrate the huge potential for the *Herschel* mission, and already provide new insight into the starforming regions in our own galaxy [Hi-GAL Zavagno et al., 2010], the abundance of SMG [H-ATLAS Clements et al., 2010] and extreme Quasar evolution [H-ATLAS Serjeant et al., 2010a].

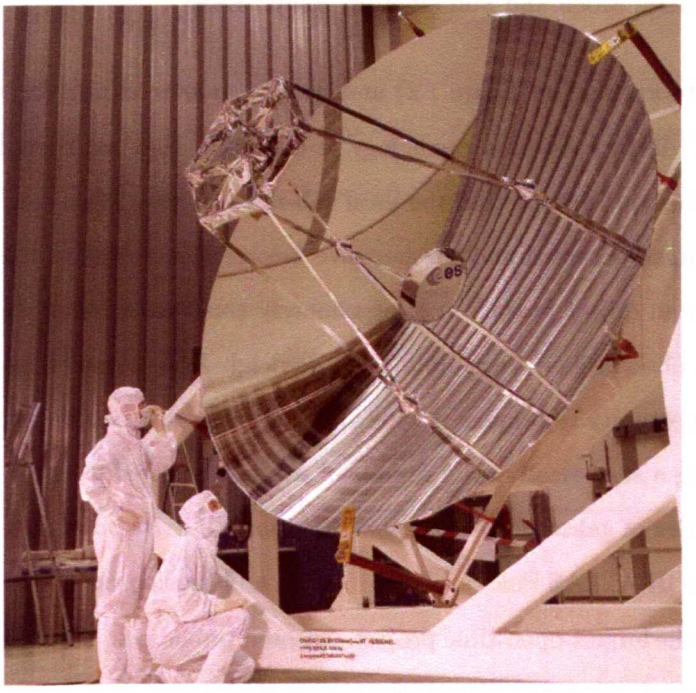

Figure 1.3: The *Herschel* Space Observatories 3.5m mirror (Picture credit: ESA).

1.3.4 H-ATLAS

Herschel is now exploring one of the remaining wavelength frontiers of observational extra-galactic astronomy. Previous sub-mm surveys have been restricted in both area and resolution,

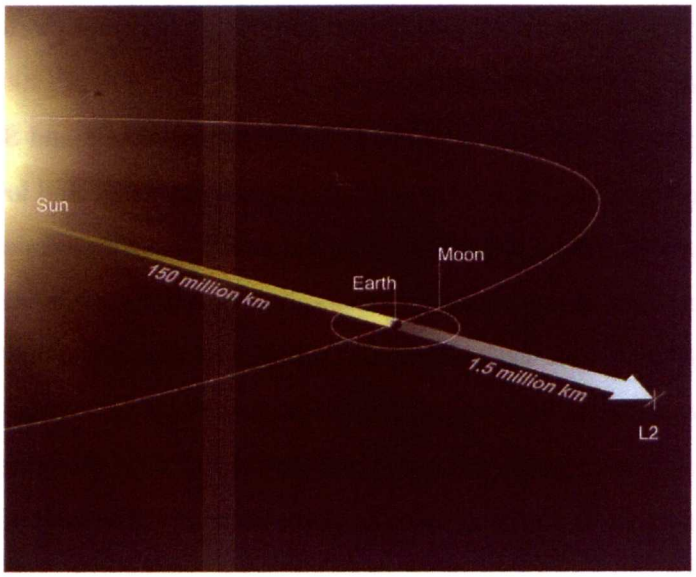

Figure 1.4: Diagram showing the L2 Lagrangian point, where *Herschel* resides and the relative positions of the Earth, Moon and Sun (Picture credit: ESA).

by atmospheric absorption (see figure 1.2) and, rather counter-intuitively, to the high redshift regime ($z \gtrsim 2.0$). In fact sub-mm cosmology is unique in that we know far more about the higher redshift sub-mm Universe that the local sub-mm universe. This can be explained due to the limit local volume observed and the negative k-correction acting in this wavelength range, which can lead to an object having an approximately constant sub-mm flux density with redshifts, as sub-mm observations are sampling the Rayleigh-Jeans slope of the SED. *Herschel* has given the first opportunity to propose a wide area survey at sub-mm wavebands. An important step toward having a statistically valid sample of sub-mm selected galaxies, which is crucial for constraining theories of galaxy formation and evolution. The *Herschel* Astrophysical Terahertz Large Area Survey [H-ATLAS Eales et al., 2010] is an ambitious proposal involving 18 institutes, which resulted in the largest open-time project accepted pre-launch, with the award of 600 hours and an overall goal of surveying $\sim$550 deg^2. The main motivations for the proposal were a lack of knowledge on the nearby Universe at sub-mm and the need for greater samples of sub-mm selected galaxies over a wide redshift range and to survey large numbers of galaxies ($>$ 100,000), with huge legacy potential. The key H-ATLAS science goals cover six main areas: 1. The local Universe, 2. Lensed galaxies, 3. AGN, 4. Large-scale structure, 5. Galactic dust, 6. Planck collaboration.

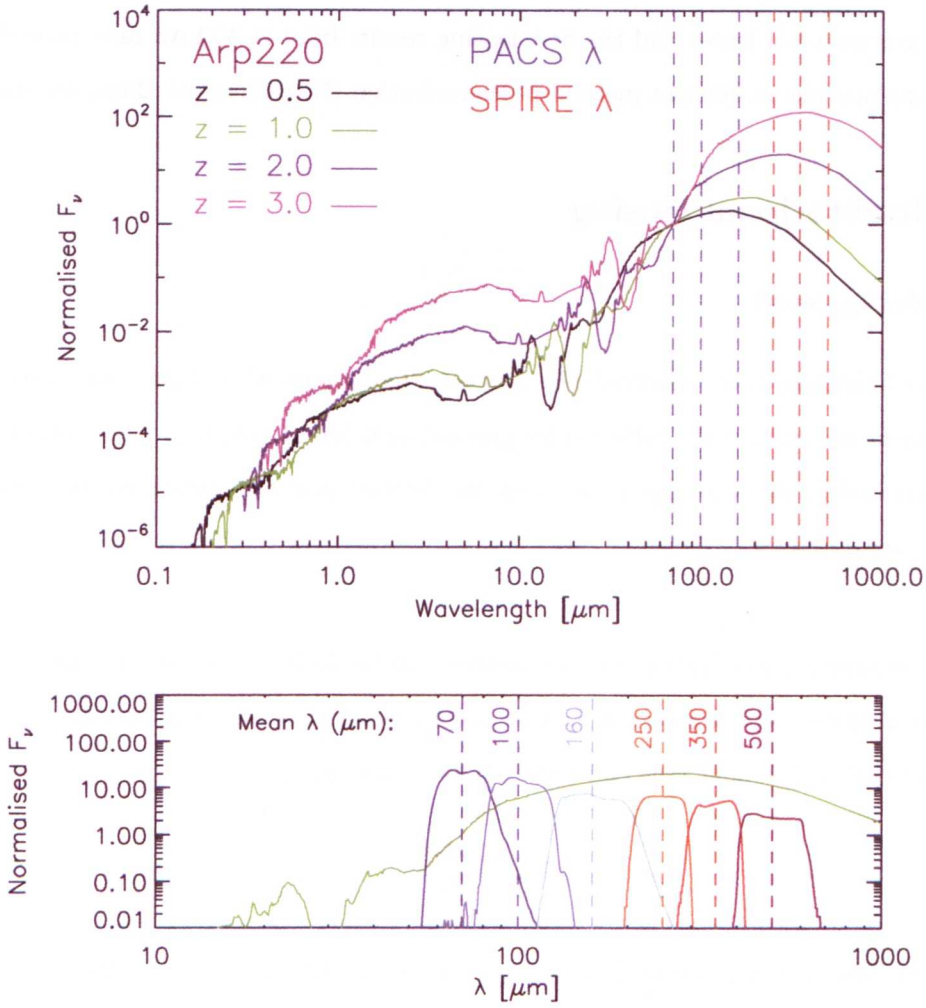

Figure 1.5: Top: Arp220 SED [SWIRE SED template library Polletta et al., 2007] shifted to several different. The dashed lines show the mean wavelength of the PACS and SPIRE instruments, showing how these wavebands sample around the peak of the SEDs. The bottom panel shows the section of the Arp220 peak at a redshift of 2, overlaid with the filter response curves for PACS and SPIRE, normalised to an area of 1 and scaled for comparison.

An important aspect of H-ATLAS is the choice of fields to observe. All fields were chosen due to already existing, or soon to be taken, comprehensive coverage at several other wavebands, therefore allowing stronger constraints on SED fitting. H-ATLAS will observe the 9h, 12h and 14h GAMA fields near to the North galactic pole and the 2h and 23h GAMA fields in the South galactic pole region. One motivation for such a significantly wide area sub-mm survey is to detect gravitational lenses and the first lensing results from H-ATLAS have proved sub-mm observations provide an efficient method of lens selection (Negrello et al. 2010; see chapter 6).

1.4 Gravitational lensing

1.4.1 Background

Gravitational lensing is an observed phenomenon that occurs when light rays emitted from a distant object are sufficiently deflected by gravitational forces, due to a large concentration of mass positioned in the line-of-sight between an observer and the source, to form distorted or multiple virtual images.

The fundamental gravitational lens equation can be derived from the geometry of a basic gravitational lens set up, as shown in figure 1.6, for a point source S being lensed by a spherically symmetric lens L. The light rays emitted by S are deflected by the angle $\tilde{\alpha}$, given by

$$\tilde{\alpha} = \frac{4GM(\xi)}{c^2\xi} \tag{1.4}$$

where G is Newton's gravitational constant, ξ is the distance from the centre of the lens and $M(\xi)$ is the mass of the lens within ξ, to form two virtual images of S (S_1 and S_2), which are observed by O. Without the deflection of the light ray from S towards O, by $\tilde{\alpha}$, the source would go unseen. The angular diameter distances D_L, D_S and D_{LS} are indicated on figure 1.6, noting that $D_S \neq D_{LS} + D_L$. Two assumptions are necessary in order to derive the lens equation, firstly that the distances are sufficiently larger than the thickness of the lens, so any deflection of the light rays can be assumed to be instantaneous (the thin lens approximation) and secondly that the angles involved are small, such that $\theta \approx \tan\theta$ (the small angle approximation), both of

which are reasonable on astronomical scales. From figure 1.6 we can write

$$\theta \mathrm{D_S} = \beta \mathrm{D_S} + \tilde{\alpha} \mathrm{D_{LS}} \tag{1.5}$$

giving

$$\beta = \theta - \tilde{\alpha} \frac{\mathrm{D_{LS}}}{D_S} \tag{1.6}$$

as α can be written as

$$\alpha = \left(\frac{\mathrm{D_{LS}}}{\mathrm{D_S}} \right) \tilde{\alpha} \tag{1.7}$$

therefore

$$\beta = \theta - \alpha(\theta) \tag{1.8}$$

for non-symmetrical lenses this can be written as

$$\boldsymbol{\beta} = \boldsymbol{\theta} - \boldsymbol{\alpha}(\theta) \tag{1.9}$$

Equation 1.9 describes the mapping of the lensed surface brightness distribution of the image plane back onto the source plane. There may not be a unique solution for the deflection θ, which reflects that possible multiple images that can be formed. The key feature of a gravitationally lensed image, making it a unique cosmological tool, is the associated magnification. A gravitational lensed image manifests a stretching of the observed source area and, as the surface brightness is conserved, an amplification of the source flux.

Since the first confirmation of a gravitational lensing event [QSO 0957 + 561 Walsh et al., 1979], there has been rapid development in exploiting gravitational lensing as an observational tool, for a range of astrophysical applications either focusing on single objects, e.g. faint or distant galaxies and exoplanets, to reconstruct the mass of the lens for both galaxy clusters or single galaxy lenses and also to study the large scale structure of the Universe. Gravitational lensing can be divided into the categories of strong, weak and micro-.

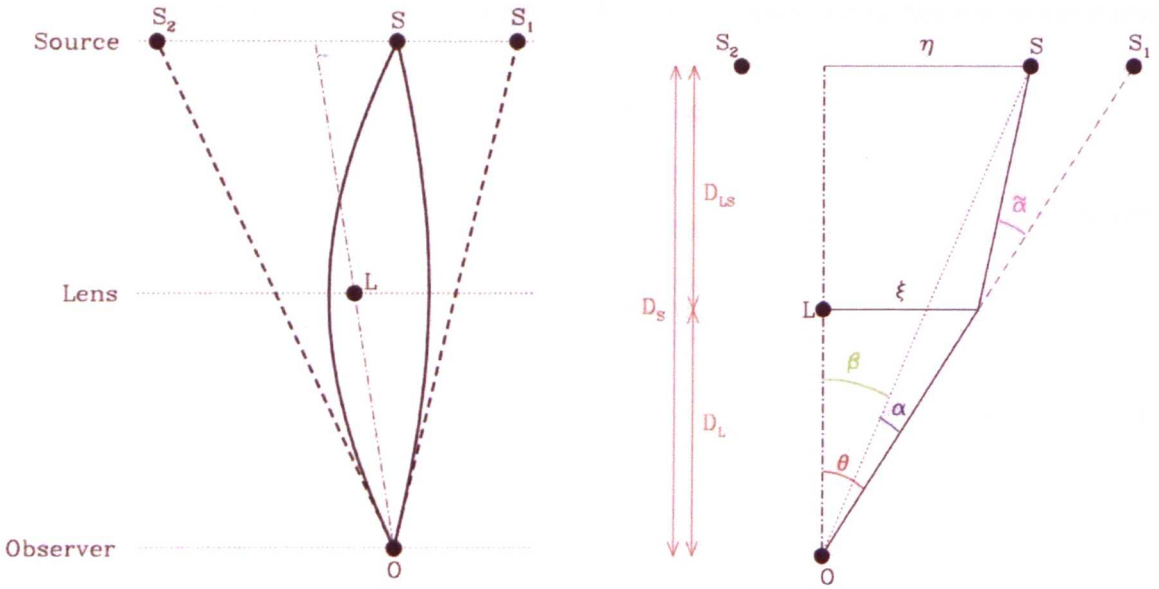

Figure 1.6: Basic gravitational lens set up (left) and the corresponding geometry (right). A source S (in the source plane) is lensed by L (in the image plane) and two virtual images are formed S_1 and S_2 and observed by an observer O. Invoking the 'thin lens approximation' allows the light rays to be approximated by their asymptotes. The lens equation 1.9 relates the angular position of the source β and the image θ. (Figure credit: Wambsganss [1998])

In the weak lensing regime background objects are still magnified and distorted (the stretching tangental to the lens is known as the shear), but these lensing effects are too small to be measured on an individual basis over the intrinsic ellipticity of the lens. Collectively, however, the underlying ellipticity of galaxies has zero mean and the distortion due to weak lensing is coherent (as lensing effects tend to vary slowly with positions). The overall pattern of distortion due to lensing can be mapped to give a shear field [Bridle, 2008; Mellier, 1999], and such fields have produced strong statistical results about the distribution of dark matter [Wittman et al., 2000].

The term microlensing refers to lensing events that form multiple images that have separations on a milli-arcsecond scale, therefore making them unresolvable with current technology. Microlensing can be a far more transient lensing event than strong lensing, occurring when a compact foreground object (e.g. a star or brown dwarf) transits the face of a more distant star, creating a temporary good line-of-sight for an observer and acting as a gravitational lens. The

brightness of the distant star is amplified giving a characteristic single event on the stars light curve (luminosity as a function of time), which distinguishes it from a variable star. Microlensing events have been used to detect Milky Way massive compact halo objects (MACHOS). Such searches have ruled out a MACHO dominated dark matter halo [e.g. Alcock et al., 2000]. Microlensing allows the search for exoplanets orbiting stars that lie beyond the range of transit photometry searches (where the planet dims the light curve of its star). If a microlensing event occurs between two stars and a planet is orbiting the foreground star, a second lensing event can occur and add an additional peak to the single light curve event. Currently there are ten exoplanets that have been detected due to a microlensing event[1].

1.4.2 Strong lensing

The most dramatic manifestation of gravitational lensing is produced by strong lensing, for deflection angles on the arcsecond scale for galaxy-galaxy lensing events to $>10''$ for lensing events due to massive clusters of galaxies. Multiple images of the background source can be formed or, for a perfect alignment of source, observer and spherically symmetrical lens, an Einstein ring. The flux amplification and area distortion observed for the background galaxy in galaxy-galaxy lensing events and for galaxies behind massive galaxy clusters, allow the observation of intrinsically faint galaxies, which would otherwise be beyond blank field sensitivities [Borys et al., 2004; Ellis et al., 2001; Ivison et al., 2010; Knudsen et al., 2010; Smail et al., 1997; Stark et al., 2007]. Such observations also provide a means to study sub-structure of galaxies at a level beyond current telescope technology [Lacy et al., 1998; Marshall et al., 2007; Nesvadba et al., 2006; Richard et al., 2010]. Importantly, gravitational lensing effects allow the constraint of the total mass of lensing systems, without regard for its dark or luminous nature [Treu, 2010]. By combining information on the distribution of visible matter, obtained through optical and near-IR imaging with the observed lensing effects, it is possible to disentangle the relative contribution of dark and luminous matter in galaxies, which is a goal difficult to achieve via other means [Gavazzi et al., 2007].

Gravitational lensing is not dependent on wavelength, but only on the mass distribution of

[1] An up to date list of planets detected via microlensing can be found at:
http://exoplanet.eu/catalog-microlensing.php

the lens and angle of approach of the light rays. However, the observed lensed images are dependent on resolution, which in turn depends on the wavelength, aperture size and (for ground based instruments) atmospheric seeing. In order to map precisely the mass of the lens, high resolution imaging (e.g. with the *HST*/ACS or *HST*/WFC3) is necessary so the structure of the lensed background galaxy image is resolved and distinct from the luminous components of the lens. This presents a challenge for heavily dust obscured lensed galaxies that are faint at optical wavelengths and unresolved at infrared or sub-mm wavelengths, due to relatively poor resolution. An example of the effect of resolution on the study of lensing events can be made between observations of the lensing cluster Abell 370 (A370). Images taken in 1985, with the 3.6m CFHT of A370 revealed 'a strange ring-like condensation' [Soucail et al., 1987], which was confirmed as the first identification of a giant lensed arc, after the re-examining of data taken in 1983 in which the arc had previously gone unnoticed. More recently A370 was re-imaged by the *HST*/ACS Wide Format Camera (WFC), producing an image that demonstrated the arc as an extraordinary lensing event, where the sub-structure of the background galaxy is visible within a distorted arc-like smear that extends around one side of the cluster core [Richard et al., 2010]. This example highlights the importance that high resolution instruments, such as the WFC, have had in the development of gravitational lensing research. The Sloan Lens ACS Survey [SLACS; Bolton et al., 2006] identify lens candidates from SDSS spectroscopic data, but only higher resolution imaging (*HST*/ACS) can reveal their true lensing nature.

Galaxy-galaxy gravitational lensing systems are strong lensing events generally observed with a central lens profile and surrounding arcs or point-like sources corresponding to the lensed background galaxy, although the precise form of the observed image is dependent on the spatial resolution of the observations. For galaxy-galaxy lensing events the lens and the image of the background galaxy can quickly become photometrically confused for poor resolution data. When strong lensing events, such as giant luminous arcs (due to galaxy lensing clusters) or Einstein rings (due to massive early type field galaxies) are observed at high resolution, e.g. *HST*/ACS or *HST*/WFC data, their geometry can be used to constrain the mass distribution of the lensing galaxy. Notable achievements by gravitational lensing research include the mapping of large scale structure of the Universe [e.g. Bacon et al., 2000], the constraint of cosmological parameters [e.g. Chae & Mao, 2003], including the Hubble constant [Koopmans & the CLASS

collaboration, 2001; Paraficz & Hjorth, 2010] and dark energy equation of state [D'Aloisio & Natarajan, 2010], and the estimate of redshifts via lensing mass model inversion [Kneib et al., 1996].

The numbers of known strong galaxy-galaxy lensing events are set to increase dramatically over the next few years with the advent of a sub-mm selection method, pioneered by H-ATLAS (Eales et al. 2010, Negrello et al 2010) and discussed in chapters 5 and 6 of this thesis. One of the main aims of building a statically large sample of these lenses is to study the properties of sub-mm galaxies and dark matter distributions with the aid of lensing.

1.5 Lensing effects on galaxy number counts

Galaxy number counts are a common method for extracting statistical information and evolutionary trends from galaxy source catalogues. These counts are expressed as the surface density of galaxies as a function of flux density. One necessity for galaxy evolution models is to recreate observed number counts taken for a range of different wavelengths, so extending the range of observed counts improves the constraints of such models. Wide and shallow surveys are more suited to probe the bright end of the counts [e.g. Rush et al., 1993, at 15 μm], and deep pencil beam surveys can constrain the faint end [e.g Hopwood et al., 2010; Metcalfe et al., 2003, at 15 μm]. The depth achieved by these latter counts (down to $\sim$0.03 mJy by *ISO* and $\sim$0.01 mJy by *AKARI*, respectively), were achieved by observing a lensed field through the gravitational lensing cluster Abell 2218. Massive galaxy clusters are the largest virialized structures known to exist in the Universe and the associated concentration of mass can offer high magnification factors toward the core, by up to factors of 30 or more, for images of background galaxies formed near to the critical lines[1] [e.g. Richard et al., 2010]. Galaxy clusters have been targeted by several sub-mm based surveys in order to beat the high confusion levels [e.g. Knudsen et al., 2008; Smail et al., 1997] including the ongoing *Herschel* Lensing Survey [HLS Egami et al., 2010], which is targeting up to 50 lensing clusters in order to find highly magnified SMG that are bright enough to be within *Herschel*'s spectroscopic capabilities. An alternative method to extend faint number counts below the detection limit is to use the probability of deflection (P(D))

[1] The critical lines are the contour of highest magnification in the source plane (theoretically the line of infinite magnification).

analysis (i.e. fluctuation analysis) [e.g. Glenn et al., 2010; Maloney et al., 2005; Patanchon et al., 2009], which does not rely on the extraction of individual sources but on the pixel density distribution, which includes the signal from both resolved and unresolved sources are considered.

Magnification effects on number counts extracted from a lensed field must be corrected to give the intrinsic counts. Lensing results in both an area distortion and, due to the preservation of surface brightness, an amplification of the source flux. The former effect leads to depletion of the counts as the true area is less than the area observed, a phenomenon known as the 'Broadhurst effect' [Broadhurst, 1995; Broadhurst et al., 1995]. Whether the counts benefit from an overall boost from the flux amplification or a depletion from the Broadhurst effect depends on the local magnification μ (which also depends on the redshift of the background source) and the slope of the unlensed counts. Assuming the differential counts are described by a power law $N_0(S) \propto S^{\alpha}$, then the magnification bias of the lensed $N'(S)$ to unlensed counts is given as (assuming a constant, i.e. flux independent, magnification factor μ)

$$\frac{N'}{N_0}(S) = \mu^{\kappa} \tag{1.10}$$

where $\kappa = -(1 + \alpha)$. This expression only considers flux amplification by lensing, which is appropriate for galaxy-galaxy lensing events. For sources lensed by a galaxy cluster the area distortion must also be factored as $\kappa = -(1 + \alpha)$ [e.g. Blain, 2002]. MIR to sub-mm counts are observed to have steep slopes, which give an overall positive magnification bias, i.e the gain from flux amplification dominates over the loss due to the Broadhurst effect. Lensed number counts, as a function of radius from the cluster core, can be corrected for magnification by comparing to the counts of an unlensed field, but for MIR counts where the statistics are generally low for the full field, and far lower as a function of radius, it is more ideal to derive magnification corrections using a mass model of the cluster (see chapter 3 section 3.12.3).

In chapters 2 and 3, the reduction, co-adding and analysis of the deepest image of the Universe at 15μm, which was taken by *AKARI* in a lensing field, is presented. A stacking analysis using the resulting 15μm extracted catalogue and *Herschel*/SPIRE data is described in chapter 4. The light profile fitting to and the characterisation of strong galaxy-galaxy gravitational

lenses are presented in chapters 5 and 6 and the conclusions and future work are discussed in chapter 7.

Chapter 2

Ultra-deep *AKARI* 15 μm observations of Abell 2218

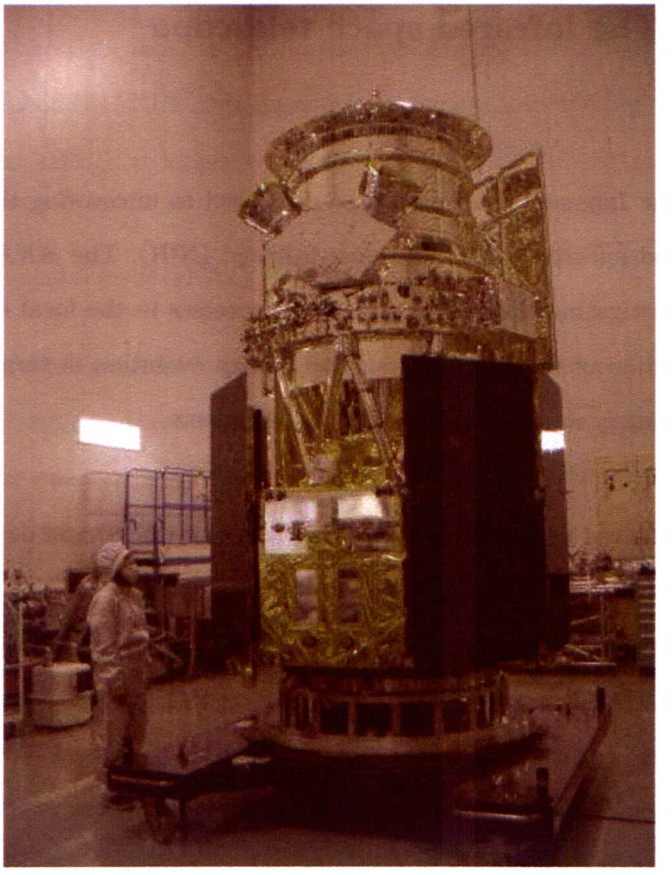

Figure 2.1: Final preparations of ASTRO-F before launch. (Figure credit: C. Pearson).

2.1 Abstract

This chapter details data reduction performed on deep *AKARI* 15 μm observations of the gravitational lensing cluster Abell 2218. Both the official pipeline for AKARI infrared camera data and bespoke post-pipeline data reduction are discussed. The main issues that required attention after running the official pipeline were offsets and rotations between the frames, scattered light remnants, field distortion, and bad pixels. In order to ensure robust source extraction and photometry could subsequently be achieved, careful attention was paid to preserve source flux during the further reduction.

This chapter contains work relating to the publication Hopwood et al. 2010, ApJ, 716, L45 and Ko, Hopwood et al. 2010, ApJ, 695, L198.

2.2 *AKARI*: The infrared space telescope

2.2.1 *AKARI*

AKARI was the first Japanese space telescope dedicated to uncovering the dusty Universe by observing in the mid-infrared (MIR) and near-infrared (NIR). The *AKARI* mission goals focus strongly on investigating the dust enshrouded processes in the local and distant Universe, including the formation of the first galaxies and galaxy evolution in terms of the cosmic star formation history, galaxy mergers and feedback mechanisms.

AKARI was conceived as the infrared imaging surveyor (IRIS) and developed as ASTRO-F (figure 2.1) by the Institute of Space and Astronautical Science (ISAS), which is part of the Japan Aerospace Exploration Agency (JAXA). ASTRO-F launched from the Uchinoura Space Centre (USC) on the 21^{st} February 2006 (UT) becoming *AKARI* (the Japanese word for 'light') upon successfully reaching a safe Sun-synchronous polar orbit, around 700 km above the Earth. *AKARI* approximately follows the Earth's night-day line and so can maintain a 90° orientation away from the Sun (figure 2.2).

AKARI houses a 0.685 m mirror and two focal plane instruments, which were cooled in a liquid helium cryostat during the first two stages of operations. Cooling to only a few Kelvin is necessary when observing longward of 8 μm, due to the increase in sensitivity to thermal emission. *AKARI*'s three phase operation plan ran to schedule, with the Helium cooled Phase I and II lasting for the predicted 550 days. After the coolant was depleted, Phase III warm NIR observations continued until the beginning of 2010. During the cooled phase of operations, *AKARI* surveyed ~94% of the whole sky in scan mode with the Infrared camera (IRC) all-sky survey (at 9 and 18 μm) and the Far Infrared surveyor (FIS) all-sky survey (at 65, 90, 140 and 160 μm). This significant investment of *AKARI* observation time produced two major public data releases in May 2010, of the FIS bright source catalogue [Yamamura et al., 2010] and the MIR IRC point source catalogue [Ishihara et al., 2010]. These catalogues improve on the all-sky survey of IRAS with greater sensitivity and number of sources, thus providing a strong tool for statistically unbiased analysis. Over 5000 pointed imaging and spectroscopic observations were also carried out with the IRC and FIS during the cooled phases. During Phase III, mechanical coolers enabled continued IRC-NIR imaging and spectroscopy, but the high thermal background ruled out further observations at longer wavelengths.

Some interesting results from *AKARI* data so far include

- the detection of a MIR excess from early type galaxies in the outer regions of local galaxy clusters, which suggests these may be the evolved form of spiral field galaxies that were accreted into the cluster and transformed to ellipticals due to the cluster environment [Ko et al., 2009];
- the use of strong redshifted PAH and silicate features in the *AKARI* MIR and FIR wavebands, to estimate the redshifts and physical characteristics of dusty star forming galaxies and AGN fraction of their bolometric luminosity [Negrello et al., 2009; Serjeant et al., 2010b];
- the combination of *AKARI* and *Spitzer*/MIPS 24 μm (MIPS24 from hereon) colours to selected dust obscured ULIRGs over the redshift range z~1.2-1.6, which exhibit characteristically strong silicate features [Silicate break galaxies Takagi & Pearson, 2005]. This population provides an extension (in redshift) of Spitzer's dust obscured galaxies [DOGs

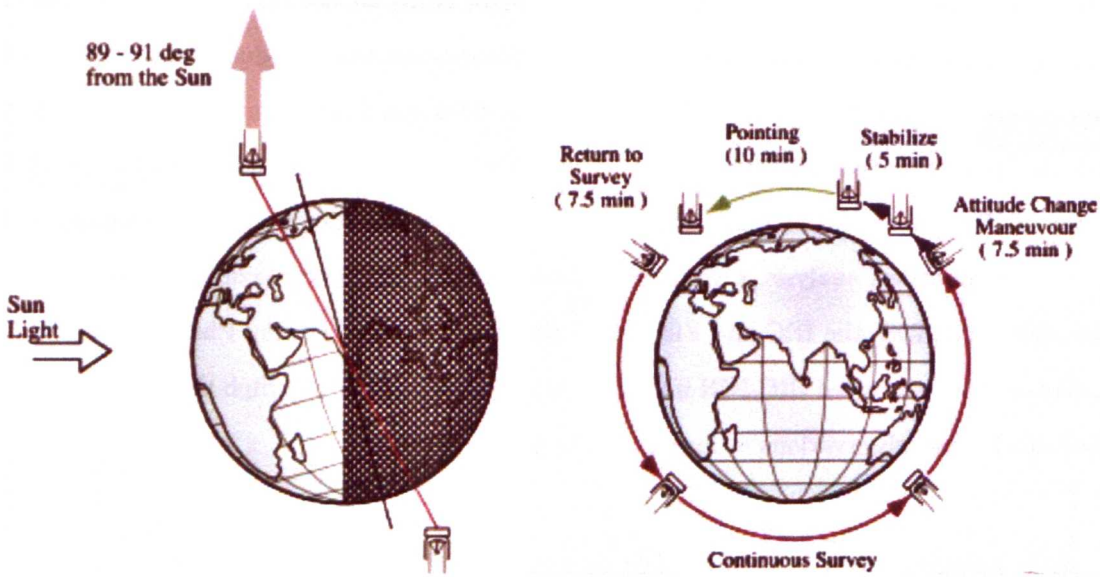

Figure 2.2: Left panel: diagram showing *AKARI*'s orbital path around the Earth, tracking the night-day line and constant orientated away from the sun [Murakami et al., 2007]. Right panel: *AKARI* can perform three pointings per orbit [Murakami et al., 2007]. Here the manoeuvre time costs are given and show the maximum 10 minutes exposure allowed per pointing, to avoid Earthshine and saturation. *AKARI* continues to observe in scan mode in-between pointings. Both panels illustrate the excellent visibility of the Ecliptic Poles, which are the North and South poles tangental to the plane of the Earth's orbit around the sun. (Figure credit: Murakami et al. [2007])

Dey et al., 2008] and shows the narrow redshift range assigned to DOGs is predominately a wavelength dependent selection effect.

2.2.2 Deep IRC observations of Abell 2218

AKARI's IRC provides continuous near and mid infrared spectral coverage from 1.8−27 μm, with a generous field of view (FOV) of nearly 10′ × 10′ and imaging and spectroscopic capabilities. Figure 2.3 compares the *Spitzer*/IRAC and MIPS24 filter coverage with that of the IRC, whose filters are more extensive than *Spitzer* and fill the gap from IRAC Ch 4 to MIPS 24. This missing Spitzer wavelength range importantly samples PAH features of star forming galaxies predicted to be at the peak epoch of star formation, with redshifts of z$\sim$ 1 − 2 [Dickinson et al., 2003b]. The MIR-S and the MIR-L are the two MIR IRC channels, which observe simultaneously with a separation of 25′. The MIR-S shares the same FOV as the NIR channel, made possible by a beam splitter (see figure 2.4 and 2.5).

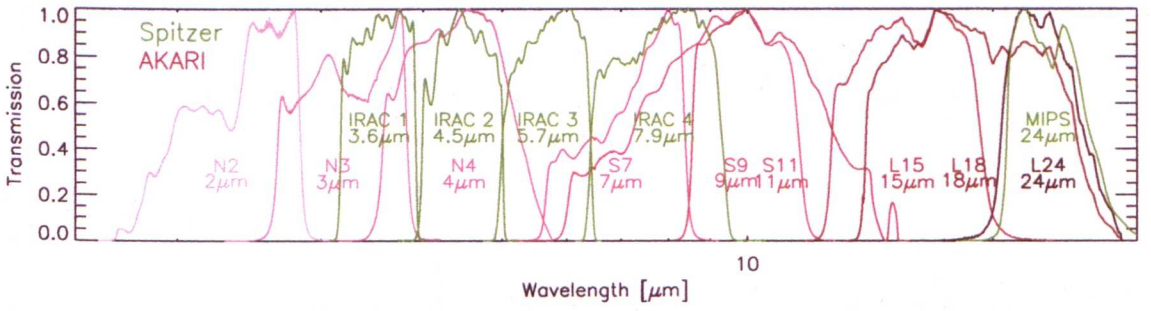

Figure 2.3: *Spitzer*/IRAC and MIPS24 filters (green) and *AKARI*/IRC filters (red). The *AKARI* coverage is more extensive and fills in the wide *Spitzer* MIR gap, including 15 μm.

Deep observations with the IRC MIR-L 15 μm filter of the galaxy cluster A2218 were proposed as an *AKARI* open time project (P.I. Stephen Serjeant). The position of A2218 near to the North Ecliptic Pole gives it high *AKARI* visibility (see figure 2.2); this, coupled with the gravitational lensing effects due to the cluster mass, made it the perfect target to achieve ultra-deep MIR data. In addition, the existence or planned complimentary multi-waveband data from u' to MIPS24 presented the necessary means to investigate sources sampled at 15 μm, which are predicted to be dominated by dusty star-forming galaxies [e.g. Elbaz et al., 2002a]. Although the cluster had been previously observed at 15 μm with the ISOCAM [Metcalfe et al., 2003], the

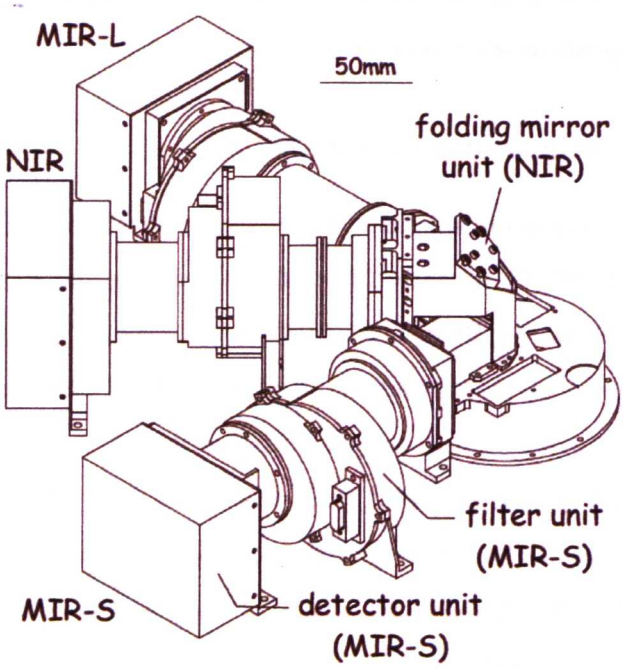

Figure 2.4: Top: The three IRC detectors covering the near and mid infrared. Bottom: The MIR-S and NIR detectors share the same FOV, which is 25′ from the FOV of the MIR-L. Lorente et al. [2008].

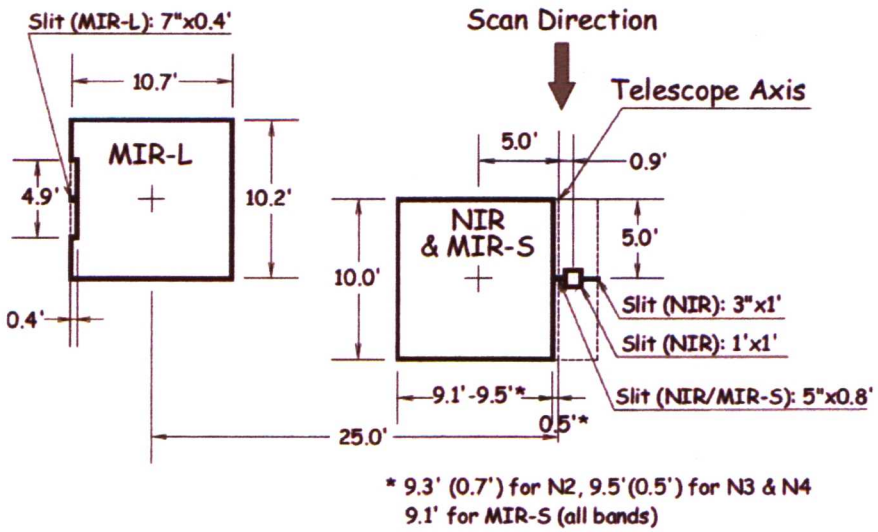

Figure 2.5: IRC schematic. The MIR-S and NIR detectors share the same field, which is 25′ from the FOV of the MIR-L. Lorente et al. [2008].

area and depth achieved were far less than the predicted *AKARI*/IRC coverage would be. The primary goal was to fully resolve the Cosmic Infrared Background at 15 μm ($CIRB_{15}$) and to understand the makeup of the constituent galaxy populations.

19 pointed observations with the MIR-L 15 μm filter (L15 from hereon) were awarded and observed during December 2006 and June 2007. Due to the design of the IRC, simultaneous 7 μm data were taken of flanking fields. The MIR-L 15 μm filter (L15 from hereon) has a wavelength response over the range 12.6 μm to 19.4 μm, with an effective wavelength of 15.6 μm. All pointed observations were taken with the IRC Astronomical Observation Template (AOT) 05, which was designed to maximise depth and has an estimated 5σ point source sensitivity for one pointing of 161 μJy. Assuming an ideal improvement in sensitivity of $1/\sqrt{N}$ with N pointings, theoretically for 19 pointings the 5σ sensitivity should improve to 37 μJy. To optimise available exposure time, no dithering is performed during a pointing with the AOT05. Dithering was therefore achieved by applying small positional offsets of translational and rotational shifts between each pointing. For each pointing there are five contiguous double frames taken, due to the repeat of the clock pattern for AOT05, which is a feature of the optimum depth design for this AOT. Each double frame consists of one short exposure and three long exposures repeated to give a double frame length of approximately 123 seconds. There are five cycles per pointing for the AOT05 giving around 615 seconds total frame integration time. The second frame of the final cycle is not always useable as it is taken within the allotted manoeuvre time between pointings.

2.3 IRC pipeline reduction

The raw L15 data were reduced using the standard IRC pipeline, version 20070912 [Lorente et al., 2008], within IRAF. The pipeline is split into three parts, named 'Boxes':

- the 'Red-Box' contains the pre-pipeline task used to split up the data into its individual exposures
- the 'Green-box' contains the main pipeline data reduction functions
- the 'Blue-box' contains the optional post-pipeline task of co-adding the data

2.3.0.1 The Red-Box

The Red-Box must be run prior to the main pipeline. The raw data is downloaded in the form of one cube per pointing, and the pre-pipeline tool divides each cube into its constituent short and long exposures. As the short exposures do not significantly add to the depth or quality of the final co-added product, they are discarded leaving around 30 long exposures of 16.5 seconds per pointing.

2.3.0.2 The Blue- and Green-Boxes

The Blue-Box performs the main pipeline tasks:

- bad or dead pixels, identified pre-flight, are masked
- A wraparound correction is applied for negative pixel values that, due to the data compression method, appear as values higher than the maximum saturation limit
- noise associated with thermal currents is removed by the subtraction of dark frames
- normalisation is performed to correct for the data compression method, where the least significant bit is dropped
- a model of low frequency sky structure, due to light scattered by the edge of the detectors, is subtracted
- single noise events due to cosmic rays are identified and replaced with the mean of the four adjoining (or nearest) pixels
- a correction for the non-linearity of the detector response for bright targets, is applied
- any pixel with a value greater than 33000 ADU is flagged as saturated
- the position of any spectroscopic slit within the IRC field of view is masked
- flat fielding is performed using super flats, which are combined pointings of zodiacal background light

- the pixel size is resampled to give square pixels

If the pipeline parameter 'co-add data' is selected, the Green-Box runs automatically at the end of the main pipeline tasks.

After an exhaustive investigation into the various parameter settings available for the pipeline, there were three parameters that were found to require non-default settings in order to optimise the reduction:

- average combine (the mean of each pixel value is taken) was chosen over median combine (the median of each pixel is taken) to optimise the signal-to-noise ratio. In fact uncorrelated noise (i.e. normally distributed random fluctuations) improves as $\sqrt{N}$ for N average combined exposures, but as $\sqrt{\pi N/2}$ for median combined. Also the IRC data user manual [IRC-DUM Lorente et al., 2008] recommends deep data be average combined to prevent loss of data due to the rotation of the non-circular PSF between pointings;

- The type of rejection for outlying pixel values was set to a sigma clipping algorithm. 'super-dark' uses dark frames taken early on during the *AKARI* mission and due to an increasing number of hot pixels this option was changed to 'self-dark', so dark frames taken at the beginning and end of each pointing were applied;

- The option for registering the astrometry with 2MASS data were kept as 'yes', however this procedure is not successful and the astrometry was subsequently registered outside of the pipeline.

The Blue-Box stage of the pipeline deals with the co-addition of the long exposures. Firstly bright reference sources are extracted with reference to the 2MASS point source catalogue [Cutri et al., 2003], secondly a median sky subtraction is performed and finally the frames are aligned and co-added. For MIR-L data there can be low numbers of reference stars detected as they tend to be faint at 15 μm and therefore the calculation of the xy-shift and rotation angle for the frames fails. In this case the median sky subtraction is performed but the post-pipeline tool 'coaddLusingS' needed to be used to co-add the reduced frames. This tool uses the corresponding MIR-S data to align and combine the MIR-L data. For each pointing, approximately 30 long exposures were average co-added and after the IRC pipeline was complete 19 frames

were reduced with an effective integration time of 8469 seconds. Here is an example of the final settings used to run the pipeline:

```
                                I R A F
                     Image Reduction and Analysis Facility
PACKAGE      =  irc
TASK         =  pipeline

(irccons     =  constants.database) IRC constants database file name
(com _mod    =  average) combine mode: average/median
(com _are    =  2) stack area: 1:common area 2:whole area
(sky _are    =  2) sky matching area: 1:common area 2:whole area
(det _sig    =  3.) Threshold in sigma for source detection
(sig _rej    =  3.) Rejection unit in sigmas
(max _itr    =  10) Maximum number of iterations
(obslog      =  irclog) output of the mkirclog
(cosmicr     =  yes) Detect and replace cosmic rays in MIRS images?
(wcs         =  no) Try to compute wcs and write it in the header?
(selfdar     =  yes) Use selfdark instead of Super-Dark?
(coaddsh     =  no) Coadd short exposure frames?
(interac     =  no) Run pipeline interactively?
(deltemp     =  yes) Delete intermediate files?
(rejecti     =  sigclip) rej in coadd:minmax|ccdclip|crreject|sigclip|avsig
(rej _sky    =  yes) Remove image(s) with outlier sky level?
(skip _L     =  yes) Skip coadding MIRL images?
(submeds     =  yes) Subtract median filtered sky in adjust _sky?
(coadd       =  yes) Coadd?
(default     =  yes) Use pipeline's default flat?
(verbose     =  no) Print verbose progress messages?

(list0       =  )
(mode        =  al)
```

The post-pipeline L15-data reduction was fully repeated several times, to improve the quality of the final image after major issues were uncovered during the data analysis. Each time the methods used were refined either with minor tweaks or with a new approach. What is detailed in the following sections are the main methods used and the path ultimately taken to achieve the deepest possible image, whilst maintaining the integrity of the source flux. The pipeline itself runs within IRAF, and several additional IRAF packages were used during the data reduction trials. For the final post-pipeline reduction a bespoke IDL routine was used primarily.

2.4 Pipeline output

Post-pipeline, the reduced data are easily categorised into two distinct groups, based on the relative scanning direction of the IRC with A2218. Due to the interval of roughly six months between the 10^{th} and 11^{th} pointings there is an approximate rotation of 180° between the first 10 frames (L15-A from hereon) and the final 9 frames (L15-B from here on). Figure 2.6 compares the post-pipeline output for one L15-A and one L15-B frame, with and without the pipeline's median sky subtraction option. This comparison illustrates the lower signal-to-noise-ratio for the L15-B data due to the high background structure from scattered light (possibly due to Earthshine), however, this issue may be related to the recently reported ghost images strongly present in the IRC L24 data[1] which would indicate this is a flat field problem and also explain why the scattering is also seen, to a much lesser extent, in the final few L15-A pointings. Warnings are given as to the accuracy of photometry for sources near the data edges due to this issue, which is a separate issue to the one directly addressed during the main pipeline, due to scattering at the detector edges.

Although the pipeline's median sky subtraction partially addresses the scattered light issue, there are remnants in the post-pipeline frames in addition to further low-frequency sky structure, introduced by the median sky subtraction. Figure 2.6 illustrates the additional low frequency noise introduced by the application of the pipeline's median sky subtraction. This increase in noise is noticeably evident around the mid to brighter sources in the frames. Combining the post-pipeline frames, produced using the optimum pipeline settings, results in uneven background structure, which is a hindrance for both extraction and photometry of potential sources. There were two ways in which the further data reduction could have proceeded; one way would be to discard the L15-B data so only the higher SNR L15-A data were combined and the second to include the L15-B frames, assuming the additional depth outweighs the additional noise. A comparison of the co-added L15-A and L15-B images[2] was made to asses the implications of excluding all 9 L15-B pointings from further use. Figure 2.7 shows the more severe sky structure seen in the L15-B data with respect to the L15-A image. This discrepancy was quantified with histograms of the half image pixel distributions giving estimates of the pixel RMS (figure 2.8)

[1] Information on the IRC ghost images can be found on the *AKARI* webpage:
`http://www.ir.isas.jaxa.jp/AKARI/Observation/DataReduction/IRC/`

[2] These images were combined after the frames were registered as described in section 2.4.2

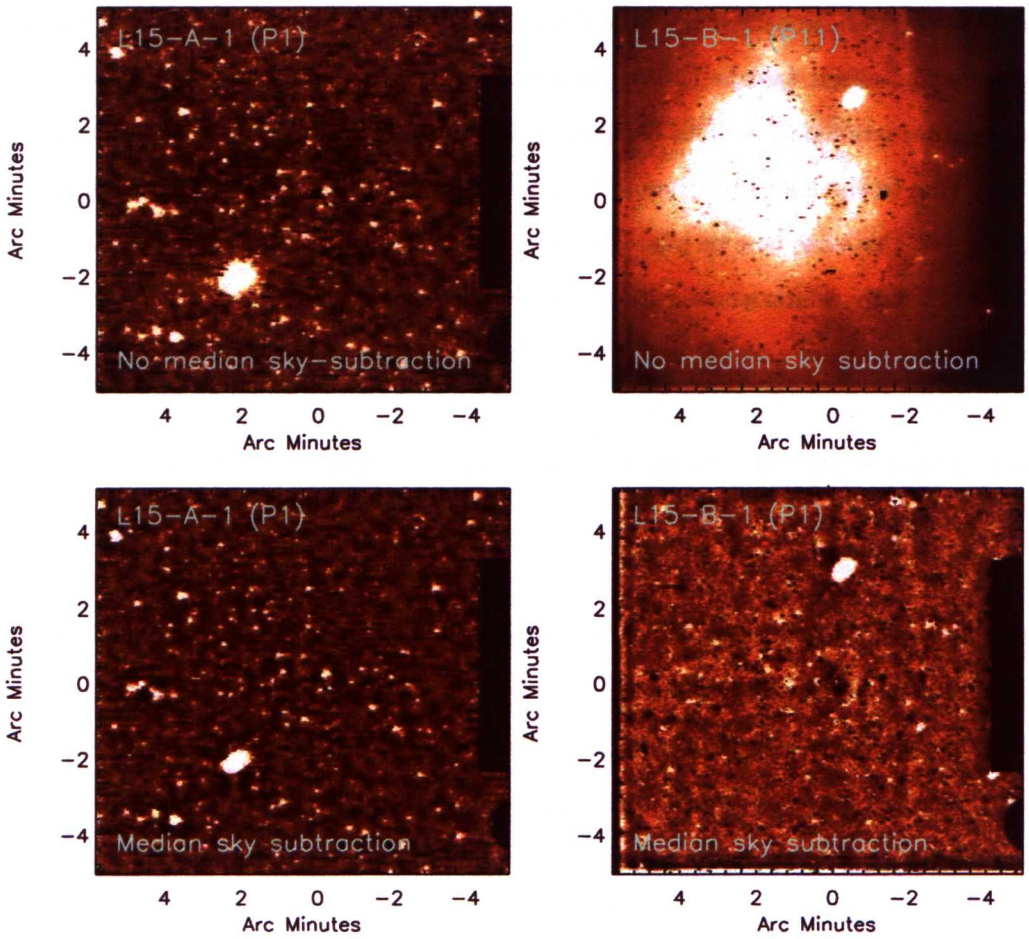

Figure 2.6: Examples of post-pipeline single frames, the first L15 pointing (L15-A:1; left column) and eleventh pointing (L15-B:1; bottom column). The top frames are reduced without the IRC pipeline's median sky-subtraction and the bottom two frames are the result of applying the sky subtraction. The issue of the scattered light is more severe for the L15-B example and this is the general trend between L15-A and L15-B. Note the difference in orientation between the L15-A and L15-B frames and the 'arms', due to masking for the spectroscopy slits within the field of view.

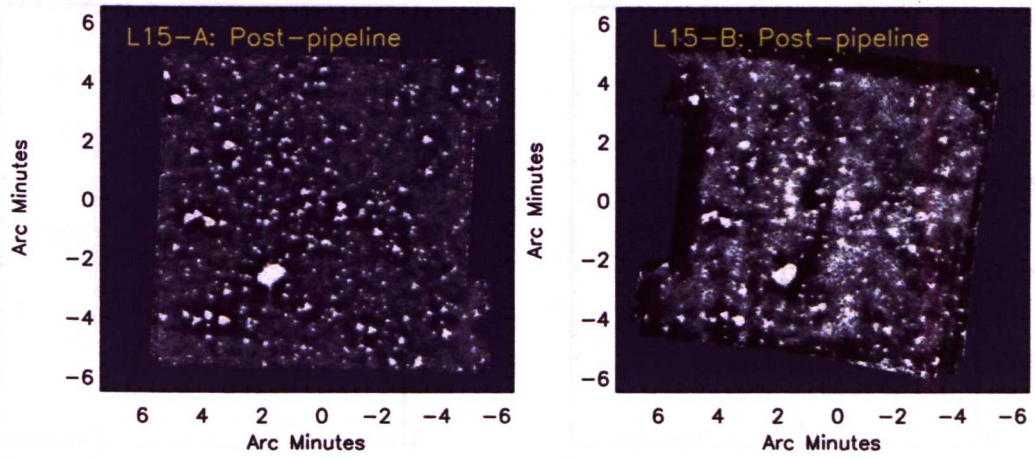

Figure 2.7: Average combined L15-A (left) and L15-B (right) 'half-images'. No further reduction was performed post-pipeline, but all the frames were aligned with respect to pointing 1 (L15-A-1) before the data were co-added. Both images show negative low frequency structure around the brighter sources. This structure is more pronounced for the L15-B image, and combined scattered light remnants also lead to brighter low frequency sky structure.

of $\sigma_{L15A}/\sigma_{L15B}$ =0.43. Despite the greater noise levels of the L15-B data, the advantage of its inclusion would be the potential improvement of sensitivity, by up to a factor of $\sqrt{\frac{19}{10}}$. Random aperture photometry were taken (following the same method as section 3.8.1) for the L15-A image and the L15-A and L15-B combined post-pipeline image (figure 2.9) giving 5σ sensitivities of 151 μJy and 324 μJy, respectively, which are significantly greater than would be expected from the IRCDUM predictions. A simple additional sky subtraction, using a box-car median filter with a kernel of width 9 pixels (21.5″), was applied to the L15-A half image and also to the combination of the L15-A and L15-B half images. Random aperture photometry were repeated for the resulting images (figure 2.9). The predicted gain in sensitivity for further reduced data is $\sim$ 10%, but this is a significant improvement for data that are approaching the confusion limit. The potential gain in sensitivity was therefore deemed desirable and the L15-B data were included in the final image. See section 3.8.1 for the sensitivity estimate of the fully reduced and combined data.

2.4.1 Post-pipeline reduction steps

The final post-pipeline reduction steps applied were as follows:

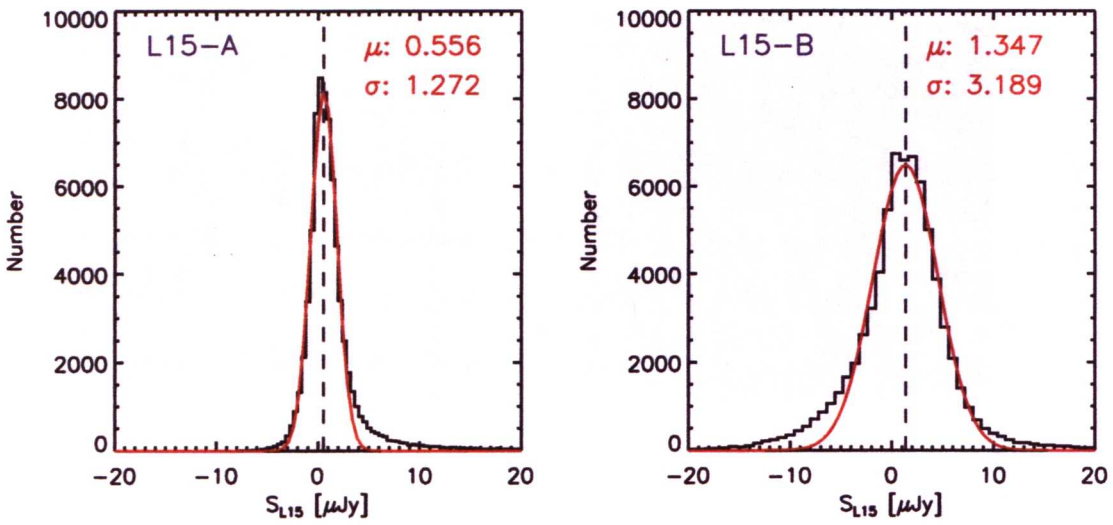

Figure 2.8: Pixel value distributions (converted to μJy) for the L15-A and L15-B average combined post-pipeline images. The RMS for the L15-B map is over double that found for the L15-A image. Both maps see a shift in the mean pixel count due to the remnants of scattered light.

- register frame astrometry
- remove edge noise
- correct hot pixels
- correct extreme cold pixels
- median sky subtraction
- correct remaining cold pixels
- remove rotation
- combine data

2.4.2 Registering the astrometry

Positional offsets between pointings, which act to dither the frames, need to be removed before combining the data. Each L15-B frame was rotated by 180° and the header astrometry updated. To address the remaining xy-shifts the IRAF tasks IMALIGN was initially used. For IMALIGN one reference frame must be nominated and bright sources within this frame must be matched

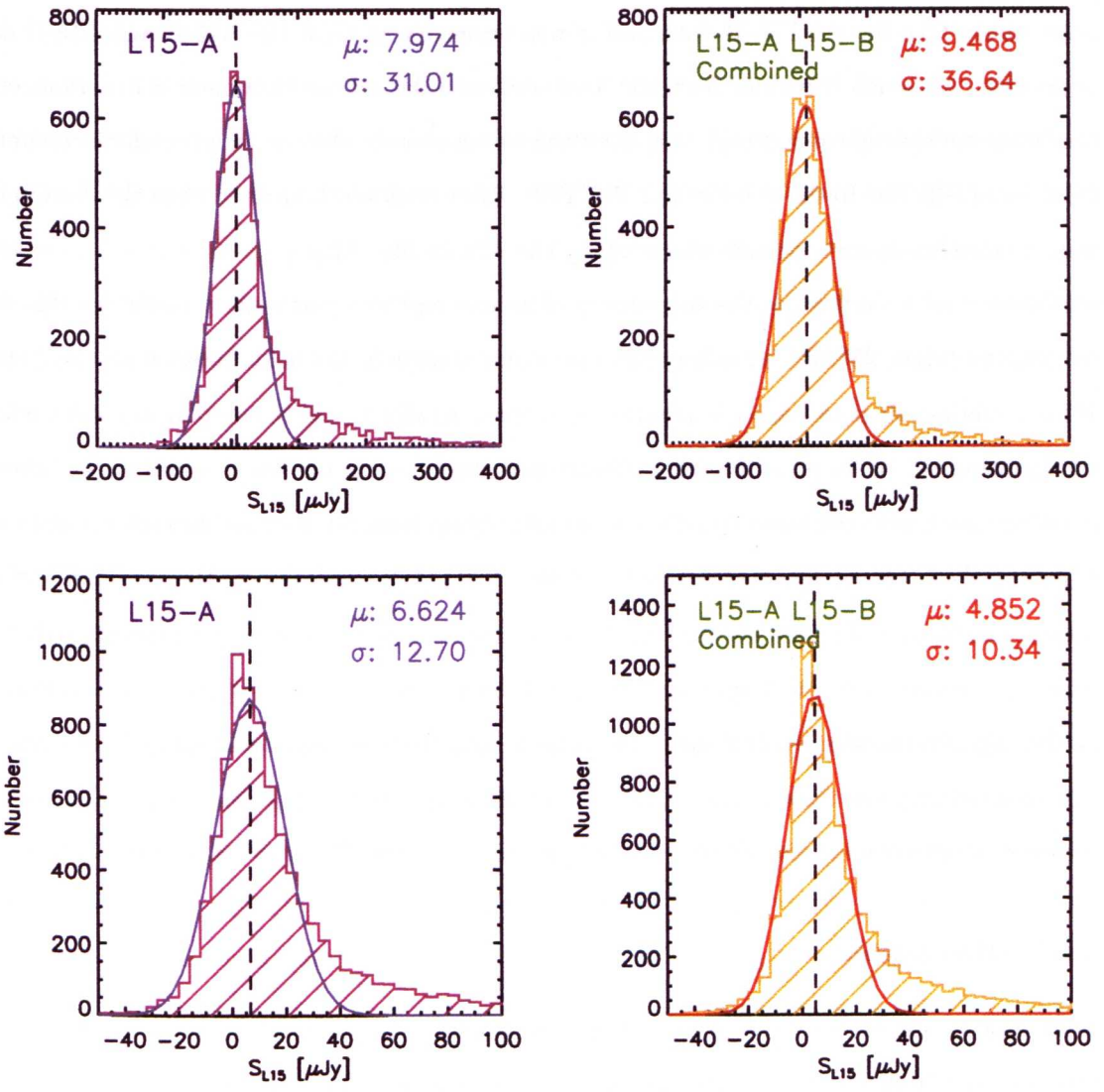

Figure 2.9: Histograms of aperture photometry taken at random positions for the L15-A half map (left panels) in comparison to the combined L15-A and L15-B data (right columns). The top histograms show the distribution of photometry obtained from the maps combined directly post-pipeline, and the bottom histograms show the equivalent distributions taken after an additional median sky subtraction, using a box-car median filter and a kernel width of 9 pixels (21.5″). The 5σ sensitivity estimate for the combined data, without further reduction, is greater that for the L15-A sensitivity estimate alone. In contrast, after the extra sky subtraction the distribution for the combined data gives a deeper estimate.

across the other images, recording the relative x and y coordinates for input as a text file. For the post-pipeline L15 data, it was difficult to find enough bright reference sources that had clear counterparts throughout the frames in order to achieve a satisfactory result. This was particularly true for the L15-B data and it was necessary to treat the L15-A and L15-B data separately. Although it is clear from the final combined data if the alignment is in serious error (i.e. from multiple ghost sources), it is not always immediately obvious when small discrepancies exist, especially due to the non-circular IRC PSF. After several attempts to align the data in this way, a more hands-on approach was sought. The Aladin Sky Atlas [Bonnarel et al., 2000] is an invaluable tool for adjusting the astrometry of images and was particularly useful for this data set with no bright 2MASS (or other) reference counterparts in the field, between all the frames. With a modest 19 pointings it is possible to employ Aladin to easily compare the data within the pointing set or to other images. Aladin was used to remove linear translations between pointings 2-19, with reference to L15-A:1, by identifying common sources through the data and adjusting the reference RA and Dec as necessary. The initial correction to the astrometry of the frames was further adjusted for the L15-B data, where necessary, when the remaining reduction steps were repeated due to improvements. Once the L15-A data were adjusted with Aladin, no further adjustment was required until the derived distortion correction was applied (section 2.5). Rotation between the frames was mainly corrected during the IDL pipeline using the fits header astrometry, although several frames needed prior corrections for minor rotational inaccuracy.

2.4.3 Bad pixels

Several other issues remained uncorrected post-pipeline that required further attention. The first and potentially most detrimental to data analysis was the low frequency sky structure, which has already been discussed at length. In addition there were incidences of bad pixels, noisy edges and an issue subsequently discovered during the multi-waveband crossmatching – a spatial distortion affecting all the L15 frames (see sections 2.5 and 3.6.2). Noise at the edge of the L15 data were removed trivially by trimming two to seven columns from the leftmost column containing data, and by one to four rows from the uppermost data row.

Both the half sets of data suffer from bad pixels, although again the L15-B data sees greater incidence of these, due to the increase in number during *AKARI*'s operation. Both positive

(hot) and negative (cold) bad pixels are present. Hot pixels are fixed in position relative to the detector and, due to their increasing number in time, only affect the L15-B data. These pixels remain an issue after the IRC pipeline as a consequence of no dithering for AOT05 pointings, which prevents the pipeline from any efficient correction or flagging. As hot pixels can appear as source-like objects in average combined data it is important that they are removed from the individual frames before co-adding. Hot pixels are fixed in the detector FOV and can therefore be identified by comparing several different frames that have rotations and translations between them. In contrast, cold pixels cannot be mistaken as real sources and are therefore more easily dealt with. Firstly one area of dead pixels, towards the centre of all the frames (this patch is visible in the top right panel of figure 2.6), was corrected by hand in the post pipeline data before any further reduction. Secondly the hot pixels were addressed. To avoid flagging any real features the hot pixels were identified by eye, taking advantage of the number of pointed observations obtained and the rotation between the L15-A and L15-B data. The L15-B frames were cross-examined to flag any potential hot pixels. The flagged positions were then compared to the corresponding positions in the L15-A combined half image, as a reliability check. A hot pixel mask was created for each L15-B frame and these were applied during the IDL extra reduction pipeline to median replace the hot pixels. Thirdly, a sigma clipping algorithm was used to correct any cold pixels, but due to the high sky variance and extensive negative sky structure, the post IRC pipeline median sky subtraction needed to be performed first, to improve the efficiency of the sigma clipping. As a compromise, an initial sigma clip was performed for negative pixel values with a significance greater than 5σ below the sky mean. After the sky subtraction the sigma clipping was applied for a second time at a 2σ level for negative pixels.

2.4.4 Median sky subtraction

A median-filtered sky model was derived for each frame, with the aim of removing the low frequency sky structure with minimal detriment to any real signal. Firstly the frames were rebinned to a finer scale, as rebinning helps to return a smoother and more accurate sky model after filtering (although this is a computationally time intensive step). To preserve source flux and improve the sky model, all pixels above some limiting value were set to zero. These zero limits were derived on a per frame basis using that frame's sky mean and variance. To min-

imise subtraction of real signal each zero limit was adjusted by comparing the residual frame to the original. Once zeroed, a linear interpolation was performed horizontally, vertically and diagonally over each of the resulting 'holes', and the mean interpolated pixel values were used to replace the zeros. A median boxcar filter was applied using a kernel width of 39 pixels. The kernel size used was three times the FWHM of the PSF scaled to that of the rebinned frames, and then rounded to the next odd integer. Using a kernel several times the FWHM ensures the maintenance of the fine scale structure of faint sources upon subtraction. The median filtered frames were then rebinned back to the original pixel scale and subtracted from the data frames. Figure 2.10 shows examples of how this median subtraction process affects sources within the data. The row profiles show the before and after of the subtraction and the median filtered mask and suggest the sky is effectively levelled, while the flux of the source is maintained. Extensive testing to the effects of the post-pipeline sky subtraction were carried out. Aperture photometry were taken for the L15 combined data, with and without the further sky subtraction, using the 5σ extracted source catalogue (see section 3.3 for details of the source extraction). Comparing the results (figure 2.11) gives an approximate 1:1 agreement at the bright end, with less of an agreement and greater scatter towards the faint end, where the flux densities tend to be greater for the median subtracted data. The conclusion drawn from this figure is that the sky subtraction successfully removes systematics associated with the low frequency sky structure, without significant detriment to subsequent source photometry. A second test was performed by adding artificial sources to the L15 data and then taking their photometry. Figure 2.11 confirms the reduction in the photometric uncertainties for the sky-subtracted data.

There remains minimal areas of extended noise for the frames that were most severely affected by scattered light. Figure 2.12 shows four corresponding postage stamp sections, taken from frame 19 (L15-B:9), of the post-pipeline output, a median filtered mask, the median subtracted result and the sigma filtered median subtracted result. This example presents the most extreme case of scattered light for all of the L15 data. Despite this the post-pipeline low frequency structure is almost entirely removed, apart from an area at the top edge of the frame.

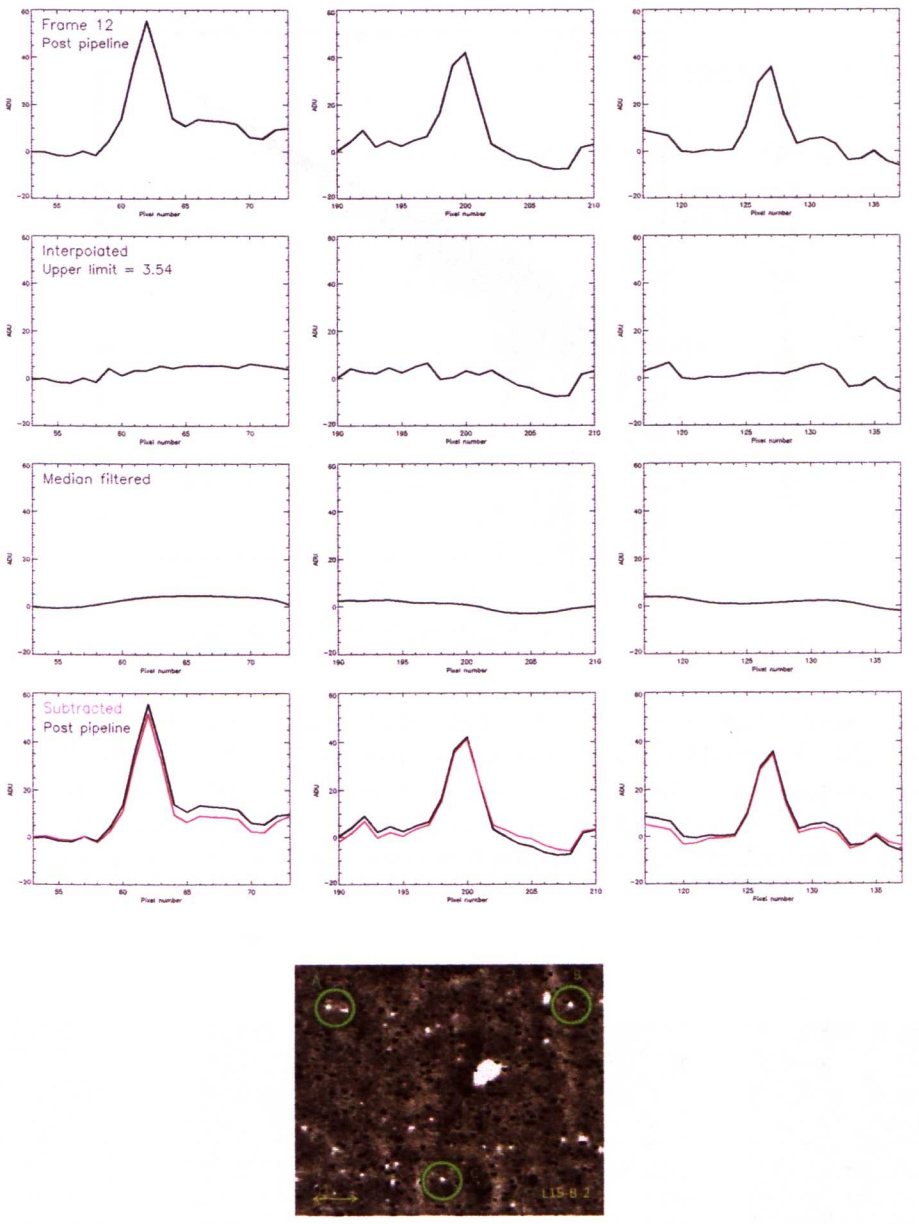

Figure 2.10: Row profiles for three medium-bright sources in the twelfth IRC pointed observation (L15-B-2), illustrating the effects of the post-pipeline sky subtraction. The sources are set to zero for all points above 3.54 ADU and the zeros are then filled with linear interpolations over horizontal, vertical and diagonal rows, before median filtering and subtracting from the data. The final row shows the residual row profile (pink line) in comparison to the initial data. The real signal is preserved and the sky is more even. For the first source the peak is slightly reduced after subtraction, but this corresponds the the removal of structure rather than signal and highlights a potential (real) reduction of photometry for this source. The sources for which these profiles were plotted are indicated with green circles in the corresponding postage stamp image.

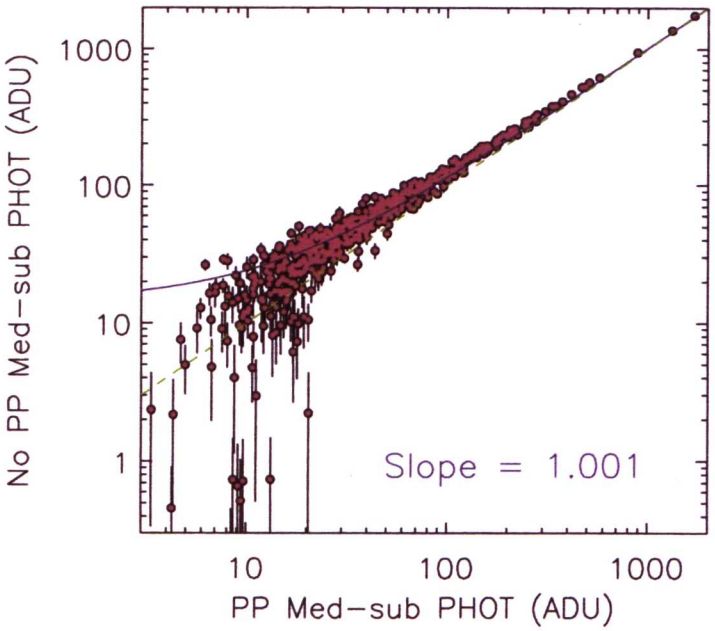

Figure 2.11: Aperture photometry for the L15-5σ source catalogue extracted from the L15 combined map with the post-pipeline median sky subtraction (PP Med-sub PHOT) and compared to aperture photometry for the L15 data combined with no additional sky subtraction (No PP Med-sub PHOT). The dashed green line is x = y and the blue solid line is the linear best fit. The 1:1 agreement indicates the source flux is preserved by this sky subtraction.

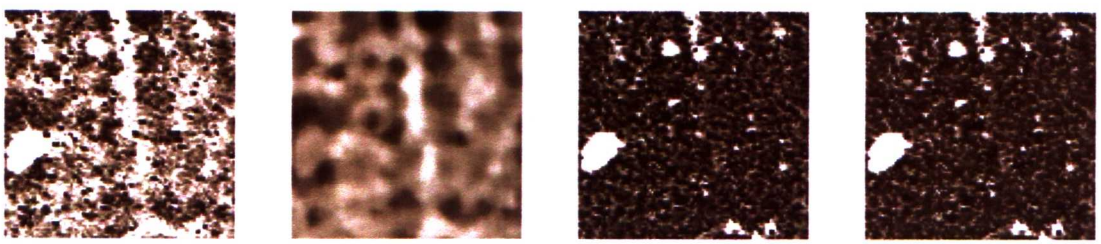

Figure 2.12: Postage stamp images ($4'' \times 4''$) taken from frame 19 (L15-B:9) illustrating the sky subtraction and sigma clipping performed during IDL extra-pipeline. The first stamp shows the post IRC pipeline output, the second the median smoothed sky model, the third is the residual image after the sky subtraction and the fourth shows the sigma clipped result. L15-B:9 is the most severely affected frame in terms of the unwanted sky structure, but even here the residual shows the noise is well subtracted, whilst maintaining the fine-scale structure of the background. There is a small residual of noise remaining at the top middle, which is not well modelled due to its near proximity to the frame's edge.

2.5 Field distortion correction

During the cross-matching process (section 3.6.2) it became clear that there were systematic positional discrepancies between sources at the edges of the L15-image and their counterpart positions at shorter wavelengths. Source extractions were performed for both reduced L15-A and L15-B 'half' images and then matched to the L15-5σ source catalogue (section 3.3). Figure 2.13 compares the x and y shifts for each half image, relative to the L15-image. These comparisons suggest there is a greater and non-linear shift, predominantly in the x-axis. Figure 2.14 shows the L15-image with the two sets of coordinates for the 'half' extractions overlaid and indicates the discrepancy lies towards the right and left edges, with a better alignment down the central part of the images. The discrepancy in position is more pronounced for the L15-B image, as the PSF for the L15-A data dominates the final result. This is due to the extra pointing for the L15-A set and the lower noise relative to the L15-B data, which is also reflected in the photometry for the half images (figure 2.15).

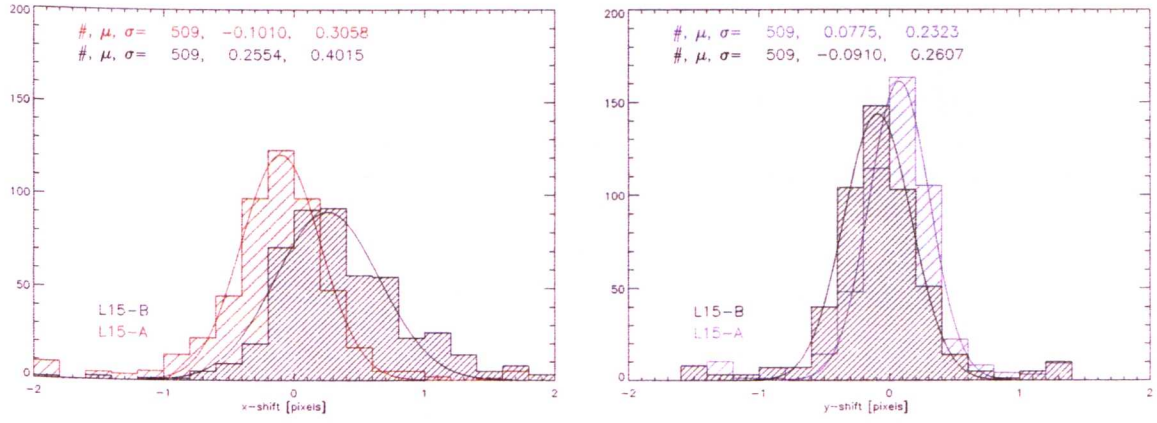

Figure 2.13: Differences in x (left) and y (right) pixel positions for sources in the L15-A and L15-B data relative to the L15-image. The largest discrepancy is for the x-coordinates of the L15-B data, although the mean shift is $< 1\sigma$.

One result of this issue was a spatially varying PSF (see section 3.7.4 detailing the PSF construction) in the L15 image, and therefore the warping was attributed to the pipeline's field distortion correction. Cubic polynomial coefficients were derived to map the L15-B data onto the L15-A data, and the resulting frames onto the Palomar i' and IRAC images by cross-matching sources in these data. The L15 image was recombined using the de-warped frames,

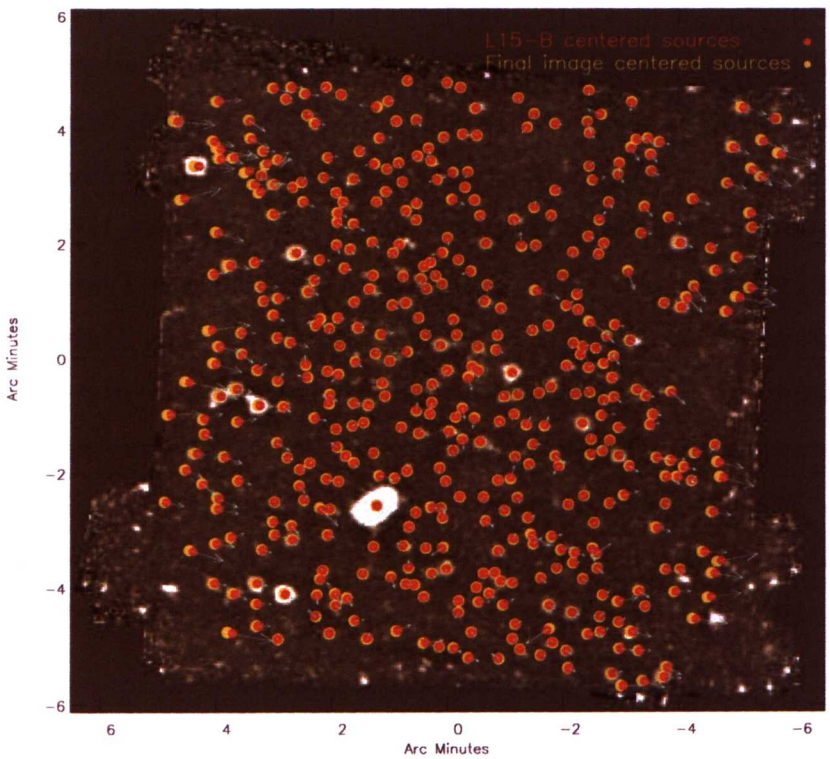

Figure 2.14: L15-image overlaid with the source positions for the L15-catalogue and the matched L15-B positions. The arrows indicate the direction of positional shifts between the L15-B and L15 positions and the length of arrow is relative to the shift. There is a non-linear shift mainly confined to the x-axis.

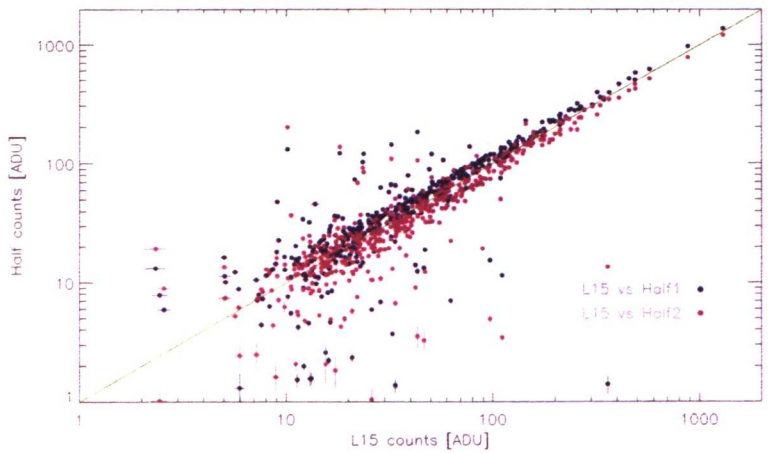

Figure 2.15: Photometry for the two half images, taken for the re-centred L15-5σ sources. There is a discrepancy between the two sets of photometry, which is most likely due to the low-frequency sky structure that affects the L15-B data more severely.

and an empirical PSF was constructed using the new image. The rebuilt PSF showed no spatial variability. Details from the corrected and uncorrected L15 image are shown in figure 2.16, for which there is a distinctly more singularly peaked PSF for the post de-warped data. The coverage plot in figure 3.4 shows some areas of the L15 image, at the top right and bottom left corners, are not covered by the available multi- wavelength data and therefore the de-warping may not be complete over these ares. Planned JHKs observations with the Canadian French Hawaii Telescope (CFHT) will provide the necessary coverage to check the persistence of this issue.

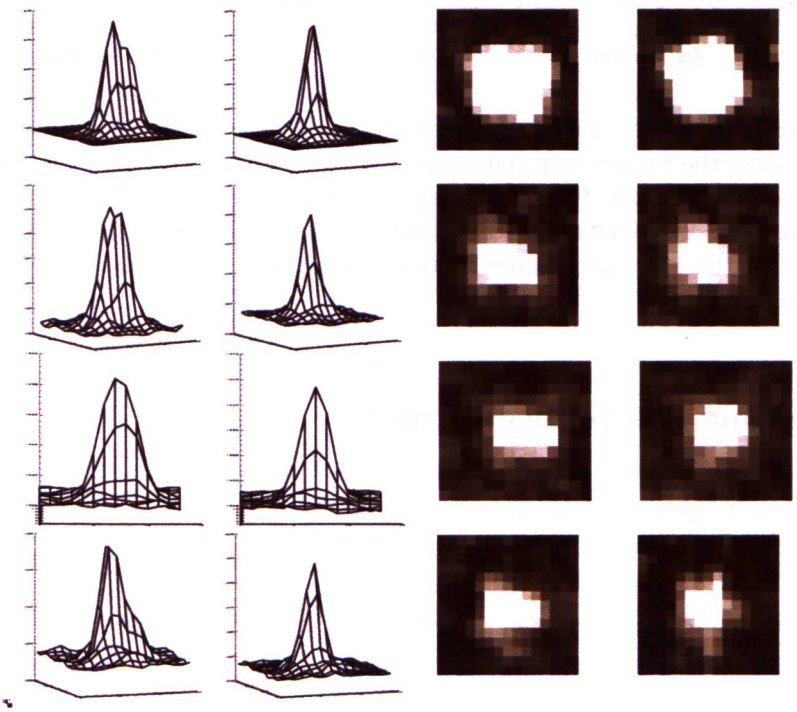

Figure 2.16: Surface plots and postage stamps for a selection of L15-sources near to the edge of the L15-map, pre- (columns one and three) and post-dewarping (columns two and four). Prior to de-warping the PSF has a broader, in some cases twin, peak due to the positional discrepancy between the L15-A and L15-B data. This discrepancy arises from incomplete distortion correction during the IRC pipeline and is compounded by the difference in orientation between these two sets of data.

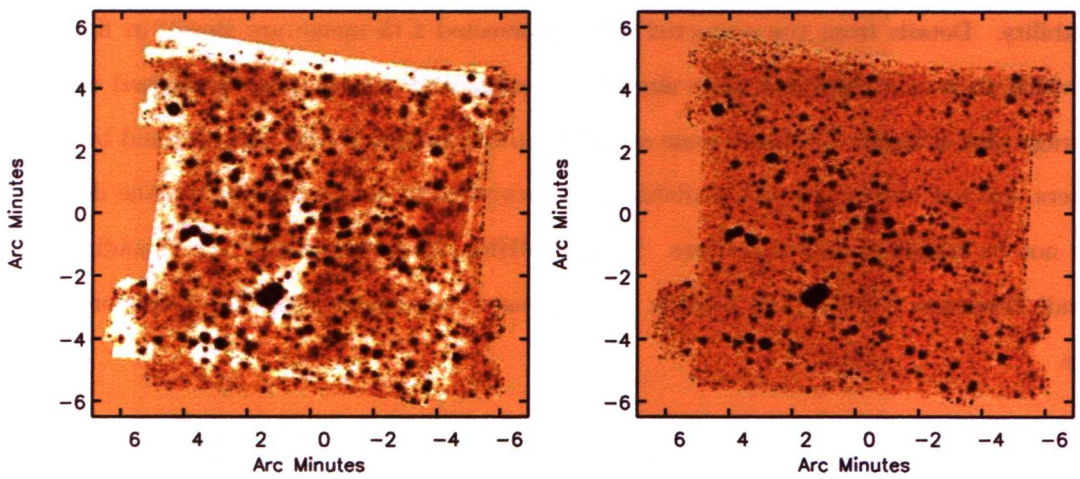

Figure 2.17: Left panel: The 19 L15 pointed observations of A2218 combined from the IRC pipeline output after the further IDL reduction is performed, but omitting the post-pipeline sky subtraction stage. Right panel: Final L15 data combined after the full IDL reduction steps were applied, including the sky subtraction step. There is a noticeable reduction of low frequency sky structure, although there is some residual towards the centre. The same pixel scaling was used to plot both images.

2.6 Co-adding the reduced frames

Once a satisfactory reduction of the L15-data were achieved, the frames were average co-added to give the final L15 image (L15-image from hereon). Due to the offsets between the frames and rotation between the L15-A and L15-B data sets, the area coverage varies. A coverage map was created during the IDL extra-pipeline by combining masks for each frame, where pixels within the field of view were set to 1 or otherwise 0. The coverage map was used to give a fair mean of the data. Figure 2.17 shows a comparison between the L15-image combined from the further reduced data and the corresponding result post IRC-pipeline (noting that the both images are plotted with the same pixel scaling). The post-pipeline data were subject to the same astrometry and de-warping corrections. The pronounced sky structure over the post-pipeline image is greatly reduced for the L15 image. It is also notable that the fine background structure is visible for the L15 image. Several tests were carried out to investigate the effect the further reduction has on subsequent photometry. A direct comparison was carried out for aperture photometry of relatively bright sources. Artificial sources with randomly assigned flux densities were added to each map and the photometry were taken with a 5″ aperture radius at

the source positions, and compared to the input (figure 2.18). The recovered flux densities have a significantly lower scatter and associated uncertainties for the L15-image in comparison to the post-pipeline version. These results confirm that the additional median subtraction is necessary for the goal of reliable photometry, especially for faint sources.

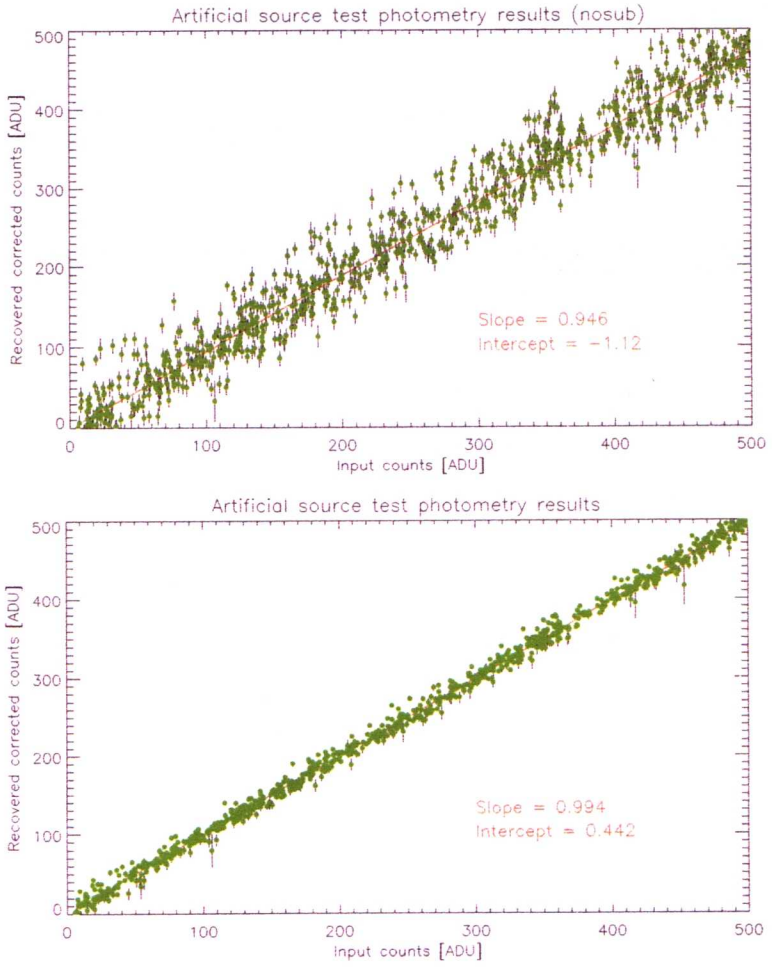

Figure 2.18: Aperture photometry for artificial sources added to the L15 combined data with (bottom panel) and without (top panel) the post-pipeline median sky subtraction. The accuracy of the photometry is improved with the post-pipeline sky subtraction and de-glitching.

Chapter 3

The deepest image of the Universe at a wavelength of 15 μm: resolving the cosmic infrared background

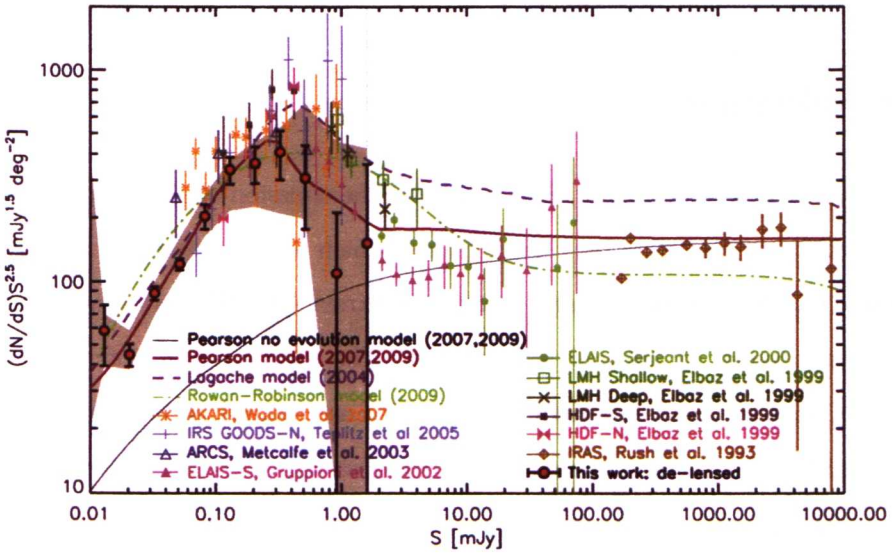

Figure 3.1: Euclidean-normalised differential galaxy number counts. The L15-de-lensed counts are compared to the P10 model counts and no-evolution model, [Pearson, 2010; Pearson et al., 2007], the Rowan-Robinson [2009] model, the Lagache et al. [2004] model, IRAS counts from Rush et al. [1993] (shifted from 12μm), ISO counts from Elbaz et al. [1999], Serjeant et al. [2000, re-calibrated following Väisänen et al. [2002]], Gruppioni et al. [2002] and Metcalfe et al. [2003], IRS counts from Teplitz et al. [2005] and *AKARI* counts from Wada et al. [2007]. The grey shaded area represents the 95% bootstrapped confidence interval for the L15-counts. Note the good agreement of the faint end of the L15-counts with the Pearson and Lagache models.

3.1 Abstract

This chapter presents the deepest image of the Universe taken by any facility at 15 μm, extragalactic number counts and a lower limit estimate for the cosmic infrared background at 15 μm. Deep pointed observations of the gravitational lensing cluster Abell 2218 were taken by *AKARI*'s IRC, giving a final map of $\sim 15' \times 15'$, as discussed in chapter 2. Multi-wavelength data were used to identify positional priors for the 15 μm 5σ source catalogue in order to de-blend with PSF fitting. Over 300 sources were recovered from the photometric confusion, giving a 5σ de-blended sensitivity of 28.7 μjy. De-magnification of the source flux densities gave 15 μm galaxy number counts that are a factor of 3 fainter than previous results, extending to a depth of ~0.01 mJy and providing a stronger lower limit constraint on the CIRB at 15 μm of $1.9 \pm 0.5\,\mathrm{nW\,m^{-2}\,sr^{-1}}$. These data probe $\gtrsim 5\times$ fainter than the blank field confusion limits and uniquely sample the normal star forming galaxy population that dominates the peak epoch of star formation.

This chapter contains work relating to the publication Hopwood et al. 2010, ApJ, 716, L45 and Ko, Hopwood et al. 2010, ApJ, 695, L198.

3.2 Introduction

The extragalactic background light (EBL) includes the emission of all galaxies over the history of the Universe, post re-ionisation. Dust grains, which are the result of intense star formation, surround star-forming regions and absorb the ultraviolet (UV) and optical stellar emission, re-radiating this energy at infrared wavelengths. The energy density of the cosmic infrared background (CIRB) and the UV/visible backgrounds are roughly equal, implying that one half of all UV/visible photons have been absorbed by dust and then re-emitted as thermal radiation. The CIRB therefore traces dusty star-formation over the history of the Universe and is an important constraint for galaxy formation and evolution models. The peak of the CIRB is around 140 μm to 200 μm [Devlin et al., 2009; Dole et al., 2006] and the galaxies responsible for this peak are the same populations that dominate the CIRB at shorter wavelengths i.e. MIR ($\lesssim 60\mu$m), because of the strong correlation between MIR and far-infrared (FIR) star-forming galaxies [Chary & Elbaz, 2001; Elbaz et al., 2002a]. Recent results from Spitzer, SCUBA and BLAST data have shown, via 24 μm stacking, that 24 μm-selected source populations account

for the bulk of 70 μm, 160 μm and 250 μm backgrounds and also dominate the 350 μm, 450 μm and 500 μm backgrounds [Devlin et al., 2009; Dole et al., 2006; Serjeant et al., 2008]. In contrast at 850 μm the 24 μm-selected source population only resolves around a quarter of the background [Serjeant et al., 2008]. In order to investigate the contribution of faint 15μm selected (gravitationally lensed) galaxies to the CIRB at 15 μm ($CIRB_{15}$), a deep source catalogue with reliable photometry and redshift estimates is required. To achieve this, sources were initially extracted from the reduced AKARI data above a 5σ significance. To gain greater depth the resulting catalogue was used as a base for photometric de-blended with PSF fitting, assisted by multi-wavelength positional priors, which were derived from ancillary data in the field. A band-merged catalogue was constructed to provide the optimum photometric coverage with the available data, and used to derived photometric redshift estimates, which are a necessary component in obtaining magnification corrections.

3.3 Source extraction

There are two publicly available source extraction packages widely used for infrared data – DAOPHOT [Stetson, 1987] and SExtractor [Bertin & Arnouts, 1996]. SExtractor was developed to deal with large data sets, in relatively low computational times. Sources are extracted using a connected pixel algorithm for pixels above a given threshold. For each detected object, de-blending is applied via a search for multiple peaks as a function of threshold level. Photometry is acquired using a specified range of aperture shapes and sizes. SExtractor has a wide range of built-in PSF convolution filters and offers the option of duel extraction, where one image is used for source detection and the second for the photometry. One inconvenience of SExtractor is the inability to input a source catalogue purely to obtain photometry, therefore having to run the extraction algorithm with the possibility of not extracting all the required sources within a given catalogue. DAOFIND (the extraction package within DAOPHOT) was developed for crowded stellar fields and identifies sources by searching for peaks, a set number of σ above the local sky level, within a radius of the given FWHM. Peaks are detected after the data is convolved with a zero sum Gaussian kernel. Centroids for the extracted sources are estimated by fitting 1D Gaussian profiles along the x and y axis. Additional DAOPHOT packages are available to further analyse the data, including those to take photometry of the extracted source

catalogue.

Both source extraction packages were applied to the L15 image to test their suitability for extracting a 5σ catalogue. A range of convolution filters and de-blending parameters were tested with SExtractor and the optimal results, in terms of number of sources extracted and levels of blending, were attained for the 5×5 pixel^2 Gaussian filter, with FWHM of 2.5, and 7×7 pixel^2 Mexican hat filter, also with a FWHM of 2.5 (see table 3.1 for the L15 image pixel scale). Although applying the mexican hat filter leads to comparatively fewer de-blended sources, it also clearly extracts numerous faint sources, beyond those selected when using the Gaussian filter and at strikingly regular intervals, which strongly suggests there are many spurious sources in the resulting catalogue. The equivalent 5σ DAOFIND extraction gave a comparable number of sources to the Gaussian filter SExtractor catalogue, with fewer clear blends i.e. one identified source which visibly has several parts. Therefore DAOFIND was adopted for the final extraction.

DAOFIND requires two main parameter inputs relating to the physical characteristics of the data, namely the FHWM of the PSF and the background standard deviation. IRAF's IMEXAMINE task was used to obtain the FWHM for several sources within the L15-image, giving an estimated mean FWHM of 2.5 pixels ($6''$). The same task was used to estimate a mean standard deviation, from predominantly sky areas, of 0.48 ADU. In order for DAOFIND to accurately estimate the local sky it is necessary to input certain fits header information for the gain, exposure time, readout noise, and for ground based observations airmass (which is redundant for AKARI data). These parameters are also necessary for several other DAOPHOT packages used during this data analysis. In particular the PSF fitting ALLSTAR task requires this information to assign appropriate uncertainties to the photometry estimates, to properly weight the fitting process and for the accurate computation of signal-to-noise ratios (SNR), sharpness and χ^2 statistics. It is therefore important to input these data in a way DAOPHOT can correctly interpret. In this case the data were average combined from several exposures and so the effective gain is given by N x gain (where N is the number of co-added frames and the gain is for one exposure) and the read noise is calculated as $\sqrt{N}$ x read noise. There is no option for setting the number of frames that have been combined and so the exposure time must be entered as the total effective exposure. See table 3.1 for the values used for the AKARI and ancillary data.

Running a 5σ DAOFIND extraction with the L15-image gave an initial 624 sources (see figure 3.2). Around 100 sources detected at the edges of the L15-image were removed as spurious, and the remaining catalogue members were then tested for reliability.

3.4 Reliability

A reliability check was performed for each remaining potential source, to identify and remove any non-robust extractions. The main reliability test exploited the 180° difference in orientation between the L15-A and L15-B data, in a similar method to the bad pixel check used during the L15 data reduction process (see section 2.4.3). Two 'half' images were combined from the final reduced and aligned L15-A frames and L15-B frames. It was then assumed that any object appearing at the same position in *both* 'half' image constitutes a reliable extraction.

Prior to checking the full catalogue, the sources in the immediate vicinity of the brightest source within the A2218 L15-map (source A), which has ten times the brightness of the next brightest source, were examined. Source A is a local galaxy that lies in front of A2218 with a spectroscopic redshift of 0.02 and a partially resolved morphology in the L15-data. Source A is bright enough to produce diffraction spikes within the tail of its PSF that could lead to spurious detections. Potential extractions within a radius of 50″ from the centre of source A were examined and compared for position and shape in each 'half' image. Due to the asymmetrical nature of the L15 PSF (section 3.7.4), sources appear with a comparatively rotated shape in either 'half' and so looking for a positional agreement and a consistent difference in profile indicates a source rather than a noise event. Postage stamp images centred on source A are shown in figure 3.3 along with the nearby extractions. The comparison between the two images shows that although the diffraction spikes of source A have a different orientation in both 'halves', the extracted sources do not change position (as would be expected for noise associated to source). Also the sources themselves are consistent with the respective PSF profile. Therefore, the extractions near to source A are not due to diffraction spikes and can be confidently included in the reliability check.

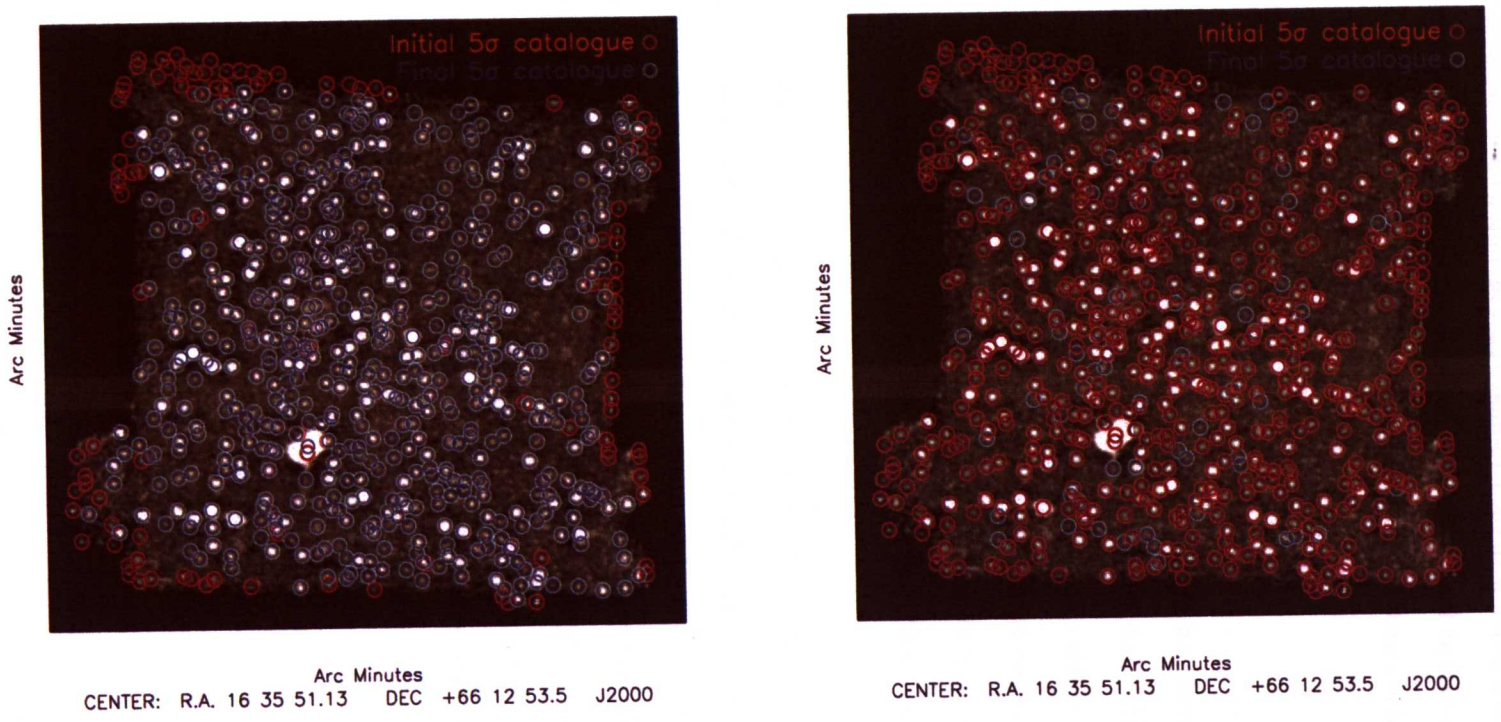

Figure 3.2: L15-image and $> 5\sigma$ source positions, extracted with DAOFIND. Left: the initial catalogue (red circles) contained many spurious detections towards the image edges, which could be immediately discarded. Further sources were rejected during the reliability check and the final catalogue (blue circles) contains 588 sources. Right: there were a number of sources added to the final catalogue from previous extractions (once checked for reliability), here the full final extraction is plotted (red circles) before any spurious sources were removed to highlight the additional members (blue circles), re-centred (where necessary) and added to the final source catalogue.

Table 3.1: A2218 data set information. The columns are the instrument name, filter used (Filt.), pixel scale (Pix), FWHM ($\theta_{\rm FWHM}$), gain (GN), readout noise (RN), number of combined frames (N), exposure time (Exp), zero magnitude (M_z), 5σ upper limits, Conv gives the pixel counts to μJy conversation factor. Note that the upper limit given for the L15-image is the 5σ sensitivity estimate for the de-blended source catalogue.

Instrument	Filt.	λ (μm)	Pix ($''$)	$\theta_{\rm FWHM}$ ($''$)	GN (e^-ADU^{-1})	RN (e^-)	N	Exp (s)	M_z	5σ (μjy)	Conv
AKARI/IRC	L15	15	2.39	5.98	6.44	14.2	517	16.36	—	28.7	1.70×10^{0}
AKARI/IRC	S11	11	2.34	6.55	6.44	14.2	30	16.36	—	84.8	3.66×10^{0}
Spitzer/MIPS	24	24	1.25	5.85	5.0	—	30-90	30.93	—	43.2	1.70×10^{0}
Spitzer/IRAC	CH4	8.0	1.22	3.8	3.3	—	587	46.8	—	7.62	3.5×10^{1}
Spitzer/IRAC	CH3	5.8	1.22	3.8	3.8	—	294	98.6	—	20.7	3.5×10^{1}
Spitzer/IRAC	CH2	4.6	1.22	3.8	3.8	—	294	96.8	—	2.87	3.5×10^{1}
Spitzer/IRAC	CH1	3.5	1.22	3.3	3.8	—	294	96.8	—	2.24	3.5×10^{1}
WHT/Ingrid	Ks	2.150	0.240	1.09	3.6	25.0	138	60	25.76	6.84	3.31^{-2}
WHT/Ingrid	J	1.250	0.240	1.09	3.6	25.0	151	60	26.82	4.43	3.00^{-2}
Palomar/Hale	i'	0.768	0.285	1.78	2.0	10.0	29	750	31.77	0.45	4.21×10^{-4}
Palomar/Hale	V	0. 550	0.284	2.90	2.0	10.0	6	1000	32.60	0.64	3.22×10^{-4}
Palomar/Hale	B	0.440	0.284	1.88	2.0	10.0	17	1000	32.32	0.19	5.02×10^{-4}
Palomar/Hale	u'	0.354	0.284	2.05	7.0	10.0	3	1000	31.53	1.12	4.10×10^{-4}
HST/WFPC2	f814	0.814	0.0498	0.349	7.0	—	2	1000	21.66	—	—
HST/WFPC2	f606	0.606	0.0498	0.299	7.0	—	2	1000	22.90	—	—
HST/WFPC2	f450	0.459	0.0498	0.299	7.0	—	2	1000	22.00	—	—

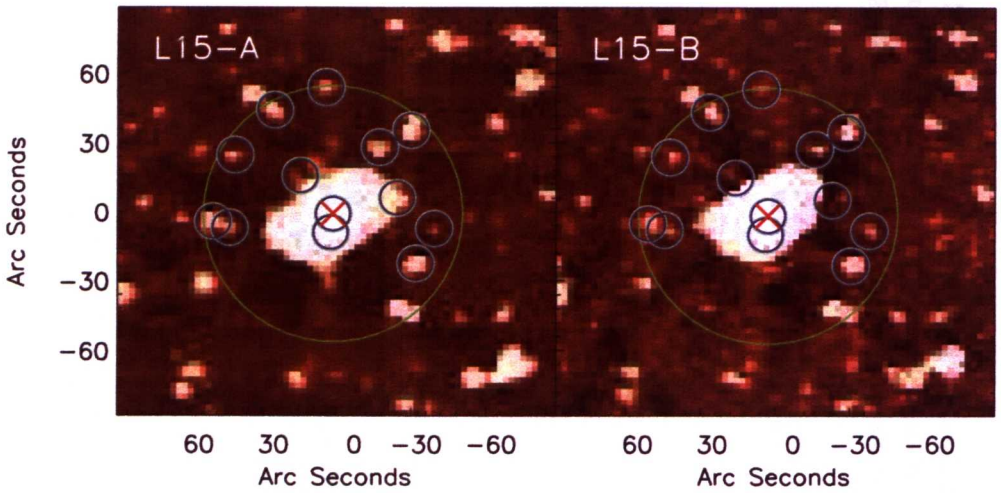

Figure 3.3: Postage stamp image of Source A in both 'half' images and the nearby sources extracted above a $5\,\sigma$ significance. A comparison of the sources in both images rules them out as occurring due to the diffraction spikes of source A.

Each member of the extracted catalogue was then examined in both 'half' images and removed from the catalogue if there was no clear presence in one of the maps. Due to improvements made to the L15-data reduction and co-addition, there are several previous extracted 5σ source catalogues that have also been checked for reliability using the half image comparison. A cross-check was performed between these 5σ catalogues and several sources, which were previously deemed reliable, were added to give the final 5σ L15-source catalogue. Although these sources may now fall just below the 5σ limit of the final L15-map, all have notable flux in both 'half' images. As the ultimate goal for the L15-data were a deep and reliable catalogue these objects were added to the L15-'5σ' source catalogue (after re-centring), giving a final total of 588 sources (see figure 3.2).

3.5 Sources per beam

The beam of a detector is the characteristic point spread function (PSF) and can be thought of as the unit of resolution for the associated data. One quantification of photometric source confusion within an image is the number of sources per beam based on an extracted source catalogue. Source confusion becomes significant in terms of identifying individual sources at

around one source per 30 beams [Condon, 1974; Hogg, 2001], beyond which the data may be described as confusion limited. The number of sources per beam is the reciprocal of the source number density, which is simply $A_{L15}/(A_{beam} \times N)$ where A_{beam} is the area defined using a radius of $1\,\sigma$ of the FHWM, where $\sigma = FWHM/(2\sqrt{2\ln 2})$ and N is the number of sources within the image area, A_{L15}. The L15 image extraction area is 70005 pixel^2 and the 5σ L15 source catalogue contains 588 sources giving 1/34 sources per beam, which implies the L15-image is confusion limited at a 5σ level. This estimate does not take into account sources that are above the confusion limit but photometric confused, thus the number of sources per beam predicted in this way is conservative. Due to the high confusion levels in the L15-image a de-blending process was employed to recover sources from photometric and background confusion.

3.6 A2218 Band-merged catalogue

3.6.1 Multi-wavelength data

Multi-wavelength analysis played a key part in de-blending the L15 5σ source catalogue, aiding in the separation of photometrically blended sources by the identification of multiple centroids and improving the precision of the centroids for other photometrically confused sources.

The available multi-wavelength coverage of A2218 was taken by several facilities: *HST* WFCP2 F450, F606 and F814, Palomar 200 inch Hale u', V, B, i' and WHT's INGRID J and Ks [Smail et al., 2001a; Ziegler et al., 2001]; *Spitzer* IRAC Ch 1 to 4 and MIPS24 [Egami, 2010, in preparation]; *AKARI* S11 [Ko et al., 2009]. The coverage offered by each data set is shown in figure 3.4 and information about the observations and data are presented in table 3.1.

3.6.1.1 *HST* data

The optical imaging taken by the *HST* provides the highest resolution, but limited area coverage of A2218 (three areas of $1.3' \times 1.3'$). Figure 3.5 shows a composite RGB image constructed using the F450, F606 and F814 data sets, recreating what may be the most famous depiction of any lensing cluster. It shows clear incidence of strong lensing in the form of multiply-imaged giant arcs.

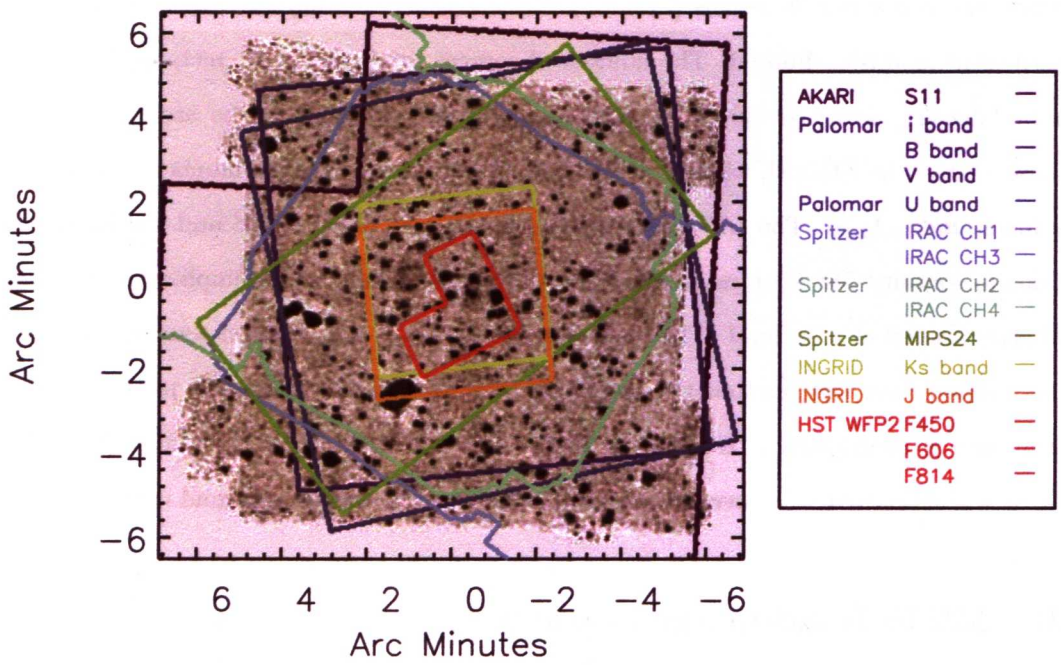

Figure 3.4: Contours indicating the relative coverage provided by the A2218 multi-waveband data set. All the images astrometry were checked and adjusted against the Palomar i' image, including the L15-image itself.

3.6.1.2 Palomar data

Ground based optical data of A2218 was taken by the 200-inch (5.1 m) Hale telescope's Large Format Camera (LFC), located at the Palomar Observatory in California. This data covers the majority of the AKARI FOV ($9.6' \times 9.6'$) and proved vital for the L15 data analysis. In particular the resolution, depth and coverage of the i-band data made it suitable to be used as the main reference image for the de-warping of the L15-data (section 2.5), astrometry alignment for all available data, the visual confirmation of cluster members (section 3.11.1) and stars, and for identifying counterparts to the L15 source catalogue (section 3.6.2).

3.6.1.3 WHT data

NIR data were observed by the William Herschel Telescope (WHT) Isaac Newton Group Red Imaging Device [INGRID Packham et al., 2003] at J and Ks wavebands. The area of the data ($4' \times 4'$) is limited to less than a quarter of the L15-map.

Figure 3.5: RGB image of the core of A2218, composed of the F450, F606 and F814 *HST* data, combined with ALADIN [Bonnarel et al., 2000]. The mass distribution of the cluster can be constrained by the geometry and relative positions of the arcs and arclets, which are manifestations of strong lensing events.

3.6.1.4 *Spitzer data*

Spitzer IRAC data were obtained from the public archive using the Spitzer Archive interface; Leopard. The data were downloaded in the form of enhanced cBCDs (corrected basic calibrated data), which are the standard pipeline level 1 output, with the artefact correction for muxstripe, muxbleed and column pulldown[1] already applied. The data were combined using the software MOPEX [Makovoz & Khan, 2005] following the standard instructions that can be found on the *Spitzer* website[2]. The software stacks the cBCDs, with the appropriate bad pixel masks, to create mosaics of the signal, the coverage and the noise maps for each channel. A median filtered sky subtraction was also applied to the signal cBCDs. The IRAC mosaic coverage consists of two contiguous square areas of $\sim 8' \times 8'$, one of which is centred on the A2218 core. The full areas of the Ch1 and Ch3 data overlap (Area A) as do the areas of Ch2 and Ch4 (Area B), however Area A and Area B only overlap by one of the contiguous squares.

3.6.1.5 *AKARI* data

As well as the primary L15-data, AKARI IRC S11 data [Ko et al., 2009] was included in the data set, although only the central region of the image is usable due to a particular noise issue experienced during part of the AKARI mission (as reported in the IRC-DUM) and fewer pointings toward the edges. Figure 3.6 indicates the region included in the counterpart identification and band-merged catalogue.

3.6.2 Cross-matching

A band-merged catalogue was constructed by cross-matching the L15 source catalogue with the multi-waveband data in order to provide positional priors for the subsequent de-blending and to provide photometric data points for the SED of each L15 source.

The cross-match was performed in two stages. For each additional wavelength a centroid search was performed to identify possible counterparts. The search was carried out iteratively within concentric circular areas of increasing radius, each centred on the L15 source and up to

[1] These are all artefacts that effect full columns or rows of an image as a consequence of a bright object or cosmic ray in the FOV causing the saturation of one or more pixels.

[2] http://ssc.spitzer.caltech.edu/postbcd/irac_reduction.html

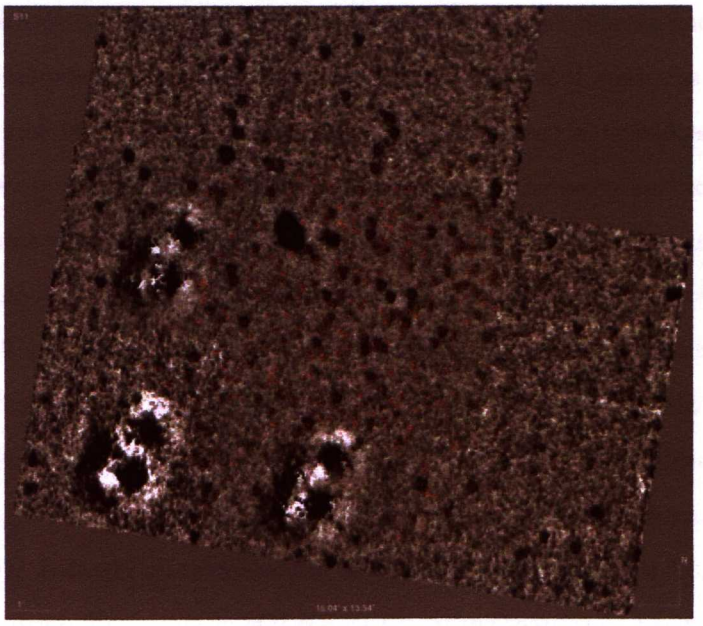

Figure 3.6: *AKARI*/S11 image of Abell 2218. The yellow circles roughly indicate the overlap with the L15-image and the red circles show the extraction area, which make up the S11 counterpart catalogue before any reliability checks were performed.

a limiting radius of 1.5σ of the L15 FWHM ($3.8''$). A maximum of three peaks were recorded per L15 source, retaining the three closest peaks to to the L15 position if more than three were identified. A distinction was made between a search that found no peaks (assigned a rank 0) and a null-search, where the L15 centroid lay outside of the image area (assigned a rank -1). To ensure the maximum number of potential counterparts progressed through to the second stage of cross-matching, all rank 0 positions were visually inspected for missed counterpart candidates. If one (or more objects) could be detected by eye, within the maximum contour, then it was added to the list of possible candidates (figure 3.7).

A cross-comparison of all available wavebands was then performed for L15 sources with potential counterparts. At each available (non-null) wavelength, a $30'' \times 30''$ postage stamp image was plotted and overlaid with the possible counterparts for that source and the surrounding area. A visual comparison of the multi-waveband stamp strips for each L15 source allowed the most likely counterpart or multiple counterparts to be chosen and re-centred where necessary. During this comparison additional L15-sources with clear L15 emission and multi-wavelength counterparts were also identified. Viewing the progression of a source through all available wavebands

minimises the wrong identification of L15-counterparts. Although the optical data provides the highest positional accuracy, it is common for a source identified as a potential optical counterpart to be, on closer inspection of the IRAC data, an unrelated faint optical source (e.g. figure 3.7). The automation of this cross-matching process would be time saving, possibly by identifying counterparts per image in order of decreasing wavelength, but due to the sampling of redshifted PAH features for star-forming galaxies there is no clear pattern of best counterpart images and a method of searching by eye appears optimum. Due to the relatively small number of sources to check and the aim of a robust band-merged catalogue, the counterparting was performed by eye once the initial IDL search was completed. During the multi-wavelength comparison, two or more additional counterparts were identified for any blended source. Approximately one third of all the L15 $5\,\sigma$ source were identified as photometrically blended, which was defined as individually extracted L15-sources within 2 L15-FWHM of any neighbouring L15 source (which was considered to significantly affect aperture photometry) or a single source that had been assigned multiple counterparts.

3.7 Photometry

3.7.1 Aperture photometry

Photometry were acquired for all sources identified as counterparts. The HST photometry were obtained from the published catalogue of Smail et al. [2001b]. For the remaining data aperture photometry were taken and a growth curve correction method was used to derive aperture corrections [Howell, 1989; King, 1971].

3.7.2 Growth curve correction

The growth curve method assumes that the PSF does not vary with position or brightness within an image. For each monochromatic image aperture photometry were taken for well separated bright sources (where possible), with concentric apertures of increasing radius. The resulting photometry is plotted for each selected source as a growth curve – flux density as a function of radius normalised to a maximum of unity – thus describing the fraction of flux within a given aperture. It is necessary to examine each growth curve and reject those without a characteristic or smooth curve. The surviving photometry were used to construct mean growth curves.

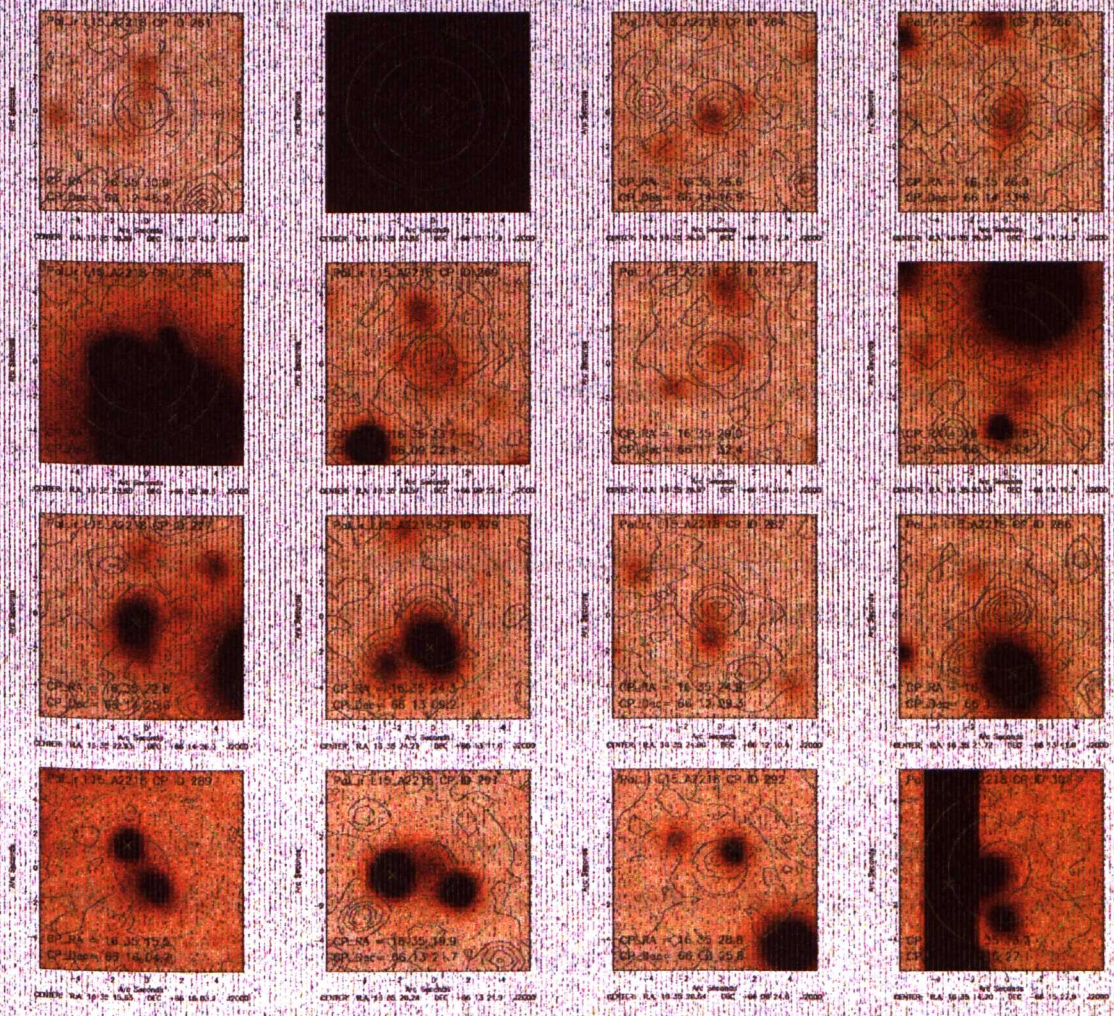

Figure 3.7: Palomar i'-band postage stamps, centred on L15 sources and overlaid with the contours of the L15 image (grey) and concentric search areas for the initial counterparting process. Potential counterparts are assigned a rank of 1 if identified within the smallest radius, a rank of 2 if between the first and second radii, a rank of 3 for the final annulus and a rank of 0 if outside of the defined search regions. Here there are examples of identified nearest neighbour counterparts that are either degenerate with another source at a similar distance (bottom left panel) or further from the L15 positions than a fainter i'-band source (panel 11) subsequently shown to be the more likely counterpart at longer wavebands. These examples illustrates the need for multi-waveband cross-comparison to maximise the probability that the correct counterpart is identified. For the sources shown in the second stamp from the left on the bottom row, comparison at longer wavelengths showed neither of the bright optical sources are linked to the central L15 source, which is bright at IRAC wavelengths.

The multiplicative aperture corrections are given as the reciprocal of the mean growth curve, with associated uncertainties estimated from the standard deviation of the photometry. For the near-infrared and optical data the images were better represented by two growth curves, one for point-like sources and one for elliptical sources. In these cases there are two distinct characteristic profiles of growth curves and so two mean growth curves can be constructed, using the method described, to give two sets of aperture corrections.

The S11 photometry were obtained after a comparison of the aperture corrections derived from the growth curve and the official AKARI S11 aperture corrections[1] showed an agreement within $\sim$ 5%. The photometry was taken with an aperture radius equal to the S11 FWHM (6.55″) and the corresponding aperture correction, derived from the growth curve, was applied.

The aperture corrections derived from the growth curves for each of the four IRAC bands agreed with the published IRAC aperture corrections[2] within 10%. The published values for an aperture of 2.44″ and sky annulus of radii 14.6″ and 24.4″, were used for the aperture photometry of each IRAC channel.

For the remaining data the growth curve aperture corrections were applied. During the mean growth curve construction and refinement process, the corresponding SNR growth curve was also calculated using the cumulative aperture photometry and associated propagated errors. The SNR growth curves were also normalised to a maximum of 1. An optimum SNR radius was chosen for each curve, where the curve approached the maximum. The sources used to build the mean growth curve were assigned the respective optimum aperture radius. However due to the crowded nature of the A2218 field, this radius was not applicable to all counterpart sources for a given image. Each source, not contributing to the mean growth curve, was plotted and overlaid with circular contours of possible radii available for aperture photometry. In this way it was possible to choose a radius for each source as near to optimum, whilst avoiding contamination from nearby sources.

[1] http://www.ir.isas.jaxa.jp/AKARI/Observation/DataReduction/IRC/
[2] http://ssc.spitzer.caltech.edu/irac/iracinstrumenthandbook/32/

Once an aperture radius and correction were assigned for each counterpart in each image, aperture photometry were taken using APER in IDL. For the S11, IRAC and MIPS24 data a straight forward conversion to flux density units was possible. The units of the S11 image are ADU and can be converted to μJy using the IRC-DUM conversion factor of 0.714 for a radius of 2.5 pixels. Each Spitzer map has the units of MJy sr^{-1}, which can be converted to μJy using the respective pixel area after converting to arcseconds squared. See table 3.1 for the full list of conversion factors. For the remaining wavebands the instrumental magnitudes were taken for up to 200 sources per counterpart catalogue. These magnitudes were converted to flux densities using on-line calculators[1], and flux density conversion factors were then derived by comparing the obtained flux densities and the equivalent aperture photometry in pixel units. These conversion factors were applied for all further photometry for the band-merged catalogue. A comparison of the Ks-band corrected aperture photometry and the published values [Smail et al., 2001b] were in good agreement, with differences $< 3\%$.

3.7.3 L15 aperture photometry and aperture correction

Due to a lack of L15 sources that are relatively bright and well separated, a slightly different approach for deriving the L15 aperture corrections was taken. To facilitate the selection of L15 sources with uncontaminated profiles, an empirical PSF was constructed using L15 standard star observations (figure 3.8). The stars were combined to give the empirical PSF corresponding to a single pointing. To best represent the L15-image, 19 versions of this PSF were taken and rotated to match the rotations applied to the L15 frames during their alignment. The growth curve for the resulting PSF was used as a guide for selected L15 sources with minimal blending. The final mean growth curve is shown in figure 3.9. Even with the standard star guide, the number of sources suitable for selection remained low and therefore the aperture corrections derived is heavily dependence on the choice of source. For three different selections of sources the variation in the corrections derived (for an aperture of the L15-FWHM) was $> 20\%$, therefore the results for the growth curve correction method were not used for the L15-image. Instead, an empirical PSF was used, and for the final photometry catalogue all aperture photometry for the L15 sources was removed in favour of the ALLSTAR PSF fitted photometry (see section 3.7.5).

[1] e.g. the NICMOS unit conversion form: `http://www.stsci.edu/hst/nicmos/tools/conversion_form.html`

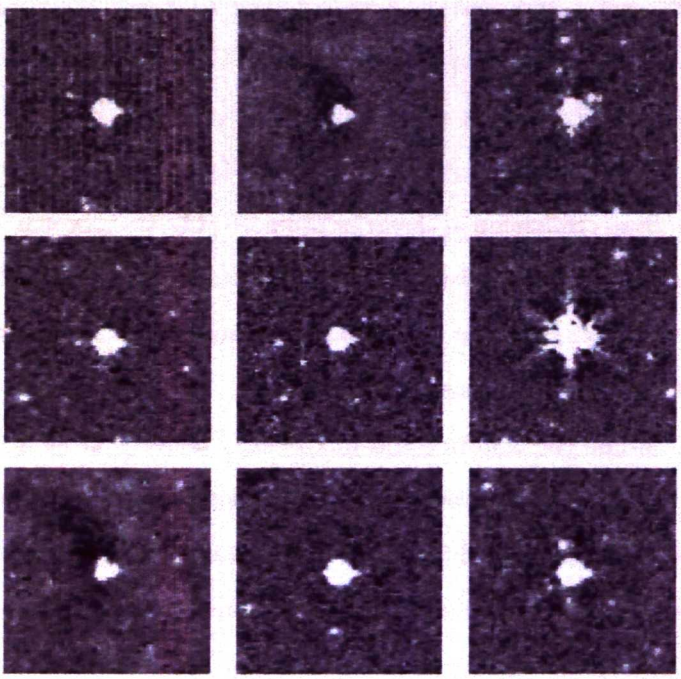

Figure 3.8: AKARI L15 standard stars used to construct the standard star PSF. A single PSF was built from eight of the nine stars (panel 6 was excluded), and orientated to match the L15-A:1 reference frame. 18 additional copies of the PSF were then rotated to match the remaining L15 frames and combined to represente the PSF of the final L15-image.

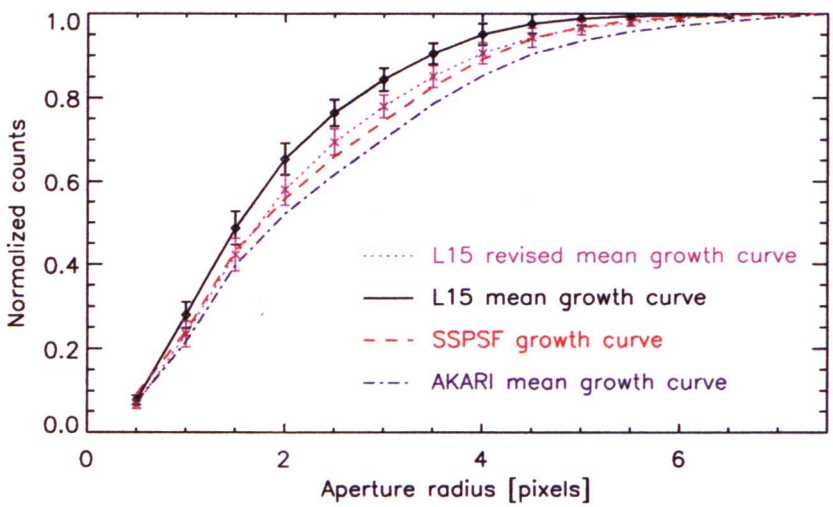

Figure 3.9: The initial mean L15 growth curve (black line) with 1σ errors in comparison to the aperture corrections provided by JAXA (AKARI mean growth curve) and the standard star PSF growth curve (SSPSF growth curve). The SSPSF growth curve was used as a guide to reconstruct the L15 mean growth curve (L15 revised mean growth curve).

3.7.4 Empirical PSF

Constructing a reliably representative empirical PSF from a confusion limited image is challenging (as already illustrated by the L15 growth curve construction). Ideally a PSF should be assembled using only high SNR sources, which are well separated from any neighbours. For the L15-image there are no sources that completely satisfy these criteria, therefore as many reasonably bright, reasonably well separated sources as possible were selected in order to statistically reduce noise in the PSF's tail. The DAOPHOT packages PSTSELECT and *PSF* (defined in italics for clarity) were used to select the L15 sources and build the L15 PSF. The output from these packages is a PSF with a physical component, from the combination of the selected sources, and an analytic component that describes the best fitting function to the PSF light profile. Each input source is weighted by its SNR and therefore adding fainter sources is possible without degrading the final SNR of the PSF. For a spatially varying PSF (e.g. such as the L15-PSF before the L15-image was corrected for distortion, as described in section 2.5) sources should be selected over the full area of the image where possible. For a non-varying PSF this is not as important, therefore allowing only the most suitable sources to be chosen. The available functions used to construct the PSF are

- 1. Gaussian, with the x and y half-width half-maximums as two free parameters
- 2. Moffat15, Moffat25, with an additional free parameter of the major axis position angle

$$f(x,y) = \alpha \frac{1}{(1+z^2)^\beta} \tag{3.1}$$

  where $z^2 = \frac{x^2}{\alpha_x^2} + \frac{y^2}{\alpha_y^2} + \alpha_{xy} xy$ and $\beta = 1.5$ for Moffat15 and $\beta = 2.5$ for Moffat25
- 3. Lorentz
- 4. Penny1 and Penny2, which are two component functions with a Gaussian core and Lorentzian wings (with a β parameter of 1.0). The difference between the first and second version is the constraint on the tilt of the two components.

No prior was imposed on the choice of function, allowing *PSF* to find the best fitting function from the functions listed above. A radius of 7.5 pixels ($18''$) was selected for the PSF based on

the full flux radius reported in the IRC-DUM and the radius derived during the growth curve construction. To avoid contamination from neighbouring sources this radius was intially set to a lower value (5.0 pixels) and then increased for the final PSF construction.

The first task for PSF construction is PSTSELECT, which required an input of the L15-image and a source/photometry catalogue in the form of the aperture photometry package PHOT output. In this case PHOT aperture photometry were taken for all the sources in the band-merged catalogue with an aperture radius equal to the L15 FWHM and a sky annulus of radii 8.5 and 14 pixels. PSTSELECT was used to manually select suitable candidates (with minimal photometric blending) for the PSF construction. The output from PSTSELECT is a list of source IDs (corresponding to the PHOT input IDs), xy coordinates, instrumental magnitudes and sky estimate in counts for the accepted candidates. The PSF can then be built using *PSF* from the PSTSELECT output catalogue.

An iterative method was applied to refine the L15-PSF following a similar method to that outlined in the appendix of the DAOPHOTII user manual [Stetson, 2000]. A residual L15-image was created with ALLSTAR, which requires the full PHOT photometry file input, the L15 image and the current PSF image. The full catalogue was subtracted and the residual image examined to assess how well the sources are subtracted, looking for systematic problems that could indicate the PSF is not representative of the L15-map. If the examination showed the L15 source catalogue was unsatisfactorily subtracted, then a second fitting was performed to subtract only the PSF sources. This second residual was used to pinpoint any source contributing to the PSF that could be responsible for the overall poor subtraction, by looking for obvious differences e.g. a reversed or oddly shaped residual. Any clearly offending sources were removed from the list and the PSF construction was repeated, starting at the *PSF* stage. This process of refinement was iterated until a satisfactory residual was achieved. In order to produce a cleaner PSF tail, the PSF source neighbours were subtracted and the PSF was reconstructed from the resulting image this time using the full PSF radius of 7.5 pixels. The final PSF (see figure 3.10) was constructed from 18 sources and the best fitting function was a Penny2, although the difference in χ^2 to the Penny1 function was $< 0.1\%$ and within $\sim 1.0\%$ of the best fit Moffat25 function.

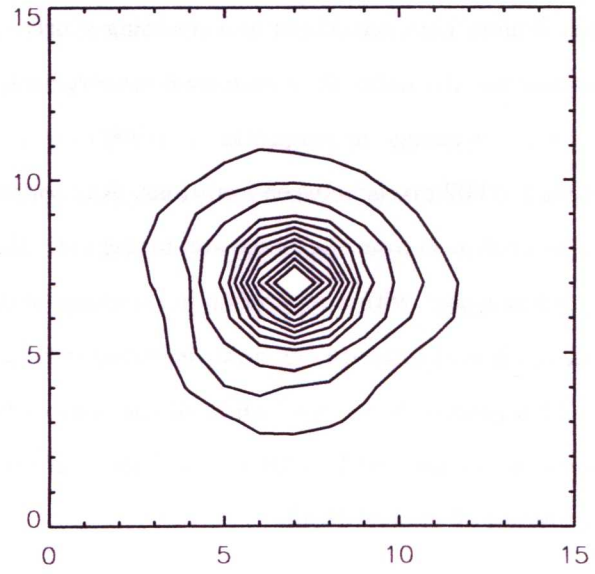

Figure 3.10: Final empirical L15-PSF (axis are in units of pixels). To construct the final PSF with a radius of 7.5 pixels (18′), 18 L15-sources were used from the L15-image after the neighbouring sources had first been subtracted. The aspherical shape indicates that the L15-A data dominates the profile.

3.7.5 PSF fitted photometry and de-blending

Many of the L15 5σ catalogue members are blends of two or more sources making aperture photometry an unsuitable method for recovering the L15 flux densities, therefore PSF fitting was performed to gain the photometry. The final empirical PSF and the positional priors from the band-merged catalogue were used as inputs to DAOPHOT's ALLSTAR package to CLEAN [Högbom, 1974] the-L15 map. A fitting radius of the L15 FWHM was chosen and ALLSTAR was allowed to re-centre the sources.

The basic ALLSTAR iteration follows the path of dividing the input sources into groups (this is purely to increase the computational speed) based on their location, brightness and separation; simultaneously performing a non-linear least χ^2 of the PSF to each source using the defined fitting radius (r), where each pixel is assigned a weight $\propto \frac{1}{r^2}$ based on the information supplied in the DATAPARS file and the error criteria parameters in the DAOPARS parameter file; subtracting all of the sources from the map using the current estimates for brightness, posi-

tion and sky; recalculating these estimates after five iterations (and then every subsequent five iterations) to check which sources have converged and rejecting sources that have fallen below the minimum SNR requirements. To qualify for a successful convergence, the version of the PSF fitted to a source must not see a change in magnitude > 0.0005 (or > 1.0 SNR) or a shift in the source centroid position > 0.002 pixels between iterations. Any source that has converged is written to the output file and removed from the image and fitting list. Also the faintest source in a group or the fainter source of a pair, with a separation in the range of 0.37 FWHM – FWHM, is rejected after the fifth, tenth and fifteenth (or final) iteration if it has a SNR < 1.0, < 1.5 and < 2.0, respectively. This process is repeated until all the sources have converged or been rejected. Figure 3.11 shows the cleaned ALLSTAR residual after an early PSF construction in comparison to an earlier version of the L15-PSF.

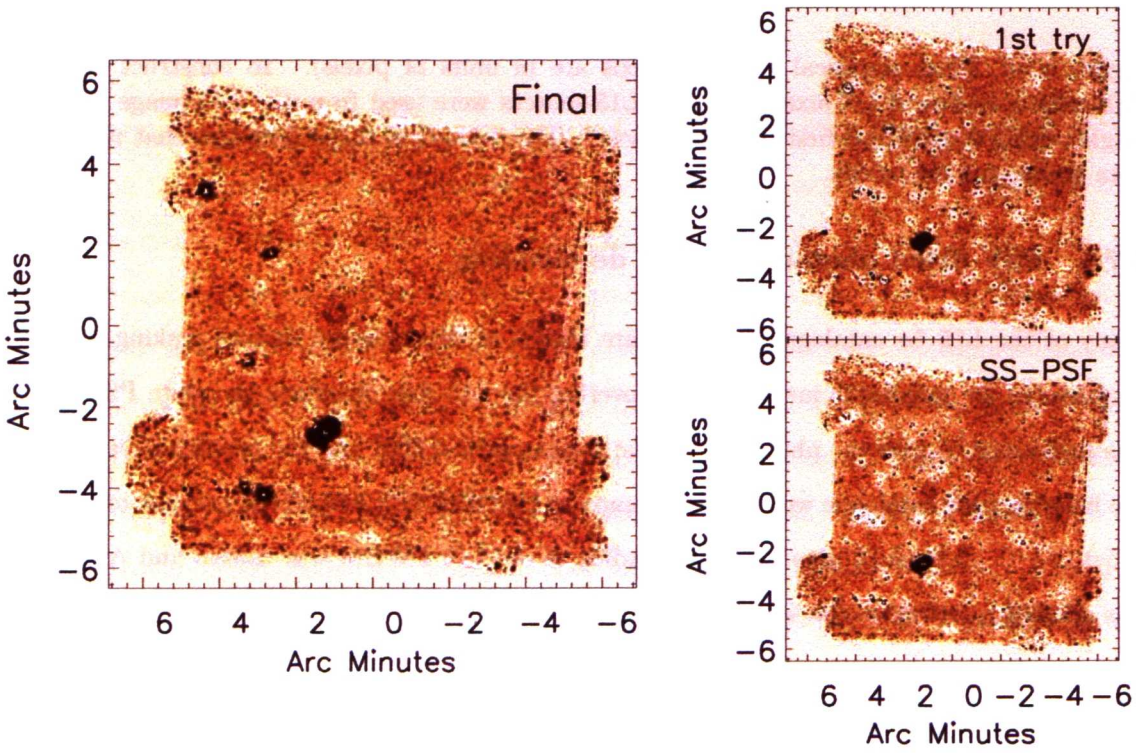

Figure 3.11: Left: Final ALLSTAR cleaned L15-image. The pronounced bright residuals (black areas) can be associated to partially resolved cluster members and foreground objects. The large-scale structure remaining is mainly residual sky structure (compare to figure 2.17). Right top: The first ALLSTAR result for the L15-image. The iterative refinement of the PSF led to a more satisfactory final subtraction. Right bottom: best ALLSTAR residual using the standard star PSF.

The source catalogue extracted by PSF fitting was cross-matched with the L15 5σ catalogue in order to assign the original ID of any blended sources to the brightest member of the de-blended component sources. Also the cross-match was used to ensure all non-blended sources retained the previous 5σ ID. All additional sources were assigned new IDs. After the PSF fitting the number of sources in the catalogue had increased by 56% from 588 to 919. As $\sim 1/3$ of the 5σ sources were categorised as photometrically blended during the multi-waveband crossmatch, this increase predicts that each blend contains an average of 2.7 sources, thus showing the importance of de-blending in order to recover sources from photometric confusion.

3.7.6 Photometry investigation

3.7.6.1 The L15-catalogues

Three main versions of the L15 source catalogue have been used to take photometry at different stages of the L15 data reduction and analysis: the initial 5σ DAOFIND catalogue; the ALLSTAR catalogue; and a version which combines aperture photometry for the sources classified as not significantly photometrically blended, from the DAOFIND catalogue, and the remaining sources from the de-blended catalogue. The flux density distributions for all three catalogue versions are given in figure 3.12. This comparison of the resulting photometry distributions shows the expected increase in lower values for an increased number of de-blended sources. It also shows that the sources in the 5σ catalogue not classed as significantly blended are affected by photometric confusion. The prediction that 1/3 of the L15-5σ sources are blends unsuitable for aperture photometry were tested by comparing aperture photometry and PSF fitted photometry (figure 3.13). The aperture photometry of blended sources showed systematically greater flux densities to the PSF photometry in comparison to approximate 1:1 agreement seen for the non-blended sources, in agreement with the classifications.

3.7.6.2 Matched filtering

A common method to obtain sub-mm photometry is to convolve the signal map with the PSF to produce a map that should be optimal filtered for point-source extraction (e.g. see Serjeant et al. [2003] and Appendix B, section B3.8.1). Each pixel in the resulting map represents the total flux of the best fit PSF. This method relies on the assumption that the sources within the data

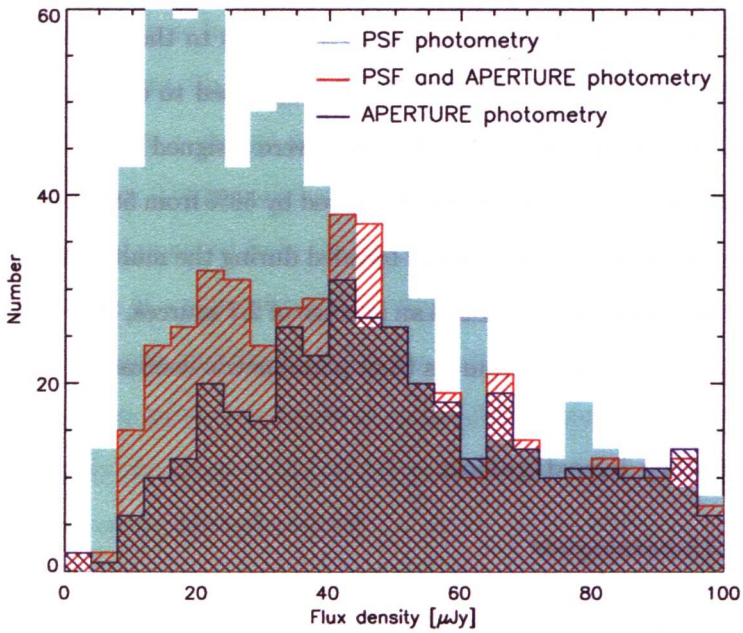

Figure 3.12: Flux density distributions for the L15 5σ aperture photometry catalogue (blue hashed), aperture photometry plus PSF-fitted photometry (red hashed) and PSF-fitted photometry only (cyan filled). The aperture photometry were taken for L15-sources categorised as not photometrically blended. The fully de-blended distribution (cyan filled) has a lower median in line with expectations.

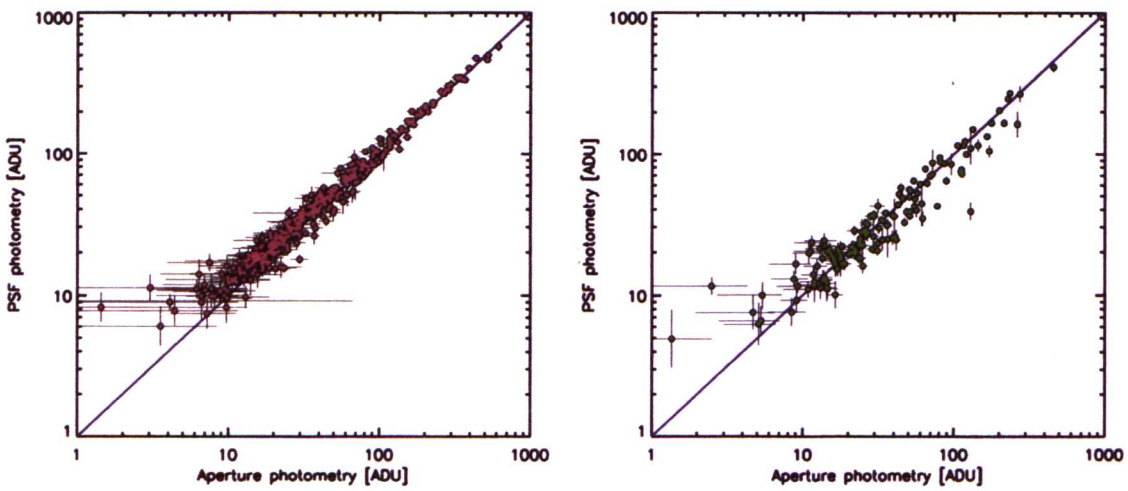

Figure 3.13: PHOT aperture photometry vs ALLSTAR PSF photometry for L15 5σ sources classified as photometrically blended (right) and those classified as suitable for aperture photometry during the multi-waveband crossmatch (left). There is the expected 1:1 agreement for the non-blended sources and a significant aperture photometry overestimate for those classed as blends.

are point-like and minimally blended, which does not describe the L15-data and sources well. In figure 3.14 aperture photometry of the L15-5σ sources that have low photometric blending are plotted in comparison to the best fit flux (obtained using an IDL routine developed for the point source extraction of SCUBA data) and shows a good agreement for bright sources, which must necessarily have high SNR. For fainter sources the best fit flux gives greater estimates, which support the unsuitability of this method for taking the L15-photometry, however performing a 5σ source extraction from the resulting best fit flux map produced a marginally greater number of sources $\sim$ 5% extra in comparison to the equivalent extraction with DAOPHOT (after edge source removal). As the necessary assumptions for this method do not hold true for the L15 data these additional sources were not included in the L15 source catalogue.

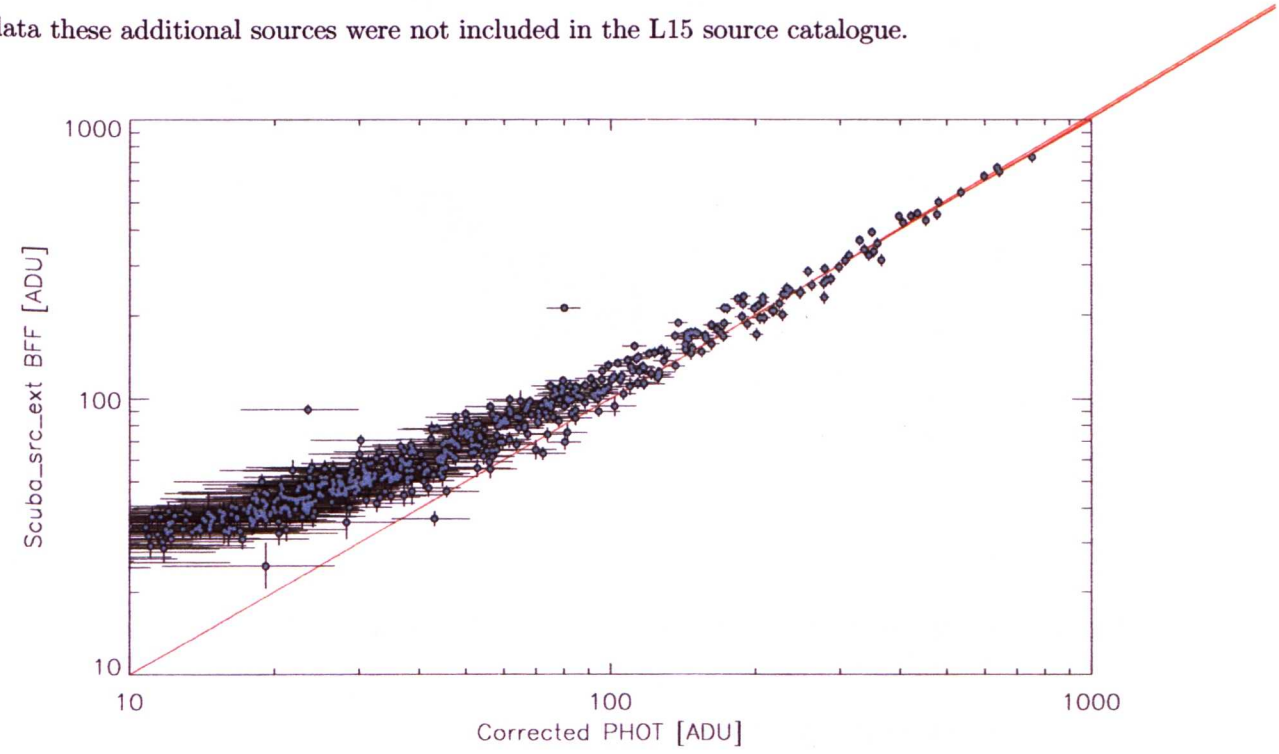

Figure 3.14: Corrected PHOT aperture photometry vs best fit flux photometry. There is a clear systematic disagreement for the fainter 2/3 of the sources. This can be explained due to the assumption of negligible blending for the matched filtering method used to obtain the best fit flux.

3.7.6.3 ISO comparison

During the investigation into the distortion correction (see section 2.5) aperture photometry were taken for the L15-5σ sources in both half images, constructed from the intermediate re-

duced L15-A and L15-B frames. The comparison of the resulting photometry (figure 3.15) shows a large discrepancy between the two halves. The cause of this difference was found to be mainly due to the subtraction and remnants of scattered light that affects the L15-B data more strongly.

In order to check if this discrepancy translates to the final L15 flux densities a comparison was made with the Metcalfe et al. [2003] ISOCAM source catalogue of A2218. A general agreement was found between the two catalogues within the 2σ errors (figure 3.16) suggesting that the problem has been resolved in the final catalogue.

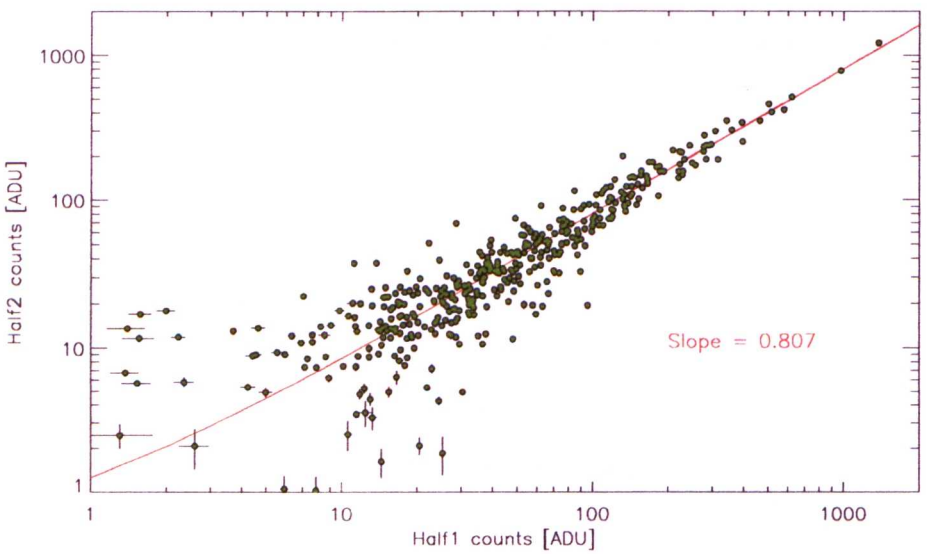

Figure 3.15: Aperture photometry taken for the L15-A combined image (Half1) and L15-B combined image (Half2), in pixel counts. There is a difference of $\sim$ 20% between the two sets of photometry, possibly attributable to the weaker PSF in the Half2 image that results from the high levels of low-frequency sky noise.

3.7.6.4 Palomar i-band

There have been several studies of the cluster members of A2218 [e.g. Jørgensen et al., 1999; Sánchez et al., 2007; Ziegler et al., 2001]. The A2218 catalogue was crossed matched with the cluster members of Ziegler et al. [2001], which were selected in the A2218 Palomar i-band image. Only seven sources were common to both catalogues, illustrating the difference between optical and MIR selections of early type galaxies. There was found to be a large ($> \times 10$) unexplained discrepancy between the i-band photometry of Ziegler et al. [2001], which was registered onto

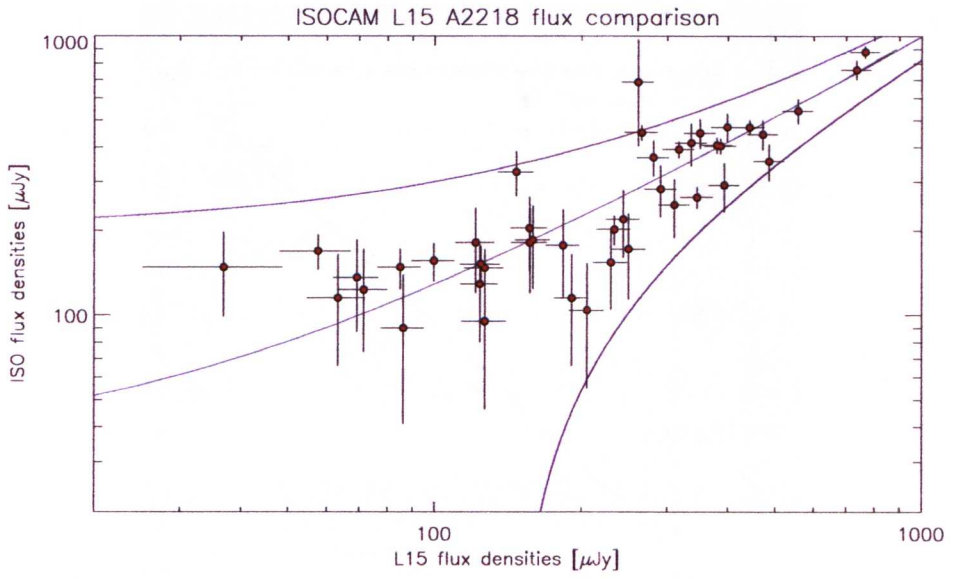

Figure 3.16: L15 and ISOCAM flux densities for sources common to the L15 source catalogue and the ISOCAM sources of Metcalfe et al. [2003]. The 2σ scatter is indicated with the purple lines. A linear fit (blue line) gives a slope of 0.96, which showing an approximate 1:1 agreement within the errors. There is not a systematic deficiency in the L15 source flux predicted by the comparison of the L15-A and L15-B half image photometry.

the I-band Johnson/Cousins magnitude system. So an alternative comparison was made with the *HST*/WFPC2 F775W flux densities of Sánchez et al. [2007], as this is the next closest available band in wavelength. Postage stamp images of each matching cluster member with the photometry comparison is given in figure 3.17 and although the number of matches is not statistically robust, there is a general agreement for the unblended sources.

3.8 Sensitivity

3.8.1 L15-image sensitivity

The depth of an image can be estimated by the point source sensitivity (although this is possibly better described as an estimate of the depth relative to the associated analysis). The sensitivity can provide an approximate flux limit, down to which sources can be reliably extracted. To estimate the L15-5σ sensitivity, aperture photometry were taken at random positions over the L15-map, excluding only the edges and a 40″ radius circular area centred on source A (figure 3.18). A histogram of the resulting aperture photometry, corrected to total flux densities, was

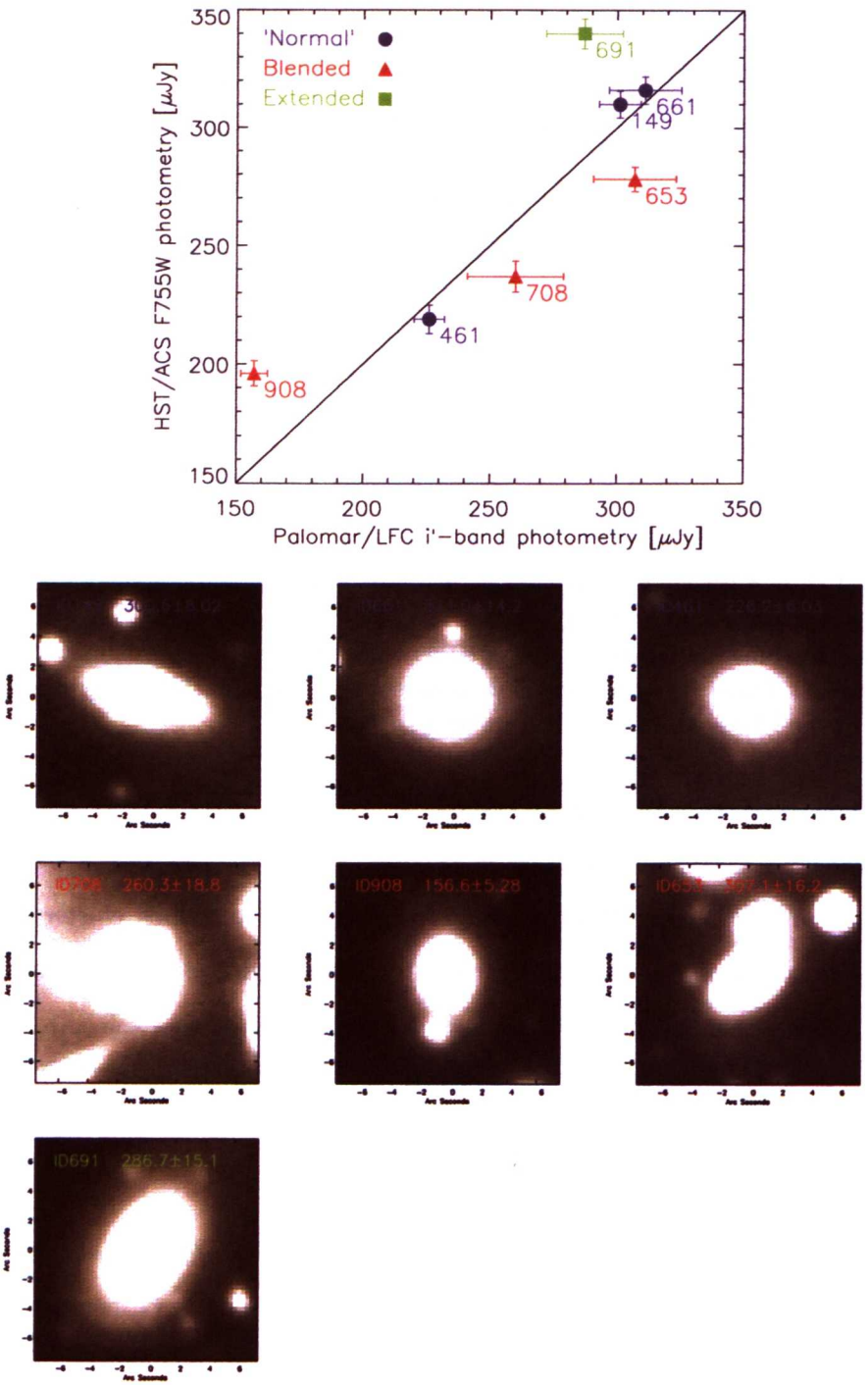

Figure 3.17: Comparison between the *HST*/ACS F755W photometry of Sánchez et al. [2007] and the band-merged Palomar i-band corrected aperture photometry. For sources classed in the L15-image as non-extended and non-photometrically blended, the comparison is good within $\sim$1 σ.

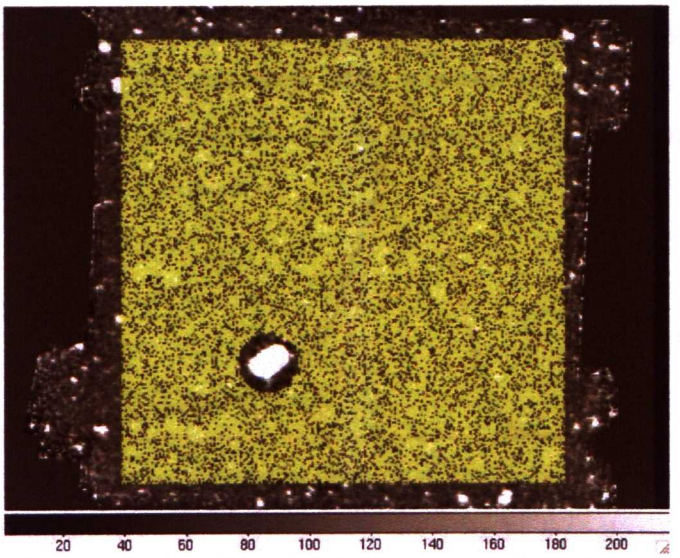

Figure 3.18: The allowed area used for random position aperture photometry for the L15 $5\,\sigma$ catalogue point source sensitivity estimate (yellow area). The edges of the map and the area around the brightest source out to a radius of $40''$ from its centroid are excluded.

fitted with a Gaussian of standard deviation $8.33\,\mu$Jy giving a 5σ sensitivity of $41.7\,\mu$Jy (figure 3.19). A second sensitivity was estimated, to represent the de-blended L15 photometry, by comparing the input and output photometry for artificial sources added to the L15 image. Random flux densities were generated within the L15 de-blended flux density range, and assigned to random positions within the area defined for the previous estimate. Artificial sources were added to the L15-map using the empirical L15-PSF. The output flux densities were obtained using the same PSF fitting method as for the real sources. Up to 40 sources were added to the L15 map per run, until photometry for around 1000 sources had been taken. Figure 3.20 gives a comparison of the input and output photometry. The standard deviation of the flux density distribution was used to derive a $5\,\sigma$ de-blended sensitivity of $28.73\,\mu$Jy. The improvement in sensitivity seen for the PSF fitted photometry reflects the greater depth that can be achieved via de-blending.

3.8.2 Upper limits

Sensitivity limits for the band-merged catalogue were derived in order to estimate upper limit, which give a level above which there is a reasonable expectation that a source will be detected.

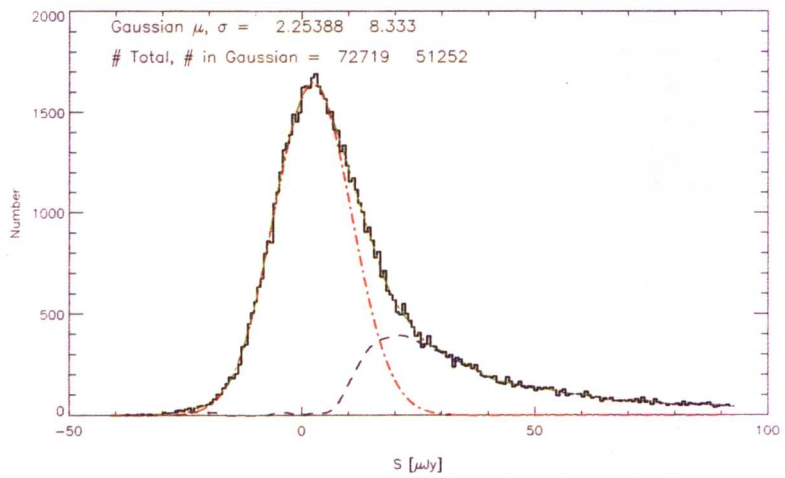

Figure 3.19: The distribution of aperture photometry, corrected to full flux densities, taken from random positions within the area indicated by yellow in figure 3.18. A polynomial was fitted to the full distribution (green dash-dot-dot line) and a Gaussian was fitted to the central distribution using a robust mean to remove the outlying tail (red dash-dot line). The residual between the two fitted curves is given by the blue dashed line. The residual represents the bright sources within the map, which give the distribution its asymmetrical bright tail. The best fit Gaussian gives a 5σ sensitivity of 41.7 μJy.

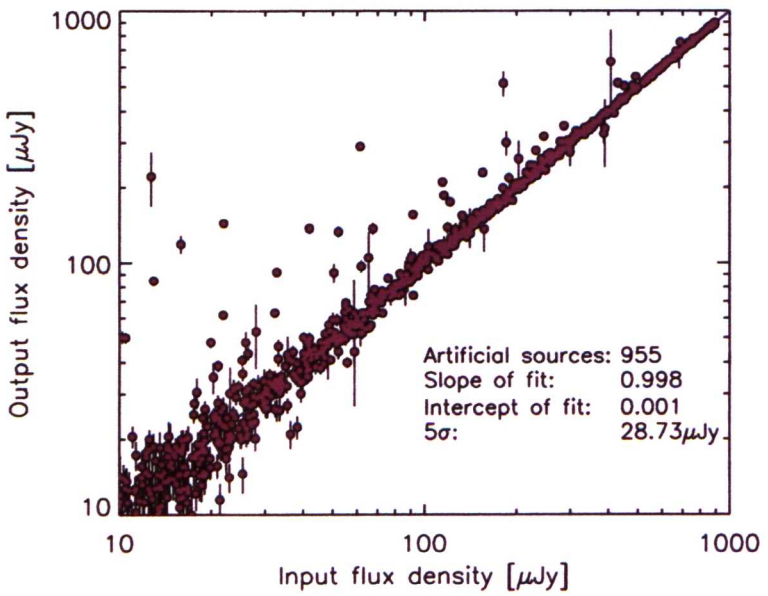

Figure 3.20: Input vs output flux densities for artificial sources randomly assigned flux densities, over the range of the L15 de-blended sources and randomly placed in the L15-map. Up to 40 sources were added to the L15-image for each set of photometry giving a total of 955 artificial sources. The standard deviation of the flux density distribution was used to derive the 5σ sensitivity of 28.7 μJy.

Upper limits for the S11, INGRID, Palomar, IRAC and MIPS24 images were derived from the standard deviation of the sky for each image. The resulting 1σ background fluctuations were scaled by the respective PSF, normalised to a peak of 1 to give the point source sensitivity. See table 3.1 for the 5σ upper limit estimates.

3.9 Completeness

3.9.1 Monte Carlo completeness test

The completeness for a source catalogue is defined as the fraction of real sources extracted from the actual number of real sources in the data, as a function of flux. Sources extracted at fainter flux densities will have lower completeness levels in comparison to brighter sources, and so a correction needs to be applied to account for the missing fraction of sources at each flux level. The two L15-source catalogues have different levels of completeness, due to the different methods used to compile them, and so two Monte Carlo completeness test were performed in order to derive completeness corrections for the L15 5σ source catalogue and the L15 PSF source catalogue. The method for the 5σ catalogue is commonly used for this type of test, and involves randomly adding artificial sources to a map and running the source extraction and photometry algorithms used on the actual data. This replicates the level of completeness seen in a catalogue and, as the actual number of sources added is known, it gives a means to calculate the resolved fraction.

3.9.2 Completeness test 1: L15-5σ source catalogue

The flux range of the 5σ catalogue was used to define 80 contiguous logarithmically spaced flux bins. Random positions were generated with a separation of at least 11 pixels from any known L15 5σ source position, and 11 pixels from all other randomly generated positions. The minimum separation was derived using the pixel values for several sources, plotted as a function of radius (figure 3.21) and taken to be twice the distance where the pixel values have decreased to the level of the noise plus one pixel. This separation was chosen so the artificial sources were not affected by flux of known sources or self-confusion with other sources being added for the same run. Randomly generated flux densities were then assigned to each random position for each flux bin. Artificial sources were added to the L15 image by convolving the random

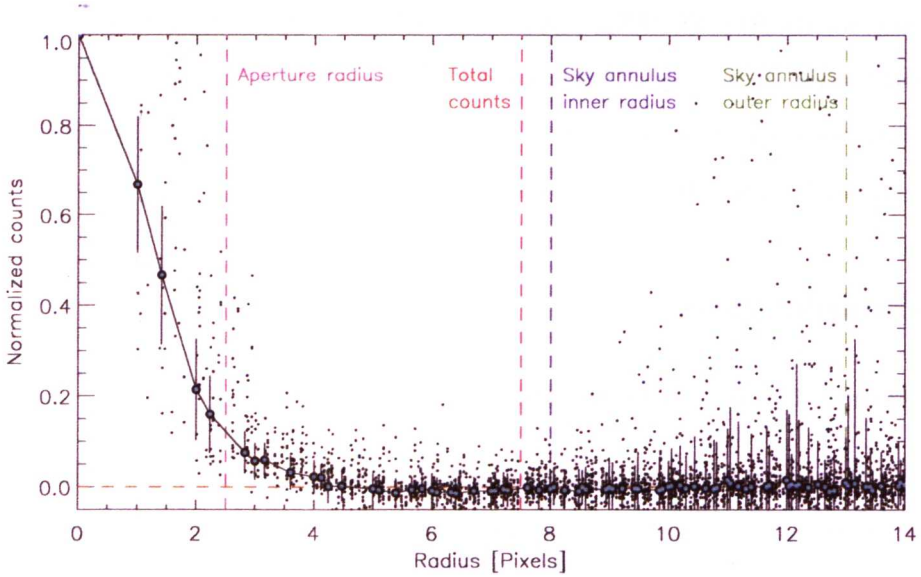

Figure 3.21: Plot of pixel values as a function of radius for the sources used to construct the L15 growth curve. The total pixel counts (red dashed line) mark the radius within which the IRC-DUM predicts that the total flux density has been taken for L15 data. The pixel values have roughly decreased to the level of the background noise at around a 5 pixels (12″) radius, therefore two sources with centroids > 10 pixels can be reasonable defined as having negligible photometric influence on each other.

flux densities with the empirical L15-PSF at the assigned random positions, which produced one artificial image per bin with up to 40 added sources per run (figure 3.22). For each image created, a source extraction was performed down to a $5\,\sigma$ level with DAOFIND, maintaining the same parameter settings used for the real L15-source extraction. Aperture photometry was taken for the resulting source catalogue, again maintaining the same settings as used previously. An artificial source was deemed successfully recovered if the extracted position was within a two pixel radius (4.8″) of the input position, which is approximately 2σ of the L15-FWHM, and the recovered photometry were within 50% of the original photometry. The test was repeated until around 20000 sources per bin were achieved.

3.9.3 Completeness test 2: L15-deblended source catalogue

For the second completeness test the same basic method was used, but adapted to represent the PSF fitting of a blended environment. The main difference between the tests was a change to the separation criteria for the random positions and known sources. Whereas for the $5\,\sigma$ sources the separation was set to avoid photometric confusion, for the de-blended sources this photometric

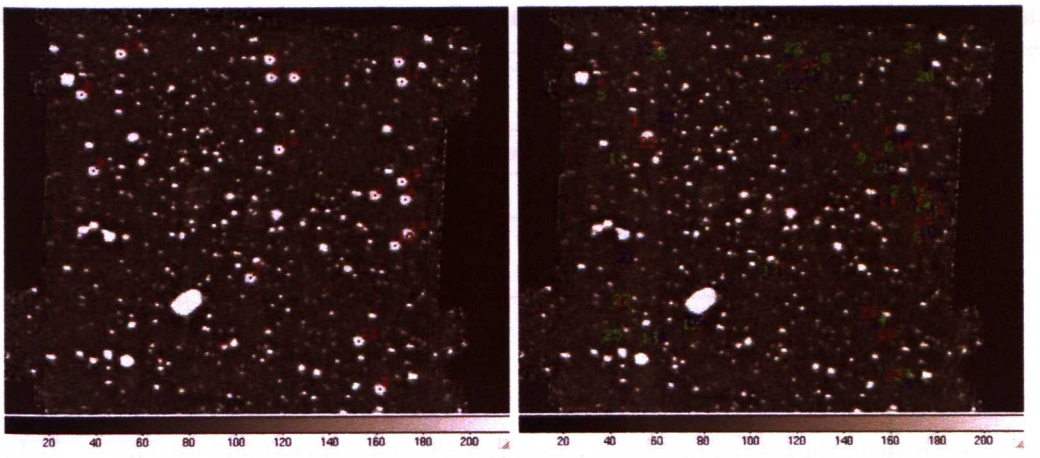

Figure 3.22: Left: an example of the artificial sources added for completeness test 1, indicated with red dots and numbers. The added sources were assigned flux densities from within one of the brightest flux bins (mid bin value of $\sim$1250 μJy) so the positions could be clearly seen. Right: the positions for three separate completeness runs are shown on the L15-map. The colour of the numbers indicate a single run. There is only a limited area within which an artificial source can be placed due to the separation criteria and crowded field, therefore out of 40 positions generated per run only $\sim$20 sources are finally added. The consequence of this could be a bias on the results due to an incomplete representation of the full map area. A second option would be to artificially generate a full map, but the additional cumulative uncertainties were estimated to be greater than those seen in the tests performed, especially due to the varying sky.

blending is a necessary component when trying to recreate the blended environment for the PSF fitting. The level of confusion given by the number of sources per beam for the L15 image (see section 3.5) was used to dictate the number of artificial sources to be added per run. Input positions continued to be randomly generated and separated from known 5σ source positions, although this limiting separation was reduced to eight pixels ($19''$) so the level of blending could be moderated. The known source positions were limited to those in the $5\,\sigma$ catalogue only, to provide a reasonable area to run the test. To ensure the number of sources added to each run provided the desired level of confusion, all the available pixel positions adhering to the separation criteria were identified and the total area for these pixels was used to define the number of sources to use for a single run. No self-separation criterion was set, except the stipulation that no two random positions could be equal. Random positions were generated, limited to the identified pixel positions, and were assigned randomly generated flux densities for each flux bin. These bins were redefined for the second test using the L15-de-blended flux range. The artificial sources were added to the L15 map as before, giving one image per flux bin. The same extraction algorithm was applied to the resulting maps to provide the base $5\,\sigma$ source

Table 3.2: Completeness test 1 and test 2 result. There is a marked increase in completeness for test 2, which represents the de-blended L15-source catalogue.

Test	Completeness				
	10%	30%	50%	70%	90%
1(μJy)	12.38	16.50	19.96	23.82	31.51
2(μJy)	20.15	26.00	30.66	35.81	47.15

catalogues. For this test the extracted source catalogue positions were not used for the PSF photometry, instead the known randomly generated source positions were used as the ALLSTAR input. This change was implemented to represent the use of positional priors for the PSF fitting of the real L15 map. A source was deemed successfully recovered under the same criteria as before. The test was repeated until around 30000 sources per bin were achieved.

3.9.4 Completeness test results

The completeness for each flux bin (C) is the fraction of successfully recovered artificial sources with associated binomial errors given as

$$\sigma_C = \sqrt{\frac{C(1-C)}{N_{Src}}} \tag{3.2}$$

where N_{Src} is the total number of artificial sources. The completeness test results are given in table 3.2. The results of the first test show, with respect to the 5σ L15 extraction, that the catalogue is 10%, 50% and 90% complete down to 20.2 μJy, 30.7 μJy and 47.1 μJy respectively. For the second test, with respect to de-blending with PSF fitting, the L15-image is 10%, 50% and 90% complete down to 12.4 μJy, 20.0 μJy and 31.5 μJy respectively. Table 3.2 and figure 3.23 show that there is a substantial shift to fainter flux limits for the second test, which translates to around a 40% increase in completeness after the de-blending.

3.10 Photometric redshifts

The analysis of the L15-data that has been described so far has no need to take into account the effects of gravitational lensing. This is also true for the estimate of photometric redshift, which should not be affected by demagnifying the source flux as this leads only to a linear scaling

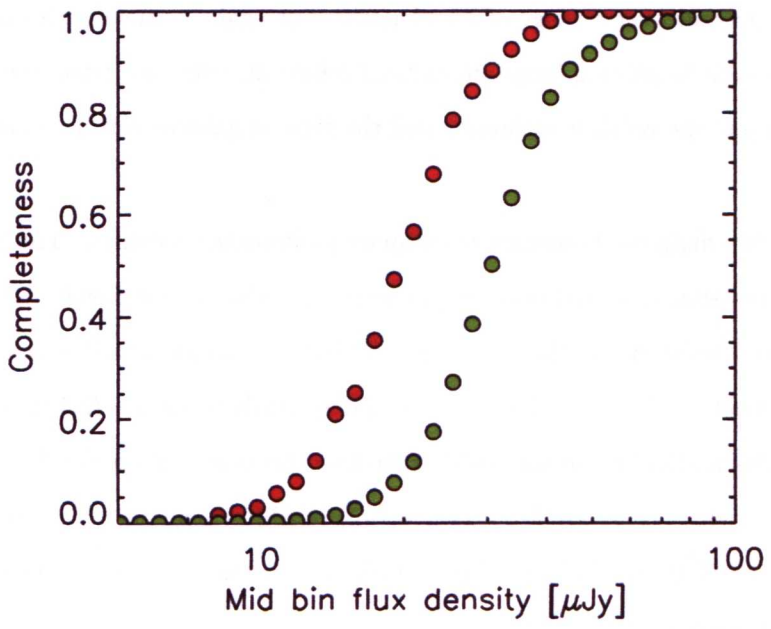

Figure 3.23: Completeness test 1 results for the L15-5σ source catalogue (red filled circles) and for the L15-deblended source catalogue test (blue filled circles). Note the improved completeness achieved via de-blending.

effect (assuming differential magnification is negligible). However, as well as the importance part redshifts play in interpreting the L15 data in the correct context they also plays a key role in gaining magnification correction estimates.

3.10.1 Introduction

In an ideal situation all the sources in a catalogue would be observed spectroscopically so their redshifts could be accurately determined from narrow spectral features. Of course this is not feasible as telescope time is limited and the inherently red nature of MIR sources, selected from deep data, can require prohibitively large integration times. The alternative option is to derive photometric redshifts from broad features that can be sampled with multi-wavelength medium and broad-band photometry, e.g. the 4000 Å break (due to a collection of metal absorption line features) and the 1.6 μm bump (which represents the emission of established stellar populations). The drawbacks for photometrically derived redshifts are the often large associated uncertainties (generally around a minimum 10% error is expected) and the redshift degeneracies that can occur between different galaxy morphologies (e.g. quiescent ellipticals and star-forming galaxies

can present similar i – K colours). Both of these issues can be minimised with high precision photometric coverage over a range of wavelengths, but again, achieving this depends on a number of factors such as gaining large amounts of follow-up telescope time, the wavelength range used to determine the redshift estimates and the type of galaxies within a catalogue.

There are two main methods used to estimate photometric redshifts. The first uses a training set of SED templates, observed and/or synthetic, to derive a relationship between the observed photometry and redshift for that set [e.g. ANNz is a sophisticated example of this 'neural network' approach Collister & Lahav, 2004]. There needs to be a sufficiently large training set available for this method to be successful, therefore this is not an appropriate method to use for the L15 sources where there are few spectroscopic redshifts available. The other commonly used method is fitting SED templates to observed photometry using a least χ^2 squares minimisation, on a source-by-source basis.

3.10.2 SED template fitting

The basic method of SED fitting involves finding the linear SED scaling factor (α) that corresponds to the minimum of the associated minimum χ^2 distribution for a range of redshifts. χ^2 is calculated as

$$\chi^2(z) = \sum_{i=1}^{N_{filter}} \left(\frac{S_{obs,i} - \alpha \times F_{pred,i}(z)}{\sigma_{obs,i}} \right)^2 \tag{3.3}$$

where $S_{obs,i}$ and σ_{obs} are the observed flux densities and associated uncertainties and F_{pred} are the model flux densities, for the corresponding N_{filter} filters, obtained following

$$F_{pred} = \int_{\lambda_{min}}^{\lambda_{max}} f(\lambda) R(\lambda) d\lambda \tag{3.4}$$

for each SED template (f) and filter response (R) normalised to unit area. For each redshift the best normalisation factor α_{best} is derived analytically, and corresponds to the solution for

$\partial\chi^2/\partial\,\alpha = 0$ given by

$$\alpha_{best} = \frac{\sum_{i=1}^{N} \left(S_{obs,i}\, F_{pred,i}/\sigma_i^2\right)}{\left(F_{pred,i}^2/\sigma_i^2\right)} \tag{3.5}$$

HyperZ [Bolzonella et al., 2000] is probably the most popular, publicly available, software for estimating photometric redshift and works with the single template fit method. The template is either generated with the Bruzual & Charlot evolutionary code GISSEL98 synthetic SED template library[1] or is from the Coleman et al. [1980, CWW] observed SED templates. The code steps over redshift and (depending on the choice of template set) age, spectral type and absorption (based on the choice of extinction law and Lyman α forest correction). More recently the EaZy photometric redshift code of [Brammer et al., 2008] was publicly released, which is aimed at data sets with no (or biased) spectroscopic redshifts available, making it suited to the A2218 data set that has few spectroscopic redshifts, mainly biased at the cluster redshifts. The main differences between EaZy and HyperZ are the adopted SED templates, the possibility to fit multiple templates simultaneously and to apply Bayesian priors in luminosity. The prior help break colour degeneracies leading to multiple probability distribution peaks e.g. featureless blue SEDs can give equally good fits at redshift $z\sim0$ and $z\sim3$. The EaZy templates set and priors are based on semi-analytical models, which the authors claim avoid the bias that can be associated to spectroscopic samples. The set pairs of templates or a linear combination of all available templates can be fitted simultaneously. To minimise with two SED templates, equation 3.3 can be extended to

$$\chi^2(z) = \sum_{i=1}^{N_{filter}} \left(\frac{S_{obs,i} - \sum_{j=1}^{2} \alpha_j \times F_{pred,i,j}(z)}{\sigma_{obs,i}} \right)^2 \tag{3.6}$$

[1] http://www.cida.ve/~bruzual/bcXXI.html

For each pair of templates (t_1 and t_2), equation 3.6 is solved as a set of linear equations to give the two best normalisation factors (α_1 and α_2).

$$\mathbf{S} = [S_{obs}], \mathbf{F} = \begin{bmatrix} F_{pred,t_1} \\ F_{pred,t_2} \end{bmatrix} \tag{3.7}$$

$$\mathbf{A} = \mathbf{F}\mathbf{F}^{\mathbf{T}}, \mathbf{B} = \mathbf{F}\mathbf{S} \tag{3.8}$$

$$[\alpha_1, \alpha_2] = \mathbf{A}^{-\mathbf{1}}\mathbf{B} \tag{3.9}$$

The EaZy SED template set consists of five templates derived from a linear combination of templates from the galaxy evolution model PÉGASE [Fioc & Rocca-Volmerange, 1997] that are trained on synthetic broadband photometry (U to K) of galaxies in the semi-analytic model of De Lucia & Blaizot [2007]. They also add one highly dust obscured starburst template. It is emphasised in Brammer et al. [2008] that as well as the application of priors, the inclusion of IRAC photometry (up to 8.0 μJy, depending on the redshift) can also be important in helping to break colour degeneracies. A comparison of HyperZ and EaZy on the few available spectroscopic redshifts gave a mild indication that EaZy (along with the application of priors) produced a better agreement, although this is far from a statistically valid result (based on 15 redshifts). Due to the results of this comparison, the greater flexibility offered in terms of the number of templates that can be simultaneously fitted and the encouragement of IRAC wavebands, the EaZy code was chosen to estimate photometric redshifts for the A2218 L15-sources. The photometry for sources with spectroscopic redshifts were fitted using EaZy with and without applying priors. Comparing the two sets of results with the known spectroscopic redshifts (see figure 3.24) suggests the option of using priors should give improved results. Although this conclusion also suffers from the same lack of statistics, priors were applied for all EaZy fitting.

Both HyperZ and EaZy (and the majority of other photometric redshift codes) rely heavily on fitting optical and NIR data to the broad 1.6 μm 'bump' spectral feature to derive redshifts, as this feature generally appears for all galaxies, with the exception of AGN and severely dust obscured galaxies, which have power-law like SEDs [e.g. Narayanan et al., 2010]. However, the dependence on this feature can lead to a relatively common degeneracy between ellipticals and dusty star-forming galaxies [e.g. see Pozzetti & Mannucci, 2000], especially when there is

incomplete NIR coverage [Gil de Paz & Madore, 2002]. There is important information in the photometry at longer wavelengths, which samples the redshifted PAH features and cooler dust emissions, to identify dusty star-formation over the old stellar populations in local ellipticals. The photometric redshift code of Negrello et al. [2009, N09 hereafter] is optimised for fitting mid-to-far-infrared PAH and silicate features seen in starburst SEDs and simultaneously minimises a linear combination of a starburst component [Takagi et al., 2003] and an AGN component [Efstathiou & Rowan-Robinson, 1995]. The code steps over redshift, age, compactness and extinction curve for the starburst component and over redshift and torus viewing angle for the AGN. Although there is currently no A2218 FIR ($\gtrsim 60\mu$m) photometry included in the band-merged catalogue, L15-SEDs were also fitted with the N09 code, which provides a useful comparison for sources with star-burst type SEDs.

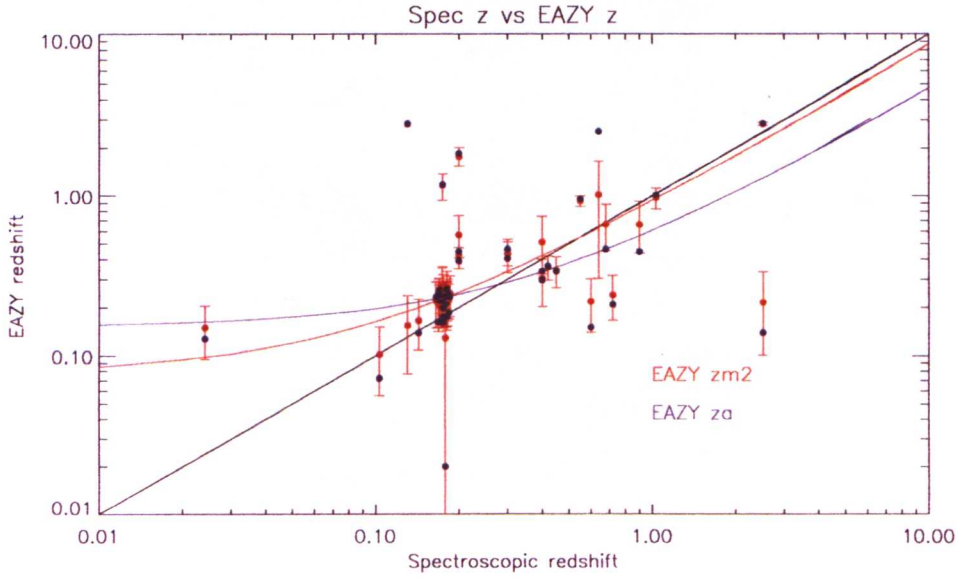

Figure 3.24: Spectroscopic redshift vs EaZy photometric redshift estimates with priors (zm2) and without priors (za). The errors are shown only for zm2 for clarity. The comparison is not conclusive, but does suggest there is an improved agreement when applying priors. The concentration of points ~ 0.18 is due to cluster members and shows EaZy's tendency to marginally overestimate redshifts for early type galaxies. The orange and blue curves are linear best fits to zm2 and za respectively. The two outliers (and one point in agreement) with the spectroscopic redshifts of 2.6 are of the same source, which is strongly lensed and has three images. The corresponding images are extended in the optical and NIR data and therefore producing poor aperture photometry for two of the lensed images. The remaining outliers (around the cluster distance) are either degenerate results or due to lack of photometric constraints.

3.10.3 EaZy photometric redshifts

Only L15 sources with coverage in four or more filters, between u' to IRAC Ch4, were included in the EaZy input catalogue. The L15-sources satisfying this criteria are shown in figure 3.25. For any waveband image with area coverage of a given L15 source but no counterpart detection, half the derived 3σ upper limits were assigned (given in table 3.1) and an equal value for the associated errors. The minimum error for each photometric point was set to 15%, to account for the discrepancies expected between the photometric calibrations of different instruments. EaZy was run allowing a linear combination of the full template set for a redshift range up to 7.0 and a redshift step size of 0.1 and the application of priors.

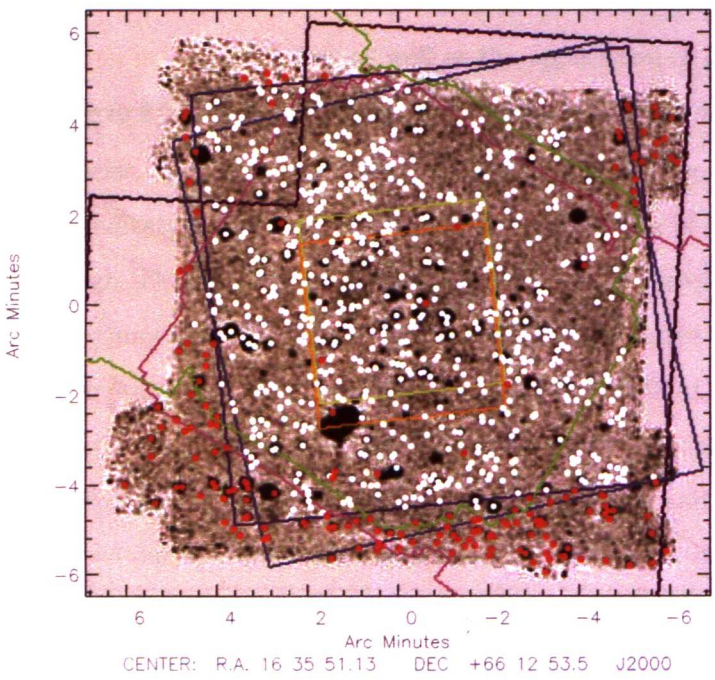

Figure 3.25: L15-image and L15 de-blended source catalogue (without cluster members) are plotted to show the number of sources with enough filter coverage to be included for photometric redshift estimation ($\geq$ 4; white dots) and without (red dots). The contours show the A2218 coverage of the S11 data (purple line), Palomar data (blue lines), IRAC data (green and pink lines) and the INGRID data (yellow and orange lines). Excluded sources shown within an area of ample coverage generally have star or local galaxy contaminated photometry.

The EaZy output file provides several redshift estimates including the estimate derived using the application of priors (zm2) and the corresponding minimum χ^2. Errors are given as 68%,

95% and 99% confidence intervals. The number of filters used in the fitting is also reported as the use of the IRAC bands is dependent on redshift. The redshift quality parameter 'odds' is provided to identify sources with either broad or multi-peak probability distributions. In order to assess the reliability of the estimates the probability of the reduced minimum χ^2 was calculated with the degrees of freedom taken as the number of data points minus the free parameters of the redshift estimate and the number of templates used. The latter value is not provided in the EaZy output, so an arbitrary value of three templates was used. The zm2 redshifts were chosen from the output file and assigned uncertainties from the 68% confidence interval.

3.10.4 SED fitting to MIR PAH

The same minimum four filter criteria was set for application of the N09 code, for the filter range from u' to MIPS24. Upper limits and minimum errors were assigned as for the EaZy catalogue. The N09 output provides the best redshift estimate, the reduced minimum χ^2 and associated probability, the torus viewing angle for the best fit AGN component and physical parameters for the best fit starburst component. The redshift estimates given for N09 are considered 'good' for probabilities > 0.01. This relatively low probability level is set as the fitting of strong spectral features, such as PAH, can lead to low probabilities for only small differences between the observed photometry and the model, e.g. if the photometric point is located on the slope of a strong feature. In comparison, the EaZy redshifts were considered reliable if the probability of the reduced minimum χ^2 are > 0.25. The redshift estimates for EaZy and N09 are compared in figure 3.26 and show a good agreement for source without a featureless SED.

3.11 Triple comparison

$30' \times 30'$ postage stamp images were taken for each source and made into strips ordered by wavelength from the available wavebands. Efforts were made to scale the postage stamp strips, using the SED of M82 (a known local starburst galaxy) in order to give fair weighting to each stamp, however this was unsuccessful due to the difference in sensitivity between the data. The stamps were, therefore, scaled by eye using several examples of sources with full waveband coverage and a typical star-forming galaxy SED shape. A triple visual comparison was performed between the postage stamp strips, and the EaZy and N09 best fit SEDs. In this way the redshift

estimates, model and observed SEDs, probabilities and the visual source morphologies could all be directly compared on a source-by-source basis (see figures 3.27 - 3.29). The triple comparison for source L15-179 is given in figure 3.27. This is an example of a non-cluster source with good photometric coverage and a spectroscopic redshift of 0.47, which the EaZy estimate replicates. The N09 estimate of 0.3 is in less good agreement, however this is due to the lack of strong MIR/FIR features. Interestingly, the optical and NIR postage stamps suggest an early type morphology, but the increase in flux density with MIR wavelength indicates higher levels of warm dust emission than expected for a quiescent elliptical, which predicts this is more likely to be a star-forming galaxy. In contrast to L15-179, the source L15-326 only has coverage in four EaZy photometric bands and no MIR-features, therefore giving unreliable estimates for both EaZy and N09, as shown in figure 3.28. Judging from the postage stamp strip, this source could be a high redshift galaxy candidate, but it is not possible to improve the redshift estimate without further photometric points. During the 'triple check', it was found that all sources with only four filter coverage in the EaZy waveband range were classified as unreliable.

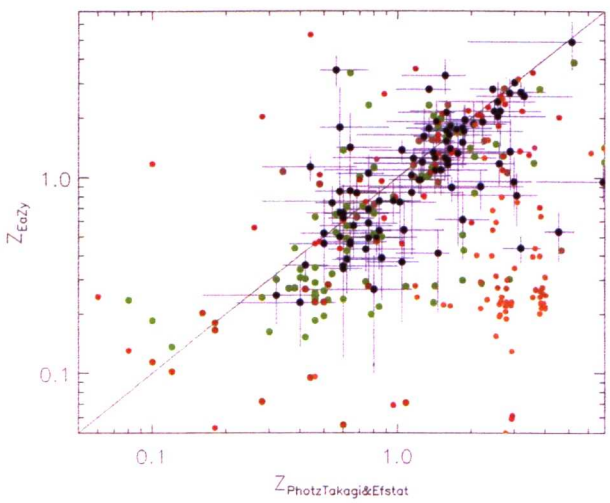

Figure 3.26: N09 ($Z_{photzTakagi\&Efstat}$) vs EaZy photometric redshift estimates. Where there are points without errors, these have been omitted for clarity. The black dots with blue error bars have 'good' associated probabilities for both codes and errors $< 80\%$. The green dots and pink dots have 'bad' N09 and 'bad' EaZy estimates, respectively. The red dots (for both codes) have large associated errors ($\geq 80\%$), the majority of which can be linked to SEDs with smooth mid- to far-infrared features. The orange points indicate elliptical-like sources, for which N09 is not designed to fit. Note that the orange points are clustered around z$\sim$0.2-0.3 for EaZy, which shows the tendency for EaZy to marginally overestimate the redshifts at the cluster distance.

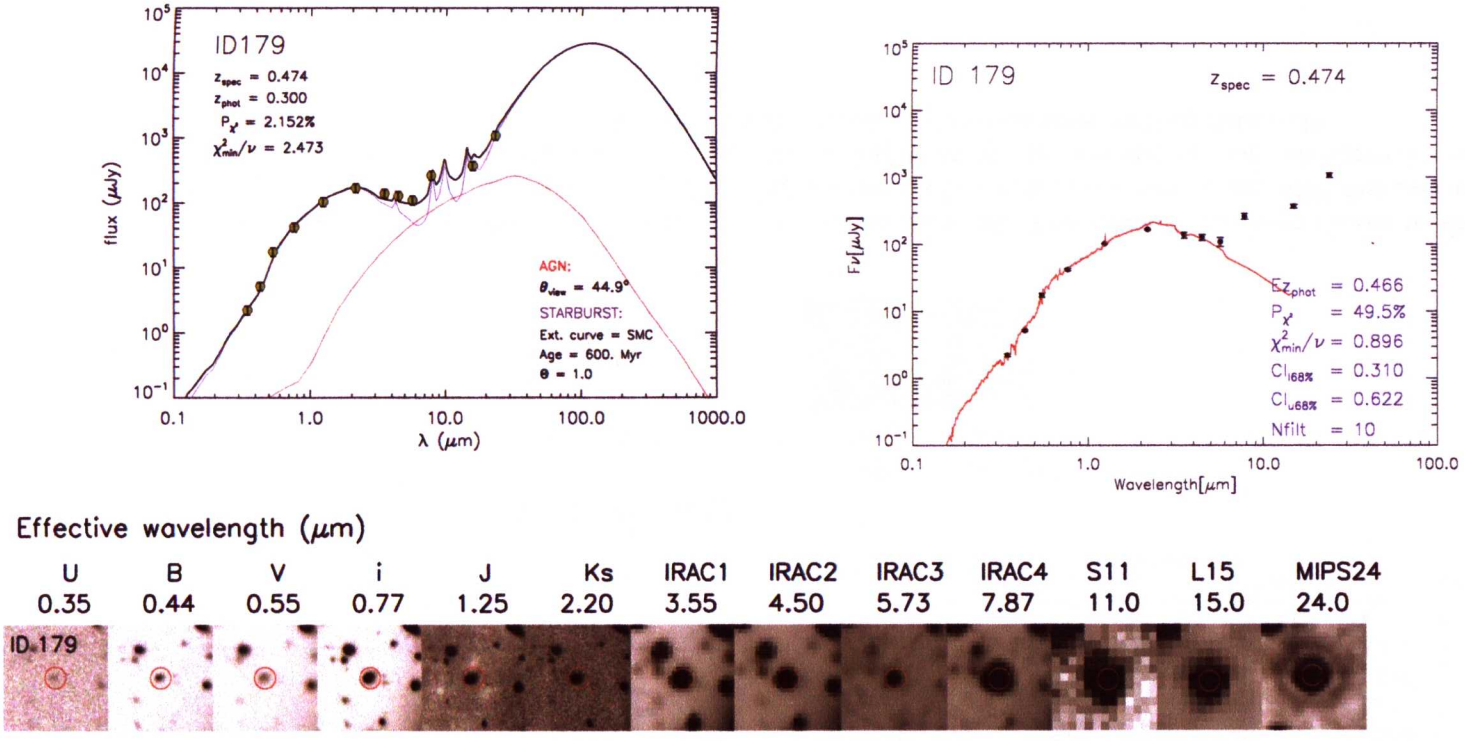

Figure 3.27: Example of the 'triple comparison' for source L15-179. Here the best fit SEDs of EaZy and N09 are compared with the photometric redshift estimates and associated statistics, the band-merged photometry and the postage stamp strip ($30'' \times 30''$ stamps) for all the available wave-bands. This is an ideal case with good wavelength coverage, which is reflected in the EaZy photometric redshift estimates agreement with the spectroscopic redshift.

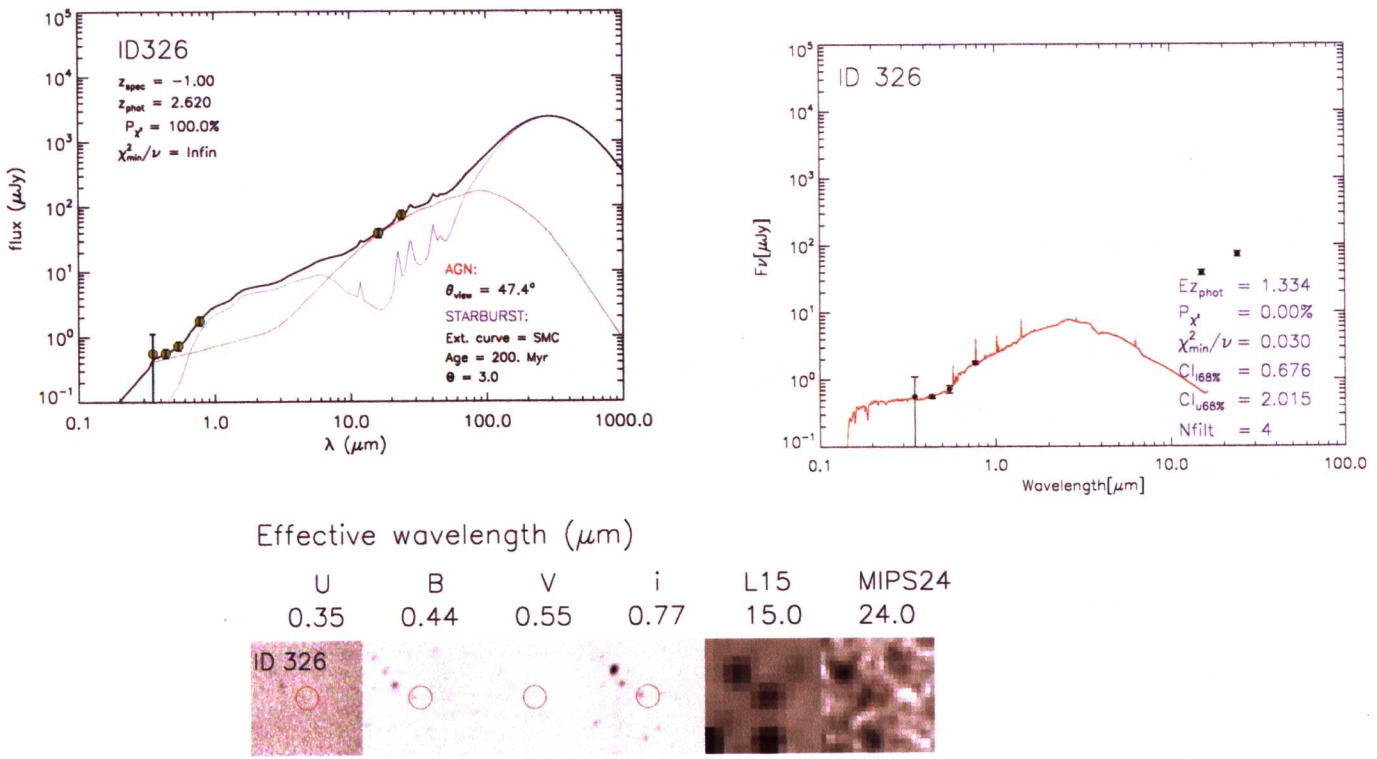

Figure 3.28: Example of the 'triple comparison' (as described in figure 3.27) for source L15-326. This example has been chosen to show the results that can occur when fitting to a source with coverage in only four photometric EaZy bands and a lack of any MIR features for N09. The photometric redshift estimates are unreliable, and this situation can only be improved by the addition of more photometric points or spectroscopic observation. Note that the infinite χ^2_ν results from having a greater number of free parameters than data to fit.

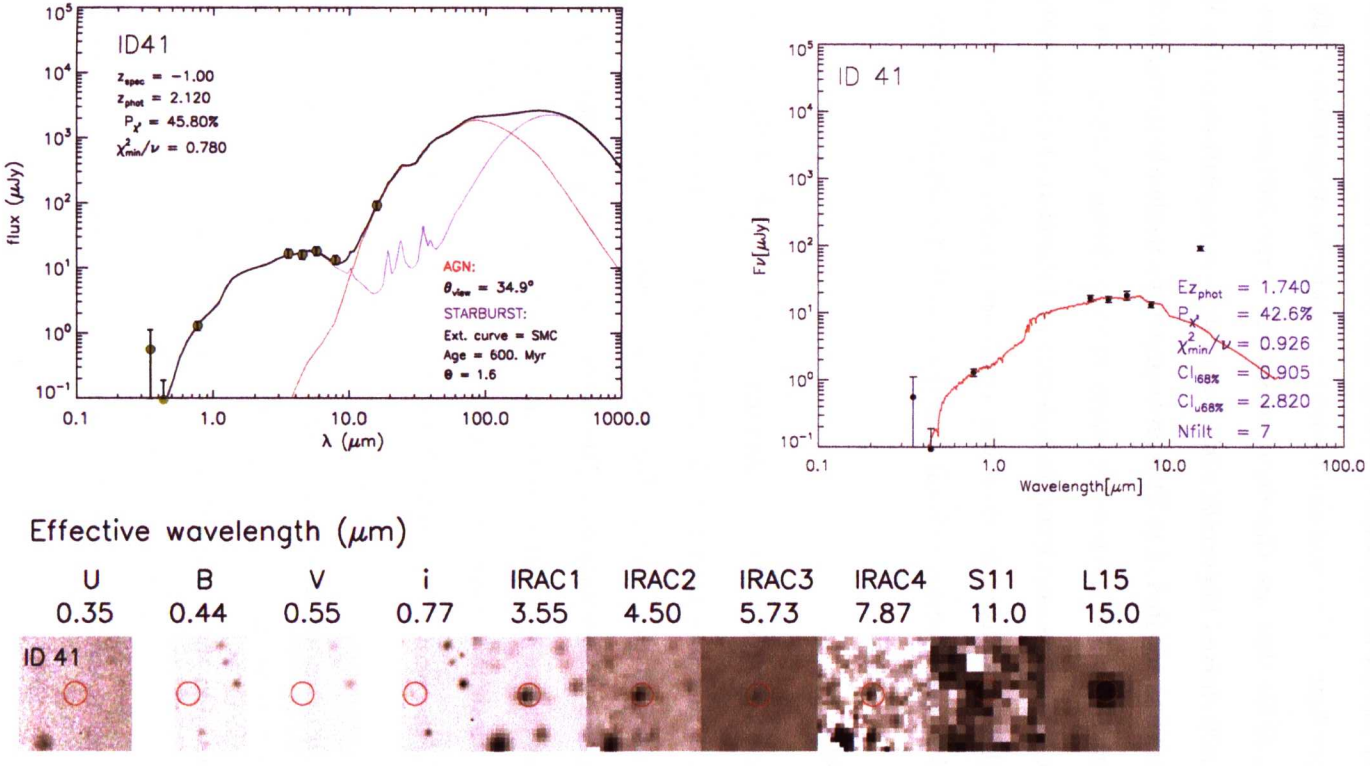

Figure 3.29: Example of the 'triple comparison' (as described in figure 3.27) for source L15-40. The comparison shows that the photometric redshift estimates are in good agreement (within the 1σ EaZy errors) and with high probabilities, and the galaxy is predicted to be a starburst with an important AGN contribution, which is supported by the morphology. For this source the EaZy photometric redshift was assigned. Note that the faint appearance in the v'- and IRAC CH3-bands is due to lower relative sensitivities. The remaining bands visually reflect the observed photometry.

For the majority of L15-sources the EaZy estimate was preferentially chosen over the N09 counterpart, due to the good correlation between the EaZy and N09 estimates for sources with pronounced MIR features (see figure 3.26) and also because a significant proportion of the L15 population have featureless SEDs that are therefore not suited to the N09 code. When the fitting of the MIR data by N09 showed important extra constraints in comparison to the EaZy output, then the N09 estimate was adopted. L15-41 is an example of a moderate-to-high redshift candidate, supported by both SEDs and the postage stamp strip as shown in figure 3.29. Here the additional constraint for N09 comes only from the L15 data and therefore the EaZy estimate was retained. The final redshift catalogue is, therefore, composed mainly of EaZy estimates, some N09 estimates and a few spectroscopic redshifts (predominantly for cluster members).

3.11.1 Cluster members

A2218 cluster members are considered to be a contaminant for the study of the background star-forming population, and therefore needed to be removed from the L15 catalogue. The cluster members were identified in three ways. The first, and most straightforward was via spectroscopic redshifts of known cluster members. The second used a colour-magnitude cut for the i' and J band magnitudes (figure 3.30), which relies on the tight relation between colour and observed magnitude for ellipticals in massive galaxy clusters [Bower et al., 1992]. This cut was carried out before obtaining the photometric redshift catalogue and was ultimately used as a check for the third method. The final method used the 'triple comparison' of SEDs and postage stamp strips to identify both extended foreground sources and A2218 cluster members. This identification process greatly benefits from the examination of the redshift estimates in context of the postage stamp images. On the whole N09 is not able to fit reliably to elliptical SEDs – mainly cluster members – as the templates chosen for N09 are aimed at fitting dusty star-forming galaxies. EaZy is able to produce estimates for this type of galaxy, but a comparison for the known cluster member's spectroscopic redshifts and EaZy estimates showed EaZy tends to over estimate the redshift by up to $\delta z \sim 0.15$ (see figure 3.26), giving cluster members an Eazy redshift range of ~ 0.1 - 0.35 with only few elliptical type galaxies given a redshift estimate as low as that of A2218's z = 0.18. Consequently during the visual inspection, redshift estimates within this range with a visual nature supporting a local elliptical galaxy were given a cluster member classification. When the cluster members identified during the 'triple comparison' were

compared with those classified by the first two methods it was found that the visual inspection selected all previously identified members. The identified cluster members constitute 16% of the full L15 de-blended catalogue.

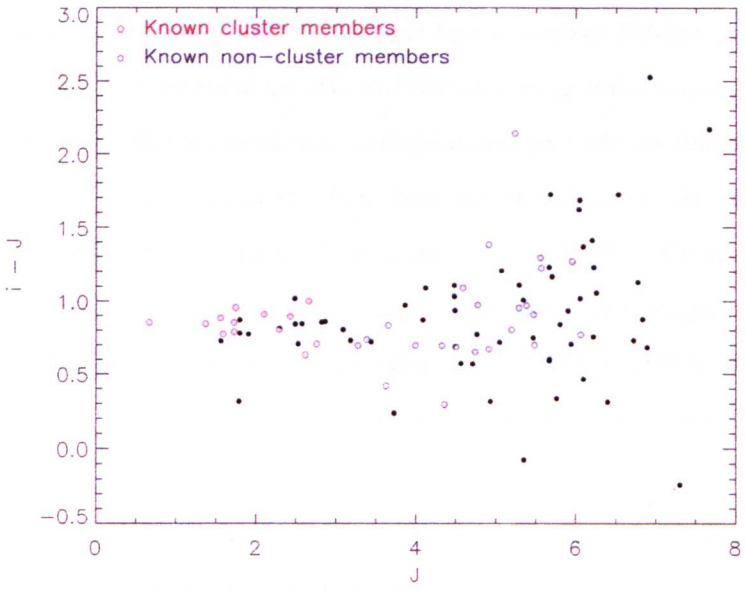

Figure 3.30: Color-magnitude plot using i'-J to identify cluster members (x-axis J magnitudes are instrumental). The known cluster members are highlighted with pink and show a clear separation from known non-cluster members with spectroscopic redshifts > 0.19 (blue).

3.11.2 Final L15-catalogue

All L15 sources considered to be contaminants, i.e. cluster members, foreground galaxies and stars, were removed from the L15 de-blended catalogue to give the final L15 source catalogue (L15-final-cat). The stars were identified simply from diffraction spikes in the optical and IRAC data. The removal of contaminants also removed all the significantly extended L15-sources. Figure 3.31 shows these contaminant sources in context of the L15-map. The distribution of redshifts of the L15-final-cat has a median redshift of 1.044±0.67 and covers a range of z ~0.3 - 5.0 (see figure 3.32), which suggests the L15-population are predominantly sampling star-forming galaxies around the peak epoch of cosmic star-formation z ~ 1-2 [Blain et al., 2004; Dickinson et al., 2003b; Hopkins, 2004]. ISOCAM HDF-N galaxies [Aussel et al., 1999; Elbaz et al., 2002a] are 98% spectroscopically complete, with a median redshift of 0.8 down to 0.5 mJy. As the

L15-sample is estimated to be 100% complete down to ~0.05 mJy at 15 μm, the higher median L15-redshift cannot be the result of incompleteness and may reflect an increase in redshift due to additional depth, which is supported by the greater estimated redshift range for the majority of L15-source of z ~ 0.35 - 3.0 in comparison to the ISOCAM HDF-N range of 0.4 - 1.3. However, it cannot be ruled out that the median redshift difference is due to the large errors associated to the photometric redshift estimates and that the median redshifts agree within these errors. For the ISOCAM source catalogue extracted from lensed fields by Metcalfe et al. [2003] the estimated median redshift for the background galaxy population is 0.65, however this estimate was based on spectroscopic redshifts for only part of the catalogue. Metcalfe et al. [2003] conclude that the main reason for the difference between the median L15 redshift estimates is due to the bias of an incomplete spectroscopic sample. As the number of sources for this field above a completeness level of 80% is just 48, of which only half have spectroscopic redshifts, statistical fluctuation could also account for this difference.

31% of the L15-final-cat are without any redshift estimate, either due to a lack of multi-wavelength coverage or a photometric estimate classed as unreliable during the triple check. For these sources the median redshift and associated error were assigned.

3.12 Gravitational lensing corrections

3.12.1 Introduction

The most interesting aspect of the observed field, which has not yet been taken into consideration, are the gravitational lensing effects of A2218 on each source in the L15-final-cat. These effects lead to some level of flux amplification and area distortion for each source. Correction factors for both the observed flux amplification and area distortion were derived using the publicly available software LENSTOOL [Jullo et al., 2007]. LENSTOOL is primarily used to construct models of the mass distribution of gravitational lensing clusters using a chosen function to describe the mass distribution, the redshift of the cluster and information on the shape and position of the cluster members and the strongly lensed images of background sources, in the form of arcs and arclets. Once a mass model is established, LENSTOOL can use the distribution of mass to predict flux and area magnification factors as a function of the observed position and redshift.

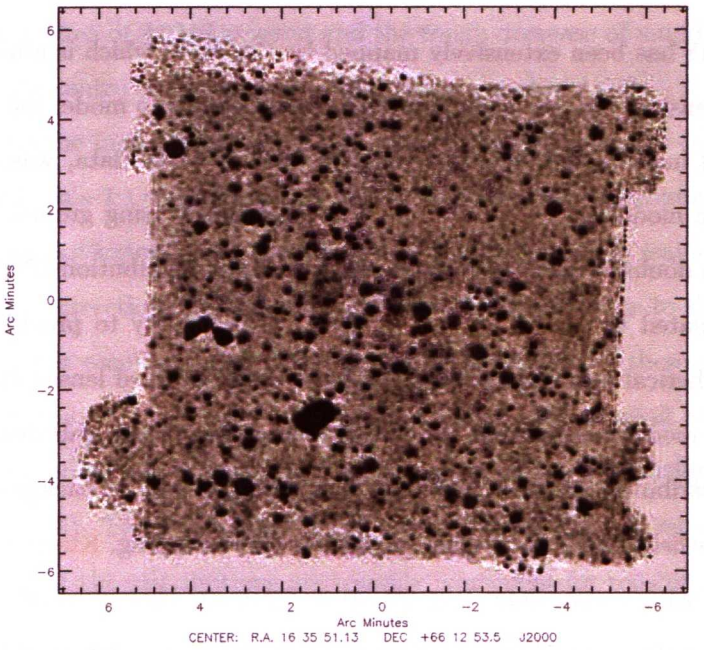

Figure 3.31: L15-sources classified as cluster members and foreground contaminants (purple circles). The cluster members are more concentrated at the centre of the cluster, as expected.

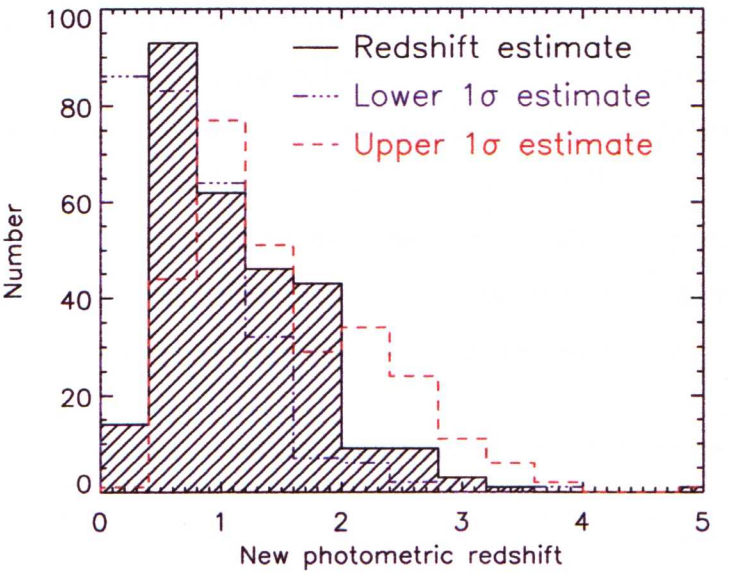

Figure 3.32: Redshift distribution of the final photometric redshift catalogue, minus cluster members, foreground objects and stars, but including the spectroscopic redshifts beyond the cluster distance.

3.12.2 A2218 mass model

The core of A2218 has been extensively mapped by the *HST*, which is able to resolve the incidence of strong lensing, e.g. the giant arcs that are necessary to model the cluster mass (figure 3.5). The A2218 mass model, based on *HST*/WFPC2 F702W data, was an extension of the initial parametric model of [Kneib et al., 1995] constructed using ground based observations. The model uses a double pseudo-isothermal elliptical mass distribution (PIEMD) for the cluster which was formulated by Kassiola & Kovner [1993] specifically to provide a lens model that would fit the aspherical lens configurations suggested by observed lensed structure [e.g. Mellier et al., 1988]. The model was based on the two most luminous cluster galaxies at the centres of the bimodal mass distribution of the A2218 core, four multiply-imaged background sources and the background shear field. With the higher resolution *HST* mapping, Kneib et al. [1996] extended the mass model using constraints from 28 other luminous cluster members, three additional multiply-imaged systems and further information on the fine structure of the multiply-imaged background galaxies. The mass model was used to estimate redshifts for a selection of observed arcs using a 'lensing inversion technique' [initially presented in Kneib et al., 1994]; in fact the observed lensed image can be defined purely by the geometrical lensing effects and the redshift of the source object. The most probable redshifts to reproduce the observed lensed images for 80 faint arclets were found, 18 of which were confirmed to within $\sim 2\%$ with spectroscopic observations by Ebbels et al. [1998] of background sources with redshifts of $z \lesssim 1.0$. These observations also provided additional redshifts for further constraining the A2218 model. Natarajan et al. [2002] added an extra 10 cluster members, but only four multiply-imaged systems with spectroscopic redshifts. The most recent version of the model [Elíasdóttir et al., 2007] uses 14 multiply-imaged systems and arcs, seven of which have spectroscopic redshifts. This model was used to gain magnification corrections for the L15-final-cat.

3.12.3 LENSTOOL magnification corrections

Flux and area magnification corrections were obtained using LENSTOOL for L15 source with redshift estimates > 0.2. LENSTOOL also provides the corresponding source plane coordinates.

The returned L15-final-cat flux amplification (μ) distribution (figure 3.33) ranges from 1.0

to 24, with the majority of factors between 1 - 1.5. The distribution has a median of μ of 1.2, which reflects the wide area of A2218 covered and the rough decrease of amplification as a function of radius from the centre of the core (see the bottom panel of figure 3.35). Comparing the flux amplification and the increased area for each source showed these are comparable factors, only deviating away from a 1:1 relationship for highly magnified sources (figure 3.33). The mass model for A2218 does not extend over the whole L15 image, therefore leaving several sources without magnification corrections toward the edge of the L15-map. Due to their distance from the cluster core, it is fair assumption that the actual magnification of these sources is close to 1. It has been reported [e.g. Knudsen et al., 2006] that there is only a weak dependence of μ on redshift for z >1. This claim was investigated by comparing the μ distribution over several redshift bins (see figure 3.34). The peak of the distribution shifts to greater values with increasing redshift up to z$\sim$1.0, but the distributions are roughly equivalent for redshifts > 1.2.

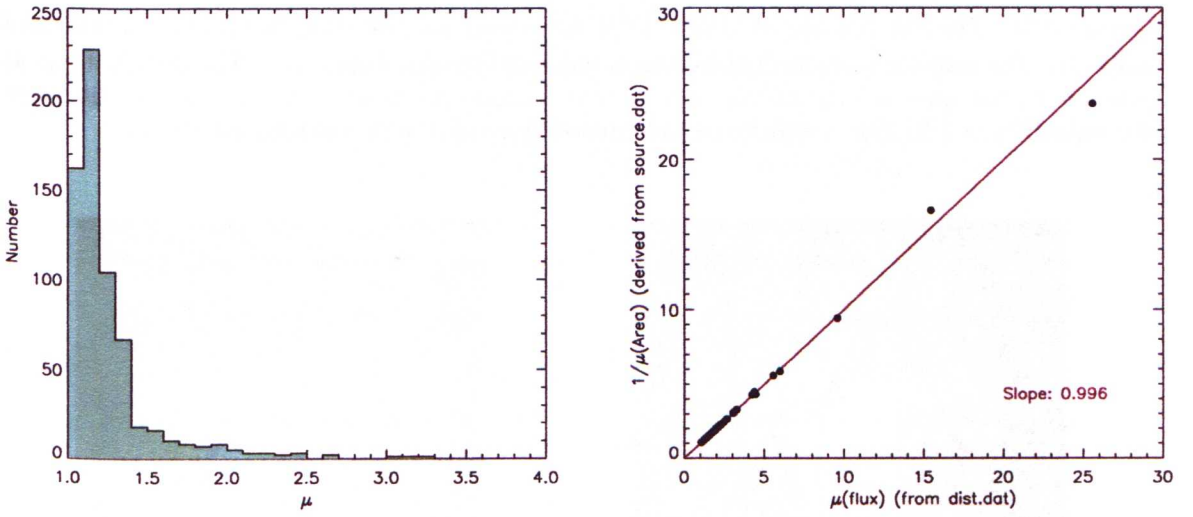

Figure 3.33: Left: Distribution of the amplification factors returned by LENSTOOL for all the L15 sources within the area covered by the mass model. The peak at low magnifications ($\sim$1.2), may be biased to lower redshifts by the inclusion of sources assigned a value of the median redshift. The distribution has been truncated at 4.0. Right: Comparison of flux magnification factors and area magnification factors, which shows a general 1:1 agreement.

A graphical depiction of the magnification map for A2218, for a source at the median redshift value of 1.044, was created by binning an area within the L15-image into a grid of input image plane coordinate. The resulting map in figure 3.35 shows the bi-modal mass distribution

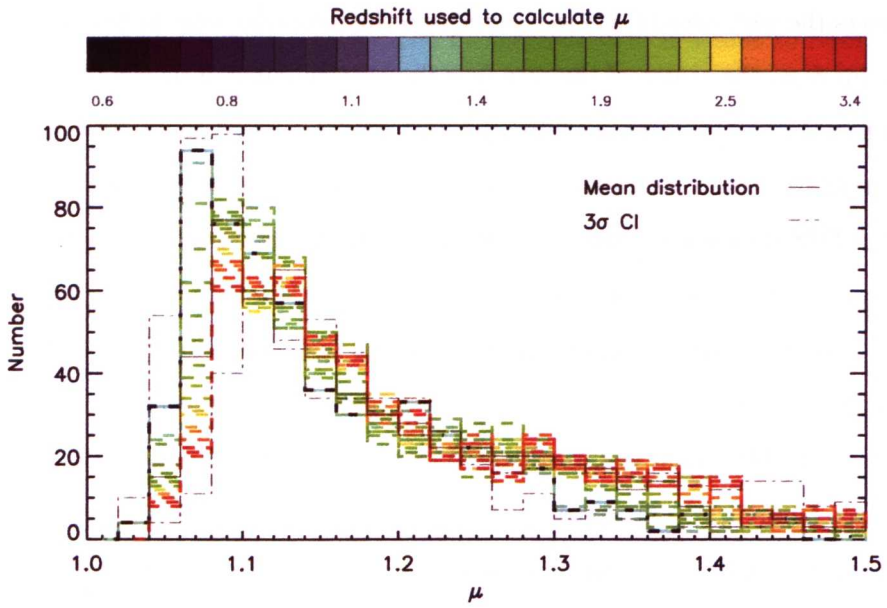

Figure 3.34: The distribution of LENSTOOL estimated amplification factors for set values of redshift. The redshift of each distribution is indicated by the colour bar. The distributions as a whole do not show a large scatter and there is a good agreement of the median amplification for redshift z > 1.2. This supports the low dependence of μ with redshifts for z>1.0.

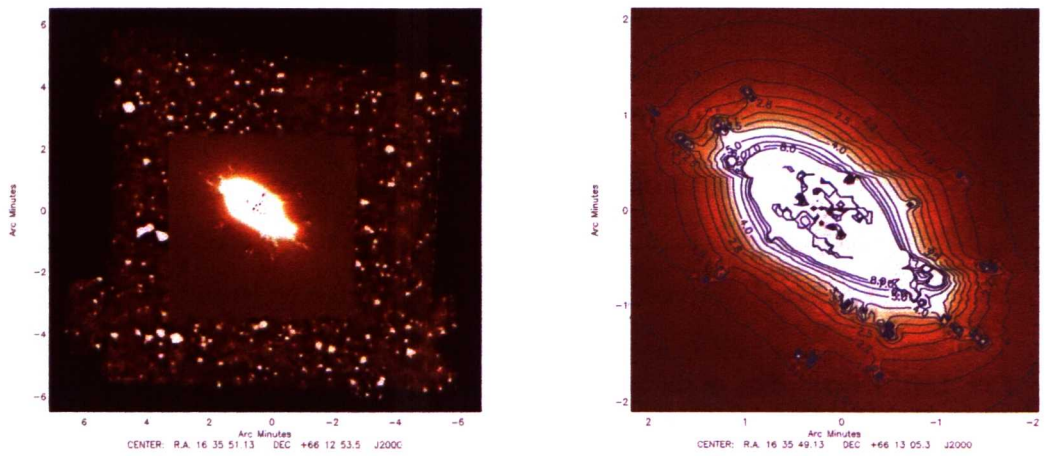

Figure 3.35: A magnification map was created by inputing a grid of image plane positions to LENSTOOL for a source with a redshift fixed to the median value of 1.044. This area does not represent the full extent of the A2218 mass model, but was chosen for computational reasons. A close-up of the centre of the magnification map is given in the bottom panel and overlaid with contours to show the decrease in amplification that would be observed for the virtual image of a lensed background galaxy.

of A2218, leading to elliptical magnification contours. The amplification factors decrease from $\mu \sim 8$ at a radius $\sim 0.5'$ from the centre of the core, to $\mu \sim 1.0$ once a radius of $\sim 2.0'$ has been reached. There are few sources in the L15-final-cat that lie within the high ($\mu > 3$) region of the map. To represent the area distortion of the L15-map, the difference between the LENSTOOL estimated source plane coordinates and the L15-final-cat image plane co-ordinates were plotted in figure 3.36. The resulting plot gives a general idea of the true area that would be observed in the absence of gravitational lensing effects.

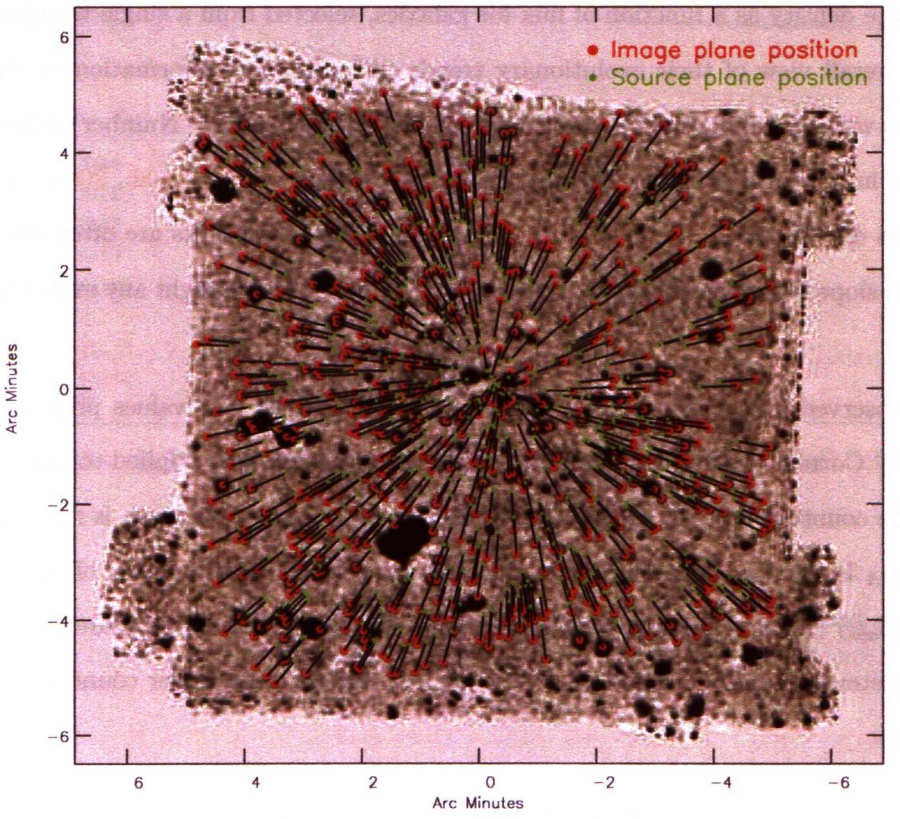

Figure 3.36: The source (green dots) and image plane (red dots) positions have been used to provide a graphical depiction of the area distortion occurring within the A2218 field.

Each source in the L15-final-cat was either assigned a flux correction and area correction or, for the sources outside the area covered by the A2218 mass model, correction factors of 1.0. There are several possible sources of error on the estimated correction factors: the photometric

redshift estimates; the source position accuracy; and the mass model itself. As the majority of the magnification factors are < 1.5, unless the associated uncertainties have a very high significance they will be negligible in comparison to the photometry errors and, for the fainter sources, to the completeness errors. Therefore no errors were assigned directly to the correction factors, but were implicitly accounted for when deriving the bootstrapped confidence interval (section 3.13.1).

3.13 Galaxy number counts

The surface density as a function of flux for galaxies, selected from a single waveband, can provide an overall view of their evolutionary trends and statistical information on their physical properties without individual idiosyncrasies causing significant bias. Number counts are usually presented in the form of either integral counts N(>S) [e.g. Coppin et al., 2006], or as differential counts dN/dS [e.g. Metcalfe et al., 2003]. The differential counts are often normalised to a Euclidean slope (i.e. spatially-flat and no expansion; $S^{-2.5}$) to highlight any evolutionary trends.

L15 observed flux densities (S_{obs}) were corrected to their true values prior to counting as $S_t = \frac{S_{obs}}{\mu}$. Corrections for area depletion and incompleteness were applied to individual sources during the counting process, assuming the relation $n_t = \frac{\mu_A}{C(S_{obs})}$, where n_t is the true number of sources, μ_A is the area correction, and the completeness (C) is a function of the observed flux density (S_{obs}) (rather than the true flux density S_t) and is obtained by linearly interpolating the completeness function over S_{obs}. The de-lensed differential number counts can therefore be written as

$$\frac{dN}{dS_t} = \sum_{S_t \in (S_{t,i} + \delta S_t)} \frac{\mu_A}{C(S_{obs,i})} S_{t,i}^{2.5} \tag{3.10}$$

3.13.1 Bootstrapping

Confidence intervals for the differential number counts were derived by bootstrapping within the photometric and redshift errors, as these are the dominant source of uncertainty for the counts. The L15 flux population was resampled without bias from the lensed L15-source catalogue. Each newly sampled population was assigned a flux density and redshift, randomly generated

within the respective 3σ photometric and redshift errors, assuming Gaussian distributions. New magnification corrections were interpolated from tabulated LENSTOOL amplification factors (see figure 3.37) and assigned to the resampled redshifts. The sources with spectroscopic redshifts were assigned zero redshift errors. 30,000 resampled populations were generated and differential counts were taken for each, following equation 3.10. Confidence intervals were derived using the median and standard deviation of the resampled counts distribution.

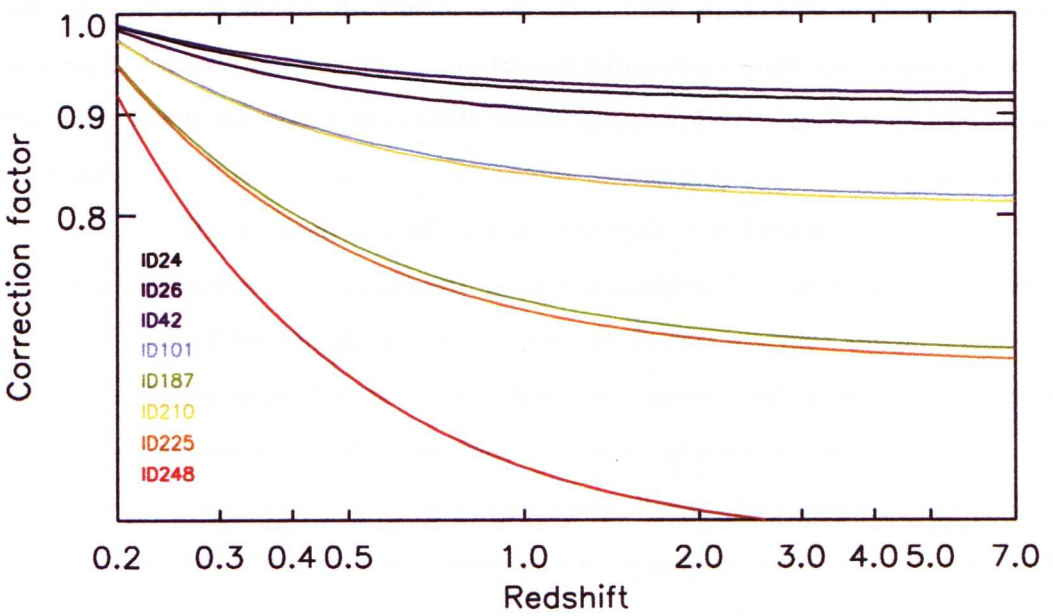

Figure 3.37: Examples of the tabulated magnification corrections $(1/\mu)$ for several sources, i.e. different positions in the observed area. The sources are listed in decreasing distance to the core of A2218.

3.13.2 Differential number count comparison

Figure 3.1 [Hopwood et al., 2010] compares the de-lensed L15 Euclidean-normalised differential number counts to a compilation of previous work and predictions based on galaxy evolution models. The grey shaded region shows the 2σ bootstrapped confidence interval. The differential number counts and bootstrapped standard deviation are presented in table 3.3. The no-evolution model provides a comparison for a non-evolving source population in an expanding Universe, which is strongly excluded by all the data. The observed counts collectively (and approximately) describe the same distinctive shape. At the bright end the counts follow the

Euclidean slope. Around 2-5mJy there is a sudden change to a steeper than Euclidean slope, which forms one side of a pronounced 'bump'. This deviation away from the Euclidean slope demonstrates strong evolution in the MIR galaxy population, which can be interpreted as increasing star formation activity and increasing numbers of dust obscured star-forming galaxies out to z$\sim$1 [Elbaz et al., 1999; Serjeant et al., 2000]. The height of the broad peak at $\sim$ 0.2 - 0.4 mJy is predicted by several previous results to be up to a factor of 3 greater than the peak of the L15-counts. Figure 3.38 shows the same comparison as figure 3.1, with a truncated flux range. The dark and light blue circles indicate the de-magnified L15-counts taken from the initial 5 σ source catalogue, therefore representing a catalogue containing sources with significant photometric blending. These 'blended' counts follow much more closely the greater peak estimated by the counts of Gruppioni et al. [2002]; Teplitz et al. [2005]; Wada et al. [2007] where complete de-blending was not applied and, therefore, the true value of the peak is more likely to be nearer to that predicted by the L15 'de-blended' counts. Towards the faint end of the flux density range the counts rapidly converge towards the no-evolution model, following a sub-Euclidean slope, which may indicate a sharp decrease in star-formation toward higher redshifts $\gtrsim$ 2 (assuming that in general fainter galaxies are at greater redshifts). The comparison of counts that extend from the peak down to fainter flux densities $\sim$0.05mJy, show a considerable scatter over the final flux bins. The L15-counts are in general agreement within the errors and scatter for these flux levels, however, there may be an issue of statistics to consider. The final data point of Metcalfe et al. [2003] contains nine galaxies at a 50% completeness level, in comparison to $>$ 100 sources at an estimated 100% completeness for the L15-data. The faint end of the counts are extended below $<$ 0.05mJy by the L15 counts alone, approximately maintaining a constant slope of -1.6, which is in agreement with the faint slope estimate of Elbaz et al. [1999]. The greater depth achieved is $\sim$ a factor of 3 fainter in comparison to the Metcalfe et al. [2003] counts. There is a possible upturn of the counts suggested by the final L15 data point, however the deviation away from the general slope is not greater than 1σ and is therefore not statistically significant. The increasing associated 1σ errors towards the faintest L15 bins reflects a decrease in completeness. Due to the movement of L15 sources to lower flux density bins after demagnification, there is a wider range of incompleteness corrections applied in comparison to the lensed counts. To give an approximate measure of the completeness, the median completeness per bin was found and showed all bins are 100% completeness down to the faintest three bins, which have median

completeness corrections of 96%, 70% and 26%, respectively. Inclusion of the final L15 bin is in line with Wada et al. [2007], who take data down to a 30% completeness level.

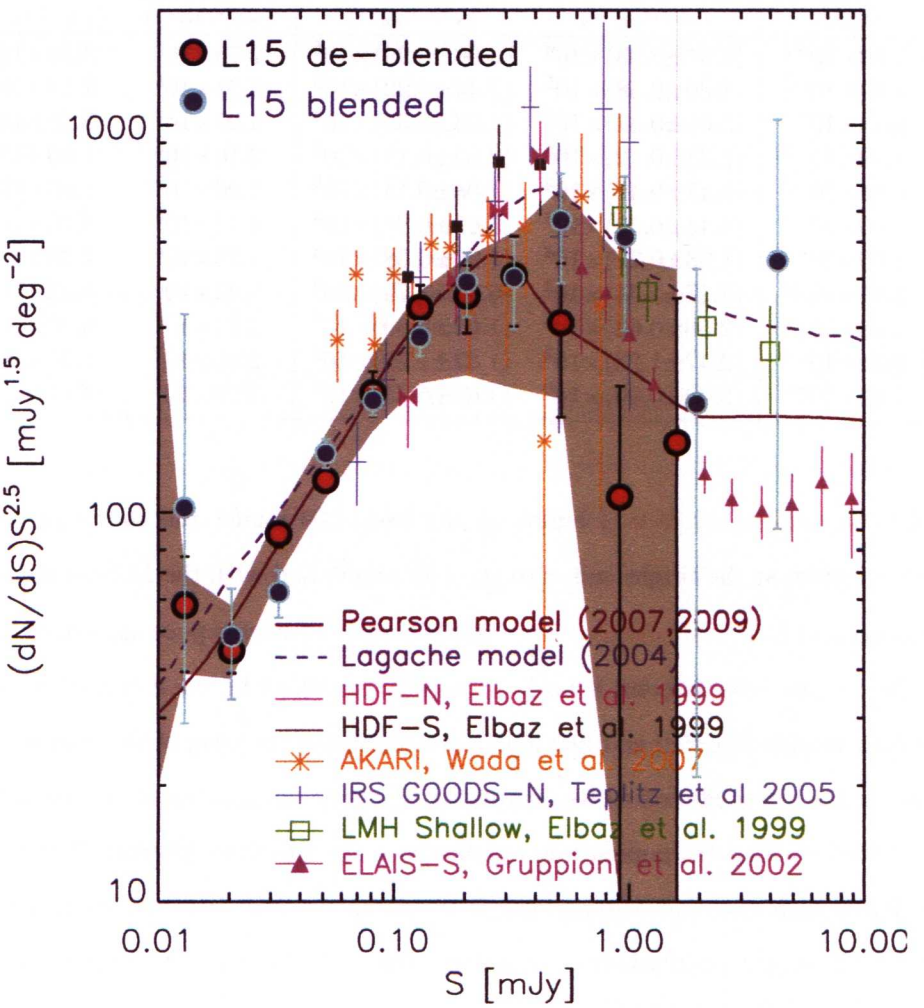

Figure 3.38: The peak of the 15 μm differential counts comparison, of figure 3.1, with the additional L15 counts taken from the L15 5σ source catalogue, which has not been de-blended). This comparison suggests blending is most significant for the bright end of the counts, and shows an improved agreement between the L15 blended counts and the counts of Gruppioni et al. [2002], Teplitz et al. [2005], Wada et al. [2007] and Elbaz et al. [1999] around the peak of the bump.

The models of Lagache et al. [2004, L04 hereafter] and Pearson [2010, P10 hereafter], compared in figure 3.1, show a good agreement with the L15 counts below $\sim$ 0.4mJy. Above this flux limit the difference between the L04 model fails to provide the correct normalisation. The

Table 3.3: Lensed ($\frac{dN(S_{ob})}{dS_{ob}}$) and de-lensed ($\frac{dN(S_{true})}{dS_{true}}$) differential number counts, corrected for incompleteness, and the associated bootstrapped median number counts and standard deviation for the de-lensed Counts. The lower bin values are presented in column one.

Bin_L (mJy) (mJy)	$\frac{dN(S_{ob})}{dS_{ob}}$ $(mJy^{-1}deg^{-2})$	$\frac{dN(S_{true})}{dS_{true}}$ $(mJy^{-1}deg^{-2})$	$\frac{dN(S_{true})}{dS_{true}}_{boot}$ $(mJy^{-1}deg^{-2})$	σ_{boot} $(mJy^{-1}deg^{-2})$
1.00×10^{-2}	$(4.37\pm0.98)\times10^{6}$	$(3.06\pm0.99)\times10^{6}$	2.76×10^{6}	3.54×10^{5}
1.59×10^{-2}	$(8.60\pm0.58)\times10^{5}$	$(7.44\pm0.92)\times10^{5}$	7.71×10^{5}	7.13×10^{4}
2.51×10^{-2}	$(3.61\pm0.81)\times10^{5}$	$(4.63\pm0.35)\times10^{5}$	4.27×10^{5}	3.28×10^{4}
3.98×10^{-2}	$(2.23\pm0.12)\times10^{5}$	$(2.02\pm0.13)\times10^{5}$	2.16×10^{5}	1.80×10^{4}
6.31×10^{-2}	$(9.42\pm9.47)\times10^{4}$	$(1.08\pm0.14)\times10^{5}$	1.06×10^{5}	1.03×10^{4}
1.00×10^{-1}	$(4.44\pm0.52)\times10^{4}$	$(5.62\pm0.81)\times10^{4}$	4.73×10^{4}	5.70×10^{3}
1.59×10^{-1}	$(1.93\pm0.27)\times10^{4}$	$(1.90\pm0.38)\times10^{4}$	1.73×10^{4}	2.73×10^{3}
2.51×10^{-1}	$(7.17\pm1.31)\times10^{3}$	$(6.81\pm1.79)\times10^{3}$	5.92×10^{3}	1.22×10^{3}
3.98×10^{-1}	$(2.56\pm0.62)\times10^{3}$	$(1.62\pm0.69)\times10^{3}$	2.24×10^{3}	6.00×10^{2}
6.31×10^{-1}	$(2.47\pm1.23)\times10^{2}$	$(1.37\pm1.29)\times10^{2}$	2.65×10^{2}	1.37×10^{2}
1.20×10^{-0}	$(0.00\pm0.00)\times10^{0}$	$(4.68\pm6.35)\times10^{1}$	4.39×10^{1}	4.01×10^{1}

model of Béthermin et al. [2010b] builds on the basic L04 model and shows an agreement in both normalisation at the bright end with the P10 model and with the L15-counts at the peak. The predictions of [Rowan-Robinson, 2009, RR09 hereafter] show a poor agreement over the full range of the counts. The different behaviours may be explained by the dominant galaxy populations for each model. For P10 and L04 starbursts dominate the peak of the counts, whereas for RR09 the counts are predicted to be dominated by quiescent galaxies at all wavelengths. The makeup of the L15-final-cat population, dominated by star-forming galaxies, strongly disagrees with the RR09 scenario. This discrepancy is surprising as both P10 and RR09 are comprised of similar base galaxy populations - quiescent, starburst, extreme star burst and AGN dust torus. The L04 and P10 models vary in the mixture of galaxy populations included (although star-forming galaxies are common to both) but they both include strong evolution $\geq(1+z)^3$ for starburst galaxies up to a redshift of $z\sim1.5$. The L15 counts and P10 model show an excellent agreement over the full L15 flux range. There are two variations of P10, the 'Bright-end' (shown here) and the 'Burst' models (which also shows a good agreement with the L15 counts). The difference between the two versions of the model is the evolution mixture for starbursts and AGN, but both predict that the upturn and bump are dominated by LIRG and more moderate starburst galaxies with redshift distributions peaking at $z = 1.2$ and $z = 0.5$, respectively. Taking an M81 SED at the L15 median redshift of 1.04, an L15 flux density at the bump peak (0.3mJy)

corresponds to an L_{IR} of $\sim 4 \times 10^{11} L_{\odot}$ – giving an LIRG classification. A key difference between P10 and previous version of the model [Pearson, 2005] is the relegation of ULIRG to a more minor role, in favour of a more dominant LIRG component.

The L15 number counts show strong evolution consistent with galaxy evolution models that incorporate luminosity and luminosity density evolution and downsizing in star formation, i.e. the P10 model predicts star formation evolution is dominated by ULIRG to LIRG to starburst with decreasing redshift.

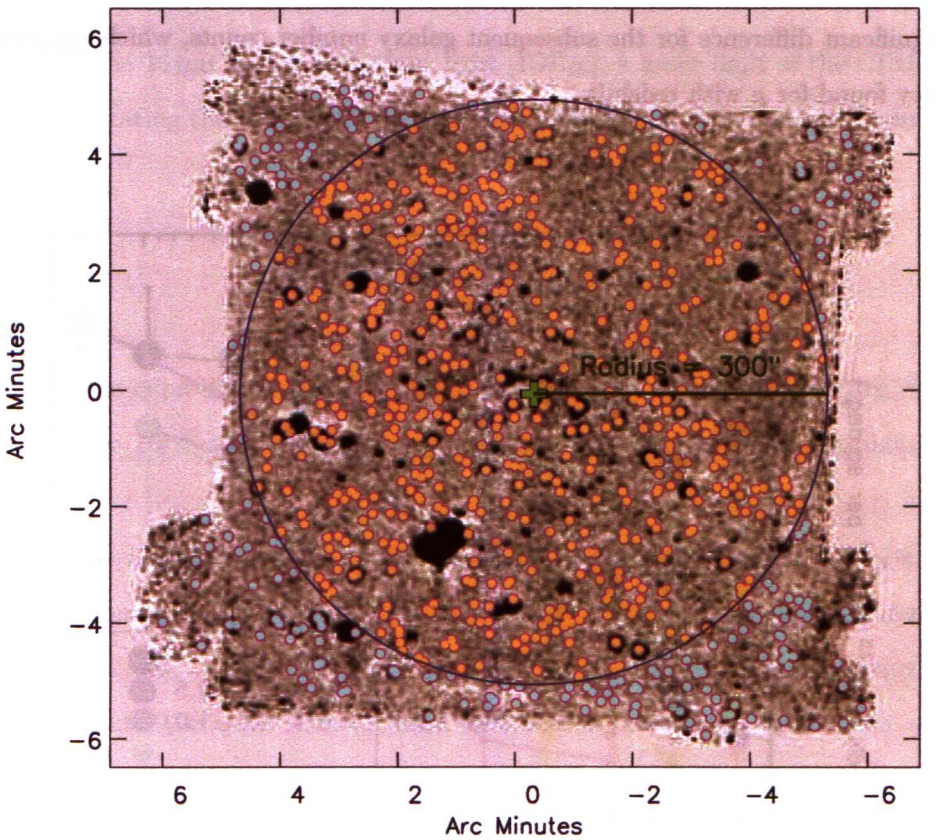

Figure 3.39: L15-image overlaid with the final L15-source catalogue with a circle of radius 5′ indicating the area of inclusion for sources used in the number counts check. The resulting counts agreed with the counts for the full catalogue, well within the bootstrapped confidence interval. These sources were also used for the counts taken in redshift bins (see figure 3.40)

3.13.2.1 Number count check

The L15 differential number counts were retaken after excluding the sources beyond a radius of 5′ from the cluster centre. This radius was chosen to removes all sources outside of the scope of the A2218 mass model and sources that could not be assigned a photometric redshift due to a lack of coverage (figure 3.39). The resulting counts were in agreement with the counts from the full L15 catalogue, within the bootstrapped confidence interval shown in figure 3.1. A second check was made focusing on the L15 sources that have no photometric redshift estimate and were assigned the L15 median redshift value. The differential number counts were retaken after reassigned these sources with a redshift of 2.0 and then again with a redshift of 3.0. There was no significant difference for the subsequent galaxy number counts, which supports the low dependency found for μ with redshift.

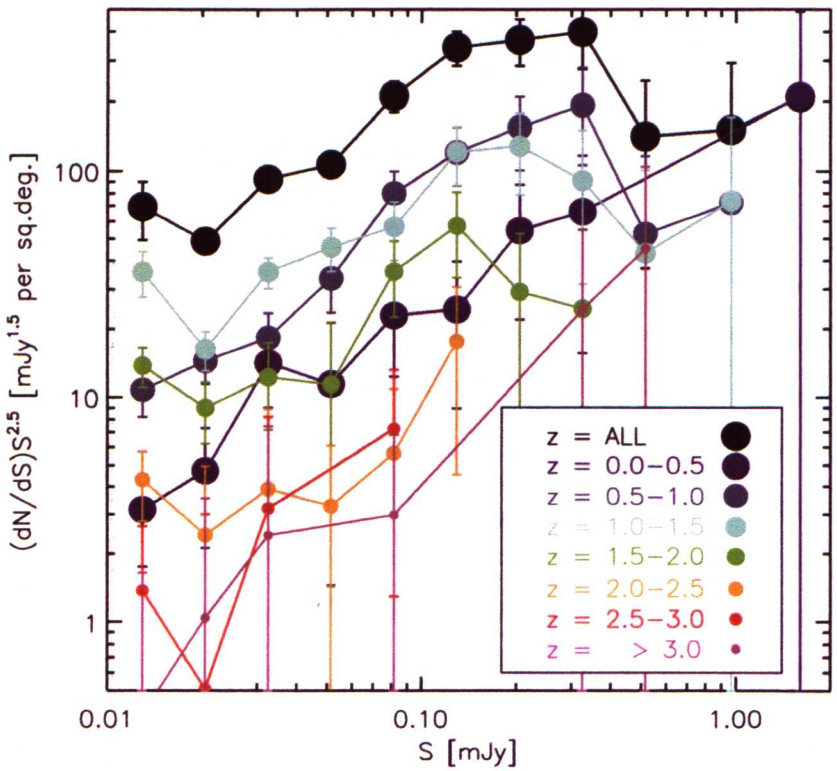

Figure 3.40: Euclidean normalised differential number counts taken for the L15 sources (with spectroscopic or photometric redshifts) in redshift bins. There are few statistics for the bins with redshift $z > 2.5$. The evolutionary bump is dominated by sources in the redshift range 0.5-1.5. The faint end of the counts have greater levels of contribution from higher redshift sources.

Number counts were also taken for the sources within the 5′ radius, after dividing them into redshift bins. A comparison of the results (figure 3.40) indicates that the 15 μm evolutionary bump, peaking around 0.2-0.4 mJy, is dominated by sources lying at redshifts ~0.5 - 1.5, which supports the median redshift of the L15 catalogue and suggests that there were high levels of dusty star formation occurring for this redshift range, in agreement with the redshift prediction of the P10 model. At the faintest end of the counts, there is a proportionally greater contribution from sources at higher redshifts, as expected.

3.14 15 μm integrated galaxy light

An estimate for the 15 μm integrated galaxy light (IGL_{15}), a lower limit of the $CIRB_{15}$, can be obtained by integrating the differential flux per unit area for the 15 μm number counts.

$$IGL_{15} = \int_{S_{min}}^{S_{max}} \frac{dN}{dS} \frac{S_{15}}{10^{20}} \nu_{15}\, dS \tag{3.11}$$

where IGL_{15} is expressed in units of nW m^{-2} sr^{-1}, dS is converted from $deg^{-2}$to sr^{-1} by $(180/\pi)^2$, 1 mJy = 10^{-20} nW m^{-2} Hz^{-1} and ν_{15} is the frequency of the 15 μm photons.

To increase the bright end of the 15 μm flux density range over which the IGL_{15} is estimated, the L15 counts were extended with the counts of Serjeant et al. [2000, re-calibrated following Väisänen et al. [2002]], Gruppioni et al. [2002] and Rush et al. [1993] giving a flux range between 0.01mJy and 10,000mJy. These counts were chosen in order to complement rather than overlap the L15 counts. Integrating over the combined counts gave an estimate of IGL_{15} = 1.9±0.5 $nWm^{-2}sr^{-1}$. Figure 3.41 shows the counts over the brighter flux range contribute < 1% of the total IGL_{15} estimate. The total IGL_{15} predicted by the P10 model, integrated over the full flux range, is 2.3 $nWm^{-2}sr^{-1}$. The P10 model provides an excellent fit to full range of the L15 counts (see figure 3.41) and if we assume the shape (but not the normalisation) of the P10 model counts, a slightly better estimate of the background contribution of 2.0±0.4 $nWm^{-2}sr^{-1}$ at ≥10 μJy is derived. Therefore, according to the best fit model, this data resolves 87±13% of the predicted $CIRB_{15}$ into individual sources.

Table 3.4: L15 IGL_{15} estimates, including those for different lower flux limits from Elbaz et al. [2002a] and Metcalfe et al. [2003]. The results give a relative, comparison to the P10 model estimate, and show the L15 data is resolving a further 19 % and 13% of the $CIRB_{15}$, respectively. RFA and RFB give the relative fractions resolved when integrating the counts and the P10 model, respectively.

limit	IGL_{15} A	RFA	IGL_{15} A	RFB
Elbaz	1.49±0.37	0.64	1.56±0.21	0.67
Metcalfe	1.64±0.38	0.70	1.70±0.24	0.73
L15	1.90±0.43	0.82	2.00±0.27	0.86

The lensed fields observed by ISOCAM (including A2218) produced 15 μm counts down to 0.03mJy and a lower limit estimation for the IGL_{15} of $2.7\pm0.62\,nWm^{-2}\,sr^{-1}$ [Metcalfe et al., 2003, and references therein], which agree with the L15 IGL estimate, within the errors. The ISOCAM result may be a slight overestimate due to confusion as no de-blending was applied and therefore the completeness could have been underestimated for the fainter bins. The result may also be affected due to the low statistics discussed in section 3.13. In order to remove the model dependency from the comparison, as both IGL estimates are based on a best fit model, the L15 IGL estimation was repeated after reseting the flux limit to several higher values. These limits included those of Elbaz et al. [2002a] and Metcalfe et al. [2003] (see table 3.4). This relative comparison predicts the L15 data are resolving a further 19% and 13% of the $CIRB_{15}$ over the estimates of Elbaz et al. [2002a] and Metcalfe et al. [2003], respectively.

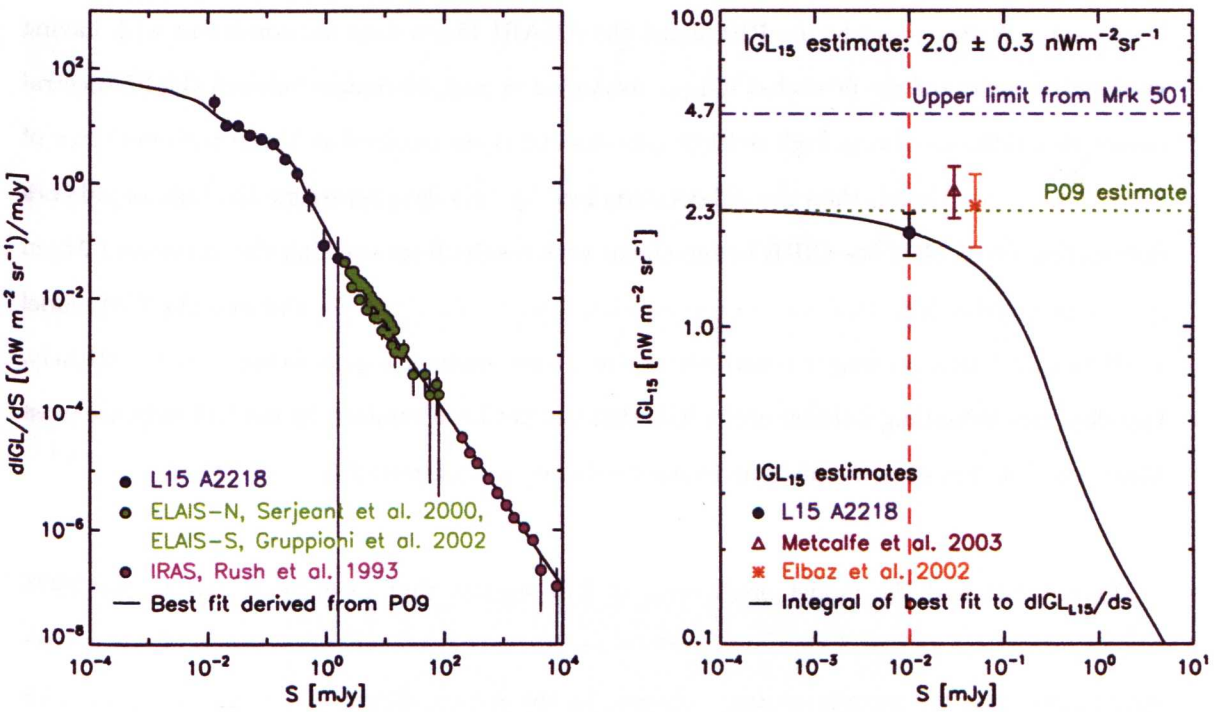

Figure 3.41: Left: differential contribution to the IGL_{15} as a function of flux density. Data shown are the L15-data, and those from Gruppioni et al. [2002]; Serjeant et al. [2000] and Rush et al. [1993], which were chosen due to the complementary (rather than overlapping) flux density ranges. The black line represents the best fit of the P10 model to the L15-data. Right: IGL_{15} estimates as a function of flux density. The L15-estimate is limited to 0.01 mJy, illustrated by the dashed red line. The Elbaz et al. [2002a] and Metcalfe et al. [2003] estimate limits are 0.05 and 0.03 mJy respectively. The IGL_{15} upper limit was derived from γ ray emission of Mrk 501 [Renault et al., 2001]

3.15 Discussion and conclusions

The L15 de-blended and de-lensed number counts are approximately commensurate with previous results and extend the faint end of the counts by $\sim 3\times$, in strong agreement with the P10 model. A strong evolution in both luminosity and luminosity density is required to explain the sharp deviation away from the no-evolution model ($\sim 2-5$mJy) and the re-convergence at fainter flux densities. The L15 data give an IGL_{15} estimate of $2.0\pm0.4\,\mathrm{nWm^{-2}sr^{-1}}$, down to $\sim$0.01 mJy. With respect to the P10 model the AKARI 15 μm data are consistent with having resolved the whole of the predicted IGL_{15}. Assuming no radical change between the IR spectral energy distributions of very high redshift galaxies and those resolved at 15 μm with median z of 1.0 [Elbaz et al., 2002a], then the galaxies resolved by this data represent the bulk of galaxies dominating the peak of the CIRB in agreement with results from stacking the unresolved 24 μm galaxy population [e.g. Béthermin et al., 2010a; Dole et al., 2006]. In addition the P10 model predicts that LIRG no longer contribute to the 15 μm number counts below $\sim$ 0.1 - 0.01mJy, therefore any remaining fraction of the IGL that has not been resolved by the L15 data are most likely a population of moderate star-forming galaxies at high-redshifts.

Figure 3.41 and the model predictions of P10 suggest that in order to ensure the 100% resolution of the $CIRB_{15}$, future observations need to probe depths in the region of one magnitude fainter than the sensitivity limit achieved by this survey, down to at least S_{15}=1μJy. This sensitivity will be required as the P10 model predicts the remaining unresolved fraction of the $CIRB_{15}$ is mainly due to high redshift moderate star bursts and LIRG, rather than ULIRG. The first possible direct measurement constraints of the $CIRB_{15}$ will come from the Japanese *SPICA* mission [Nakagawa, 2004].

Chapter 4

Stacking analysis of the contribution of mid-infrared galaxies to the sub-millimetre integrated galaxy light

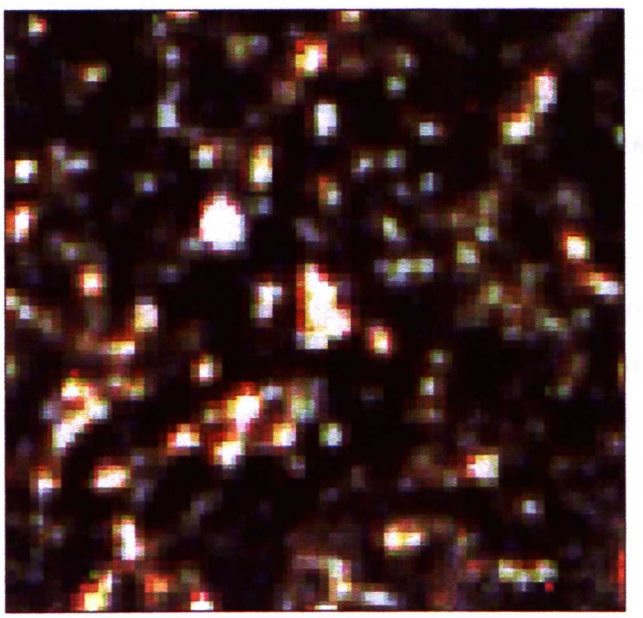

Figure 4.1: RGB image of Abell 2218, combined from the SPIRE 250, 350 and 500 μm maps.

4.1 Abstract

This chapter presents a stacking analysis of deep *AKARI* 15 μm selected sources at 250 μm, 350 μm and 500 μm with *Herschel/SPIRE* data. Stacking analysis takes advantage of the improved resolution at shorter wavelengths, and allows deeper analysis beyond the limiting confusion experienced at the SPIRE wavelengths. We investigate the effect of co-adding and stack ordering as a function of flux and redshift, and the contribution of AKARI 15 μm selected galaxy populations to the cosmic infrared background (CIRB) around its peak. We compare the 15 μm resolved fraction of the CIRB to the fractions resolved with previous results, obtained by stacking 24 μm selected populations at far-infrared wavelengths, with *Spitzer*, SCUBA and BLAST. This comparison shows 15 μm selected populations represent at least 40% of the galaxies responsible for the peak of the CIRB, in comparison to the direct measurement of FIRAS.

4.2 Introduction

The cosmic infrared background (CIRB) provides an important diagnostic for galaxy formation and evolution models, as it is dominated by dust emissions associated with star-formation and AGN accretion and thus traces the star-formation and black hole accretion histories of the Universe [see reviews by Hauser & Dwek, 2001; Lagache et al., 2005]. Great strides have been made towards resolving the monochromatic backgrounds into their individual galaxy components with galaxy number counts [e.g. Hopwood et al., 2010; LeFloc'h et al., 2009; Metcalfe et al., 2003; Papovich et al., 2004; Rodighiero et al., 2004]. In addition, stacking analysis has been successfully applied to estimate the unresolved contribution to the CIRB at far-IR/sub-millimetre wavelengths. Creating a 'stack', by combining image data at the position of sources selected from a higher resolution image, produces a single 'point source' from which an estimate of the total signal can be derived. Stacking deep mid-infrared Spitzer 24 μm selected populations has been previously performed with SCUBA (Sub-millimetre Common-User Bolometer Array) and BLAST (Balloon-borne Large-Aperture Sub-millimetre Telescope) imaging [Béthermin et al., 2010a; Devlin et al., 2009; Dole et al., 2006; Serjeant et al., 2008]. Stacking analysis, such as these, rely on the correlation between mid-IR and far-IR emission in star-forming galaxies, and assume the bulk of the galaxies responsible for the CIRB, at its peak ($\sim$140 μm-200 μm [Devlin et al., 2009; Dole et al., 2006]), are also those being sampled at mid-IR wavelengths. Results

to date have suggested that the CIRB at 70 μm, 160 μm and 250 μm can be mainly accounted for by the populations observed at 24 μm, and also that 24 μm populations are representative of the galaxies which dominate the CIRB at 350 μm, 450 μm and 500 μm [Béthermin et al., 2010a; Devlin et al., 2009; Dole et al., 2006; Marsden et al., 2009; Serjeant et al., 2008]. In contrast, at 850 μm the 24 μm population only resolves around one quarter of the background [Serjeant et al., 2008]. There is some debate as to these claims and Chary & Pope [2010, CP10 from hereon] conclude that the fraction of the CIRB being resolved at FIR wavelengths is actually closer to one half, and previous claims have been overestimated due to photometric blending and multiple flux counting.

Taking deep source counts at 15 μm is interesting due to the sensitivity of MIR observations to redshifted polycyclic aromatic hydrocarbon (PAH) and silicate features, which translates to deep 15 μm observations sampling galaxy populations that dominated the crucial epoch of peak star-formation [Blain et al., 2004; Dickinson et al., 2003b; Elbaz et al., 2002a; Hopwood et al., 2010]. Deep 15 μm number counts are limited by source confusion, however with *AKARI*'s IRC (*AKARI*: Murakami et al. [2007]; IRC: Onaka et al. [2007]), coupled with the exploitation of gravitational lensing effects due to observing through a gravitational lensing cluster, it has been possible to take deep observations that probe beyond the blank field sensitivity of AKARI. These data sample 'normal' galaxy populations as well as those highly luminous in the IR i.e luminous infrared galaxies (LIRG; $10^{11} < L_{IR}/L\odot < 10^{12}$) and ultra luminous infrared galaxies (ULIRG; $10^{12} < L_{IR}/L\odot < 10^{13}$), which has strongly constrained the faint end of the 15 μm galaxy number counts [Hopwood et al., 2010], extending previously reached depths by around a factor of 3. Utilising the effects of gravitational lensing on the faint galaxy population behind the cluster Abell 2218 (A2218 from hereon), which gives magnifications up to at least a factor of 10 towards the core, produced a deep 15 μm source catalogue (see chapter 3, section 3.3). With this catalogue the strength of the correlation between galaxies sampled at 15 μm and those at the SPIRE wavelengths (250 μm, 350 μm and 500 μm) has been investigated.

In this chapter a stacking analysis is presented of an ultra deep population of 15 μm selected sources at SPIRE wavelengths and comparative IGL are given. The data and data reduction used to produce the source catalogue, used for the stacking, are discussed in detail in chapters 2 and

Table 4.1: IRC and SPIRE information.

Instrument	$\lambda(\mu m)$	Pixel scale($''$)	θ_{FWHM}(pixels)
IRC	15	2.38	2.5
SPIRE	250	6.00	3.0
SPIRE	350	10.0	2.5
SPIRE	500	14.0	2.5

3. In the current chapter, SPIRE data is presented in section 3, stacking analysis methodology is outlined and the results discussed in section 4. In section 5 simulated stacking is performed, and the results and comparison to other works are presented in section 6 and discussed in section 7. From here on we will refer to the 250 μm, 350 μm and 500 μm maps as the SW, MW and LW maps respectively.

4.3 *Herschel*/SPIRE data

A2218 has been observed at all three SPIRE bands during Herschel's scientific demonstration phase (SDP). Two sets of public data were obtained from the Herschel Science archive[1] for each SPIRE waveband. The level 2 HIPE[2] output [Ott et al., 2010] were combined to give both signal and instrumental noise SW, MW and LW maps, see figures 4.1 and 4.2. The area of the SPIRE maps is greater than that observed by AKARI, placing the full L15-catalogue well inside the low signal-to-noise SPIRE map edges. A slight discrepancy was found between the astrometry of the SPIRE and L15 data, and therefore the SPIRE data was re-registered onto the L15-image astrometry. The level 2 HIPE products are calibrated to units of Jy/beam, although the maps have not been convolved with a point spread function (PSF) filter. All three SPIRE maps were converted to mJy/pixel using the respective beam areas of $\pi\theta^2_{FWHM}/(4\ln 2)$. See table 4.1 for the SPIRE pixel scales and θ_{FWHM}.

[1] http://archives.esac.esa.int/hsa/
[2] See Appendix B for a description of HIPE.

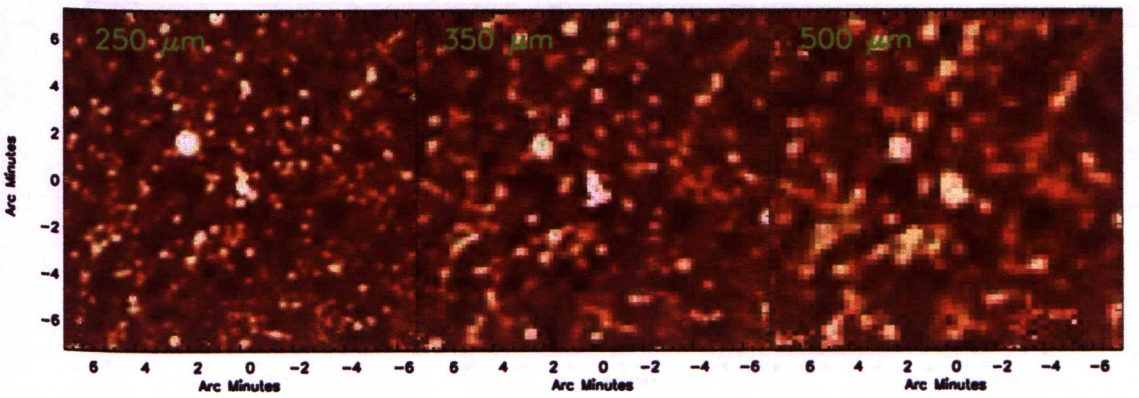

Figure 4.2: Combined and cropped SPIRE SW (left), MW (middle) and LW (right) maps of A2218.

4.4 Stacking analysis of the 15 μm population

4.4.1 Resolved fraction

A source extraction is performed on each SPIRE map and then the stacking analysis progresses in three stages. Firstly, for each SPIRE map, counterparts are matched with L15 cluster members, using a search area with a radius of 1σ of the respective SPIRE θ_{FWHM}. Any identified cluster counterpart with significance greater than $3\,\sigma$ is subtracted. Secondly, high signal-to-noise SPIRE sources ($> 5\,\sigma$) that have an L15 counterpart were subtracted from the SPIRE maps to give the resolved galaxy contribution. Thirdly, the residual maps are stacked to give the unresolved contribution.

Our de-blended AKARI 15 μm source catalogue (L15-catalogue hereafter) of 918 sources, including cluster members, stars and foreground objects, was constructed using multi-waveband priors (see chapter 3 section 3.6.1) and PSF fitting (see chapter 3 section 3.7.5). An initial PSF fitting of the SPIRE maps was performed. Gaussian PSFs were constructed using the θ_{FWHM} of the SPIRE wavebands - 18″, 25″ and 34″. These PSFs, with added nominal sky noise (necessary for use with DAOPHOT [Stetson, 1987]), and the 15 μm source positions were used to CLEAN [Högbom, 1974] each SPIRE map via PSF fitting with ALLSTAR [Stetson, 1987]. ALLSTAR rejects sources iteratively based on their signal-to-noise ratio (more details of the ALLSTAR algorithm are given in section 3.7.5). For the SW map the number of sources fitted by ALL-

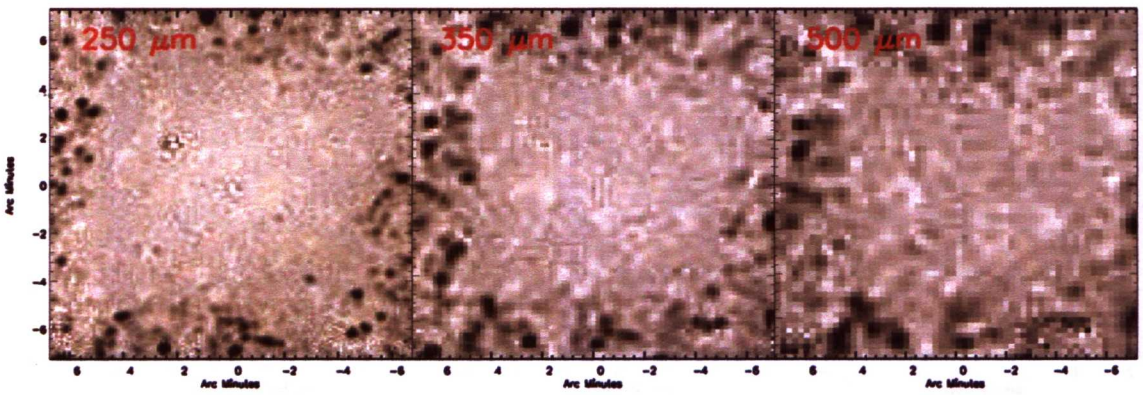

Figure 4.3: ALLSTAR residual maps of Abell 2218. The SW map (left) was cleaned using the full AKARI source catalogue for PSF fitting with ALLSTAR. The MW map (middle) and LW map (right) were cleaned with an edited version of the L15-catalogue after applying lower limits of 20 μJy and 40 μJy respectively. There were 414, 304 and 122 sources extracted from the maps by ALLSTAR, respectively.

STAR was 414. For the MW and LW maps the input L15-catalogue was reduced in size using cuts in flux density of 20 μJy for the MW map and 40 μm for the LW map, which corresponds approximately to the 50% and 100% completeness levels for the 15 μm map. This cut was necessary to allow ALLSTAR to run efficiently within the maximum number of iterations due to the large number of faint sources rejected from the full L15-catalogue. The number of sources subtracted by ALLSTAR from the MW map was 304 and 122 from the LW map, which reflects the reduction of resolution and increasing confusion levels with wavelength. It should be noted that as ALLSTAR re-centres source positions during the fitting iterations, the output positions will not generally match those of the input catalogue. The cleaned maps (figure 4.3) show some residual structure, mainly at the centre of the cluster where there is high photometric blending and at the position of the brightest extended foreground galaxy. An area of 50″ radius, around the brightest extended source (source A) was excluded from stacking for both the SW and MW maps. This exclusion was not necessary for the LW map where source A is more point-like and well subtracted with a Gaussian PSF.

It was necessary to remove foreground galaxies, stars and cluster members from the image prior to stacking, to avoid any bias on the results. Stars are only weakly detected (if at all) at all three SPIRE wavebands. Cluster members within the L15 sources were identified during the

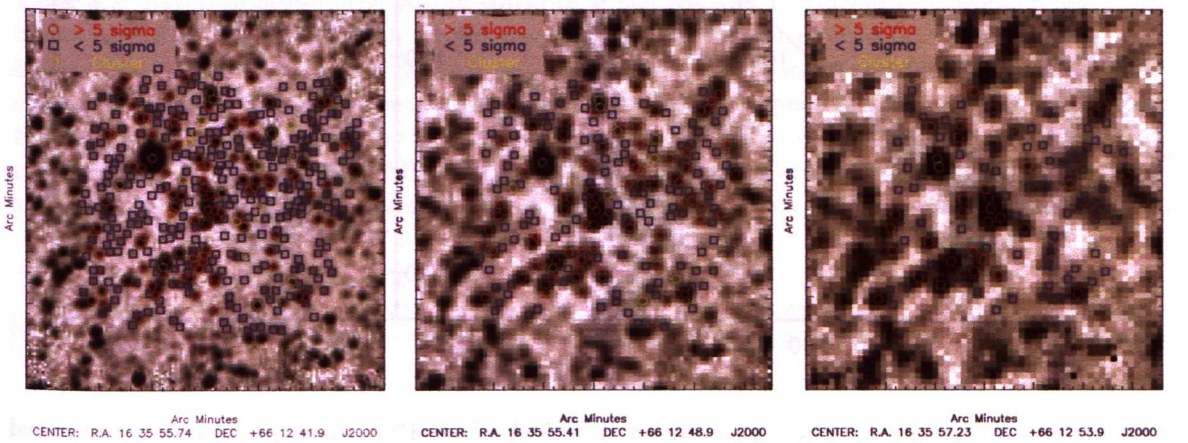

Figure 4.4: SPIRE SW (left), MW (middle) and LW (right) maps of Abell 2218. Overlaid are the results of PSF fitting with ALLSTAR, showing the matched cluster members and sources above and below $5\,\sigma$. The two cluster members shown for the LW map were merged to a single source before subtraction.

construction of the photometric redshift catalogue (see chapter 3, section 3.10) or from spectroscopic redshifts. The position of all cluster members in the L15-catalogue were crossmatched with each ALLSTAR catalogue to identify SPIRE counterparts. The nearest neighbour within a radius of 1σ of the θ_{FWHM} to an L15 source was considered a match. All cluster counterparts with signal-to-noise > 3 were considered possible contaminants to the stacks, and therefore were subtracted from the maps, using a Gaussian PSF and the ALLSTAR position and flux estimate. For the SW image there were 20 cluster members identified and subtracted, the positions are shown in figure 4.4. 11 cluster members were subtracted from the MW map and only the brightest foreground galaxy (previously mentioned) was removed from the LW map.

Stacking analysis can be used to resolve the galaxy population within a confused image by applying positional priors obtained from higher resolution data. One problem that is inevitable when stacking confusion limited data, and in this case a crowded field, is the possibility of summing source flux multiple times. To minimise this issues we followed a similar method to that presented in CP10, who argue that masking the central area of a source, once included in the stack, is essential to minimise the effects of confusion noise on the resulting photometry.

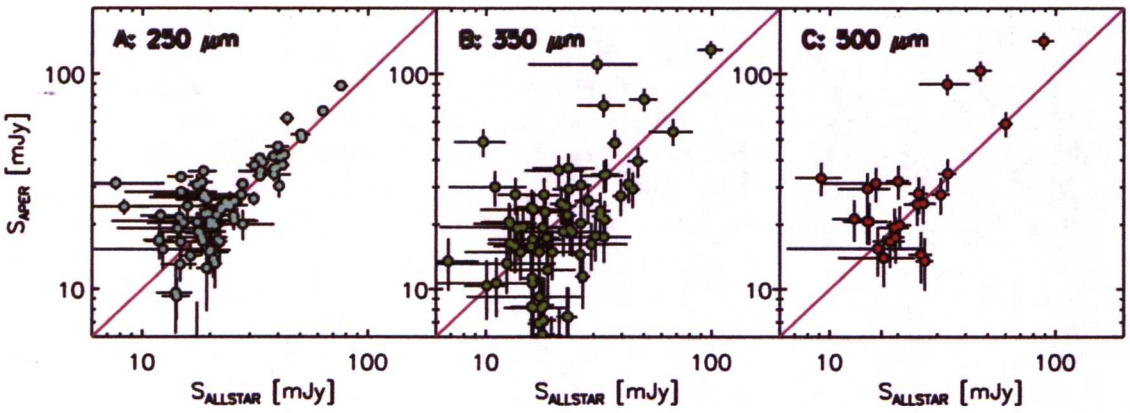

Figure 4.5: Corrected aperture photometry and ALLSTAR PSF fitted photometry, compared for the $> 5\sigma$ sources for each SPIRE waveband. This comparison shows a largely one to one trend, but has an increased scatter at the fainter end due to photometric confusion of the SPIRE sources. The bright outliers in the SW and MW comparisons are the result of increased photometric blending with wavelength, therefore they are not as significant for the SW comparison.

4.4.2 Unresolved fraction

Stacking for all three SPIRE wavebands followed the same method. For each map we selected sources from the respective ALLSTAR catalogue, above a 5σ level, and performed a nearest neighbour search against the edited L15-catalogue (with the foreground, stars and cluster members removed). The search criterion was set to within 1 SPIRE θ_{FWHM} of an L15-centroid, see table 4.1. Figure 4.5 shows a comparison of corrected aperture photometry[1] for the resulting sources, and the PSF-fitted photometry recovered via ALLSTAR. Full flux densities for the aperture photometry were achieved by applying a corrected factor, derived from aperture photometry of the respective Gaussian PSF, normalised to an area of 1. As expected, this comparison is close to 1:1 at the bright end, with a greater scatter for fainter sources, due to the photometric confusion within the SPIRE maps.

The high sigma sources matched to L15 counterparts were subtracted from the map using the ALLSTAR positions and a Gaussian PSF, normalised to the ALLSTAR photometry for each source. Magnification corrections were derived for the 15 μm sources using LENSTOOL [Jullo et al., 2007], with a mass model of A2218 [Elíasdóttir et al., 2007; Kneib et al., 1996], (which

[1] All aperture photometry of the SPIRE maps were taken with an aperture radius of the respective SPIRE θ_{FWHM}.

Table 4.2: IGL estimates derived from stacking at the AKARI 15 μm source catalogue positions in the A2218 SPIRE maps, both for the resolved ($> 5\sigma$) and unresolved ($< 5\sigma$) stacks. S_{L15ord} stacks are ordered by L15 flux density, z_{ord} are ordered by redshift, and for the MW and LW stacks the limiting flux densities and redshifts were applied, respectively. λ is the wavelength of the map being stacked and C is the completeness of the unresolved stack, due to masking. Also presented are the total ALLSTAR photometry obtained (minus cluster contribution). The total stack IGL estimates are compared to the measurement by Fixsen et al. [1998].

Order	λ (μm)	C	$> 5\sigma$ (nW m^{-2} sr^{-1})	$< 5\sigma$ (nW m^{-2} sr^{-1})	$S_{ALLSTAR}$ (nW m^{-2} sr^{-1})	FIRAS (nW m^{-2} sr^{-1})	S_{stack}/ FIRAS
S_{L15ord}	250	0.74	2.126±0.038	2.091±0.094	4.218±0.101	10.4±2.3	0.41
z_{ord}	—	—	—	1.921±0.091	—	—	0.38
S_{L15ord}	350	0.48	1.259±0.052	0.564±0.057	2.361±0.039	5.4±1.6	0.34
z_{ord}	—	—	—	0.451±0.066	—	—	0.32
S_{L15ord}	500	0.31	0.279±0.016	0.361±0.054	1.341±0.026	2.4±0.6	0.27
z_{ord}	—	—	—	0.332±0.067	—	—	0.27

has been extensively tested for reliability via spectroscopic comparison [Ebbels et al., 1998]), and the L15 redshift catalogue (see chapter 3, section 3.12 for details). The flux densities for the high sigma sources were then corrected for magnification, and a simple sum was taken to give the contribution of the resolved sources to total IGL estimate. After lensing correction, the total flux density of the 5σ sources was reduced by around 40% for each SPIRE waveband. Towards the core of A2218 the magnifications factors are up to 16×. Overall the median flux amplification factor for the full L15-catalogue is ~1.2, which reflects the size of the field. The total of the demagnified ALLSTAR photometry was taken and used for comparison to the resulting total stack photometry (listed in table 4.2).

4.4.3 Stacking by brightness

Three methods of stacking the residual maps, with the cluster members and $> 5\sigma$ sources subtracted, were tested. Firstly stacking in the order of the 15 μm photometry (brightest first), which was compared to stacking in order of SPIRE brightness and by MIPS 24 μm brightness. Secondly the stacking was repeated using the order of the L15 redshift catalogue, from high to low. The first two methods were also used to stack in bins (i.e. in flux bins and then in redshift bins), which guided the flux or redshift limit estimates to be applied to the full stacks. Finally the limits for both brightness ordering and redshift ordering were combined. A comparison of

the methods used to combine the stacks and take the subsequent photometry is discussed at the end of this section, for which all the photometry was taken using PSF fitting of the stack, after combining using a simple sum.

For each SPIRE map the identified and subtracted 5σ sources were removed from the edited L15-catalogue. The resulting catalogues (L15 stacking catalogues) were then ordered by descending brightness. Initially no flux density limit was imposed, and the maps were stacked at all of the remaining 15 μm source positions. Starting with the brightest L15 source position, a postage stamp image was cut out and added to the stack after correcting for magnification. The widths of the stamps were set to 13 pixels for each SPIRE map, i.e. $1.3'$ for SW, $2.2'$ for MW and $3.0'$ for LW. A region of the map, centred at the position of the source coordinates, with radius of 2 pixels from the central pixel position (i.e. 2.5 pixels), was set to zero after each stamp was taken. An example of a masked image, after the stacking has been performed, is shown in figure 4.6. Masking the central area of the sources in this way minimises the number of times the flux of any source contributes to the final stack. A simple sum was taken of the resulting stamp cube, and a completeness correction applied. This completeness correction is required particularly for sources in close proximity to bright sources, which have already been stamped, and will therefore have a large portion of their stamp already masked by zeros. The completeness is the fractional number of non-zero pixels (see table 4.2), and each simple sum stack is divided by the estimated completeness. The photometry of the stack was taken by centring and normalising the corresponding PSF to the stack peak, and converting to surface brightness in MJy sr^{-1}, using the area of the AKARI map minus the area occupied by cluster members and the excluded area around the brightest foreground galaxy. This photometry method is discussed further in section 4.4.5. The surface brightness taken for data of wavelength λ, was converted to units of nW $\mathrm{m}^{-2}\,\mathrm{sr}^{-1}$ using the relation:

$$1\,\mathrm{nW\,m^{-2}sr^{-1}} = \frac{\lambda/\mu\mathrm{m}}{3000}\,\mathrm{MJy\,sr^{-1}} \tag{4.1}$$

To assign errors to the stacked flux densities, the stacking procedure was repeated using a bootstrapping method. For each SPIRE map the L15 stacking catalogues was resampled, with-

out bias, after randomly assigning a new flux density to each source within the corresponding 3σ photometric errors, giving a new population equal in number to the stacking catalogue. This new catalogue was then sorted into descending order of brightness, before proceeding with stacking. For each SPIRE image this resampling and stacking was repeated 10,000 times, and the distribution of the resulting photometry was fitted with a Gaussian to obtain the 1σ errors.

The initial stacks showed minor astrometry offsets, which were corrected by subtracting the offset from the header astrometry for each map and then restacking. This correction was repeated until the resulting stacks were centred. The initial stacks, with corrected astrometry, are shown in figure 4.7. The SW stack is well behaved, whereas the MW and LW stacks have a somewhat weaker signal at the centre and considerable sky structure around the edges. To reduce this structure the stacks were retaken, with the nth stamp rotated by $n\pi/2$ [Dole et al., 2006]. The bottom panels of figure 4.7 illustrate that applying this rotation method reduces the structure, but not entirely removes it.

To rule out cluster contamination as a source of this structure, from faint cluster members $< 3\sigma$ in the SPIRE maps, the remaining cluster member positions (not already subtracted from the respective maps) were added to the L15 stacking catalogues used for stacking. The stacks were retaken, firstly for the L15 stacking catalogues plus cluster sources and then purely for the cluster members, to test if any appreciable signal could be detected (see figures 4.8 and 4.9). The cluster members make negligible difference to the results and show no discernible signal when stacked at MW and LW.

Another cause of the structure could be due to the stacking order itself. The stacks are taken in the order of decreasing brightness according to the L15 stacking catalogues, which therefore relies on the assumption that this order translates to SPIRE flux densities. Comparisons of the $> 5\sigma$ SPIRE source flux densities and the corresponding L15 photometry, show there is no apparent relation between the two (figure 4.10). Therefore, the order of stacking could well lead to bright SPIRE sources appearing at the edge of stamps centred on fainter sources, as the bright sources have yet to be masked. Subtraction of the brightest L15 source that remained in the edited L15 stacking catalogues illustrates this point. This source is at low redshift ($z =$

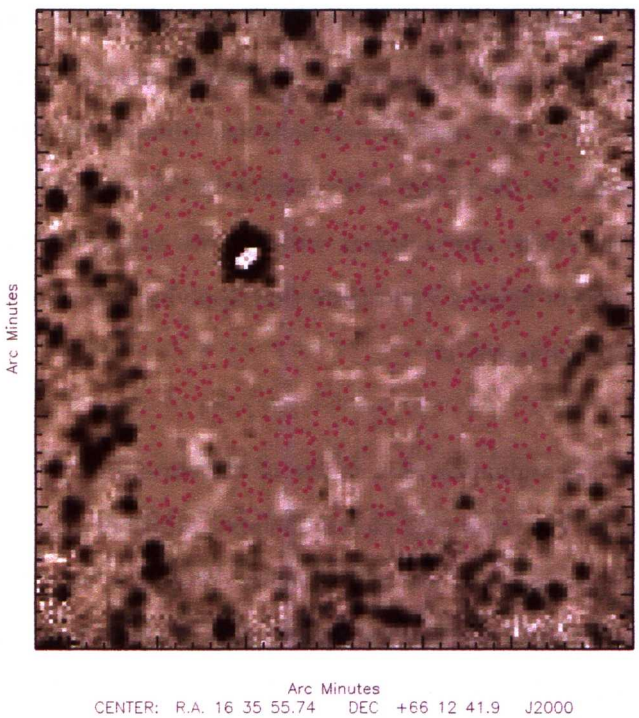

Figure 4.6: SPIRE 250 μm residual image, after stacking the sources $< 5\,\sigma$ and applying a zero mask at the position of each stacked source for each stamp taken and overlaid with the L15 extraction catalogue (marked with pink circles). The identified SW cluster members and $> 5\sigma$ sources counterparts to the L15-source catalogue were removed prior to stacking.

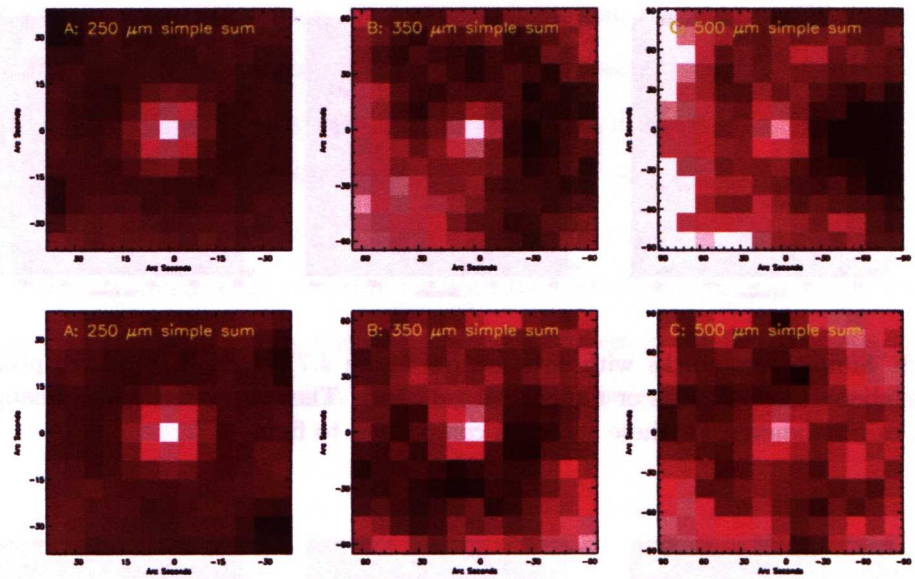

Figure 4.7: Simple sum co-added stacks (A-C top) compared to the same stamps obtained with the nth stamp rotated by $n\pi/2$ (A-C bottom), following Dole et al. [2006]. The structure present at the edges of the MW and LW stacks is notably reduced using the rotation method.

0.3), and could be a cluster member with an over estimated photometric redshift (see chapter 3, section 3.10 for a discussion on the minimum limit for an EaZy derived photometric redshift), and is a factor of 4 brighter than the next brightest L15 source. This source also has no detectable counterpart in any of the SPIRE maps. Subtracting this source prior to stacking had a noticeable affect on the resulting MW and LW stacks and stack photometry. As this is not likely to be an isolated case, it can be assumed that L15 sources, at the bright end of the catalogue, are contributing the final edge structure, via relatively faint SPIRE sources being masked early on in the stacking process.

To evaluate the stacking order as a cause of the edge structure, the L15 stack catalogues were roughly reordered using the pixel values at the source positions in each SPIRE map. The stacks were retaken without rotation, firstly for all positions and then for all those positions with positive central pixel values followed by stacks of just those positions with negative pixel values. During the stacking, each stamp has the median stamp value subtracted and therefore the negative central pixel values occur as cumulative random fluctuations about the sky level, however due to correlated noise on the scale of the PSF, stacking the negative positions leads to

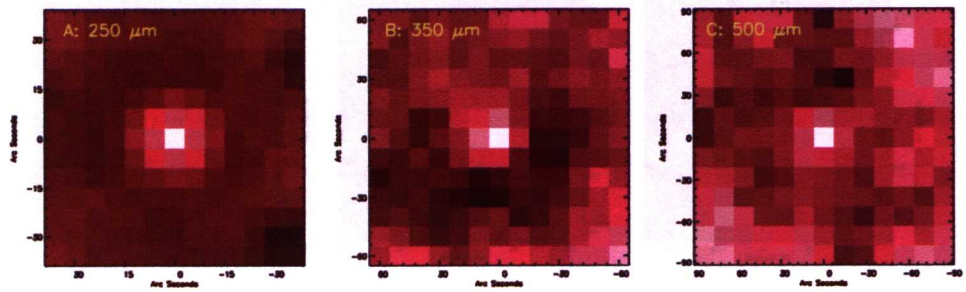

Figure 4.8: Simple sum stacks with rotation (as figure 4.7) of the L15 source positions and cluster members (but not stars or foreground galaxies). There is no noticeable change to edge structure, or photometry, for these stacks in comparison to figure 4.7.

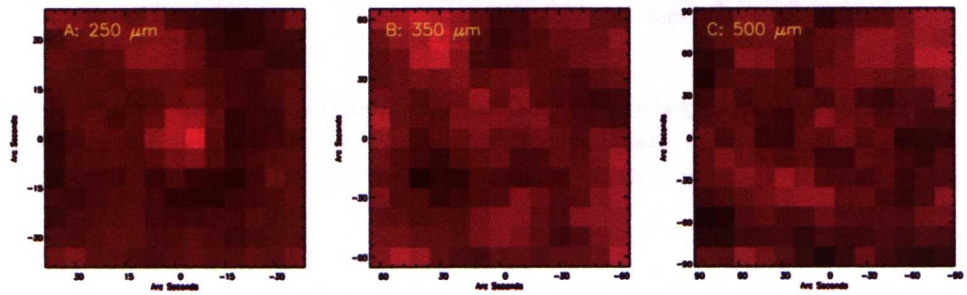

Figure 4.9: Stacks of cluster member positions. There is no detection at MW and LW, and a faint detection at SW, which proves that faint cluster members are not adding to the edge structure seen in the MW and SW stacks.

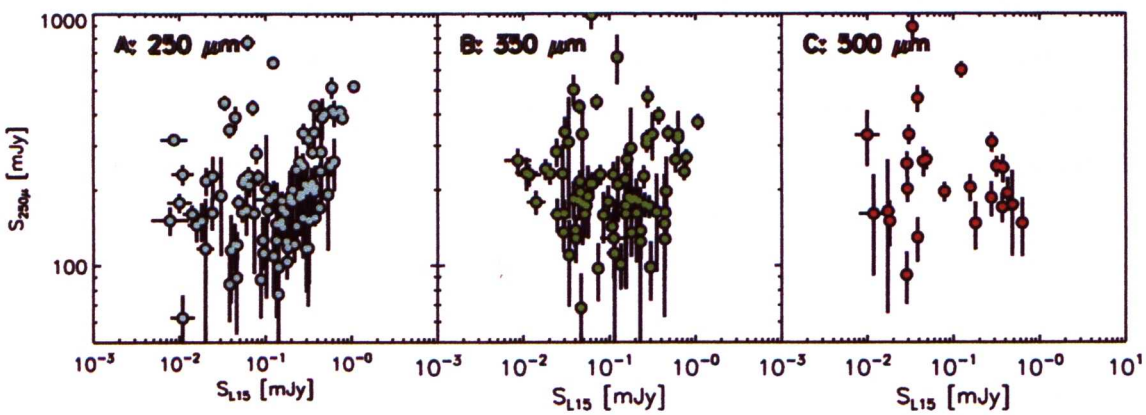

Figure 4.10: L15 flux densities vs SPIRE flux densities (SW left, MW middle and LW right) for the $> 5\sigma$ SPIRE sources, with L15 counterparts. This comparison shows little correlation between the sets of flux densities, and therefore strongly suggests that ordering the stacks using L15 brightness is not an ideal method to avoid flux contamination of the stamp edges.

what is effectively a negative source. Of course such random fluctuations will be canceled out by positive random fluctuations, barring any Eddington bias, so the effect on the final stack is assumed to be negligible. The resulting stamps are shown in figure 4.11. Stacking by SPIRE brightness provides a comparison for the optimum stacking order that can be achieved with the stacking catalogue begin used. Comparing the stacks in column A of figure 4.11 and the top row of figure 4.7 show a similar edge structure for both the SPIRE ordered and L15 ordered stacks. This suggests the structure mainly results from bright sources in the SPIRE maps with no L15 counterparts, as they would be high in the SPIRE stacking order and quickly masked otherwise.

4.4.3.1 Stacking in flux bins

Four logarithmically spaced flux density bins were defined for each SPIRE map, and stacks were taken using the positions of the L15 stack catalogue sources within each bin. The stacking was carried out starting with the brightest bin first, with cumulative masking over all four bins. The stacking was carried out for ordering based on the L15 flux densities, the SPIRE pixel values and the MIPS24 pixel values. The comparison was made with MIPS 24 μm brightness, as several previous stacking analyses have been performed using catalogues extracted from MIPS μm data [e.g. Béthermin et al., 2010a; Dole et al., 2006; Serjeant et al., 2008]. The L15 sources within the MIPS 24 μm coverage were reordered very roughly using the MIPS pixel values, which did not discriminate between the lower and higher signal-to-noise areas of the MIPS 24 μm image. For each sub-stack (i.e. stack for one bin), the corresponding pixel value distributions were taken noting the number of sources and completeness per bin. Figure 4.12 and figures in Appendix 1 (A1 - A8) show the resulting distributions and stacks and indicate that the resulting stacks are highly dependent on stack position ordering.

The most interesting feature of the resulting stacks, comes from the comparison between different orderings for the SW map. Figures 4.12 and A2 (in Appendix A) show the MIPS24 ordered stacks are more similar in relative intensity of detection, and number of sources in each bin, to the SPIRE ordered stacks that to the stacks ordered by L15 brightness. This trend is not however seen for the MW and LW maps, where the pattern of stacks and pixel distributions is far similar between the MIPS and L15 orderings. These results suggest that for the galaxy

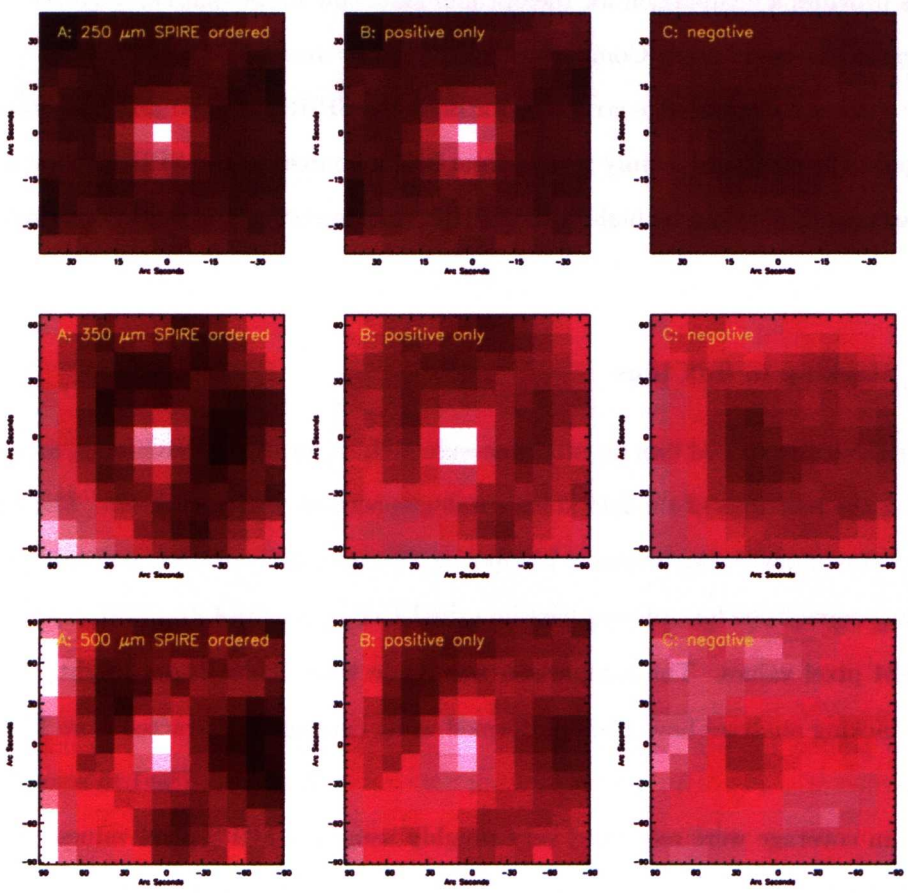

Figure 4.11: Stacks from SPIRE ordered stacking. The order was roughly defined using the respective SPIRE map pixel values at the L15 source position. The left panels show the resulting stacks from the full L15-catalogue. The middle panels show stacks taken only for the positive pixel values and the right panels show the negative pixel value only stacks. The stacks were taken without rotation to maintain a fair comparison and for each waveband the stacks were plotted using the same pixel scaling. The SW stack shown little relative contribution from the stamps associated with the negative pixel values. For the MW and LW the negative stacks contribute some structure to the edges of the stacks, but not the majority. The correlated noise on the scale of the PSF is clearly visible, giving a negative source into the centre of each negative pixel stack. The random positive fluctuations will approximately cancel out this negative source in the total stack (ignoring any Eddington bias).

populations sampled at 15 μm, there is a stronger correlation between the 24 μm and 250 μm emissions than between the 15 μm and 250 μm, implying that a 24 μm selected population will be more representative of the population dominating the 250 μm background than a 15 μm population. This is in contrast to the $\gtrsim$ 350 μm stacks, where the 15 μm and 24 μm ordered stacks show a similar difference to the SPIRE ordering.

The moderate to low numbers of statistics involved with stacking in bins, for these L15 stacking catalogues, leads to large uncertainties in the sub-stack photometry, and therefore the stacks in brightness bins method was not applied for the final unresolved contribution estimate. However, it is a useful exercise to compare the results across the bins, indicating possible lower limits in flux density for the MW and LW L15 stacking catalogues. The L15 ordered and MIPS24 ordered stacks of the faintest two bins for the LW map make no substantive contribution to the combined total photometry. For the L15 ordered stacks this is also true for the MW map, whereas there is a faint detection for the MIP24 ordered results. For the faintest SW bin the completeness is approximately 0.3. The MW and LW maps suffer lower completeness levels in their final bins due to their greater pixel scales (i.e. fewer pixels per stack) and therefore the lower limits were set to achieve approximately a 0.3 completeness in the final bin, and the best agreement between the simple sum and weighted mean methods of co-adding for the full stacks. Using this completeness based criteria gave L15 flux density limits of 23 μJy for MW and 50 μJy for LW. The stacks in bins resulting from these flux cuts are shown in Appendix 1 (figures A9 - A14). Once the limits are applied there is a visible detection in the final bin for the LW map, and the corresponding photometry make a positive contribution to the total. For the final stacks, ordered by L15 flux density, the lower limits of 23 μJy for the MW map and 50 μJy for the LW map were applied.

4.4.4 Stacking by redshift

Negative K-correction at SPIRE wavelengths (especially 500 μm) leads to sources having approximately constant flux densities for redshift $z > 1$, whereas the 15 μm selected sources do not benefit in same way. Low redshift sources ($z < 1$) that have depleted dust levels are more likely to be faint at SPIRE wavelengths, therefore, to avoid top order stacking at the positions of bright low redshift L15 sources, with faint SPIRE counterparts, the L15-catalogue was ordered

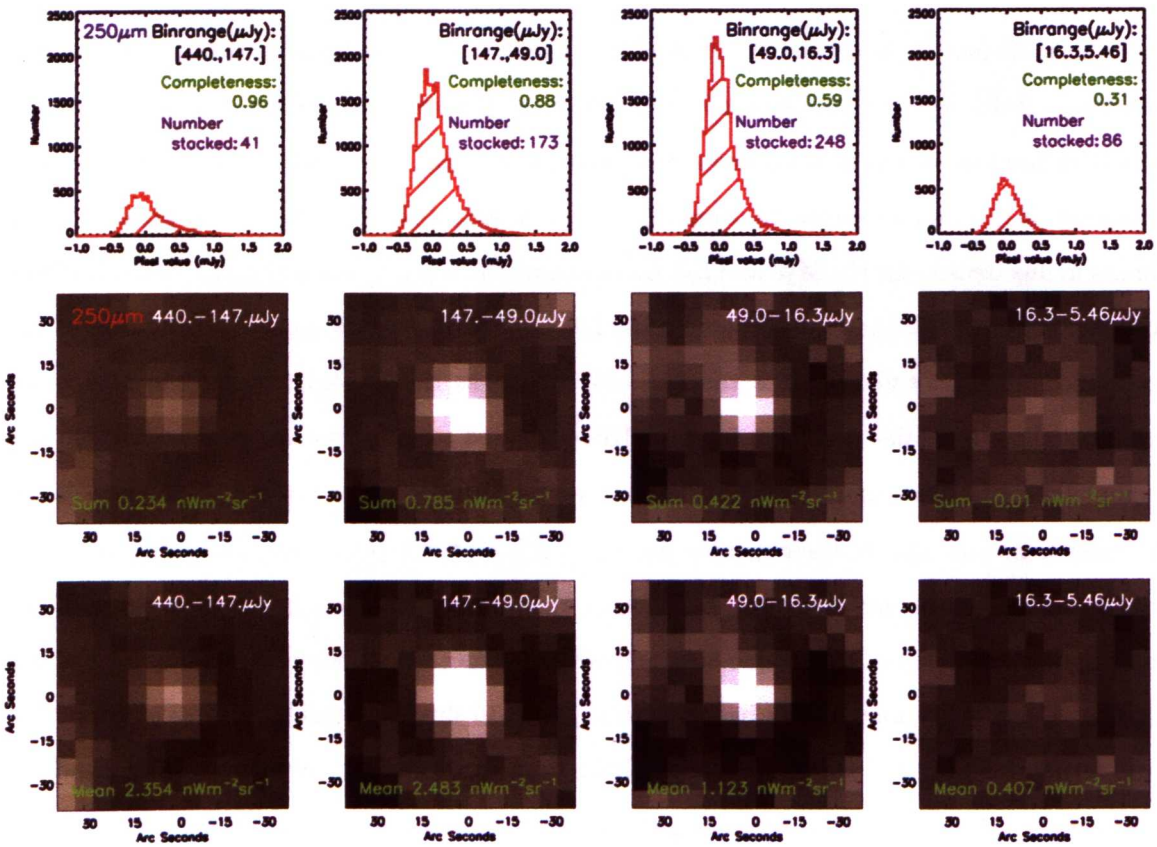

Figure 4.12: L15 flux density ordered stacks, taken in flux bins for the SW map. The stacks with the strongest detection (for both the simple sum - middle row, and weighted mean - bottom row) occurs in the second brightest bin (49.0 - 147 μJy), with the highest number of statistics in the next faintest bin (18.3 - 49.0 μJy). The brightest bin has only a comparatively weak detection, showing the correlation between the brightness of L15 sources and SPIRE sources is poor.

from high to low redshift. This redshift ordering is biased by the number of sources assigned the median L15 redshift of 1.044, but should place the majority of higher redshift sources near the beginning of the stacking list, as a greater number of higher redshift sources are detected towards the core due to the boosting in flux density due to gravitational lensing. These sources are also more likely to have a robust photometric redshift due to greater multi-waveband coverage.

4.4.4.1 Stacking in redshift bins

When ordering by L15 redshift, defining stacking bins is not as straightforward as for the L15 flux bins, due to the number of sources assigned the median redshift. Therefore the bin limits were adjusted by hand to achieve a more fair spread of sources for the middle two bins. As with the stacks in flux bins, the SW stacks were resistant to change for the stacks taken with and without applying a lower redshift limit and therefore no limit was set. For the MW and LW stacks the limits were set at 0.4 and 0.8 respectively based on the completeness of the final bin (see figures A16 and A18).

Using a redshift ordered catalogue gave improved results for the MW and LW stacks in terms of reduced edge structure and more consistent photometry. Comparing the results of stacking by redshift order to those of stacking by L15 flux density suggests stacking in redshift gives a more representative ordering with respect to the SPIRE maps. This is most evident for the MW and LW maps, where the comparison with the SPIRE ordering shows that using the redshift ordering does indeed prioritise the masking of sources bright at SPIRE wavelengths first, and an overall improved ordering of bright to faint SPIRE sources across the bins.

4.4.5 Stack co-adding and photometry

Weighted mean and simple sum methods of coadding stacks have been used by previous authors. For example Dye et al. [2006] used a weighted mean, weighting with the error associated to the beam-convolved map, whereas Dole et al. [2006] used a simple sum after applying a rotation of $\pi/2$ to each stamp, with no sigma clipping of any outlying stamps. CP10 also use the simple sum method of coadding, with no rotation or sigma clipping of the single stamps. The stacks

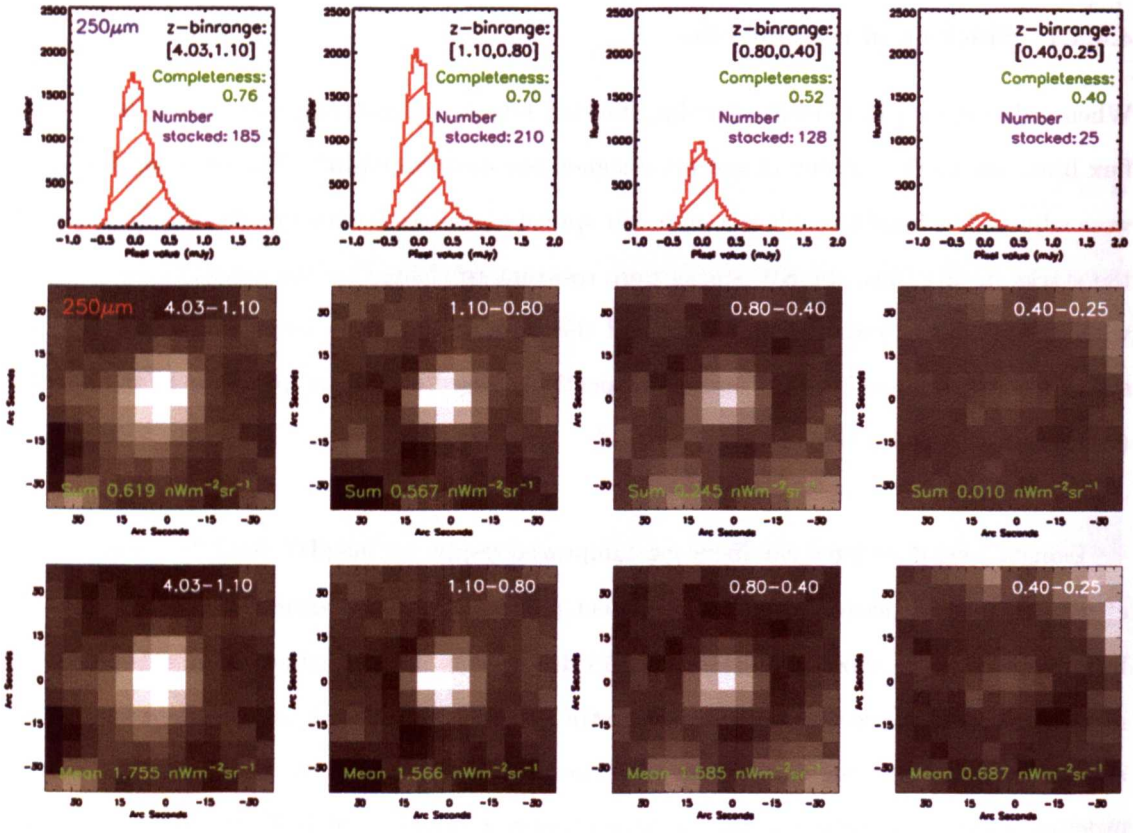

Figure 4.13: Redshift ordered stacks taken in L15 redshift bins for the SW map, both co-adding with a simple sum (middle row) and the corresponding pixel value distributions (top row) and a weighted mean sum (bottom row).

and photometry obtained when combining the stamped data with a simple sum or a weighted mean approach are compared. The weighted mean sum ($\bar{S}_{i,j}$) and associated error ($\bar{\sigma}_{S_{i,j}}$) for each pixel at position (i,j) for N stamps are given as

$$\bar{S}_{i,j} = \frac{\sum_{i=0,j=0}^{N-1} S(p_{i,j})\sigma^{-2}_{S(p_{i,j})}}{\sum_{i=0,j=0}^{N-1} \sigma^{-2}_{S(p_{i,j})}} \tag{4.2}$$

$$\bar{\sigma}_{S_{i,j}} = \frac{1}{\sqrt{\sum_{i=0,j=0}^{N-1} \sigma^{-2}_{S(p_{i,j})}}} \tag{4.3}$$

There is no need to apply the stack completeness correction to the weighted mean stack as the zero pixel positions as a result of the masking are omitted from the mean sum. The SPIRE noise maps represent the instrumental noise only, and as the signal maps are dominated by confusion noise, using a noise-weighted coadding of the stamps results in an unfairly weighted stack. Instead of the associated noise per pixel per stamp, the mean noise per pixel of the stack was applied to the first set of weighted stacks (Weighted mean 1). A second weighting was applied of the the L15 source population completeness (see chapter 3, section 3.9), added in quadrature to the pixel RMS, giving a second set of weighted stacks (Weighted mean 2). This L15 completeness accounts for the fraction of real sources detected in the L15-catalogue, as a function of flux.

Aperture photometry of the stacks is hampered by the relatively small size of stamp and the sky structure seen towards the edge of the stack, which although reduced by rotating the stacks and ordering by redshift, is still present in the final stacks. The photometry taken in this way should be with an isophotal aperture that covers the masked area. Large uncertainties are associated with the photometry obtained as the local sky is assumed to be zero. To avoid these issues and any bias from the edge structure, PSF fitted photometry was taken. A Gaussian

PSF, with θ_{FWHM}, set by the respective SPIRE map, was initially re-centred to match the stack centroid (to within a factor of one tenth of a pixel), and then normalised to the peak of the stack. The residual achieved after subtraction of the normalised PSF were generally unsatisfactory and therefore the PSF fitting was repeated using more degrees of freedom. The centroid (within a radius of 1 pixel), the θ_{FWHM} (limited to ± 0.2 of the map θ_{FWHM}) and the peak (with an upper limit of the maximum stamp value) were taken as (limited) free parameter and a χ^2 minimisation was performed to obtain the best fit PSF. A comparison of the residuals obtained for different PSF fitting methods illustrate the improve fit that is achieved by increasing the degrees of freedom (figure 4.14).

Examples of the resulting photometry for the different methods of co-adding (simple sum, Weighted mean 1 and Weighted mean 2), using the χ^2 minimisation PSF fitting to take the stack photometry in each case, are presented in table 4.3. For the final stacks, a simple sum (with stamp rotation) was chosen as this method gave more consistent results for the stack simulations.

The final stacking photometry, corrected for magnification, are summarised in table 4.2. When ordered by L15 flux density, the SW stack gives a total estimate for the IGL at 250 μm of 4.2 ± 0.1 nW m^{-2} sr^{-1}, which is in perfect agreement with the total ALLSTAR photometry (minus cluster members). The "faint" SW stack contributes 50% of the total SW IGL estimate, and the total estimate is 41% of the background measured by FIRAS. When ordering with redshift, the SW results agree with those obtained from L15 brightness ordering, within the errors. The MW and LW stacks represent a lower fraction of the respective FIRAS measured backgrounds, with 34% of the MW background and 27% of the LW background recovered. The total estimate for the L15 brightness ordered MW stack is 1.8 ± 0.1 nW m^{-2} sr^{-1}, where the "faint" stack ($< 5\sigma$) is contributing 31% and for the LW map the "bright" plus "faint" stack give a total estimate of 0.6 ± 0.1 nW m^{-2} sr^{-1}, where the "faint" stack contributes the greater fraction. The "faint" stack ordered by redshift agrees with the L15 brightness ordered stack for the LW map, whereas for the MW map the redshift ordered estimate is 20% lower. For the MW and LW wavelengths the total IGL estimates constitute fractions of 0.77 and 0.48 of the total corresponding ALLSTAR recovered photometry, respectively.

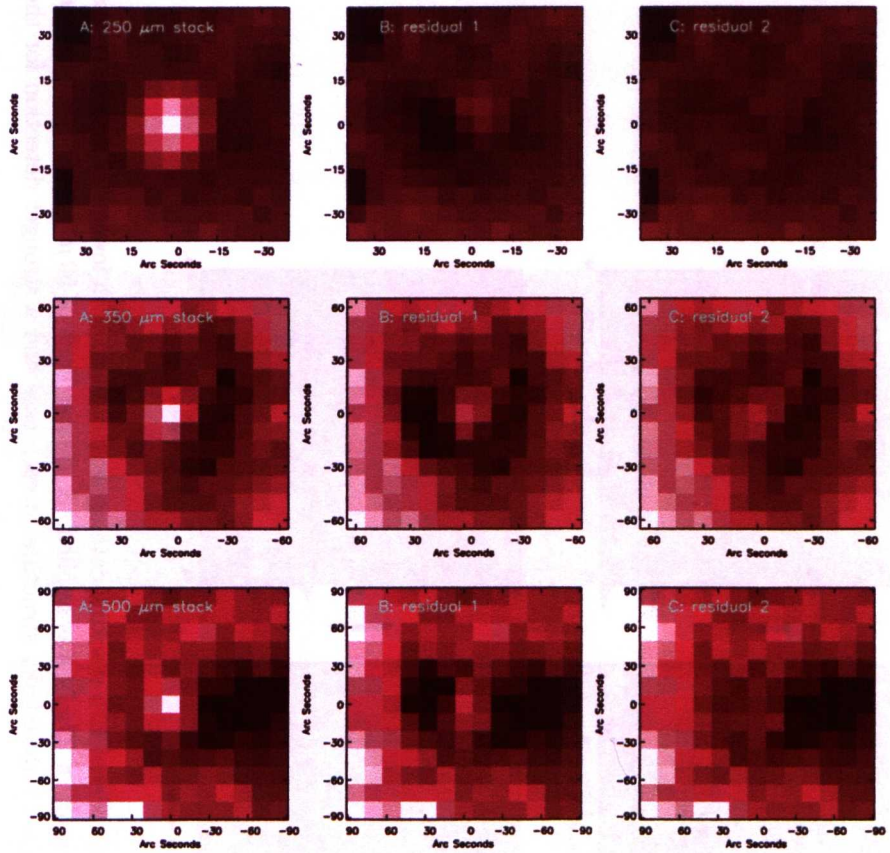

Figure 4.14: The left column (A panels) show the initial stacks, which have been taken using a simple sum coadd, for the L15-flux density ordered catalogue with no prior stamp rotation. The B panels show the residuals achieved from subtracting the PSF after re-centring and normalising to the peak value and the C panels show the residual after a χ^2 minimisation to obtain the best fit. There is notably less residual at the centre of the C panel stacks. The residuals indicate that both methods of PSF fitting may be underestimating the stack at 350μm, although any underestimate is reduced with the minimisation method.

A comparison of the full final stacks, taken using a simple sum co-add, and with and without the flux density limits, and redshift limits applied is given in figures 4.15 and 4.16. The SPIRE ordered and MIPS24 ordered stacks are also shown in figure 4.17, for comparison. The MW stack is still weak, even for the SPIRE order, but stronger when ordering by MIPS24 pixel value.

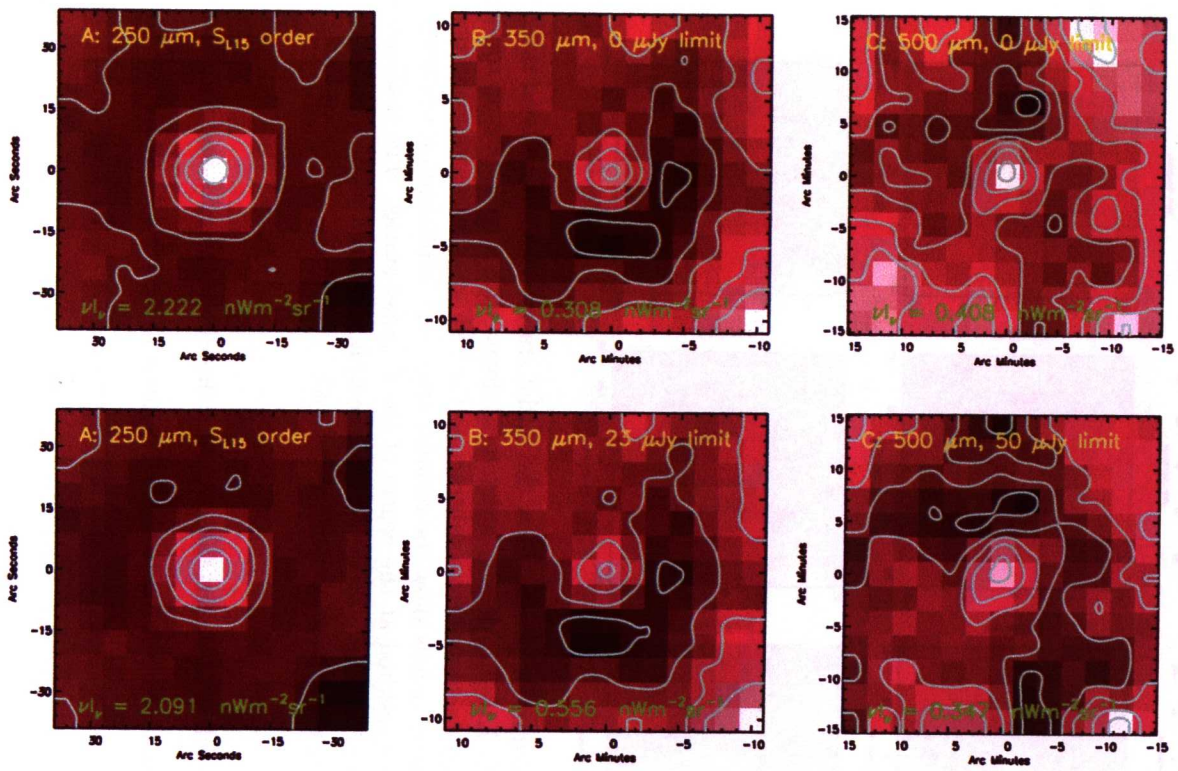

Figure 4.15: SW, MW and LW (left to right) stacks taken using the flux ordered L15 stacking catalogues (top) and with lower flux density limits applied (bottom). For the bottom SW and MW stacks a flux density limit of 23 μJy was applied. A greater limit of 50 μJy was applied when taking the LW stack in the bottom right panel. Applying the limits gives reduced sky structure in each case and a stronger detection for the MW stack (middle bottom)

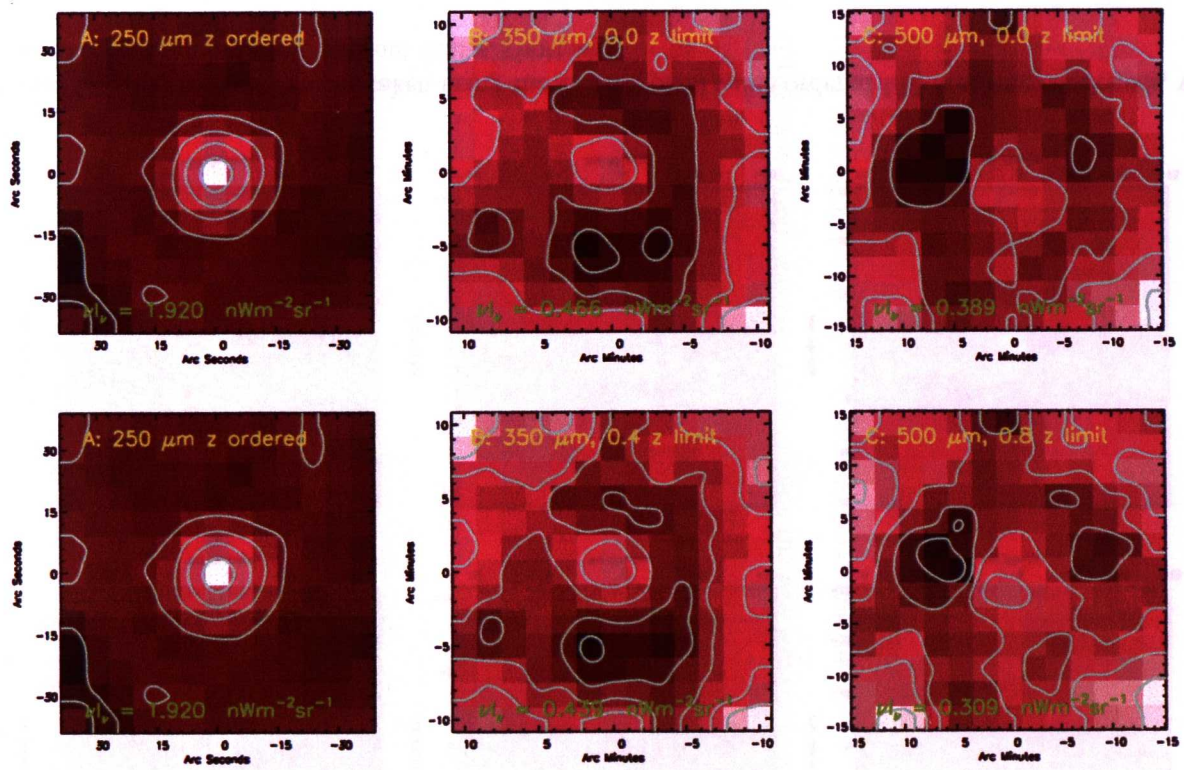

Figure 4.16: SW, MW and LW (left to right) stacks taken using the redshift ordered L15 stacking catalogues (top) and with lower redshift limits applied (bottom). For the MW stack a limit of z = 0.4 was applied and a limit of z = 0.8 was applied when taking the LW stack. Applying the limits gives a stronger detection for the MW and LW stacks (middle bottom and right bottom panels).

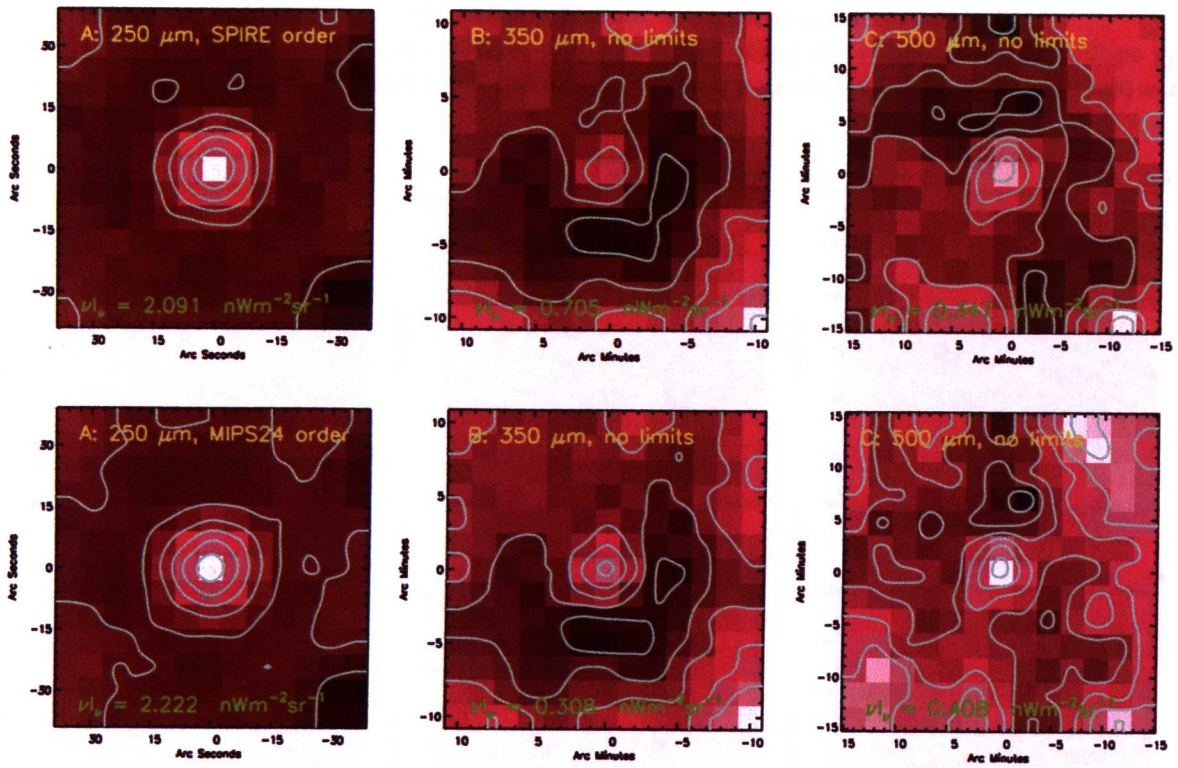

Figure 4.17: SW, MW and LW (left to right) stacks taken using the SPIRE pixel value ordered L15 stacking catalogues, without a limiting flux density (top) and for the MIPS 24 μm ordering, without limits, (bottom).

4.5 Simulations

4.5.1 Simulating the stacks

Simulated maps were created to assess the stacking methodology, including the effect of masking on the results. Three simulations were run:

- simulation A: to simulate the unresolved stacks, catalogues of SPIRE flux densities were created by reassigning each 15μm source with a new flux density and redshift (within the respective 3σ errors) and a corresponding magnification correction. For each new L15 flux density, a random SED from the model of Takagi et al. [2003] was used to generate the corresponding SPIRE flux density. Artificial SPIRE maps were generated by populating a blank array with SPIRE sources. One image for each new catalogue, at each SPIRE waveband, was created by adding the new sources (using a Gaussian PSF) to the existing L15 positions. Normally distributed random noise, with a standard deviation of the corresponding map RMS, was then added. Each map was stacked in-line with the method used for the real stacking analysis. Stacks, ordered by the simulated L15 flux densities, were taken for 1000 catalogues. The simulated stacking was repeated after ordering by redshift, SPIRE pixel values and MIPS pixel values, and also repeated with the derived flux density and redshift limits enforced for the MW and LW maps;

- simulation B: simulation A only takes into account the systematic noise of the SPIRE maps, but not the confusion noise. There are numerous faint neighbours to the L15 source positions being stacked in the real data. To test if these neighbours affect the errors associated to the stacking or the stack photometry itself, simulation A was rerun after additional artificial sources were added at random positions. These additional sources were assigned random flux densities from a $< 3\sigma$ catalogue, generated using the same method as for the artificial L15 catalogues. Comparing the results of simulation B with simulation A confirmed that confusion noise only serves to increase the associated stack uncertainties.

- simulation C: the third simulation was run using the cleaned SPIRE maps to provide background noise. These maps should give a more realistic estimate of the actual noise seen by the SPIRE maps, although the noise is expected to be marginally greater due

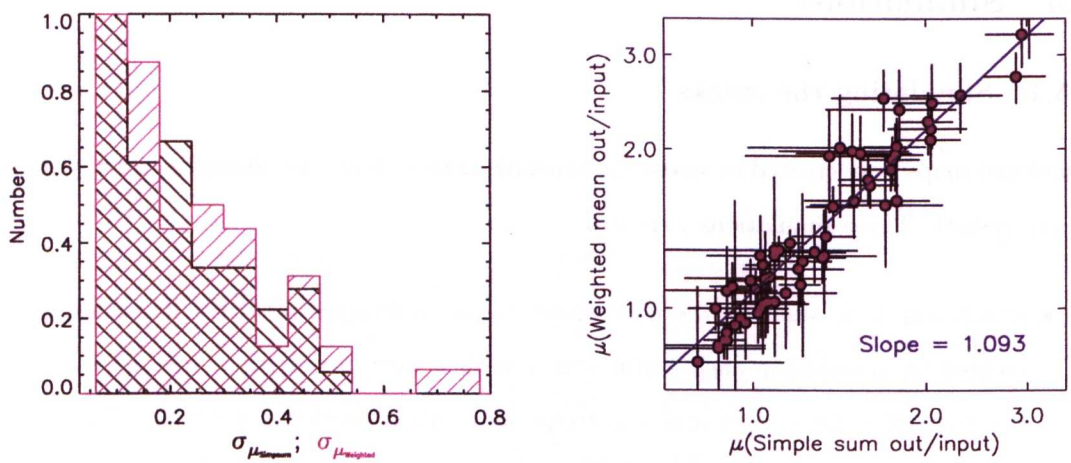

Figure 4.18: Left: distributions for the 1 σ uncertainties associated with the output/input simple sum and weighted mean co-added simulated stack distributions. The histograms have been normalised to a peak of 1 and show the two distributions are similar. Right: Flux ratios (μ) of the output/input distributions for simulation A, comparing the methods of combining the stacks with a simple sum or weighted mean sum. Each data point represents a simulation of 1000 catalogues of sources and includes simulations for each wave band. The Weighted mean tends to give IGL estimates around 10% greater than taking the simple sum of the stack.

to the PSF used to subtract the sources by ALLSTAR. ALLSTAR requires a PSF with an inbuilt sky noise estimate. The noise of the PSF, most significantly at the wings, is therefore folded into the map noise during subtraction, giving a higher noise level in the residual map. Sources were added to the cleaned maps following simulation A.

Both the results for simulation A and simulation C pointed to a general overestimate for the output stack photometry of between 7 - 10%. The associated error distribution for the output flux densities for the simple sum and weighted stacks are similar (see figure 4.18), but comparing the output/input flux density ratios for simulation A shows the weighted mean systematically overestimates the output photometry by 10%. Therefore, the final IGL estimates were taken for the stacks combined using a simple sum (and rotation).

Comparing the simple sum results for simulation A, gives a 1:1 agreement for the SW input vs output νI_ν estimates (see figure 4.19). The output for both the MW and LW simulated stacks, are generally greater than the input. These trends are similar for the equivalent comparison for simulation C (figure 4.19). The systematic overestimates for the output photometry for

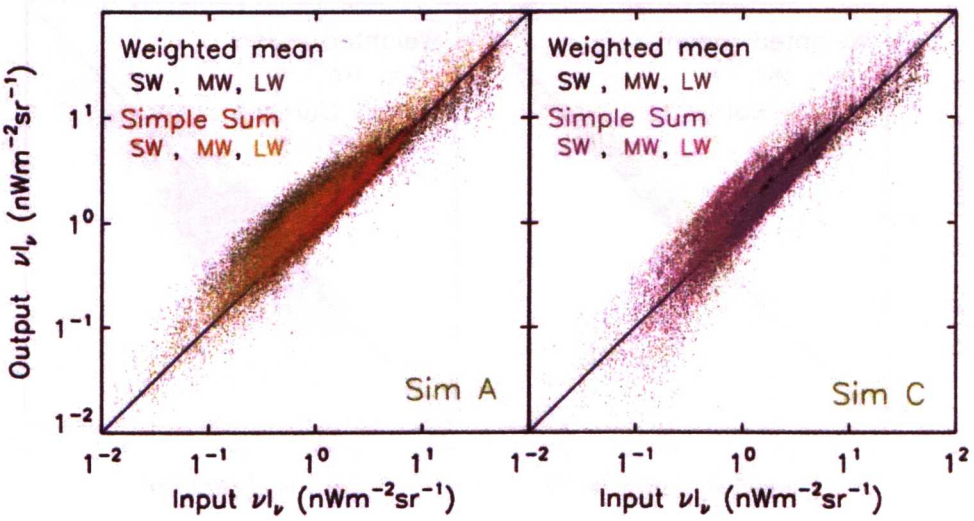

Figure 4.19: Comparison of input νI_ν and output νI_ν for Simulation A (left) and Simulation C (right), for both a simple sum and weighted mean stacking method, employing the same masking and PSF fitting photometry methods as for the real stacks. All ordering methods are included in the results. Each SPIRE waveband are identified by colour. Results from simulation C (right panel) distinguishes more clearly between wavelengths and shows less scatter for the MW and LW simulated stacks, but also shows greater overestimates for the LW stacks, in comparison to the results for simulation A (left panel). the overestimates are mainly due to the inclusion of the redshift ordering in these results (see figure 4.20).

the MW and LW artificial maps, were checked by comparing the input and outputs separately for each ordering. Ordering by redshift was found to be the main cause of the offset. The left panel of figure 4.20 repeats the comparison shown in the right panel of figure 4.19, with the redshift ordered results removed. There is a clearly improved agreement for the MW and LW input/output. To test the order of the resampled redshifts, simulation A was re-run and the original redshifts were randomly assigned to the new flux densities. Stacking the catalogue in order of the random redshifts resulted in a mean increase between the input to output flux of a factor 1.41, therefore suggesting that ordering by redshift for the resampled catalogue is similar to a random ordering and leads to the overestimates of the output photometry. Therefore, the redshift ordered simulations were not included for the remaining simulation tests. This poor ordering is due to the large photometric redshifts uncertainties of the L15 redshift catalogue. Figure 4.21 illustrates the comparatively greater errors assigned to the photometric than for the

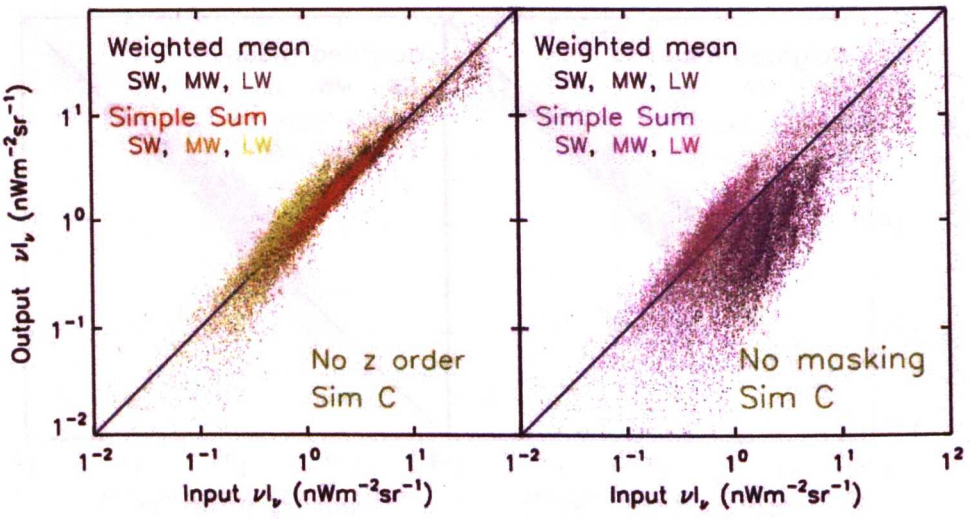

Figure 4.20: Input vs output νI_ν for simulation C, omitting the z ordered results (left), and with no z ordering or masking (right). The results for each SPIRE waveband are identified by colour. In comparison to figure 4.19 the scatter and overestimates for the output MW and LW results are both reduced. The results without masking show a significant increase of the spread of results, and shows that for the SW and MW images the output is are generally underestimates. This goes against expectations, which might logically suggest the unmasked stacks would tend to give an overestimate. This result could reflect that the unmasked signal contributing to the tails of the stacked signal, giving a less well-defined stacked source and affecting the PSF fitting used to take the photometry.

L15 photometric uncertainties. Consequently the resampled redshifts are liable to far greater scatter than the resampled flux densities, which could lead to a bias on the stacking order.

Flux density limits are imposed on the final stack for the real data, therefore the input and output photometry were compared for the results of simulation C with and without the limits applied (figure 4.22). For the simulation, enforcing such limits for the LW stacks gives a 1:1 agreement between input and output photometry. One final comparison was made with the simulation C results taken without applying masking. The right panel of figure 4.20 makes this comparison and shows a substantial increase in the scatter between the input and output photometry. More interestingly, although the LW outputs are generally overestimated, the MW and SW are underestimated, which is counter-intuitive.

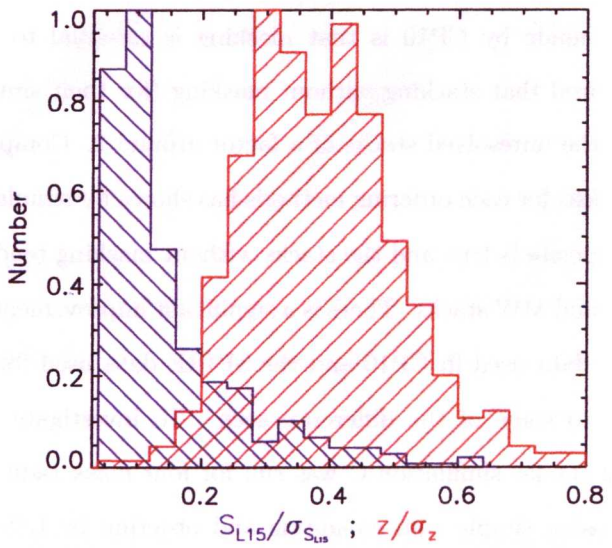

Figure 4.21: Distributions of $S_{L15}/\sigma_{S_{L15}}$ and z/σ_z for L15 sources with photometric redshifts. The distributions have been scaled to a peak of 1. The photometric redshift errors are significantly greater than the flux density uncertainties.

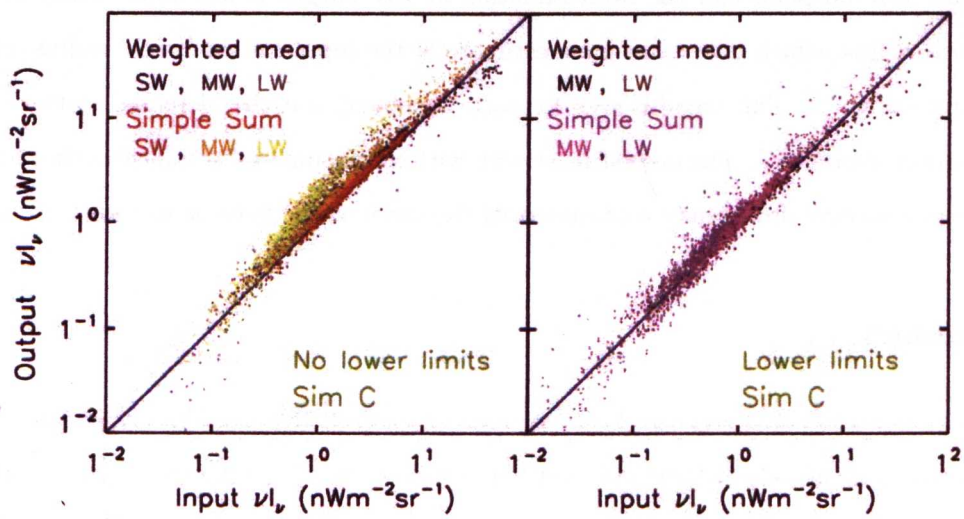

Figure 4.22: input νI_ν vs output νI_ν for simulation C. The stacks have been ordered by the resampled L15 flux densities without lower limits (left) and with lower limits (right). No limits were applied for the SW simulations. For the MW and LW stacks limits of 23 μJy and 50 μJy were applied, respectively. There is a substantial reduction in the overestimate of the LW results when lower limits are applied.

4.5.2 Stack masking

One of the key points made by CP10 is that masking is essential to obtain a least biased IGL estimate. CP10 found that stacking without masking (for their simulated stacks), gave a mean overestimate for the unresolved stacks of a factor around 2. Comparing the masked and unmasked simulated stacks for each ordering methods has shown for simulation A and simulation C that generally the opposite is true and the stacks without masking tend to underestimate the flux density for the SW and MW stacks. There is a significant improvement of resolution between the MIPS and BLAST data used in CP10 and the SPIRE data used for the current stacking, which may contribute to some of the difference seen. To investigate the affect of masking radius on the resulting stacks, simulation C was run for four mask radii (see figure 4.23). The simulations were run using simple sum co-adding and ordering by L15 brightness. The first notable feature of the plots in figure 4.23 is that the scatter for all four radii is lower than for no masking (as seen in figure 4.20). Secondly, the radius chosen for the real stacking (radius (r) of 2, which translates to a mask with a width 5 pixels (2r + 1)), gives the best agreement. Thirdly, the same dramatic trend seen for no-masking, of underestimation of the input stacks by the SW and MW outputs, and the overestimation at LW output is not seen. There is a clear trend with radius, which follows an underestimate of the input for the lowest radius and overestimate for radii > 2. This trend is seen for each waveband, but the increased scatter for the LW comparison dominates. The overestimate seen with increasing radius indicates that flux from neighbouring sources are already contaminating the stack as the mask is too wide.

4.6 Summary

Using a deep 15 μm selected source catalogue we have stacked SPIRE data to investigate the correlation between 15 μm selected galaxies and FIR populations. Ordering the stacks by L15 flux density in flux bins, showed the brightest L15 sources do not correlate strongly with the brightest SPIRE sources for all three wave bands. In contrast, ordering by MIPS24 implied a stronger correlation between the 24 μm emission of the L15 sources and the SW emission, in comparison to the 15 μm emission. The 24 μm ordering did show comparable results for the L15 brightness ordered MW and LW stacks. Ordering with redshift gave a stronger order in terms of stacking the brighter SPIRE sources first, for both the SW and MW data. The redshift

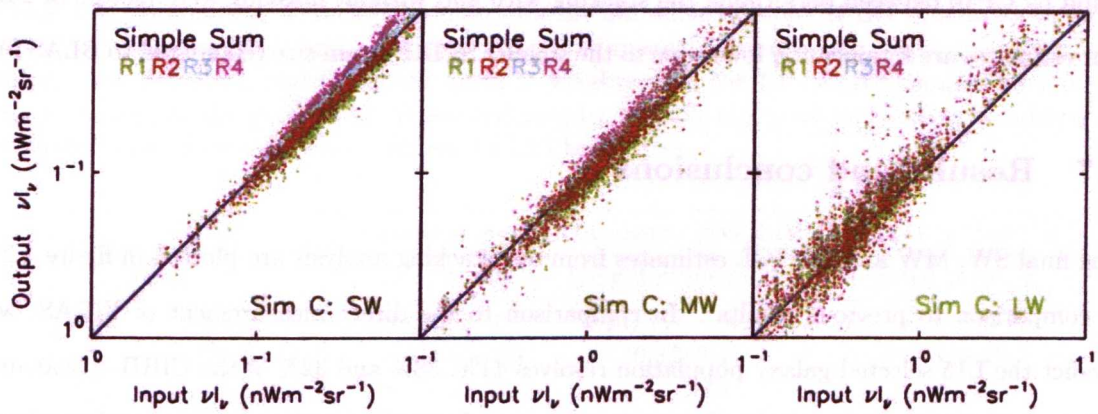

Figure 4.23: Comparison of input νI_ν vw output νI_ν for simulation C. The stacks were taken using L15 flux density ordered catalogues and simple sum co-adding. The simulation was taken for masking widths of $2\times$R + 1 pixels (ie R1 gives a mask width of 3 pixels) and then for masks with width 2r + 1, for each SPIRE waveband. A mask radius of R2 (mask width of 5 pixels) gives the closest to 1:1 comparison. For the greater radii, the output shows a general trend of overestimating the input flux (although the considerable scatter seen for the LW band degrades any clear trend). For a mask of 1 pixel (R1) the output results suggest using this mask width marginally underestimates the stack, but shows a larger scatter.

ordering gave similar stacks as the L15 brightness ordered bins for LW. The final stacks were taken for both L15 flux density and redshift orders, using the simple sum method of co-adding, with the additional rotation applied per stamp. The resulting IGL estimates (brightness and redshift ordered) agreed within the 1σ errors for three SPIRE bands. CP10 simulated bias factors for their stacks at 250 μm of 1.16, 350 μm of 1.14 and 500 μm of 1.20, by taking the ratios of masked stack flux to simulated input flux. By comparing all of the stacks obtained by different orderings and co-adding method we found similar results for unmasked to masked stacks, which gave median factors of 1.18, 1.21 and 1.21 (table 4.4). Although this is not a like-for-like comparison, as we followed a similar stacking method to that presented in CP10 the general agreement suggests our stacks, taken with masking, may overestimate the IGL by only a few percent. Simulated stacking results for stack photometry taken using a mask width of 5 pixels and without masking are given in tables A1 to A3 (in Appendix A) and predict the IGL estimates taken for unmasked SW data will be greater than the results taken with masking, by $18 \pm 3\%$, for the MW data the difference is predicted to be $24 \pm 10\%$ and for the LW stacks, 30% - 15%, which agree with the bias factors estimated from the observed stacks. The difference

found by CP10 between performing the stacking with and without masking were factors of 2-3. Our estimates are significantly lower due to the smaller SPIRE beam size (compared to BLAST).

4.7 Results and conclusions

The final SW, MW and LW IGL estimates from our stacking analysis are plotted in figure 4.24 in comparison to previous results[1]. In comparison to the direct measurement of FIRAS, we predict the L15 selected galaxy population resolves 41%, 38% and 32% of the CIRB at 250 μm, 350 μm and 500 μm, respectively. Comparing these results to the fractions resolved with stacking analysis of 24 μm selected populations (by CP10) of 54% at 250μm, 52% at 350μm and 43% at 500μm shows $\sim$ 10%-15% less of the galaxy emissions contributing to the total IGL (at SPIRE wavelengths) are represented by 15 μm selected galaxies, with respect to galaxies selected at 24μm. This is only a moderate difference and strongly suggests the bulk of these two galaxy populations are sampling the same populations. Our results also show that over half of the galaxy emission responsible for the IGL_{250} and $\sim$ 65% of the IGL_{350} and IGL_{500} are not represented by the 15 μm population. The missing fraction are most likely SMG with extreme infrared luminosities (e.g. LIRG and ULIRG) that formed most of their stars at redshifts > 2. This 15 μm galaxy population has resolved 74%-100% of the IGL_{15} and therefore predicts there is a marked difference between the galaxies dominating the $CIRB_{15}$ and the CIRB at $\gtrsim$ 250μm.

[1]Figure 4.24 was plotted using the publicly available IDL code (and necessary data), that can be obtained from the IAS infrared model homepage: `http://www.ias.u-psud.fr/irgalaxies/model.php`

Table 4.3: Comparison of stack photometry for the unresolved ($< 5\sigma$) SPIRE stacks, for different stack co-adding methods and orderings. 'Weighted mean 1' weights each image stamp with the mean noise per pixel, and 'weighted mean 2' weights with the L15 source completeness added in quadrature to the pixel RMS. When ordering by redshift the three methods of co-adding are in better agreement that when ordered by L15 brightness.

Order	limit	Coadded stack photometry [SW/MW/LW ($\mathrm{nW\,m^{-2}\,sr^{-1}}$)]		
		Simple sum	Weighted mean 1	Weighted mean 2
S_{L15}	0μJy	2.09/0.72/0.73	2.23/0.30/0.42	2.22/0.31/0.41
S_{L15}	23μJy	—/0.56/0.53	—/0.32/0.41	—/0.33/0.41
S_{L15}	50μJy	—/—/0.36	—/—/0.61	—/—/0.59
z	0	1.92/0.48/0.41	1.96/0.42/0.38	1.96/0.42/0.37
z	0.4	1.86/0.45/0.40	2.06/0.44/0.37	2.06/0.44/0.38
z	0.8	—/0.42/0.33	—/0.57/0.36	—/0.57/0.37
S_{L15} & z	23μJy & 0.4	1.64/0.38/0.48	2.05/0.43/0.42	2.05/0.44/0.42
S_{L15} & z	50μJy & 0.8	—/0.3/0.20	—/0.88/0.59	—/0.89/0.61
S_{SPIRE}	none	2.13/0.65/0.80	2.07/0.70/1.12	2.07/0.70/1.12
S_{SPIRE}	0 mJy	2.17/0.72/0.70	2.70/1.65/1.92	2.70/1.66/1.92
S_{MIPS}	none	2.50/0.71/0.71	4.22/0.56/0.58	4.23/0.57/0.57

Table 4.4: Comparison of flux ratios taken for the unresolved stacks, with and without masking. The fractions given in the table are masked/unmasked. The mean result given in the final row were calculated from all the fractional results for that wavelength. The mean sum was weighted with the stack pixel RMS added in quadrature to the L15 completeness.

Order	limit	Simple sum			Weighted mean		
		SW	MW	LW	SW	MW	LW
S_{L15}	0 μJy	0.851	0.983	0.850	0.841	0.872	0.872
S_{L15}	25 μJy	—	0.955	0.851	—	0.885	0.826
S_{L15}	50 μJy	—	—	0.850	—	—	0.857
S_{SPIRE}	none	0.850	0.958	1.225	0.822	0.834	40.80
S_{SPIRE}	0 mJy	0.846	0.856	0.491	0.834	0.831	2.389
S_{MIPS}	none	0.843	0.967	0.812	0.828	0.761	0.734
z	0.0	0.854	1.059	0.770	0.818	0.865	0.752
z	0.4	0.825	1.055	0.771	0.853	0.869	0.754
z	0.8	—	—	0.762	—	—	0.661
z	0.9	—	—	0.767	—	—	0.801
S_{L15} & z	23 μJy, 0.4	0.848	0.984	1.123	0.821	0.823	0.658
S_{L15} & z	50 μJy, 0.4	—	0.942	0.863	—	0.794	0.782
S_{L15} & z	50 μJy, 0.8	—	—	0.818	—	—	0.676
S_{L15} & z	50 μJy, 1.0	—	—	0.835	—	—	0.632
	Median	0.851	0.827	0.824			
	Mean	0.875	0.806	0.803			

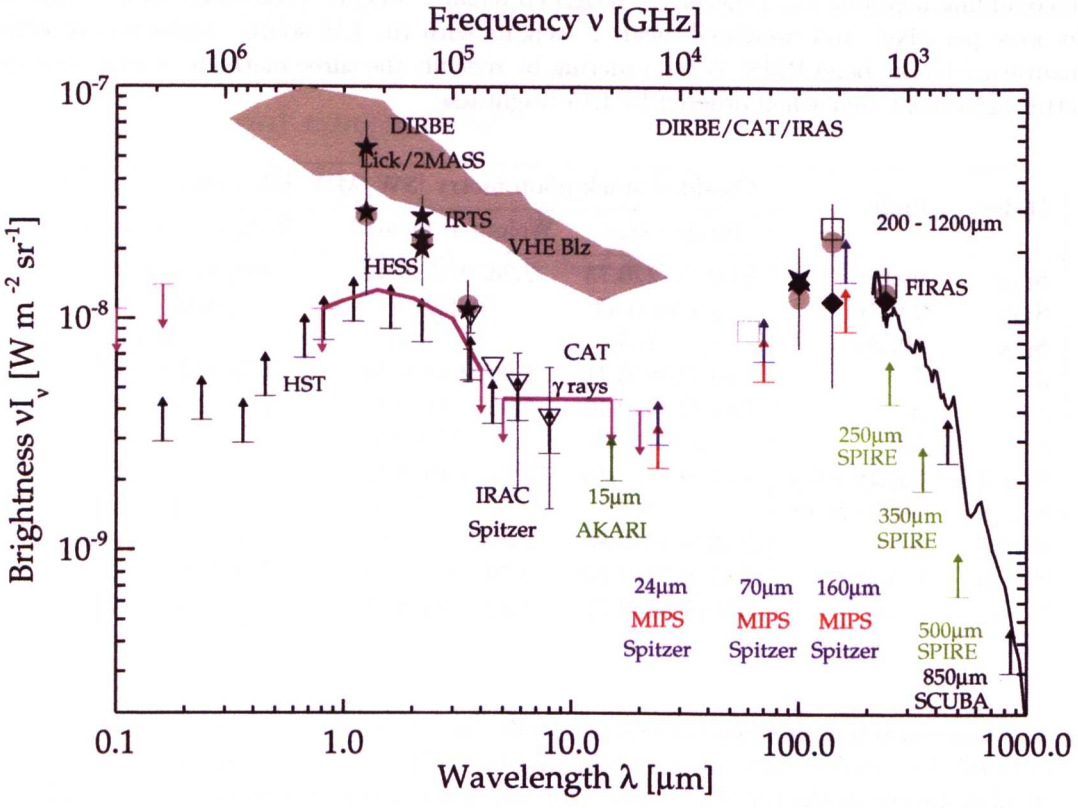

Figure 4.24: Current measurements of the COB (0.1 μm - 8 μm) and CIRB (8 μm - 1 mm). Black arrows (lower limits): Brown et al. [2000] and Gardner et al. [2000] with HST/STIS (lower limits); Spitzer IRAC 3.6, 4.5, 5.8 and 8.0 μm lower limits from number counts by Fazio et al. [2004]; Smail et al. [2002] lower limit at 850 μm from number counts with SCUBA; Hopwood et al. [2010] lower limit at 15 μm using number counts with AKARI (green arrow); Béthermin et al. [2010a] lower limit estimates at 24 μm, 70 μm and 160 μm from number counts and stacking analysis (red arrows) and total extrapolated CIRB due to infrared galaxies (blue arrows). Magenta arrows and lines (upper limits) and the remaining estimates: Edelstein et al. [2000] at 0.1 μm using Voyager UVS; Madau & Pozzetti [2000] and Thompson [2003] with HST ; Gorjian et al. [2000] at 2.2 and 3.3 μm using DIRBE and Lick; Schroedter [2005] Very High Energy Blazar upper limit (grey region); Aharonian et al. [2006] HESS upper limit P0.55 (solid line between 0.8 and 4 μm); Renault et al. [2001] upper limits from 5 to 15 μm using CAT (γ-rays) on Mkn501; Wright [2001] at 1.25 and 2.2 μm using DIRBE and 2MASS (five branch star); DIRBE values from Wright [2004] from 1.25 to 240 μm (grey circles); Savage & Oliver [2005] from fluctuation analysis with IRAC by (open triangles); upper limit at 20 μm by Stecker & de Jager [1997] on Mkn421; fluctuation analysis at 60 μm in IRAS data from Miville-Deschênes et al. [2002] (open grey square); an estimate of the CIB at 100 μm using CAT and DIRBE Renault et al. [2001] (four branch star); Lagache et al. [2000] at 100, 140 and 240 μm using DIRBE and WHAM (diamond) and spectrum between 200 μm and 1.2mm using FIRAS (solid line above 200 μm); Hauser et al. [1998] at 140 and 240 μm using DIRBE (open square). The IDL script to plot this figure is available at: http://www.ias.u-psud.fr/irgalaxies.

Chapter 5

Light profile fitting of a strong gravitational lensing system

Figure 5.1: A strong galaxy-galaxy lensing event in the GOODS-S field.

5.1 Abstract

This chapter focuses on the decoupling of the light profiles of a strong galaxy-galaxy lensing system discovered in the GOODS-S survey, in order to measure photometric redshifts and constrain physical characteristics of the lens and source galaxies.

5.2 Introduction to Light profile fitting

To gain useful information on the constituent galaxies of a gravitational lensing system, e.g. the mass distributions of the lensing galaxy or the intrinsic morphology and star formation rate of the background source, the luminous components of lens and source must be precisely disentangled. When high resolution imaging gives a good separation between the lens and source (i.e. a separation greater than several FWHM between the lens and source peaks) and the aim is to model the lens galaxy only, then the lensed structure of the background source may be masked out e.g. Treu et al. [2006]. This method can be extended to study the source on subtraction of the lens model, but care must be taken for a precise subtraction to avoid residual structure around the level of any faint lensed structure [Bolton et al., 2008a]. For data not satisfying such a separation criteria, photometric blending of the lens and source can be expected. An approach to the decoupling of lens and source components when there is partial blending between them (i.e. individual peaks of the lens and source components can still be identified) is via the simultaneous fitting of light profiles, which describe the intensity as a function of radius, to each component in a system. However, if there are no distinct components a prior knowledge of the spatial distribution of the lensed structure may be required. GALFIT [Peng et al., 2002] is a light profile fitting software designed with a wide ranging functionality to handle complex galaxy structure, such as spiral galaxies. GALFIT uses non-linear parametric least-squares minimisation via a Levenberg-Marquardt method [Press et al., 1992]. This is a 2D least-squares minimisation algorithm that explores parameter space searching for minima that can provide a convergence. A damping factor (also know as the step size) moderates the speed of convergence at each iteration as the step size is reduced if there is a reduction in the associated error of the last step, but augmented if the opposite is true. GALFIT is capable of simultaneously fitting multiple component profiles, with a range of base functions and parameters, making it perfect for fitting galaxy-galaxy gravitational lensing systems.

The light profile of a galaxy has a characteristic shape, commonly ellipticals can be well described by a Sérsic profile [Sersic, 1968] as

$$\mathrm{I(r)} = I_0\, exp\left[-\left(\left(\frac{r}{r_\alpha}\right)^{\frac{1}{n}-1}\right)\right], \tag{5.1}$$

where I(r) is the mean intensity at radius r, $\mathrm{I_0}$ is the intensity at the centre of the profile, r_α is the radius for which intensity has decreased by e^{-1} and n is the Sérsic index, which governs the slope of the profile. GALFIT uses the modified form of equation 5.1, which gives the pixel surface brightness as a function of r ($\Sigma(r)$)

$$\Sigma\mathrm{(r)} = \Sigma_e\, exp\left[-\kappa\left(\left(\frac{r}{r_e}\right)^{\frac{1}{n}-1}\right)\right]; \tag{5.2}$$

r_e is the effective (or 'half') radius, containing half the total flux, Σ_e is the pixel surface brightness at r_e and κ is not a free parameter, but linked to the index to ensure that the definition of r_e holds. The Sérsic function is particularly flexible due to n, which allows a wide range of profiles to be represented (figure 5.2). There are several special cases of the Sérsic function, depending on the value of n. A Gaussian function is given by n = 0.5, whereas n = 1 describes an exponential disk and n = 4 (and $\kappa = 7.67$) gives the de Vaucouleurs profile (see figure 5.2), which has been shown to be a good approximation to the light profiles of early type galaxies [Burkert, 1993]. If n is allowed to be a free parameter when fitting to elliptical galaxies, a wide range of n for the resulting best fits can be expected n $\sim$ 0.5-16 [e.g. Caon et al., 1993], unless some prior is enforced. n is correlated with luminosity and mass [Graham & Guzmán, 2003; Hjorth & Madsen, 1995] and is generally $\lesssim$ 1 for dwarf galaxies.

5.2.1 An introduction to GALFIT

GALFIT is an easy and mainly intuitive package to use, with thorough supporting documentation[1]. There are several required steps to take before beginning a GALFIT run. GALFIT requires a fits image input, containing the source or sources to be fitted, a corresponding σ-image and an appropriate PSF. If there are nearby neighbours within the fitting region, they must either be assigned a profile and included in the model (which is necessary if they encroach on the

[1] http://users.obs.carnegiescience.edu/peng/work/galfit/galfit.html

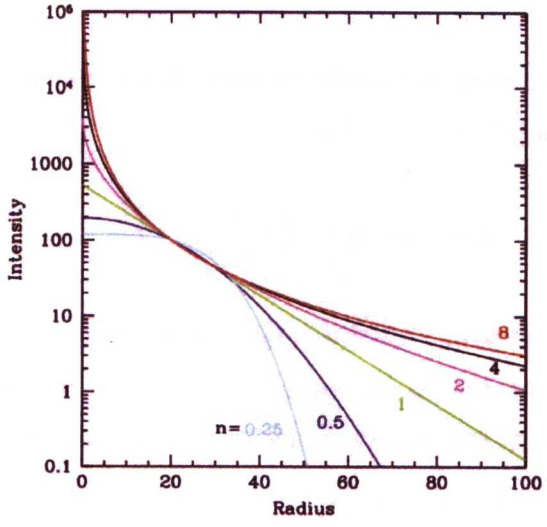

Figure 5.2: Sérsic profile for various index (n) values. Special cases of the Sérsic profile occur for n = 0.5, 1 and 2, producing a Gaussian, exponential or de Vaucouleurs profile, respectively. (Figure credit: GALFIT user manual
`http://users.obs.carnegiescience.edu/peng/work/galfit/galfit.html`.

source of interest) or removed separately with fitting or masking. The fits header is required to contain the exposure time (EXPTIME; in seconds), GAIN (with units of $e^{-}ADU^{-1}$), read noise (RDNOISE; with the units of electrons) and the number of frames combined (NCOMBINE) to allow the conversion of the data to electrons, so the noise can be calculated. Here consideration must be taken for the data units and, if the image is a combination of separate exposures, the method used to combine the data. The pixels should have the units of ADU counts so that the GAIN will convert to units of electrons, unless the data has been normalised to counts per second, and then the EXPTIME should to be set to 1 second. If the data were average or median combined, the GAIN and RDNOISE required is that for one exposure with NCOMBINE set to the number of frames combined. If the data were summed then the effective GAIN and RDNOISE should be used, given as NCOMBINE x GAIN and $\sqrt{NCOMBINE}$ x RDNOISE, whilst setting NCOMBINE to 1. GALFIT can estimate a σ-image using the GAIN, RDNOISE and NCOMBINE information and this is the recommended course of action by the GALFIT manual, however the information provided in the header must be complete and accurate or the fitting may be seriously affected. If a user-made σ-image is provided then it needs to represent 1 standard deviation of the counts for any given pixel, assuming Poisson statistics, and may be a necessary input for images without straightforward units, e.g. $mJy\,sr^{-1}$. GALFIT can

progress without a user supplied PSF, therefore performing no convolution with the model, but the results may have little physical meaning. An input PSF should peak at the centre of the PSF image, regardless of an odd or even pixel width, and have a zero sky. Also recommended is that the PSF be Nyquist sampled, with a FWHM > 2 pixels regardless of the input data's FWHM, therefore possibly requiring a finer pixel scale for the PSF image when the data is undersampled. GALFIT recommends (in order of preference) that the input PSF should be either an empirical PSF, e.g. constructed from a postage stamp image of a neighbouring star, a Tiny Tim[1] PSF e.g. for *HST* or *Spitzer* data, or an analytic function, e.g. a 2D Gaussian function is a good representation of *Herschel*/SPIRE data.

The basic GALFIT iteration follows the path of creating a model from the chosen profile function and convolving the results with the PSF, then minimising to find the best fit parameters and finally using these parameters to construct a new model. The χ^2 is found as

$$\chi^2_\nu = \frac{1}{N_{\rm dof}} \sum_{x=1}^{nx} \sum_{y=1}^{ny} \frac{(f_{\rm data}(\mathrm{x,y}) - f_{\rm model}(\mathrm{x,y}))^2}{\sigma(\mathrm{x,y})^2} \tag{5.3}$$

summed over all nx and ny pixels. $N_{\rm dof}$ are the number of degrees of freedom, defined as (number of pixels - number of free parameters), $f_{\rm data}$, $\sigma(\mathrm{x,y})$ and $f_{\rm model}$ are the input data, the σ image (one standard deviation of the counts at each pixel) and model data, respectively. The number of free parameters depend on the chosen GALFIT function, but each free parameter can be fixed within the input parameter file. This GALFIT process is iterated until the χ^2_ν minimised.

When beginning to construct a GALFIT input model, it is a good idea to start simply by using the minimum possible components needed to obtain a reasonable output (low residual levels and appropriate centroid positions) before building complexity. For each component profile, inputs of the profile centroid (in [x, y] pixel position) a position angle (which ranges from 90 to -90, left to right) and a magnitude are required. There is a default input/output magnitude type for each function, which is an integrated magnitude for the Sérsic profile. It is possible to select an alternative magnitude output by appending a suffix to the name of the function, which indicates to GALFIT what normalisation to apply. The alternatives to the default (given by stipulating

[1]Tiny Tim is a publicly available software that generates PSF for several *HST* instruments and also for *Spitzer*/IRAC

'function-name#') are central surface brightness ('function-name1) the surface brightness at a radius that also depends on the function ('function-name2') or for a truncated function, the surface brightness at a radius of 99% of the flux ('function-name3'). There are three standard starting parameter inputs for the choice of Sérsic function, or two for the special cases of this function previously mentioned, when n is fixed. The first is the effective radius, r_e, for which a good starting value is the FWHM of the PSF (in pixels). The second is the Sérsic index, n, and the third is the ellipticity, defined as the minor/major axis ratio (a/b), which should therefore be between 0 for infinite ellipticity and 1 for circular symmetry. Each parameter can be left completely free or fixed, using the adjacent Boolean operator, or assigned soft constraints in a separate text file that is then called from within the main parameter file. Using soft constraints allows limits to be assigned to prevent wild movements within the parameter space, but also parameters can be linked between profiles, e.g. setting limits on the ratio of the effective radius for two profiles or requesting the magnitude colour between two profiles stays below a particular limit. To maintain the initial simplicity and to avoid unnecessarily bias on the results or constriction of the best parameter space being explored, it is wise to introduce fixed parameters or soft constraints if the iteration catastrophically fails, or the results are clearly unphysical. It is worthwhile taking time to give GALFIT a best guess starting point, so that the parameters are more likely to converge toward the probable global minimum as the Levenberg-Marquardt algorithm is sensitive to the initial input. If a parameter is persistently badly behaved (e.g. tending to infinity or zero), temporarily fixing or strictly limiting it, and allowing the other parameters to converge, may allow this 'bad' parameter to converge to a desired solution.

There are hidden parameters within GALFIT that can be activated by their addition to the input file. These additional parameters include diskyness/boxyness, Fourier, bending and truncation modes, which allow complicated profile shapes to be created, such as spiral arms and bars. When fitting elliptical or point-like galaxies, there is little need to use these additional features, however, for gravitationally lensed images the bending parameter is useful to recreate lensed arcs. There are three bending options; B1 shear, B2 banana shape and B3 S-shape. For galaxy-galaxy lensing events in the field the B2 banana bending parameter is the most useful.

Once a model has been produced there are options to output the image block (stamp, model,

residual) without further optimisation. Each profile in a model can be included or omitted from the output, which is useful in the case of modelling a lensing system as the residual obtained after subtraction of the lens or source profiles can be examined.'

5.3 The GOODS-South lens

5.3.1 Serendipity

A common event in astronomy is the serendipitous discoveries (see Fabian [2009] for an interesting discussion on serendipity in astronomy). With respect to other disciplines, the higher incidence of chance and beneficial findings is due to the nature of astronomy, where wide field surveys and large databases lend themselves to rare object discovery. As the frontiers of observational astronomy have expanded, for example in wavelength, area, depth and (necessarily) technology, so the number of chance discovery of interesting objects (or even new populations) have also grown. Of the $\sim$ 200 confirmed galaxy-galaxy gravitational lenses a significant number can be classed as serendipitous discoveries [e.g. Allam et al., 2007; Ratnatunga et al., 1995; Reimers et al., 2002; Schneider et al., 2000]. One such lens was spotted by Open University Postdoctoral Fellow, Dr Mattia Negrello, in the Southern field of the Great Observatories Deep Survey [GOODS; Dickinson et al., 2003a], whilst browsing the *HST*/ACS coverage, and I would like to thank him for giving me the opportunity to work on this object.

The majority of known lenses were, however, found with dedicated surveys[1] and therefore it is worthwhile summarising several of the most well known and important examples of surveys designed to identify gravitational lenses.

- the Sloan Lens Advanced Camera Survey SLACS [Bolton et al., 2006] pre-selected lensing candidates from over a million optical Sloan Digital Sky Survey (SDSS) spectra. 'Anomalous' spectra were identified, which were indicative of the superposition of a local massive early-type galaxy spectrum (a quiescent continuum) and that of a higher redshift star-forming galaxy (with strong spectral emission features). The selection method, requiring high quality SDSS spectra that can only be obtained for relatively local sources, imposed

[1] An online database of known gravitational lensing systems can be found at the CfA-Arizona Space Telescope LEns Survey website[2]

a redshift bias on the resulting lens population ($z \leq 0.5$). Multi-waveband *HST* follow up imaging was initially obtained for suitable candidates with the *HST*/ACS at V, I and H and then the *HST* Wide Format Camera and NICMOS NIC2 camera, when the ACS ceased to function. To date, 85 of the ~100 SLACS sources imaged with the HST have been confirmed as gravitational lensing events [Auger et al., 2009]. The selection method ensures spectroscopic redshifts are derived for both galaxies in each system, and a velocity dispersion for the massive elliptical. The availability of both spectra and high resolution imaging for each lensing system have provided a range of scientific results including: the characterisation of SLACS early type lens galaxies [Auger et al., 2009; Bolton et al., 2008b; Gavazzi et al., 2007; Treu et al., 2006], the reconstruction of the source galaxies [Koopmans et al., 2006] and the detection of the weak-lensing signal for massive early type galaxies [Gavazzi et al., 2007]. The latter result predicts the combination of strong and weak lensing analysis will be able to decouple the dark and luminous mass components, but requires a more complete sample of lens galaxies (i.e. including those at higher redshifts).

- The Cosmic Lens All Sky Survey [CLASS; Myers et al., 2003] searched for lens candidates in a preselected sample of ~16,500 sources with flat radio spectra. Snapshots were taken with the Very Large Array (VLA) looking for multiple components objects, which were then observed with MERLIN to give higher resolution radio imaging to resolve any extended structure. 22 active nuclei with multiple images formed the final CLASS lenses, 13 of which make a statistically well defined sample, i.e. within the set image separation and flux density ratio criteria [Browne et al., 2003]. This gives CLASS a lensing rate of $1{:}1690 \pm 190$. One of the main results from CLASS has been the constraint on H_0 [Koopmans & the CLASS collaboration, 2001; York et al., 2005]

- The SDSS Quasar Lens Survey (SQLS) looked for quasars with multiple components in spectra from the SDSS DR3 spectroscopic catalogue [Schneider et al., 2005]. An imposed redshift range for candidates of $0.6 \leq z \leq 2.2$ restricted quasars to those with a reasonable lensing probability and less chance of being extended (rather than multiple components), as seen in the SDSS imaging for low redshift sources, and avoided misidentification of stars with high redshift quasars. The gravitational lens selection criteria were based on extended emission and similar colour of adjacent objects and resulted in 11 gravitationally lensed quasars [Oguri et al., 2006, 2008], which have been used to derive cosmological constraints.

The DR3 sample is only $\sim$ 40% of the full SDSS data available, and currently the DR5 release is also being used to search for further lens candidates.

5.3.2 GOODS

GOODS is not a survey dedicated to finding lenses (such as SLACS), but aims to investigate galaxy formation and evolution, dark and luminous matter distribution, cosmological parameters and the extragalactic background light. GOODS was designed to gather deep, high quality, multi-wavelength data for two relatively small fields ($10' \times 16'$), one in the Hubble Deep Field North (HDF-N) and one in the Chandra Deep Field South (CDF-S). These areas were chosen as both had pre-existing multi-waveband coverage. Currently GOODS-S has imaging data from CTIO[1]/Mosaic (U), ESO/VIMOS[2] (U and R), *HST*/ACS (U, B, i, z), ISAAC (J, H, Ks), *Spitzer*/IRAC Channel 1 - 4 and MIPS 24μm, which is all publicly available[3] Observations with *Herschel* have also been taken (or are planned), however these are still proprietary.

The study of gravitational lenses was not a planned priority issue for GOODS, and the initial results saw no mention of lenses [Giavalisco et al., 2004], but the available high resolution, multi-colour ACS data lends itself to the search of gravitational lenses (as seen with SLACS). There are currently $\sim$40 either confirmed or candidate galaxy-galaxy lenses reported in Fassnacht et al. [2004] and on the GOODS lenses web page[4], which were identified with a systematic search of the ACS data based on colour and morphology. Fassnacht et al. [2004] searched for massive early-type galaxies within a redshift range of $0.3 < z < 1.3$ in order to select galaxies most likely to produce strong lenses, and modelled each potential lens galaxy to derive archetypal magnitudes and colours of any residual features for comparison to the un-subtracted ACS data. The initial search gave 1092 candidates, which were examined in combined ACS F435W (B_{435}), F606W (V_{606}) and F775W (I_{775}) data. Any potential lens galaxy was modelled and subtracted to identify residual that could be related to a lensed morphology. The final number of candidates considered 'good' numbered 48. Currently the data is undergoing further searches by applying an algorithm that performs a fit to all reasonable galaxy candidates in the field, and should find

[1] Cerro Tololo Inter-Americam Observatory
[2] European Southern Observatory; VIsible MultiObject Spectrograph
[3] All GOODS publicly available data can be obtained via the GOODS webpages.
[4] http://www.stsci.edu/science/goods/

tens more lenses. The criteria for the initial selection of GOODS lens candidates required a z magnitude < 23 and a colour of B - i > 0.2, all taken with an aperture radius of $0.2''$. The latter limit was derived from a (i - z) vs (B - i) colour-colour diagram (figure 1 of Fassnacht et al. [2004]), to select only low redshift ellipticals and reject star forming galaxies. The new lens candidate reported here has a z magnitude, within the specified aperture, of 24.4 and therefore would not have qualified to be included in the initial candidate catalogue. Interestingly the B - i and i - z colours are 1.98 and 0.26, which the colour-colour diagram suggests is an Sb galaxy or elliptical galaxy at redshifts below the range desired by Fassnacht et al. [2004]. The new candidate shows a more compact configuration than the typical GOODS lens (see figure 5.3 top left and bottom panels) and therefore an aperture radius of $0.2''$ may not be sufficiently small to avoid significant contamination of the colours by the source galaxy.

5.3.3 The GOODS-South lens candidate

The new GOODS-South (GOODS-S) lens candidate (G-lens from hereon) lies at co-ordinates J2000 RA 03:32:21.26 Dec -27:49:29.6 and is situated in section 33 of the ACS coverage (as named on the GOODS web site). This data set is v2.0 of the GOODS ACS Treasury program. Each ACS image segment has a pixel scale of $0.03''$ and is 8,192 pixels $\times$ 8,192 pixels. There are a total of 18 sections covering the CDF-S and section 33 is centred on J2000 03h32m07s -27d48m00s. G-lens is identified as a single source (COMBO-17 30295) on NED[1]. An RGB image was constructed from the B_{435}, V_{606} and I_{775} maps, which shows a clear colour differential between the central object and surrounding ring-like structure (shown in comparison to figure 2 of Fassnacht et al. [2004] in figure 5.3). This is a typical morphology seen for both GOODS and SLACS lenses, with a red lens component (suggesting a massive early-type galaxy) and a bluer lensed source component (suggesting a star forming galaxy), in this case with four peaks. There is strong evidence from this visual inspection alone that supports G-lens as a lensing event, however further evidence is required for a convincing case. One aspect of a galaxy-galaxy lens is the confused nature of its spectra, as utilised by SLACS to identify lensing systems by subtracting the ellipitical's continuum and identifying the remaining strong features. The combination of this typical morphology plus dual spectra is almost irrefutable proof of a lensing event. In the absence of spectroscopic observations, G-lens was modelled with GALFIT to

[1]NASA/IPAC Extragalactic Database: `http://nedwww.ipac.caltech.edu/`

decouple the foreground lens and background source in order to derive photometric redshifts.

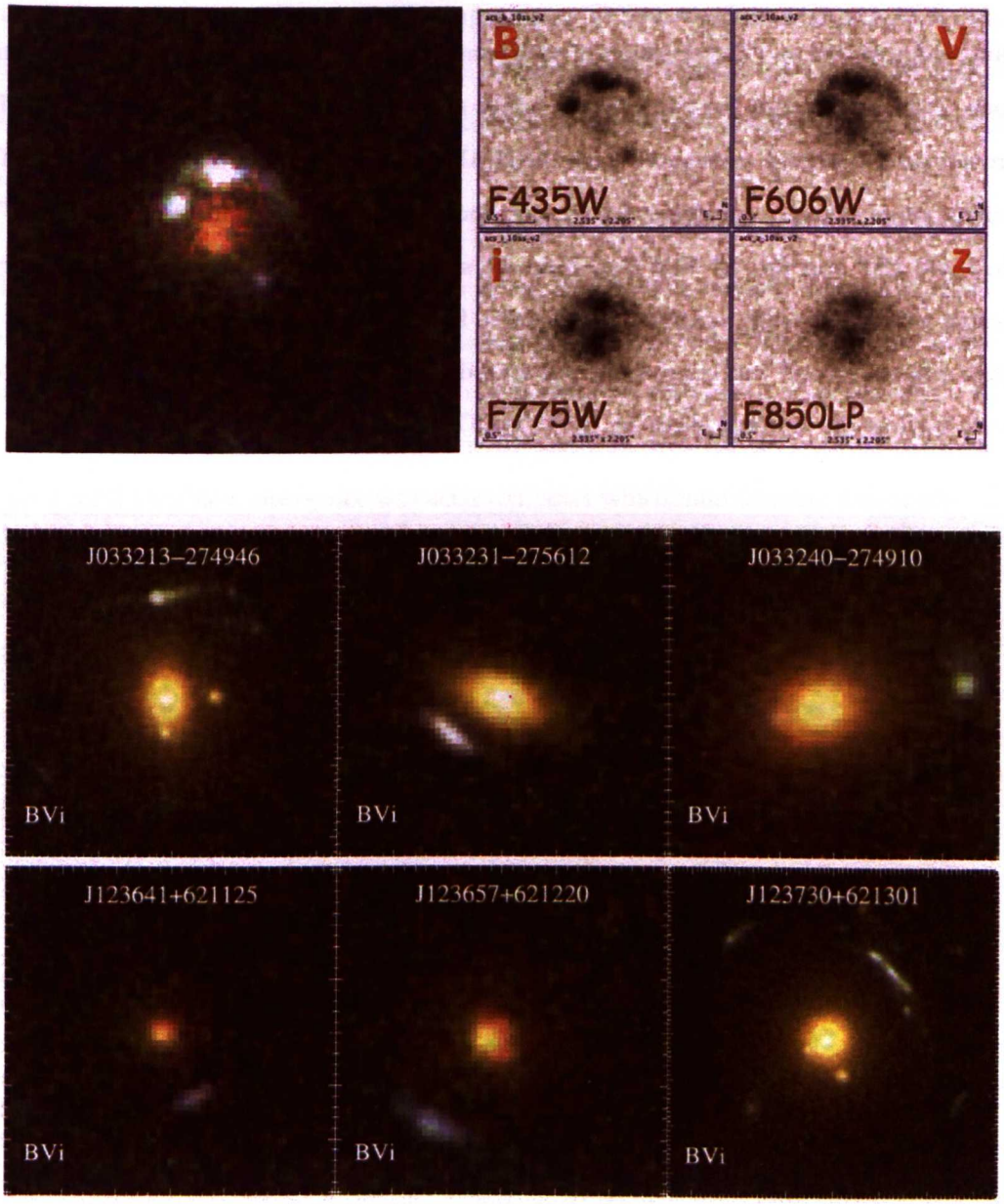

Figure 5.3: Top left: $2.0'' \times 1.8''$ postage stamp RGB image of G-lens. Top right: All four ACS band data for G-lens, plotted as $2.5'' \times 2.2''$ stamps. The lens is brighter in the longer wavelength data and therefore red in the RGB image, whereas the surrounding emission from the background source is brighter at shorter wavelengths and therefore bluer in comparison to the lens. Bottom: Figure 2 from Fassnacht et al. [2004], showing six examples of GOODS lens candidates. The stamps are $3'' \times 3''$ except for the bottom right panel which is $4.5'' \times 7''$. All RGB images shown are the combination of B_{435}, V_{606} and I_{775} ACS data. G-lens is significantly more compact at $\approx 0.5''$ in diameter than the typical GOODS lensing system, and was too faint to be selected during the official search. The morphology for each gravitational lens is similar, with a red object at the centre of a bluer, more extended surrounding structure.

5.4 Decoupling G-lens with GALFIT

To gain peak centroid and flux densities of each component of G-lens, empirical PSFs were made for each of the ACS bands from the closest bright and unsaturated star in the field. The PSFs and rough peak positions (estimated with IMEXAMINE in IRAF) were used with ALLSTAR[1] to provide more strongly constrained centroids and instrumental magnitudes. The ALLSTAR residual and PSF star for the ACS B_{435} data are shown in figure 5.4. On subtraction, a residual image without strongly negative and positive features at the position of the lens was only achieved when a second lens component was introduced. The resulting positions and photometry were used as the starting guess for the GALFIT models.

Figure 5.4: ACS B_{435} data of the local star used for the empirical PSFs (top left corner) and the ALLSTAR residual of G-lens (bottom right corner). The subtraction is not clean as ALLSTAR subtracts only point sources, i.e. no extended structure is accounted for, but does provide estimates for the centroid of each component and rough magnitudes. Initial residuals were poorly subtracted at the position of the lens, and required a second lens component.

Initially G-lens was modelled for each ACS band using six Sérsic profiles. The best results produced clean residuals with total pixel counts $< 5\%$ of the input data. A visual comparison of the input stamps and corresponding models and residuals showed a less than satisfactory result for the B_{435} and V_{606} residuals and the I_{775} and Z_{850} models (see figure 5.5), in particular for the lowest SNR ACS data – Z_{850}. This is not hugely surprising for a model with many profile

[1] See section 3.7.5 for details on the use of ALLSTAR.

components, as there are numerous possible degenerate solutions. The number of degenerate paths can be minimised with higher SNR input data. To improve the SNR, the ACS data were median combined over all four bands on the assumption that, although the relative luminosity of lens and source differs from band-to-band, the centroids and general profile shapes should remain approximately constant.

The input positions and magnitudes were recalculated for the combined ACS data, after constructing a PSF by co-adding postage stamps of the nearby star for each band, in the same manner as for the G-lens stamps. Four Sérsic profiles for the lensed structure (S1 - S4) and two Sérsic profiles for the lens were adopted (L1 and L2). Initially no bending parameter was employed until a stable convergence was achieved, after which mild bending was applied to each of the four source profiles, to give the final best fit. During the fitting iterations (which consist of a GALFIT run followed by a visual check of the model and residual) soft constraints were used due to the highly degenerate nature of fitting six profiles each with at least six free parameters. For the initial GALFIT iterations the constraints were set to extremely soft so as to not introduce any bias, but to prevent an unphysical result. The constraints were then progressively tightened, relaxed or temporarily fixed at the end of a run, depending on the behaviour of the parameters for each profile. The resulting lens components suggest one lens is around an order of magnitude fainter that the other, having instrumental magnitudes of L1 = 36.7 and L2 = 37.6.

In order to assess the need for a second lens component, the GALFIT modelling was repeated after replacing the double lens with a single component (L3) and using the previous best fit model profile as the first guess for profiles S1 - S4. Figures 5.6 and 5.7 compares the double and single lens models, and the final GALFIT parameters are given in table 5.1. The resulting best fit was found to be less well representative of the data due to the poor fitting lens component. This assessment is based on a visual inspection rather than on the fit statistics, which show the single and double profile models achieved identical minimum χ^2, with much greater parameter uncertainties for the double lens ($\sim 20 - 50\%$) compared to the single lens ($\sim$10%). These uncertainties do not represent the true picture as many of the parameters were eventually fixed for the single lens model, to prevent an unphysical convergence. The double lens model was, therefore, adopted as the most likely scenario for G-lens.

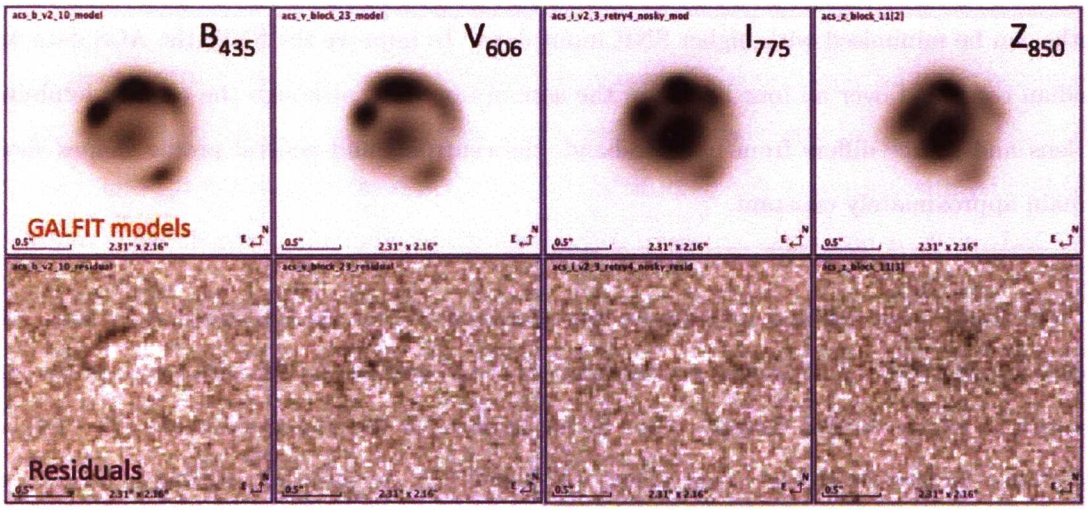

Figure 5.5: ACS single band GALFIT models (top row) and the corresponding residuals (bottom row). The resulting Sérsic profiles for both the lens and source components do not see an agreement in the orientation, effective radius or bending parameter across the bands. Z_{850} could be visually considered to give poorest source model (in comparison to figure 5.3), despite providing the cleanest residual and lowest χ^2. This discrepancy is due to the relatively low SNR of the Z-band. To improve the SNR the data were combined and a single GALFIT model was constructed.

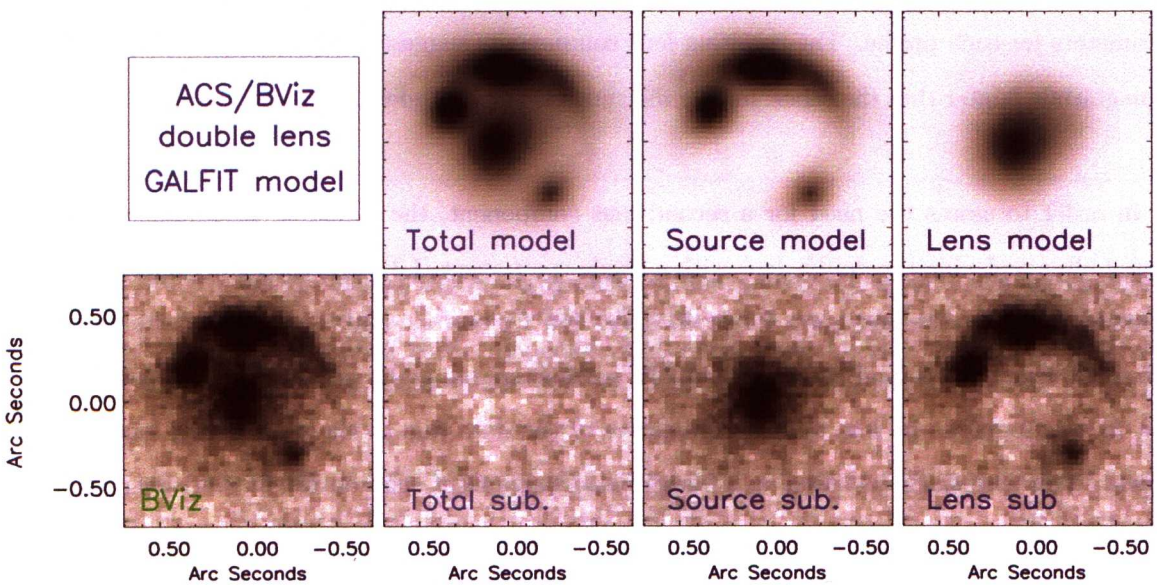

Figure 5.6: Combined BViz data GALFIT double lens model. The BViz stamp is compared to the residual image that results from subtracting the best GALFIT model. Also shown are the separate source (S1 - S4) and lens (L1 and L2) models above the associated residual image. There is no significant residual structure on the subtraction of the total model.

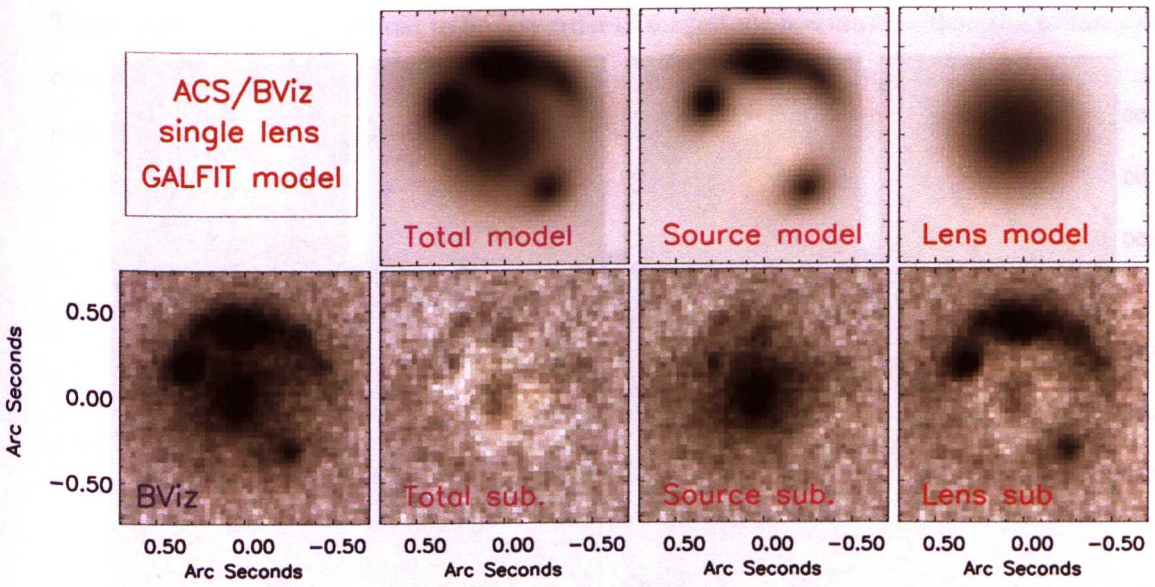

Figure 5.7: Combined BViz GALFIT single lens model. In comparison to figure 5.6 there is noticeable residual on the subtraction of the total (S1-S4 and L3) and lens only (L3) models.

The best fit combined BViz double lens model was refitted to each separate ACS band, allowing at least the GALFIT magnitudes to be free parameters, but fixing the L1 position angle. Fixing this one parameter proved crucial to maintaining the general configuration whilst obtaining a good fit. It was not necessary to add any further constraints for the B and V data. Due to a numerical error during the i-band minimisation, with no obvious cause, soft constraints were added to the previous stipulated L1 conditions. For the i-band it was possible to have relaxed constraints, but for the z-band data they required considerable tightening to ~5-10% of the initial limits, to avoid several parameters (but mainly the bending parameter) leaving the desired parameter space. The final best fit models and corresponding residuals are shown in figure 5.8.

A second model of G-lens was provided by Neal Jackon and his lens modelling code IGLOO[1] (figure 5.9). IGLOO derives the positions of the lens, in this case modelled as a Singular Isothermal Ellipsoid, and of the source to best reproduce the observed positions of the multiple peaks associated to the lensed structure. The IGLOO model also found that two lens profiles were required to produce a good fit, providing independent evidence for a double lens system.

[1]Interactive Gravitational Lens Optimisation Olgorithm: IGLOO

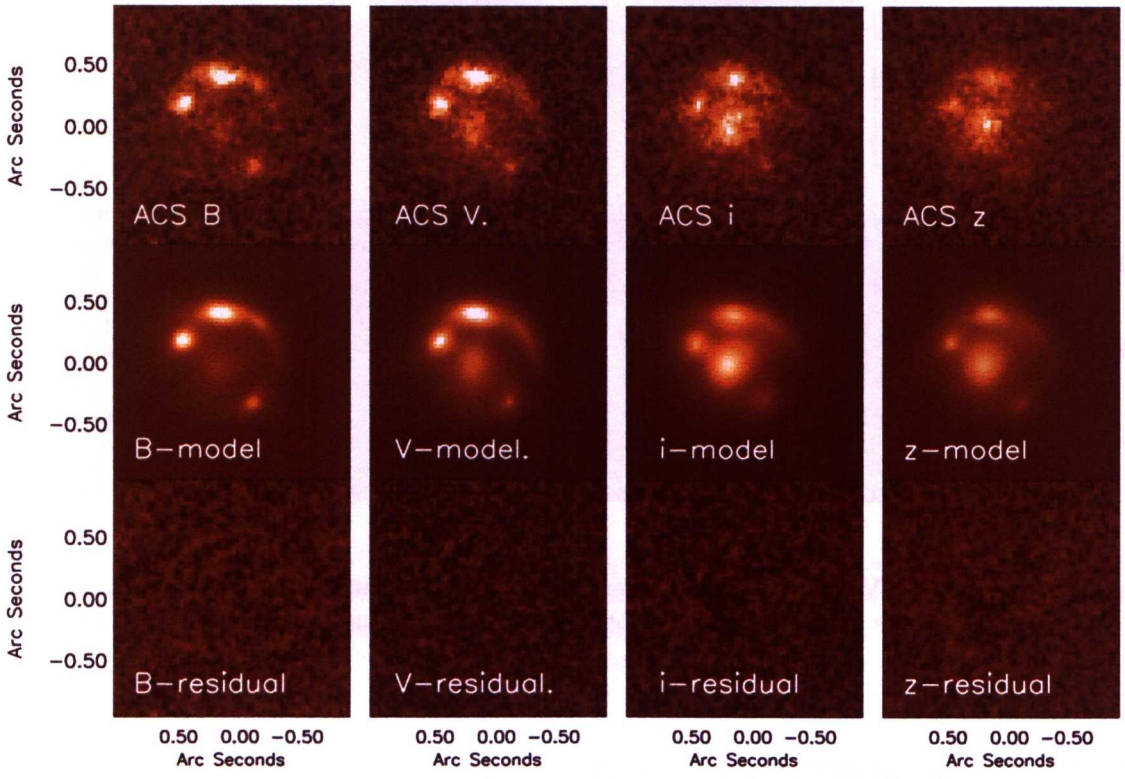

Figure 5.8: Final GALFIT models for the GOODS-S ACS coverage of G-lens. Each model has two lens components and four source components, and are the result of fitting to the combined BViz model to each ACS band. For the B and V bands, only a constraint on the position angle of the brighter lens component was applied. For the i-band additional soft constraints were also necessary for all but the magnitudes, to avoid numerical errors during the fitting. For the z-band it was necessary to give harder constraints, except for the magnitudes, due to the tendency for the sudden diversion of the bending parameters. There is a marked improvement in each model and residual in comparison to figure 5.5. All the data postage stamps were plotted with identical pixel scaling.

Table 5.1: GALFIT best fit parameters for the BViz combined model.

Component	$R_e('')$	n	b/a	PA	B2
L1	0.180	0.801	0.857	0.00	—
L2	0.185	0.293	0.742	-80.1	—
S1	0.221	7.150	0.502	-33.8	0.95
S2	0.247	1.864	0.223	84.5	0.92
S3	0.244	1.135	0.108	41.7	1.90
S4	0.220	4.509	0.399	-49.9	2.52
L3	0.229	0.401	0.987	9.99	—

The secondary lens is predicted to be one order of magnitude less massive than the primary one, consistent with being a satellite and ideal for studying the distribution of baryonic plus dark matter in interacting galaxies [e.g. Suyu & Halkola, 2010].

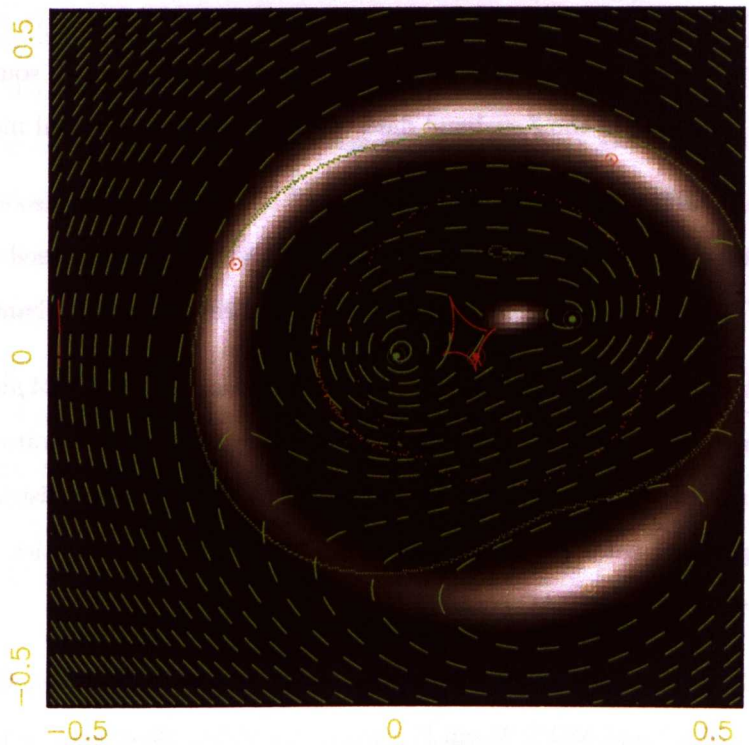

Figure 5.9: Best-fit IGLOO model to the multiple source image configuration of G-lens, indicated by the orange and yellow circles. IGLOO assumes a Gaussian profile background source lensed into the grey extended structure. The model required two lensed components (green contour peaks) to give a good fit to the observed structure. The axes scale are in arcseconds and the contours represent the magnification. Figure credit: Neal Jackson.

5.5 G-lens multi-waveband coverage

The extensive GOODS multi-waveband coverage has been used for several publicly available catalogues:

- GOODS/ACS B_{435}, V_{606}, I_{775} and Z_{850} source catalogue [Giavalisco et al., 2004] was extracted using SExtractor from v2.0 of the ACS mosaics. Noise weighted source extraction was based on detection in the Z_{850}-band data, using the SExtractor dual mode.

- GOODS/ISAAC JHKs $5\,\sigma$ source catalogue [Retzlaff et al., 2010] was also extracted with SExtractor, using a Gaussian filter. Dual mode with the Ks band was used to extract the sources. The catalogue presents colours and full magnitudes for the Ks band.

- GOODS/Spitzer IRAC and MIPS 24 μm third data release and MIPS 24 μm source catalogue (Dickinson et al. in preparation, Chary et al. in preparation). No IRAC catalogues were directly provided, but the supplied MIPS 24 μm source list is derived from the upcoming IRAC catalogues of Chary et al., for MIPS flux densities $>80\,\mu$Jy and within $0.6''$ of the nearest IRAC centroid.

- FIREWORKS v2 Ks based band-merged catalogue for ESO WFI[1] U_{38}, B, V, R and I, ACS, ISAAC, IRAC and MIPS 24 μm [Wuyts et al., 2008]. SExtractor was used in dual mode, with the Ks band as the extraction image, to extract catalogues for each optical and NIR image, after converting to the Ks image pixel scale ($0.15''$). PSF fitting was applied to the IRAC, MIPS and WFI data. Colours are presented for the 16 photometric bands, and the full flux densities are also given for the Ks and MIPS sources.

- MUSIC v2 is also a band-merged source catalogue with wavelength coverage from 2.2ESO[2] U_{35}, VLT-VIMOS U_{38}, ACS, ISAAC and IRAC [Grazian et al., 2006]. A modified version of SExtractor was used to extract a z band based ACS source catalogue, and additional sources were added from a Ks based source extraction. Colours for the ACS data were those provided by SExtractor, and for the IR and UV data a PSF-matching algorithm was employed [ConvPhot; de Santis et al., 2007], which uses information from the higher resolution data to de-blend at lower resolutions.

[1] Wide Field Imager at ESO's La Silla facility
[2] The 2.2m Max-Planck-Gesellschaft telescope at La Silla.

- COMBO-17 source catalogue [Wolf et al., 2004], which provides photometry for 17 narrow and medium width passbands from 350 to 930 nm acting as a low-resolution spectra. The sources were extracted using SExtractor and aperture photometry was taken with MPIAPHOT [Roeser & Meisenheimer, 1991].

A cross-catalogue comparison, after accounting for the difference in aperture corrections, showed that the COMBO-17 and FIREWORKS band merged catalogues and the ACS and ISAAC catalogues have a general 1:1 agreement with relatively low scatter, whereas the MUSIC catalogue showed a poorer correlation with all other catalogues (figure 5.10). As the FIREWORKS catalogue provides the widest waveband coverage and is consistent with the ISAAC and ACS catalogues, it was adopted to construct an SED for G-lens (albeit a lens plus source SED). An inspection of the FIREWORKS ISAAC and Spitzer photometry for G-lens, the corresponding appearance of G-lens in each image and the shape of the SED suggested the FIREWORKS values for JHKs, IRAC and MIPS24 may be affected by photometric blending from neighbouring sources, despite the PSF fitting method used to gain the photometry. This conclusion was based on the expectation that the IRAC and MIPS24 photometry will be dominated by the background source. Aperture photometry of G-lens was taken for the ISAAC J, H and Ks data, with an 8 pixel aperture radius to give approximately 100% flux densities. The radius was chosen using a plot of flux as a function of radius for bright sources in the field for each band. No decoupling using GALFIT is possible for the ISAAC data, due to the low resolution, and therefore the ISAAC aperture photometry provides the total lens plus source flux density. For the IRAC and MIPS data, empirical PSFs were constructed, and PSF fitting with ALLSTAR was performed to gain photometry. Due to the faint nature of G-lens, and high confusion with neighbouring sources in these data, it was found necessary to perform the PSF fitting to a localised, area otherwise ALLSTAR rejected G-lens as too faint. G-lens is situated in a small and relatively isolated group of other sources, so this group was used as the input catalogue for the fitting after first subtracting the bright nearby sources. Figure 5.11 shows the IRAC and MIPS data with the corresponding residuals after PSF fitting. Despite the faintness of G-lens in the IRAC Channel 3 and Channel 4 data, ALLSTAR was able to perform a fit once the brightest surrounding sources had been removed. In order to normalise the new G-lens photometry to the aperture of the FIREWORKS catalogue, the ISAAC aperture photometry and *Spitzer* ALLSTAR photometry were repeated for all of the FIREWORKS sources and then compared

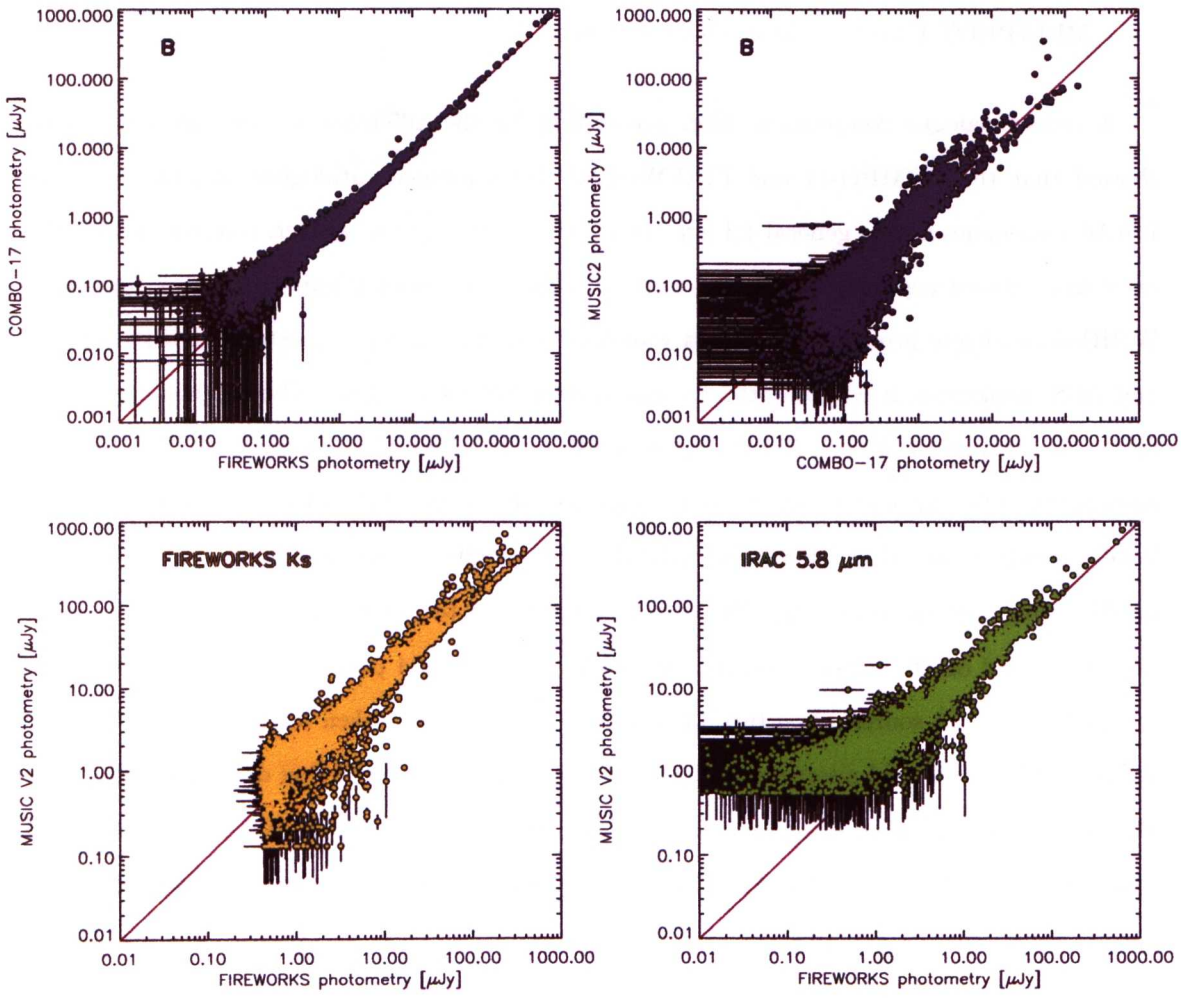

Figure 5.10: GOODS photometric catalogue comparison for the B_{435} ACS band, between the COMBO-17, FIREWORKS and MUSIC catalogues (top panels) and the FIREWORKS and MUSIC catalogues' ISAAC Ks band photometry (bottom left) and IRAC Ch3 photometry (bottom4). There is a generally a good agreement seen for the FIREWORKS and COMBO-17, as seen for the B_{435} comparison, but the MUSIC catalogue tends to give systematically greater estimates. Wuyts et al. [2008] report that (in comparison to their FIREWORKS catalogue) MUSIC may overestimate flux densities of blended sources taken with SExtractor's MAG-AUTO aperture, which does not take into account blending in the PSF tails. They also report an error with the version of the IRAC PSF and PSF smoothing kernel used for the MUSIC IRAC PSF fitting, that was partially dealt with for the MUSIC V2 catalogue (used for the comparison), but still leads to the observed offsets.

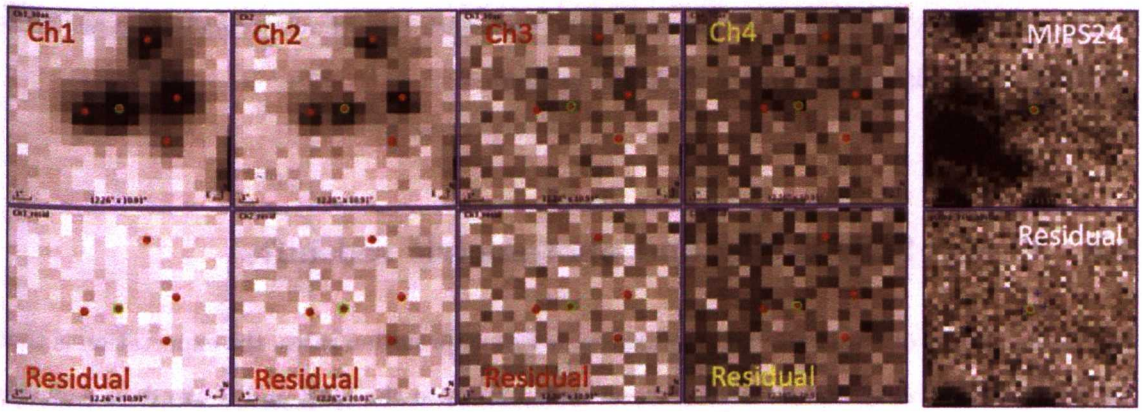

Figure 5.11: IRAC and MIPS24 data (top row) and the corresponding residuals products from PSF fitting and subtraction. The red dots show the positions of sources from the MUSIC catalogue, with the central green and red dot indicating the position of G-lens. **Note** that the MIPS postage stamp is $45'' \times 42''$ and the IRAC postage stamps are $12'' \times 11''$. The brightest sources in the MIPS plot (lying outside the IRAC stamp area shown) were subtracted at the IRAC wavebands before PSF fitting. Note the faint appearance of G-lens and the nearby sources in all but the Channel 1 and Channel 2 data, however ALLSTAR was able to extract these faint source at each waveband.

to the respective FIREWORK photometry to derive correction factors. A 'best' SED for G-lens was constructed from the FIREWORKS U to Ks photometry, the new ISAAC aperture photometry and the IRAC/MIPS24 ALLSTAR results. The COMBO-17 data were also included for comparison, due to the general good agreement found with the FIREWORKS photometry, within 1 σ errors.

The total pixel counts for the components (L1 and L2 and S1-S4) of the final GALFIT ACS models were converted to flux density (S) in μJy following

$$S = \frac{\lambda}{\nu} \times PHOTFLAM \times 10^{39} \tag{5.4}$$

where PHOTFLAM is the pixel counts to flux conversion factor taken from the respective fits header, λ is the wavelength, ν is the frequency and $10^{39}\lambda/\nu$ is the conversion from erg/s/cm^2/Å to μJy. The GALFIT provided uncertainties, associated to the parameters of each profile function, were propagated to give the total lens and total source flux density errors for each band. Finally, the photometry was normalised to the FIREWORKS catalogue to ensure an agreement with the new ISAAC and Spitzer photometry. A 10% correction was applied to the lens and

source photometry based on a comparison of the total with the overall normalisation of FIRE-WORKS. The collated photometry is plotted in figure 5.12.

5.6 G-lens SED fitting and photometric redshifts

Due to the nature of local early type galaxies of low star-formation rates, the expectation is that the background galaxy makes the dominant contribution to the MIR and warm dust emission at IRAC and MIPS24 wavelengths. However, as the decoupled ACS photometry suggests that there is substantial blending at optical wavelength due to the high contribution from the source galaxy (possibly indicating the source galaxy is at a relatively low redshift); this level of blending may also extend to the ISAAC and possible IRAC wavebands and, therefore, offers a particular challenge to SED fitting for the purpose of deriving photometric redshifts for both the lens and the source. The photometric redshift was initially taken with EaZy in order to compare with the estimates given by the COMBO-17 catalogue of 0.69±0.1 and 0.96±0.2 [Mobasher et al., 2004; Wolf et al., 2004]. The results (see figure 5.13) agree with the COMBO-17 estimates, within the errors, but as these estimates are based on blended photometry (including the emission of the background galaxy) they are not a reliable estimate for the lens galaxy.

In order to estimate photometric redshifts for both the foreground and background galaxies of G-lens simultaneously, the double template fitting EaZy method (chapter 3, equation 10) was extended to take into account the decoupled ACS photometry giving the best SED normalisation factors of α_{Lens} for template 1 (t1) and α_{Source} for template 2 (t2), solved as

$$\left[\alpha_{Lens}, \alpha_{Source} \right] = \mathbf{A^{-1}B}$$

where

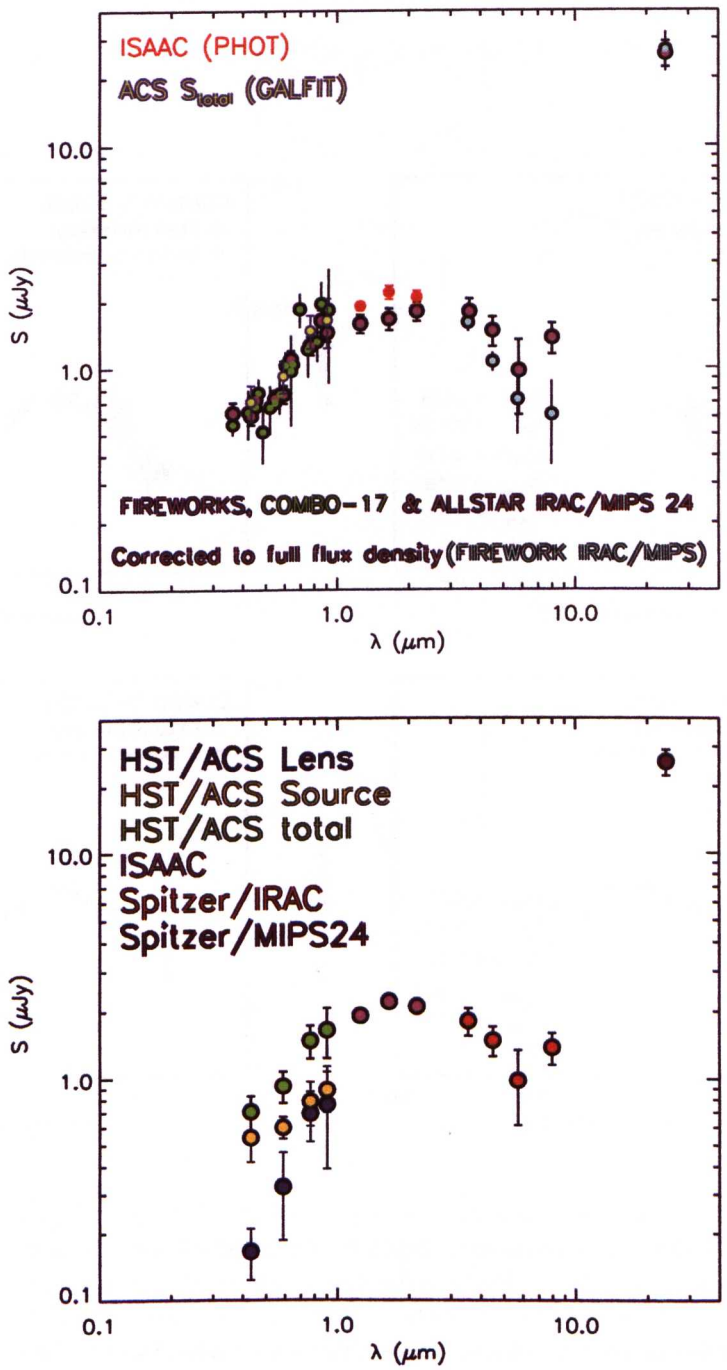

Figure 5.12: G-lens SED. Left: the COMBO-17 (green/black) and FIREWORKS UV and optical photometry (pink/black up to Ks) are combined with the new ISAAC aperture photometry (red) and the PSF fitted IRAC and MIPS24 photometry (also pink/black), and compared to the the IRAC and MIPS photometry from the FIREWORKS catalogue (turquoise/black). The right version of the SED is included to show more clearly the decoupled ACS flux densities, that were obtained using the combined BViz GALFIT model (yellow/black for the background galaxy, dark blue for the lens galaxy and blue for the total). The total is simply the sum of the two parts of each band. The SED follows a familiar shape to that of a star forming galaxy, with an increase in flux contribution at long wavelengths from thermal emission (i.e. the MIPS24 data point).

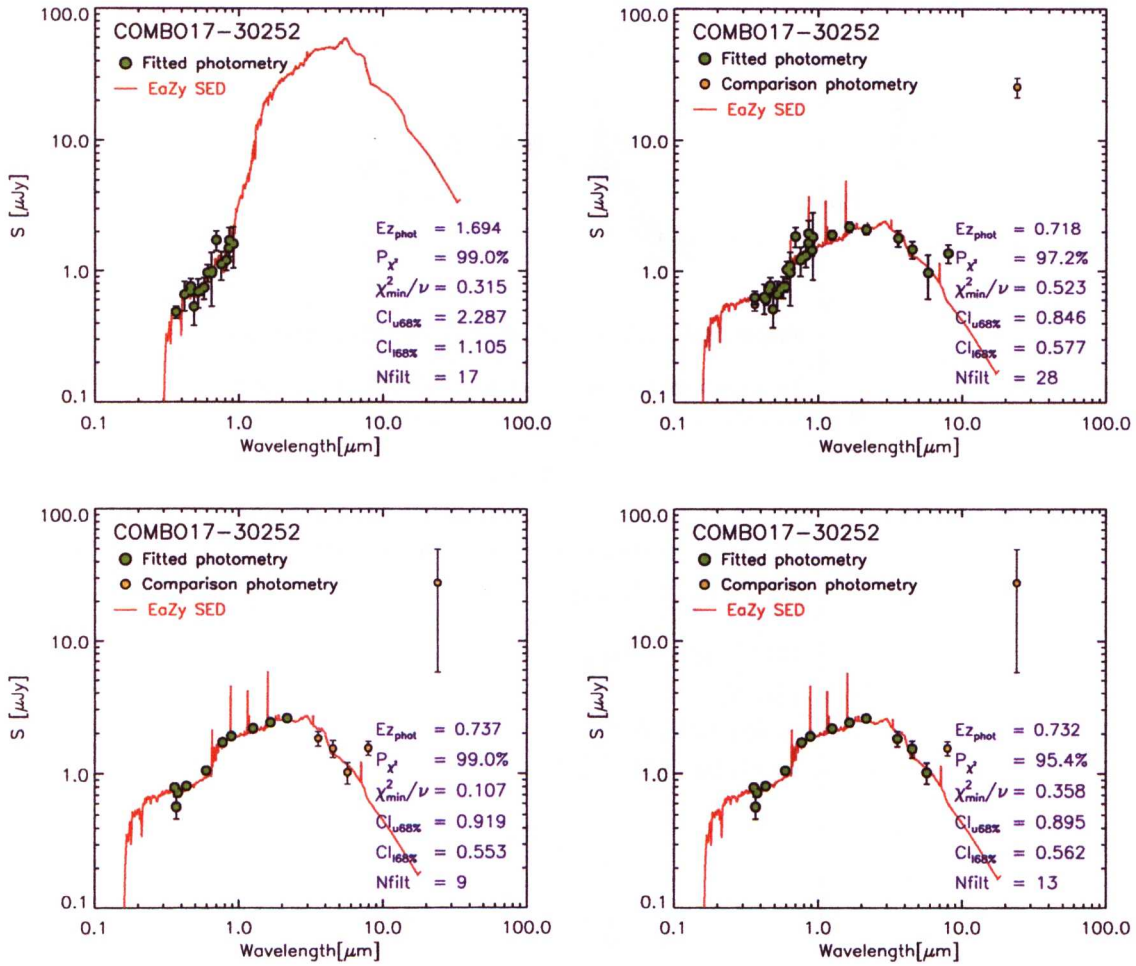

Figure 5.13: EaZy estimates of the photometric redshift of G-lens. Top left: EaZy estimate using only the COMBO-17 photometry. Top left: COMBO-17 and the new ISAAC and IRAC photometry are used to gain an EaZy redshift. Bottom left: EaZy estimate based on the MUSIC catalogue photometry. Bottom right: optical MUSIC photometry plus ALLSTAR IRAC photometry are used to gain an EaZy redshift estimate (although the IRAC Channel 4 band data were included in the EaZy input catalogue it was not fitted by EaZy). The resulting EaZy best fit SED is wildly unconstrained without NIR data, but in this case (due to the predicted moderate redshift of the objects involved) additional IRAC data gives only a marginal difference to fitting with the ISAAC data.

$$\mathbf{A} = \begin{bmatrix} A_1 + A_2 & A_1 \\ A_1 & A_1 + A_3 \end{bmatrix} \tag{5.5}$$

$$\mathbf{B} = \begin{bmatrix} B_0 + B_2 \\ B_1 + B_3 \end{bmatrix} \tag{5.6}$$

$$\tag{5.7}$$

with

$$\mathbf{A_1} = \sum^{N_{filter_{i=1}}} \frac{S_{1,i}S_{2,i}}{\sigma^2_{Total,i}}, \; \mathbf{A_2} = \sum^{N_{filter_{i=1}}} \frac{S^2_{1,i}}{\sigma^2_{Lens,i}}, \; \mathbf{A_3} = \sum^{N_{filter_{i=1}}} \frac{S^2_{2,i}}{\sigma^2_{Source,i}}$$

and

$$\mathbf{B_0} = \sum^{N_{filter_{i=1}}} \frac{S_{1,i}F_{All,i}}{\sigma^2_{Total,i}}, \; \mathbf{B_1} = \sum^{N_{filter_{i=1}}} \frac{S_{2,i}F_{All,i}}{\sigma^2_{Total,i}},$$

$$\mathbf{B_2} = \sum^{N_{filter_{i=1}}} \frac{S_{1,i}F_{Lens,i}}{\sigma^2_{Lens,i}}, \; \mathbf{B_3} = \sum^{N_{filter_{i=1}}} \frac{S_{2,i}F_{Source,i}}{\sigma^2_{Source,i}}$$

Applying this method, the best fit templates and values of α_{lens} and α_{source} were found for the individual ACS photometry and the combined ISAAC and Spitzer bands. Pairs of SED template were selected from the SWIRE template library[1] [Polletta et al., 2007]. The SWIRE library contains 25 galaxy SED templates including ellipticals, spirals and starbursts, generated by the GRaphite and SILicate (GRASIL) code [Silva et al., 1998], which specialises in systems with dusty spectral evolution. For the spirals and starbursts the SWIRE SEDs were combined with observed *Spitzer*/IRS spectra over the region dominated by PAH and silicate features (5-12 μm).

[1] http://www.iasf-milano.inaf.it/~polletta/templates/swire_templates.html

The IDL code used to carry out the double template χ^2 minimisation, steps over redshift for each template set, which consists of one elliptical to represent the foreground lens and one dusty star forming galaxy for the background source. For each loop the chosen templates are shifted to the desired redshift following

$$S_{\nu_{ob}}(\lambda) = \frac{(1+z)L_{\nu_{em}}}{4\pi d_L(z)^2} \tag{5.8}$$

where $S_{\nu_0(\lambda)}$ is the observed flux density (erg/s/Hz/cm^2), $L_{\nu_{em}}$ is the emitted luminosity at the emitting frequency ν_{em} and $\nu_{em} = \nu_0(1+z)$, $d_L(z)$ is the Luminosity distance (cm) at redshift z. The shifted SED templates are then convolved with the corresponding response function of the filter (R), providing the model flux densities (S_T)

$$S_T = \int_{\lambda_{min}}^{\lambda_{max}} S_{\nu_{ob}}(\lambda)\mathrm{R}(\lambda)d\lambda \tag{5.9}$$

where λ_{min} and λ_{max} are the minimum and maximum values of the wavelength range where the function R is defined. The minimum of the resulting χ^2 distribution is used to identify the most likely redshift estimates for a given pair of templates.

Initial fitting trials using the photometry plotted in the right panel of figure 5.12 (total and decoupled ACS, ISAAC, IRAC and MIPS24), gave poor results for the combination of templates tried, which were unable to simultaneously fit to all the photometric points within the 3 σ errors. Therefore, only the ACS and MIPS24 photometric points were retained for the minimisation, as these data are either assumed to be fully disentangled or in the case of the MIPS24 photometry, dominated by only one galaxy. Several combinations of template pairs were considered. Each of three elliptical SWIRE templates (Ell2, Ell5 and Ell13) and an S0 template, which range in warm dust emission, were coupled with templates corresponding to local star burst galaxies NGC 6090 and M82 and ULIRGs Arp220 and IRAS 20551-4250 (I20551). Also used for the background galaxy template were two SWIRE spiral galaxies (Sdm and Spi4) and a LIRG equivalent template from the Chary & Elbaz SED library[1] [Chary & Elbaz, 2001]. The foreground redshift range for t1 was limited to $z_1 = 0.2 - 1.0$ (allowing for a lower minimum redshift than that given in Fassnacht et al. [2004]) and for the background template $z_2 = 0.7 - 3.0$ (assuming the

[1] http://david.elbaz3.free.fr/astro_codes/chary_elbaz.html

source is $> 2\times$ the lens redshift and not likely to be at higher redshifts than $z = 3$, due to the relatively significant optical emission), with the added criteria that $z_1 < z_2$. Figure 5.14 shows examples of the resulting best fits for Ell2/M82, Ell2/IRAS 20551-4250, Ell2/$LIRG_{C\&E}$ and Ell13/Arp220. The best fits (plotted in figure 5.14) predict the background galaxy is a modest star forming galaxy at a redshift ~ 1.6. Overlaying the ISAAC and IRAC photometric points illustrates a major problem with these results. Due to the low numbers of constraints, there is a strong disagreement between the NIR and IRAC data points and the best-fit models, by more than an order of magnitude. A similar result to the best fit SED estimated by EaZy is achieved without NIR data (figure 5.13). The reason for these unsatisfactory results could be due to several factors: a difference in normalisation between the ACS photometry and the remaining data being fitted; the uncertainties of the MIPS24 photometric point; the limited shape of templates used; or the lack of consideration given to the double lens component, which may consist of two galaxies with markedly different SEDs. The SWIRE I20551 template provides the 'best' fit and tentatively indicates a more significant young stellar population (i.e greater emission at UV) may be necessary to allow a better agreement with the background source emission.

Assuming the issue with the poor best fits is due to an inconsistent normalisation between photometry (i.e. the ACS total and decoupled photometry and the IRAC Channel 3 and Channel 4 photometry) as a result of the normalisation with the FIREWORKS catalogue, the G-lens SED was retaken directly from the initial photometry (i.e. ACS GALFIT, ISAAC aperture and IRAS and MIPS24 photometry). The resulting SED has the same general shape as in figure 5.12 (identical for the ACS and ISAAC photometry and within the σ for the IRAC and MIPS photometry) but with a higher normalisation by a factor ~ 1.5.

In order to take into consideration the second lens component during the SED fitting, the double template fit method was extended again to incorporate a third template, contributing to the foreground emission. Combinations of two ellipticals, or one elliptical and one spiral galaxy, were used and the greatest improvement in the resulting fits came from an elliptical and the SWIRE S0 template for the second lens component. S0 galaxies are spiral galaxies with low levels of star formation and disk structure. In the Hubble classification scheme they lie as an intermediary stage between spiral (Sa) and elliptical (E) galaxies [Hubble, 1936], although

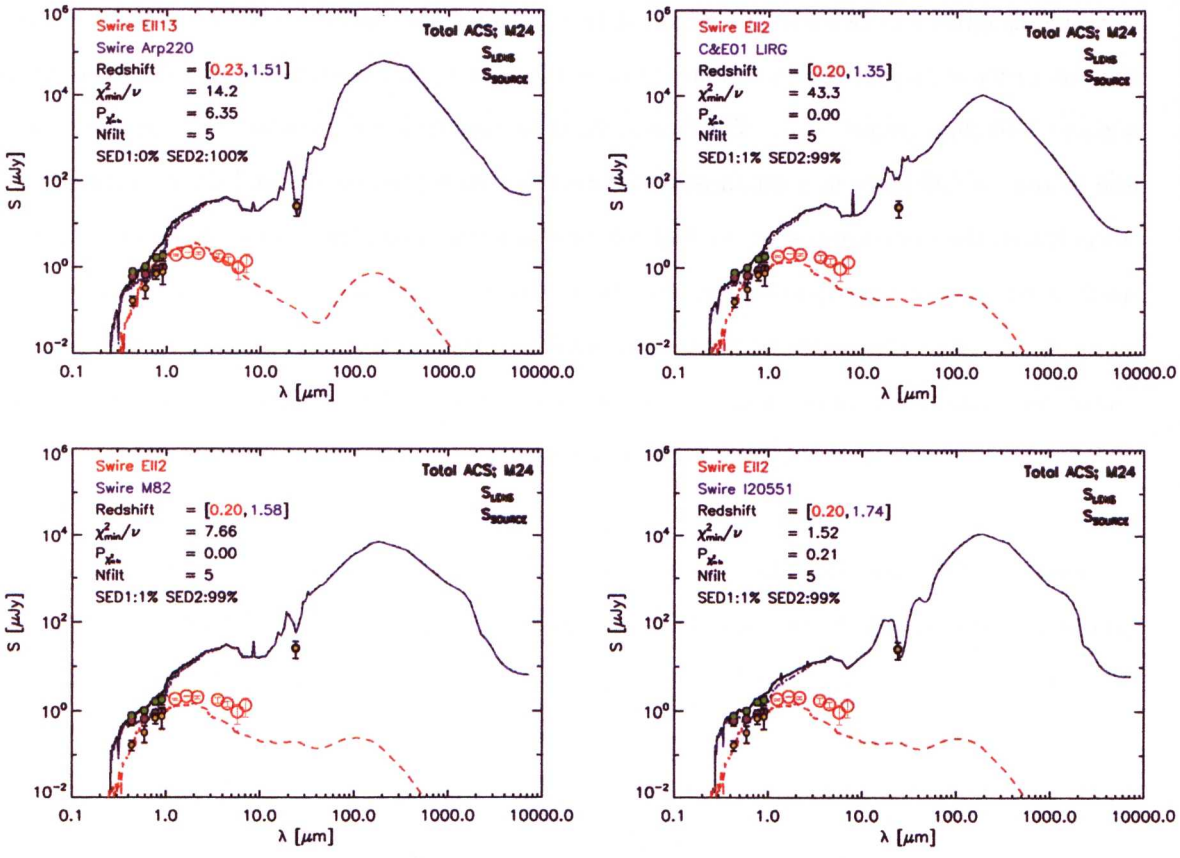

Figure 5.14: Examples of the best fit SED templates to the ACS and MIPS24 photometry, using the double fit method. There is a consensus on photometric redshift of the background source, over the range 1.3-1.8. Overlaying the ISAAC and IRAC photometry (red circles) shows the resulting fits are poor in comparison, and these models are ruled out due to the overestimate of the NIR and MIR by $\sim 10\times$.

more recently it has been suggested that the morphology of S0 galaxies is an environmental consequence, rather than an evolutionary step [van den Bergh, 2009]. S0 galaxies tend to be fainter than Sa or E galaxies, thus making an S0 a good choice for the fainter lens component. Both lens templates were assigned the same redshift.

Figure 5.15 gives the resulting best fit for the template triple of Ell2/S0/I20551, which although giving the overall best agreement at NIR and optical within the errors, it still lacks the necessary UV feature to fit to all of the ACS data points for the background galaxy. The contribution of the S0 galaxies to the warm dust emission appears to be key in allowing an agreement with both the NIR and MIR, but still does not contribute $> 1\%$ to the total IR emission.

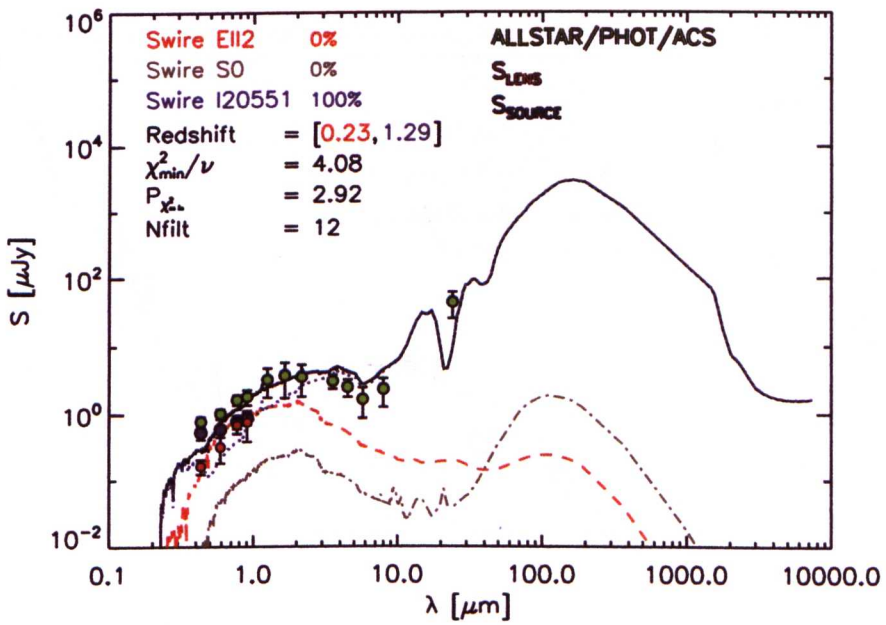

Figure 5.15: Best triple SED template fit of the ACS, ISAAC, IRAC and MIPS24 photometry with the SWIRE Ell2, S0 and I20551 templates. There are significant improvements over the double template fit, helped by the renormalisation of the non-ACS photometry and the increase of the ISAAC uncertainties. Interestingly the best normalisation of the S0 puts the optical emission approximately an order of magnitude below the main elliptical, as predicted by the GALFIT model. There is room for improvement in terms of the background SED, which has a poor agreement with the shortest two ACS decoupled photometric points. Integrating over 3-1000μm gives L_{IR} estimates of 1.0^9 $L_\odot$ and 3.5^8 $L_\odot$ for the two lens galaixes and 2.3^{11} $L_\odot$ for the background galaxy.

The next step for this fitting process was to employ a more sophisticated set of SED templates to provide an increased flexibility in both profile and additional parameters, such as dust extinction and stellar population. A quiescent SED component was adopted for the lens [Efstathiou & Rowan-Robinson, 1995], describing the diffuse emission of the interstellar dust in galaxies, which is heated by stars and emits in the infrared (infrared cirrus), and a starburst galaxy component for the source from the model of Takagi et al. [2003]. A simultaneous minimum χ^2 fit was performed following the method of N09. The results (figure 5.16) indicate a higher redshift for both the lens and source components of $z_{lens} = 0.62$ and $z_{source}=1.92$. The best fit SEDs predict an almost dust-free elliptical lens, with low star-formation rates (although this could be contributable to the satellite lens galaxy) and a young star-forming source galaxy, with strong MIR PAH emission.

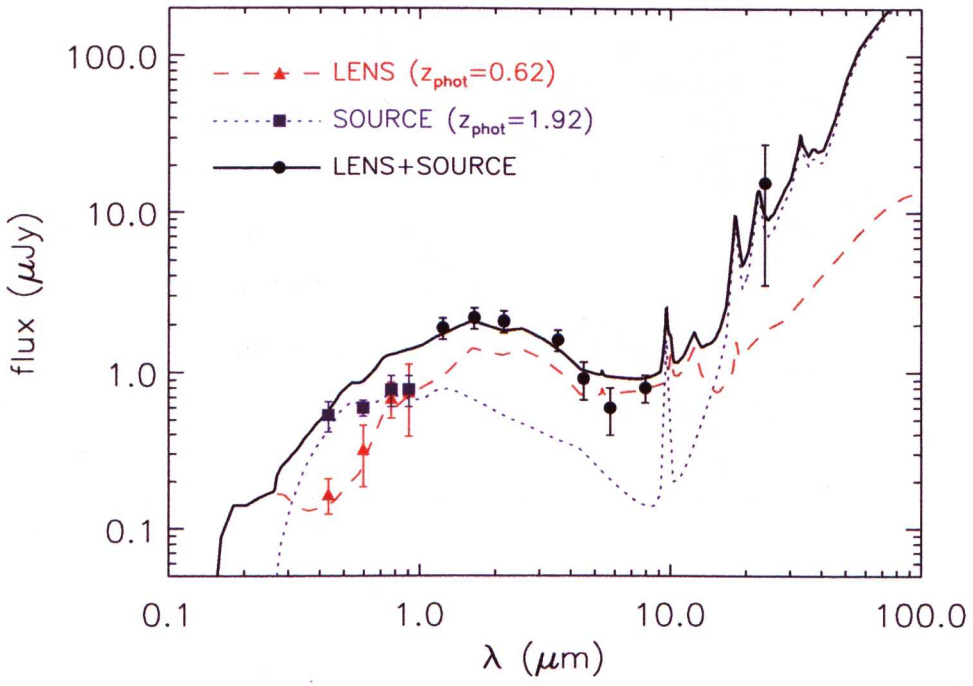

Figure 5.16: Simultaneous SED fitting to the lens, with a cirrus model [Efstathiou & Rowan-Robinson, 1995] and the source, with a star-burst model [Takagi et al., 2003]. The best fit predicts an elliptical with relatively high MIR emission and a young star-forming galaxy at high redshift (z = 1.92), with strong MIR features and warm dust emission. Figure credit: Mattia Negrello

A spectroscopic redshift of the background may be required to help fully separate the remaining coupled data in order to improve the robustness of the redshift estimates, which are $\sim 0.23 - 0.62$ and $\sim 1.28 - 1.92$ for the lens galaxies and background galaxy, respectively. The main lens profile for the GALFIT model has a Sérsic index of 0.8, which is toward the lower limit considered acceptable for an elliptical. This low index value may related to the issue of blending in the profile tail, due to the close proximity of several other profiles, or a second component of an exponential disk may be required to better describe the L1 profile. The result still indicates an elliptical lens, but one of low mass and low luminosity. Some conclusions can be drawn about the physical characteristics of the component galaxies. If assuming two lens components, one lens galaxy may dominate the FIR emission and star formation activity. The background galaxy probably lies at moderate to high-redshifts (> 1.0) and is a normal star forming galaxy, typical of SLACS lenses, although it has a relatively high optical brightness (even when taking flux amplification due to lensing into account) in comparison to the population found by Bolton et al. [2006]. By integrating the best fit SED over the wavelength range $3 - 1000\,\mu$m, the L_{IR} was estimated for each of the three (triple fit) galaxy components, giving 1.0×10^9 $L_\odot$ and 3.5×10^8 $L_\odot$ for the two lens galaxies and 2.3×10^{11} $L_\odot$ for the background galaxy. Confidence intervals were derived by assuming 50% errors on the photometric redshift estimates, and rerunning the SED fitting using the extreme redshift values giving $[7.8 \times 10^8, 1.7 \times 10^9]$ for the brighter elliptical, $[0.0, 2.5 \times 10^9]$ for the fainter elliptical (the minimum limit is physically possible as the fit can reject the extra template when the normalisation factor becomes negative) and for the background galaxy $[1.1 \times 10^{11}, 2.5 \times 10^{11}]$. The limiting values of these confidence intervals are quite significant, which is a good reflection of the uncertain nature of the SED fits. The estimated redshift and L_{IR} support the predictions that a second lens component would be significantly fainter than the primary lens object. As the magnification of background galaxies in typical strong galaxy-galaxy lensing event is $\gtrsim 10$ [Negrello et al., 2007], then the source galaxy of G-lens would be an intrinsically faint infrared galaxy ($L_{IR} < 10^{11}\,L_\odot$). Much uncertainty surrounds these results and more work is required to derived robust redshift estimates and understand the nature of the galaxies involved.

Although the G-lens system still lacks crucial information, such as spectroscopic redshift for both components, the light profile fitting with GALFIT, presented in this chapter, proved

extremely valuable 'training'. These methods were subsequently applied to the first gravitational lenses identified from a population of sub-mm bright lensing events, recently discovered with the *Herschel* Space Observatory (Negrello et al. 2010). For these lenses more comprehensive multi-waveband photometry and spectroscopy was available, including IRAC data for two of the lensing systems, making it possible to decouple the lens and source in both cases, as discussed in Chapter 6.

5.7 Summary and future work

There is strong evidence to support G-lens as a gravitational lensing event. It shows a typical strong galaxy-galaxy lens morphology and colour differential consistent with the lensing senario. The decoupled photometry in combination with the best fit SED from the multi-waveband photometry, are in-line with two low redshift ($z \lesssim 0.2$-0.6) elliptical galaxies, at least one of which has higher than average levels of star formation for early-type galaxies, which are usually dust depleted and therefore have minimal star formation rates. This assessment is supported by the initial colour-colour comparison made with figure 1 of Fassnacht et al. [2004], which predicted a low redshift elliptical or Sb galaxy as the lens component of G-lens. There is also strong evidence to support the double lens hypothesis from the ALLSTAR PSF fitting and GALFIT and IGLOO best fit models, which all require a second lens to produce a good result. This second lens is found to be $\sim 10\times$ fainter than the main elliptical, and may be a satellite galaxy that is contributing the MIR excess. The background galaxy of G-lens is a star-forming galaxy at redshift of $z\sim1.2$, with magnified L_{IR} that classes it as an LIRG. Once the intrinsic L_{IR} magnification is recovered, after de-magnification, this estimate will decrease to possibly sub-LIRG levels, giving an intrinsically faint star-forming galaxy. Both the double-lens and faint L_{IR} of the source make G-lens an interesting object for follow-up studies. Gravitational lens satellite galaxies are rare in the literature, e.g. Jackson et al. [2010, and references therein], who predict that faint satellites ($\sim 10\%$ of the primary lens galaxy brightness) are predicted at a rate of just $\sim 0.001\%$ (although this rate has been found to be anomalously high for CLASS lenses). Such satellites have been used to explain flux anomalies of lensing systems that were initially misidentified as lensed sub-structure [McKean et al., 2007; More et al., 2009; Schechter & Moore, 1993], and provide in each case a key component to producing a good model for the lens. Suyu

& Halkola [2010] used light profile modelling in conjunction with lensing effects to model the lens mass distribution in order to measure the dark halo of the associated satellite galaxy for the gravitational lensing system SL2S J08544-0121. They showed a difference between the position angles for the satellite's total mass distribution and light distribution. More studies of lenses with satellite galaxies, such as G-lens, are required to support such results.

The clear gravitational lensing nature of G-lens plus the identification of a satellite galaxy, make this a highly interesting object. In order to more precisely constrain the component redshifts of G-lens and provide tighter constraints on the physical characteristics of the lensing galaxies, spectroscopic observations are required. For follow-up spectroscopy, a strategy of two slit positions, one to be dominated by lens emission and the second placed orthogonally to allow contributions from both lens and the source, would be adopted. This strategy would allow the separation of lens from source spectra, by identifying strong features in both. If it were not possible to associate any spectral features to the lens then the SLACS strategy would be applied to subtract the elliptical continuum. An ideal study would provide the means to separate the two lens component. Spectroscopic observations will allow a better SED fit with less degeneracy and uncertainties and, therefore, a better constraint on the physical parameters of G-lens. The final goals are to accurately model the mass distribution of G-lens and to detangle the dark and luminous component.

Chapter 6

Investigating the properties of the first sample of sub-mm gravitational lenses detected by H-ATLAS

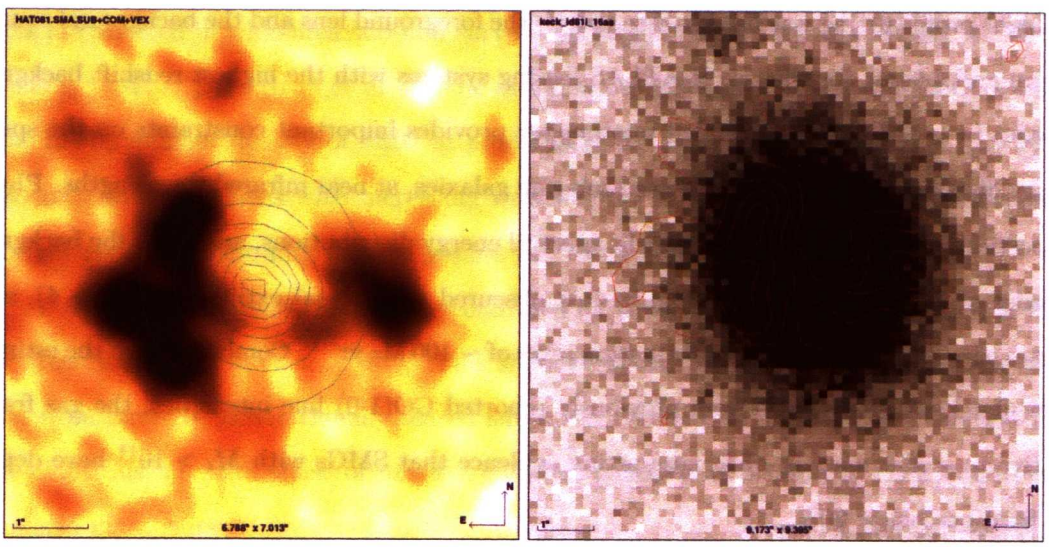

Figure 6.1: SMA imaging (left) and contours (red), and Keck i-band imaging (right) and contours (blue) for the sub-mm lens ID81.

6.1 Abstract

This chapter presents the first strong galaxy-galaxy gravitational lenses to be selected in a blank field at sub-mm wavelengths. Early data from the *Herschel* Astrophysical Terahertz Large Area Survey (H-ATLAS) and a time-effective gravitational lens selection method – developed by the H-ATLAS lensing group – has been used to prove that wide-area sub-millimetre surveys are perfectly suited to finding gravitational lensing events at close to 100% efficiency. The inaugural results show that essentially *all* star-forming galaxies at redshifts $z > 1$, with flux densities above 100 mJy at 500 μm are lensed. Traditional optical lens selection methods would have missed these lensing events entirely, due to severe dust obscuration of the lensed galaxies. H-ATLAS (and future wide field *Herschel* surveys) will provide a large sample of strong gravitational lenses for astrophysical and cosmological studies. This sample will be less biased in both mass and redshift of the lensing galaxy, in comparison to lenses selected by previous dedicated surveys, as the selection method is based on the emissions of the background galaxy only.

Light profile fitting was used to disentangle the foreground lens and the background source at 3.5 μm and 4.6 μm, for the two H-ATLAS lensing systems with the highest redshift background galaxies ($z > 2.5$). The decoupled photometry provides important constraints on the spectral energy distribution (SED) of the lensed sub-mm galaxies, at near infrared wavelengths. Physical properties were derived from the best fit spectral energy distributions, and show the background galaxies of these two lenses are highly dust obscured with visual extinction ($A_v > 4$), stellar masses of $\sim 3\times10^{11}\,M_\odot$ and star formation rates of $\sim 100\,M_\odot yr^{-1}$. Combined with the estimated molecular hydrogen masses from previously reported CO(1-0) line intensities, the gas fraction relative to stellar mass is ~5%, supporting evidence that SMGs with $M_\star > 10^{11}$ have depleted gas fractions below 20%.

6.2 Introduction

The majority of the known ~200 galaxy-galaxy strong lensing events have been identified via dedicated searches. These systematic searches have relied on high numbers of optical spectra or radio imaging for the initial candidate selection, which must then be followed up with imaging in order to identify multiple images of single lensed objects in sub-arcsecond resolution These

selection methods are time intensive in both person and telescope hours, often inefficient, e.g. CLASS has a lensing rate of $\sim 0.14\%$ [Browne et al., 2003], and subject to bias on the selected lens population by design e.g. SLACS are limited to low redshift lenses, due to the initial search based on high quality SDSS optical spectra that can only be obtain for galaxies with redshifts $z \lesssim 0.5$ [Bolton et al., 2006]. An ideal gravitational lens selection method would be time efficient *and* without any bias on the lens mass or redshift distribution. The latter requirement is necessary to produce a statistically large and unbiased sample of lenses, which could be used to address the nature of how dark matter distribution of galaxies evolved with cosmic time [Chae & Mao, 2003; Gavazzi et al., 2007; Koopmans et al., 2006] and constrain galaxy formation models [e.g. LeFloc'h et al., 2009], study galaxies beyond the sensitivity of current technology [Borys et al., 2004; Ellis et al., 2001; Ivison et al., 2010; Knudsen et al., 2010; Lacy et al., 1998; Marshall et al., 2007; Nesvadba et al., 2006; Richard et al., 2010; Smail et al., 1997; Stark et al., 2007] and measure cosmic parameters [Chae, 2003; Koopmans & the CLASS collaboration, 2001; Paraficz & Hjorth, 2010; York et al., 2005] including dark energy density and equation of state [Oguri et al., 2008]. A possible way to fulfil this goal is a methodology where gravitational lens candidates are selected in wide-area sub-mm surveys, as suggested by several authors Blain [1996]; Negrello et al. [2007]; Perrotta et al. [2003]. Sub-mm observations have shown there is a steep decline in the number density of SMG at moderately to bright flux densities (e.g. $\gtrsim 20\,\mathrm{mJy}$ at $500\,\mu\mathrm{m}$), which steepens with increasing wavelength [Devlin et al., 2009]. A shallowing at the bright end of the sub-mm number counts ($\gtrsim 100\,\mathrm{mJy}$ at $500\,\mu\mathrm{m}$) was predicted [Negrello et al., 2007], and recently observationally confirmed by *Herschel*'s Science Demonstration Phase (SDP) results [Clements et al., 2010]. This shallowing can in part be explained by a contribution from strongly gravitationally lensed sub-mm galaxies (SMG). SMG are believed to be 'proto-ellipticals' i.e. the phase of massive elliptical galaxies when most of their stars formed in a single giant burst [Lilly et al., 1999]. Negrello et al. [2007] predict the surface density of *unlensed* proto-ellipticals is effectively zero by $\sim 100\,\mathrm{mJy}$ at $500\,\mu\mathrm{m}$, and therefore SMG detected above this threshold are *all* gravitationally lensed. So it is possible, just by setting a suitable sub-mm flux limit, to select only the lensed SMG population as illustrated by figure 6.2.

The derived cut in flux also selects other populations, such as local ($z \leq 0.1$) spiral and starburst galaxies [Serjeant & Harrison, 2005], and blazars [radio-loud AGN; de Zotti et al.,

2005], however these are readily identifiable in shallow optical and radio imaging. It is necessary to have observations over a wide area to obtain a statistically valid sample of lensing events as the surface density of lensed SMG is low $\lesssim 0.5$ deg^{-2}. Although these objects are rare, the lensing rate for SMG is high (relative to other galaxy populations), as these objects typically lie at high redshifts, with a median redshift of $z = 2.2$ [Chapman et al., 2005], and therefore have a higher probability of chance alignment with a foreground galaxy and an observer. It is also necessary to have coverage with shallow optical and radio data, for the elimination of contaminants to leave only lensed SMG. There are many pre-existing wide area optical and radio surveys that provide such data, e.g. the SDSS [Abazajian et al., 2003] DR6 imaging includes the northern Galactic cap imaging survey, which covers 7668 deg^2, and an additional area of 749 deg^2 from the SDSS Legacy survey in the southern Galactic cap [Adelman-McCarthy et al., 2008]. The proposed selection method of gravitational lenses, based on the background galaxy emission, should necessarily impose no bias on the redshift or mass of the associated foreground lens population.

Herschel has provided – for the first time – a means for a proof-of-concept test for sub-mm selection of lenses, with H-ATLAS. H-ATLAS is the first survey to provide sub-mm coverage over a substantially large area of the sky, with a total area of 550 deg^2. planned. No previous test of this method has been possible due to the limitations of high confusion noise, because of poor spatial resolution [e.g. BLAST; Devlin et al., 2009], or limited area surveys [e.g. surveys with the Submillimetre Common-User Bolometer Array (SCUBA), the Submillimeter High Angular Resolution Camera 2$^{\rm nd}$ generation (SHARC-2) and the Large Apex BOlometer CAmera (LABOCA); Kovács et al., 2006; Mortier et al., 2005; Weiß et al., 2009]. It is worth mentioning that at millimetre wavelengths the South Pole Telescope recently mapped an area of more than 80 square degrees [Vieira et al., 2010] and found an 'excess' of sources that could be accounted for by a gravitationally lensed population.

Lenses were selected in SPIRE 500 μm SDP data of the H-ATLAS GAMMA-9h field. The area observed is only $\sim 3\%$ of the planned total for H-ATLAS, but provided a source catalogue of $> 6,000$ sources that was used for the initial selection criteria [Rigby et al., 2010]. The longest wavelength *Herschel* channel (500 μm) is the most favourable for selecting lens candidates, as

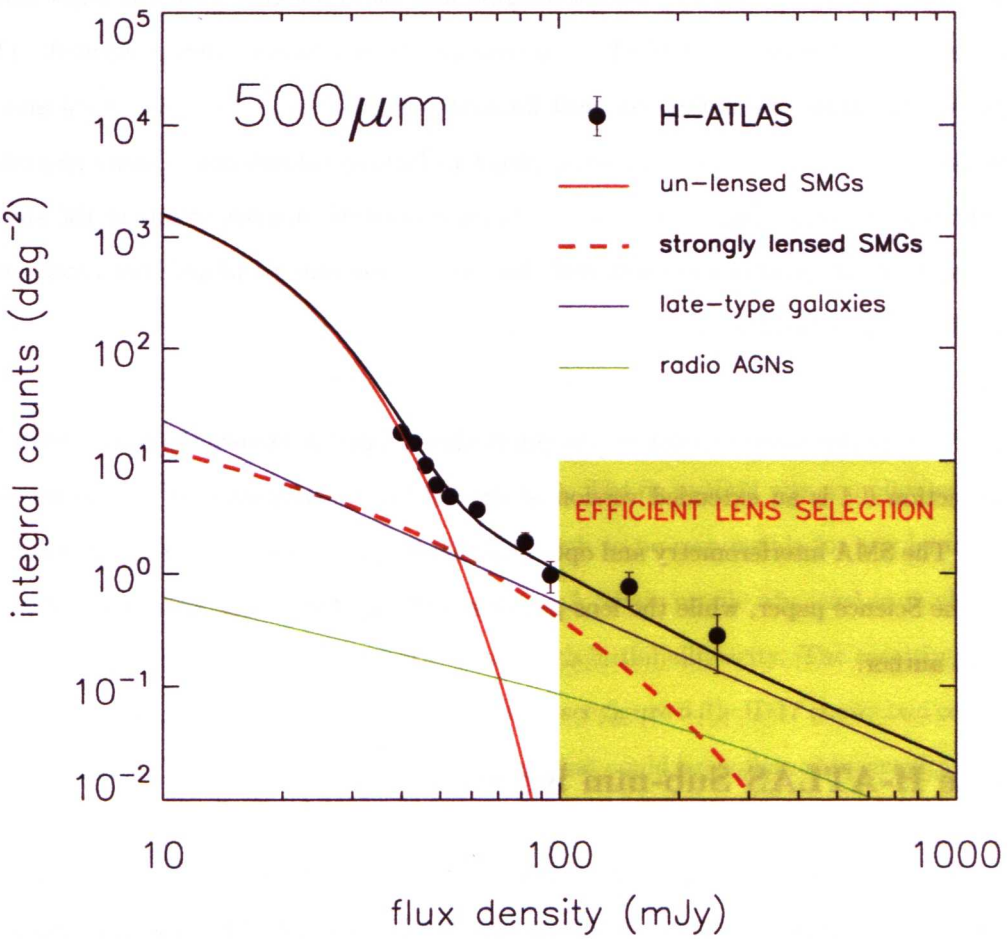

Figure 6.2: Selection of gravitational lenses at sub-mm wavelengths. The total 500 μm galaxy number counts (black line) consist of three different populations Negrello et al. [2007]: high-redshift dust-obscured star-forming galaxies (i.e. SMGs); low redshift $z < 0.1$ late type galaxies (starburst plus normal spiral); and radio sources powered by active galactic nuclei. Strongly lensed SMGs dominate at very bright fluxes where the count of un-lensed SMGs falls off dramatically (yellow shaded region). Therefore a simple cut in flux density selects gravitational lenses with high efficiency. The major contaminants in the bright tail of the sub-mm counts are local ($z < 0.1$) spiral-like galaxies and bright radio AGNs. These are easily identifiable in shallow optical and radio surveys. The data points are from H-ATLAS Clements et al. [2010]. The model curves are from Negrello et al. [2007]. (Figure: N10)

the slope of sub-mm number counts steepens at longer wavelengths [e.g. Clements et al., 2010; Devlin et al., 2009]. Using the optimum flux density limit of 100 mJy at 500μm, 11 lens candidates were selected from the full SDP catalogue. On inspection of ancillary data in the field – optical Sloan Digital Sky Survey (SDSS) imaging and radio imaging from the Faint Images of the Radio Sky at Twenty-cm (FIRST) – several non-lensed sources were identified. These 'contaminants' consisted of one Galactic star forming region [Thompson et al., 2010] and one radio-loud AGN [González-Nuevo et al., 2010], plus four local spiral galaxies – easily identifiable by their SDSS morphology [see Baes et al., 2010, for a detailed analysis of one of the spirals]. Once the contaminant objects were removed, five lens candidates remained, hereafter named ID9, ID11, ID17, ID81 and ID130.

Section 6.3 contains work relating to the publication Negrello, Hopwood, et al. (2010, Science) and section 6.4 is an extended version of the publication Hopwood et al. (2010, ApJL submitted). The SMA interferometry and optical/sub-mm spectroscopy was conducted by other authors of the Science paper, while the lens profile modelling of the Keck and *Spitzer* data was done by this author.

6.3 The H-ATLAS Sub-mm lenses

The appearance of a sub-mm bright galaxy-galaxy lensing system holds certain expectations. The system should appear point-like at 500 μm, due to the large SPIRE beam size and a redshift expectation of z $\gtrsim$ 1. At sub-mm wavelengths the background source will dominate the emission, with negligible contribution from the foreground lens – lensing galaxies are usually massive ellipticals that are 'red' and 'dead' i.e. with old stellar populations and minimal dust. Conversely, at optical wavelengths the lens should have the appearance of an elliptical with only low levels of flux contributed from the background galaxy – as SMG are severely dust obscured. High-resolution optical imaging from the twin 10 m telescopes of the W. M. Keck Observatory, in Hawaii (on the summit of Mauna Kea), provided a means to check the latter assumption. Observations of each lens candidate were taken with the Low Resolution Imaging Spectrometer [LIRS; McCarthy et al., 1998; Oke et al., 1995] on KeckI. G-band data were taken with the Blue arm of the LRIS and i-band data with the Red arm (N10, Hopwood et al. 2010 in preparation).

Effective integration times of 330 second and 180 seconds were achieved for the g- and i-bands, respectively, and 1 second snap shots of nearby stars were also taken. The reduced data (supplied to us by A. Cooray) show morphologies consistent with elliptical galaxies (figures 6.3 and 6.4), and no evident background source contributions.

In order to assess the contribution of the background galaxies in the Keck data, a light profile model of each lens was subtracted to reveal the presence of any lensed structure behind the lens galaxy. To this end empirical PSFs were prepared using postage stamps of the respective star snap-shots. GALFIT models were then constructed for each candidate in the i-band, as these data have the higher SNR. No hard or soft constraints were applied to the fitting parameters so as to avoid any prior on the galaxy morphological type. ID9 proved straight forward to fit, with a single Sérsic profile, giving a χ^2_ν of 1.1 and a clean residual, with no evident structure that could be related to the background source (see figure 6.3). The fit to ID11 was complicated by a nearby edge-on spiral, which although it is not close enough to be responsible for any lensing effects, is close enough to affect the GALFIT minimisation. A Sérsic profile was used to model the lens of ID11 and a second Sérsic for the spiral, with a high initial ellipticity. The resulting fit had a χ^2_ν of 1.0, and again there was no significant residual (see figure 6.3). ID17 shows two components in the Keck imaging, but neither have a morphology that could be explained by gravitational lensing effects, which suggests they constitute a dual foreground lens. There is possibly a similarity for one of ID17's foreground components to an edge-on spiral galaxy. Two Sérsic profiles were used to model ID17 and a good χ^2_ν (of 1.1) and good residuals were achieved (see figure 6.3). The two remaining candidates are the optically brightest ($\sim$10$\times$ greater than the other three), and have the most extended optical morphologies. Both ID81 and ID130 were better fit by the combined profile of one Sérsic plus a more extended exponential disk, i.e a power law Sérsic with an index of 1. No suggestion of structure related to the background galaxy was revealed on subtraction of the best fit models (see figure 6.4 and 6.5). Plotting the pixel flux density as a function of radius for each of the ID81 and ID130 profiles, showed the total contribution is dominated by the Sérsic component (figure 6.6). Table 6.1 [adapted from N10 supplementary on-line material (SOM)] presents the GALFIT model parameters. The best fit profiles for ID9 and ID11 have Sérsic index of 5.4 and 3.0, respectively, which are consistent with an early-type morphology [Caon et al., 1993]. For ID17 both profiles have a relatively small Sérsic index (0.5 and 1.0),

which is more consistent with dwarf elliptical galaxies. The Sérsic profiles for ID81 (n = 2.8) and ID130 (n = 1.2) also suggest early-type morphology. Assuming an elliptical morphology, GALFIT models for ID81 and ID130 were optimised after fixing the Sérsic indices to 4 – a de Vaucouleurs profile – again including the additional exponential disk profile. The best fit models gave a comparable χ^2_ν in each case and a plot of the flux as a function of radius showed a relative contributions for ID81 similar to that of ID130 (figure 6.6).

Table 6.1: GALFIT parameters for the five sub-mm lens galaxy models and g- and i-band upper limits for the background sources. R_e is the effective radius, n is the Sérsic index, b/a is the ellipticity, PA is the position angle measured east of north and $3\sigma_{ul}$ are photometric upper limits. (Adapted from N10 SOM)

ID	func.	χ^2_ν	$R_e('')$	n	b/a	PA deg.	g-$3\sigma_{ul}$ (μJy)	i-$3\sigma_{ul}$ (μJy)
9	Sersic	1.07	0.85	5.36	0.72	56.76	0.162	0.641
11	Sersic	1.03	1.10	3.97	0.65	39.61	0.229	0.442
17	Sersic	1.07	0.61	0.54	0.71	63.25	0.202	0.404
	Sersic	–	1.36	0.91	0.69	12.83	–	–
81	Sersic	1.13	0.70	2.82	0.78	36.45	0.130	0.202
	ExpDisk	–	1.20	–	0.72	0.62	–	–
130	Sersic	1.00	0.32	1.23	0.52	56.83	0.198	0.351
	ExpDisk	–	1.11	–	0.55	-54.64	–	–

6.3.1 Spectroscopic redshifts of the sub-mm lenses

Deriving two distinctly different redshifts for a gravitational lens candidate – one for the lens and one for the source – is strong evidence of a lensing event (see chapter 5). Traditionally, spectroscopic redshifts are derived from optical and NIR spectra, but high dust obscuration and the presence of an optically bright lensing galaxy do not lend themselves to this method for lensed SMG. It has recently become possible to use sub-mm and mm spectroscopy to obtain lensed SMG redshifts, with the development of instruments that are able to detect Carbon Monoxide (CO) lines from molecular gas over a wide redshift range [Daddi et al., 2009; Weiß et al., 2009]. CO lines trace dust associated with star formation and are therefore not likely to belong to the dust depleted elliptical lens galaxies. Each of the five lensed systems were observed by the Z-spec spectrometer at the Caltech Submillimeter Observatory [Bradford et al., 2004; Naylor et al., 2003] and ID81 and ID130 were also observed by the the Plateau de Bure Interferometer [Guilloteau et al., 1992], with a followup observation from the NRAO Robert C. Byrd Green

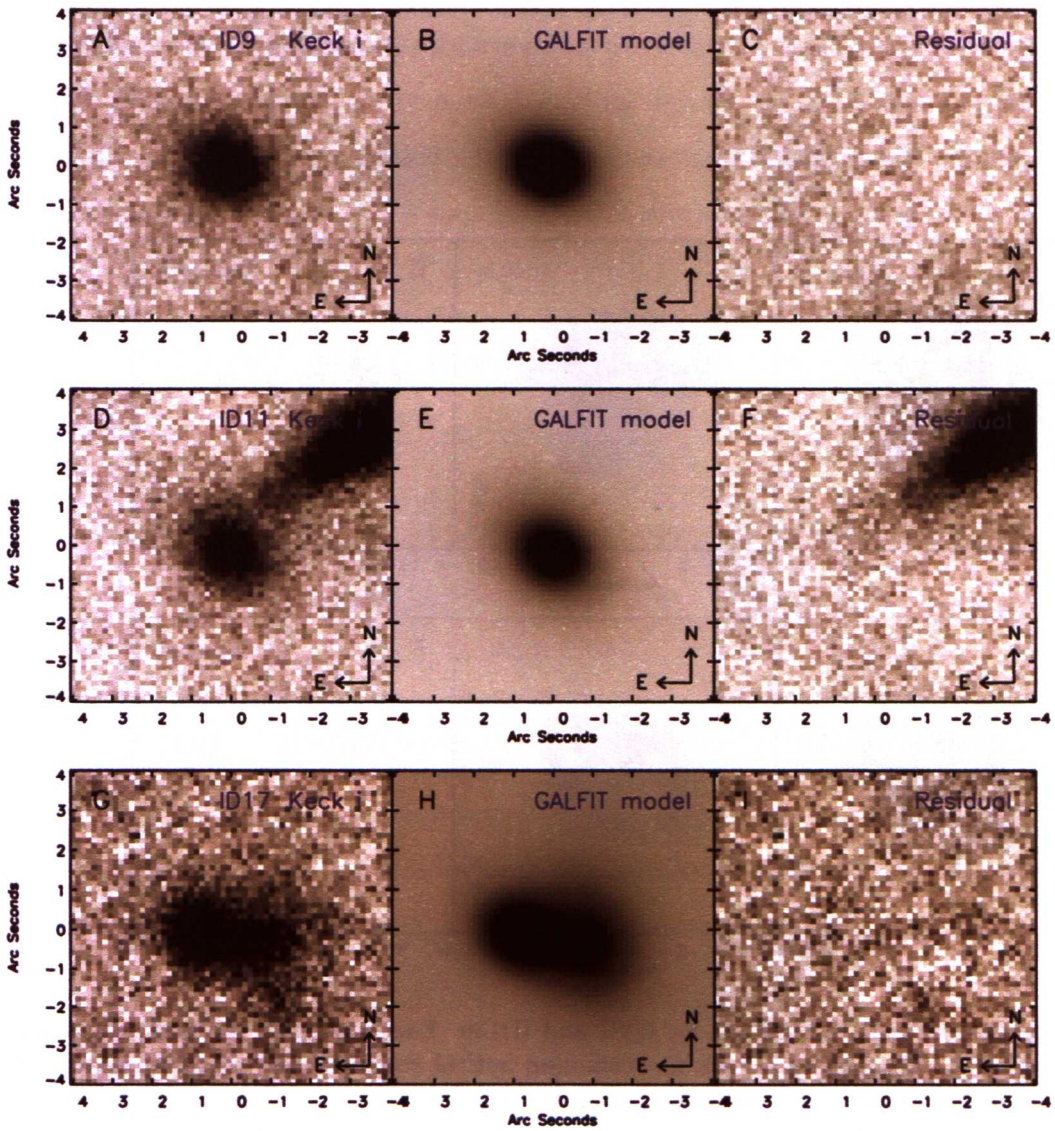

Figure 6.3: Best fit GALFIT models for ID9, ID11 and ID17. Each row gives the data, the model and the residual. ID11 has a close edge-on spiral neighbour and a profile was included for this during the fitting, but not in the model output. The best fit profiles for ID9 and ID11 have Sérsic indices that are consistent with an elliptical morphology. ID17 was fitted by two Sérsic profiles (see figure 6.5), which both have Sérsic index marginally consistent with ellipticals, but more commonly found for dwarf ellipticals. There is negligible optical residual for all three lenses confirming the dust obscured nature of the background galaxies. (Figure: N10 SOM)

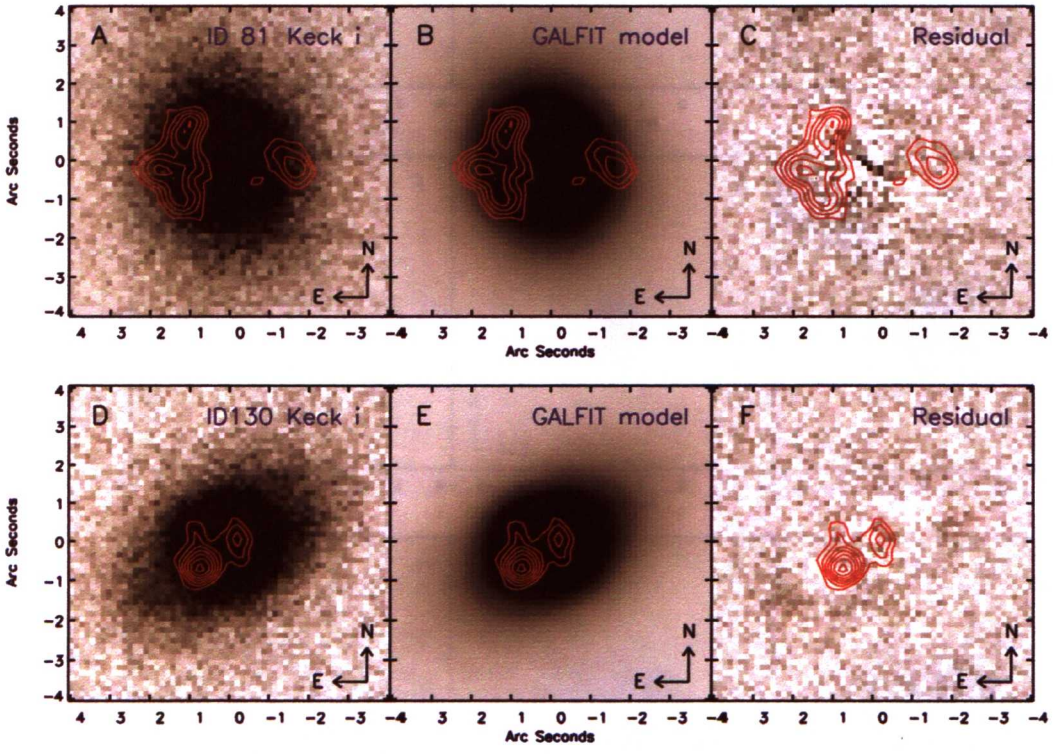

Figure 6.4: Best fit GALFIT models for ID81 and ID130. Each row gives the data, the model and the residual. The residuals have no remaining optical structure and therefore show that the background lensed galaxy (despite flux amplification due to lensing) is severely obscured by dust that is emitting almost all of its radiation at longer wavelengths. The SMA contours are overlaid in steps of 6σ, 8σ, 10σ, etc. (Figure: N10 SOM)

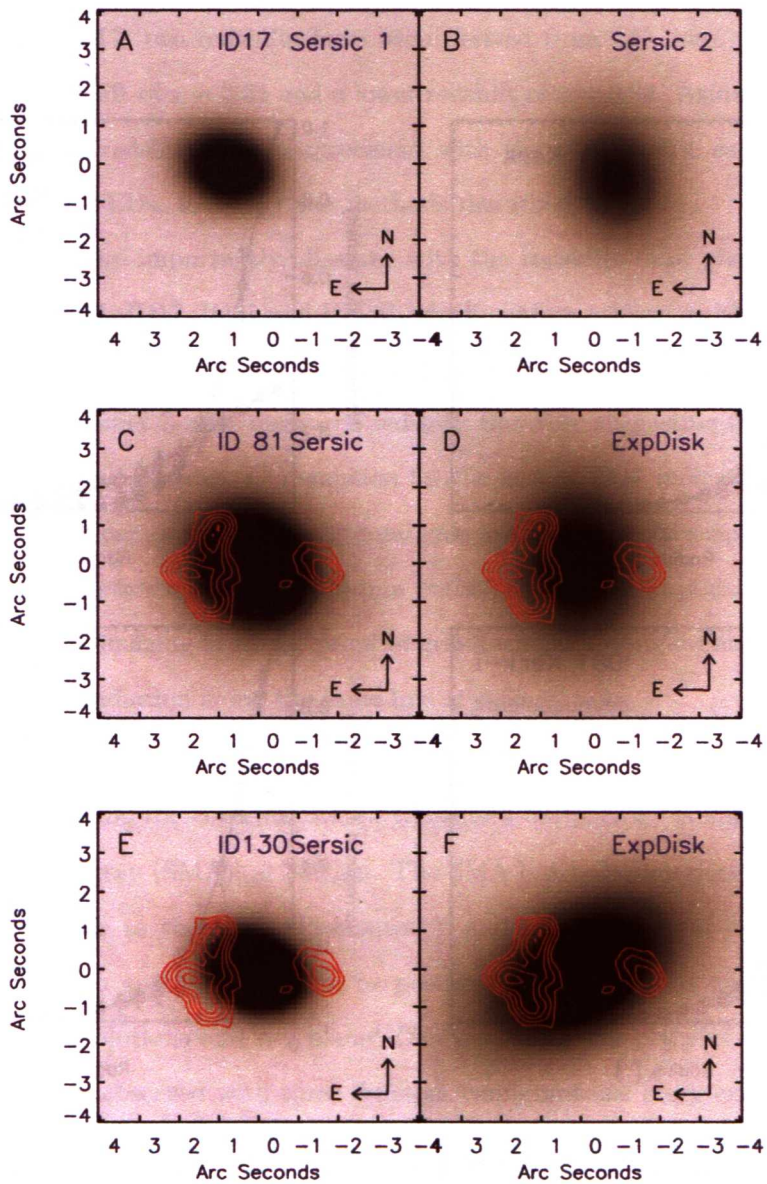

Figure 6.5: GALFIT models components for the three lensing systems that required two profiles for the foreground lens galaxy model. For ID81 and ID130, the SMA contours are overlaid in steps of 6σ, 8σ, 10σ, etc. The second component for ID17 shows a high ellipticity, supporting the visual suggestion of a side-on spiral from the i-band data. Both ID81 and ID130 have a Sérsic and exponential component. A notable relative rotation can be seen for the two components of ID130. (Figure: N10 SOM)

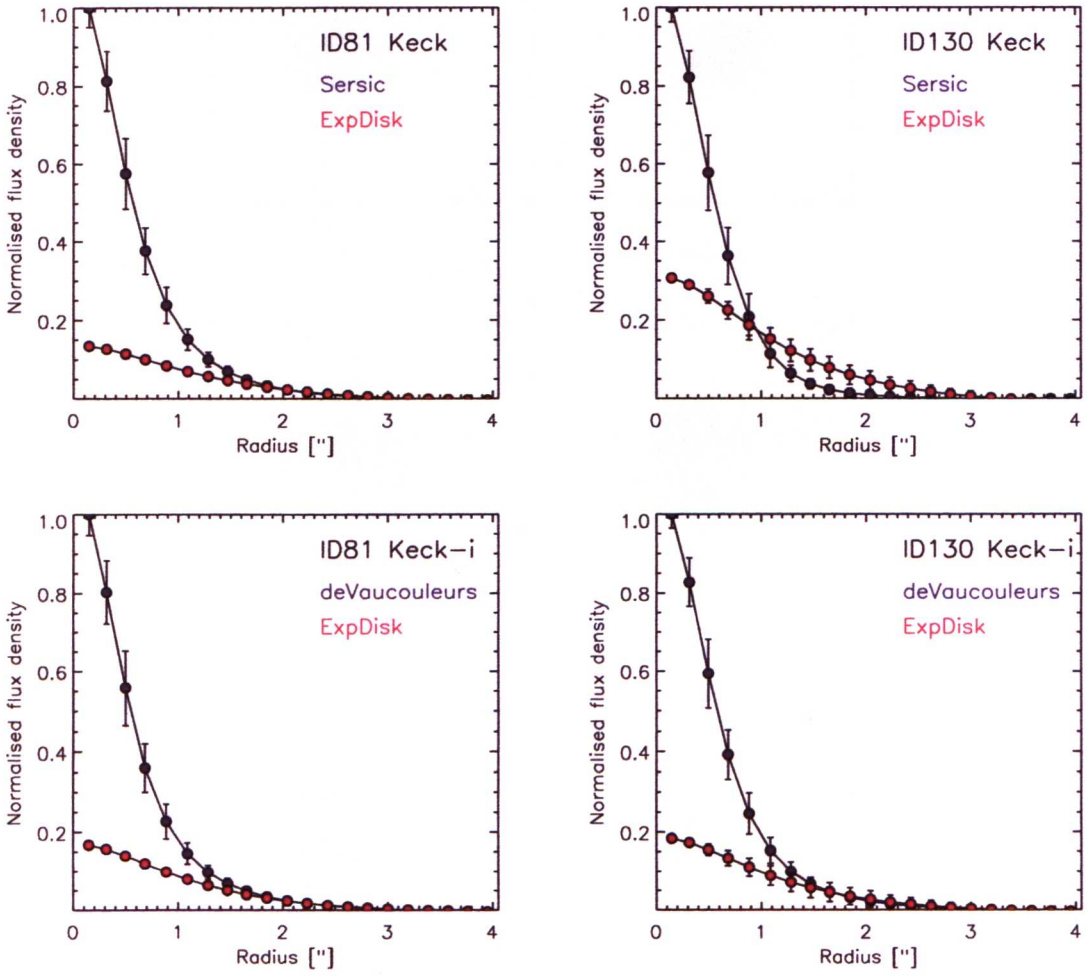

Figure 6.6: Flux density for the GALFIT Keck i-band model components, as a function of radius(″). The Sérsic/exponential disk model is compared to the Sérsic of index 4 (de Vaucouleurs profile) and exponential disk for both ID81 and ID130. The de Vaucouleurs assumes an elliptical morphology and shows a more comparable fit for both, with approximately the same goodness of fit as for a free Sérsic index, thus confirming the elliptical morphology of these lens galaxies.

Bank Telescope's Zpectrometer instrument [Harris et al., 2007]. The resulting redshifts [Frayer et al., 2011; Lupu et al., 2010] place ID81 and ID130 at the highest redshifts of z = 3.04 and z = 2.63, respectively, with ID9 and ID11 at more moderate redshifts of z = 1.58 and z = 1.79, respectively. For ID17, two redshifts have been derived from CO lines, measured by Z-Spec, giving one high redshift of z = 2.31 and a lower redshift of z = 0.94. Aside from the lower ID17 measurement, these redshifts are in agreement with the photometric estimates derived from sub-mm/millimetre SEDs, following the methods described in Aretxaga et al. [2003]; Hughes et al. [2002], and more importantly, disagree with the redshifts (and photometric redshift for ID9) derived for ID11, ID17, ID81 and ID130, which confirm a lower redshift for the optical ID of these sub-mm bright objects of between 0.2 and 0.9 (Table 6.2). For ID17 the optical redshift does agree with the lower Z-Spec measured redshift, therefore suggesting this redshift should be assigned to the lensing galaxies. CO emission for the lens of ID17 indicate some molecular gas is present in at least one of the two foreground galaxies. This spectroscopic evidence combined with the disparity between the high sub-mm emission and the elliptical morphology for the galaxies in the Keck imaging is strong proof of gravitational lensing events – i.e. there are two different sources of radiation along the same line of sight.

For ID81 and ID130 the configuration of the lensed morphology is known via imaging with the Submillimeter Array (SMA), at 880 μm. The SMA is a radio interferometer that is located on Mauna Kea (near to the Keck Observatory), and can achieve sub-arcsecond resolutions. There are eight radio antennas that can be positioned into several configurations, to provide different angular resolutions and u-v plane[1] (Fourier transform plane of the image) coverage. The two lenses were observed with three different configurations (very extended, compact and sub-compact), in order to resolve all of the structure. The combined data is given as contours in figure 6.4 and are in line with expectations from a lensing event, suggesting an Einstein ring-like structure for ID81 with a more compact double image for ID130.

[1]Radio interferometers rely on collecting samples in the Fourier transform plane (u-v plane) of the image, because a Fourier transform is a similar mathematical operation to that of interference fringes. Each point in the u-v plane corresponds to an orientation and baseline in the interferometer and many samples are required to build up the u-v plane image. This is achieved by either an array of antennas, forming different baselines, or by the relative motion of the antennas and the target (usually due to the rotation of the Earth).

Table 6.2: Photometric and spectroscopic redshifts of the five lens candidates. Spectroscopic redshifts were derived from optical lines for the lens [$z_{\rm spec}^{\rm (opt)}$] and from CO lines for the background source [$z_{\rm spec}^{\rm (CO)}$]. Photometric redshifts are based on UV/optical/NIR photometry for the lens [$z_{\rm ot}^{\rm (opt)}$] and H-ATLAS plus SMA and Max-Planck Millimeter Bolometer (MAMBO) photometry for the background source[$z_{\rm phot}^{\rm (sub-mm/mm)}$; using the photometric redshift code of Aretxaga et al. [2003]; Hughes et al. [2002]]. The quoted errors on the redshifts correspond to a 68% confidence interval. (Table adapted from N10.)

SDP ID	$z_{\rm phot}^{\rm (opt)}$	$z_{\rm spec}^{\rm (opt)}$	$z_{\rm phot}^{\rm (sub-mm/mm)}$	$z_{\rm spec}^{\rm (CO)}$
9	0.679±0.057	–	$1.4^{+0.3}_{-0.4}$	1.577±0.008[1]
11	0.72±0.16	0.7932±0.0012[2]	$1.9^{+0.4}_{-0.3}$	1.786±0.005[1]
17	0.77±0.13	0.9435±0.0009[2]	$2.0^{+0.4}_{-0.3}$	0.942±0.004[1]
				2.308±0.011[1]
81	0.334±0.016	0.2999±0.0002[3]	$2.9^{+0.2}_{-0.3}$	3.037±0.010[1]
				3.042±0.001[4][5]
130	0.239±0.021	0.2201±0.002[6]	$2.6^{+0.4}_{-0.2}$	2.625±0.001[4]
				2.6260±0.0003[5]

[1] Datum is from CSO/Z-Spec [Lupu et al., 2010]
[2] Datum is from the William Herschel Telescope
[3] Datum is from SDSS
[4] Datum is from GBT/Zpectrometer [Frayer et al., 2011]
[5] Datum is from PdBI
[6] Datum is from the Apache Point Observatory

6.3.2 Spectral energy distributions of the sub-mm lenses

In addition to SDSS and FIRST data, the SDP field has Galaxy Evolution Explorer (GALEX) UV and optical imaging, NIR imaging from the UKIDSS Large Area Survey (LAS), and NRAO Very Large Array Sky Survey (NVSS) radio imaging. SEDs were collated for each gravitational lens from the available data, depending on the coverage. Two SEDs were constructed per system: one for the foreground lens, assuming it has negligible emission at wavelengths longwise of the NIR; and one for the background galaxy, where the emission at NIR and shorter wavelengths is negligible. Each lens is covered with at least five optical and NIR photometric bands, and up to 12 for ID81. The background galaxies have no photometry at wavelengths below PACS wavebands, and ID81 is too faint in the H-ATLAS SDP data to have any PACS photometric points, so was assigned PACS upper limits. ID130 is not within the final PACS map area, but further PACS imaging has been obtained at 100 μm and 170 μm (Valtchanov in prep.), giving better constraints for both ID81 and ID130 (see section 6.4). ID130 has the least well constrained background galaxy SED, with only upper limits below 250 μm (although subsequent

photometry was added from IRAC band imaging, see section 6.4). Where there are UKIDSS and Keck data, photometric upper limits were assigned for the lensed galaxies. These upper limits were derived by taking random aperture photometry in the nearby field, using a 1.5″ radius aperture and fitting the resulting flux distributions with Gaussians (3σ upper limits are presented in table 6.1). The choice of aperture radius was based on the estimated Einstien radii as discussed in section 6.3.3.

For the lens galaxies, the UV to NIR SEDs (excluding ID17) were fit with the model of da Cunha et al. [2008], assuming passively evolving objects. ID17 was excluded from the fit as the observed photometry is a blend of two lens galaxies. For the lensed galaxies, the observed data (>NIR) plus the optical and NIR upper limits were again fitted with the model of da Cunha et al. [2008], calibrated to reproduce the UV-to-infrared SEDs of local, purely star-forming ULIRGs [da Cunha et al., 2010] (figure 6.7). A visual extinction[1] of A_V >2 is required to be consistent with the derived UKIDSS and Keck upper limits, which confirms severe dust obscuration of the SMG.

6.3.3 Discussion

The best fit SEDs provide estimates of the physical characteristics for the lensing systems. As there are only upper limits below the PACS wavebands for the SEDs of the background galaxies that, despite having precise redshifts, physical parameters derived from optical and UV emission (such as stellar mass and star formation rates) are poorly constrained. Table 6.3 presents the physical estimates for the lens galaxies and the L_{IR} for the lensed SMG, as this quantity is dominated by the cold dust component. For the lens galaxies, the predicted stellar mass (M_*) is of the range (4 - 15) $\times 10^{10}\,M_\odot$, with low predicted star formation rates of <0.8 $M_\odot\,yr^{-1}$, which are in-line with the characteristics of typical ellipticals. The high A_V of the lensed galaxies, which is necessary to fit the optical and NIR upper limits, indicates these lensing events would not have been identified using traditional optical selection methods. Each background SMG has an observed L_{IR} that would initially define it as a HLIRG, however these estimates are not corrected for magnification. It is not unreasonable to expect magnification factors $\sim$ 10 or greater

[1] A_V is the difference between the observed (dust obscured) V-band magnitude and the intrinsic (dust free) V-band magnitude.

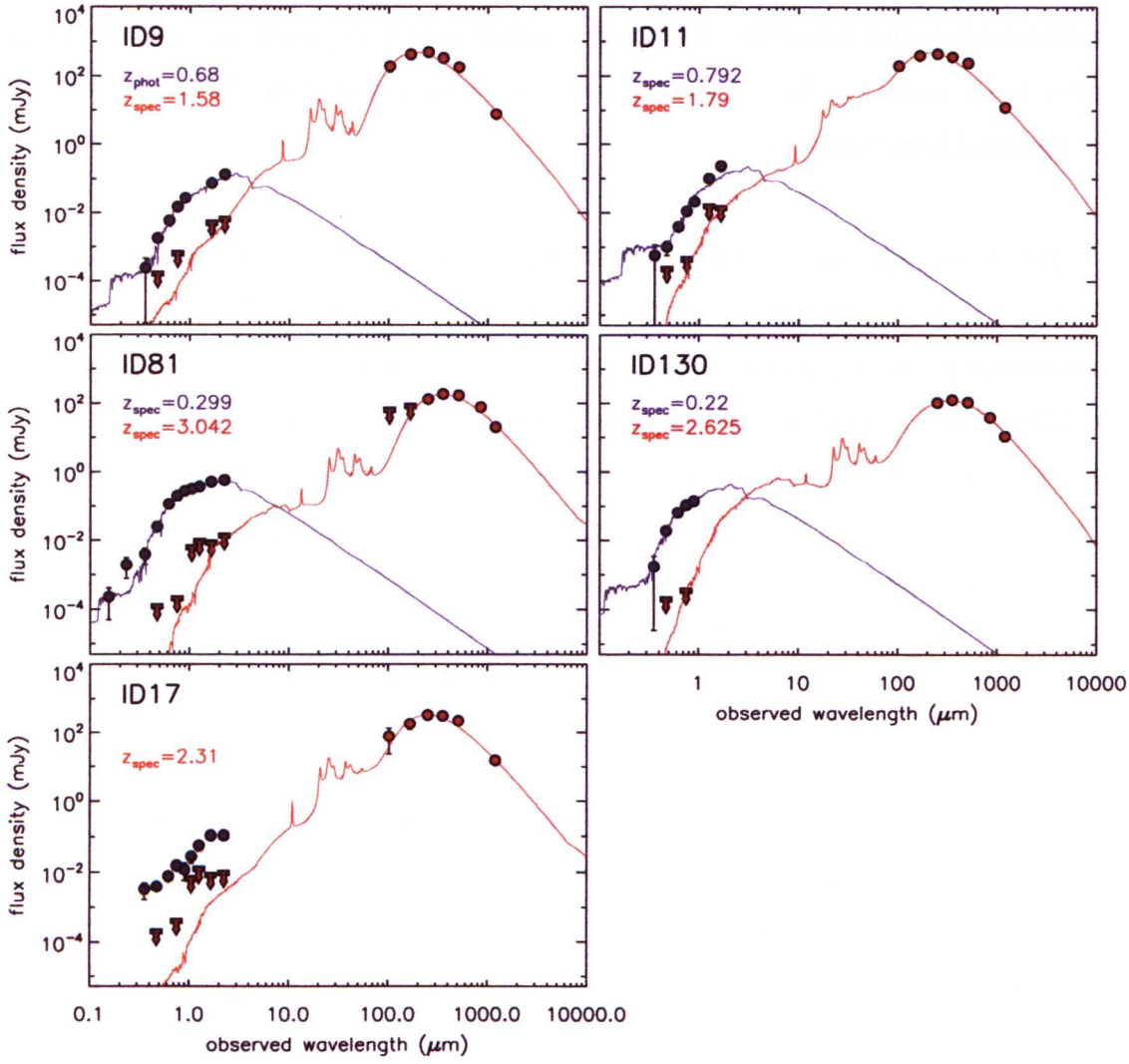

Figure 6.7: Observed SEDs and best fit SED models [da Cunha et al., 2008] for the five sub-mm lenses. The background source, responsible for the sub-mm emission, is a heavily dust obscured star-forming galaxy (red curve), whereas the lens galaxy, which is responsible for the UV/optical and NIR part of the spectrum, is characterised by passive stellar evolution (blue-curve). The UV, optical and NIR data points (blue dots) are from *GALEX*, SDSS and UKIDSS LAS, respectively. The sub-mm/mm data points (red dots) are from PACS/Herschel, SPIRE/Herschel, SMA and Max-Planck Millimeter Bolometer (MAMBO)/IRAM. Upper limits for ID81, at *Herschel*/PACS wavelengths, are shown at $3\,\sigma$. There are no upper limits for ID130 as it lies outside the region covered by the SDP PACS map. (Figure: N10)

for strong lensing events [Negrello et al., 2007], and therefore these objects are more likely to be ULIRGs. The magnification factors for ID81 and ID130 were estimated from a model of the lensing systems (see N10; SOM), giving 25 ± 7 for ID81 and 6 ± 1 for ID130. The greater associated uncertainty on the magnification factor for ID81 is due to the source galaxies position close to the caustic[1] (therefore giving the near Einstein ring observed). Any small change in the source position, therefore, translates to a large change in magnification. Correcting for flux amplification using these magnification estimates, gives L_{IR} for ID81 and ID130 in the ULIRG range $\sim 5 \times 10^{12} L_{\odot}$.

These results suggest that *all* of the brightest SMGs detected in the H-ATLAS SDP field are being lensed, and therefore un-lensed SMG that are intrinsically brighter than 100 mJy at 500 μm (e.g. HLIRG) at redshifts $z < 4$ are rare, with a predicted surface density of < 0.32 deg^{-2}, having implications for models of the formation and evolution of the most massive galaxies in the Universe.

The total dark plus luminous mass of a lensing galaxy, enclosed within the circular area defined by the Einstein radius, can be derived directly from the Einstein radius. The Einstein radius is the radius into which a source would be lensed for a circular symmetric lens directly along the line of sight, between an observer and the source. The Einstein radii for ID81 and ID130 were derived from the average radius measured from the lens centre to the peaks of the lensed structure in the SMA data. Peaks with a SNR > 8 were selected – 4 peaks for ID81 and two peaks for ID130 – giving Einstein radii of $1.62 \pm 0.02''$ and $0.59 \pm 0.02''$ for ID81 and ID130, respectively. The associated uncertainty was estimated using the positional error on a point source within the SMA image. Assuming uncorrelated noise and accurate astrometry, the RMS on the point source position is $\sqrt{2}\sigma/\mathrm{SNR}$, where $\sigma = \mathrm{FWHM}/2\sqrt{2ln2}$. The mean FWHM of the SMA synthesised beam is $0.75'''$ for ID81 and $0.77''$ for ID130. For a minimum SNR of 8 for the SMA peaks, the maximum positional RMS of the SMA data is estimated at $0.06 \pm 0.01''$ for both ID81 and ID130. Assuming a singular isothermal sphere (SIS), the mass within the

[1] The caustic curve indicates the position in the source plane of maximum magnification

Einstein ring ($M_{\rm E}$) is given by

$$M_{\rm E} = M(< \theta_{\rm E}) = \pi \, \Sigma_{\rm cri} \, \theta_{\rm E}^2 \tag{6.1}$$

where $\theta_{\rm E}$ is the angular distance from the centre of the mass distribution and $\Sigma_{\rm crit}$ is the critical surface density as

$$\Sigma_{\rm crit} = \frac{c^2}{4\pi G} \frac{D_{\rm S}}{D_{\rm L} D_{\rm LS}} \tag{6.2}$$

where c is the speed of light, G is the gravitational constant and $D_{\rm S}$, $D_{\rm L}$ and $D_{\rm LS}$ are angular diameter distances (see chapter 1, figure 1.6). The estimated values of $M_{\rm E}$ are $(11.59 - 11.61) \times 10^{10}{\rm M}_{\odot}$ for ID81 and $(10.56 - 10.64) \times 10^{10}{\rm M}_{\odot}$ for ID130. A comparison estimate for the measured Einstein radius was obtained from the line-of-sight stellar velocity dispersion, $\sigma_{\rm v}$, which can be derived from the Faber–Jackson relation [FJR Faber & Jackson, 1976]. This relation is between the luminosity and $\sigma_{\rm v}$ for elliptical galaxies as ${\rm L} \propto \sigma_{\rm v}^4$. Using the B-band luminosity derived from the best fit models, the Einstein radii estimated using the FJR are $1.51 \pm 1.0''$ for ID81 and $0.81 \pm 0.5''$ for ID130. These estimates have large associated uncertainties, due to the scatter of the FJR, but are consistent with the estimates from the lens geometry.

To test the hypothesis that the physical properties of sub-mm selected lensed galaxies are consistent with other known lens elliptical at a similar redshift, a comparison of the lens V-band mass-to-light ratio was made with SLACS lens galaxies. ID81 and ID130 are consistent with the average trend for SLACS galaxies (figure 6.8). In addition ID130 suggests sub-mm selected lenses will extend the lower mass and luminosity limits seen for SLACS lenses.

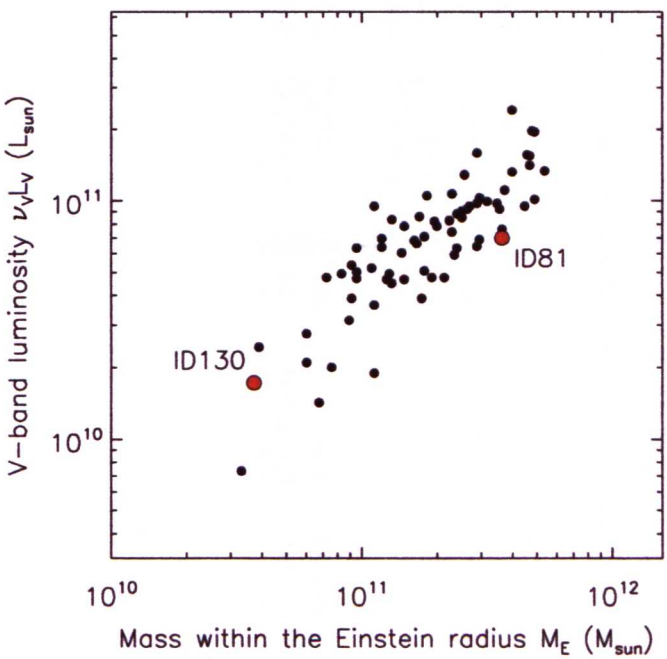

Figure 6.8: Mass vs V-band luminosity for the lensing galaxy in ID81 and ID130. The rest-frame V-band luminosity was derived from the best-fit SED to the UV/optical/NIR photometric data; the mass within the Einstein radius is that measured directly from the SMA images. The light versus mass relation inferred for ID81 and ID130 (red dots) is consistent with that observed for the SLACS lenses (black dots from Bolton et al. [2008a]). (Figure: N10)

Table 6.3: Derived physical parameters for the five sub-mm gravitational lenses. Estimated mass in stars ($M_\star$) and Star Formation Rate (SFR) of the foreground galaxy, derived from the best-fit to the UV/optical/near-IR part of the SED; the Einstein radius measured from the SMA images (θ_E); mass within the Einstein radius (M_E), estimated from θ_E; line-of-sight stellar velocity dispersion (σ_v^{FJ}), derived from the Faber-Jackson relation and the B-band luminosity produced by the best-fit to the UV/optical/NIR SED; Einstein radius (θ_E^{FJ}), calculated from σ_v^{FJ}; infrared luminosity of the background source (L_{IR}), without correction for magnification, derived by fitting the sub-mm/mm part of the SED and the upper limits at optical and NIR wavelengths; and visual extinction parameter (A_V), inferred for the background galaxy. All the quoted errors correspond to a 68 per cent confidence interval. For ID17 only the infrared luminosity and the extinction parameter of the background source are quoted because of the presence of two lensing galaxies, that can only be disentangled in the Keck images. (Table adapted from N10)

H-ATLAS ID	$\log(M_\star)$ ($M_\odot$)	$\log(SFR)$ ($M_\odot\,yr^{-1}$)	θ_E (arcsec)	$\log(M_E)$ ($M_\odot$)	σ_v^{FJ} ($km\,sec^{-1}$)	θ_E^{FJ} (arcsec)	$\log(L_{IR})$ ($L_\odot$[a])	A_V
9	$10.79^{+0.16}_{-0.11}$	$-0.51^{+0.20}_{-0.27}$	–	–	232^{+75}_{-56}	$0.77^{+0.49}_{-0.34}$	$13.48^{+0.07}_{-0.06}$	$6.7^{+1.5}_{-1.0}$
11	$11.15^{+0.09}_{-0.10}$	$-0.08^{+0.18}_{-0.24}$	–	–	258^{+82}_{-62}	$0.91^{+0.59}_{-0.40}$	$13.61^{+0.06}_{-0.06}$	$5.1^{+1.6}_{-0.7}$
17	–	–	–	–	–	–	$13.57^{+0.08}_{-0.06}$	$5.3^{+1.4}_{-0.6}$
81	$11.17^{+0.04}_{-0.08}$	$-1.66^{+0.46}_{-0.14}$	1.62±0.02	11.56±0.01	242^{+77}_{-58}	$1.51^{+0.98}_{-0.67}$	$13.71^{+0.07}_{-0.07}$	$3.5^{+3.4}_{-0.3}$
130	$10.65^{+0.06}_{-0.08}$	$-1.17^{+0.39}_{-0.58}$	0.59±0.02	10.57±0.04	174^{+55}_{-42}	$0.81^{+0.52}_{-0.36}$	$13.45^{+0.08}_{-0.09}$	$1.9^{+0.3}_{-0.3}$

6.3.4 Conclusions

Out of five gravitational lens candidates, selected above 100 mJy at 500 μm in the H-ATLAS SDP data, all five have been confirmed as gravitational lensing events, thus validating the selection method presented here and in N10. Using a simple cut in flux in conjunction with shallow optical and radio data, which already exist over a large fraction of the sky, will allow strong galaxy-galaxy lensing systems to be selected with a success rate of $\sim$100%. H-ATLAS is a blind survey and so can detect lensing events over a range of scales, from galaxy to galaxy cluster, which extends the mass scale from previous sub-mm surveys that searched for lensed objects in cluster fields. In addition, H-ATLAS selected lenses will not suffer the bias of previous dedicated lens search survey (i.e. biased towards low redshift and high mass lenses), shown by the wide range redshift of the first five H-ATLAS lenses – $z \approx 0.2 - 0.9$ and low predicted mass of ID130. Extending the SDP findings of five gravitational lenses in 14.4 deg^2, the full H-ATLAS survey area will produce more than one hundred sub-mm lenses. This sample of lenses will allow the question of how the mass distribution of galaxies evolved with cosmic time, which is crucial to test models of galaxy formation and evolution *and* will extend our current understanding of the physical characteristics of SMGs.

6.4 Spitzers NIR view of the H-ATLAS sub-mm lenses

The successful proof-of-concept test for sub-mm based gravitational lens selection, identified five sub-mm bright strong lensing systems, in the H-ATLAS SDP field (Negrello et al. 2010; N10 from hereon). These lensing events were confirmed with follow-up observations. IRAC Channel 1 (Ch1) and Channel 2 (Ch2) imaging were taken as part of the *Spitzer* program 548 (PI A. Cooray) for the two lenses with the highest redshifts sources galaxies – ID81 and ID130. Both targets were observed with a 36-position dither pattern, and a 30 second exposure per frame. This observing strategy gives a mapping grid depth with a coverage of 36 pointings, at the position of each of the targets. The IRAC 'corrected basic calibration data' (cBCD), which are the official pipeline output (pipeline version S18.18.0) pre-processed by the Spitzer Science Centre (SSC), were aligned, resampled to give a pixel scale of 0.6″, and combined to give the final mosaics, using MOPEX[1] [Makovoz & Khan, 2005].

GALFIT was used to construct models of the light profiles for each lensing system. Postage stamp images were taken for both IRAC channels, centred on each lens (25″ × 25″ stamps for ID81 and 20″ × 20″ for ID130). Corresponding stamps of the standard deviation noise maps were also taken. There are no nearby neighbours present in the ID130 image stamps, but for ID81 several other sources, within the stamp area, needed to be masked. The additional sources are all beyond a 10″ radius from the lens, and therefore can be considered to have negligible photometric blending with the main source. Masking of these sources was achieved by replacing the pixel values with normally distributed random noise, at the level of the local sky (figure 6.9). Initially empirical PSFs, constructed from several bright and unsaturated sources in the maps, were used, however, the GALFIT residual images for ID81 and ID130 were not well subtracted by the resulting best fit models, nor were blank field tests on other sources within the IRAC maps. These PSFs were replaced with the official PSFs[2], provided by the SSC. The size of the PSF were reduced to coincide with the the lens postage stamp image sizes. These PSFs have been produced with a pixel scale of 0.3″ as the inherent IRAC PSF is under-sampled.

Before fitting profiles to ID81 and ID130 in the IRAC data, and in order to take advantage

[1] MOPEX is the official IRAC data reduction software provided by the SSC
[2] The IRAC PSFs can be found on the official website: IRAC-PSF

of the Keck optical imaging –higher resolution and the presence of only the lens galaxy (see section 6.3)–, single de Vaucouleurs profile models were constructed for the Keck i-band data, in addition to the Sérsic plus exponential disk models already described in section 6.3. To look for any structure in the IRAC data that could be linked to the background galaxy, the resulting best fit de Vaucouleurs Keck models were scaled and fitted to the IRAC Ch1 and Ch2 data. The scaling was achieved simply by converting the effective radius to the IRAC pixel scale and then fixing the effective radius and ellipticity. The centroid, magnitude and position angle were kept as free parameters. On subtraction of the results, and in comparison to the SMA contours, the residuals strongly suggests a more complex structure, associable to the background galaxies, is present for both sources, in both IRAC channels (see figure 6.10). For ID130 a significant emission was uncovered to the south-east, which is not seen in the Keck images. This extra flux can be linked to a small peak towards the edge of the SMA contours, and therefore points to either a second sub-mm galaxy (most likely at a different redshift) or to a more extended structure than predicted for the background source.

In order to more precisely detangle the lens and background components, further Sérsic profiles were added to each model, with centroids roughly at the positions of the sub-mm contour peaks that correspond to the residual flux remaining after the single profile. Three profiles were added for ID81 and two for ID130. After initial trials, an exponential disk profile was added to model the lens galaxy for ID130. The lens and source profiles were fitted simultaneously. The fitting process for each lens in each channel is described in more detail in the following sections.

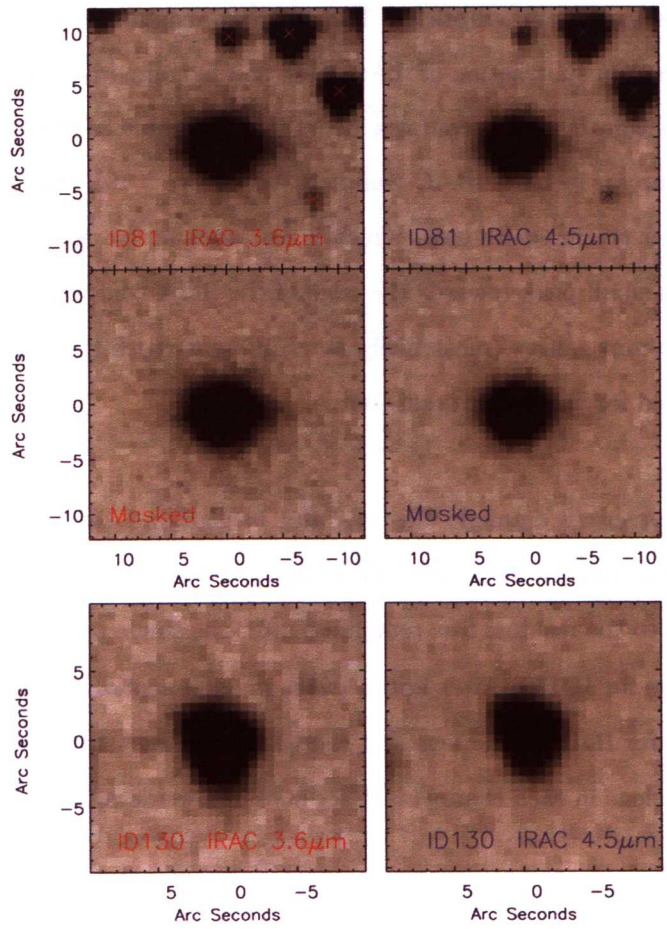

Figure 6.9: Top: $25'' \times 25''$ postage stamp images of IRAC CH1 and CH2 for ID81, before (top) and after (bottom) masking of the nearby sources. Bottom: $20'' \times 20''$ postage stamp images of IRAC CH1 and CH2 for ID130

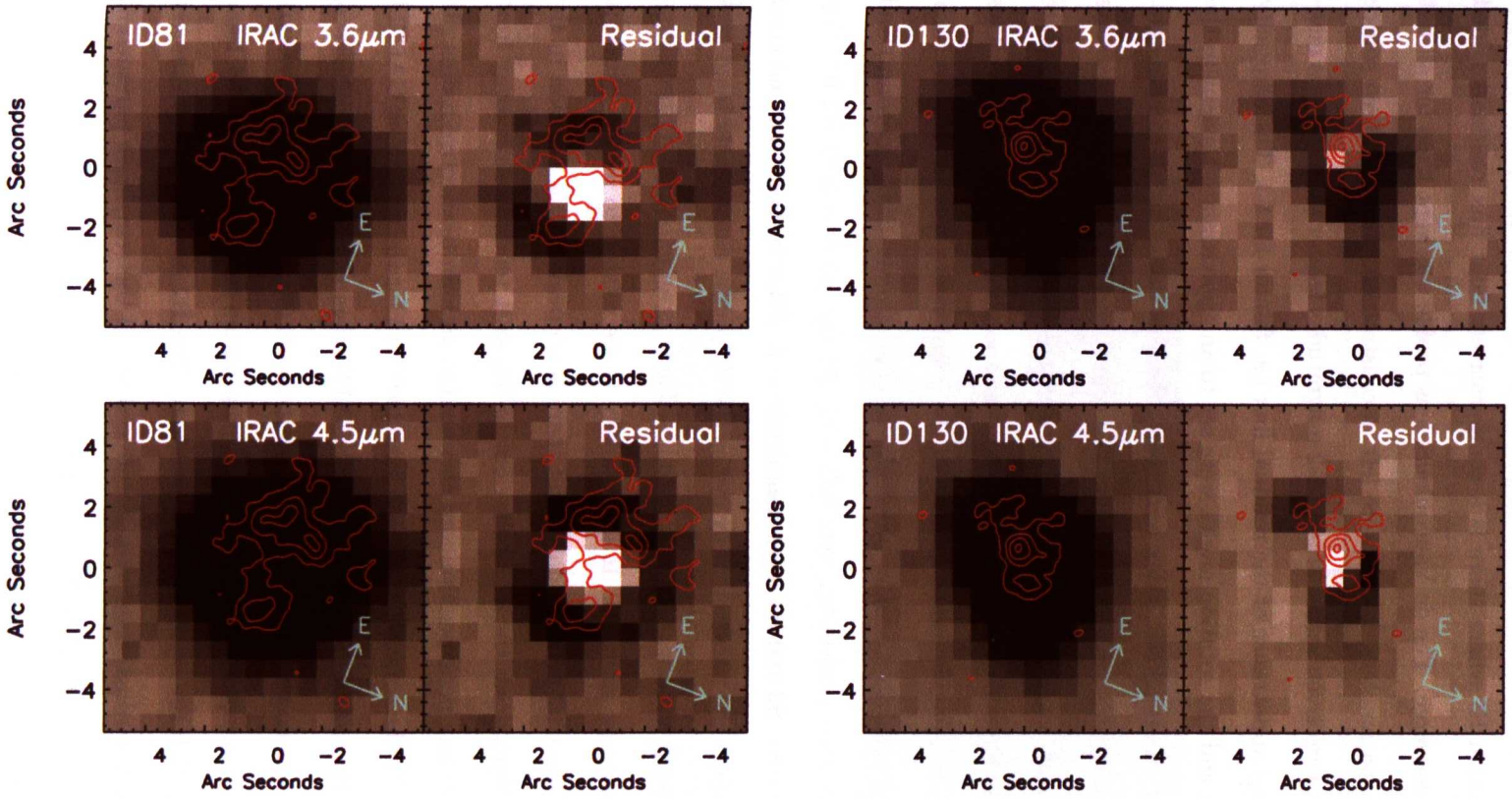

Figure 6.10: IRAC Ch1 and Ch2 postage stamp images for ID81 and ID130, and the corresponding residuals after subtraction of single de Vaucouleurs profile GALFIT models. Each stamp is overlaid with contours from SMA imaging. The profiles are fitting to the foreground lens galaxy, and for all four cases show residual structure in line with the SMA contours, strongly suggesting there is lensed structure of the associated background galaxy present in all these data. Assuming a 0.1″ error on the astrometry between the IRAC and SMA data and a point source positional RMS for the SMA data of 0.06″ (see section 6.3.3) gives a total uncertainty on the SMA contour position of 0.11″. (Figure: N10)

6.4.1 ID81 CH1

Two profiles were added to the ID81 CH1 model, shown as positions S1 and S2 on figure 6.11), with a third profile (at position S3 where there is a comparatively faint flux residual) added after GALFIT struggled to converge. The de Vaucouleurs lens profile was kept fixed for all but the magnitude and position parameters, which were left unconstrained. For the three source components the magnitudes were given values around 1-2 magnitudes fainter than the lens magnitude, adjusted by the visual appearance of the residual flux i.e. fainter for S3. The ellipticity was increased for S2 and S3 and the rotation angles were set to an approximate tangent to the lens centre. The effective radius and Sérsic index were set to the lens values for all components. GALFIT was then run without additional constraints. The source component parameters were adjusted at the end of each run, where necessary, based on a visual examination of the separate and combined model for S1, S2 and S3, along with the corresponding residual image. This process was repeated until a reasonable model (where all the components remain close to their input position and have converged to a profile, physically relatable to the SMA contours) and a residual, with no clear structure remaining, were achieved. At this point a mild B2 bending parameter was introduced for S1, S2 and S3, with magnitude < 2. After further trial and error it was found necessary to adjust the parameters by eye as the S2 profile consistently bend convexly, and the S3 profiles effective radius tended to infinity. There is an extended diffuse signal to the north of S3, which may be spurious. It is not likely to be related to lensed structure as it lacks a counterpart in the Ch2 or Keck data, and there is no peak at this position in the SMA contours. This extra flux causes the odd behaviour of S3, as it tends to shift away from the nearby corresponding sub-mm peak position and also tend to an infinite effective radius. To force 'good' behaviour from S3, the rotation angle was fixed to 0 (up) for the remaining GALFIT runs. As well as an option for optimising the model, GALFIT offers the alternative choice of outputting the total model, the image block or the subcomponents (without further iteration). These outputs provide ample comparison, so the model parameters can be adjusted by hand and checked before running with the optimisation turned on. The B2 parameter was removed from the S3 component and soft constraints were introduced for all the remaining parameters, including the lens profile parameters. These constraints allowed around a 20% movement for each parameter. This is not a quick process and would not be a feasible approach for large numbers of galaxies, but in this case it does provide a means to a solution which may not be

achieved otherwise. Once satisfied with the model and residual, all constraints were removed to check that the convergence was real and not just bounded by the limiting parameter values. The resulting model (see figure 6.12) follows the SMA contour structure and residual, after the subtraction of the lens model. The final parameters for the lens component remained similar to the best fit input model, with the effective radius, ellipticity and rotation angle within 10%, a change of 0.1 magnitudes and only a fractional centroid position shift. The full output parameters are given in table 6.5.

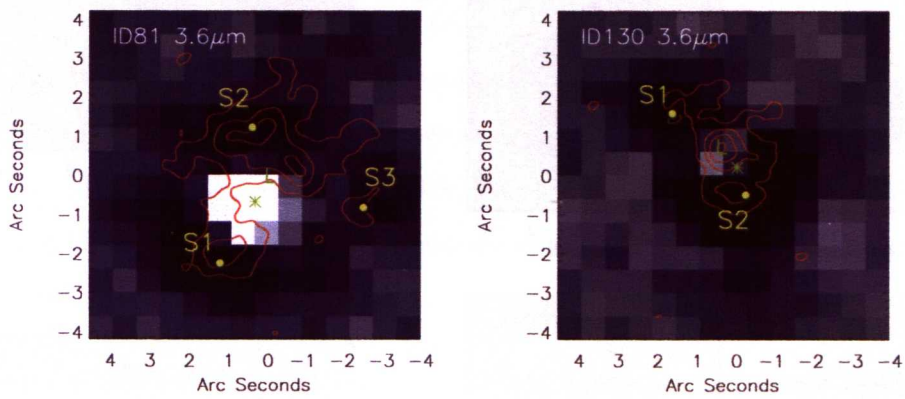

Figure 6.11: Residuals after the subtraction of the best fit GALFIT single de Vaucouleurs profile models for ID81 and ID130, IRAC CH1 data overlaid with SMA contours (black line). The initial GALFIT lens component (L) and background galaxy components (Sn) centroids are also shown.

6.4.2 ID81 CH2

The fitting for ID81 CH2 was simplified by taking the best fit model for CH1 as a starting point. The lens component was replaced by the de Vaucouleurs profile produced by the single profile fit and the equivalent S3 profile was adjusted to a lower Sérsic index and ellipticity, and the fixing of the position angle was removed. The magnitudes for the source components were also altered, using the offset between the CH1 and CH2 lens profile magnitudes. After the first GALFIT runs, there were clear issues with the resulting model. Examining the sub-components showed the main problem to be that S1, S2 had moved within the SMA contours, closer to the lens centroid that predicted. To solve the problem the magnitude of the lens was decreased and the S1 and S2 components were moved further from the lens centroid and given tight positional constraints. The lens parameters were given loose constraints and the bending parameter of S2

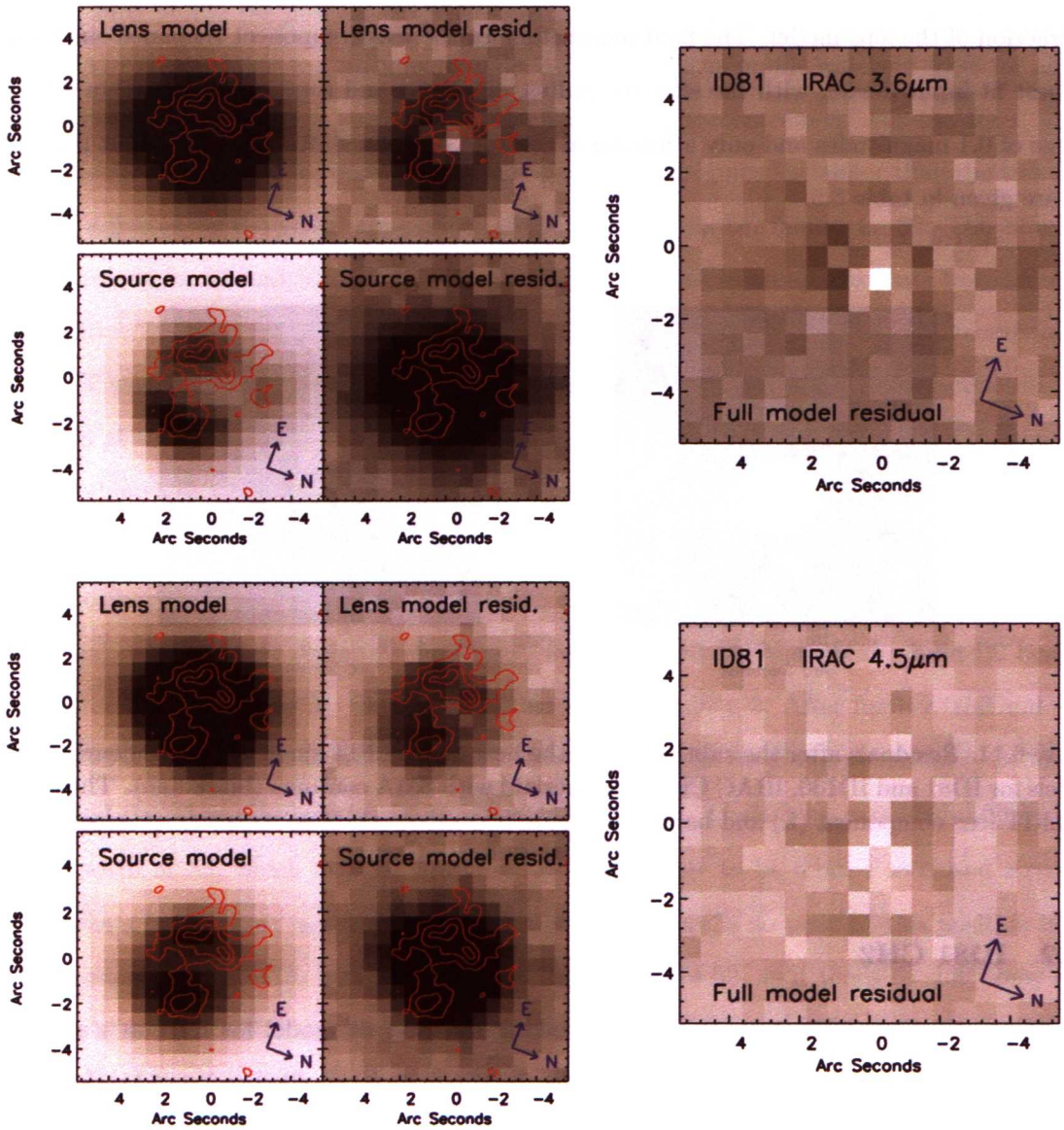

Figure 6.12: Multi-component light profile models for ID81 Ch1 and Ch2. The block of smaller postage stamps each show the lens model (top left) and model fitting the lensed structure (bottom left) with the respective residuals (top and bottom right). The larger stamps show the results of subtracting the combined lens and source models for each channel. The red contours represent the corresponding SMA data. The best fit models for the background galaxy (in each channel) show a partial ring-like structure and are constructed from three Sérsic profiles. Note the clean residuals for each combined model.

was removed. Once the lens dominated over S1 and S2 profiles, the parameter constraints were loosened and the Sérsic index was reset to 4.0. At this point the model was adjusted by hand and then run with constraints, as with CH1, after reinstating the bending parameter for S2. The final model is in good agreement with the SMA contours and has a clean residual (figure 6.12). The final GALFIT parameters for the best fitting model are given in table 6.5

6.4.3 ID130 CH1

Figure 6.10 (right hand panels) illustrates the compact nature of the lensed structure in ID130, in comparison to ID81. Consequently the multi-component GALFIT model must accommodate at least one source profile with centroid close to the position of the lens, $< 1''$ in separation (see figure 6.11). To facilitate the GALFIT fitting process, the model for ID130 was expanded by two extra component to represent the lensed structure. The Keck i-band data were previously modelled with a de Vaucouleurs profile plus an exponential disk profile, giving a marginally improved χ^2 over the single profile fit. The double profile lens model was adopted for ID130. Indeed after initial GALFIT trials with the single ID130 profile lens for the IRAC CH1 data, substantial residual structure remained after subtraction, which was not in-line with the SMA contours (see figure 6.13). The structure resembles closely the type of residual one might expect for poor GALFIT subtraction. Again the main lens parameters (for both profiles) were kept fixed and the positional coordinates were given tight constraints (within 0.05 pixels), due to the nearby background source component. Soft constraints were necessary for the remaining parameters during the full GALFIT fitting procedure to prevent the lens profiles switching to a source profile and vice versa. Once the output model became reasonably stable, bending parameters were introduced for the two source profiles. After several further attempted GALFIT runs the bending was removed from S2, as this produced repeatedly poorer results, and the ellipticity was increased to compensate. An adequate model was ultimately achieved, but only after the de Vaucouleurs lens profile was changed to a generic Sérsic profile, with a non-fixed Sérsic index and a discrepancy between the two lens profile centroids, of $\sim 0.3''$ in the y-axis direction, was allowed. Also the model exhibits a lack of stability (non or undesirable convergence with looser constraints), all of which suggests the different component galaxies may not be cleanly represented in the final model and therefore the associated photometry will be relatively uncertain.

After fitting to the Ch2 data, the resulting model was used for a second attempt at the Ch1 data and gave a more stable result. The residual (see figure 6.14) is, well subtracted and the best fit gave a χ^2_ν of 1.69. The final GALFIT parameters are given in table 6.6.

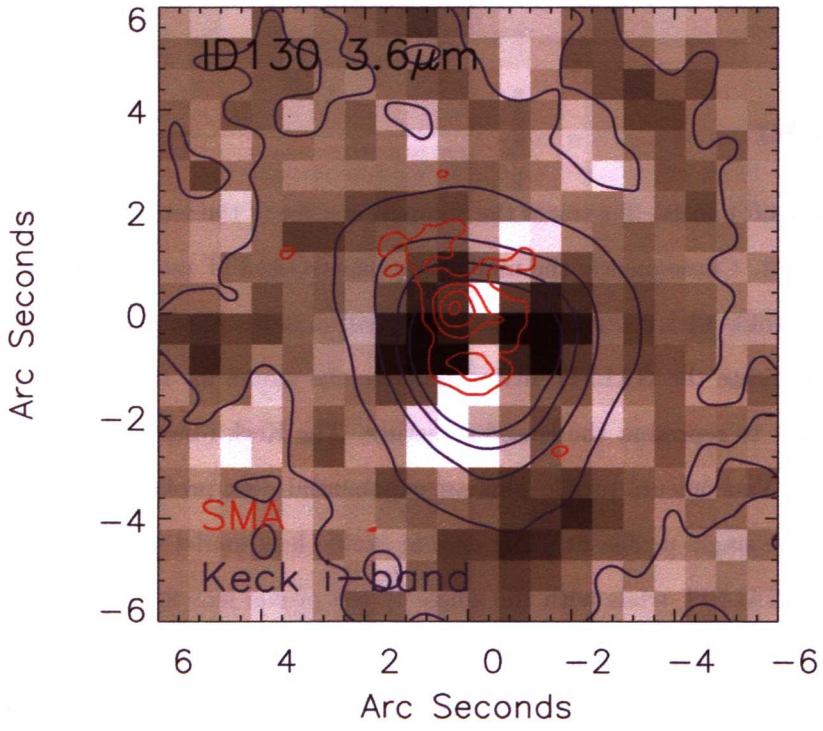

Figure 6.13: Residuals after the subtraction of the best fit GALFIT multi-profile model for ID130 CH1. The related model consist of one de Vaucouleurs for the light profile of the lens galaxy and two Sérsic profiles for the light profile of lensed background galaxy. SMA contours (red) represent the lensed structure and Keck i-band contours (blue) represent the lens galaxy and suggest the excess flux is related to a poorly subtracted lens.

6.4.4 ID130 CH2

Discounting the shortfalls of the ID130 CH1 model, this was used as a base for the initial CH2 GALFIT input, and despite expectations converged with relatively minimal adjustment to give a stable result. The double lens profile was again adopted and the CH1 lens components were replaced with the best fit Keck-i ID130 CH2 profiles. The bending parameter for S2 was retained from the CH1 fit. For the first few runs the Sérsic index for the non-exponential disk profile was not constrained and in fact no constraints file was used during the iterations of GALFIT

Table 6.4: Photometry, χ^2_ν and degrees of freedom (Ndof) are given for the IRAC CH1 and CH2 GALFIT models for ID81 and ID130.

ID/channel	S_{lens}(mJy)	S_{source}(mJy)	χ^2_ν	Ndof
ID81/CH1	0.354 ± 0.043	0.062 ± 0.044	1.45	1653
ID81/CH2	0.254 ± 0.047	0.169 ± 0.054	1.61	1570
ID130/CH1	0.213 ± 0.034	0.044 ± 0.015	2.33	1061
ID130/CH2	0.230 ± 0.005	0.047 ± 0.003	1.69	1061

Table 6.5: Best fit parameters for the multi-component GALFIT models for ID81. Values given in square brackets indicate a fixed parameter. Values marked with asterisks are flagged as extremes. The magnitudes given are instrumental magnitudes with a zero point of 25 ($m = -2.5\log_{10}\left(\frac{S}{mJy\,sr^{-1}}\right) + 25$.

Parameter	Ch1				Ch2			
	L	S1	S2	S3	L	S1	S2	S3
Magnitude	20.95	23.56	24.21	24.59	21.31	22.76	23.18	24.45
R_e	1.49	1.64	1.43	1.70	1.21	1.50	1.61	2.48
n	[4.00]	0.05*	0.05*	16.11*	2.35	0.50	0.05*	3.57
Ellipticity	0.73	0.16	0.13	1.00	0.74	0.60	0.10	0.99
Pa	78.8	60.1	89.2	[0.0]	66.3	75.0	87.4	24.7
B2	—	-1.54	0.53	—	—	-0.53	-0.81	—

run and model adjustment. This time the model was adjusted by hand where necessary before re-running with GALFIT. The final model proved stable enough to reinstate the de Vaucouleurs profile for the generic Sérsic lens component, although the χ^2_ν is relatively high, at 2.331, in comparison to the CH1 model. The model and residual maps are shown in figure 6.14 and the parameters are provided in table 6.6.

The final models for the background galaxy components of ID81 in both channels (see figure 6.12) show a partial Einstein ring-like structure, which corresponds to the main SMA contour peaks. For ID130 the resulting best fit profiles for the lensed galaxies do follow the SMA contours and the combined model subtracts cleanly, suggesting a successful lens/source disentangling (see figure 6.14). This morphology, however, has to be confirmed, and the planned *HST*/WFC3 observations of ID81 and ID130 will provide the necessary higher resolution data.

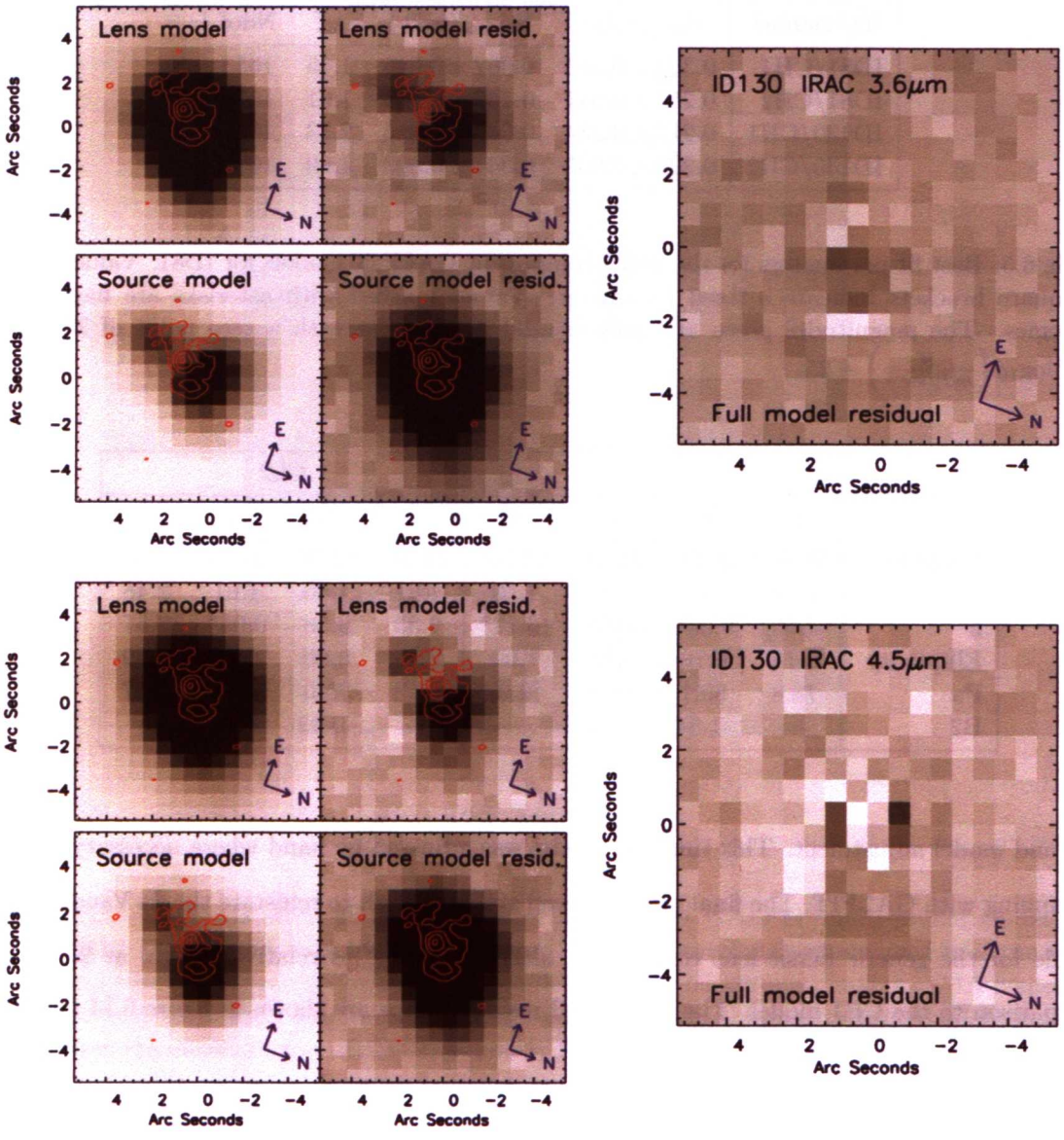

Figure 6.14: Multi-component light profile models for ID130 Ch1 and Ch2. Each block of four postage stamps each show the lens model in their respective top left, and model fitting the lensed structure (bottom left) with the respective residuals (top and bottom right). The larger stamps show the results of subtracting the combined lens and source models for each channel. The red contours represent the corresponding SMA data. The best fit models for the background galaxy (in each channel) matches well with the SMA data, which has an estimated positional error of $0.11''$ (the error for a point source within the SMA data folded with the astrometry uncertainties between the data sets). Note the clean residuals for each combined model.

Table 6.6: Best fit parameters for the multi-component GALFIT models for ID130. Values given in square brackets indicate a fixed parameter. Values marked with asterisks are flagged as extremes. The magnitudes given are instrumental magnitudes with a zero point of 25. The lens profile parameters are given in the L1 (Sérsic) and L2 (exponential disk) and the source profile parameters are given in the S1 and S2 columns.

Parameter	Ch1				Ch2			
	L1	L2	S1	S2	L1	L2	S1	S2
Magnitude	22.36	22.16	24.80	23.49	22.33	22.03	25.19	23.31
R_e	0.49	0.89	0.67	0.76	0.41	0.96	0.02*	0.55
n	1.51	[1.00]	0.10	0.05	[4.00]	[1.00]	0.71	1.27
Ellipticity	0.71	0.46	0.04*	0.45	0.62	0.55	0.85	0.14
Pa	89.1	15.7	71.6	-48.0	-46.0	25.9	-12.41	-40.8
B2	—	—	—	0.38	—	—	—	0.55

6.4.5 Sub-mm lenses SEDs with added NIR constraints

For each model, uncertainties on the photometry were derived from the GALFIT magnitudes distribution, taken over all the GALFIT trails that converged (providing between 40 and 100 results per profile per model). The estimated total uncertainty on the magnitude for each profile was then propagated to give an error for the lens and source model photometry. The GALFIT integrated magnitudes for each component of the best fit ID81 and ID130 models, were converted to mJy sr^{-1} using the zero point magnitude of 25 (set for all the GALFIT minimisations), and then to flux densities (see table 6.4). To assess the significance of the residuals obtained, on subtraction of the lens galaxy models for ID81 and ID130, they were compared with residuals derived for other (not-lensing) elliptical galaxies in the field, after fitting with single Sérsic profile. For both the lensing systems and the elliptical residuals, aperture photometry flux ratios were taken of the residual image to the corresponding un-subtracted data. To minimise the effects on the aperture photometry of positive and negative residual, i.e. tending to a zero sum, pixel values $> 2\sigma$ below the background level were replaced with the median local sky. The lensing system residuals were found to have flux ratios of factors around (3-5)$\times$ greater than those taken for the random elliptical galaxies.

The resulting ID81 and ID130 flux densities were added to the existing multi-waveband photometry of N10 (see section 6.3.2), to extend the coverage of their SEDs to the NIR. For ID81 a

new photometric measurement was also added at 160μm and an upper limit at 70μm; these data come from PACS re-imaging of the lensed H-ATLAS sources (Ibar et al. 2010; Valtchanov et al. in prep). For the goal of deriving physical properties, the IRAC photometry adds particularly important constraints to the SMG SEDs, which previously consisted of just upper limits below 250μm for ID130 and below 160μm for ID81. The SEDs of both the lensing galaxy and the background SMG were re-fitted using the models of da Cunha et al. [2008]. The best fit to the foreground galaxies confirm the previous results, of galaxies that are elliptical in nature with stellar masses of between 4.0 $\times$ 10^{10} $M_{\odot}$ and 1.5$\times$$10^{11}$ $M_{\odot}$, and low star formation rates $<$ 1 $M_{\odot}$ yr^{-1} (table 6.7). For the background galaxies, the da Cunha et al. [2008] models were applied as before: calibrated to reproduce the ultraviolet-to-infrared SEDs of local, purely star-forming Ultra Luminous Infrared Galaxies [da Cunha et al., 2010]. The resulting physical characteristics of the SMGs, derived from the best fit SEDS (see figure 6.15), are presented in table 6.8. The visual extinction required to be consistent with the IRAC photometry and upper limits, remains high ($A_V > 4$), predicting these are highly dust obscured galaxies. Such high extinction is consistent with other examples of ULIRGs and SMGs [e.g. Geach et al., 2007; Hatsukade et al., 2010; Michałowski et al., 2010a,b; Takata et al., 2006]. There are only minor changes to the re-estimated L_{IR}, for both SMG. Before correcting for lensing the predicted infrared luminosity (L_{IR}) are consistent to those of HLIRG ($L_{IR} > 10^{13}$ $L_{\odot}$). Using magnification estimates of 25 $\pm$ 7 for ID81 and 6 $\pm$ 1 for ID130 to scale the results, redefines the background galaxy of both lensed systems as ULIRG ((2.0 $\pm$ 0.6) $\times$ 10^{12} and (5.6 $\pm$ 1.2) $\times$ 10^{12} $L\odot$), with high intrinsic SFRs in the range of 74 $\pm$29 $M_{\odot}$ yr^{-1} for ID81 to 152 $\pm$51 $M_{\odot}$ yr^{-1} for ID130. The L_{IR} is dominated by cold dust emission and therefore the further constraints at NIR and not strongly influential on the resulting estimates or associated errors. On the other hand the parameters derived from the optical and UV part of the spectrum are more significant constrained by the NIR photometry (see figure 6.15). Both SMGs have high intrinsic SFRs in the range of 74 $\pm$29 $M_{\odot}$ yr^{-1} for ID81 to 152 $\pm$51 $M_{\odot}$ yr^{-1} for ID130.

The IRAC measurements allow us to estimate the stellar masses ($M_{\star}$) of the two background sources. We find demagnified $M_{\star}$ that are consistent with $\sim (2-5) \times 10^{11}$ $M_{\odot}$ for both sources, though the overall uncertainty is larger due to errors in the magnification factors and lack of optical and UV constraints. While the $M_{\star}$ is similar, we find a factor of $\sim$3 variation in the

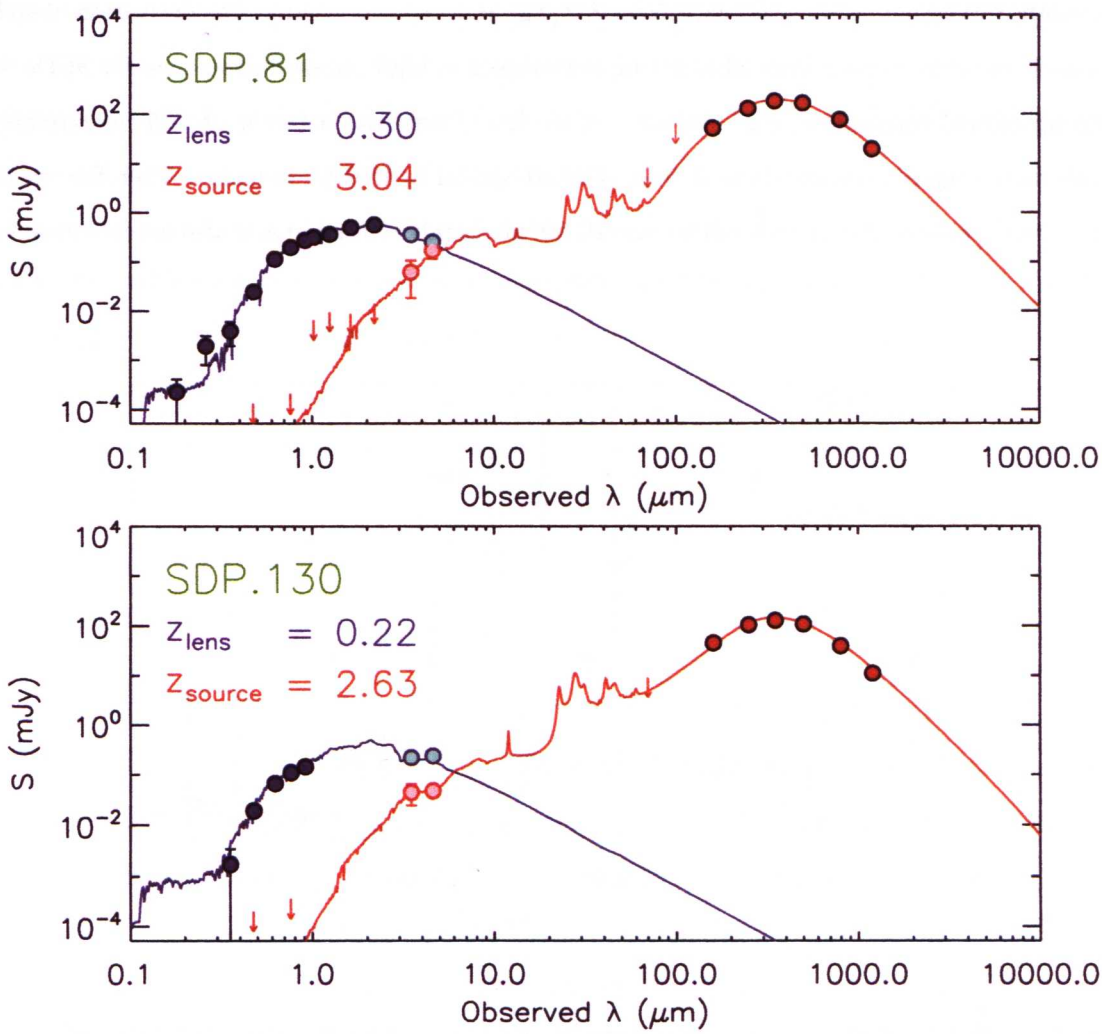

Figure 6.15: Photometry and best fit SEDs for the foreground elliptical (blue) and background galaxy (red) for ID81 and ID130 (N10). The photometric points and upper limits are from GALEX, SDSS, UKIDSS, PACS, SPIRE, SMA and MAMBO data. Photometry from the best fitting light profiles to the IRAC data have been added for the foreground lens galaxies (turquoise points) and for the background SMG (pink points). The photometric SEDs were fitted using the models of da Cunha et al. [2008] and provide information on the physical properties for the lensed systems (see table 6.8). High levels of visual extinction of the SMG were required ($A_v >$ 4) to be consistent with the optical to NIR data.

dust mass from 3.4 × 10^8 $M_\odot$ for ID81 to 11 × 10^9 $M_\odot$ for ID130. Strong evolution in the dust masses of galaxies is found in H-ATLAS [Dunne et al. in preparation; Gomez et al. in preparation], and the dust and stellar masses predicted for ID81 and ID130 are in-line with other high redshift SMG galaxies sampled with *Herschel* [e.g. Santini et al., 2010]. The derivation of stellar masses and dust masses from SED fitting are subject to high uncertainties, even for SEDs with strong optical constraints, e.g. Wardlow et al. [2010] estimate a factor of ∼ 5 uncertainty in their stellar mass estimates derived with 17-band optical to MIR photometry. Therefore we caution that the estimates given for ID81 and ID130 are highly uncertain and also model dependent.

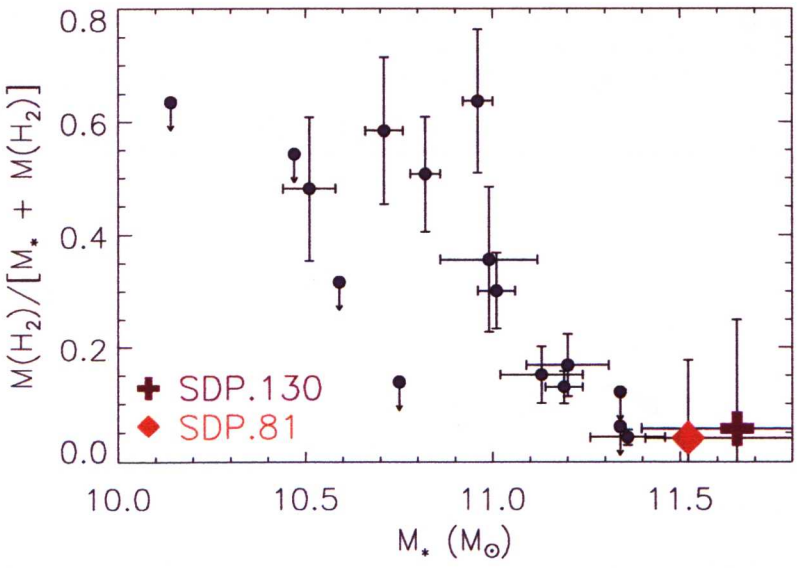

Figure 6.16: Gas fraction μ_g vs stellar mass for a sample of SCUBA-selected SMGs and the two lensed H-ATLAS sources. The molecular gas masses come from CO emission line observations [Frayer et al., 2011]. The two H-ATLAS sources support the overall trend seen in a sample of SCUBA sources where SMGs with larger stellar masses, especially above 10^{11} $M_\odot$ have gas fractions below 20% (Hainline et al. 2010).

The CO(1-0) line intensity measurements for the two sources constrain the molecular gas mass $M(H_2)$ to be 1.4 × 10^{10} $M_\odot$ for ID81 and 2.7 × 10^{10} $M_\odot$ for ID130 [Frayer et al., 2011]. The estimated gas fraction $\mu = M(H_2)/[M_\star + M(H_2)]$ is at the level of 5% to 8%. This ratio is mostly independent of the lensing model and the magnification, and thus is better determined than $M_\star$ alone.

We compare these measurements for the two SMGs in H-ATLAS with a sample of SCUBA-selected SMGs (from Hainline et al. 2010) in figure 6.16. The two lensed H-ATLAS SDP sources occupy the lower right region, with high values for $M_\star$ and low values for the gas fraction. The overall trend in figure 6.16 is such that galaxies with $M_\star > 10^{11}$ $M_\odot$ have gas masses less than 20%. Therefore these SMGs are likely to be at the end of their rapid starburst phase, where the SFRs exceed 300 $M_\odot$ yr^{-1} with lifetimes in the order of a few tens Myrs. While we have studied 2 lensed SMGs in the H-ATLAS SDP data, with the full 550 deg.^{2} survey area, H-ATLAS will recover a sample of 200 or more lensed SMGs. Multi-wavelength followup observations will eventually enable us to study the properties of not only the foreground lenses, but also the physical properties of the background SMGs. As these sources have intrinsic fluxes well below the *Herschel* confusion noise, studies such as this will become necessary to further understand the nature of sources that make up the bulk of the cosmic far-infrared background.

6.5 Summary

We determine physical properties of two of the first five strong gravitational lensing systems selected purely at sub-mm, in the H-ATLAS SDP data. The lensed background SMGs have sub-mm bright observed flux densities of > 100 mJy at 500 μm, but are not visible in optical imaging, where only the lens ellipticals are detectable. We have fitted multi-component light profiles to each lensing system in *Spitzer* IRAC data 3.6 and 4.5 μm data and have successfully disentangled the foreground lens and background source components, providing important constraints on the SMG spectral energy distributions at near-IR wavelengths. The best fit SEDs required high dust obscuration in the optical and NIR for the SMG with $A_v > 4$. After demagnification, the derived physical properties for both SMG are consistent to other high redshift (z > 2) ULIRG, with stellar masses of $\sim 3 \times 10^{11}$ and star formation rates of 74 and 152 $M_\odot y^{-1}$. Combined with H_2 molecular masses from previously reported CO(1-0) line intensities, the gas fraction relative to stellar masses for the ID81 and ID130 is at the level of 5% to 8%, which is in agreement with SMGs of high stellar mass having depleted gas fractions < 20%.

Table 6.7: Photometry and derived parameters of the foreground lens for ID81 and ID130. The redshifts given are spectroscopic. The core radius is taken as the GALFIT best fit effective radius. $M_{\rm E}$ is the estimated lens mass within the Einstein radius. The symbols $\rm M_\odot$ and $L_\odot$ denote the total mass and the total luminosity of the Sun, respectively, and correspond to $M_\odot = 1.99 \times 10^{30}\,\rm kg$ and $L_\odot = 3.839 \times 10^{33}\,\rm erg\,s^{-1}$

Instrument	Parameter	ID81	ID130
	Redshift	0.299	0.220
SDSS	u (μJy)	3.87 ± 2.0	1.7 ± 1.7
	g (μJy)	24.9 ± 1.1	19.4 ± 0.7
	r (μJy)	115 ± 2.1	66.1 ± 1.2
	i (μJy)	198 ± 3.6	109 ± 2.0
	z (μJy)	278 ± 7.7	143 ± 6.6
UKIDSS	Y (μJy)	321 ± 22	—
	J (μJy)	367 ± 24	—
	H (μJy)	508 ± 46	—
	K (μJy)	574 ± 73	—
Spitzer/IRAC	3.6 μm flux (mJy)	0.35 ± 0.04	0.213 ± 0.03
	4.5 μm flux (mJy)	0.25 ± 0.04	0.230 ± 0.01
	core radius ($''$)	1.63	1.11
	$M_{\rm E}$ (10^{10} $\rm M_\odot$)	36.3 ± 1.1	3.7 ± 0.4
	$\rm L_V$ (10^{10} $\rm L_\odot$)	6.4	1.8
	$M_{\rm star}$ (10^{10} $\rm M_\odot$)	15 ± 1	4.0 ± 0.3

Table 6.8: Photometry and derived parameters of the background SMG for ID81 and ID130. The redshifts given are spectroscopic, the 8-1000 μm L_{IR}, star formation rates (SFR), stellar mass ($M_\star$) and dust mass (M_{dust}) are derived from the best fit SED. The H_2 molecular mass is taken from [Frayer et al., 2011]. The gas fraction is calculated as $\mu = M(H_2)/[M_\star + M(H_2)]$. The PACS upper limit at 70 μm and PACS photometric point 160 μm are from Valtchanov et al. in preparation. The derived parameter values are intrinsic quantities corrected for magnification and the errors quoted accounts for the tabulated uncertainty in the magnification.The symbols $M_\odot$ and $L_\odot$ denote the total mass and the total luminosity of the Sun, respectively, and correspond to $M_\odot = 1.99 \times 10^{30}$ kg and $L_\odot = 3.839 \times 10^{33}$ erg s^{-1}

Instrument	Parameter	ID81	ID130
—	Redshift	3.042	2.625
	Magnification	25 ± 7	6 ± 1
Keck/LRIS	g (μJy)	< 0.13	< 0.20
	i (μJy)	< 0.20	< 0.35
UKIDSS	Y (μJy)	< 6.27	—
	J (μJy)	< 9.23	—
	H (μJy)	< 8.52	—
	K (μJy)	< 13.5	—
Spitzer/IRAC	3.6 μm flux (mJy)	0.062 ± 0.04	0.044 ± 0.01
	4.5 μm flux (mJy)	0.126 ± 0.05	0.047 ± 0.01
Herschel/PACS	70 μm flux (mJy)	< 8.0	¡ 9.0
	100 μm flux (mJy)	< 62	—
	160 μm flux (mJy)	51 ± 5	45 ± 8
Herschel/SPIRE	250 μm flux (mJy)	129 ± 20	105 ± 17
	350 μm flux (mJy)	182 ± 28	128 ± 20
	500 μm flux (mJy)	166 ± 27	108 ± 18
SMA	880 μm flux (mJy)	76.4 ± 3.8	39.3 ± 2.3
IRAM/MAMBO	1200 μm flux (mJy)	19.6 ± 0.9	11.2 ± 1.2
—	L_{IR} (10^{12} $L_\odot$)	2.0 ± 0.6	5.6 ± 1.2
	A_v	4.4 ± 0.6	4.93 ± 0.48
	SFR [$M_\odot$ yr^{-1})	74 ± 29	152 ± 51
	M_{H2} (10^{10} $M_\odot$)	1.4	2.7
	$M_\star$ (10^{11} $M_\odot$)	2.5 ± 1.7	4.5 ± 2.5
	$M_{\rm dust}$ (10^8 $M_\odot$)	3.4 ± 1.0	11 ± 2.2
	μ_g	0.05 ± 0.01	0.08 ± 0.01

Chapter 7

Conclusions and future outlook

7.1 This work

This thesis has investigated the faint MIR star-forming galaxy population behind a strong gravitational lensing galaxy cluster and the first sample of strong galaxy-galaxy lensing systems detected by *Herschel*. A uniquely deep 15 μm selected source catalogue has been extracted from the *AKARI* L15 image of A2218. This catalogue probes beyond the blank field sensitivity of AKARI via the exploitation of gravitational lensing and careful de-blending. The photometric redshift distribution of the *AKARI* sources peaks around 1, which translates to 15 μm observations sampling the rest frame wavelength of $\sim 8\,\mu$m – i.e. PAH emission, which are associated with dusty star formation. The faint flux densities reached by the L15 galaxy number counts, coupled with the redshift distribution, indicate this catalogue is sampling the more normal dusty populations that dominate star-formation around redshifts of z$\sim 1-2$, whereas previous 15 μm counts have been dominated by galaxies with high infrared luminosities, i.e. $\gtrsim$ ULIRG. Measuring the faint end of the 15 μm galaxy number counts provides important constraints to models of galaxy formation and evolution, and has given a stronger lower limit estimate of the cosmic infrared background (CIRB) at 15 μm of $2.0 \pm 0.4\,\mathrm{nW\,m^{-2}\,Hz^{-1}}$– resolving between 70% – 100% of the individual galaxy emissions contributing to the IGL at 15μm. Assuming no significant change in the IR SED of high redshift galaxies and those that dominate the 15 μm CIRB at redshifts z$\sim$1 [e.g. Elbaz et al., 2002b], the deep 15 μm selected galaxy population is, therefore, representative of the bulk of galaxies that dominate the peak of the CIRB $\sim 170\,\mu$m. The performed 15 μm stacking analysis implies this correlation is weaker at longer wavelengths

($\gtrsim$ 250 μm). IGL estimates taken at *Herschel*/SPIRE wavelengths from stacking, suggests 41% of the IGL is resolved at 250 μm, by the L15 selected galaxies, reducing to around one third of the IGL at 350 μm and to one quarter at 500 μm with respect to the IGL measured by FIRAS. This result implies the bulk of the CIRB at 500 μm is produced by distinctly different galaxy populations, e.g. massive high redshift sub-mm galaxies, rather than those sampled at 15μm (far more moderate star bursts at lower redshift). Stacking in brightness bins suggested that a 24 μm selected population is more representative at 250 μm, in comparison to 15 μm selected galaxies.

A second measure of the number density of dust obscured galaxies came from the study of strong galaxy-galaxy lensing events. The new technique of selecting a population of sub-mm gravitational lenses in the sub-mm with *Herschel* will revolutionise our ability to study SMG – over a wide range of sub-mm flux densities, redshift and mass. The first sample of sub-mm bright lenses detected by H-ATLAS (presented in Chapter 6) provide constraints on the numbers of un-lensed sub-mm bright galaxies. Of the five SMG with 500 μm flux densities greater than 100 μJy, all were found to be lensed, therefore predicting un-lensed sub-mm bright galaxies are extremely rare events on the sky. Applying this gravitational lensing selection method to the whole of H-ATLAS will provide a statistically significant sample of strongly lensed SMG (>100). Decoupling of the lens and source light profiles for two of the H-ATLAS sub-mm lenses was achieved in NIR IRAC data and provided stronger constraints on the source galaxy SED, which is vital for SED fitting due to the faint optical nature of these sources.

7.2 Future work

Future work is planned in both the development of the L15 selected source catalogue and multi-waveband photometry (L15 band-merged catalogue), with the aim for public release, and the modelling and characterisation of the H-ATLAS sub-mm bright lensing systems.

7.2.1 Investigating the ultra deep 15 μm selected band-merged catalogue

Further constraints on the L15 band-merged catalogue SEDs will come from NIR imaging data at J, H and Ks wavebands (PI: Hopwood) in the process of being observed by the Canadian

French Hawaii telescope (CFHT), plus PACS FIR data taken as part of the PACS Evolutionary Probe survey (PI D. Lutz), which is due to finish its preparatory period before the end of the year. In addition the PSF fitting applied to the SPIRE A2218 data, during the stacking analysis, illustrated this as a feasible method to obtain 250 μm, 350 μm and 500 μm photometry for a high proportion of the L15 sources. These three data set each cover the full L15 A2218 field, offering a way to estimate photometric redshifts for those L15 sources that previously lacked adequate coverage and to improve the robustness for the photometric redshift estimate for the remaining catalogue.

The L15 galaxies represent a unique sample of star-forming galaxies, which will be analysed in the context of galaxy formation and evolution models and of the interplay of AGN feedback and star-formation, building on the achievements presented in this thesis. The L15 galaxies trace the dusty emission of the Universe and their NIR emissions are sensitive to the established stellar mass. The extensive CFHT data will constrain the 1.6 μm bump feature (i.e. the emission from the established stellar population) for the majority of the L15 source SEDs, enabling the stellar mass to be investigated as a function of redshift. This will be achieved by fitting the multi-waveband photometry with template SEDs, which will also allow galaxy morphologies to be categorised. The fraction of dusty AGN within the L15 catalogue and the extent of star-formation in galaxies with AGN-like emission, can also by determined by SED fitting, following Negrello et al. [2009]. This is because the MIR is a powerful diagnostic for the AGN fraction of a galaxy's bolometric luminosity [Serjeant et al., 2010b]. By using colour-colour selection, S[Ks]/S[J] $>$ 1.7 and S[L15]/S[J] $>$ 200, galaxies with extremely red mid-infrared colours can be selected at redshifts around 1.5 (analogous to *Spitzer* Dust Obscured Galaxies [Dey et al., 2008]), which have a significant to dominant AGN contribution to their SED. Such populations may represent a key evolutionary phase between high redshift SMG and local massive quiescent galaxies.

The MIR/FIR correlation is an important relation upon which many recent results have relied. 24 μm populations have been used for stacking analysis at SPIRE wavelengths using BLAST data, giving estimates on the resolved fraction of the IGL at 250 μm that range from ~56% (CP10) to 100% by Devlin et al. [2009] (although this latter claim has been disputed by CP10). Taking the lower limit estimate of 56% suggest 24 μm catalouges are more representa-

tive of 250 μm populations than 15 μm by at least 15%, as they resolve a larger fraction of the 250 μm background. 24 μm samples the rest frame PAH at redshifts z$\sim$2. The 24 μm galaxy number counts also have an evolutionary 'bump' feature, similar to that observed at 15 μm, but at fainter flux densities ($\sim 0.3 - 0.4$ mJy). This 24 μm bump may, therefore, be sampling an analogous population to the star-burst galaxies that dominate the 15 μm counts [Chary et al., 2004; Gruppioni et al., 2005, e.g.], but at higher redshifts due to the redshifted PAH. However models of galaxy formation and evolution have struggled to fit the counts at both wavelengths simultaneously without some evolution of the MIR SED over redshifts $1 < z < 2$ [Pearson, 2005]. It has been suggested that a new population of luminous infrared galaxies, not predicted by the 15 μm counts, are required to explain the 24 μm counts [e.g. Papovich et al., 2004]. The latter theory is tentatively supported by the L15 stacking analysis, which suggests that the 15 μm to 250 μm correlation shows a distinct difference to the 24 μm to 250 μm correlation. The validity of this relation will be explored further by extending the 15μm/24μm stacking analysis comparison to PACS wavelengths.

In addition to the AKARI imaging observations, we have AKARI NIR spectroscopic observations of three of the A2218 L15 sources (PI: Hopwood). These sources have high photometric redshift estimates ($z > 2.5$) and therefore were proposed as targets for spectroscopy in order to identify redshifted Hα. Hα recombination lines are a strong star-formation rate indicator, as they represent the re-emission by gas of the UV output for young stellar populations. By redshift z$\sim$2.6 Hα emission lines are shifted into the lower wavelength range of AKARI's spectroscopic capability. If these spectral features are detected for the L15 targets, then star formation rate (SFR) can be estimated from the stellar mass ($M_\star$; that will have been derived from the CFHT NIR photometry) and the Hα luminosity as $dM_\star/dt$. The specific SFR $(1/M_\star)dM_\star/dt$ can then be derived from $(1/M_\star)dM_\star/dt = dlnM_\star/dt$, which will shed light on where the evolutionary stage lies between star-burst and AGN.

Eleven faint L15 sources ($\lesssim$ de-blended 5σ sensitivity) have been matched with several SPIRE counterparts with SNR >5, all with SED indicative of high redshift star-forming galaxies. All but three have no previous identifications and therefore make potentially interesting targets for follow-up spectroscopy. Of the three source with IDs, one is a well known lensed SMG

at redshift z = 3.188, identified with SCUBA [SMM J163541.2+661144 Knudsen et al., 2006]. The other two previously identified sources have been detected in deep PACS imaging of the core area of A2218 (see figure 7.1) by the PACS evolutionary probe survey [PEP; Altieri et al., 2010]. By deriving magnification corrections and perfoming SED fitting on the multi-wavelength photometry, the LIR can be derived and a direct comparison of the luminosity and redshift range, plus the surface density of these SMG lensed by a gravitational lensing cluster, can be made with the H-ATLAS sub-mm bright lens population that are selected in a blank field. Also identified in the L15 map and the SPIRE 250 μm ALLSTAR map (resulting from the stacking analysis presented in chapter 4) is the high redshift (z = 4.04) compact SMG (SMM J163556+661300) of Knudsen et al. [2010]. Although the work relating to this object is not included in this thesis, it will be the subject of future papers. Additional constraints to the SED have been added at 15 μm and for 24 μm (to replace the upper limit used by Knudsen et al. [2010]). This source resides close to the core of A2218 and suffers high photometric blending with neighbours, which is made more severe by high magnification factors. SED fitting suggests a discontinuity between the sub-mm/mm and NIR/MIR SED, which could be explained by differential magnification as a consequence of the disturbed SMG morphology. Adding de-blended SPIRE photometry will highlight any significant differential magnification that is occurring, which can then be investigated further.

7.2.2 A new population of gravitational lenses

For the H-ATLAS bright sub-mm lenses, follow-up observations with IRAC showed it is possible to decouple the lens and source of a photometrically blended system without high resolution imaging. The high dust content of the source galaxy is beneficial to lens galaxy SED fitting, as there is negligible contribution at UV and optical wavebands and so, in contrast to typical SLACS lenses, median resolution imaging (e.g. by Keck/LRIS) is adequate to constrain the lens population SED (without contamination). G-lens is an example of a strong galaxy-galaxy lens, with typical SLACS and GOODS lens colours, but a more compact morphology. For G-lens the disentangling of the lens and source galaxy components proved more challenging than for the sub-mm lenses (ID81 and ID130), as the background galaxy has lower optical obscuration by dust, and therefore contributes significant emission to the optical and NIR wavebands. The decoupling of G-lens is difficult despite having high resolution ACS imaging. Although no high-

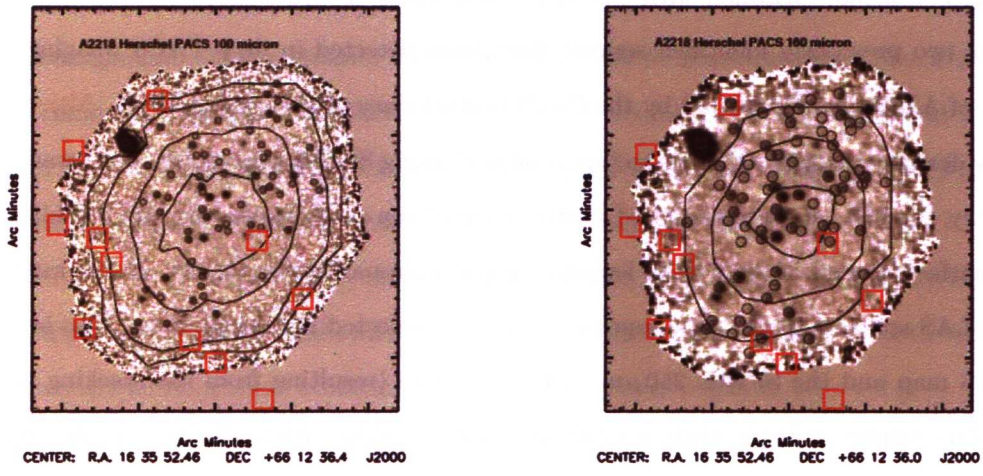

Figure 7.1: PACS maps of A2218 (left: 100 μm, right: 160 μm), taken as part of the PEP survey. Red squares indicate the L15 sources of interest that have been matched with SPIRE counterparts and black circles show the PEP identifications. SMM J163541.2+661144 is identified by the red square closest to the centre of the PEP maps. These sources mainly have no IDs as they lie towards the edge of the A2218 core. Adapted from figure 1 of Altieri et al. [2010]

resolution optical data was necessary to decouple ID81 or ID130, SMA imaging was required to provide the essential ingredient of positional priors on the lensed structure to de-blend the IRAC data. Co-ordinated follow-ups with the *HST* (for high-resolution NIR imaging), *Spitzer* (NIR imaging), SMA (880 μm imaging), PdBI (spectroscopy for the detection of CO lines) and several other instruments are planned (or have been proposed) for the existing lenses and for the new candidates from H-ATLAS and the *Herschel* Multi-tiered Extragalactic Survey [HeMES: a less wide but deeper survey than H-ATLAS; Oliver et al., 2010], where several interesting lens candidates have been identified (Clements, private communication). Apart from the individual lensed SMG studies that will require photometric decoupling with light profile fitting and SED fitting to derive physical characteristics, the large sample of lensing systems predicted will form the basis of cosmological study. Immediate results will come from stronger constraints on predictions of the low surface density of bright un-lensed SMG, which will have significant implications for models of galaxy formation in terms of the upper limits on high redshift mass assembly. Also the mapping of dark and baryonic mass distributions for the lenses will be possible, including disentangling the relative contributions, which will constrain the cosmic evolution of the mass-to-light ratio of elliptical galaxies, something that will be hard to achieve without gravitational lensing.

In addition to the work relating to gravitational lensing, the PACS de-glitching modules are currently undergoing testing within the official H-ATLAS pipeline and will be applied for the next H-ATLAS data release. Work on optimising the code is ongoing.

Appendix A

Several figures and tables are presented that relate to Chapter 4. The following figures show the results of stacking the A2218 SPIRE maps using the L15 stack catalogues, divided into flux bins. Three methods of ordering were applied: by L15 flux density; by SPIRE pixel values; by MIPS24 pixel values. Each figure presents the simple sum (middle rows) and weighted mean stack (bottom rows) for each brightness bin, and the corresponding pixel value histogram for the simple sum stacks (top rows). The MIPS24 map has a smaller area than the L15-image, and therefore the related histograms contain fewer statistics. Although this is only a rough comparison, the MIPS24 ordered stacks and pixel distributions are more similar to the SPIRE ordered results for the SW data, rather than to the L15 ordered stacks and pixel distributions.

These figures imply that when ordering by brightness there is a stronger similarity between the SPIRE ordered stacks, at 250 μm, and those ordered by MIPS24 in comparison to those ordered by L15 brightness. However, this trend is not observed for the MW and LW stacks. A comparison of the stacks obtained when stacking by L15 brightness and those ordered by redshift, suggest ordering by redshift produces 'better behaved' stacks that may provide more robust photometry. It is clear that there are too few statistics to produce reliable stacks over several flux or redshift bins for the MW and LW data, and therefore the final stacks are taken of the full stacking catalogues for all three SPIRE wavelengths.

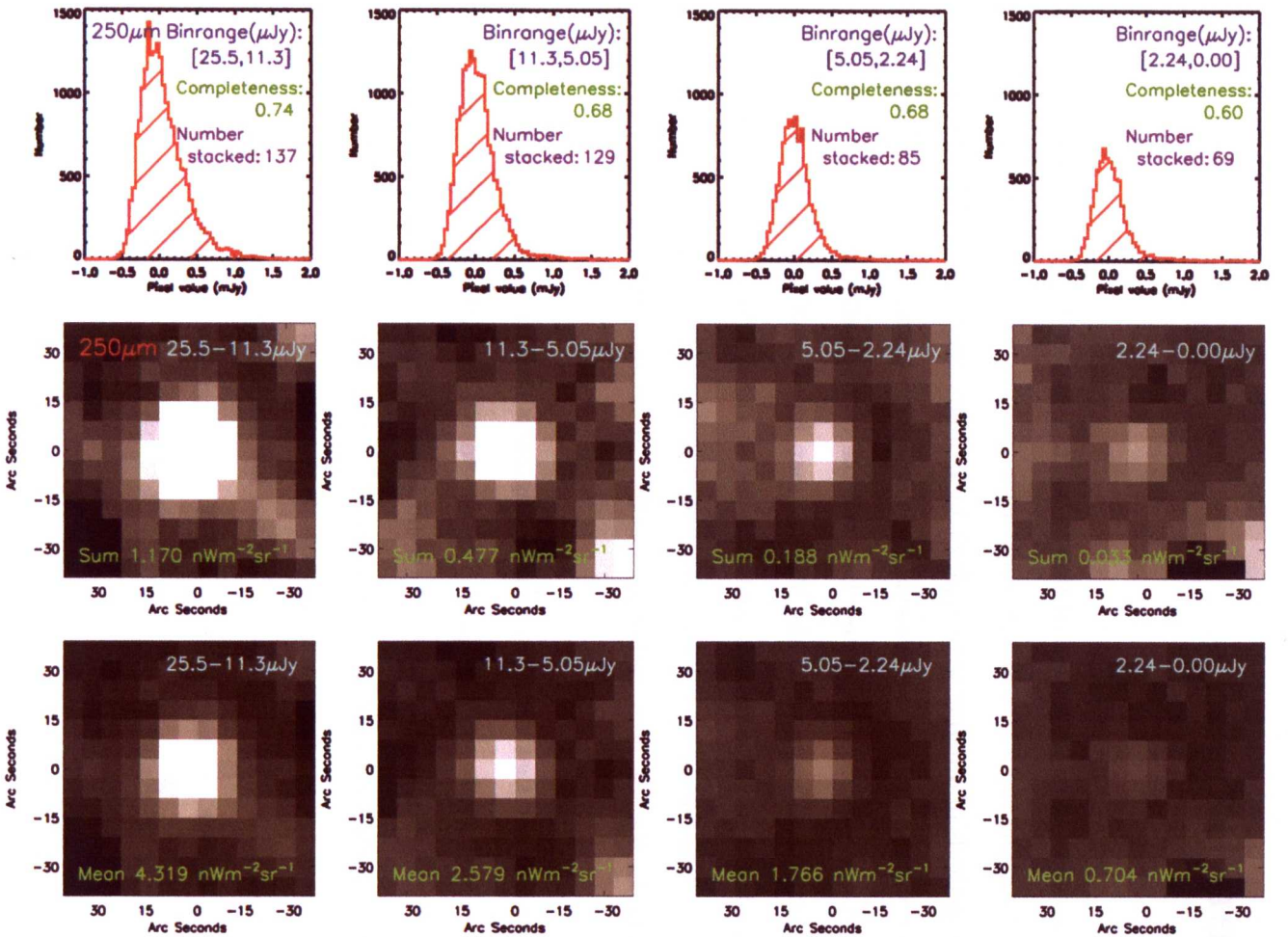

Figure A1: SPIRE pixel value ordered stacks, taken in flux bins for the SW map. As expected, the SPIRE ordered stacks follow the logical path of brightest detection in the brightest bin to faintest in the faint bin.

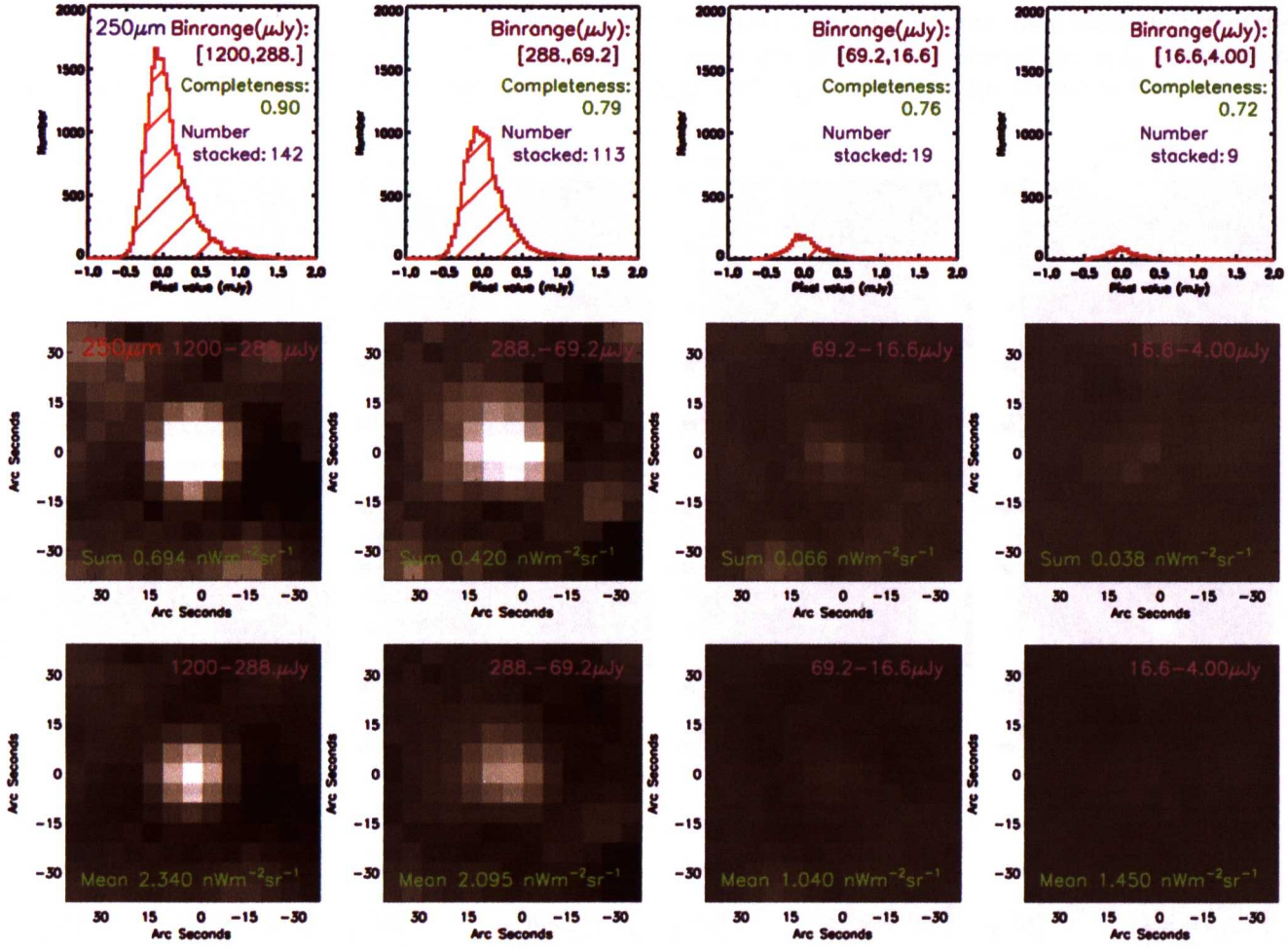

Figure A2: MIPS 24 μm pixel value ordered stacks, taken in flux bins for the SW map. Interestingly ordering by MIPS24 pixel values produces well behaved bright bin stacks, with the strongest detection in the brightest bin, suggesting there is a significantly stronger correlation between the L15 population at MIPS24 and SPIRE SW wavelengths that for L15 and SW.

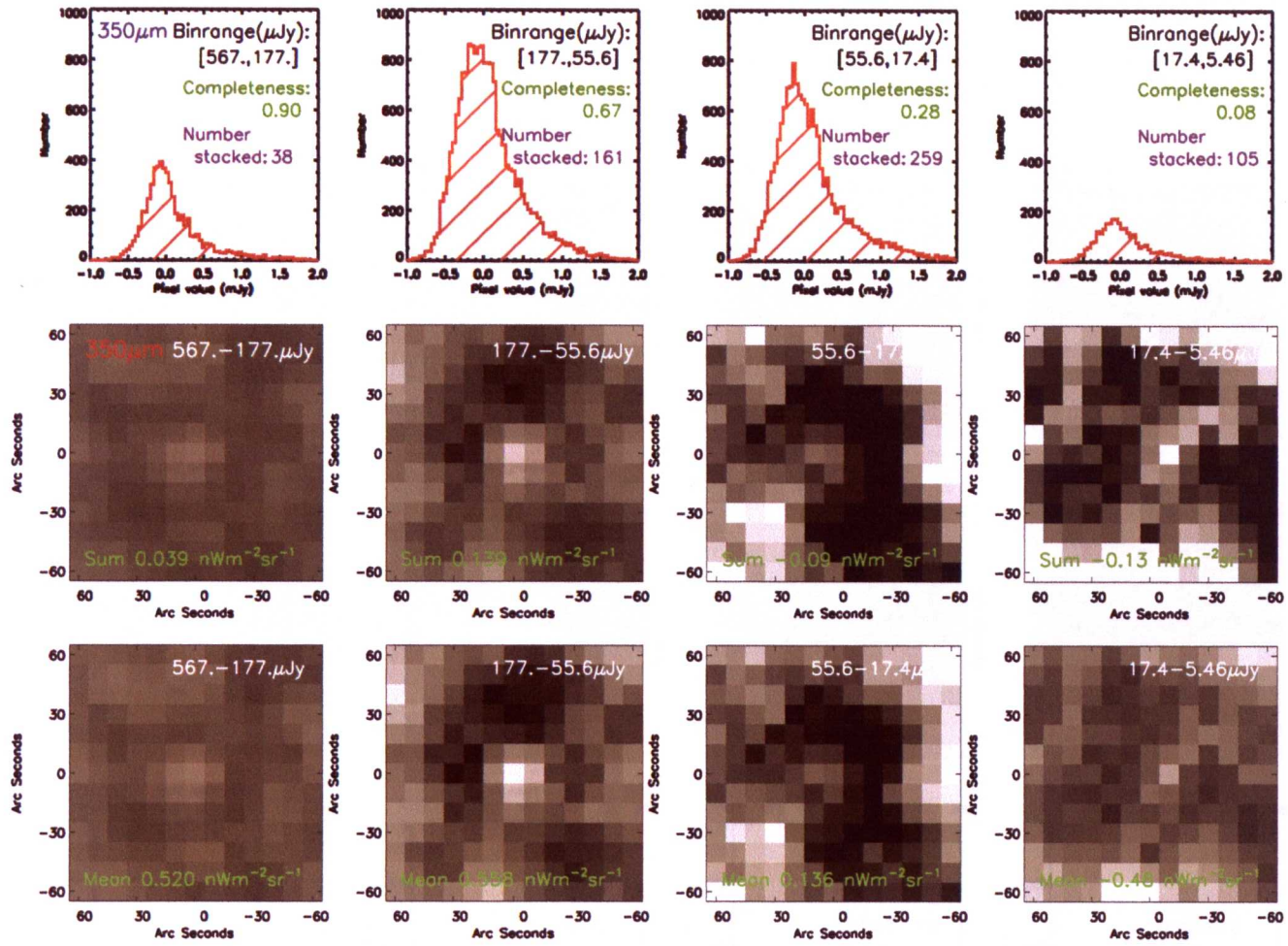

Figure A3: L15 flux density ordered stacks, taken in flux bins for the MW map. The stacks for the second faintest bin (17.4 - 55.6 μJy) are strongly affected by noisy structure, which provides a guide for setting a lower flux limit when stacking the MW L15 stack catalogue. Due to number of sources being stacked it is not statistically robust to take the final stack photometry from these stacks in brightness bins.

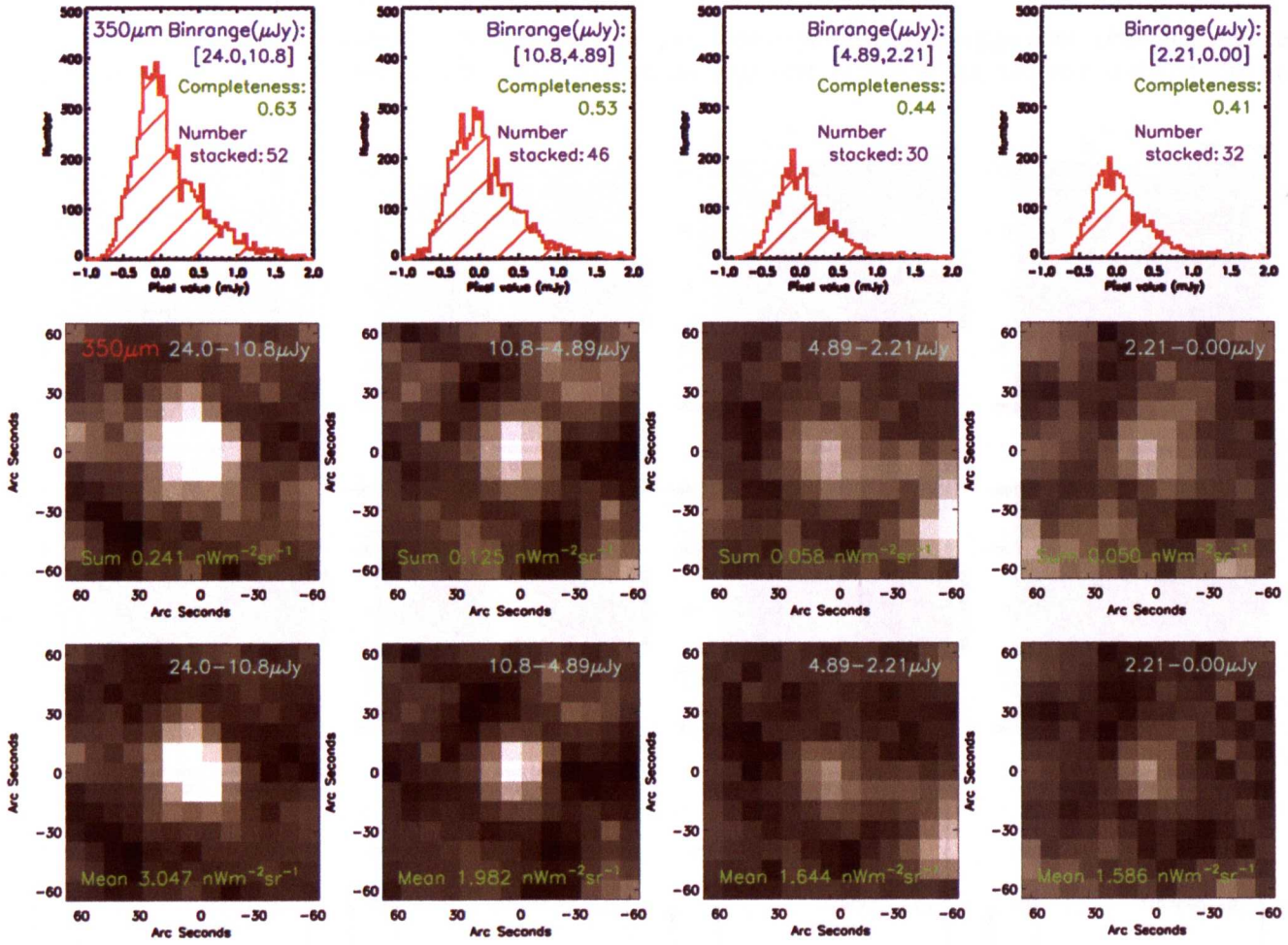

Figure A4: SPIRE pixel value ordered stacks, taken in flux bins for the MW map. As with the SW map, the stack detections follow a logical path from brightest to faintest for the bright to faint bins.

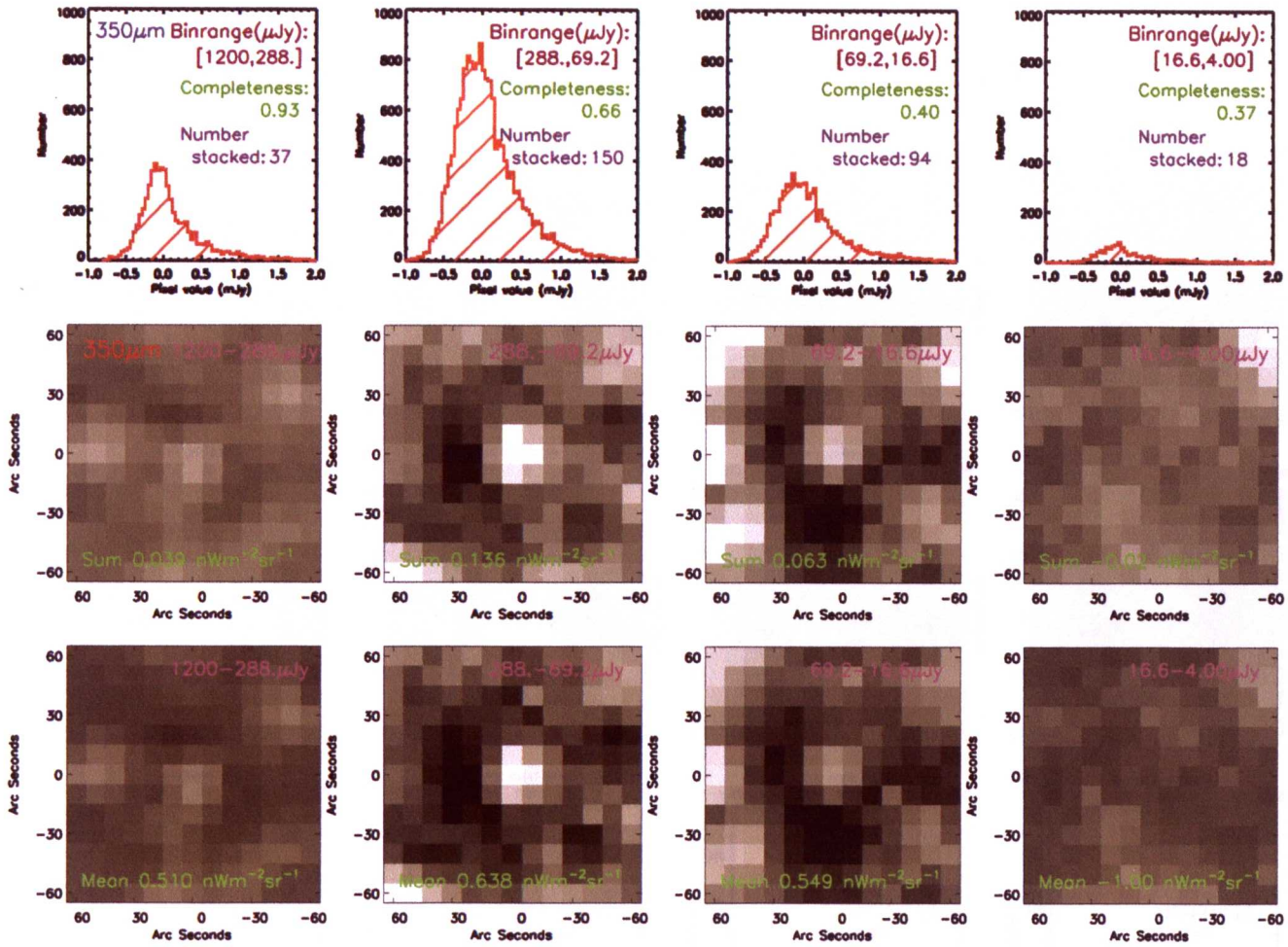

Figure A5: MIPS 24 μm pixel value ordered stacks, taken in flux bins for the MW map. These stacks and pixel distributions are more similar to the ones obtained for the L15 flux density ordered L15 stack catalogue than those obtained for the SW map. Implying that the L15 and MIPS 24 μm wavebands are sampling much more similar populations at 350μm.

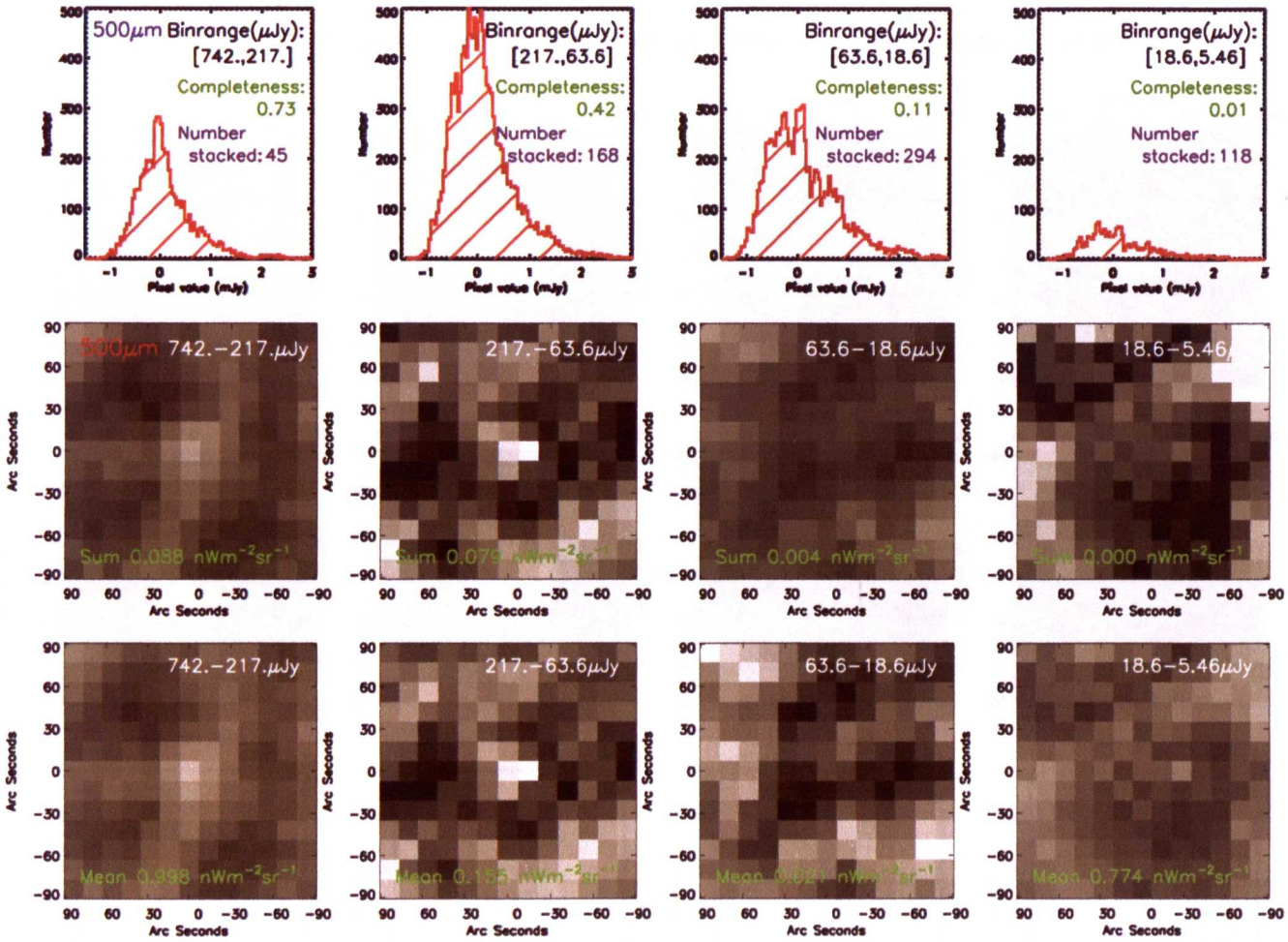

Figure A6: L15 flux density ordered stacks, taken in flux bins for the LW map. The progression of the stacks and pixel distributions over the bins are similar to that seen for the MW map.

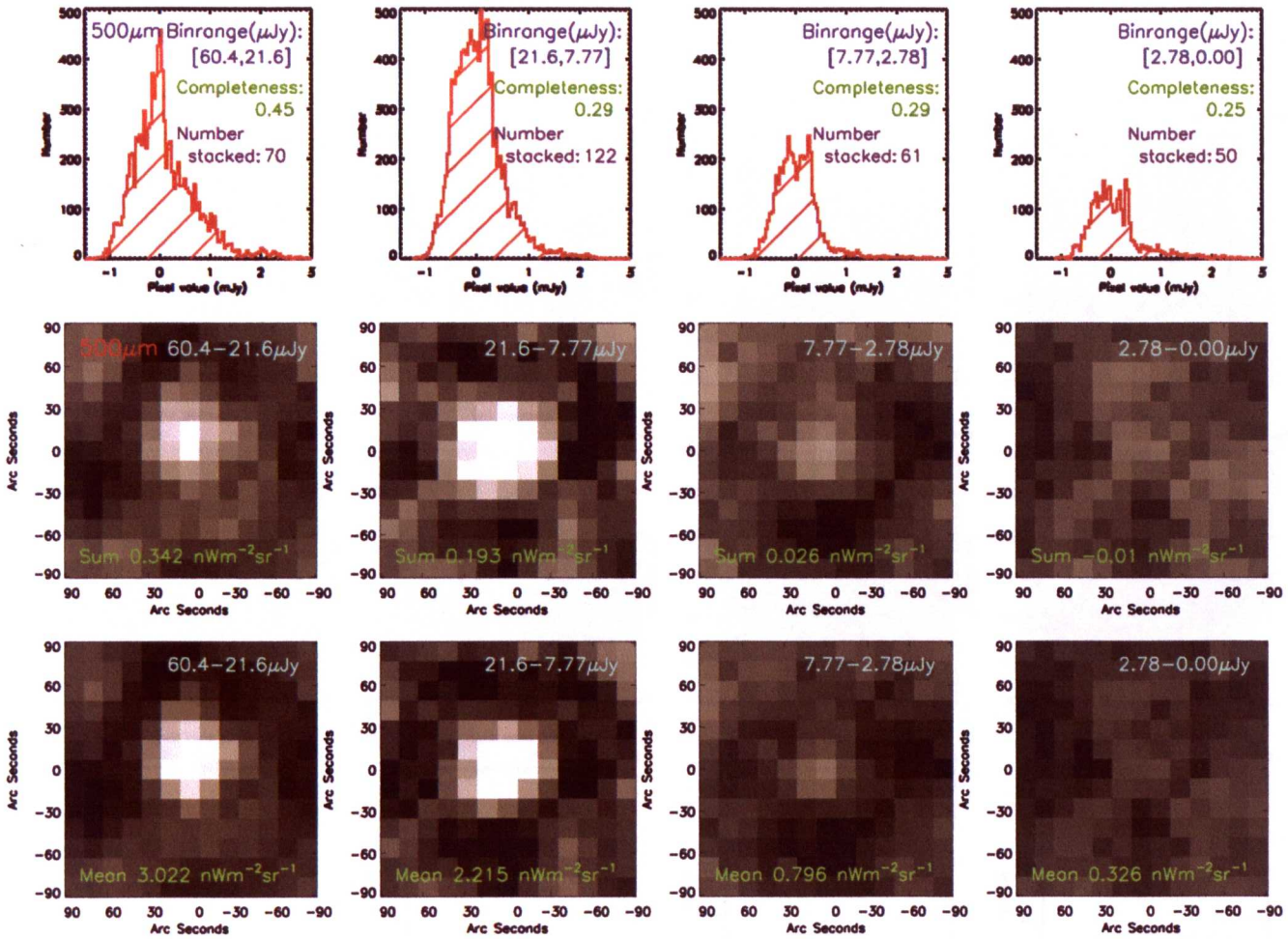

Figure A7: SPIRE pixel value ordered stacks, taken in flux bins for the LW map.

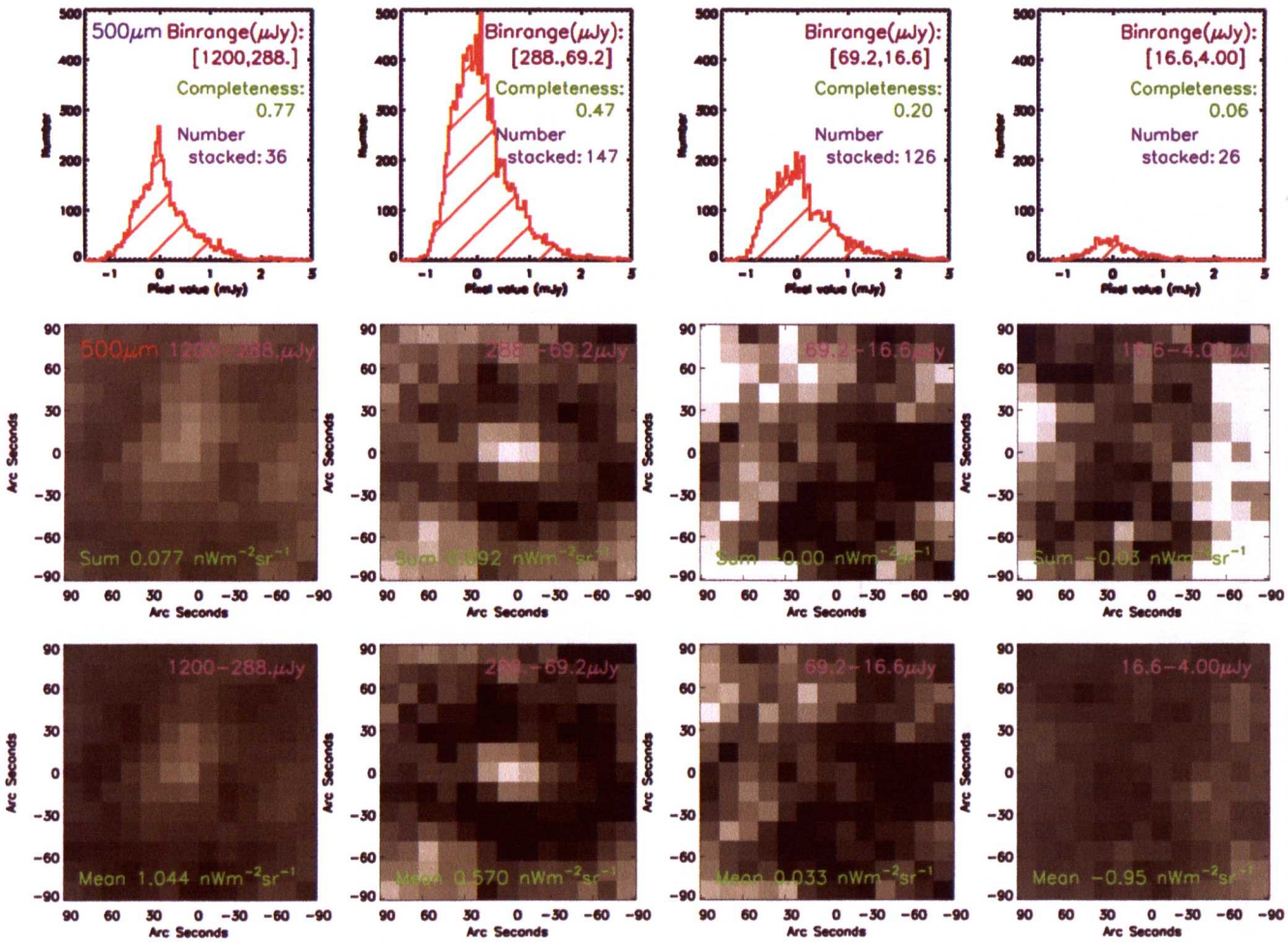

Figure A8: MIPS 24 μm pixel value ordered stacks, taken in flux bins for the LW map. The stacks and pixel distributions are similar to the corresponding L15 ordered stacks and distributions.

The following figures present the simple sum stacks (middle rows) and corresponding pixel value distributions (top rows), and the mean weighted stacks (bottom rows) for the MW and LW maps, when stacking the respective L15 stacking catalogues after enforcing a lower flux density limit based on the completeness. The statistics per bin are reduced, but show that even the faintest bins have a detection when the highest flux cut is applied.

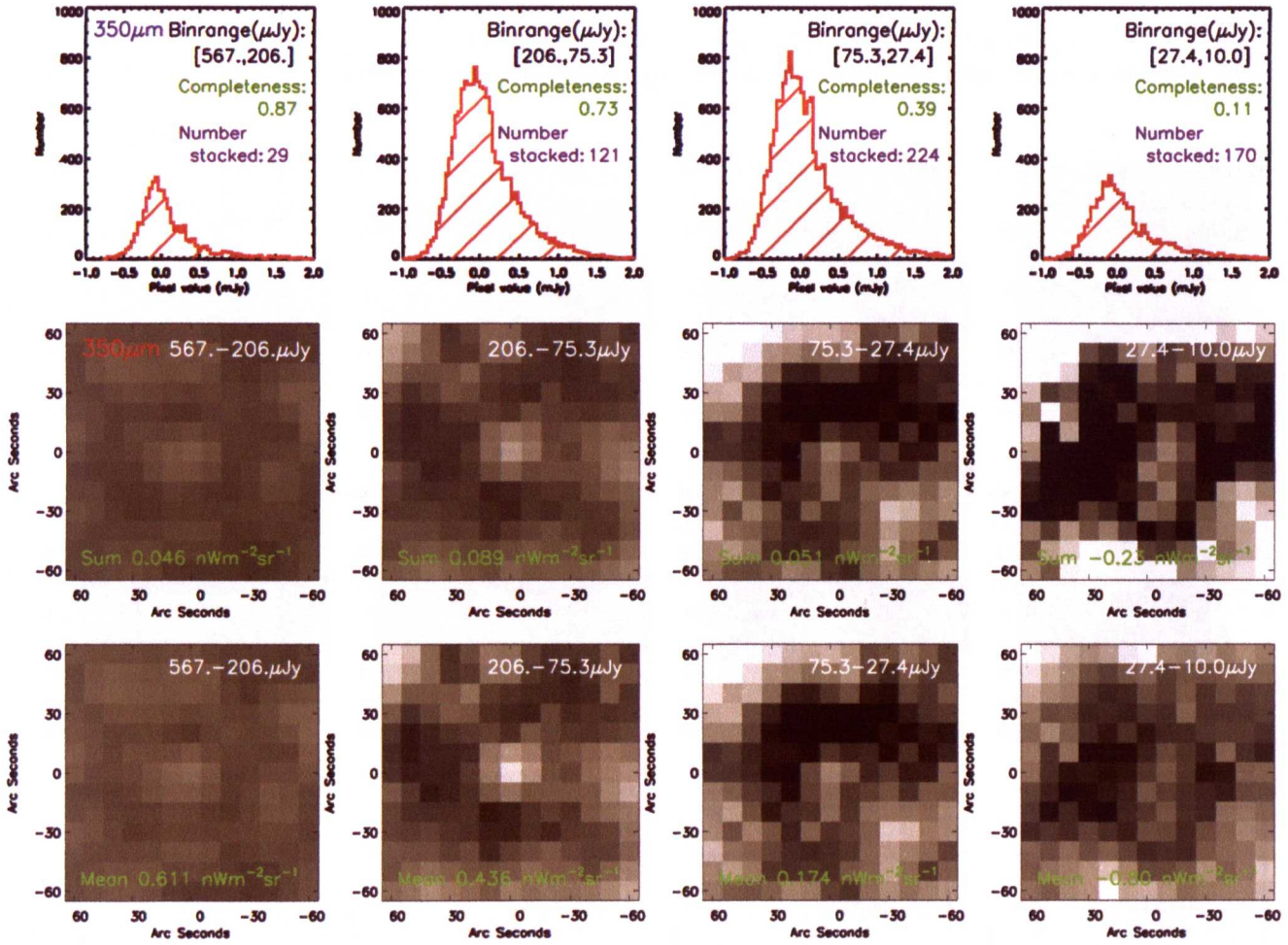

Figure A9: L15 flux density ordered stacks, taken in flux bins for the MW map with a lower flux limit of 10 μJy applied. There is may be a marginal detection in the faintest bin for the simple sum stack, but it is too weak to gain reliable photometry. This lower limit achieves a completeness of 11% in the final bin.

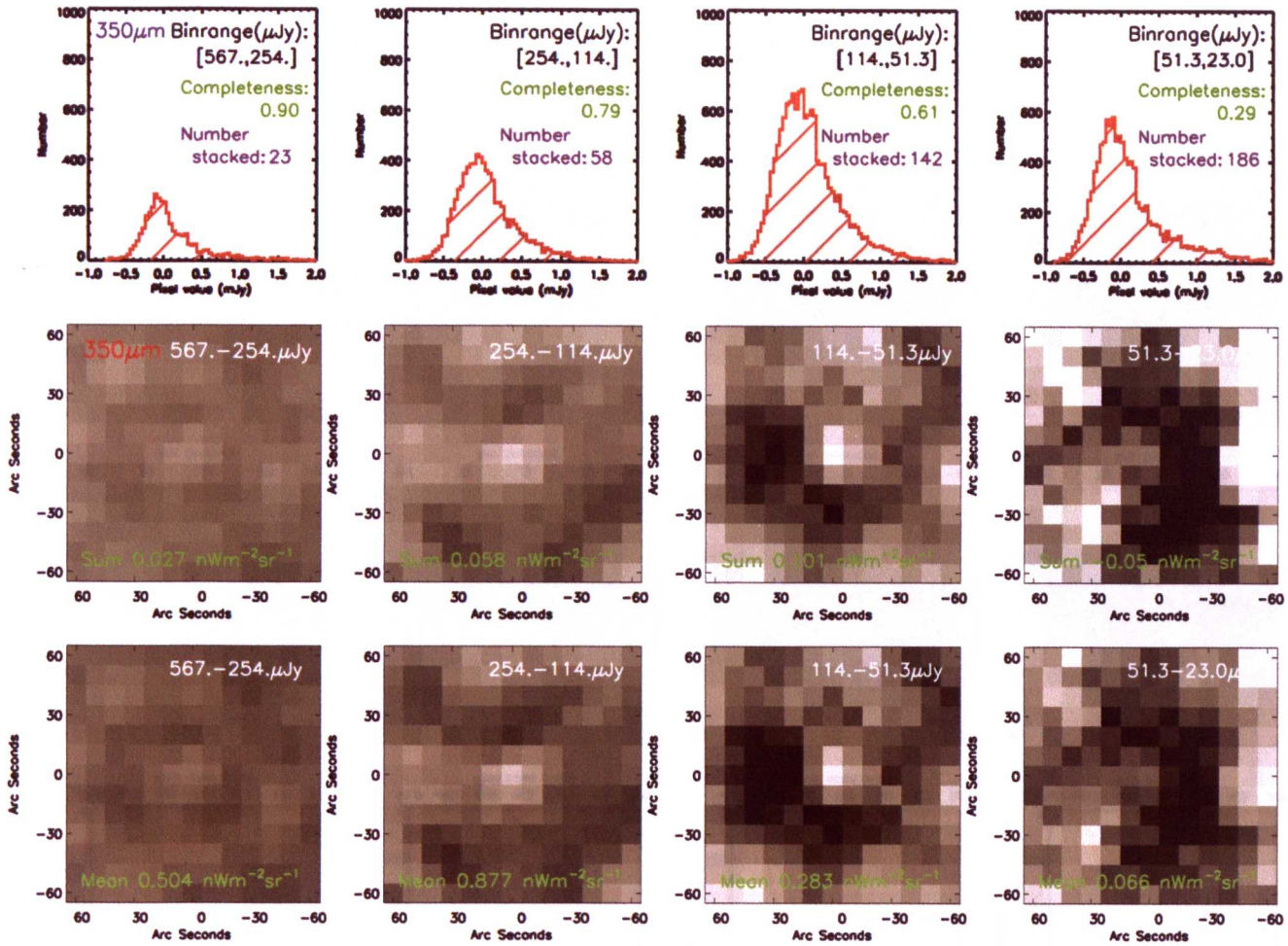

Figure A10: L15 flux density ordered stacks, taken in flux bins for the MW map with a lower flux limit of 23 μJy applied. There no real detection in the faintest bin for the simple sum stack. This lower limit achieves a completeness of 29% in the final bin.

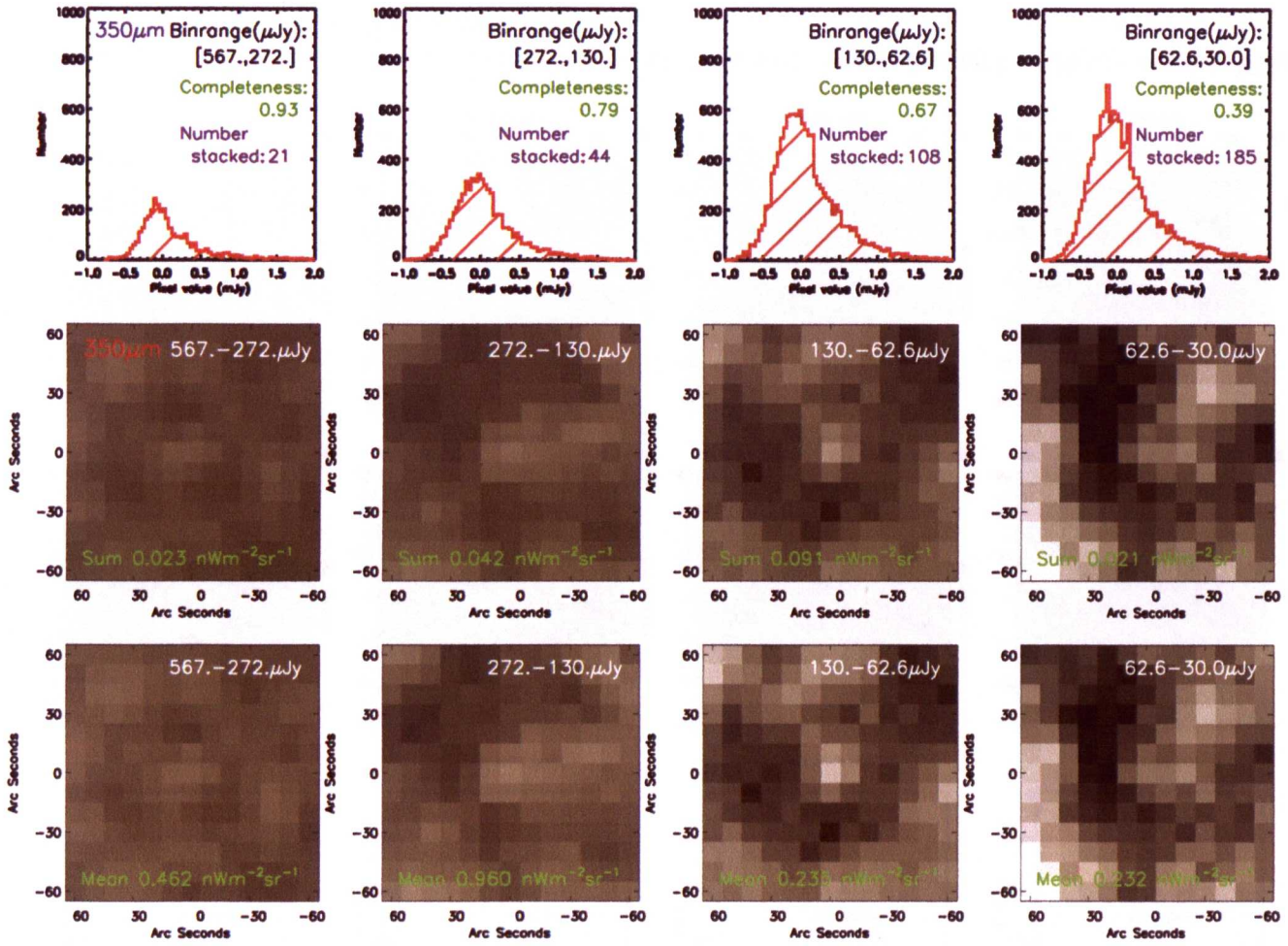

Figure A11: L15 flux density ordered stacks, taken in flux bins for the MW map with a lower flux limit of 30 μJy applied. There is a marginal detection in the faintest bin for the simple sum stack. This lower limit achieves a completeness of 40% in the final bin.

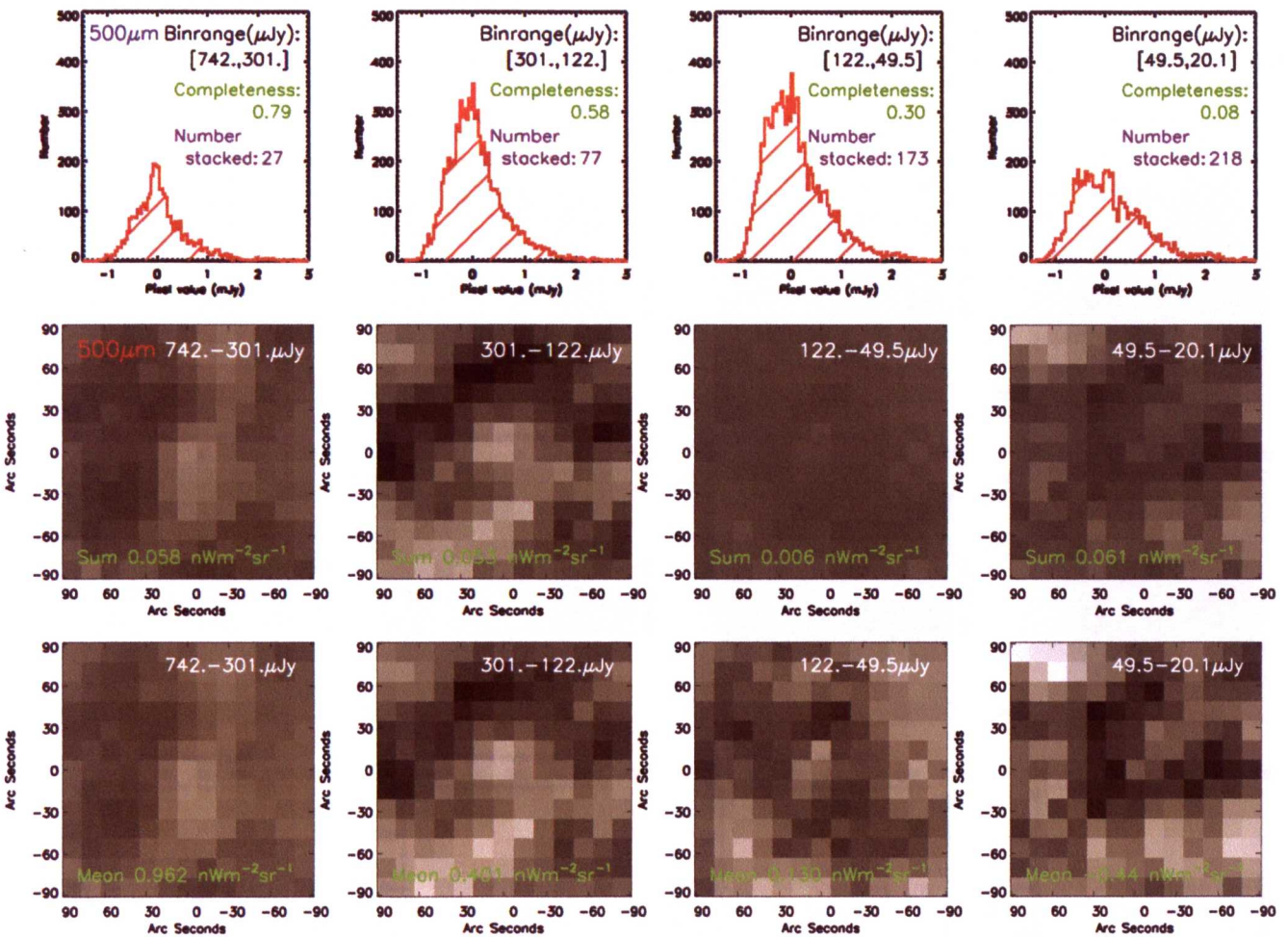

Figure A12: L15 flux density ordered stacks, taken in flux bins for the LW map with a lower flux limit of 20 μJy applied. There are no notable detections in either of the faintest two bins for the simple sum stacks.

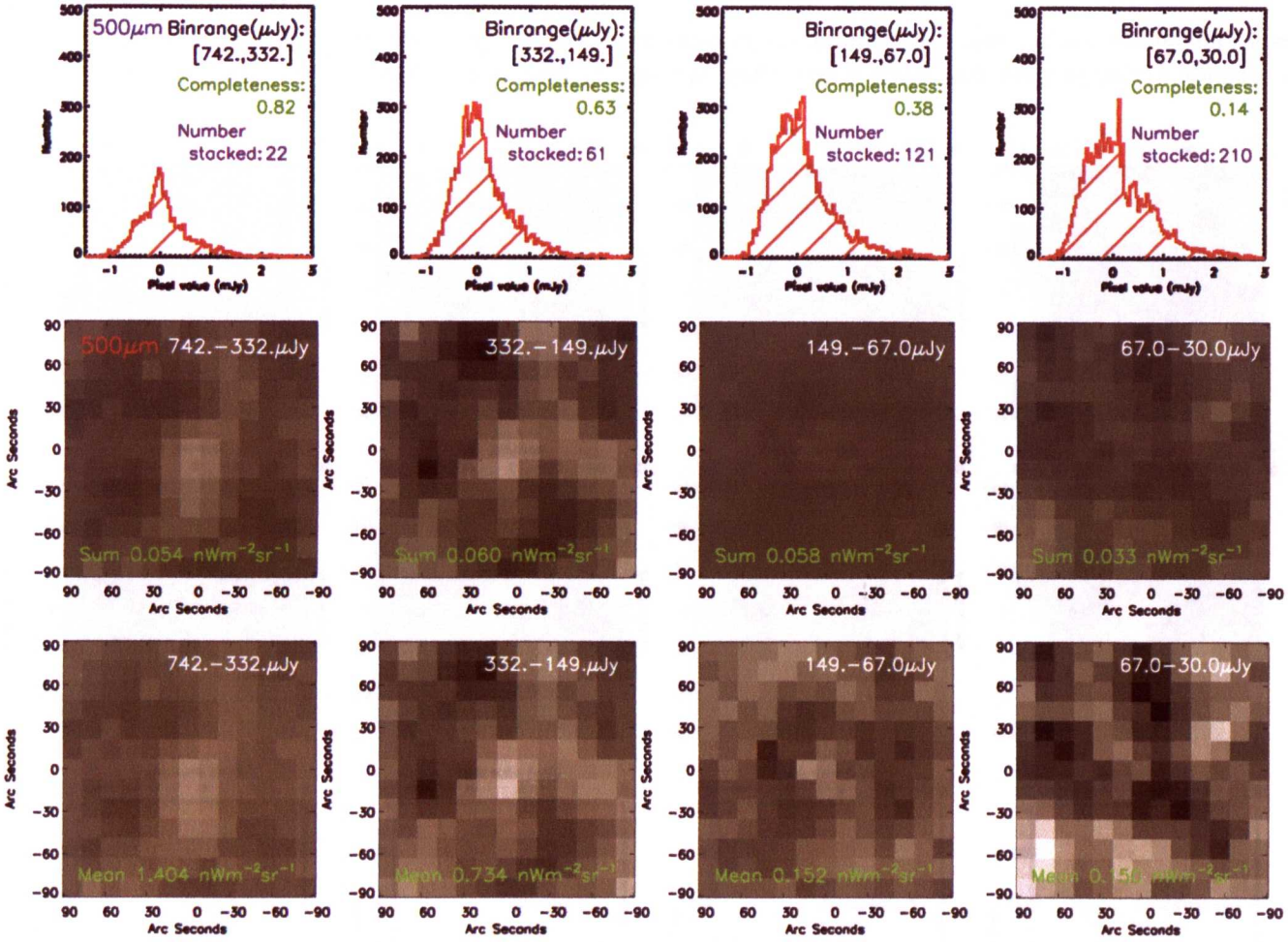

Figure A13: L15 flux density ordered stacks, taken in flux bins for the LW map with a lower flux limit of 30 μJy applied. There may be weak detections in both of the faintest two bins for the simple sum stacks.

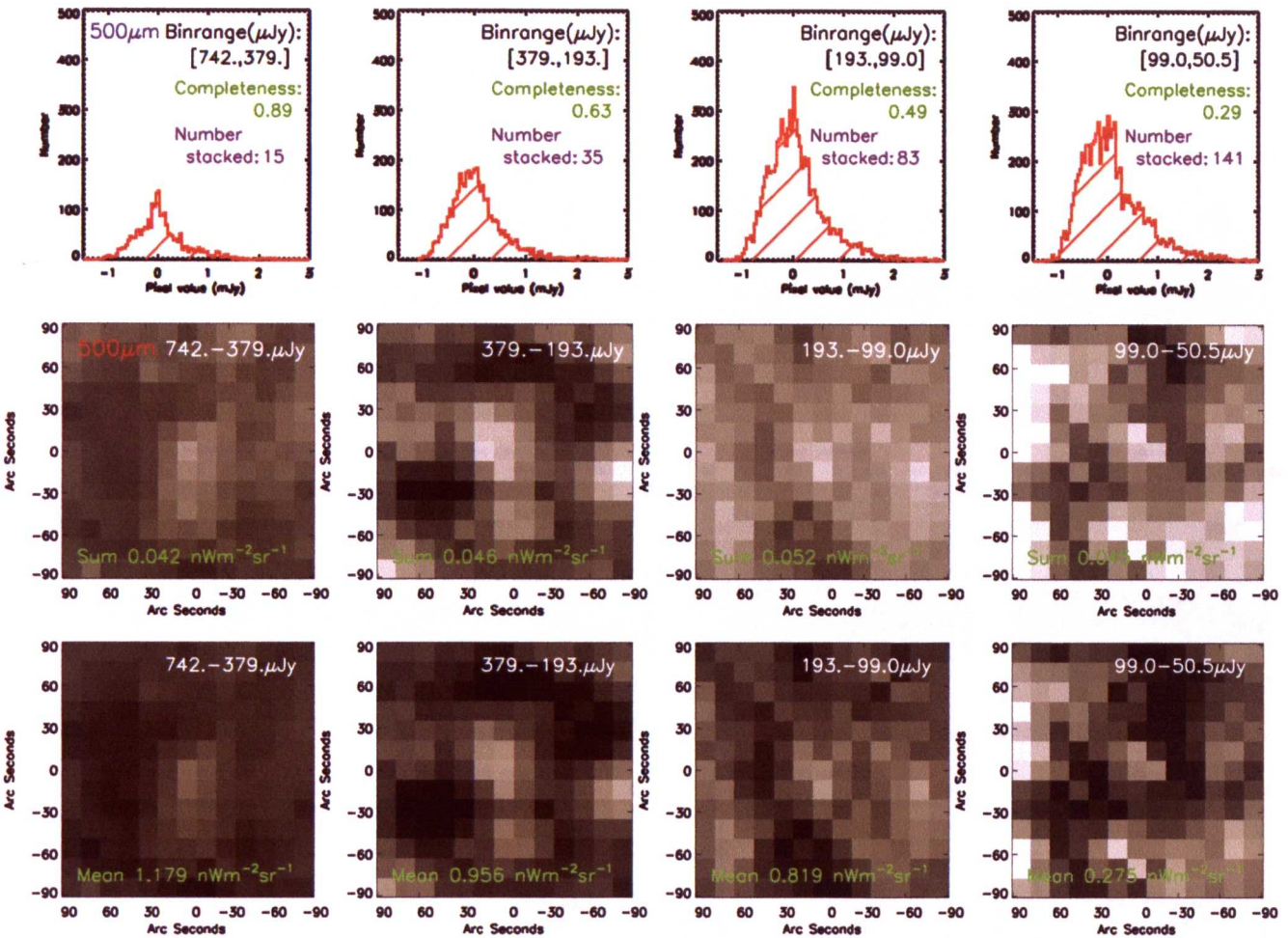

Figure A14: L15 flux density ordered stacks, taken in flux bins for the LW map with a lower flux limit of 50 μJy applied, which achieves a completeness of 29% in the final bin. There are hints of a detection in both of the faintest two bins for the simple sum stacks, however the statistics for these bins is greatly reduced to the previous flux limit.

The following figures A15 to A18 show the results of stacking when the L15 stacking catalogues are ordered by redshift and stacked in redshift bins for the MW and LW maps. The SW results are shown in the main text of chapter 4, section 4.4.4.

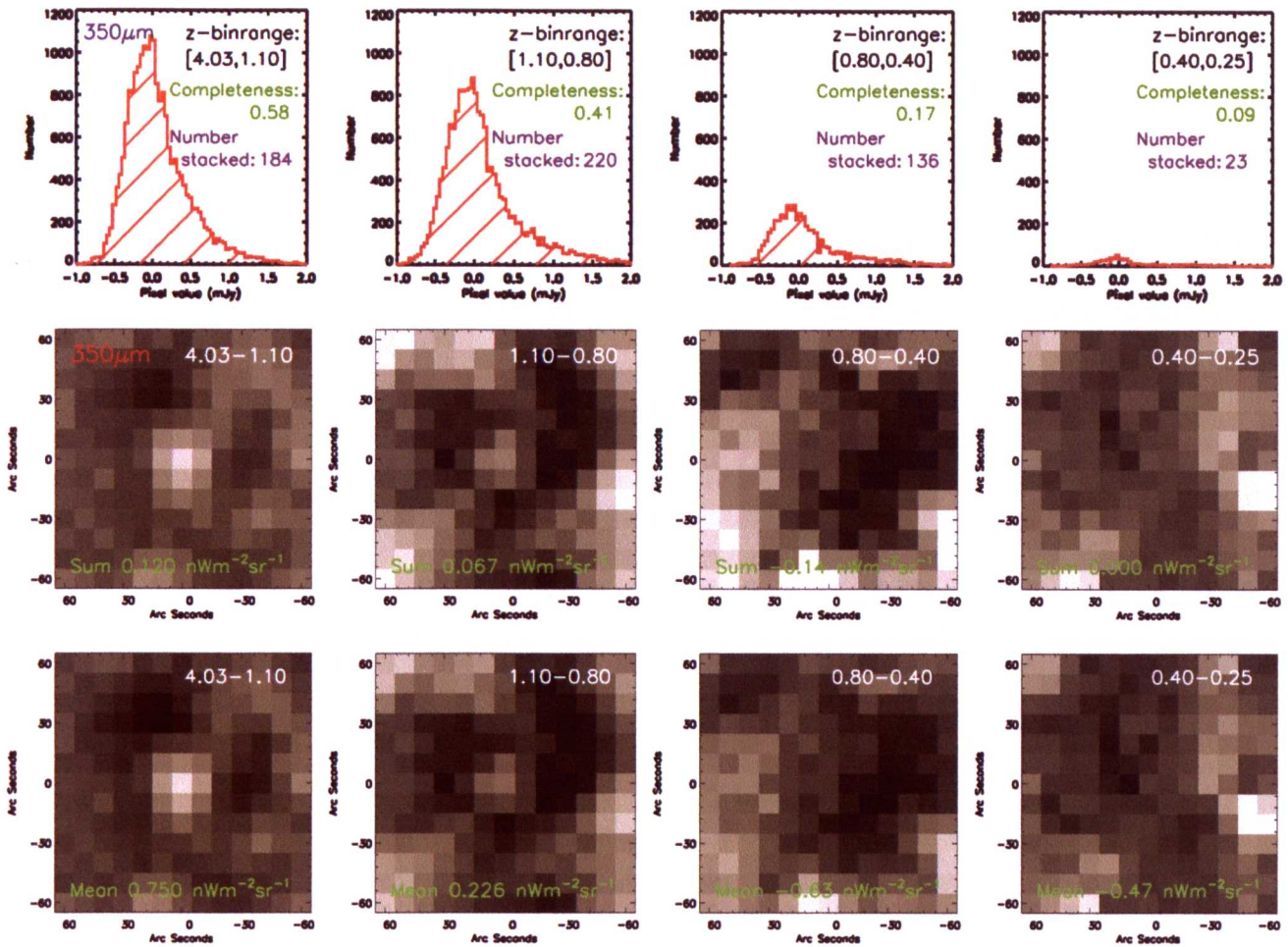

Figure A15: Postage stamp plots of the stacks taken in L15 redshift bins, for the MW map, both co-adding with a simple sum (middle row), and the corresponding pixel value distributions (top row) and using a weighted mean sum (bottom row). No lower redshift limit was set.

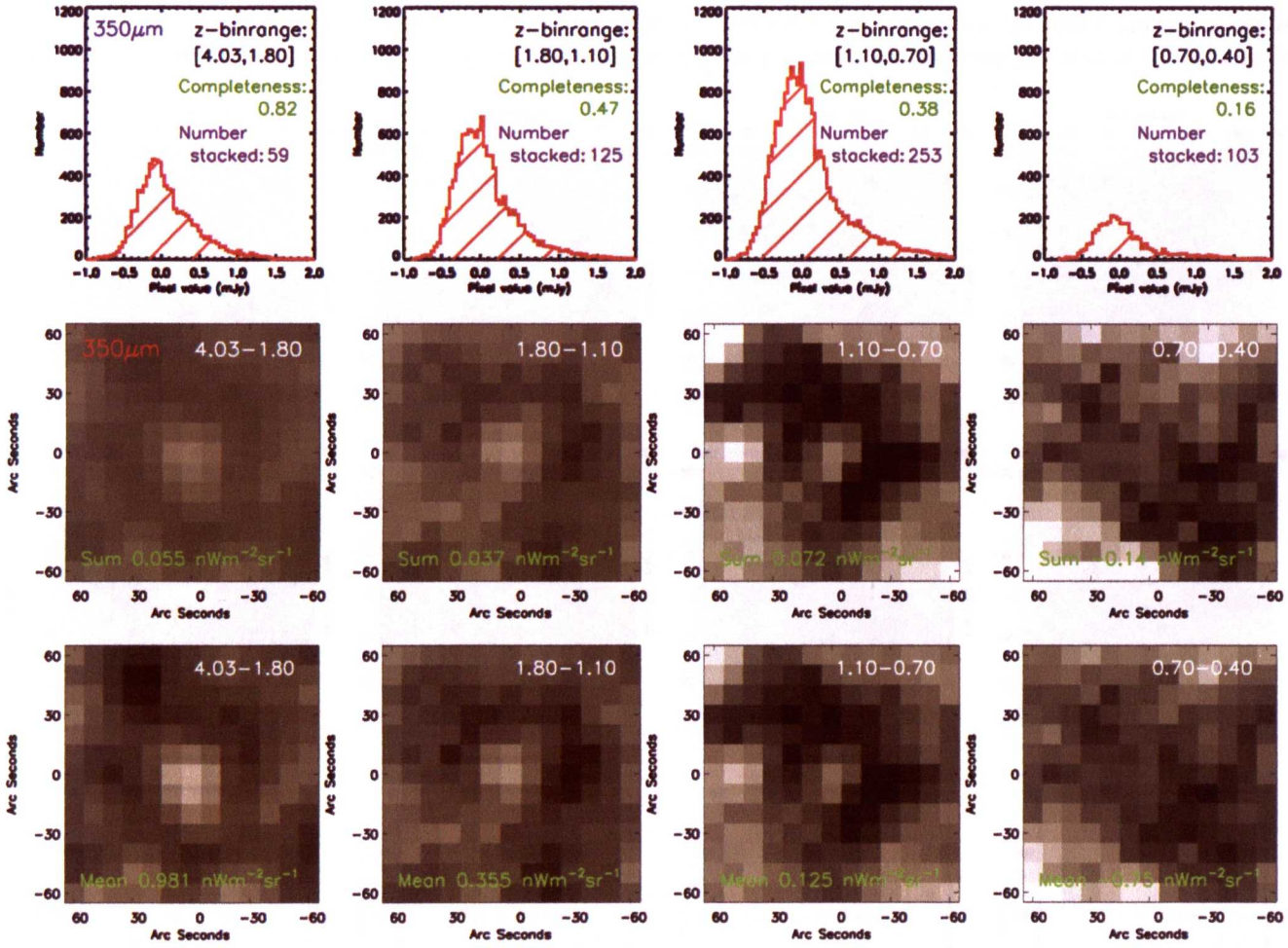

Figure A16: Postage stamp plots of the stacks taken in L15 redshift bins, for the MW map, both co-adding with a simple sum (middle row), and the corresponding pixel value distributions (top row) and using a weighted mean sum (bottom row). A lower redshift limit of 0.4 was set.

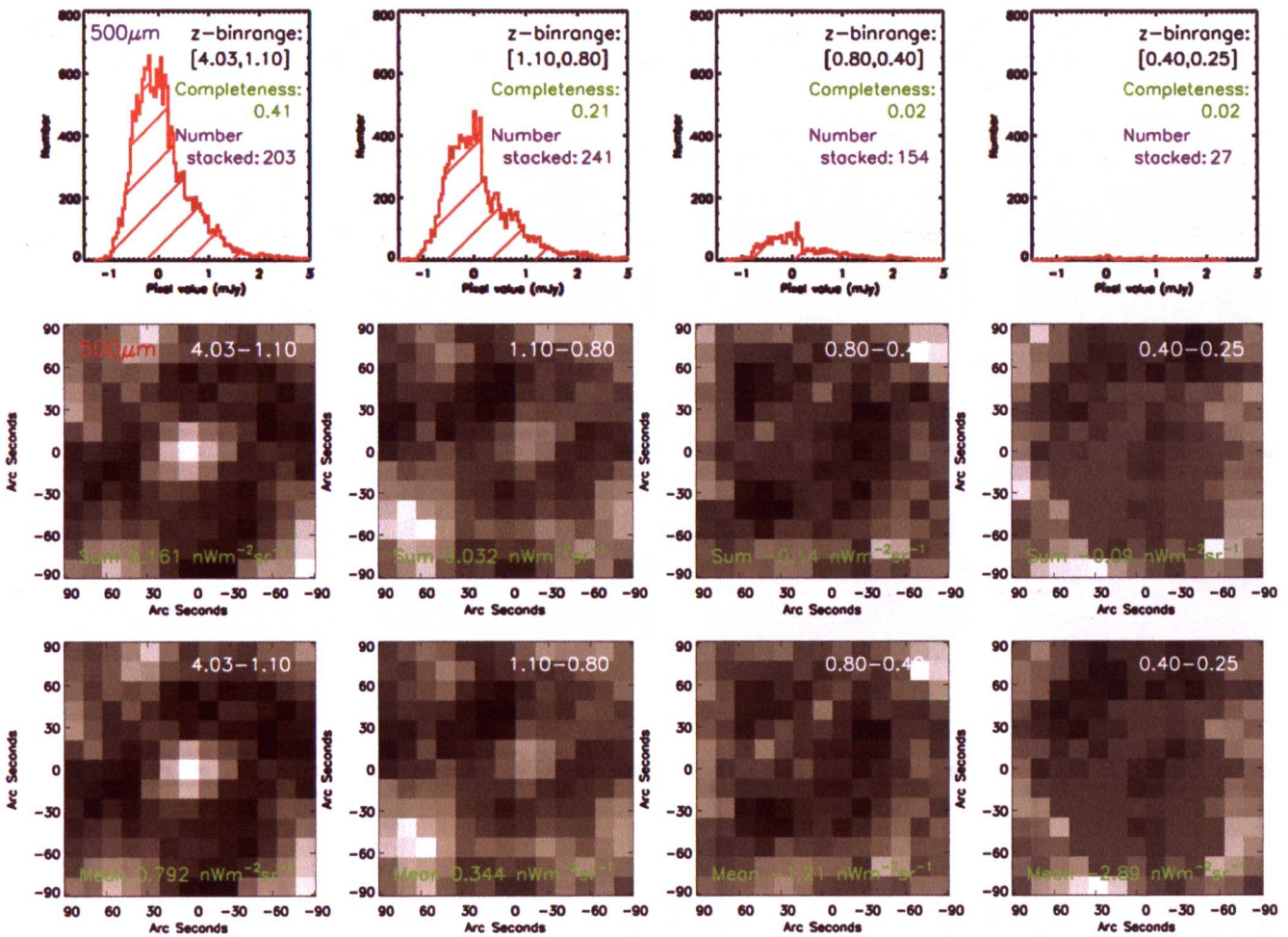

Figure A17: Postage stamp plots of the stacks taken in L15 redshift bins, for the LW map, both co-adding with a simple sum (middle row), and the corresponding pixel value distributions (top row) and using a weighted mean sum (bottom row). No lower redshift limit was set.

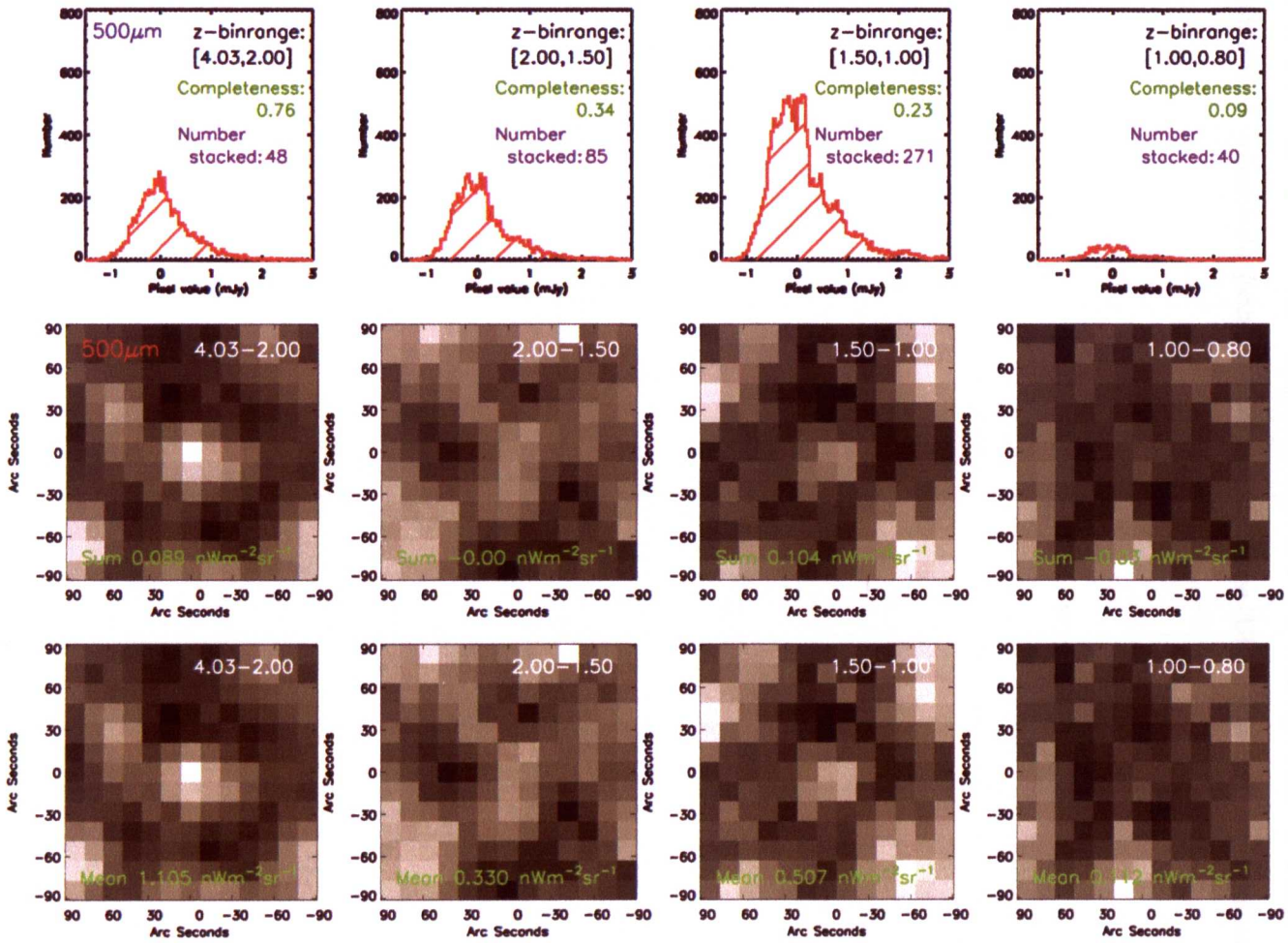

Figure A18: Postage stamp plots of the stacks taken in L15 redshift bins, for the LW map, both co-adding with a simple sum (middle row), and the corresponding pixel value distributions (top row) and using a weighted mean sum (bottom row). A lower redshift limit of 0.8 was set.

The following figures present examples of the bootstrapping used to assign uncertainties to the stack photometry taken with PSF fitting. Each histogram represent 10,000 resampled populations from the corresponding L15 stacking catalogue. The resulting distributions were found to be highly symmetric and therefore the errors were estimated from the standard deviation of a fitted Gaussian curve. For each SPIRE waveband, six example stack photometry distributions are plotted

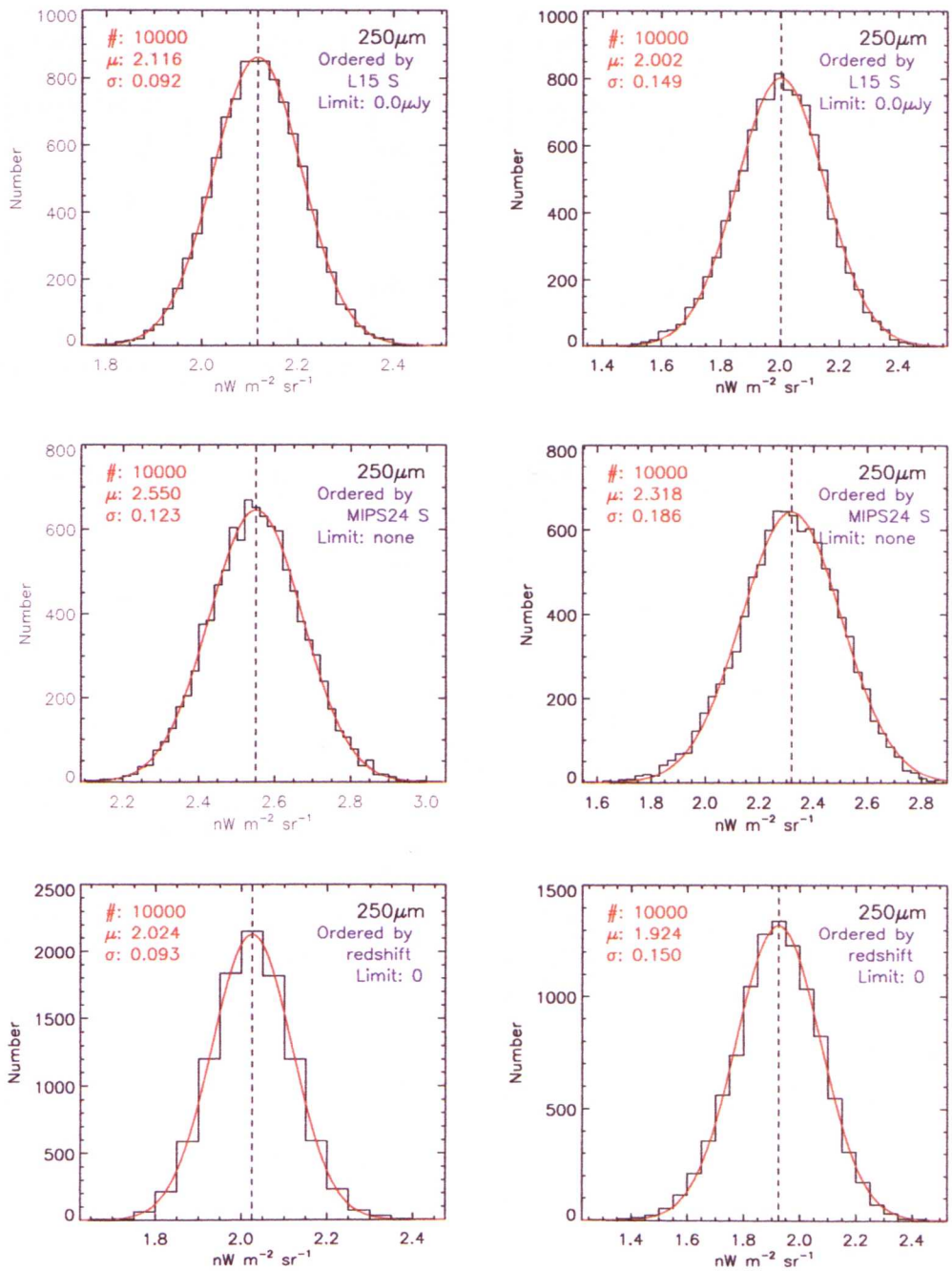

Figure A19: Examples of bootstrapped distributions to used to derive 1σ errors for SW stacked photometry, for different methods orderings.

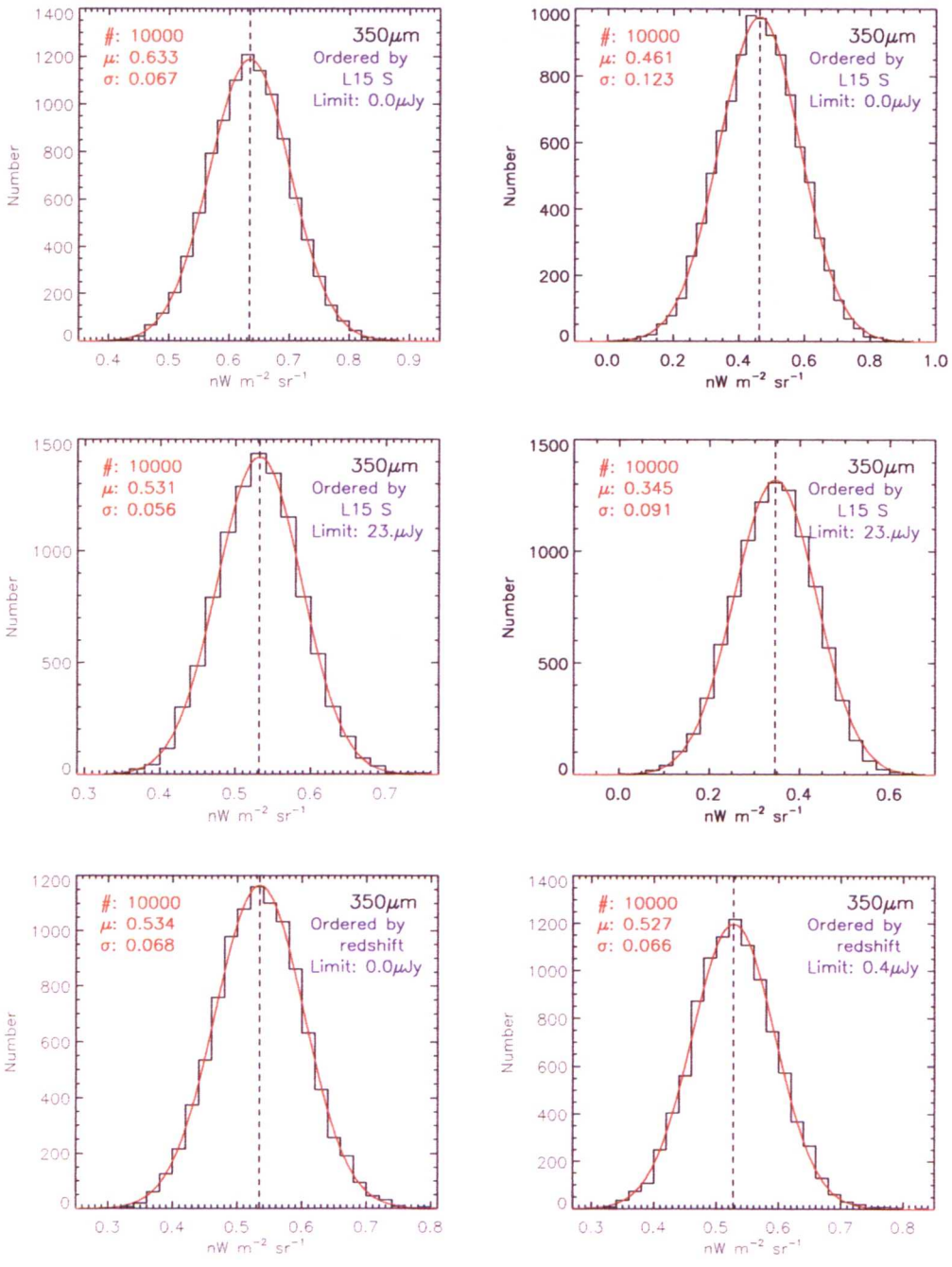

Figure A20: Examples of bootstrapped distributions used to derive 1σ errors for MW stacked photometry, for different methods of orderings.

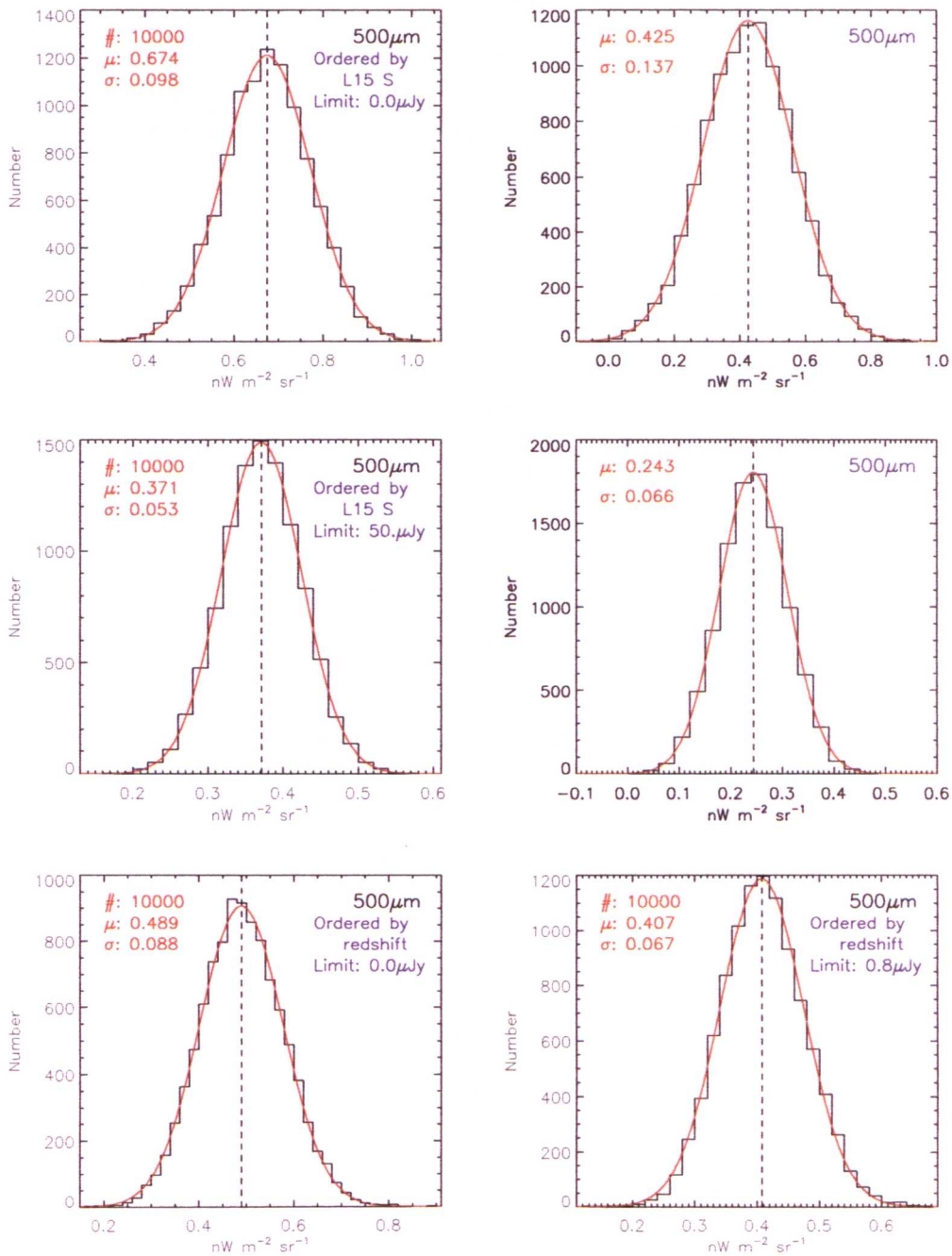

Figure A21: Examples of bootstrapped distributions used to derive 1σ errors for LW stacked photometry, for different methods of orderings.

The following tables present simulated stacking results for each SPIRE waveband. Masked and unmasked flux ratios to the input photometry are given, with associated errors. The mask width used for all of the stacks was 5 pixels.

Table A1: Stacking simulation results, comparing the masked and unmasked output/input photometry for the SW map. For the simple sum method of co-adding, with masking, the full input is recovered to within 1-2σ. The equivalent weighted mean results recover the input to within 1-3σ. The mean difference between the masked and unmasked results show without masking the output is overestimated between 15% and 21%.

Order	limit	Simple sum		Weighted mean		Mean difference
		Masked	Unmasked	Masked	Unmasked	
S_{L15}	0μJy	1.01±0.07	1.18±0.08	1.09±0.09	1.24±0.11	0.16
S_{L15}	20μJy	0.90±0.06	1.05±0.07	0.90±0.06	1.03±0.09	0.14
S_{SPIRE}	none	0.92±0.06	1.07±0.09	1.10±0.11	1.26±0.13	0.17
S_{SPIRE}	0mJy	0.86±0.09	1.00±0.11	1.00±0.09	1.15±0.12	0.15
S_{MIPS}	none	0.90±0.07	1.05±0.08	0.87±0.07	1.00±0.08	0.14
z(sim)	0.0	1.09±0.07	1.26±0.09	1.26±0.08	1.44±0.10	0.18
z(L15)	0.0	0.96±0.09	1.18±0.11	1.15±0.09	1.40±0.11	0.24
z(sim)	0.4	1.04±0.07	1.21±0.08	1.21±0.08	1.39±0.10	0.20
z(L15)	0.4	0.94±0.09	1.16±0.11	1.13±0.09	1.37±0.11	0.21
S_{L15}&z(sim)	23μJy&0.4	0.95±0.06	1.11±0.06	0.96±0.06	1.10±0.07	0.15
S_{L15}&z(L15)	23μJy&0.4	0.89±0.07	1.09±0.08	0.90±0.06	1.10±0.08	0.20

Table A2: Stacking simulation results, comparing the masked and unmasked output/input photometry for the MW map. The weighted mean results are marginally greater than those taken for the simple sum co-added stacks. The redshift ordering shows the highest overestimate for both the masked and unmasked stacks. The mean difference between the unmasked and masked stacks range from 14% to 33%.

Order	limit	Simple sum		Weighted mean		Mean difference
		Masked	Unmasked	Masked	Unmasked	
S_{L15}	0μJy	1.28±0.17	1.47±0.19	1.28±0.16	1.46±0.18	0.19
S_{L15}	20μJy	1.06±0.14	1.22±0.16	1.03±0.13	1.17±0.15	0.15
S_{L15}	23μJy	1.02±0.13	1.17±0.15	0.98±0.12	1.11±0.14	0.14
S_{SPIRE}	none	1.03±0.20	1.18±0.22	1.26±0.24	1.42±0.26	0.16
S_{SPIRE}	0mJy	1.69±0.32	1.91±0.35	2.49±0.33	2.77±0.37	0.25
S_{MIPS}	none	0.97±0.14	1.12±0.16	0.94±0.14	1.07±0.16	0.14
z(sim)	0.0	1.75±0.20	2.03±0.25	1.91±0.20	2.16±0.23	0.27
z(L15)	0.0	1.41±0.27	1.73±0.33	1.68±0.26	2.01±0.31	0.33
z(sim)	0.4	1.59±0.18	1.84±0.20	1.75±0.18	1.98±0.21	0.24
z(L15)	0.4	1.36±0.25	1.68±0.30	1.63±0.24	1.94±0.29	0.32
z(sim)	0.8	1.38±0.14	1.60±0.13	1.56±0.14	1.77±0.17	0.22
z(L15)	0.8	1.18±0.20	1.46±0.24	1.45±0.20	1.74±0.23	0.29
S_{L15}&z(sim)	23μJy&0.4	1.32±0.13	1.52±0.14	1.25±0.13	1.42±0.15	0.19
S_{L15}&z(L15)	23μJy&0.4	1.24±0.17	1.53±0.201	1.19±0.16	1.43±0.19	0.27

Table A3: Stacking simulation results, comparing the masked and unmasked output/input photometry for the LW map. The overestimate of the input photometry is greatest for the LW map, which is expected due to the decrease in resolution. The MIPS ordering and L15 flux density ordering (limited to $> 50\mu$Jy) give the results closest to the input. The mean difference between the unmasked and masked stacks range from 15% to 44%.

Order	limit	Simple sum		Weighted mean		Mean difference
		Masked	Unmasked	Masked	Unmasked	
S_{L15}	0 μJy	2.04±0.32	2.34±0.37	2.18±0.297	2.48±0.33	0.30
S_{L15}	23μJy	1.50±0.27	1.72±0.30	1.60±0.24	1.82±0.27	0.22
S_{L15}	50μJy	1.04±0.21	1.19±0.24	1.02±0.20	1.17±0.22	0.15
S_{SPIRE}	none	1.36±0.39	1.57±0.45	1.94±0.42	2.23±0.48	0.25
S_{SPIRE}	0mJy	1.42±0.44	1.63±0.52	2.01±0.52	2.30±0.61	0.29
S_{MIPS}	none	1.05±0.29	1.21±0.34	1.14±0.26	1.31±0.31	0.17
z(sim)	0.0	2.94±0.40	3.39±0.45	3.27±0.43	3.69±0.47	0.44
z(L15)	0.0	2.20±0.55	2.70±0.65	2.99±0.56	2.70±0.65	0.53
z(sim)	0.8	2.02±0.21	2.32±0.25	2.25±0.30	2.53±0.33	0.29
z(L15)	0.8	1.66±0.39	2.04±0.45	2.25±0.42	2.68±0.51	0.41
z(sim)	1.0	1.78±0.22	2.06±0.24	2.02±0.27	2.29±0.30	0.28
z(L15)	1.0	1.58±0.39	1.94±0.44	2.13±0.40	2.54±0.48	0.46
S_{L15}& z(sim)	50μJy&0.8	1.21±0.10	1.39±0.10	1.11±0.10	1.25±0.11	0.16
S_{L15}&z(L15)	50μJy&0.8	1.13±0.15	1.39±0.18	1.05±0.40	1.27±0.17	0.24
S_{L15}& z	50 μJy&1.0	1.11±0.15	1.37±0.18	1.05±0.14	1.27±0.17	0.19

Appendix B: Data analysis and early science results from H-ATLAS and PACS

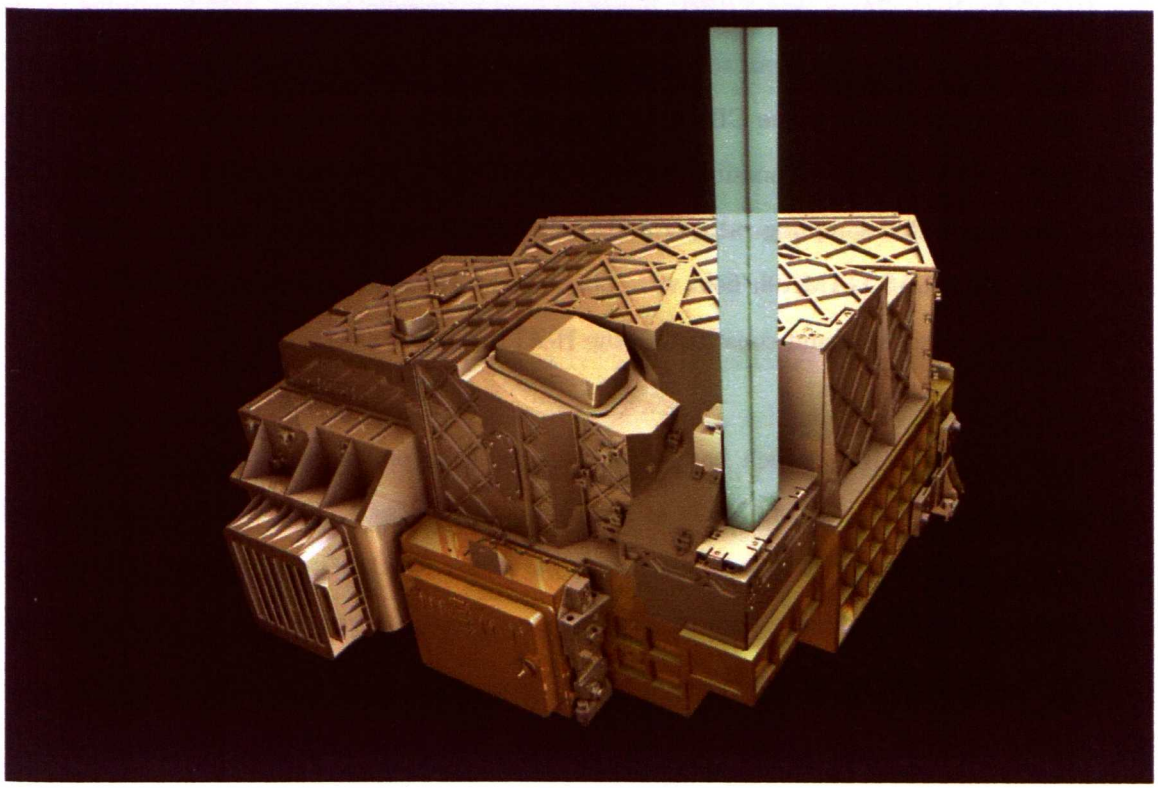

Figure B1: Artistic illustration of *Herschel*'s Photodetector Array Camera & Spectrometer instrument PACS. (Illustration: ESA - C. Carreau)

B1 Abstract

The poorer than expected performance of the *Herschel* Space Observatory's FIR instrument PACS has provided a strong data reduction challenge. In this chapter various PACS data reduction issues and methods are explored with the H-ATLAS SDP data. The reduction is tackled with both IDL and HIPE, with a focus on removing both chronic and occasional spurious features, to provide data suitable for the science goals of H-ATLAS. Data were reduced both for the purpose of optimal point source extraction, using the OU IDL pipeline, and as a contribution to the official H-ATLAS PACS pipeline.

B2 Exploring the PACS Green data with IDL

For H-ATLAS both PACS and SPIRE data is taken in parallel mode. PACS parallel mode offers the choice of Blue or Green, to accompany the Red scan. Green was chosen to give better coverage around the peak of the CIRB, which is in-line with the science goals of HATLAS. To make such a wide are survey possible the data is taken at a fast scan rate of 60″ per second, giving Green and Red sampling rates of 5 Hz and 10Hz, respectively. In November 2009, 14.4 deg^2 of the H-ATLAS GAMA9h field were observed by Herschel, providing around 3% of the total planned survey area and constituting the H-ATLAS SDP data.

In contrast to SPIRE, which has so far performed beyond expectations, PACS has not reached the predicted depths of 67 mJy at 100 μm and 94 mJy at 170 μm, and has also provided a steep challenge in terms of data reduction, in particular for the Green channel. The current explanation for PACS relatively poor performance is unclear, and so the best possible efforts are required to give science grade products.

Several basic investigations of the SDP Green data were carried out in order to better understand the data and the issues that were proving problematic for initial data reduction attempts. The raw PACS Green data is a 3D cube array of the form [t,x,y], where t is the temporal axis $\sim$ 130,000 frames in length, and x and y form the spatial axes of 64×32 pixels. Plotting a slice through the t axis (figure B2) shows the Green subarray structure. Visible in the slice are several bad pixels, which are flat along t or saturated. Example sections for two timelines are

shown in figure B3 and illustrate the digitised nature of the signal. The data suffers from high levels of low-, mid- and high-frequency noise[1] (discussed in detail in section B3.2) that lead to problems in the projected maps in terms of source extraction and photometry.

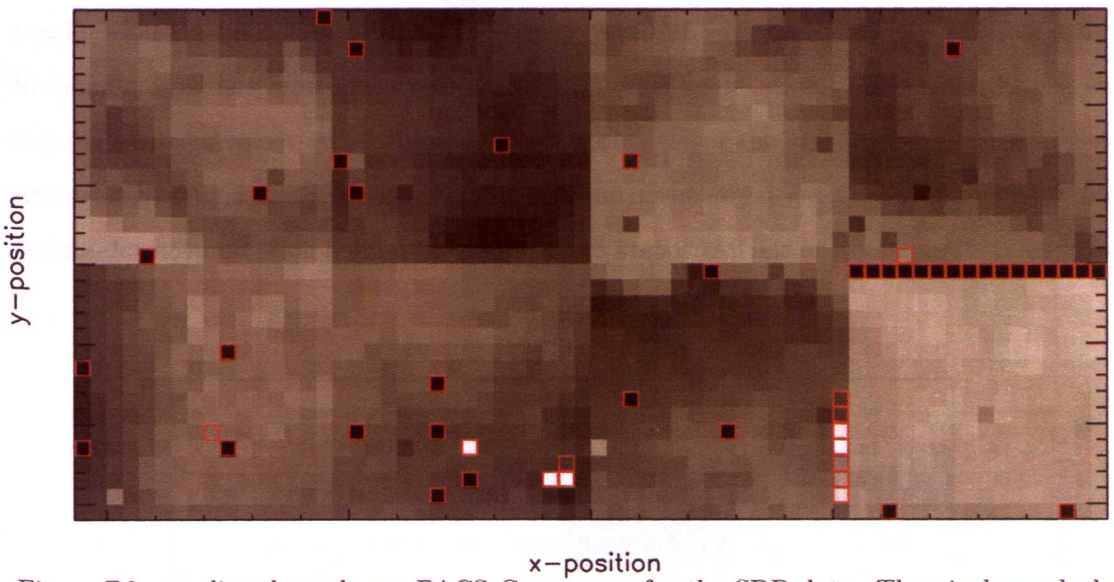

Figure B2: xy slice through one PACS Green scan for the SDP data. The pixels marked with red squares are considered bad either because they are flat (i.e. no real signal) or saturated. The 4 by 2 sub-array structure (of 16×16 pixel sub-arrays) shows strong correlated noise from pixel-to-pixel.

Theoretically, low frequency noise such as 1/f noise (originating from temperature drifts in the detector and background) can be removed from data by selecting and omitting the appropriate frequency modes in Fourier space. Information about the frequency of noise contained within a data set can be graphically represented by the plotting the power spectrum (P(k)). P(k) is a plot in frequency domain of Fourier space of the energy per unit time (i.e. power) as a function of frequency. Plotting P(k) gives a measure of the power of any particular frequency over the full timeline and can be achieved in IDL with the fast Fourier transform (FFT) as P(k) = ABS(SHIFT(FFT(timeline,-1),centre))^2, where -1 indicates the direction of the FFT and the centre for SHIFT must be specified as the mid point of the timeline. By plotting the timeline P(k) it should be possible to identify the 1/f 'knee' (where the background fluctuations begin to dominate over the white noise) and therefore remove low frequency structure below this frequency. For the H-ATLAS SPIRE SDP data this knee was found to lie at angular scales greater than that of the maps (> 5 deg) (see figure 2 Pascale et al. [2010]), therefore allowing

[1] mid to low frequency noise are on the scales of a few times the FWHM of the PSF to the size of the FOV.

the 1/f noise to be removed without any danger of affecting real structure. In contrast the P(k) of the PACS Green data (see figure B4) shows an almost constant slope. The power spectrum should be dominated by the PSF at higher frequencies and for data with purely Poisson noise the slope, becomes flat at lower frequencies. For data containing (ideal) 1/f noise the P(k) should exhibit a slope of -1. Examining the PACS P(k) showed it is dominated by 1/f noise plus a source of additional noise (as the slope is not -1), which may come from the large number of glitches present in the timelines. Cleaning up the initial timelines by removing these glitches should, therefore, give a cleaner power spectrum with which it may be possible to investigate the interference pattern present in the PACS data or to identify correlated noise between sub-arrays.

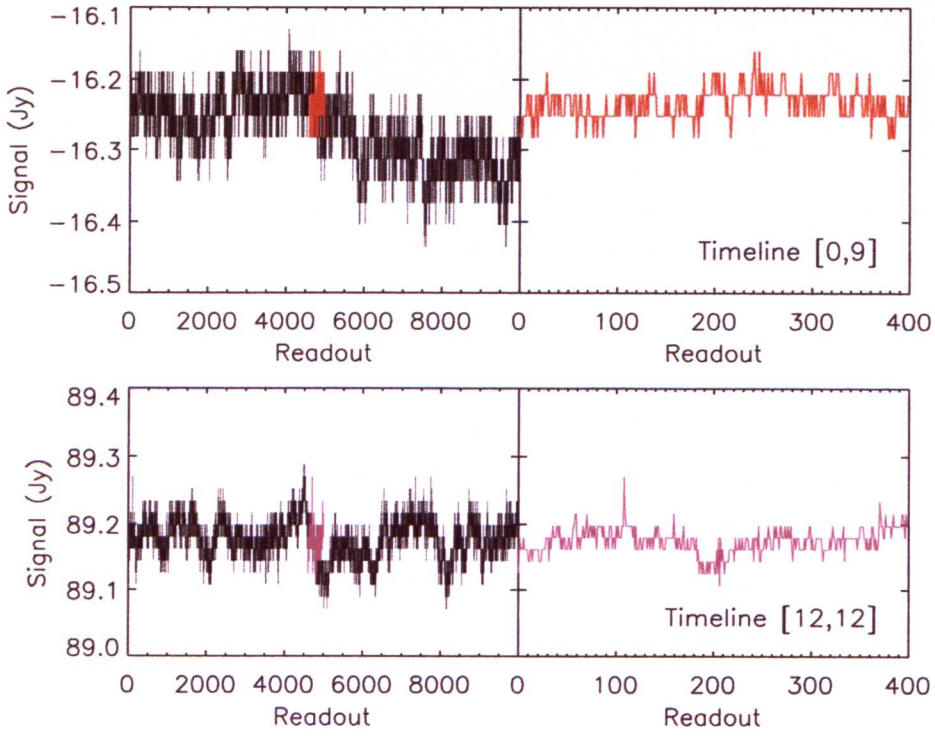

Figure B3: Example timeline sections for timelines at xy-positions [0,9] (top panels) and [12,12] (bottom panels). The right-hand panels show a zoomed version of the left hand plot, for the section highlighted with colour in the left-panels. Note the digitisation of the data and the variation in the background levels.

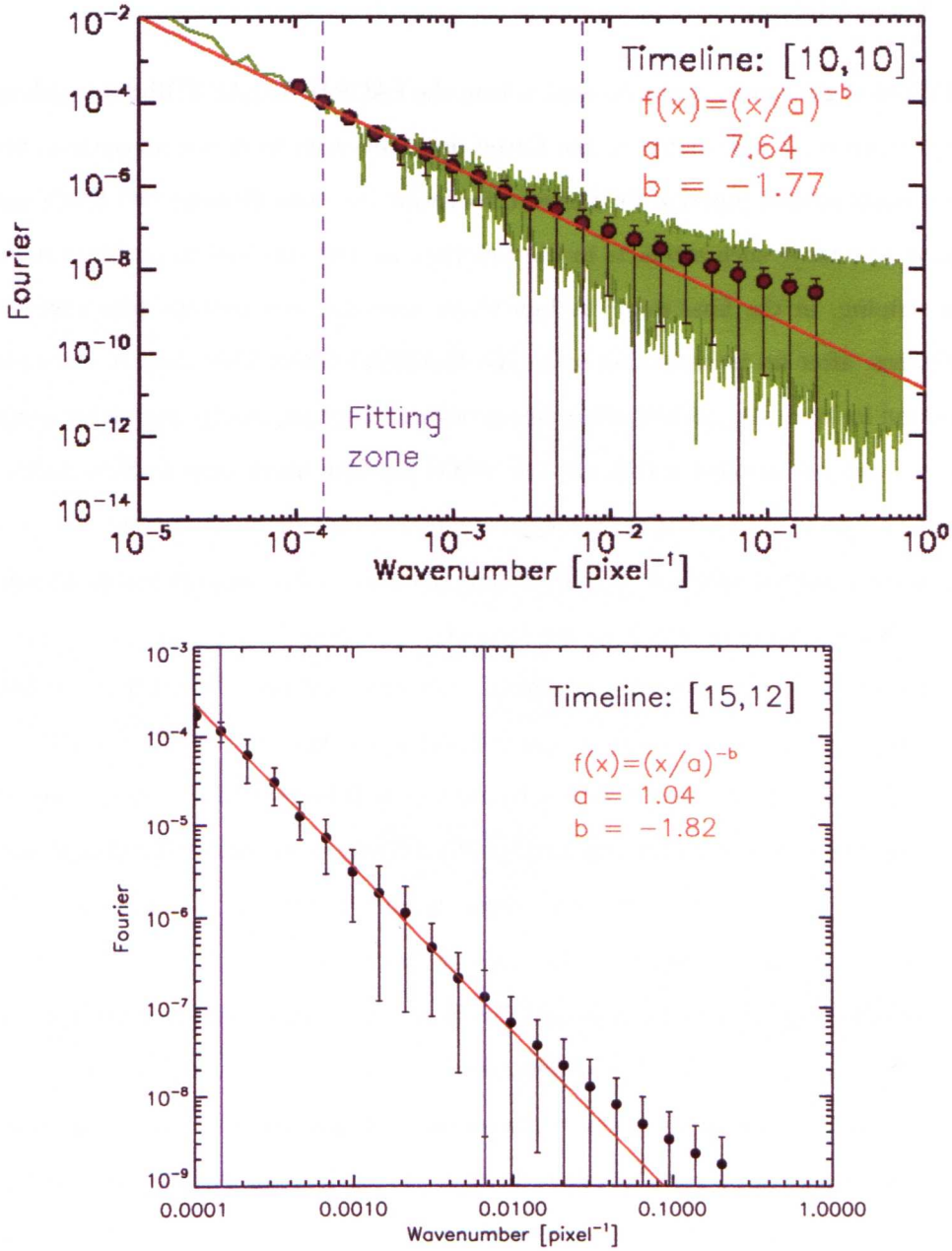

Figure B4: Example power spectra for Green 1342187170 timelines [10,10] and [15,12], showing only the rebinned version used for fitting in the later case. For idea 1/f noise a power spectrum is expected to have a slope $\sim$ -1 for lower frequencies, which is not the case for these examples, or the PACS data in general. There is also no clear 1/f knee. For both examples there is a deviation away from the fitted straight line around scales of around 200″, which is not a large enough to consider removing the 1/f noise in Fourier space.

B3 The OU PACS Pipeline

B3.1 Introduction

Several types of glitch were found to exist within the PACS H-ATLAS SDP data, although these can be predominantly associated to the Green data. In order to derive an optimal filter or an empirical point spread function for the zero footprint (i.e. non-filtered) OU PACS maps, it is imperative to remove such artefacts in the timelines as they can lead to problematic structure, such as striping, in the final map. A four stage approach was initially formulated to tackle these glitches, after an investigation using the H-ATLAS Green SDP data as a template. The final method for each stage follows the same straightforward approach - search for a feature and remove it - and was applied within the OU PACS pipeline using bespoke IDL code. The OU IDL pipeline begins with a HIPE [*Herschel* Interactive Pipeline Environment Ott et al., 2010] reduced level 1 output and uses a noise-weighted matched filtering approach, similar to that used for SCUBA data reduction [e.g. see Mortier et al., 2005; Serjeant et al., 2003] to optimise the extraction of point-like sources, assuming a non-confused field. The four-point de-glitching plan precedes the 1D and 2D filtering, and is detailed in a flow chart of the full IDL pipeline in figure B5. The aim for this de-glitching is to produce well behaved timelines by removing sharp features and therefore minimising the number of artefacts in the final map. Due to the filtering methods used in the subsequent timeline steps, the introduction of low frequency noise during de-glitching was deemed acceptable. As there are a wide range of features seen in the Green data, a small fraction are inevitably missed but the code was optimised to correct the maximum possible. One undesirable side effect of addressing glitches can be the addition of high frequency noise, comparable to the noise being corrected so care was taken to check and remove such by-products. In general the implemented de-glitching significantly reduces the number of artefacts in the timelines and provides the best possible input to the 1D filtering, using this approach.

B3.2 Glitches

Glitches within the SDP Green data can be roughly categorised into three groups – spikes, faders and steps.

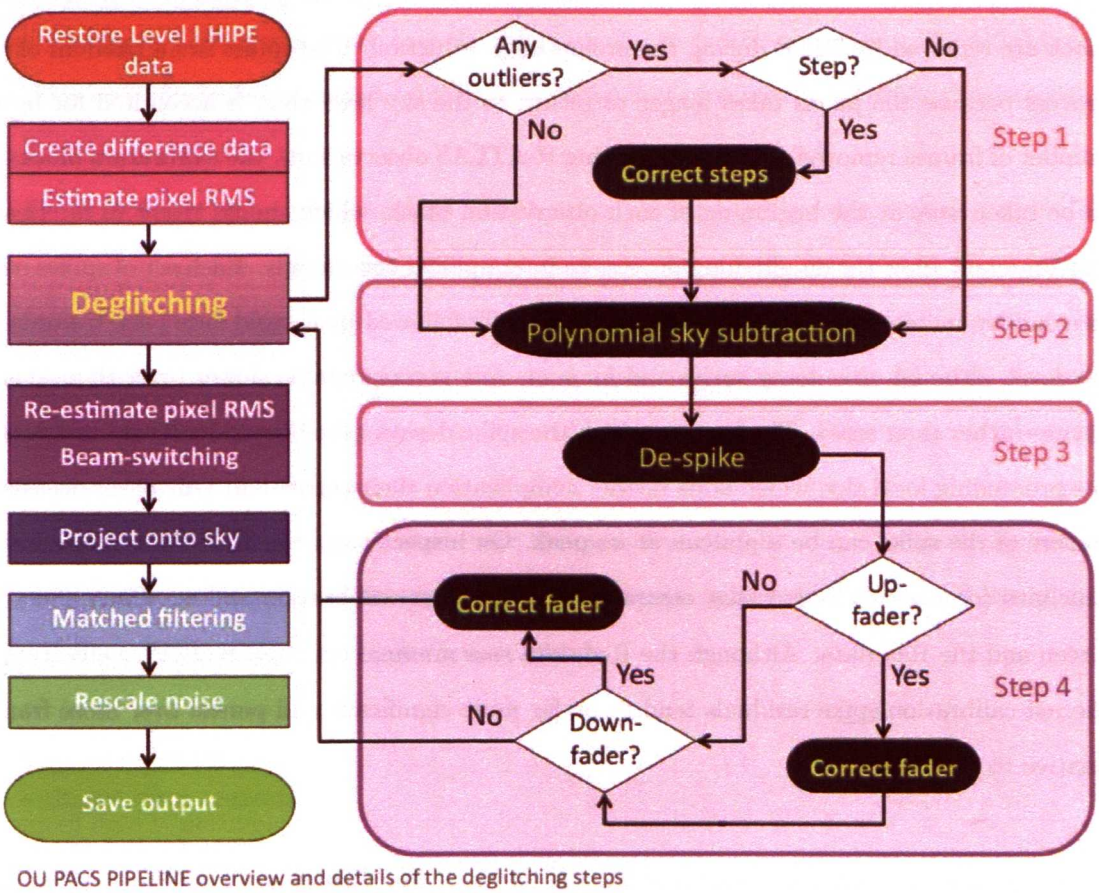

Figure B5: Flow chart of the OU PACS pipeline, detailing the de-glitching stage.

For the SDP data set (OU version) used to derive the de-glitching, a large proportions of features that occur are related to the removal of calibration blocks and appear at regular easily derivable positions, as sets of either positive or negative features (spikes; see figure B6). In general as *Herschel* scans a wide area field, a calibration observation lasting ~30 seconds is taken at the beginning of each observation block and repeated every ten scans. The calibration is taken to monitor any temperature drifts seen in the detector response, and is performed by the focal plane chopper [Krause et al., 2006][1]. A set number of frames at the position of each calibration block are removed by HIPE during the preliminary reduction. The spikes are a residual of this process because the pixels takes longer to return to the sky level than is accounted for by the number of frames removed. For the remaining H-ATLAS observations, the calibration blocks are to be taken *only* at the beginning of each observation block, which should result in far cleaner timelines and allow the de-glitching process to be simplified accordingly. Each set of spikes occur as a sudden increase or decrease in the signal, usually followed by a rapid fade back towards the sky level, although this decay varies and for some sets is considerable slower (over thousands of frames rather than tens). The level to which the spike decays can show a significant different to the proceeding local sky, which adds further complication their correction. One other occasional feature of the spike can be a plateau at its peak. On inspection of the SDP data, there are few timelines (or possibly none) that completely escape these calibration spikes, which effect the Green and the Red data. Although the Red data sees minimal occurrence of other glitch types, the red calibration spike residuals tend to be far more significant and persist over more frames, relative to the Green.

In addition to calibration spike sets there is another class of similar glitch (faders) that have the same general profile – a jump in signal followed by a decay (but never a plateau). Unlike spikes, faders occur randomly within the timelines, but may reoccur over as many as 16 pixels, i.e. the width of a Green sub-array, but with a tendency to decrease in intensity after the first incidence. Within the fader class several sub-classes have be defined. As faders are often

[1] Chopping and nodding is a technique used for infrared and sub-mm observations to allow an accurate sky estimated. For a pointed observation at optical or NIR it is common to observe both the source and also the nearby sky for calibration purposes, but for longer wavelengths the high thermal background are not adequately accounted for by this. Instead the telescope beam is alternated (chopped) between source and sky, but as the sky in the source beam will be at a slightly different level to the sky in the sky only beam, the process is then reversed to swap the beams so the telescope chops between sky and source. The 'nod' is the movement of the detector itself to allow the source to be observed in the alternative beam position.

(but not always) more significant than spikes and tend to decay at a slower rate and due to their persistence over several pixels, the prefix 'mega' has been assigned giving the sub-classes of Mega-up-, mega-down- and mega-cosmic-fader. Mega-up and -down-faders are the closest to calibration spikes, whereas mega-cosmic-faders, which are extreme examples of mega-up-faders with a rapid decay, are similar to single frame events, most likely caused by a cosmic ray incident. Again for these faders, the following mean sky is not necessarily approximate to the level preceding it, and for the the most significant (positive) fader features there can be an additional dip below the sky level, which increases the difficulty of a successful correction. The third type of glitch are step-like features (steps), which are a sudden and sustained jump in the timeline signal.

The removal of steps was found to be reasonably trivial, with a high success rate. The correction of Mega-faders features (which are similar to those seen in ISOCAM scans [e.g. see Metcalfe et al., 2003, figure 3], is also relatively straight-forward and generally produces satisfactory results, once secondary corrections to remove residual spikes are applied. As spikes have a variety of strength and profile two approaches were explored, one (an extremely simple approach) involving the replacement of a short strip of data immediately after the start of the spike, and the other a more complicated curve fitting approach. The simple method was adopted for the IDL de-glitching, due to the comparibly good results achieved with minimal loss of data. The final four IDL de-glitching stages are as follows:

- Stage1: step correction
- stage2: polynomial sky subtraction
- stage3: calibration spike removal
- stage4: mega-glitch correction

B3.3 Step correction

Prior to de-glitching the only required task is to load the necessary level1 PACS data from the HIPE output fits files. The data is in the form of a fits cube with 18 fits extensions. For the OU pipeline we are only interested in the timeline data, which are a 3D image located in extension

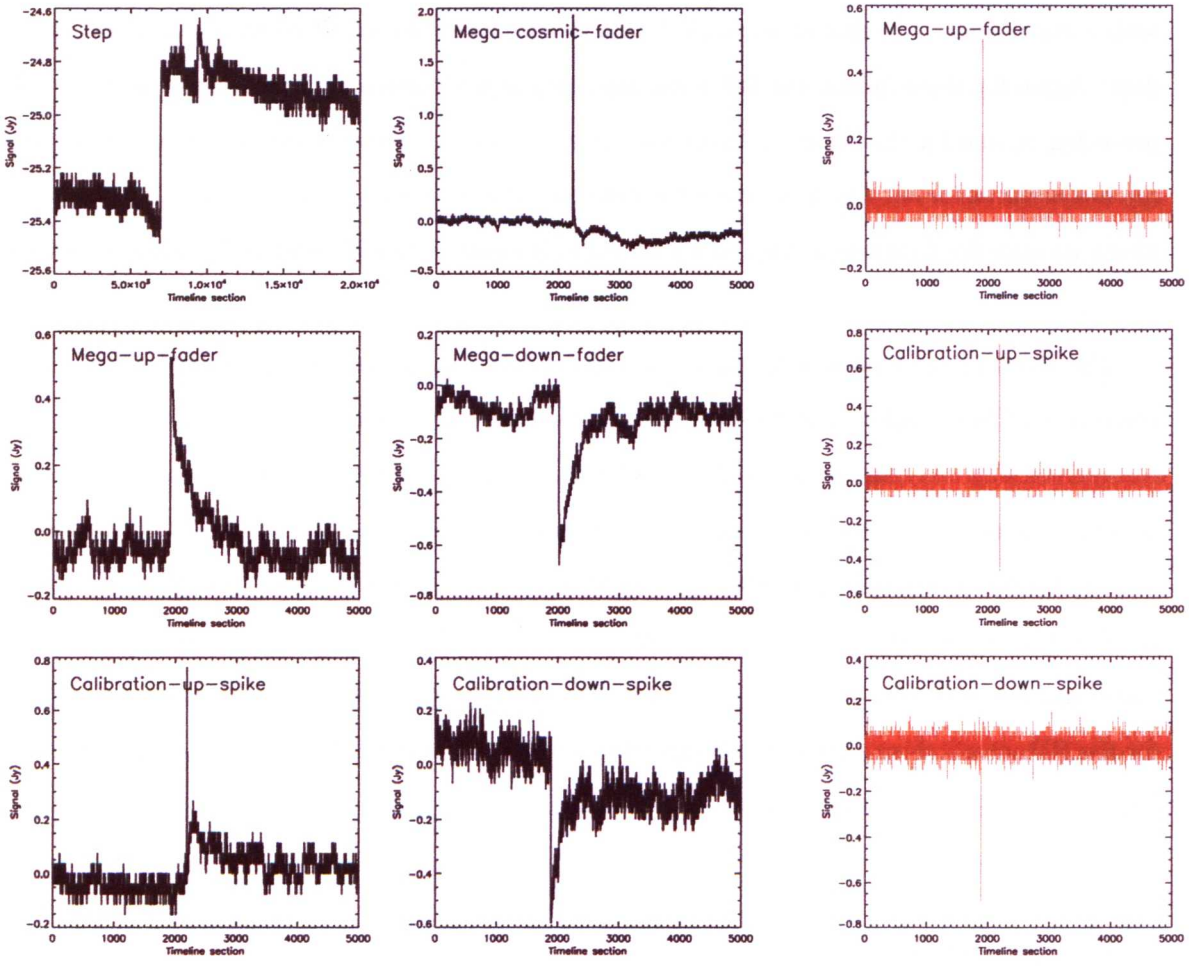

Figure B6: Left and middle: timeline sections of PACS Green data that contain a strong feature. Right: The corresponding difference timeline for three of the timeline sections. Each point of the difference timeline is the difference between the readout value at that frame and the preceding frame. Peaks in the difference timelines can be used to identify potential features, taking into account the peak in the timeline is positioned one to the left relative to the difference timeline. The middle right panel shows a difference timeline section that illustrates calibration-up-spikes may be represented by a positive followed by a negative peak, which can be used to define the calibration-spike plateau. In contrast the difference timeline of a calibration-down-spikes are less likely to have this double feature, as seen in the bottom right panel.

1, and the corresponding RA and Dec images of the same dimensions, which are found in extensions 17 and 18 of the fits cube. The timeline data has already been partially processed with '1st level de-glitching' in HIPE. This removes the calibration blocks, which truncates not only the timelines but also the RA and Dec data, and the flagging of single frame noise events with Multi-resolution Median Transform (MMT, see section B4.1). In several of the de-glitching stages, a difference timeline is used to identify outlying signal. This is found from the difference between sequential readouts of a timeline (see figure B6), giving a 1D array with one less frames than the corresponding timeline. All glitch types in these data begin with a sharp jump in the signal and therefore should appear as a spike in the difference timeline, which is usually at a significantly greater level than the background frame-to-frame difference. Identifying features as outliers in the difference timeline is assumed to avoid the mistaken identification of any real source signal, which should see a less extreme difference from one frame to the next due to the PSF profile.

Steps are corrected in the first part of the de-glitching procedure, before a rough sky subtraction is applied to facilitate the remaining glitch corrections. To identify possible step positions, outlying points $> 5\ \sigma$ above the mean difference (~ 0) are flagged in the difference timeline ($\mathrm{D_{TL}}$) using the 68% confidence interval of the median of the absolute deviation (MAD). For median ($\tilde{\mathrm{D}}_{\mathrm{TL}}$)

$$MAD = \tilde{\mathrm{D}}_{\mathrm{TL}}(|\mathrm{D_{TL}} - \tilde{\mathrm{D}}_{\mathrm{TL}}|) \tag{1}$$

Firstly all steps are assumed to be positive (which holds true for the OU version of the Green data, however both up and down steps are addressed in later versions of the de-glitching performed in HIPE) and therefore only positive outliers are considered. Secondly the remaining outliers are checked to retain only step-like features. Steps are classified as a sustained jump in the overall signal and therefore the long term sky level before and after a jump should see a marked difference. Median values are estimated from a 2000 frame long timeline section, where possible. This length is necessary to avoid unstable signal that can occur near to a glitch. Initial tests showed steps were more frequently identified by taking the post-step median level starting 2000 frames after the outlying difference position. Introducing this gap avoids the misidentification of long ranging faders as steps, but at the same time, steps of low significance in a

pronounced gradient may be missed, however these are likely to be then successfully corrected as a fader. A simple criteria using the difference between the two median values ($\tilde{TL}_1$ and $\tilde{TL}_2$) in comparison to the pixel RMS $(\tilde{TL}_2 - \tilde{TL}_1)/(\mathrm{RMS}_{TL} > 5)$ is then applied to identify step features. Once a step is identified it can be corrected by simply equalising the sky levels either side of the outlier. The left median value found during identification is subtracted from the section of timeline to the left of the outlier and from the right segment the median of the following 2000 frames is subtracted. Four frames at the position of the outlier itself, starting one position to the left, are set to the local sky level.

To test the effectiveness of step identification and correction, each timeline in one full Green scan was examined and all timelines featuring a step were noted. There were around 25 timelines, out of 2048, found to have a noticeable step that is not associated to a spike positions. Timelines with a range of calibration spike sets and those with faders were also identified for subsequent testing and to check the incidence of mis-identification and mis-correction of steps. This set of test timelines were used to test the de-glitching methods, assuming no statistical difference between Green scans. The step identification success rate is more sensitive to the σ clipping level applied to the difference timeline compared to the minimum level of difference set between the segment median values and the timeline RMS. Some consideration was taken while trying to optimise the criteria set for step selection due to the range of step-like-features within the SDP data, including those at a low significance above the sky (see figure B7 right panel[1]). A high σ clipping level that puts forward fewer outliers to the secondary sorting can miss less significant steps, on the other hand a low sigma clip can increase the number of potential steps significantly, to tens and in a few cases hundreds. The de-step algorithm was applied to the test timelines for a range of σ for both criteria. For timelines containing step features, a $5\,\sigma$ clipping level identified and corrected all but one step (96%), $6\,\sigma$ removed 92%, $7\,\sigma$ removes 83% and $9\,\sigma$ removed only 79%. The single step not identified with a clipping level of $5\,\sigma$ remains unidentified when the clipping limit (or median comparison limit) is lowered as it fails to appear as a distinct spike in the difference timeline. This is an issue common to a small fraction of glitches and arises when the initial jump is spread over more than one frame. The de-step algorithm is not time intensive and therefore even with each iteration checking tens of outliers, the pipeline run-time

[1]The position of a timeline is denoted as [x,y].

for a σ of 5 is only increased by a few minutes.

The de-step algorithm was run on timelines with non-step type glitches. Using the median value taken directly adjacent to the outlier, results in several examples of mis-corrected fader. When using this median further along the timeline, fewer unnecessary correction were performed and any that were applied to a non-step feature arose due to an uneven sky level, before and after a fader. The resulting correction tended to be negligible or give a more level sky on which to correct the fader itself, not an undesirable outcome.

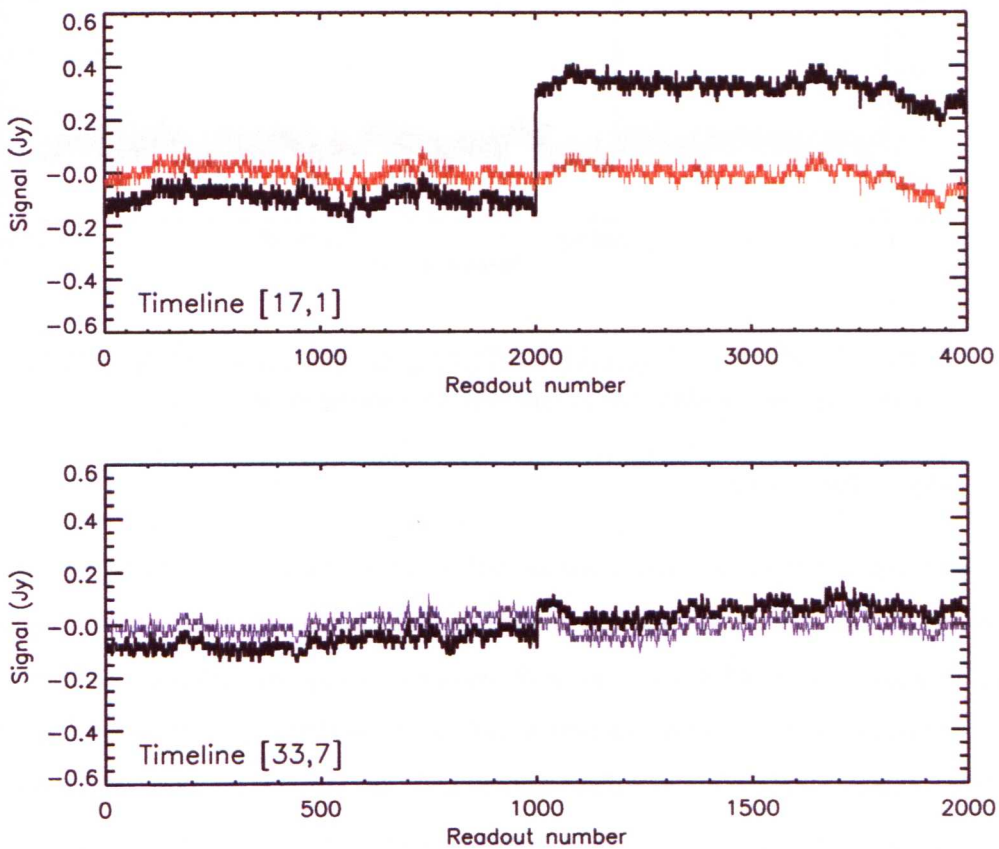

Figure B7: Two examples of step corrections. The black line shows the uncorrected timeline section and the coloured line shows the corrected results. The steps were were identified from the first outlying point checked, for timeline [17,1], and the second outlying point checked, for timeline [33,7]. These steps vary, comparatively, in signifiance, but are both eqally well corrected.

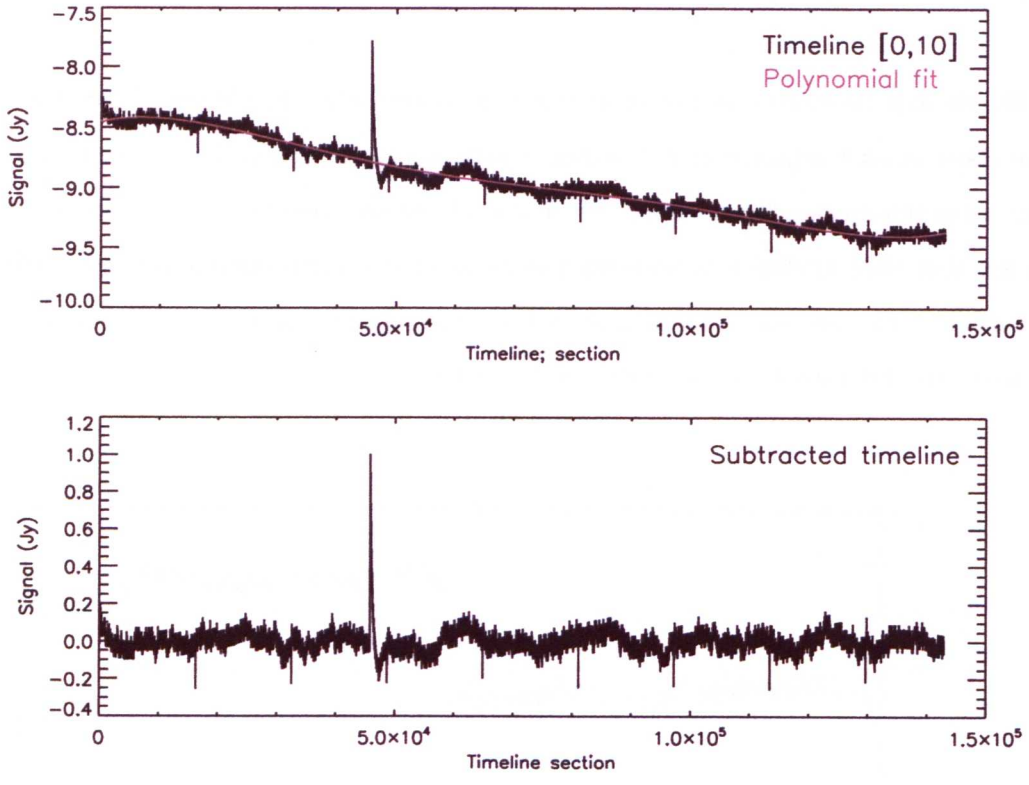

Figure B8: Example of a 5^{th} order polynomial fit to timeline [0,10] (top), which is then subtracted (bottom). This rough sky subtraction is repeated for each timeline.

B3.4 Sky subtraction

Removal of step-features leaves the timelines with an approximately continuous sky level, albeit one with significant 1/f noise. Hence it is then possible to perform a sky subtraction at a low enough frequency (> 10,000 frames) so as to avoid all sources and glitches. The 1/f noise can lead to steep local gradients at the position of a glitch, so removing the 1/f noise can facilitate the correction of mega glitches (up- and down-faders) and calibration flashes (up- and down-spikes). A 5th order polynomial was fitted and subtracted from each timelines (see figure B8). In the final version of the IDL de-glitching code the subtracted sky is added back to the timelines after the de-glitching process is completed, but before the 1/f noise is addressed at the 1D filtering stage (see section B3.8.1).

B3.5 Fader correction

B3.5.1 Primary fitting method

Mega-up- and mega-down-faders are similar in shape to calibration-spikes but generally with wider profiles and a tendency towards slower decay back to the local sky. Mega-cosmic-faders are relatively rare, with only a few occurring in the Green SDP data, and therefore the fader correction procedure was initially tailored towards correcting the more common glitch profile, using a 5th order polynomial to fit the mega-glitches and a power law function to fit the calibration spikes

$$f(x) = \frac{1}{\mathrm{P}_0} x^{\mathrm{P}_1} + \mathrm{P}_2, \tag{2}$$

where P_0, P_1 and P_2 are free parameters.

One reason behind the choice of a polynomial curve was due to the badly defined peak identified for some mega-up-faders, an example of which is shown in figure B9. Using a polynomial generally leads to a good fit to the profile of most faders at the peak end, but can also lead to the necessity for several subsequent corrections, due to the addition of mini-steps at the start and/or tail end of the fitting range, plus a mini-spike residual at the beginning of the fitting range. These added features can be easily dealt with (apart from those experience by mega-cosmic-faders), but there is clearly an associated run-time cost. Examples of the addition and correction of features introduced as a consequence of best fit subtraction, are shown in figure B10, B11 and B12. Corrections of features added by the subtraction of a best fitting function are hereafter referred to as secondary corrections.

An important factor to consider when choosing between de-glitching methods, is the addition of new features at a frequency that would not be well dealt with at the 1/f noise removal stage, such as new fader-like features. Although the polynomial fitting tends to introduce only mid-to-low frequency (i.e. tens of pixels and greater) noise, it can also introduce low significant steps. As it would be better to avoid additions of this type, alternative functions were tested to try and achieve an equally good fit whilst minimising the number of added residual features.

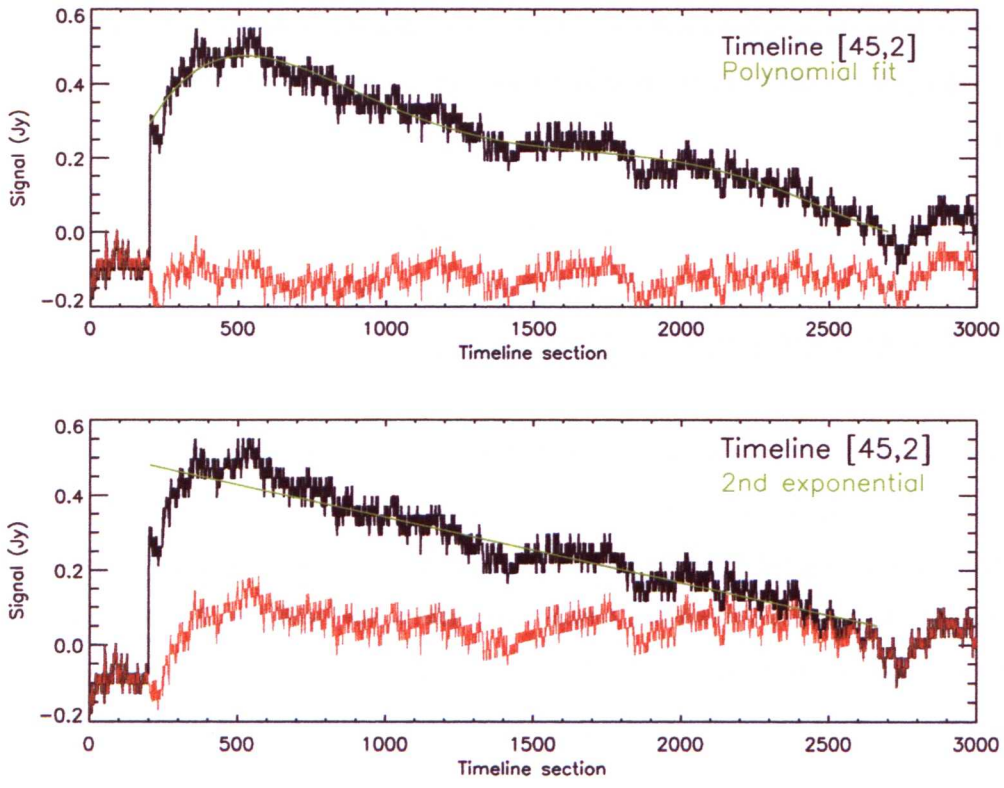

Figure B9: A mega-up-fader present in timeline [45,2] with a badly behaved peak, which does not initially decay. The results of fitting and subtracting a polynomial (top) and an exponential function (bottom). Both methods give a satisfactory result (after secondary corrections). The black line indicates the timeline section containing the feature, the green line shows the best fit and the red line the residual timeline after the fit has been subtracted and any secondary corrections have been performed. The '2nd exponential' in the right panel indicates this fit was initially rejected during an investigation into the χ^2 limit in order to allow a wide range of mega-faders (including this type) to be accepted for corrected.

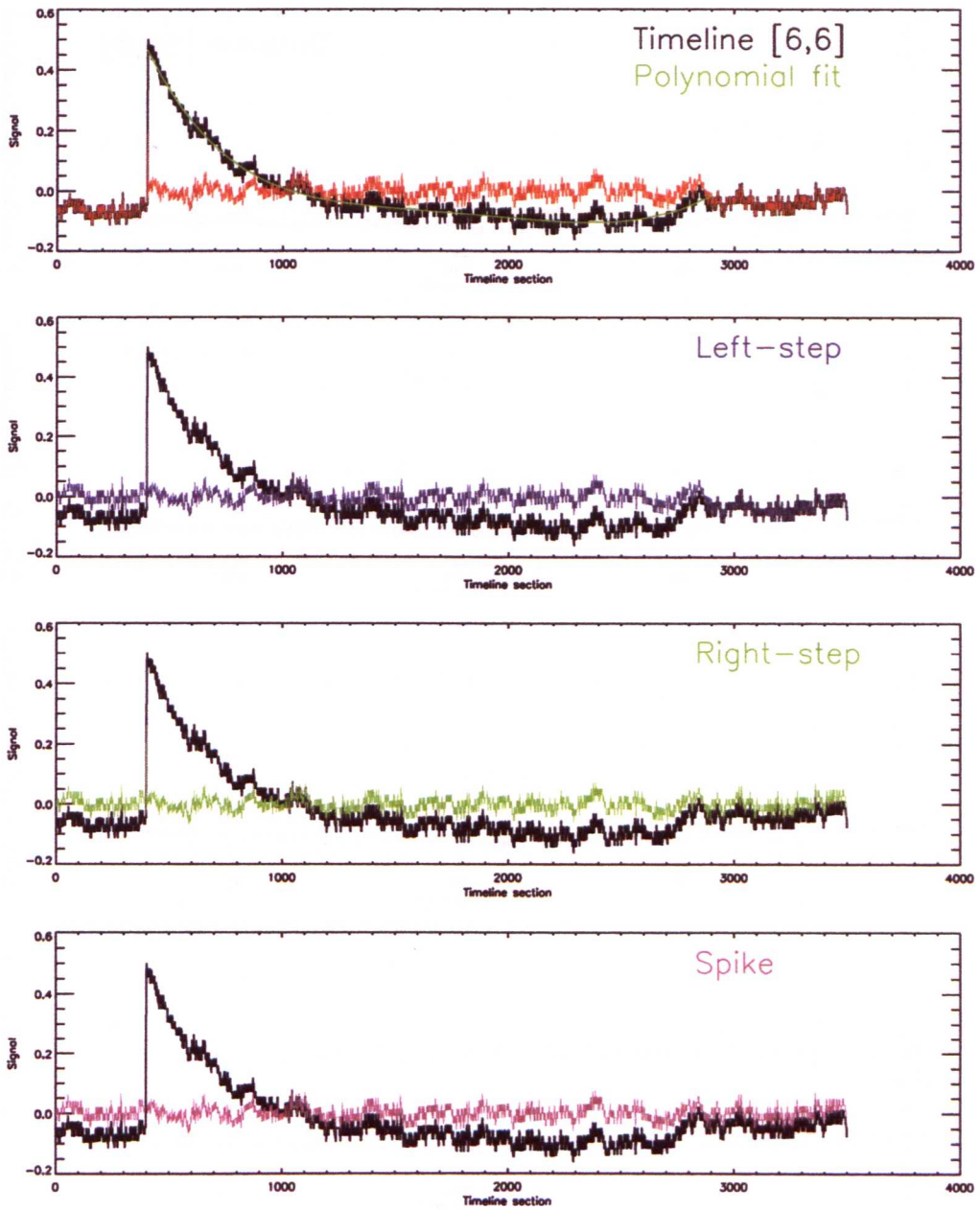

Figure B10: An example of the polynomial fitting and correction of a mega-up-fader, present in a section of timeline [6,6]. The primary subtraction of the polynomial leads to the addition of new features, at the either end of the fitting region. The top panel shows the primary fit (green line) and residual (red line), the remaining three panels illustrates the subsequent secondary corrections that were carried out, although it should be noted that the right step correction is minimal. Rarely are all three secondary corrections required, this is usually only for the mega-cosmic features (see figures B11). Fitting and subtraction the same feature with an exponential function requires no secondary corrections.

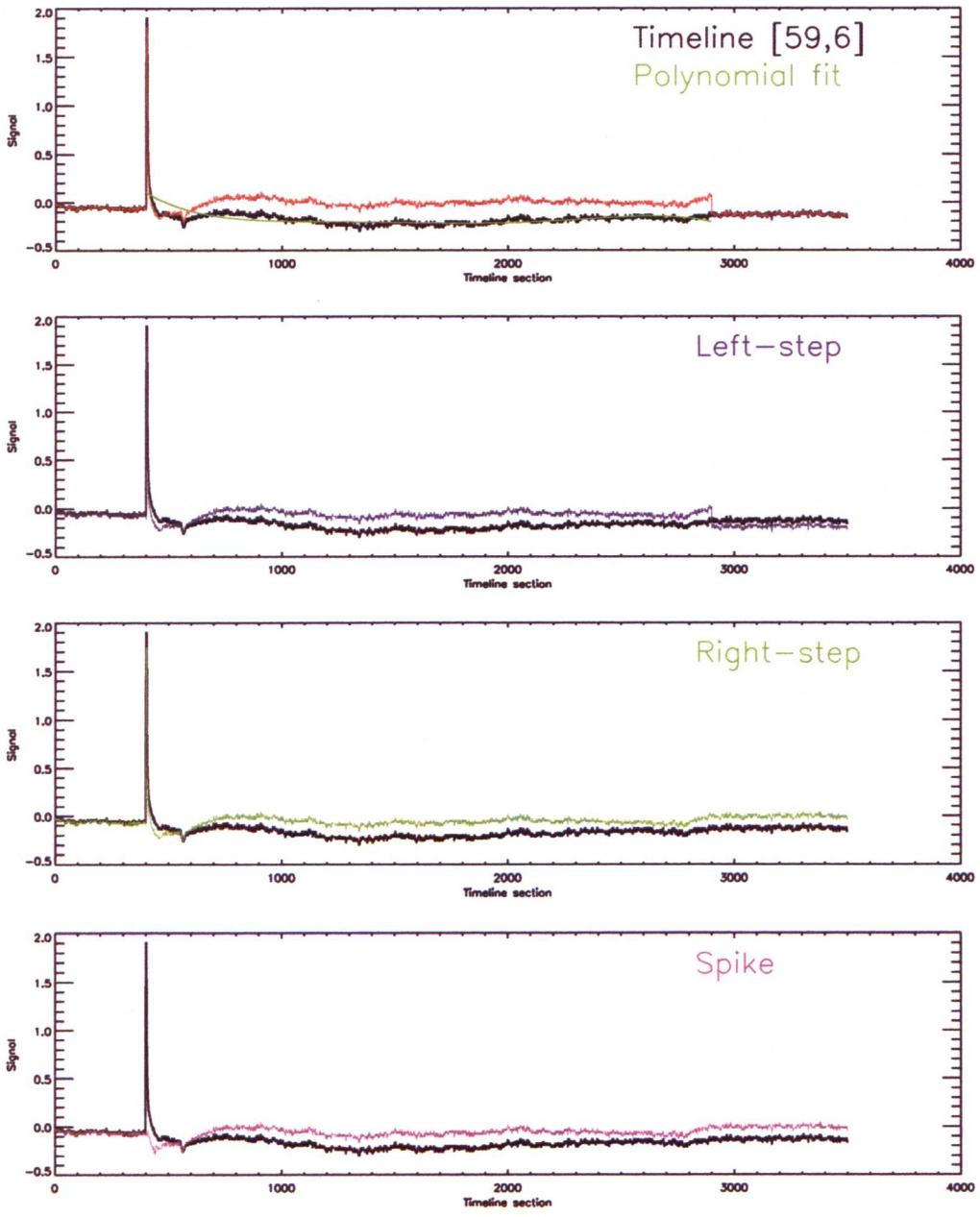

Figure B11: A section of timeline [59,6], showing the primary (top panel) and secondary (remaining panels) corrections for a mega-cosmic-fader by fitting with a polynomial. The primary fit (top; green line) is very poor and does not significantly subtract the feature. The peak is only corrected with the final secondary correction (fourth panel), although as the fit was rejected this correction was achieved by setting a short number of readouts to the local sky level. The respective residuals are shown with red (for the initial fit), blue (after the left-step secondary correction), green (after the right-step secondary correction) and pink (after the residual spike secondary correction).

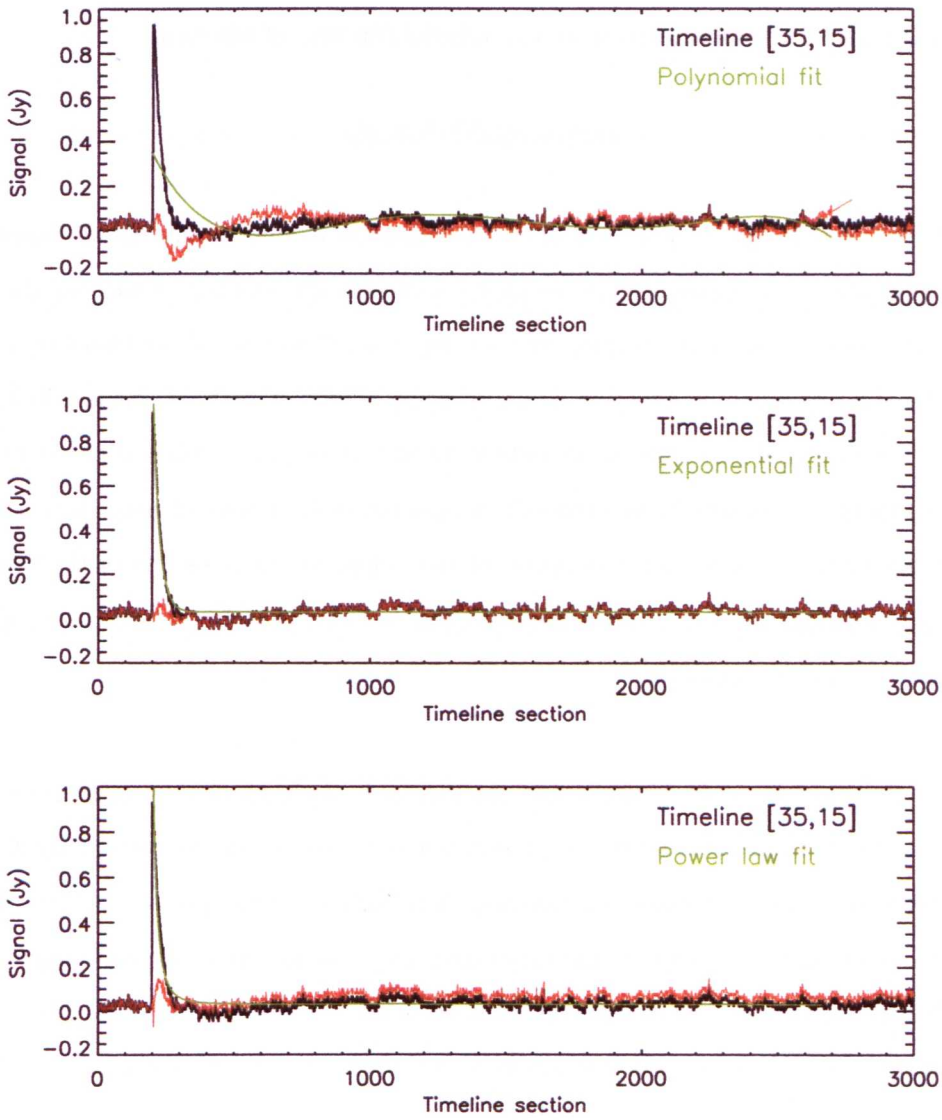

Figure B12: A section of timeline [35,15], showing the correction of a mega-cosmic-fader using 1. a polynomial fit (top). Three secondary corrections were required after the primary subtraction (top panel). 2. an exponential fit (middle panel). No secondary corrections were applied after the primary subtraction. 3. a power law (bottom panel). The addition of a step to the outlier position needed correction. For all panels the black line represents the uncorrected timeline, the green line shows the fitted function and the red line is the residual timeline after the primary best fit subtraction.

Fitting a power law to the mega-features generally led to an unsatisfactory results for all the mega-faders tested, although this can successful correct mega-cosmic-faders (see figure B12), so a third approach was applied, fitting an exponential function of the form

$$f(x) = P_0\, e^{-P_1 x} + P_2 \tag{3}$$

where P_0, P_1 and P_2 are free parameters. This function is able to address all types of mega-glitches and calibration spikes, except the most cosmic-ray-like features (which can then be dealt with using a power law or by flagging and setting a small section of the timeline to the local sky level). This exponential function deals, to some extent, with those mega-glitches that do not decay initially, but does tend to introduce significant negative spikes at the start of the fit (however this type of feature is rare and can be reasonably dealt with by secondary corrections). A secondary pass to remove any new spikes or mini-steps at the peak end of the fitting region is required, although the need for such corrections is reduced in frequency. The tail-end step correction is no longer required.

After inspecting the SDP Green timelines, a sizeable assumption that only up to one mega-up-fader and one mega-down-fader are present per pixel was made. Consequently a maximum of two mega-faders can be treated per timeline. Although this assumption holds true for the OU SDP data, it can not be ruled out that other data may contain more that two mega-faders. Indeed this was found to be the case for different versions of the same data set and so the method was extended to incorporate the correction of multiple mega-faders per timeline (detailed in section B4.2).

Figures B13 and B14 show examples of mega-fader correction with the polynomial and exponential fitting methods. Each method follows the same basic path. Again outliers are identified from the difference timeline, retaken post step correction. Only up-faders are corrected, so it is necessary to run this part of the de-glitching twice to deal with down-faders, using the inverted timeline. All outliers that correspond to negative difference timeline values are discarded and the outlier with the highest signal is then retained. A timeline section is then fitted with the

exponential function using the IDL routine MPFIT [Markwardt, 2009][1]. The goodness of the fit is assessed using the reduced χ^2 (χ^2_ν) and the curvature of the resulting model. A fit deemed acceptable it is subtracted, otherwise an alternative fitting is carried out and checked. Secondary corrections are applied to the residual of a fit if necessary. A comparison of the number of successful corrections and an examination of the residuals for each fitting function showed the exponential function gave by far the most consistent results and was therefore chosen as the primary fitting function. A power law was selected for the secondary fitting.

The fitting length needs consideration to account for the variety of different fader profile widths. Faders can range from a few hundred to a few thousand frames, but the longer the fitting length the more likely residual features will be added at the tail end. For mega-faders, the majority were selected and successfully corrected with a clipping limit of 10σ and a fitting length of 2500 readouts (this length was selected to cover the widest mega-faders with the minimum possible number of frames). To improve the number of fader features being selected, the clipping limit was sequentially reduced from 10 to 5σ. Most mega-features are identified at a 9σ or 8σ level, but this level must be lowered to 5σ to successfully catch all features in this category, for the test set of timelines. As this clipping level is being applied to the difference timeline it is a safe assumption that the low clip level avoids real sources, which will have a more gradual slope in their profile.

B3.5.2 Goodness of fit criteria

The primary fit of an exponential function to a timeline section 2500 frames in length was considered good if the returned $\chi^2_\nu < 22$. This relatively high value was set after tests showed this was the minimum to allow the full range of fader profile types, seen in the Green SDP data, to progress to the subtraction phase. In particular features with a sharp decay and, therefore, long fit tail can lead to a high χ^2_ν, despite any good agreement at the peak end. A χ^2_ν far lower than the set limit can arise when the fit has a low curvature, which is usually as a result of no feature being present. The curvature is estimated by finding the difference of the best fit model (again in terms of sequential readout differences). If the total of the curvature difference model is < 0.2 or the $\chi^2_\nu < 22$, the fit is classed as bad, the alternate fitting stage is invoked and

[1] MPFIT was developed by C. Markwardt and can be downloaded via `http://purl.com/net/mpfit`.

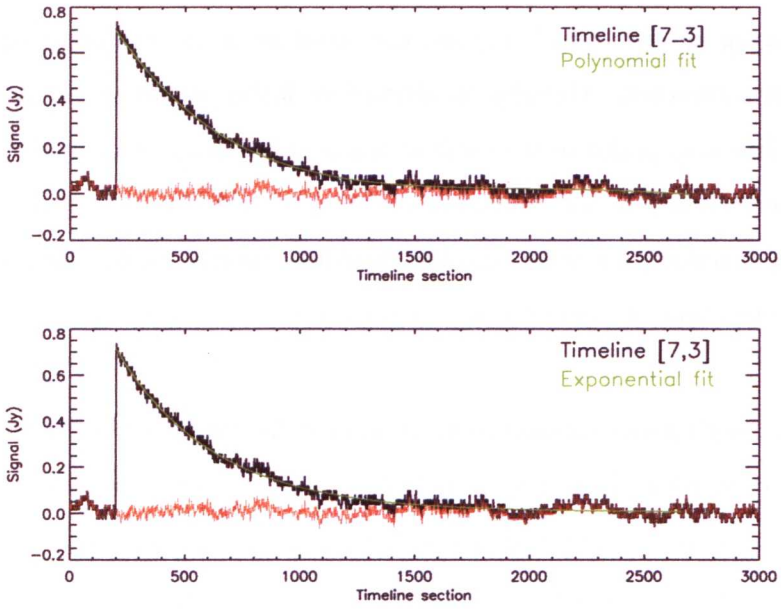

Figure B13: A section of timeline [7,3] (black lines) with a well behaved mega-up-fader that was subtracted using a polynomial (top; green line) and also an exponential fit (bottom; green line). Both methods give a clean subtraction (red lines).

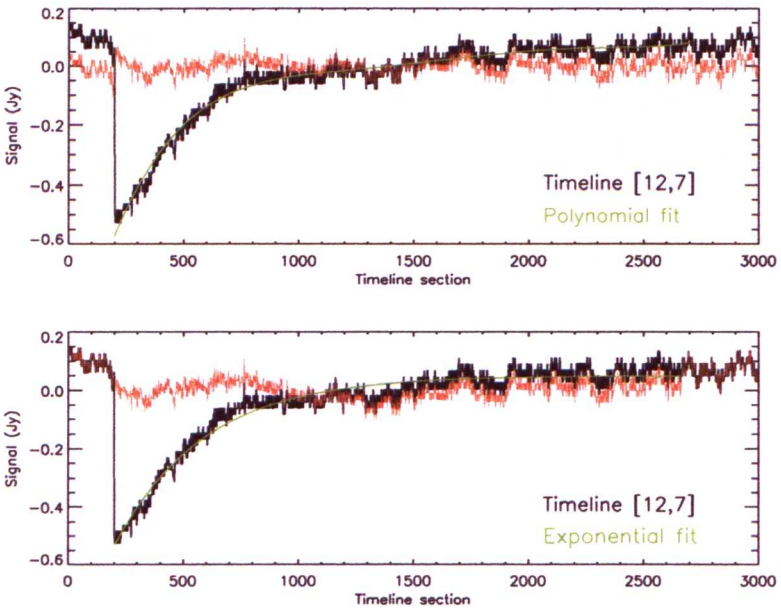

Figure B14: A section of timeline [12,7] (black line) with a mega-down-fader that has been corrected with a polynomial (top; green line) and an exponential fit (bottom; green line), where the residual is represented by the redline. After the polynomial fit subtraction, secondary corrections for an introduced left step followed by an introduced right step were performed. The residual on the left shows the left step was not completely corrected for the polynomial fit.

an alternative power law fitting is performed. Otherwise, for a fit classed as good, the best fit model is subtracted and secondary corrections are carried out as follows. A check is performed to look for steps added to the beginning of the fitting region. This is performed, as before, by comparing the median sky levels either side of the outlier position, however the number of frames used to calculate the median values is reduced to 500. A detected step is corrected using the usual median subtraction method. A local difference timeline is then taken around the same outlying positing to check for residual faders. An exponential (of length 50 frames) is fitted if an outlier is found, and the fit is accepted if the $\chi^2_\nu < 20$ and the curvature is > 0.01 (the curvature is substantially reduced to account for the shorter fitting length).

B3.5.3 Alternative fitting method

It is at this point that a power law is fitted if an outlier has been identified, but not yet qualified for correction. The same fitting length (of 50 frames) and goodness of fit criteria as the secondary corrections were used. The power law fit is subtracted from the timeline if deemed a good fit and five frames at the position of the outlier are set to the local sky level. If this fit is rejected, a section of 13 frames are then set to the local median sky level. Whenever a section of the timeline is set to the local sky value (either around the starting point of the best fit or around the outlier, if no good fit is achieved), random noise is added just below the level of timeline RMS. This is to avoid biasing the subsequent noise estimates and 1D filtering. A value of 0.8 RMS is chosen to compensate for using non-digitised noise. Even when a fit is deemed good, a few frames are set to the local median sky value, which takes into consideration the possible difference in starting point of the fit with respect to the initial outlier position.

B3.5.4 Secondary corrections

The Secondary corrections necessary after a subtraction at either the exponential fitting stage or the subsequent power law fitting stage, are dealt with in the order of left-step and then residual spike. The mini-steps are removed similarly to major-steps, but on a more local scale (in terms of lengths use to calculate the sky medians). Any new step is (necessarily) introduced at the start position of the fitting region, and therefore the correction begins at the second median difference check stage. The difference in the local median sky, calculated from two 100 length timeline strips before and after the starting fit position, is required to be $> 3\sigma$ above the time-

line RMS in order to qualify for correction. The step correction then proceeds as with the main step-features. For the secondary residual spike correction, a local difference timeline is taken for a strip of 99 readouts, centred on the initial peak. If an outlying point is identified above 4σ within 20 readouts, either side of the peak centre, a correction is deemed necessary. The outlier is identified as positive or negative and then corrected with an exponential fit, using a shorter fitting length of 40 frames. If the exponential best fit has a χ^2_ν >20 or total difference of <0.01 then a power law function is fitted. If the power law fit does not pass the goodness of fit conditions a strip of length 15 is set to the local sky value. If the fit of either the exponential or the power law was successful then the best fit model is subtracted and a section of six readouts (around the outlying position) is set to the local sky value. Mega-down-faders are corrected for in exactly the same way as mega-up-faders, after temporary inversion of the respective timeline.

B3.6 Calibration spikes

For the H-ATLAS SDP PACS data there are nine positions per timeline where calibration block spike residuals can occur (figure B15). These positions are encoded into the data cube, but not in a way IDL can easily decipher. It is straightforward to identify these positions by summing the timelines across the spatial axes and taking the nine most outlying points as the spike set positions. The first position for the Green data is at around frame 40, and is excluded from the calibration spike set that are corrected at this stage, however if there is a significant feature at this position it is generally corrected as a step or a fader. Initially the calibration spikes were addressed after the fader-correction to avoid possible confusion between less prominent mega-faders and the calibration spikes present and in a similar manner, however this part of the de-glitching now occurs between the temporary sky subtraction and the fader de-glitching to avoid possible confusion between less prominent mega-faders and the calibration spikes present. The main aim of each de-glitching stage is to retain as much usable data as possible and so the possibility of a using a fitting method was initially explored and although not applied in the IDL de-glitching was incorporated during the HIPE de-glitching performed for the OU data (see section B5).

A search for outliers within the difference timeline, near to the known spike positions (within

10 frames), was used to identify whether the timeline contains a notable calibration spike set, and if so, precisely where each spike starts (noting that there is little change in starting positions between timelines of any given scan). Figure B16 shows an 'ideal' example of the profiles of a calibration-up-spike set, with a short flat peak and a rapid decay. Theoretically in this ideal situation the only data that needs to be removed is the plateau. The start and end points of the plateau, which broadens the peak, can be identified from the difference timeline. A sharp rise and fall either end of such a plateau leads to a pair of peaks in the difference timeline (one positive and a smaller negative one), which define the plateau width. Although this type of profile can be easily corrected for by removing the data corresponding the to plateau and fitting the decay with either an exponential or power law, it is also not a common case for spike sets. In fact a range of significance, shapes and widths, with and without plateaux are seen over the full Green data set. When testing the fitting method of correction, if no good fit (in this case defined totally by the curvature) was found then several frames at the calibration-spike position were set to the local sky level around the start position. Figure B16 illustrates that for the ideal case, the calibration spikes can be modelled and subtracted, with only a minimum number of frames lost, i.e. set to random noise at the level of the local sky.

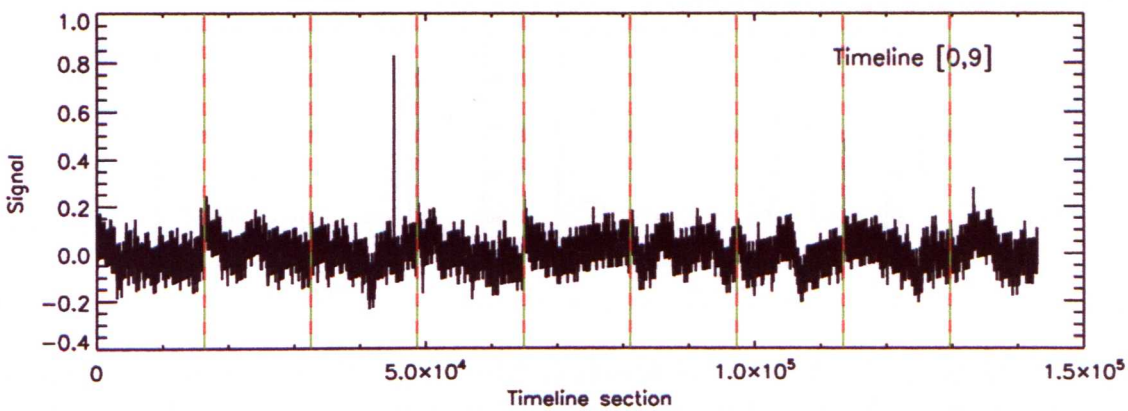

Figure B15: Calibration spike positions are shown with red lines. The Green dashed lines show the positions identified by looking for peaks in the difference map around the known positions. Note that peaks lying away from the known positions are ignored, as is the first calibration residual position at frame 40.

After considering the varying nature of the spike sets throughout the Green data and the difficulty of consistent correction without the introduction of residual features with respect to

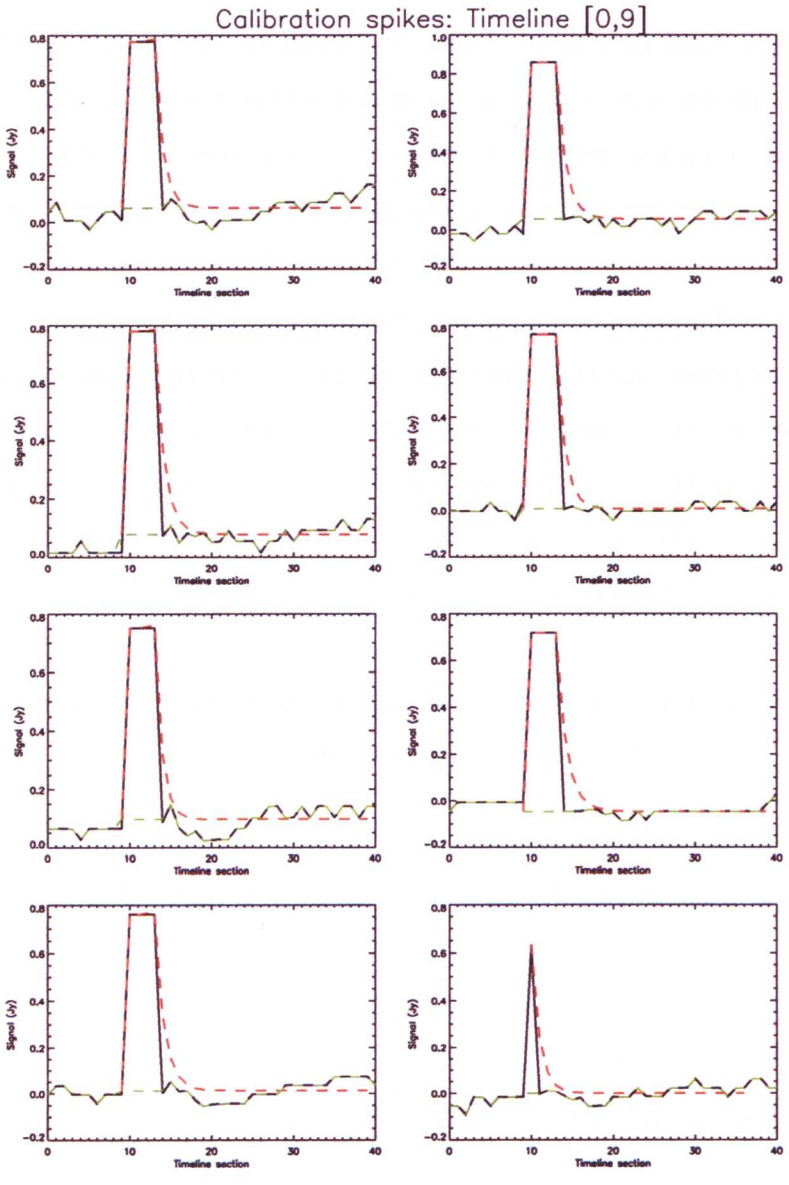

Figure B16: Sections of timeline [0,9] showing an 'ideal' set of calibration-up-spikes. The plateau for each peak can be defined by looking for a close peak and trough in the corresponding difference timeline. An exponential function may then be fitted from the end frame of the plateau. if the fit is not acceptable a power law is fitted. If a good fit is achieved then the length of the defined plateau is set to the local sky level and the best fit is subtracted. The black line shows the uncorrected timeline, the red dashed line shows the spike model and the Green dashed line shows the corrected timeline. For this ideal case the feature correction works well, however most calibration spikes sets are less well defined. See figure B17 for the correction of timeline [0,9] using the simple method.

the potential quantity of data that could be recovered, this method was abandoned in favour of a more simple approach.

During the examination of each Green timelines, the majority (or possibly all) exhibited some level of calibration spike features. Therefore, prior to mega-fader correction the known calibration spike positions are used to define a timeline strip at each of the nine set positions, 44 readouts in length with 3 frames prior to the spike start. The gradient between the end positions of each strip (over the spike regions) are then used to fit these parts of the timeline with straight lines. Finally random noise at the RMS level of the timeline is added to each fitted slope. The strip length was the minimum found to deal will all the spikes tested. Figures B17, B18 and B19 show examples of timeline calibration spike sets before and after this removal method has been applied.

B3.7 Testing HIPE

All the IDL based de-glitching procedures discussed so far have the potential to be converted to Jython and run within HIPE. To illustrate this point the IDL de-step routine was converted to a Jython script and then applied to simulated timelines within HIPE. The results (see figure B20) showed that the de-stepping is equally successful. This conversion was straightforward as there are some similarities between IDL and Jython syntax, and illustrates it would be possible to achieve the IDL de-glitching with Jython based scripts within the HIPE environment.

B3.8 IDL de-glitching results

An example timeline ([0,10]) before and after IDL de-glitching is shown in figure B21. Present in [0,10] is a mega-up-fader and noticeable calibration spikes, but in order to demonstrate each stage of the de-glitching plan for a single timeline, an artificial step was introduced between the sixth and seventh spike. The 'after' timeline shows that all glitches have been successfully removed. Before progressing to the 1D filtering stage of the IDL pipeline, the polynomial sky is added back. The remaining sky structure noticeable in the 'after' timeline is then addressed during the 1/f noise removal. Postage stamp images of the IDL pipeline filtered SNR Green map product (single scan), with and without the IDL de-glitching applied, are shown in figure B22. There is a clear improvement in the de-glitched data for the examples shown. These incidences

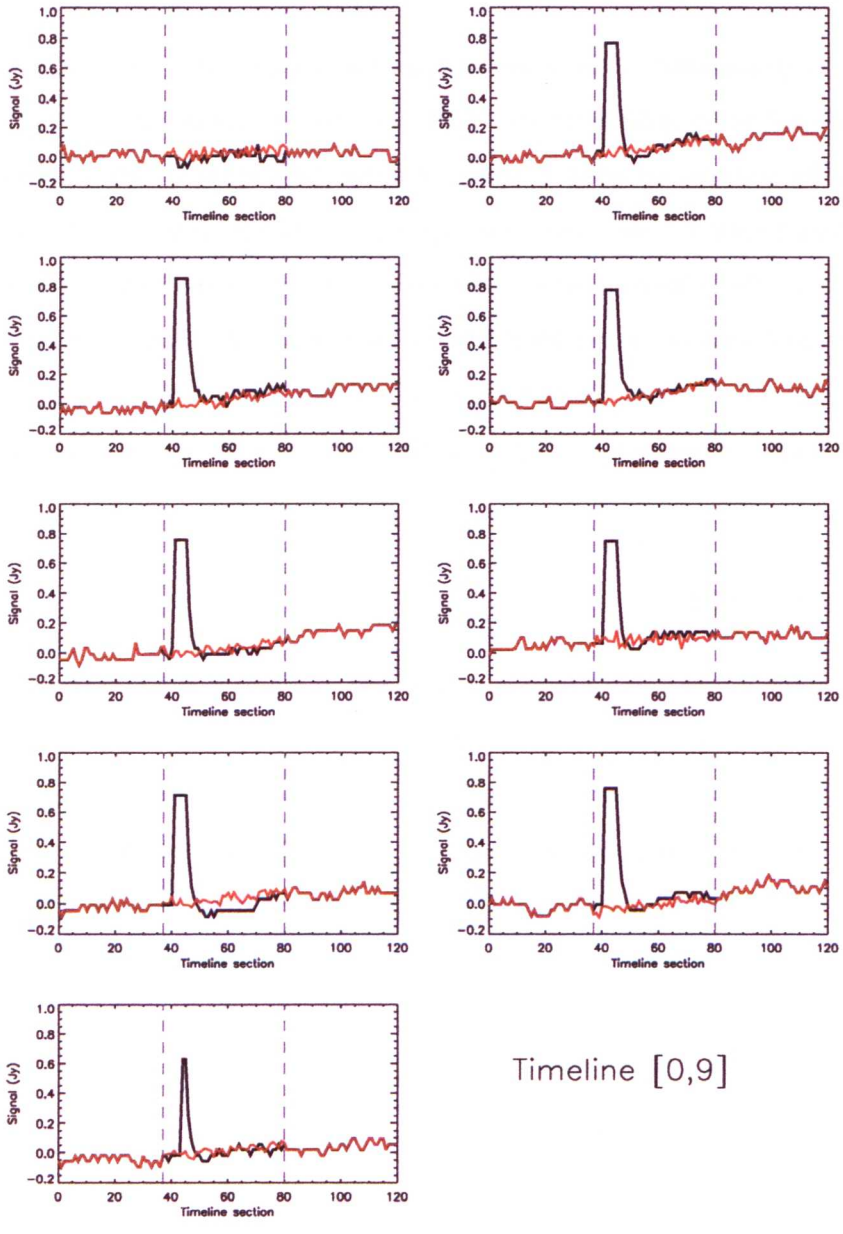

Figure B17: Sections of timeline [0,9] corrected with the strip replacement method. The black line shows the timeline section, the redline shows the corrected timeline section and the blue dashed lines indicate the region over which the correction took place. For this 'ideal' spike-set case, up to 30 readouts of potentially usable data are lost. See figure B17 for the correction to the calibration spikes for this timeline using the fitting method and figures B18 and B19 for the correction of less than ideal calibration spike set cases.

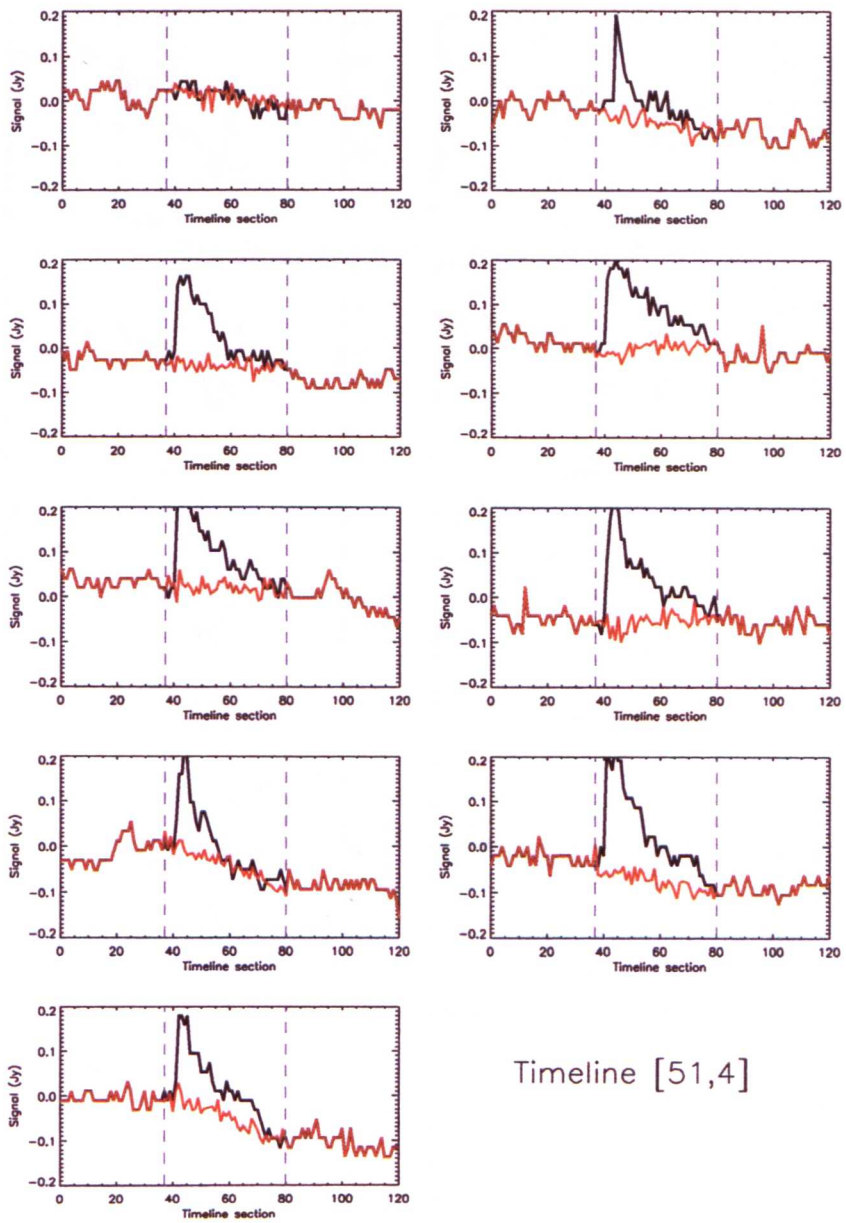

Figure B18: Sections of timeline [51,4] showing the non-'ideal' set of calibration-up-spikes. There is no well defined plateau and the features vary in significance and profile. The black line shows the timeline section, the redline shows the corrected timeline section and the blue dashed lines indicate the region over which the correction took place.

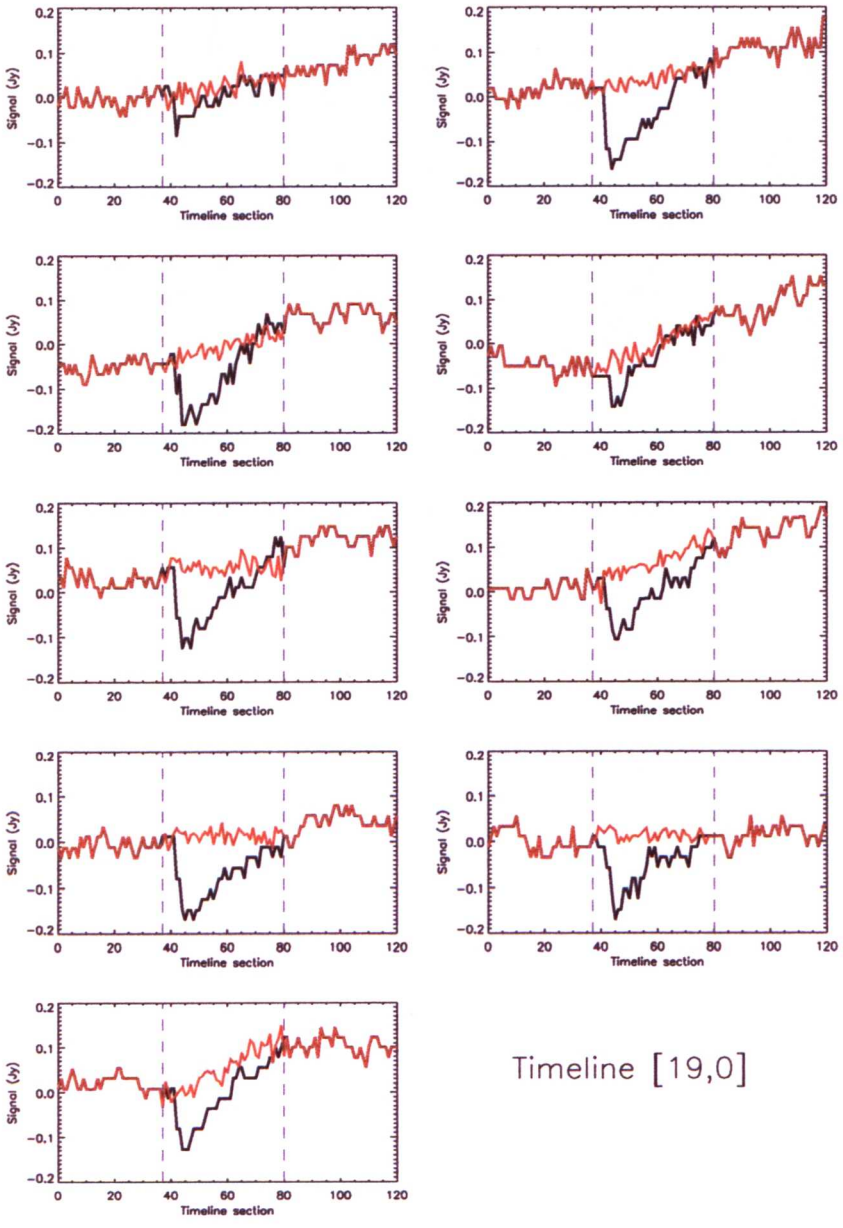

Figure B19: A non-'ideal' set of calibration-down-spikes present in timeline [19,0]. The width of data replaced is just adequate to remove the features. The black line shows the timeline section, the redline shows the corrected timeline section and the blue dashed lines indicate the region over which the correction took place.

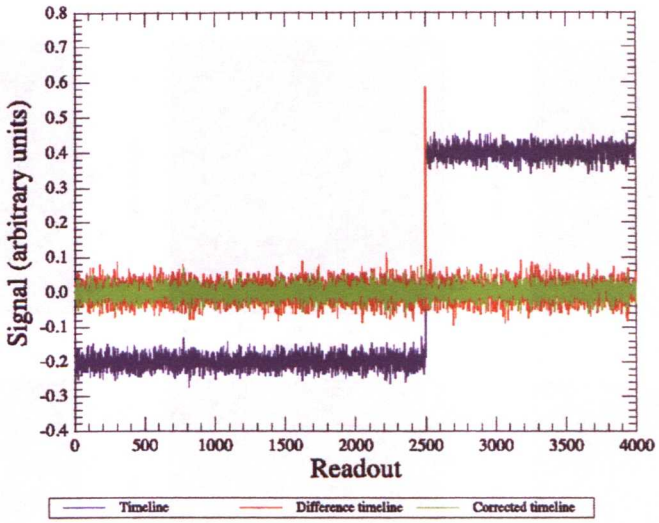

Figure B20: A simulated timeline section, with an added step and background noise. The Jython conversion of the IDL de-step routine was applied to successfully correct the step. The blue line shows the simulated timeline section, the red line shows the associated difference timeline and the red line gives the corrected timeline.

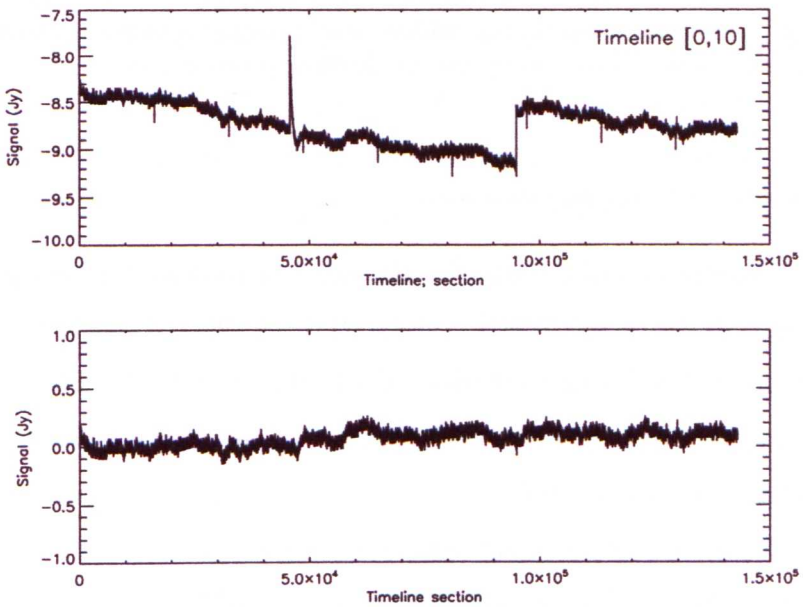

Figure B21: Timeline [0,10] before (top) and after (bottom) de-glitching. An artificial step was added, before any corrections, so that all four stages of de-glitching could be represented. The mid-frequency sky structure (i.e. not of the scale of the corrected features or 1/f noise) is still noticeable within the 'after' version of the timeline, however this is something that is addressed at the 1D filtering stage.

of noise, if left uncorrected, lead to many spurious detections and the masking of real sources.

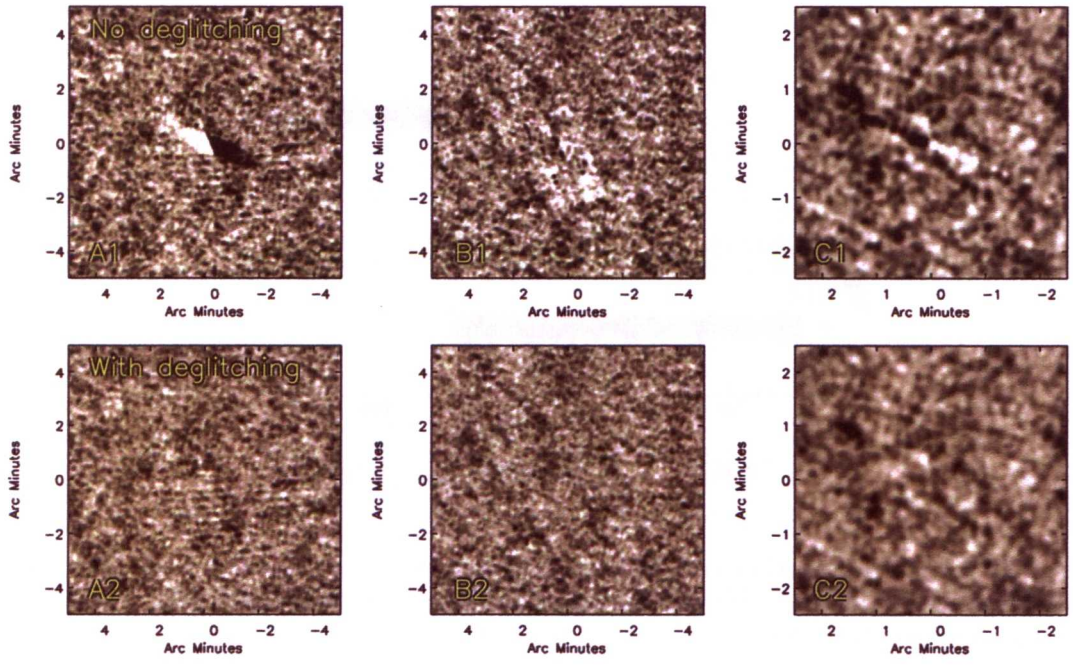

Figure B22: Postage stamps of the filtered SNR maps for one Green SDP scan. The stamps of the map reduced with no de-glitching (top row) show examples of noise relating to mega-up-faders (top left), calibration spikes (top middle) and possibly a mega-down-fader (top right). Each noise example is well corrected by the de-glitching (bottom row).

B3.8.1 Post de-glitching pipeline tasks

The OU PACS pipeline's focus is towards point-source extraction. For data with uniform sky noise convolving with the intrinsic PSF provides an optimally filtered map [e.g. Eales et al., 2000]. For data with non-uniform background noise, such as the Green PACS data, a χ^2 minimisation for each pixel can be achieved by performing a noise weighted convolution ($\otimes$) with the zero-footprint map and the intrinsic PSF [Serjeant et al., 2003]. The product is a map where each pixel represents the minimum χ^2 point source flux density or 'best fit flux'. The following formulae can be applied in 1D or 2D with the appropriate kernel (K)

$$S_{BFF} = \frac{\frac{S}{\sigma^2} \otimes \mathrm{K}}{\frac{1}{\sigma^2} \otimes \mathrm{K}^2} \tag{4}$$

The corresponding noise is found as

$$\sigma_{BFF} = \frac{1}{\sqrt{\frac{1}{\sigma^2} \otimes \mathrm{K}^2}} \tag{5}$$

and therefore the SNR as

$$SNR = \frac{\frac{S}{\sigma^2} \otimes \mathrm{K}}{\sqrt{\frac{1}{\sigma^2} \otimes \mathrm{K}^2}} \tag{6}$$

where S_{BFF} is the best fit flux density and σ_{BFF} is the corresponding noise. Sources can be optimally extracted from the resulting SNR map and for each source the pixel value at the corresponding position in the best fit flux map gives the full flux density (as each pixel represents the total of the best fit PSF). This method assumes the sources are point-like (i.e. not spatially resolved) and free from confusion. For the PACS data these are reasonable assumptions.

Prior to de-glitching the pipeline accesses the necessary data - timeline, RA and Dec images, and then creates a blank 2D sky-array array to be filled with the 1D timelines after de-glitching and 1/f noise removal. The dimensions of the sky-array are set using the RA and Dec images, from which a basic astrometry can be created to form a corresponding fits header. The next stage is to estimate the RMS per pixel, where one pixel corresponds to the xy-position of one timeline. The RMS is derived from the standard deviation of the difference timeline after clipping outliers above and below the 99st and 1st percentiles, respectively. There are several flat timeline, which correspond to bad pixels, giving zero sum difference timelines and these are flagged by assigning a high noise. The resulting noise array has the same dimensions as the timeline image, but is constant along the temporal axes, before any further frames are flagged. Once the noise array has been created the de-glitching is carried out, as detailed above, and in the order of removing steps, temporary sky-subtraction, correcting for spikes, addressing faders (up-faders followed by down faders) after which the noise array is re-estimated and the temporary sky is added back. There are several post de-glitching steps to produce the final 2D data product.

Firstly the 1/f noise needs to be removed, which is achieved via modelling and subtracting the sky. A 1D convolution of the timeline is performed, using equations 4 and 5. This is the

equivalent of smoothing the data on a scale set by the 1D Gaussian kernel width. It is usual when filtering data to use a kernel width $\gtrsim 3 \times$ FWHM the PSF to avoid structure on the scale of the PSF remaining in the smoothed image, which would then remove source flux on its subtraction from the data (see chapter 3). To allow the use of a kernel with smaller width, a technique developed for radio astronomy and referred to as beam-switching is applied [Kraus, 1966]. The beam-switching mimics a Mexican Hat or Vio filter [Vio et al., 2002]. All real sources within the data are assumed point-like and have the same characteristic PSF that is approximately symmetrical along the scan direction, and it is this information that is key to the beam-switching.

The most basic beam-switch method for one timeline would involve taking the mean of two frame values separated by a width (w) and subtracting this mean at the mid-point between the pixels, then repeating for each pair of pixel along the timeline. As a Gaussian kernel is convolved the timeline, so results in each frame representing the total of the best fit estimate of the Gaussian kernel at that position. The timeline is then beam-switched by shifting a copy of itself by w and finding the mean of the resulting timeline copy and the untranslated timeline. A copy of the noise timeline undergoes the same shift and is then added in quadrature to the untranslated noise. This gives a sky-timeline and corresponding sky-noise timeline. The frames within one width of the sky-timeline ends are flagged at the corresponding frames in the noise image. Subtraction of the sky-timeline removes all low frequency noise, but also higher frequency structure as well. This is where the symmetry of the PSF comes into play. Figures B23 and B24 shows an example of the results of beam-switching on an ideal timeline (one with zero shot and confusion noise). As shown in the figures, beam-switching introduces negative side lobes that change the profile of the PSF, but not the symmetry. This change applies to all point sources present in the map, but does not produce such an affect for noise as this tends to be asymmetric. An appropriate filter needs to be chosen to recover the flux density and/or a flux correction derived by applying the same reduction technique to a calibration source.

A preliminary investigation into the choice of the convolution kernel width and beam-switch width was carried out by adding artificial 1D sources to the single timelines. The result agreed with figures B23 and B24 that the wider the beam-switching width the less source is subtracted,

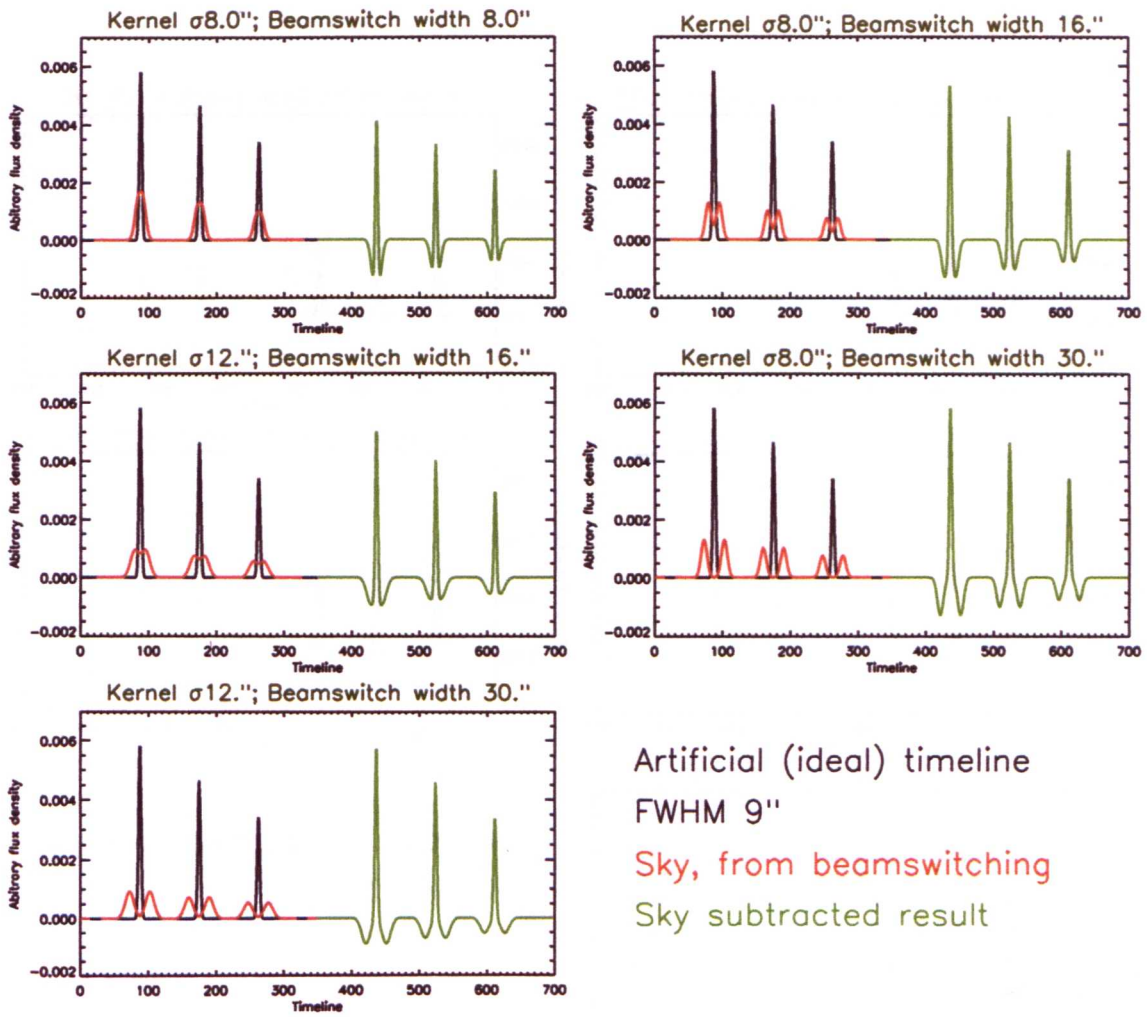

Figure B23: Beam-switching performed on an ideal timeline that contains only source flux. Three artificial sources with a 9″ FWHM [Ibar et al., 2010], treated with the same 1D filtering/beam-switching technique used for the real data and then subtracted from the ideal timeline. The Kernel width and beam-switched width were varied for comparison. The source peak is preserved for a kernel width $\gtrsim$ twice the FWHM. The choice of width for the real data needs to take into account the σ of the SNR histogram of the resulting 2D filtered maps.

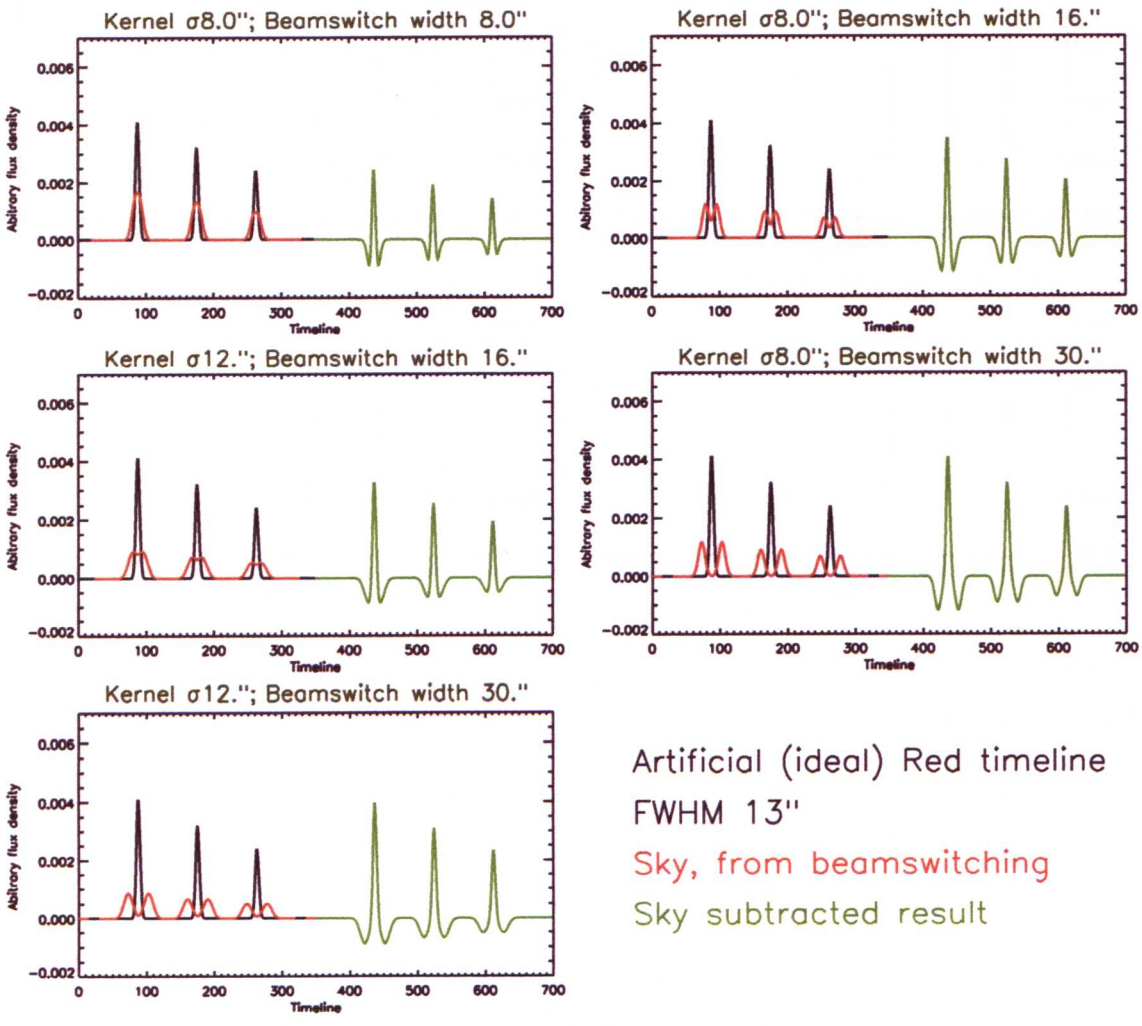

Figure B24: As figure B23, but for the PACS Red data. The profile of the PSF is changed by the beam-switching, but the symmetry is preserved.

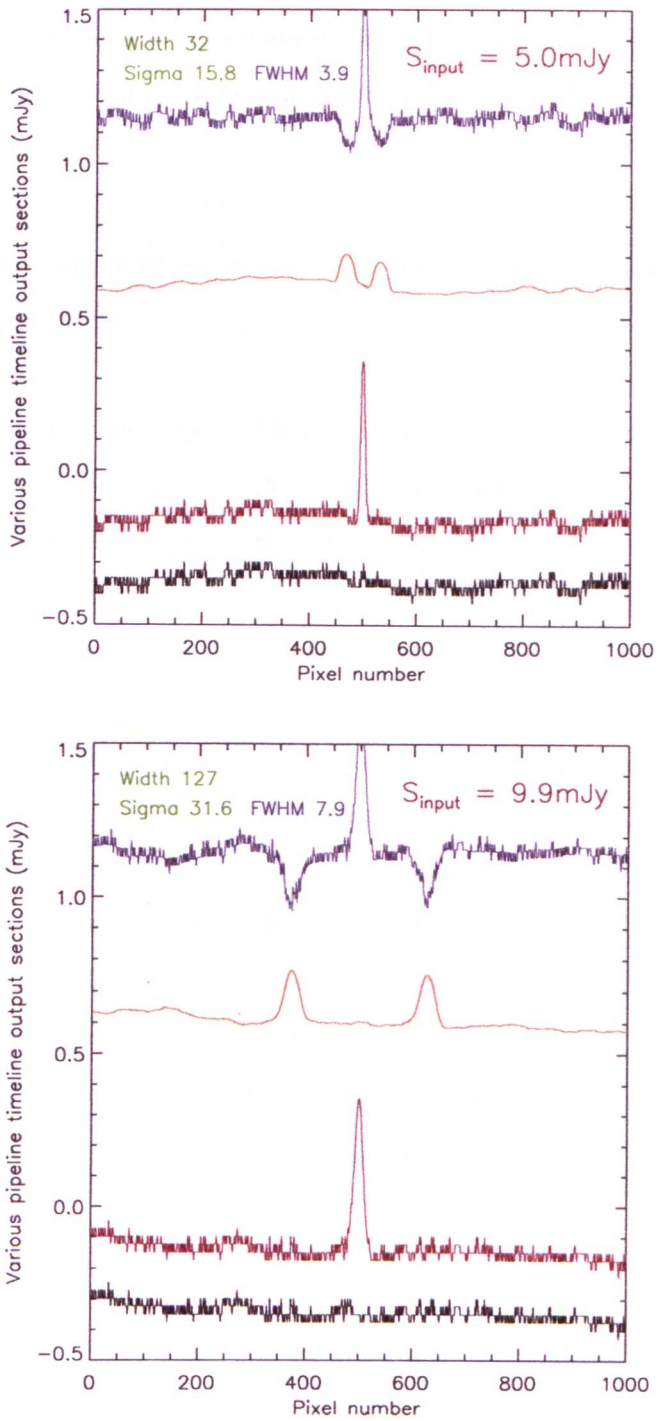

Figure B25: Real timeline sections (black) with an added point source (maroon) are filtered (red) and then beam-switched (blue), the timeline sections are offset for clarity. The FWHM of the added source is 8″ (top) and 19″ (bottom). For a beam-switch width substantially > the kernel FWHM, the source flux is completely preserved, but the negative side lobes separate from the main PSF and the 1/f noise is not completely removed (bottom).

however for a width several times larger than the kernel width the negative side lobes becoming disassociated with the source and the 1/f noise is not completely removed (figure B25). A kernel width of twice the FWHM gives a good compromise between preserving source flux and noise removal.

After 1/f removal the sky-subtracted 1D timelines are projected onto the 2D array, constructed at the start of the pipeline, and a noise-weighted co-addition is performed to give the zero-footprint signal and noise maps. The final pipeline stage is matched filtering using a 2D Gaussian filter, which is by default set to the FWHM, based on the resolution of the detector. This FWHM (7″) underestimates the PSF of the raw timelines, which is affected by the *Herschel* scan speed. Due to the sampling rate the PSF is elongated along the scan direction and estimated to be $\sim 9''$ for the Green and $\sim 12''$ for the Red data [Ibar et al., 2010]. However after the beam-switching the PSF will be narrower, with negative side lobes. An empirical PSF was constructed from the zero-footprint signal map and fitted with elliptical profiles (see figures B26 and B27). The central profile fitted to the positive component gave an FWHM estimate of 4.9″ and 3.3″, showing a significant reduction in the estimated raw FWHM corresponding to the scan direction. An initial investigation into the combined effects of the 1D and 2D filter kernel widths and the beam-switched widths, showed that for a circular 2D Gaussian filter the noise of the filtered SNR map was a substantially increased ($> 2\times$) for a 1D kernel width and beam-switch width of 14″ and a 2D kernel width of 9″. After varying all three quantities the results were inconclusive and therefore suggest a circular 2D Gaussian is not able to optimise the filtering. A more in-depth investigation into filter shape is required, including the use of the empirical PSF.

B3.8.2 Results and future work

The four point IDL de-glitching approach was derived to address the artefacts seen in the PACS Green data. All de-glitching stages have been successfully implemented into the OU PACS pipeline and checked for effectiveness (i.e. how well the feature is removed against the recovery/loss of data).

An optimally filtered 2D SNR map is expected to have a pixel distribution with a variance

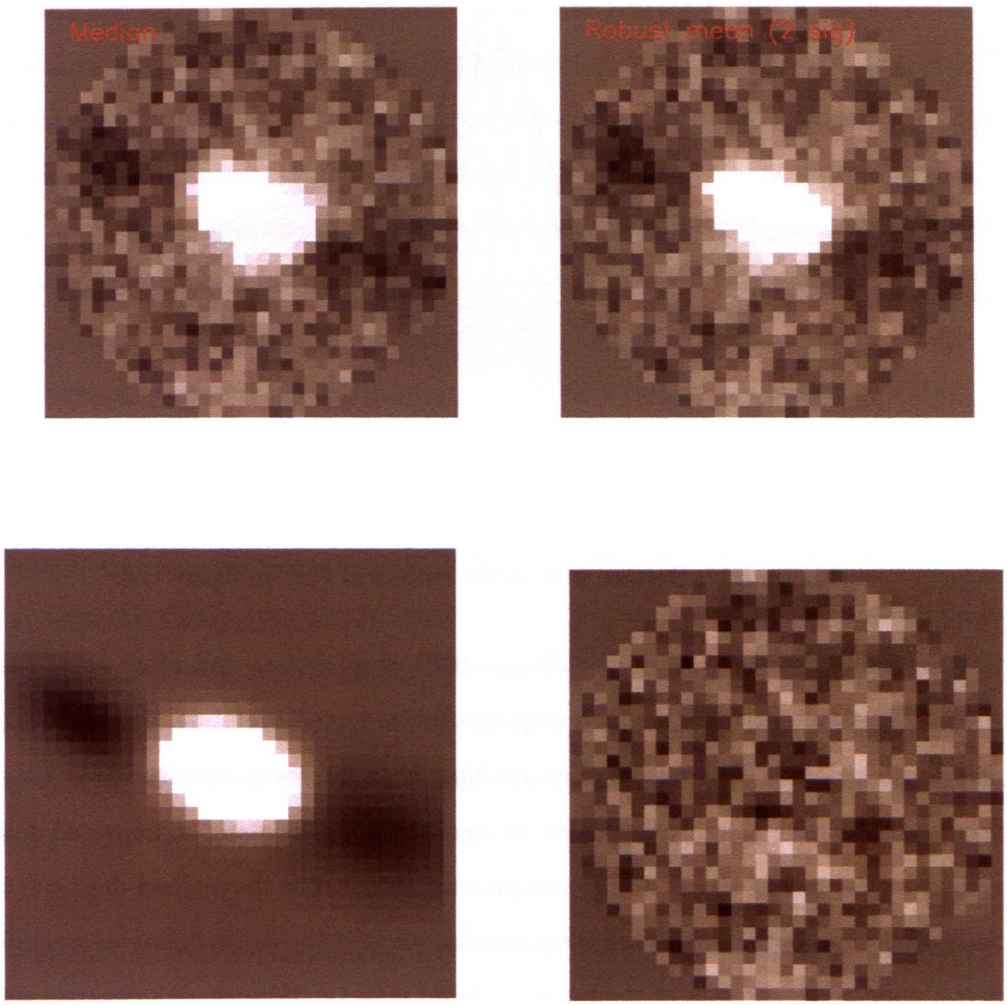

Figure B26: PACS Green empirical PSF constructed from the zero footprint map for one SDP scan, with a median combine (top left) and a robust mean (top right). The PSF was modelled with three profiles (bottom left) and the subtracted residual is shown bottom right. The PSF has negative side lobes introduced by the beam-switching.

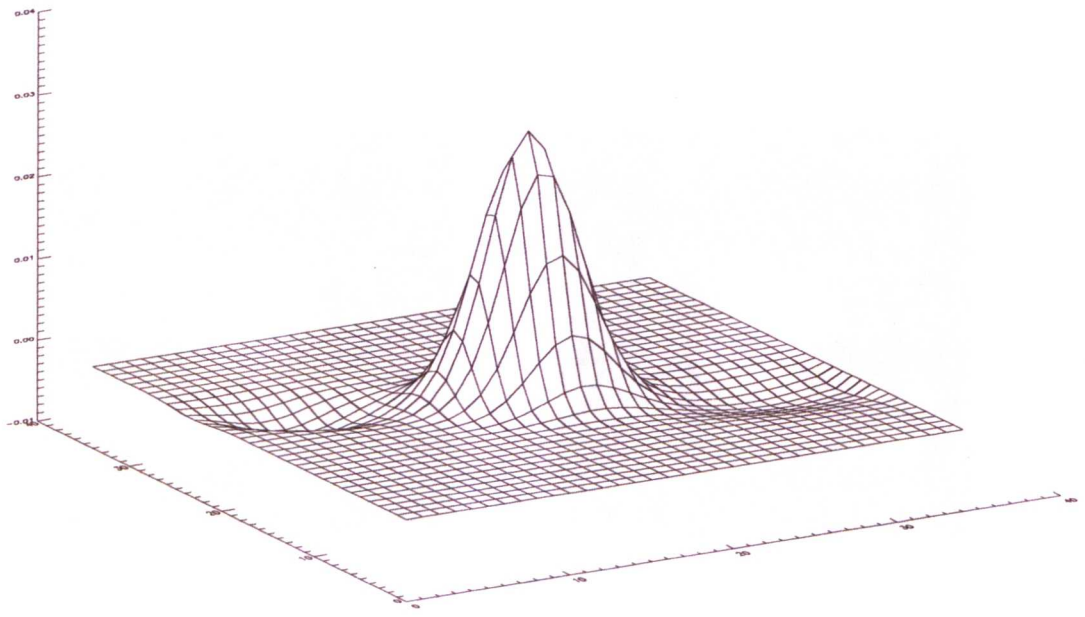

Figure B27: Surface plot of the empirical PSF in figure B26

of 1. Pixel value distributions of the filtered SNR map, before and after deglitching, were fitted with Gaussian curves. The noise map sees an improved σ of 1.65, compared to 1.82 for the non-deglitched data. The results of de-glitching is an improved noise estimate although the variance is still far from 1, indicating either an incorrect noise estimate, an improved de-glitching is required or the loss of signal during the pipeline steps. The de-glitched data will facilitate the derivation of an optimal matched filter and has allowed the constructing an empirical PSF, which is a good representative of the beam-switched map i.e. thinner with negative side lobes.

B4 De-glitching with Jython

B4.1 The official H-ATLAS PACS pipeline

After circulating details on the OU IDL pipeline de-glitching methods, to the H-ATLAS data-reduction working group, I was invited to convert the IDL code to Jython, to be integrated into the official H-ATLAS PACS pipeline [Ibar et al., 2010].

The Herschel Interactive Pipeline Environment (HIPE) is a JAVA based tool that has been developed for processing *Herschel* PACS and SPIRE imaging and spectroscopic data. As the name suggests HIPE is an interactive programming environment (similar in style to Eclipse), for the purpose of retrieving data from the Herschel archive and running it through the appropriate HIPE pipeline, or applying user written code. Although HIPE was developed in JAVA it also has Jython capability. Jython is the Java/Python interlink language, incorporating most of the user friendly Python features, whilst being compatible in a JAVA environment. Care must be taken when writing Jython code for use with HIPE, due to HIPE's incomplete Jython capabilities, so it is advisable to write within the JIDE environment using available HIPE specific functions, where possible. Although Jython shares some similar syntax with IDL, making the conversion reasonable straightforward, Jython is case sensitive and encourages an object oriented approach to programming. HIPE was primarily designed for reducing pointed and small area observations, rather than wide-area surveys such as H-ATLAS. Consequentially HIPE has a potentially prohibitive memory usage for such large data sets. For example, to process a single Green H-ATLAS scan can require up to 60GB of memory. To facilitate fast and memory efficient testing, the PACS data was split into individual timeline, which could then be loaded into HIPE either in groups or individually (this method of testing was also applied for the IDL de-glitching). Initial tests, performed whilst converting and developing the de-glitching, were carried out solely on Green PACS data, with additional Red testing after the conversion was complete.

The official H-ATLAS PACS pipeline was developed in-house by the H-ATLAS data reduction team [Ibar et al., 2010]. The main steps of the pipeline (as it stands at the time of writing, however it continues to be developed and optimised) from level 0 are as follows. Calibration blocks are remove, with an increased number of frames flagged per block with respect to the default number (as is implemented with the OU version of the data). An extra 15 seconds are removed, which at fast scan speeds translates to 75 frames for the Green data and 150 for the Red. Any bad or saturated pixels are masked before converting the frame signal from ADUs to Volts, and then to units of flux density (Jy). MMT de-glitching is the standard HIPE level 1 de-glitching applied in the pipeline, this uses wavelet filtering [Starck & Murtagh, 1998] to flag single frame events, such as cosmic rays, and can differentiate between single frame glitches

and real signal – except in fast scan mode and for bright compact sources such as quasars. Therefore to avoid potential cropping of real source flux the first transformation from level0 to level1 data is carried out without applying the MMT de-glitching. Instead the data is projected straight to 2D, followed by a comparison between the cross scans to identify sources ($> 3\sigma$). As the cross scans are taken with a near 90° angle offset, any source detected in both resulting 2D maps is considered real. All sources above 3σ, extracted in this way, are masked out to approximately a radius of the relative FWHM, before the data is de-projected back to the 1D timelines. MMT de-glitching is then applied to the data where there is no source mask. A sigma clipping method is used to reject outlying frames at a significance of $> 10\sigma$ for the masked data, taking advantage of the multiple frames that contribute to each pixel ($\approx$30 for the green data and $\approx$15 for the red). A high-pass median filtering is applied to subtract the timeline backgrounds. The data is re-projected to a 2D map, using a naive mapping technique (HIPE task PhotProject) before co-adding the cross scan products to give the final reduced map.

The reason behind the need to incorporate further de-glitching in the pipeline, after the level1 de-giltching, is to flag and correct glitches that fail to be picked up by the MMT de-gliching task and produce well behaved timelines that may have cleaner power spectrums and will not produce spurious source like objects at the high-pass filtering stage.

B4.2 From IDL to Jython

While converting to Jython, various steps of the de-glitching method were altered either to improve the method, to comply with stipulations required for the input and output data or just due to switching from one language to another. Extra consideration had to be taken due to the following points:

- no alterations were to be carried out to the timelines themselves
- corrections must include the masked frames
- newly flagged frames must be set to Not a Numbers (NaNs)

The first request, namely that the data itself is not be corrected, led to the largest change in the de-glitching process. Instead of correcting the timelines, corresponding correction timelines

are created at each stage and cumulatively filled with derived corrections over all the stages, which is simplified as all the corrections are additive. The corrections can then be applied to the data in a single operation. Figure B28 shows two correction timeline, combined from corrections for all the de-glitching stages.

Secondly, the corrections must be interpolated over the existing flagged positions indicated by NaNs in the initial data. This is because in contrast to the OU data, which sees no restrictions placed on the y-movement of one or more sections of timeline or to a timeline as a whole, the data for the official pipeline needs to maintain a relative normalisation to the frames flagged with NaNs, which correspond to both those from the first map-making stage (i.e. real signal) and also those from the following MMT level1 de-glitching (i.e. spurious signal). Examples of the NaN positions for a section of timeline are shown in figure B29. The anonymous nature of the NaNs mean these positions cannot be differentiated to protect the source flux, so when a timeline section is corrected, without considering the flagged frames, the result could affect source flux. Extending a correction over the related NaN positions ensures that the flux is maintained at the relative level for any flagged frame. To achieve this the method followed is the same regardless of glitch type. The positions of the input timeline, where the frames are not NaNs, are recorded and a truncated timeline is formed from just these positions. A blank correction timeline, the same length as the truncated timeline is created. Corrections required are derived using the shorter signal timeline and added to the correction timeline, then any newly flagged frames that need to be set to NaN are recorded separately. After all corrections for a particular de-glitching step are found, the timeline and correction timeline are placed back into the initially recorded no-NaN positions for the full-length timeline. This gives a full frame length correction timeline with only the pre-existing NaNs (and a corrected version of the timeline for sanity checks). Each NaN in the correction timeline is then replaced one block of NaNs at a time, from the left, using the frame value one place to the left of the first NaN. This is because the corrections are found from left to right to maintain the normalisation of the timeline when the corrections are applied. If the first block of NaNs starts at frame 0, then this block is replaced with the frame value just to the right of the last NaN of that block. Thirdly, after all the NaNs have been replaced with this simple interpolation, the newly flagged frame positions in the truncated correction timeline are filled with NaNs and it is this version that is finally placed into the interpolated full-length

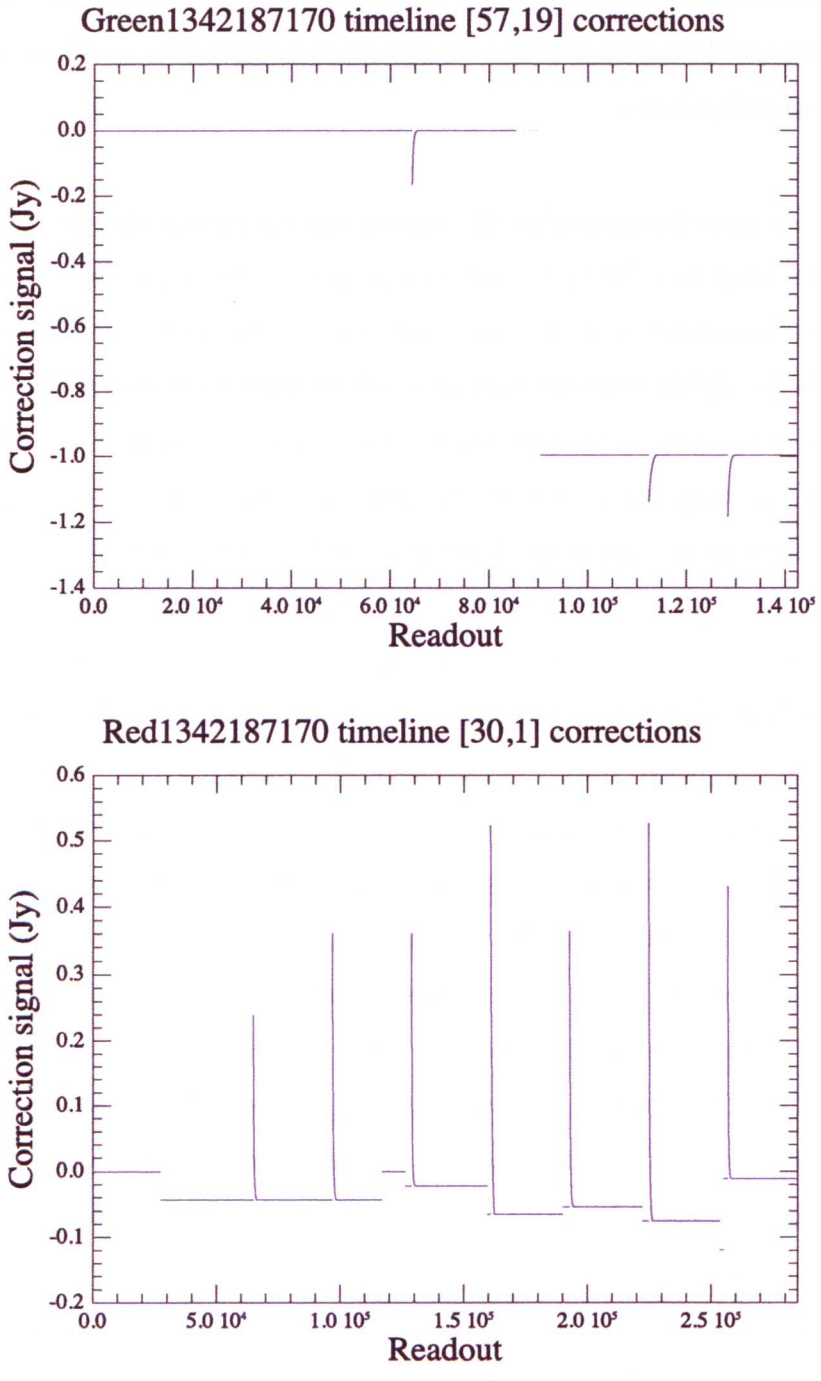

Figure B28: Final correction timeline for one Green timeline example (top) and one Red timeline example (bottom). Both examples show step and fader corrections were derived during the deglitching process. Note that the corrections are contiguous in the x-axis as all gaps were filled to maintain the relative normalisation of any flagged source flux.

correction timeline. For the first de-glitching step a copy of the timeline is also corrected, which is then propagated to and cumulatively corrected at each of the following stages to avoid features begin assigned corrected more than once. After the de-glitching is complete the sum of the correction timelines from each stage give the final corrections (see figure B28)

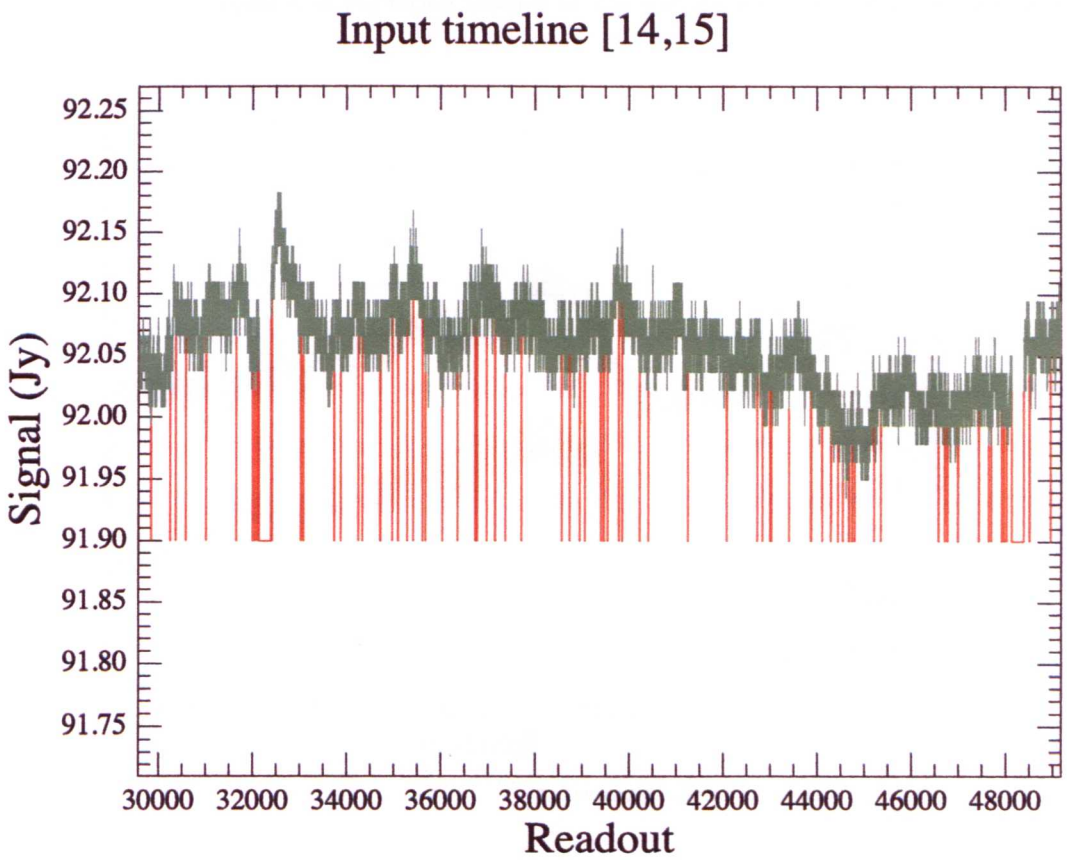

Figure B29: Section of a 'raw' timeline (Green 1342187170 [14,15]). The NaN positions in the timeline are highlighted with red (by setting them to an arbitrary value for plotting purposes). These NaN positions mainly correspond to single frame glitches, but some are at the positions of real sources.

Along with these global changes to the code, some more local changes were implemented. The method of de-stepping was altered so that the right hand side of the outlying frame was aligned with respect to the left hand side, allowing the left section to remain anchored, up to the first identified glitch. This not only allows the normalisation of the timeline to be maintained in-line with point two of the new stipulations, but was also found to gives fewer misalignments

between the timeline either side of the corrected step. Due to this improvement in the step correction method (although still not infallible), it is less important to ensure that steps and faders are differentiated during the step correction. It is still favourable to correct faders as faders, but an incorrect identification as a step and subsequent correction tends only to lead to the addition of low frequency noise, which can be dealt with during the high-pass filter sky subtraction (see figure B30 for an example of a fader corrected as a step).

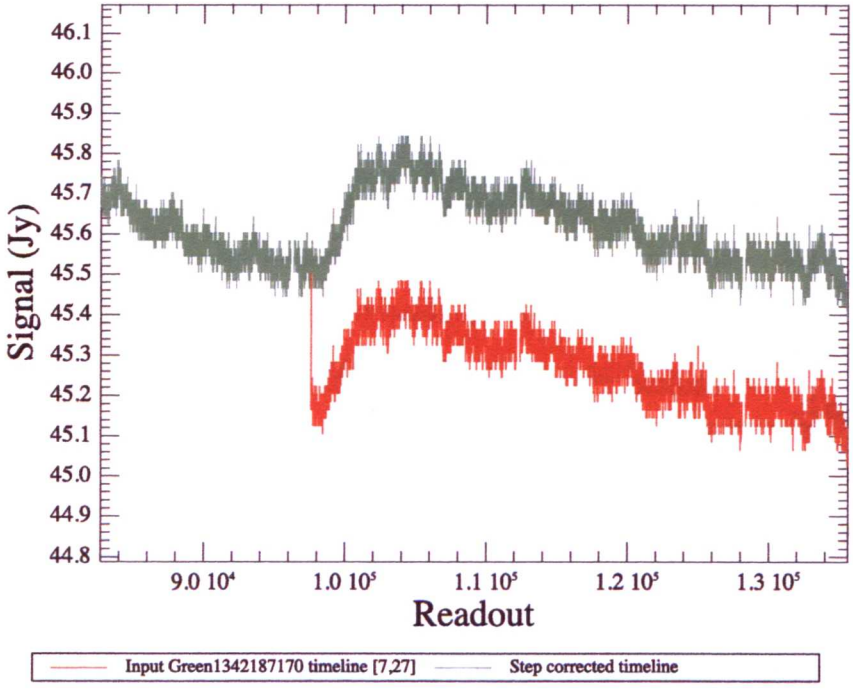

Figure B30: Section of timeline Green 1342187170 [7,27] before and after the step correction of a fader glitch. The resulting timeline (green line) shows that even though the fader was mis-identified as a step the resulting correction has not added any high frequency noise. The additional low frequency noise will be subtracted during the high-pass filtering.

An extra condition was added to the step correction function, so that any outlier < 50 frames from the start of a timeline were rejected. There is commonly a calibration residual around this position, which regularly leads to a mistaken step to be identified and poor correction, due to the short section of timeline available to calculate the left median value used in step identification process. In addition the overall normalisation of the timeline can suffer without this extra condition. Modifications were also necessary to accommodate a new down step feature, not

present in the OU version of the data. The same Jython de-step function was used to deal with down-steps, but the criteria for their detection required altering for Green data. This is due to the underlying negative gradient of the timelines, therefore reducing the difference between the comparison median values, taken either side of the step. To account for this difference, the comparison σ level was reduced to 2, see table B5 for the final levels used.

For the Red data, no standalone steps were found in the timelines checked. There are numerous small steps associated to the calibration block residual spikes, including both up and down steps. These 'mini-steps' do not generally get identified via the difference image as they are also often combined with a poorly defined spike. Therefore the correction step order was changed for the red data, so that faders are addressed prior to the steps. This order change greatly increases the number of step/spikes corrected and also prevents over correction, as show in figure B31. The calibration block residual spikes will no longer be such a significant issue for further H-ATLAS data, when only one calibration block will be taken at the beginning of an observation block. However for both Red GAMA9h SDP data these glitches remain a problem throughout the timelines.

The tackling of faders was revised to allow greater functionality in order to address wide and narrow, more and less significant and up and down faders with one function. To achieve this the sign of the difference timeline is taken for all identified outlying points, which indicates the necessary orientation of the timeline during each fader correction. At the beginning and end of each correction loop the timeline is multiplied by the sign of the difference timeline to invert for negative feature correction. The first fader correction stage tackles any greatly significant faders, $> 35\sigma$, for which the classification of mega-fader is now redefined (with the remaining faders referred to as just faders from hereon). The relatively fast decay of mega-faders is often accompanied by a large step and therefore no fit is attempted. At the position of a mega-fader a 5000 frame section of timeline is flagged. The remaining frames, to the right of the glitch, are treated with a step correction. Figures B32 shows an example of a timeline affected by a mega-fader glitch, with a large associated step, in comparison to the timeline corrected with the normal fader method and after correcting using the mega-fader method. Correcting for mega-faders in this way allows some simplification of the remaining fader correction code and also minimises

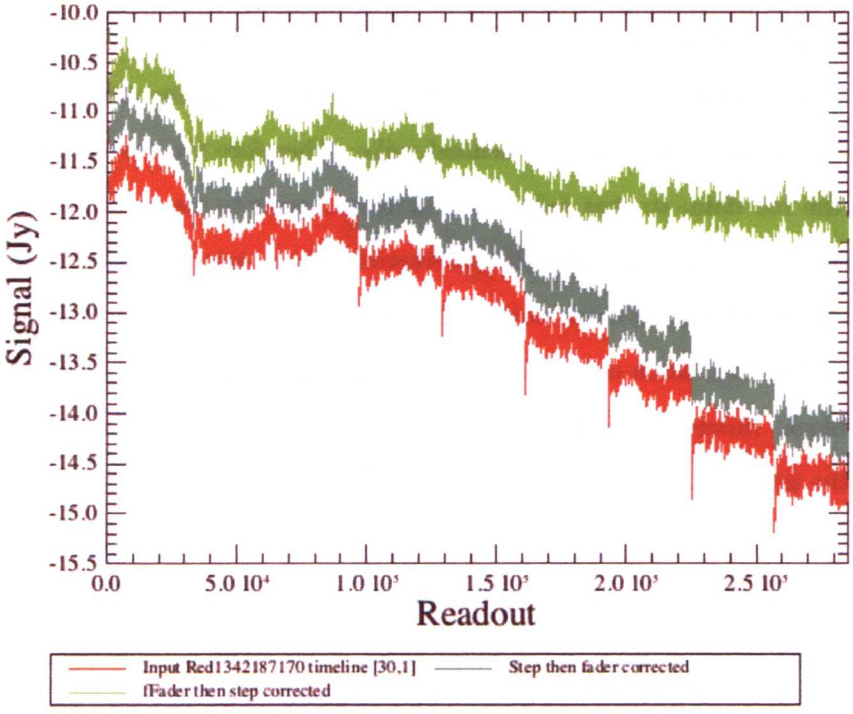

Figure B31: Red timeline 1342187170 [30,1] is show prior to correction (timeline 1; red), after corrections are applied in the order of steps then faders (timeline 2; dark Green) and also for the correction order of faders then steps (timeline 3; Green). The corrected timelines have had an arbitrary value added to their signal to allow them to be viewed separately. Although timeline 2 show several faders (at the position of steps) are corrected, the steps themselves are not. Timeline 3 shows a far more desirable result, where the steps and faders are successfully removed.

the possibility of adding significant high frequency residuals. Faders of such significance are rare (none have so far been found when examining the Red data and few examples exists in the Green data). Considering the number of frames that contribute to each pixel in the final map (~30 for the Green) the benefits of masking 5000 frames per mega-fader outweighs the loss of potentially good data.

The second stage of the fader correction function deals with all remaining faders, regardless of their orientation. Outliers are not considered if they are within 50 frames of the beginning of the timeline or 40 frames from the end. The fitting then proceeds in two stages. Firstly a 'short' 1500 frame section of timeline is considered, starting from the outlying frame position and checked for flatness (as explained below), if the local timeline passes the flatness test it is then fitted with an exponential function, of the same form described for the IDL de-glitching code (equation 3). If the resulting model does not pass the goodess of fit criteria (see table B5) then a second fit is attempted for a 'long' 5000 frame length of timeline, again starting at the outlying frame. If the longer fit passes the goodness criteria then a step correction at the position of the outlier is derived along with the model subtraction. Using this approaches allows both the spike like faders and the longer ranging faders to be addressed. Figures B33 and B34 shows some examples of 'flat' timeline sections as well as the initial guesses and best fit results for short and long timeline sections.

Due to the wide range of faders seen in the Green data and extensive calibration spike residuals present in the red, finding a ubiquitous initial guess for exponential model starting parameters, which allows the fitting algorithm to converge without error in all cases, is potentially impossible. For each parameter the code attempts a guess to better tailor the starting model to the feature being considered. A good guess also reduces the run time, as the number of fitting iterations can be substantially reduced, however having numerous conditions and criteria does complicate the code. For the first parameter, which controls the hight of the faint end of the curve, the sign of the initial guess was set by comparing the median values taken of the first and last third of the timeline, which gives a rough idea if the curve should be exponentially decaying or growing. Due to digitisation of the data it is possible for these median sections to be equal,

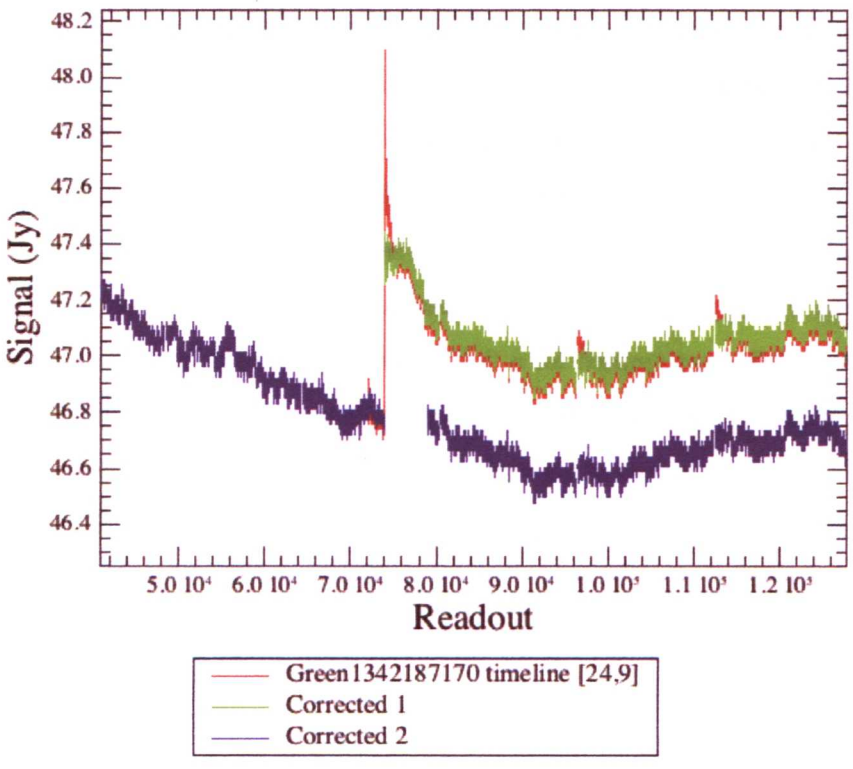

Figure B32: Section of timeline Green 1342187170 [24,9] showing the revised method for corrected significant faders (mega-faders) before (red), after applying a normal fader correction (Green) and after applying a mega-fader correction (blue). Clearly the former correction is not acceptable, whereas the later correction removes the glitch and leaves the timeline in agreement either side of the flagged frames.

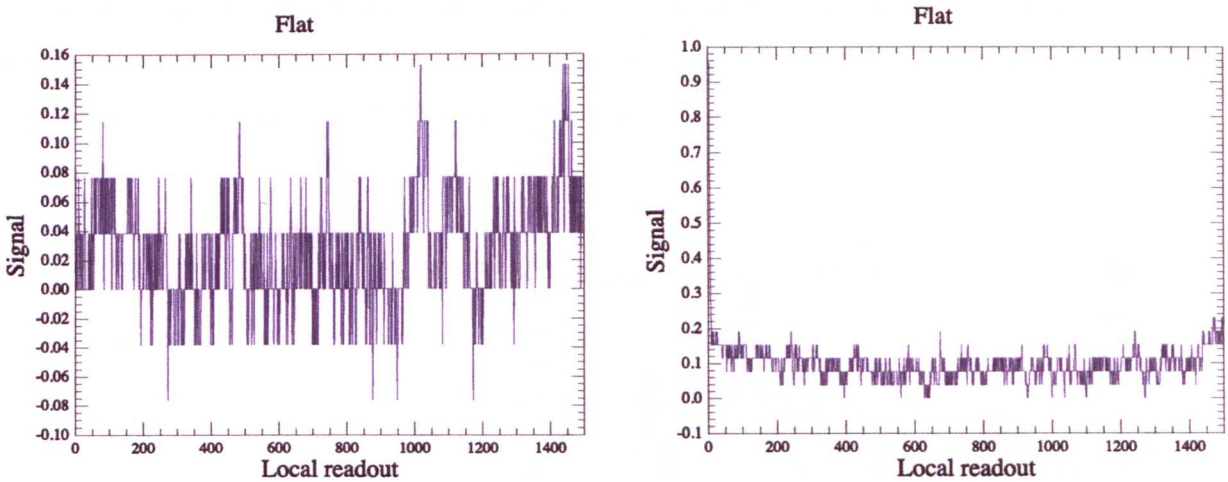

Figure B33: Two examples showing timeline sections that were considered for short length fitting (1500) frames, but failed the flatness test. The median values are taken for the first third and last third of the timeline section and if they are equal the outlier is not allowed to pass onto the fitting stage. There is a considerable chance for these values to be exactly equal, due to the digitisation of the data. The right panel shows a clear case of flatness over the majority of the local timeline but has a significant glitch at the start (dealt with by flagging the data once a flat timeline is declared), whereas the left panel shows no clear glitch, but is quite flat.

which is taken to indicate a flat timeline section and then the outlier is rejected from the fitting process. For the initial guess the height was kept low to assist the fitting of less significant faders (see figure B34, top right panel), as for more significant faders the fit is likely to succeed regardless of the initial guess (within reason). The second parameter controls the decay speed of the slope, and if this is high the fit can quickly tend to infinity leading to fewer successful fits, therefore this value is kept conservatively low (see table B5 for the final initial guess settings). The first and second parameter values used also depend on the colour of the data, the length of fit and the median comparison. The third guess parameter (the y-asymptote) was estimated by taking the median of the timeline section being used for the fit, which by itself greatly reduced the number of non-fits.

The goodness of fit conditions are similar to those for the IDL de-glitching code, based on the curvature and χ^2_ν. Again the limiting χ^2_ν is set reasonably high for the previously given reason reason – to allow long ranging features to be pass (see figure B34, bottom left panel) as these tend to have a higher χ^2_ν due to low frequency undulations over the length of the timeline

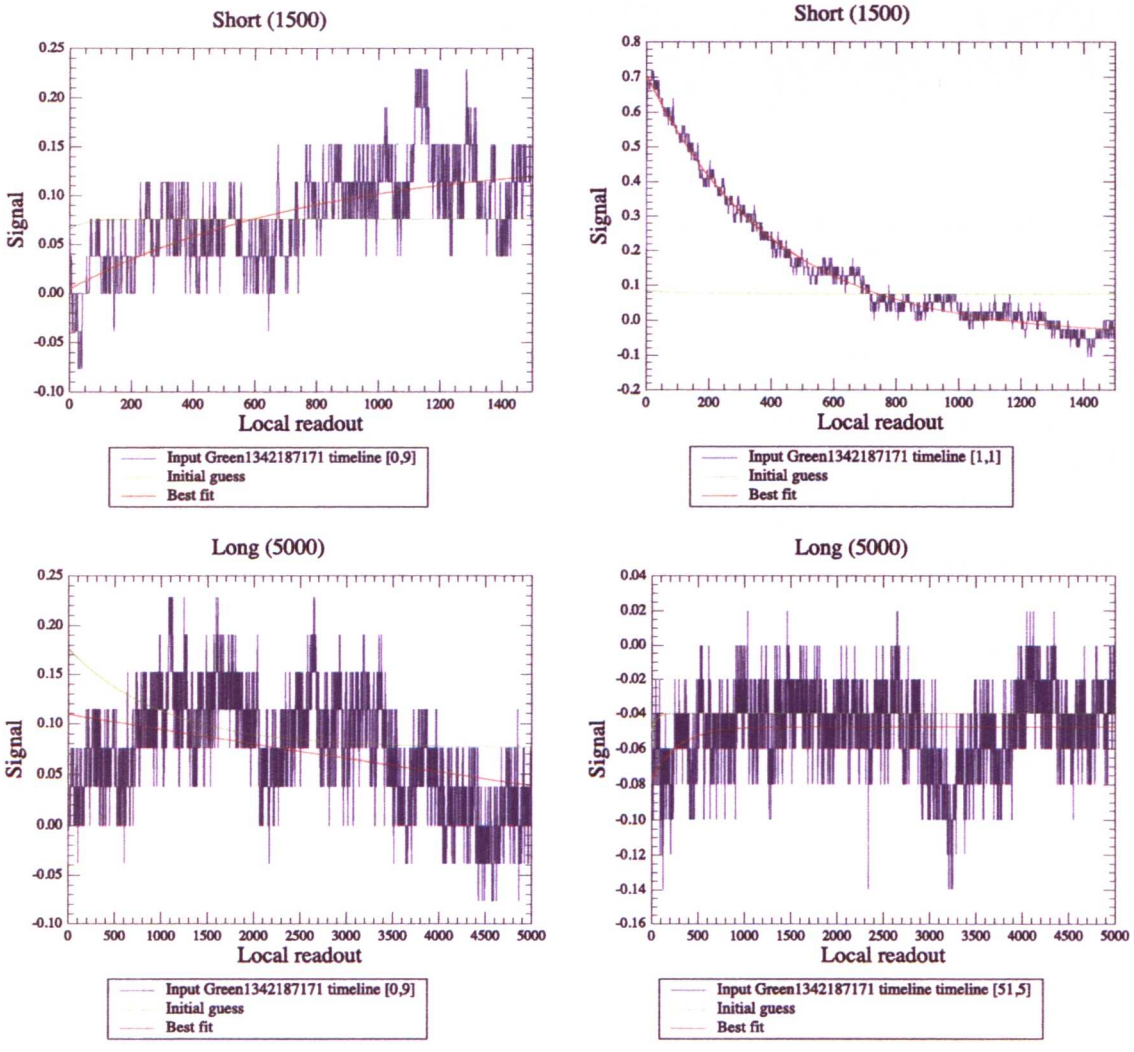

Figure B34: Examples of the fitting process to faders. The top panels show examples of the best fitting exponential models to the short fit length. The initial guess for the top right example is not accurate, but converges due to the faders significance. The bottom panels show the results of fitting to the longer timeline sections, which are carried out only if the fit to the short length fails to pass the goodness of fit criteria.

section, which impact the faint end of the fit. The curvature measurement excludes the first 30 frames of the best fit model for the short length and the first 100 frames for the long length. To ensure that both long ranging features with high χ^2_ν and high curvature and sharply decaying features with lower χ^2_ν but also low curvature, two criteria were set to give a fair chance to both types at both lengths of fit (see table B5). There is a fine balance between optimising the number of successfully corrected features and allowing unwanted corrections, or over corrections to non-glitches, but tuning the parameters and conditions using several 100 timeline gave more than satisfactory results. Several examples of de-glitched timelines are shown in figures B35 to B39.

The IDL de-glitching tasks were successfully converted to Jython scripts. The de-step function was adapted to meet the requirements of the HIPE pipeline and led to an improved correction method. The fader correction was extended to allow the correction of all identified faders per timeline, rather than a maximum of two. The fader correction process was developed to run in three stages, mega-fader correction, fader short fit and fader long fit. Due to a greater number of calibration block frames having been flagged for this version of the Green and Red SDP data, the calibration block correction was not applied, but any remaining spike residuals were dealt with in the new fader correction function. No polynomial sky subtraction is now performed, as the glitch corrections runs smoothly despite the 1/f noise background.

B5 De-glitching the OU data in HIPE

Upon testing the Jython versions of the de-glitching modules and comparing the results with those from the progenitor IDL code, it was found that the Jython code allowed a wider range of glitches to be addressed and introduced fewer high frequency residuals for secondary correction, therefore it seemed prudent to take advantage of these improvements and apply them to the OU data. Instead of converting the new Jython functions back to IDL, they were adapted to process the OU version of the PACS data within HIPE.

As the OU data has fewer frames removed with regard to the calibration blocks, the associated spikes remain a chronic issue, especially for the red data. Prior to implementation of the

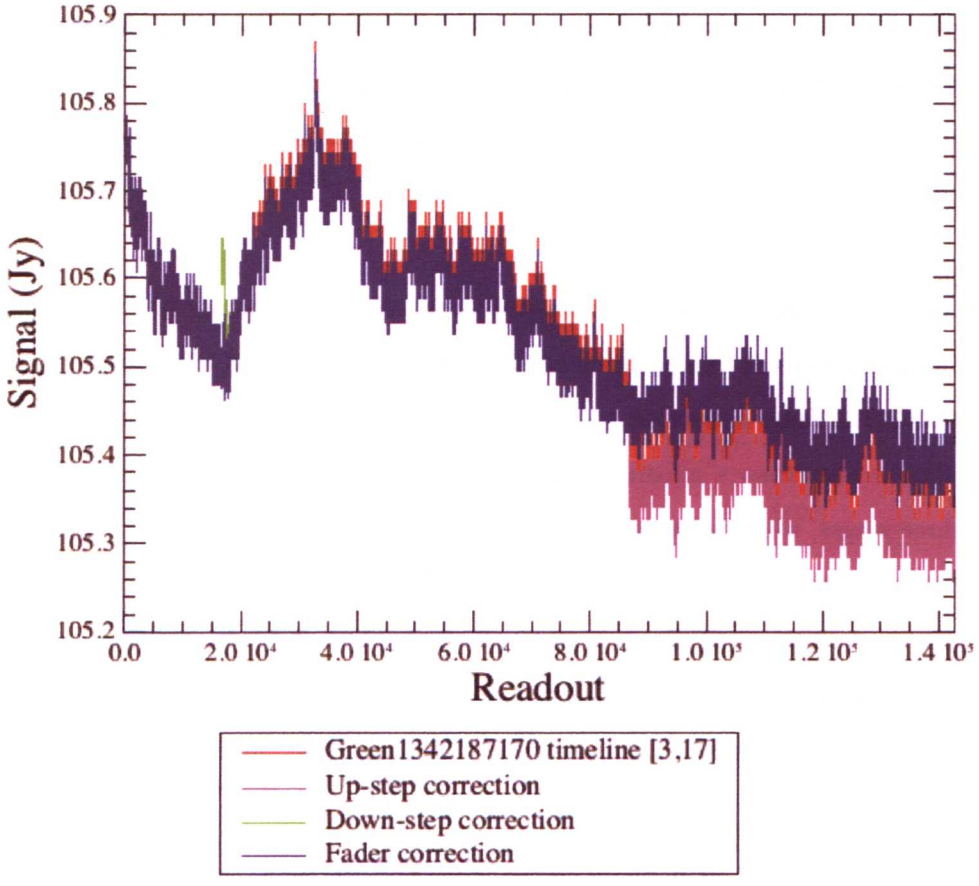

Figure B35: An example of a Green 1342187170 timeline ([3,17]) with a fader and step feature (red), showing the intermediate stage timelines (pink, green) and the final corrected version (blue). The corrections are cumulative over the order of up-step, down-step and fader. The apparent sharp peak ~frame 3×10^4 is not a sudden jump in the signal and so was not identified in the corresponding difference timeline as an outlying point. Zooming in on this frame shows a more gradual undulation that the full length image suggests and should not produce a strong feature after high-pass filtering. The remaining low-frequency noise will also be removed by high-pass filtering.

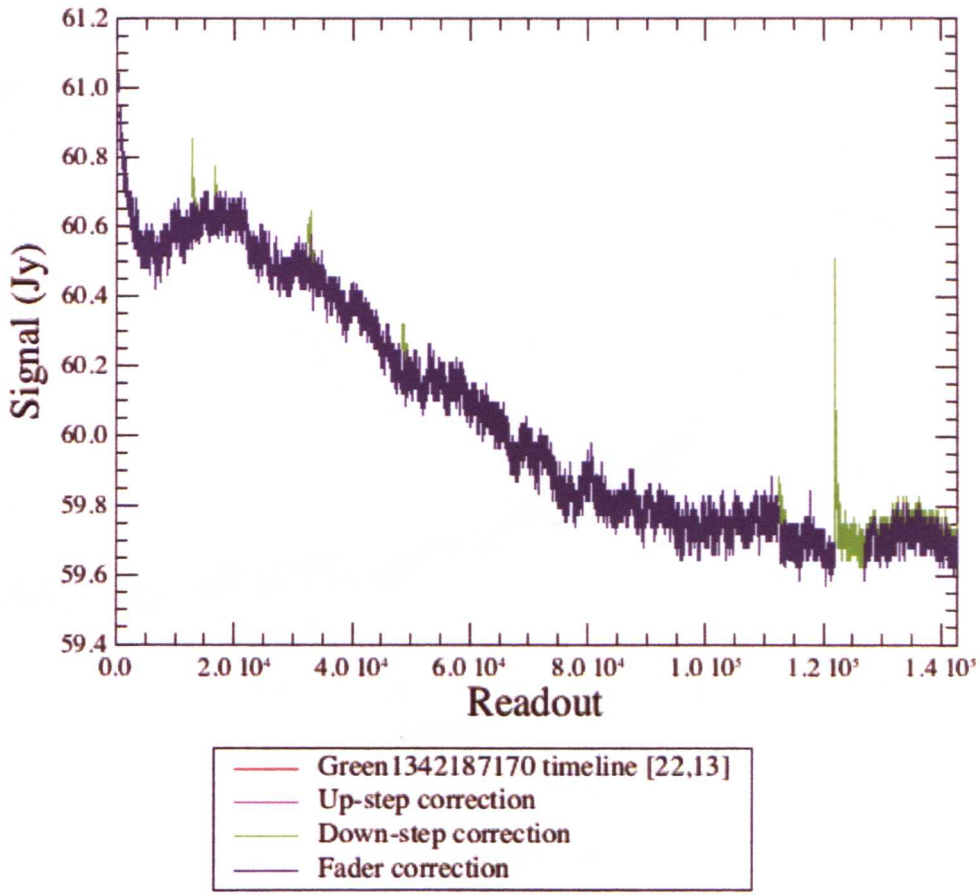

Figure B36: An example of a mega-fader and several faders for Green 1342187170 timeline [22,13] (green line). The alignment between the mega-fader correction ends is good (blue line). All features are satisfactorily corrected. No step corrections were performed and all features were corrected at the fader correction step.

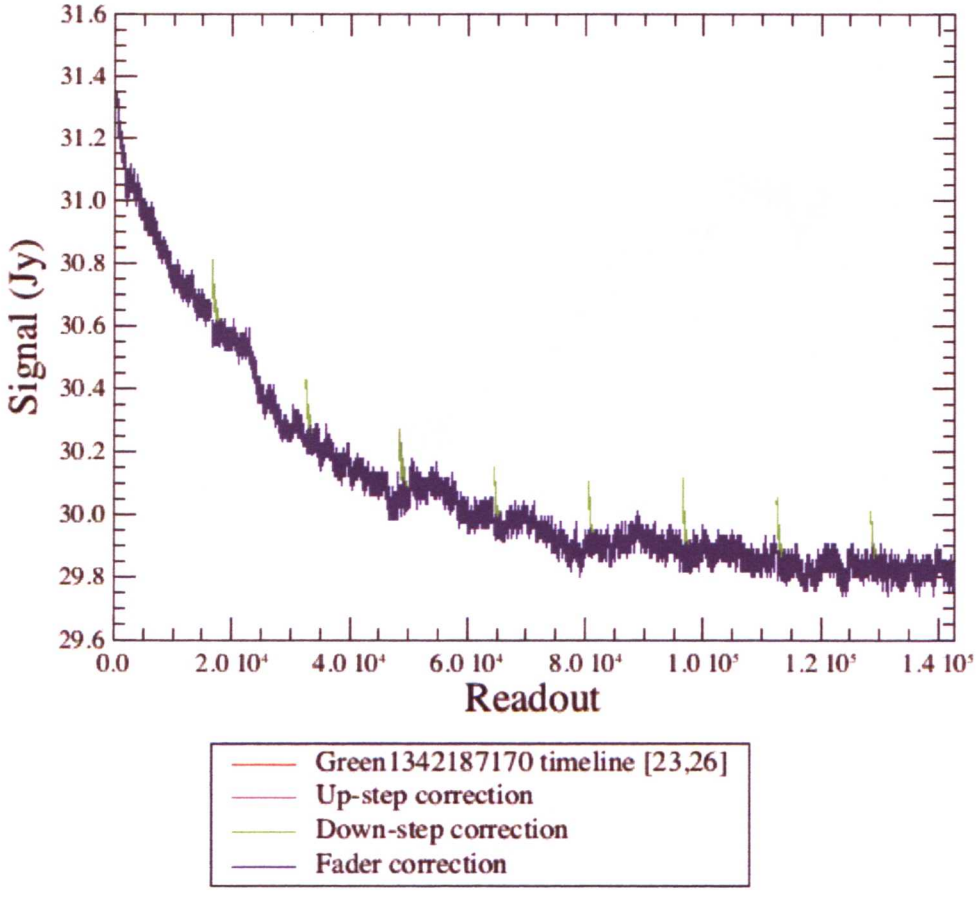

Figure B37: A set of Green 1342187170 calibration spike (shown in the green line) are corrected for timeline [23,16]. No other corrections were necessary, however all spikes are well corrected (blue line).

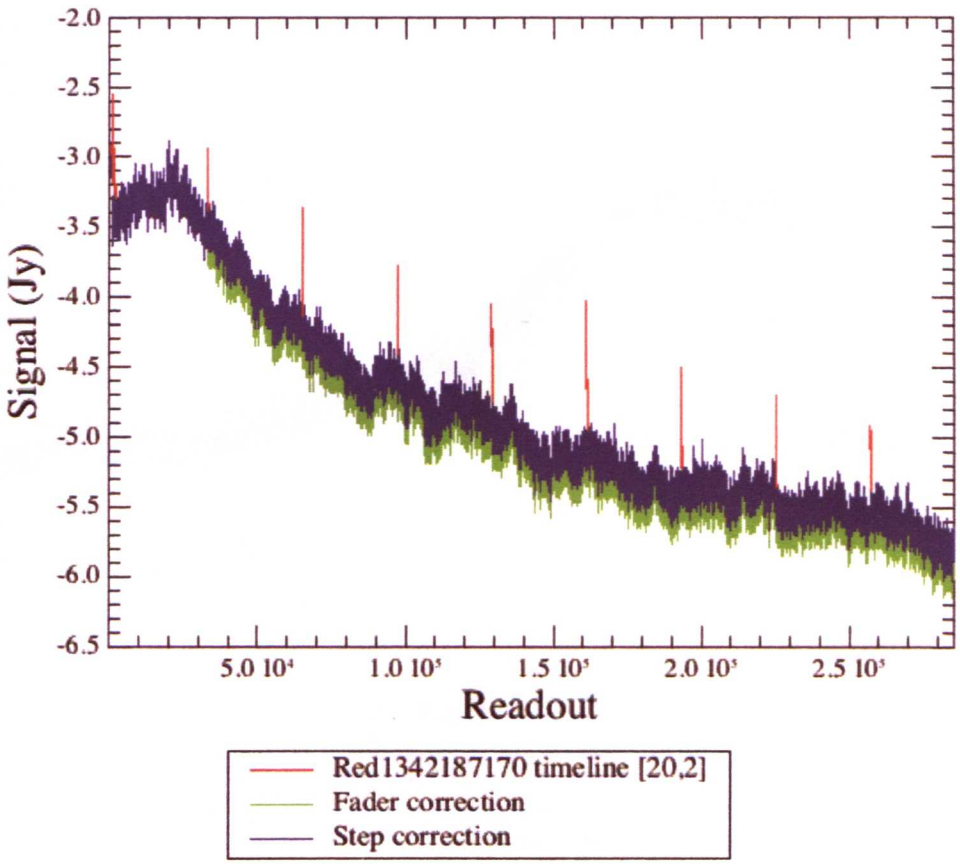

Figure B38: an example of a Red 1342187170 timeline ([20,2]) spike set with higher significance that for figure B37 (red line). The corrections are cumulative over the fader then (green line) then up and down step corrections. A step correction at the second spike position was corrected giving better alignment for the final corrected timeline (blue line).

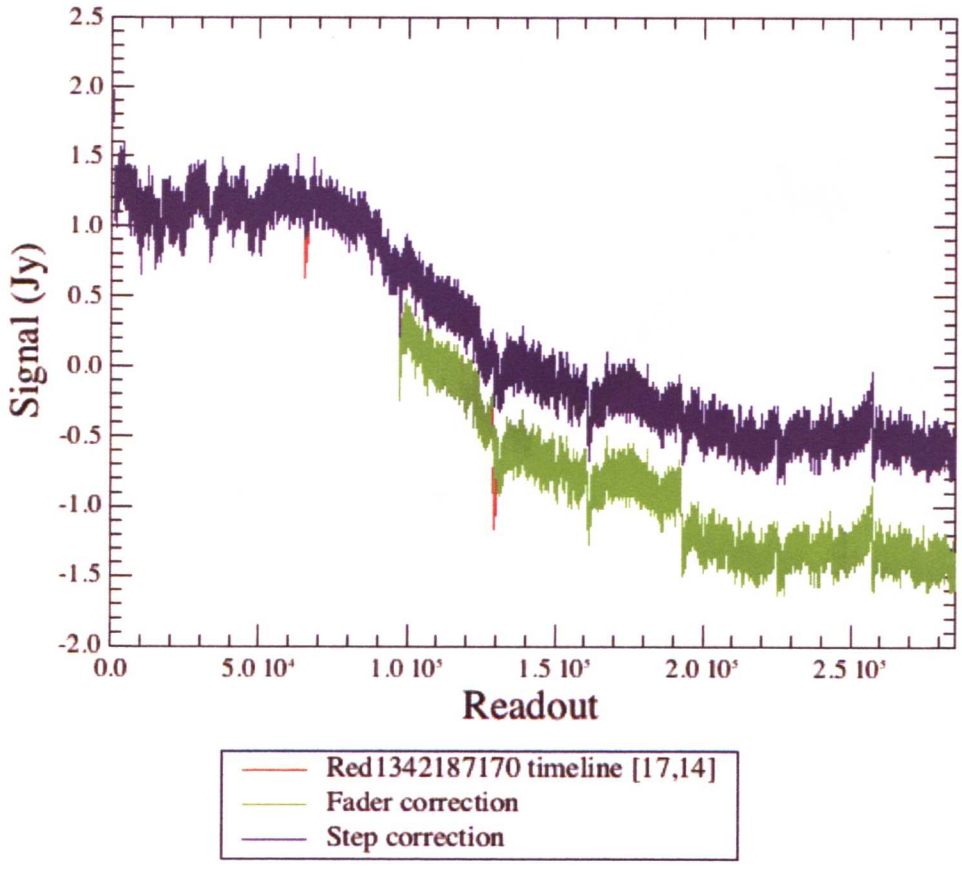

Figure B39: Red 1342187170 timeline [17,14] that has an down-spike set, which varies with significance with frame position. There is some success for both the fader correction (green) and the step correction (blue), but several small features appear uncorrected in the final timeline. See figure B40 for a closer look at the main uncorrected glitch at frame 256500.

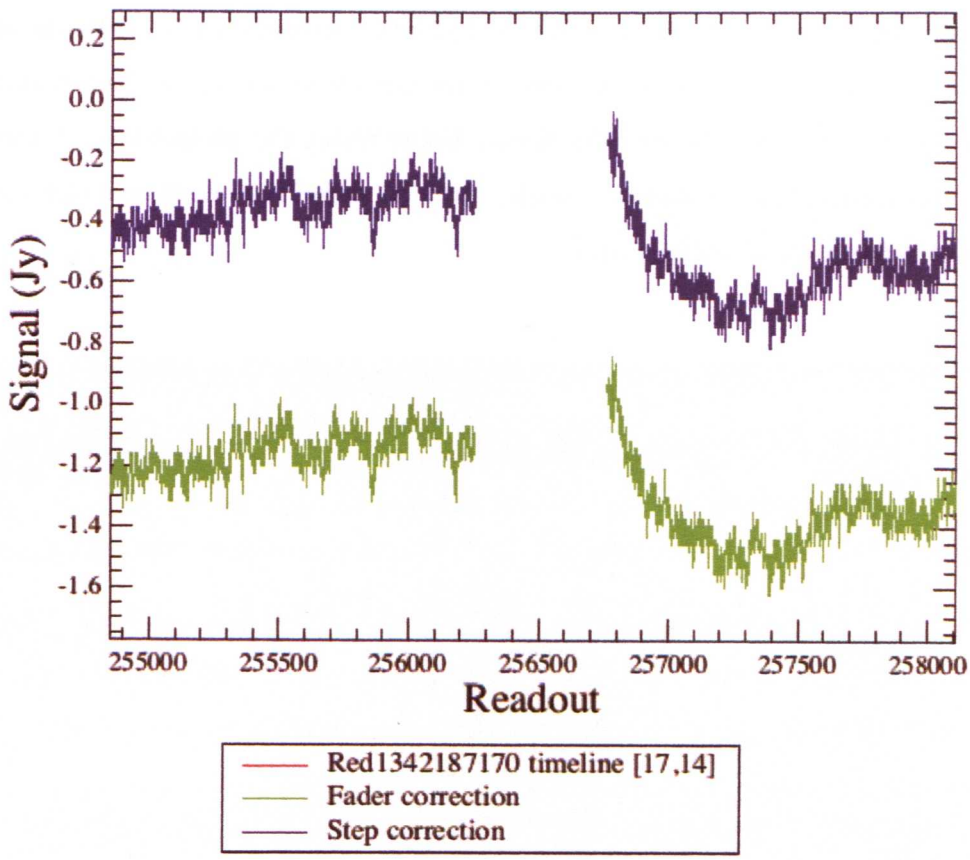

Figure B40: Section of the corrected Red 1342187170 [17,14] timeline, at the position of a glitch that was not well corrected for during the de-glitching. The difference between the end points either side of the NaN frames (which are at the position of the gap), is not great enough for the associated difference timeline (which is a truncated version without the NaN frames) to have an outlying spike at that position.

IDL de-glitching, this issue was corrected in the red data by masking strips of 2000 frames after all positions with a signal greater than a set threshold, which deals with the most significant spikes. As a consequence of correcting in this way the reduced data exhibited an additional sky structure (figure B41). Using the positional priors for the sets of spikes a new function was written to correct the residual spikes using the same basic method that was employed in the IDL code, where a strip of frames over the glitch are replaced by a straight line. This method was extended to replace a larger number of frames (70 for the Green data and 540 for the Red) and a step correction was added to better align the timeline either side of the 'bad' frames, which reduces the slope between the gap edge frames before fitting the straight-line. A comparison between the results for two calibration spikes, with and without the additional step correction, are shown in figure B42.

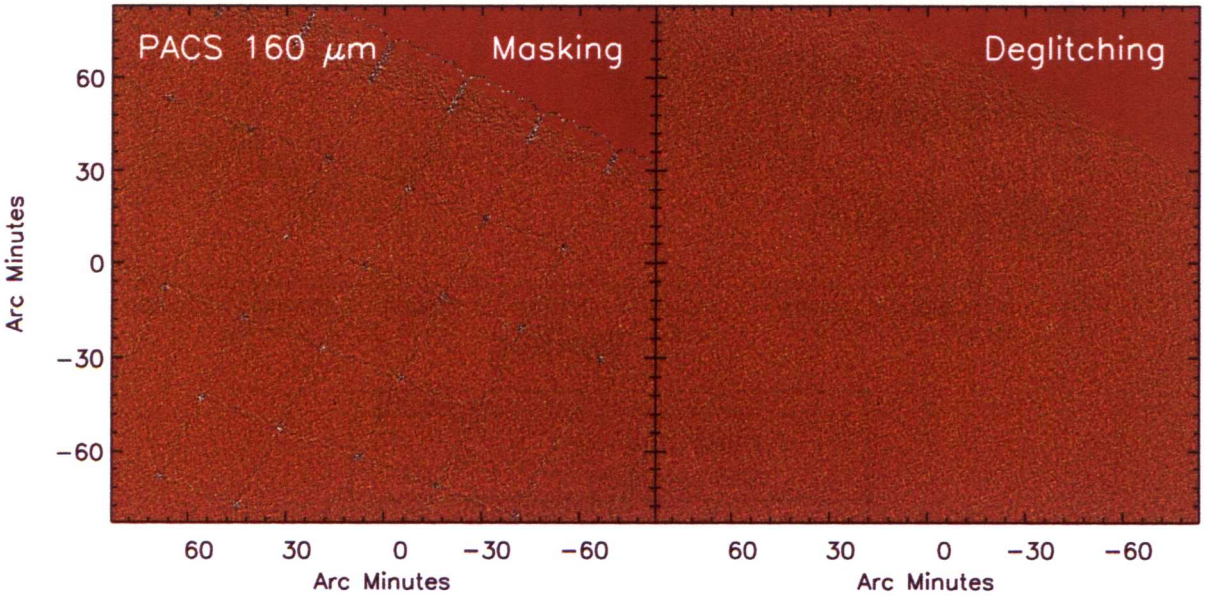

Figure B41: Reduced, projected and coadded OU red data. The grid of structure seen in the left panel is removed when correcting at each calibration spike position.

This method of flagging timeline strips for each calibration cumulatively leads to a substantial data loss, so in an attempt to reduce the number of flagged frames the previously tried fitting method was revisited. Firstly an exponential function is fitted to each of the calibration spike positions for each timeline, after a step correction is performed, if found to be necessary. In line with the other fit based corrections, a length of timeline is flagged around the glitch position.

In this case, if the fit is not deemed good, then the alternative correction method of flagging a timeline strip is invoked. Generally, correcting using a fitting method to the red data introduces low frequency noise (e.g. the top panel of figure B46), however this is far more preferable to the mini-steps that can be introduced otherwise and the additional noise is subtracted at the 1/f noise removal stage.

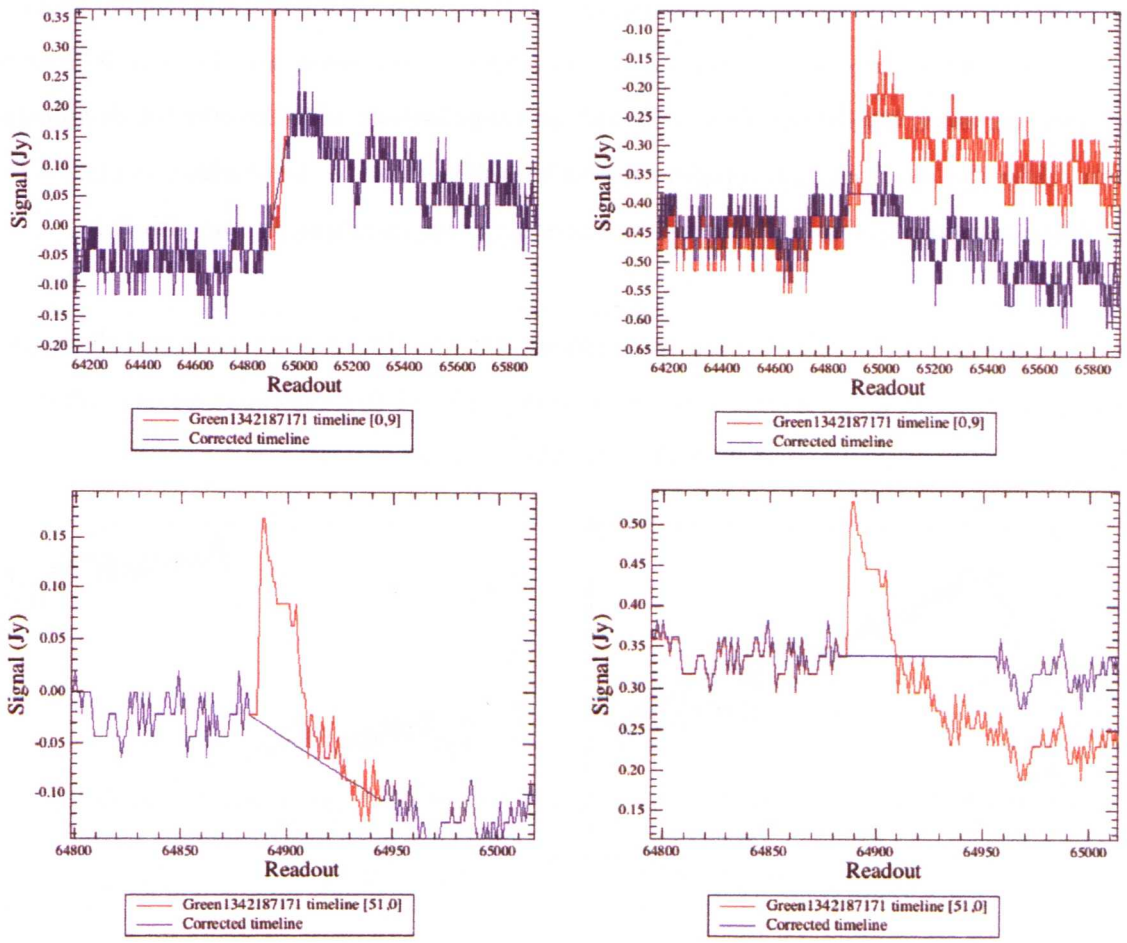

Figure B42: Examples of single calibration spike corrections. Timeline sections are shown before (red) and after (blue) the correction at the spike position. The data corresponding to the spike is replaced with a straight line in all panel, but with an additional step correction for the data in the right hand panels. The step correction aligns the timeline either side of the gap allowing a smoother continuation over the replaced feature and the following frames.

The additional mega-fader correction was removed as the majority of faders do not have the same associated and significant step. All faders, regardless of significance, begin their correction at the short fitting stage. To make sure any small steps that may occur in the sky level due to

a fader feature are removed, an extra step correction is carried out (if necessary) at the end of the short fitting stage, as with the long fit stage, but only for the Green data. For up-faders, the starting guess for parameter 1 was increased to 0.05, to reduce the mega-fader fitting time for the Green data (there are no mega-faders in the SDP Red data). The basic procedures for correcting steps and faders was otherwise mainly unchanged, however some simplifications were possible/necessary. As there is no need to handle NaN values and maintain the normalisation for the input OU data, so the left interpolation over the NaN positions is redundant. There is also no need for a correction timeline and the timelines are corrected directly. A NaN mask to indicate any newly flagged positions is created, and cumulatively added to over the de-glitching steps. After the de-glitching is complete the NaN mask is added to the timelines to place NaNs at all the flagged positions, so only one data product needs exporting for use with IDL.

A comparison was made between the resulting IDL OU de-glitched results and the Jython based OU de-glitching. Figure B43 is the equivalent plot of the sections of timeline shown in figure B9 and in figure B7, and show the corrections are comparable.

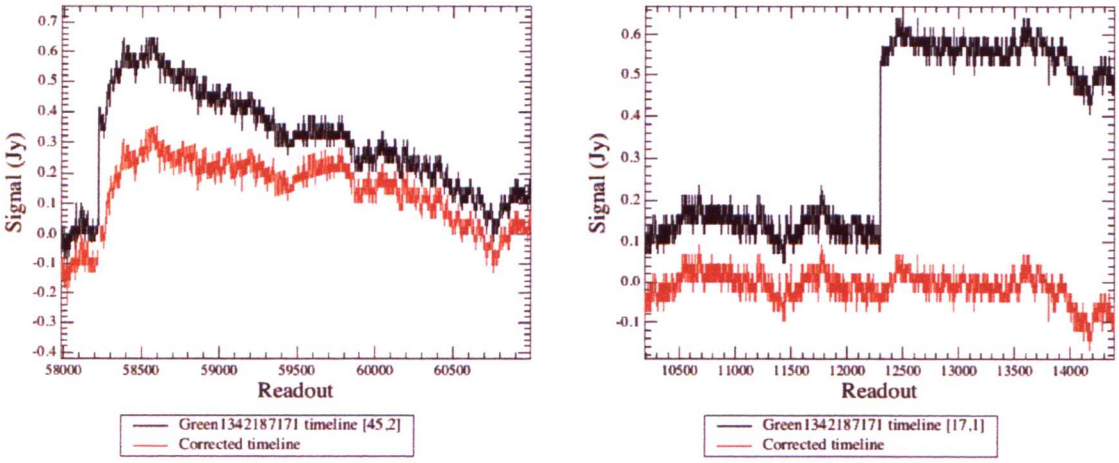

Figure B43: Jython de-glitched OU timeline sections. Left: The same feature as shown in figure B9. The comparison between the IDL and Jython de-glitching methods for this glitch shows a similar result. The corrected timeline (red) has the flagged NaN frames added from the mask output to illustrate the data version passed to IDL. Right: Jython based step correction for the step featured in figure B7, showing an identical correction is achieved.

Once the OU version of the PACS data is run with the final Jython de-glitching code and exported as a data cube from HIPE, it is ready to be run through the remaining IDL pipeline,

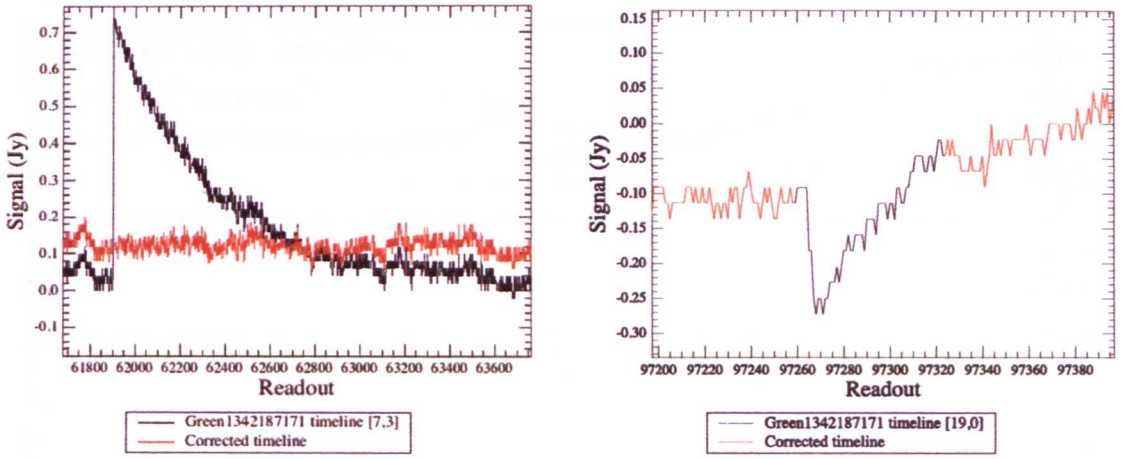

Figure B44: Jython de-glitched timeline sections. Left: A corrected fader also shown in figure B13 (bottom panel) after IDL based correction, showing an equivalent correction. Right: The results for one calibration spike after setting the data to NaNs at the position of the glitch, which is the equivalent to the correction seen in figure B19 (7^{th} panel). This illustrates the intermediate spike correction method, before the implementation of the fitting procedure or strip replacement with step-correction.

once the new NaNs at flagged positions are accounted for. The only change necessary for the IDL pipeline is the earlier creation of a blank mask array during the first noise estimate, which is filled with random normal noise, scaled by the respective pixel RMS, at all the NaN positions in the timeline image. Then for each block of NaN frames a step-correction is performed and a straight line is fitted between the adjoining data frames to replace the NaNs. By adding the mask array to the timeline image, each fitted line sees the addition of the appropriate level of random noise, which minimises any bias to the beam-switching and subsequent noise estimate. The mask is then reset to 1 at all non-zero positions. The remaining pipeline tasks remain unchanged, but a scaling of the filtered noise map was added to produce a SNR map with a variance of 1. The scaling was achieved simply by iterating $\mathrm{Map}_{noise}/\sigma_{SNR}$, retaking the SNR map at each loop until σ_{SNR} converged toward 1. Examples showing a timeline prior to HIPE de-glitching, post HIPE de-glitching and the final beam-switched, sky-subtracted timeline are given in figures B45 and B46.

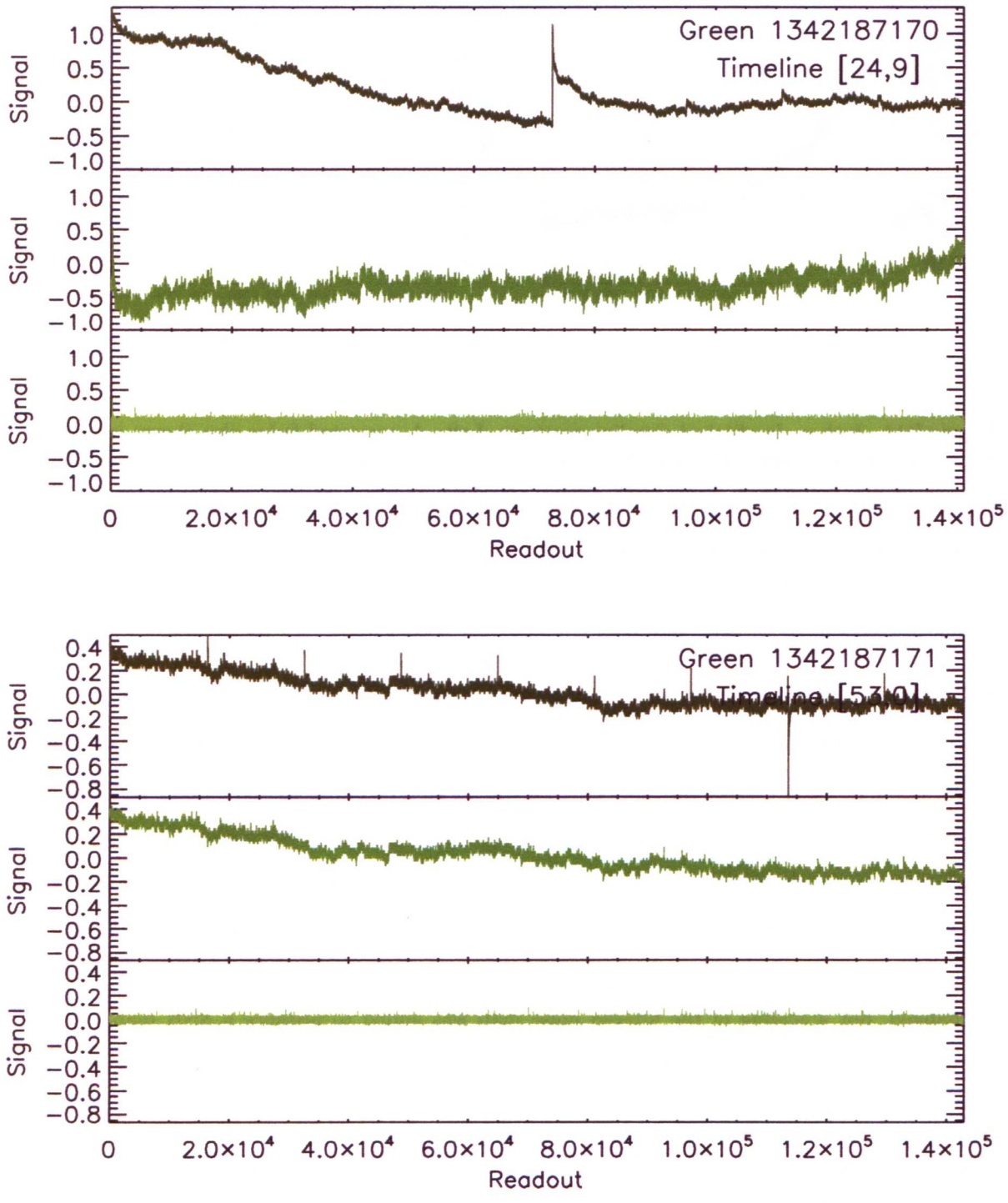

Figure B45: Timeline at three stages during the OU reduction process for each Green scan. Timeline [24,9] for Green 1342187170 (top level) and timeline [53,0] for Green 1342187171 (bottom level). For both plots he level1 'raw' timelines are shown in the top panels, the post HIPE de-glitched timelines are shown in the middle panels and the final IDL reduced timelines are shown in the bottom panels. Glitches and 1/f noise are successfully removed in both cases.

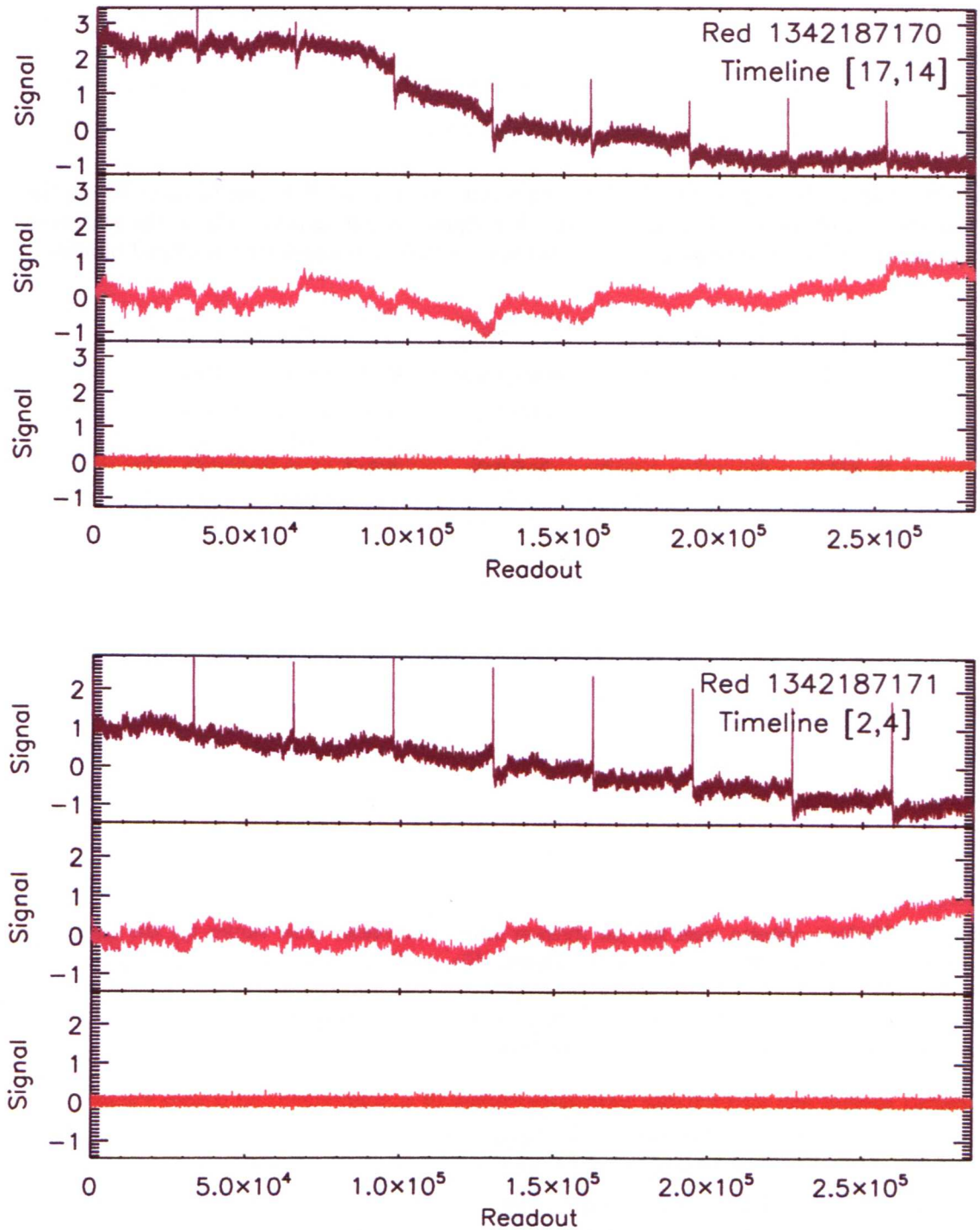

Figure B46: Timeline at three stages during the OU reduction process for each Red scan. Timeline [17,14] for Red 1342187170 (top level) and timeline [2,4] for Red 1342187171 (bottom level). The level1 'raw' timelines are shown in the top panels, the post HIPE de-glitched timelines are shown in the middle panels and the final IDL reduced timelines are shown in the bottom panels. There is the addition of low (or mid) frequency noise during the correction of timeline [17,14], which is removed at the beam-switching stage. The high frequency glitches are all well corrected.

Table B4: Sigma clipping levels, glitch identification criteria and flag lengths used during the Jython versions of the de-glitching modules. The Spike column applies only to the OU data. The values given in parenthesis are for the Jython moduals developed for the official pipeline.

Limit	Spike		Step		Fader(mega)	
/Criteria	Green	Red	Green[up,down]	Red	Green	Red
σ_{Clip}	—	—	[4.0,4.5]	4.0	6.5(35)	6.5(35)
σ_{Step}	3.0	3.0	[5.0,8.0]	5.0	3.0	3.0
σ_{Step2}	—	—	[8.0,2.0]	5.5	—	—
N_{flagged}	70	540	5	5	(5000)	(5000)

Table B5: Various criteria used for the Jython fader correction. The values for the short and long fitting for the fader are given for the Green (G_{short}, G_{long}) and for the Red (R_{short}, R_{long}, including the criteria use for the additional step-corrections and the two best fit conditions (F_A and F_B) for the curvature (C) and the χ^2_ν. N_{fitted} and N_{flag} correspond to the number of frames fitted to during the fader correction and the frames set to NaN.

Type	Up[P_1, P_2]	Down[P_1, P_2]	N_{fitted}	F_A[>C,< χ^2_ν]	F_B[>C,< χ^2_ν]	N_{flag}
G_{short}	[0.01,-0.05]	[-0.01,-0.02]	1500	[0.2,10]	[0.06,2.4]	15
G_{long}	[0.1,-0.001]	[-0.1,-0.002]	5000	[0.15,13]	[0.06,10]	110
R_{short}	[0.2,-0.008]	[-0.2,-0.008]	1500	[0.2,10]	[0.06,2.4]	15
R_{long}	[0.1,-0.001]	[-0.1,-0.002]	5000	[0.15,13]	[0.06,10]	110

B5.1 De-glitch testing

To test the impact of de-glitching on the final data product, the OU pipeline was run with all the SDP data using the default setting for each set of cross scans, firstly for the data with no de-glitching, and secondly after the implementation of the de-glitched data. Each set of filtered and projected scans were combined using a noise weighted mean sum to give four final maps (Green and Green de-glitched and Red and Red de-glitched).

The pixel distributions for each resulting SNR maps were taken (prior to rescaling) to assess any reduction in the map noise due to de-glitching, as shown in figures B47. A Gaussian was fitted to each distribution to find the 1 σ noise, showing a reduction in RMS of around 0.2 for both sets of data due to the removal of glitches. This comparative reduction is less for the red data, as the data with no de-glitching has masking at the most significant calibration spike positions. Note the difference to both values of σ reported in section B3.8.2. This difference is due to the use of two scans that have been combined with a noise weighted sum and a change in the mean wavelength used for the Green data (originally taken as 110μm). The expectation that the SNR of an optimally filtered map will have a pixel distribution with a variance of 1 is achieved for the Green de-glitched data, however not for the red data. The Red σ estimate may see an improvement for future H-ATLAS data that has fewer calibration observations performed. There is also a reduction in the scatter at the bright end of the distributions, reflecting the removal of large scale glitches.

B5.2 Source extraction and photometry

The primary reason for de-glitching is to remove large scale glitches that can present themselves as significant features in the final maps (see figure B22). Such features can lead to multiple false source detections, which are either time consuming to remove from an extracted catalogue or are miss identified as real. It is therefore advantageous to remove the root cause at the timeline stage, but here must be an emphasis on the removal of these glitches without the introduction of noise on the scale of the PSF. In order to assess the impact of de-glitching on sources extracted from the final maps, a connected pixel extraction algorithm (that looks for a minimum number of connected pixels above a given σ level and then identifies peaks) was performed with the

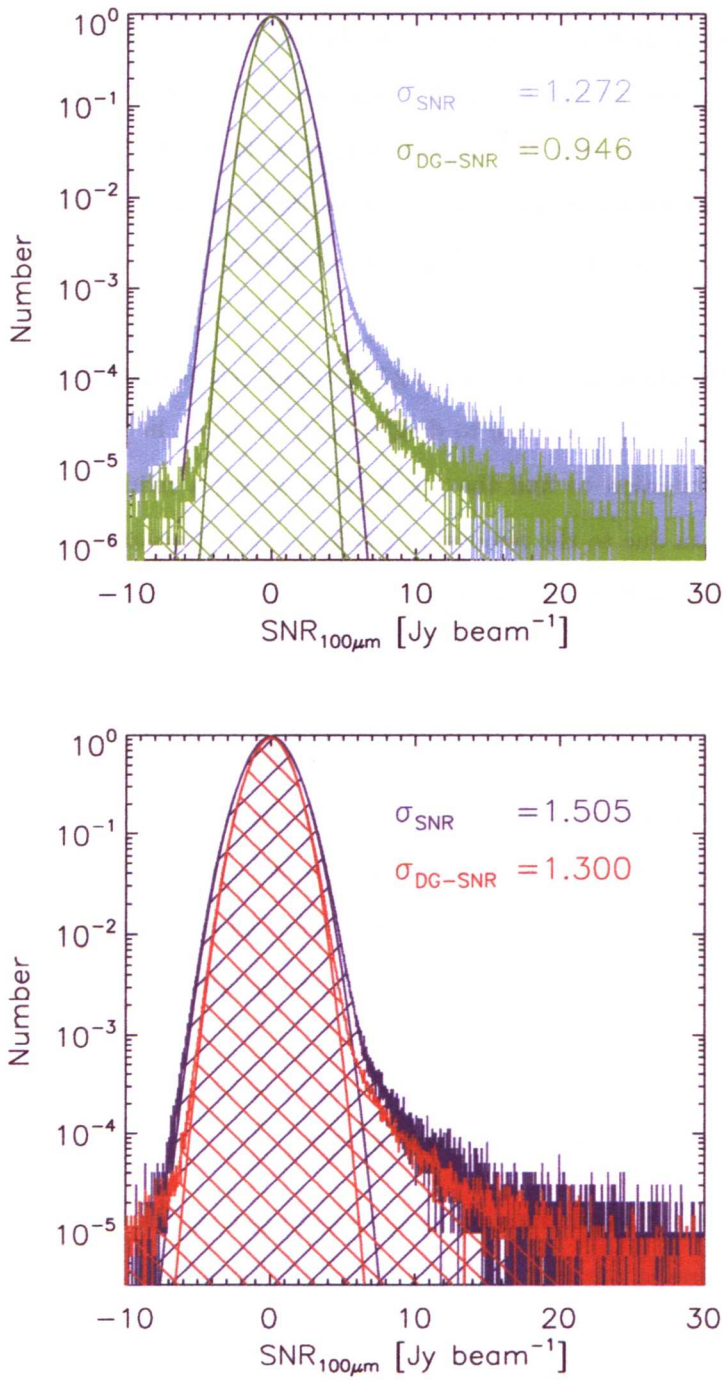

Figure B47: Pixel distributions for the projected and combined Green (top) and red (bottom) SDP scans. A comparison is made between the non-deglitched and deglitched data, although for the red data a simple masking of the significant calibration flashes was make for the non-deglitched data. De-glitching reduces the width of the resulting distributions in both cases by $\sim$0.2 and significantly reduces the scatter in the bright tail (less so for the red as the large scale glitches were already addressed to some extent).

Green and Red SDP maps. Extractions were performed at a 3σ level for each map and then the resulting source catalogues were compared between maps of the same colour. The cross match was performed with a separation tolerance of $2''$ for the Green data and $4''$ for the red, which takes into account the difference in pixel scale. Of particular interest are sources that appear in one map but not the other, however due to the difference in noise level between the data a 3σ extraction for the de-glitched map is not the equivalent to that for the comparison data, leading to a difference in the number of sources extracted at the fainter end. Therefore, the comparison was made looking primarily at at the areas surrounding major glitches, rather than assessing the extracted catalogues as a whole. Examples of this comparison are shown in figures B48 and B49, where many spurious sources are extracted at the site of projected glitches. The numbers of spurious extractions due to these significant glitches are many hundreds per map.

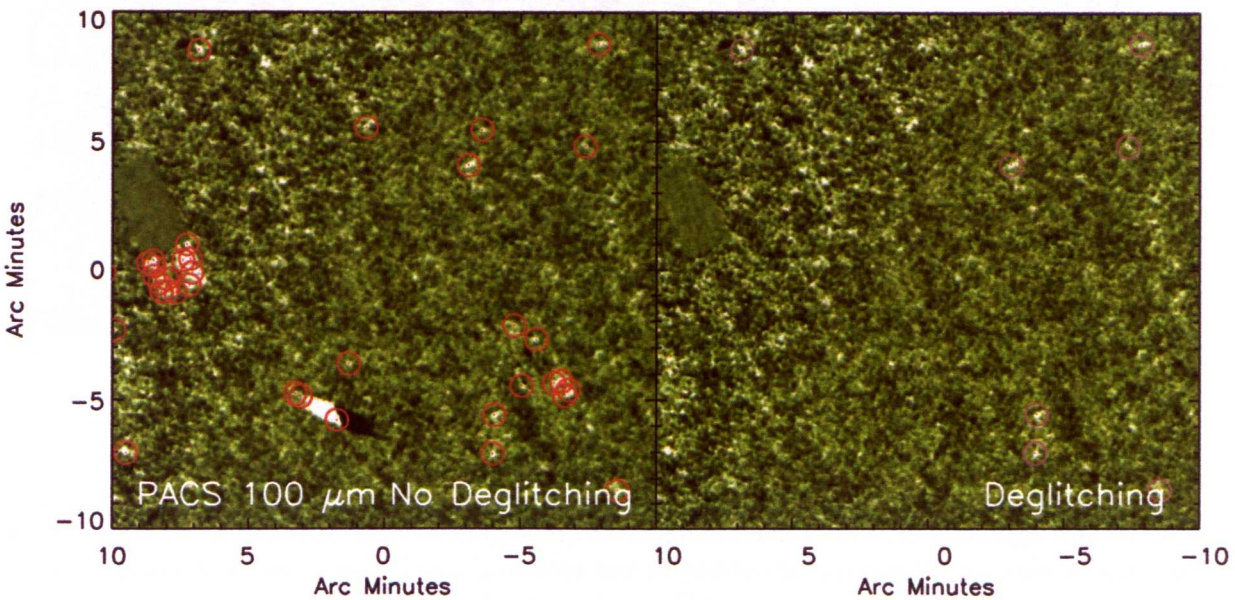

Figure B48: Section of the IDL reduced and co-added Green SDP scans, before (left) and after (right) de-glitching in HIPE. A source extraction on both maps shows several spurious sources are extracted around the glitchy regions. In particular there are many fake detections around the glitch associated to a calibration block (left hand side at $0'$). There are some differences in the number of real sources extracted due to the difference noise levels in the maps.

For each extracted catalogue the photometry was taken by simply finding the pixel value at each centroid position, as the filtered maps represent the best fit flux per pixel and are in units of Jy/beam. To quickly calibrate the photometry a comparison to the official catalogue was performing for each catalogue. The OU source catalogues were crossmatched with the official

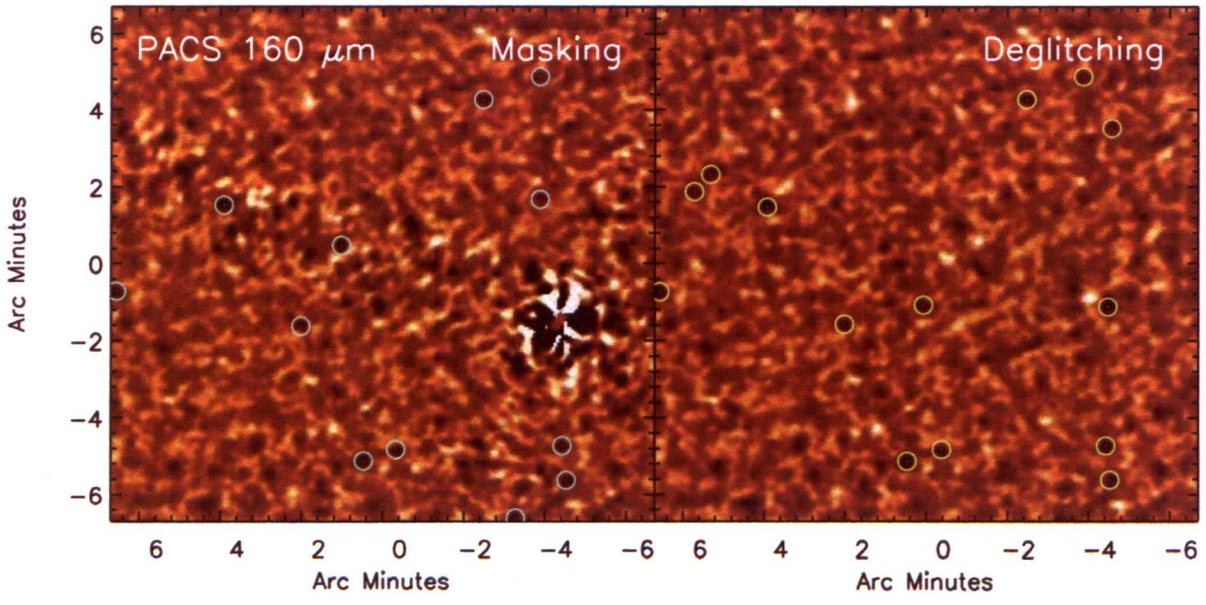

Figure B49: Section of the IDL reduced and co-added Red SDP scans, before (left) and after (right) de-glitching in HIPE. Apart from the extensive calibration spikes within the Red data (which are masked), the vastly lower number of other glitches seen in the Red data leads to a reduced number of spurious detections in the non-de-glitched map. The de-glitching more successfully deals with the calibration spikes leading the the geometric structure in the left map (seen more clearly in figure B41) and reduces the number of spurious sources extracted due to this feature.

source positions, using a limiting separation of 2″ and 4″ for the Green and red catalogues, respectively. The resulting flux densities are compared in figure B50. For the Green data a calibration factor of 13.5 was derived, which may suggest the FWHM for the Green data is more extended in the scan direction, relative to the extension for the red data, where a calibration factor of just 5.3 was estimated. As the FWHM for the 1D filtering was based on the wavelength and pixel scales, a greater difference between the filter width and the actual FWHM would lead to a greater deficit of flux. There is an overall 1:1 agreement seen for both comparisons, but at the very brightest end there is an indication that the OU sources have a further reduced flux density in comparison to the official source flux, noting that for each comparison the three brightest sources were removed from the plot as outliers, but also follow this trend. One explanation for this may be due to the HIPE MMT-de-glitching task used to create the level1 OU data. As explained previously, for the PACS fast scan mode, the sampling rate does not allow the MMT-deglitcher to differentiate between single frame events and the brightest sources, therefore possibly cropping the flux for bright sources in the OU data. However, the brightest sources were also treated differently in the official pipeline for the current version of the source catalogue and so this could also be the cause. To account for this deficiency a flux dependent calibration factor may need to be derived.

A second comparison was made between the final OU maps before and after HIPE based de-glitching was applied (figure B51). The sources are assumed to be real, to focus on any effect on source flux due to the de-glitching. There is a good agreement between the Green flux densities and slight difference seen of 5% is due to a small difference in wavelength ($\sim$4 μm) used for deriving the FWHM. There is an interesting scatter seen for the Red flux density comparison, which is more likely due to the masking of the non-de-glitched data as the comparison of the de-glitched data with the H-ATLAS catalogue did not show a similar structure. The line of best fit does not show a good fit towards the bright end as a consequence of the distribution at fainter flux densities, but suggests the flux agreement is probably close to 1.

Another test for the OU reduced and de-glitched data was made with the photometry of the five sub-mm lenses of Negrello et al. [2009] (see chapter 6). The PACS flux densities were taken for four of the lenses, and Red photometry and a Green 3σ upper limit for the fifth (ID81) as it lies to the edge of the combined maps, in a region of low signal-to-noise. For ID17 and ID81 the

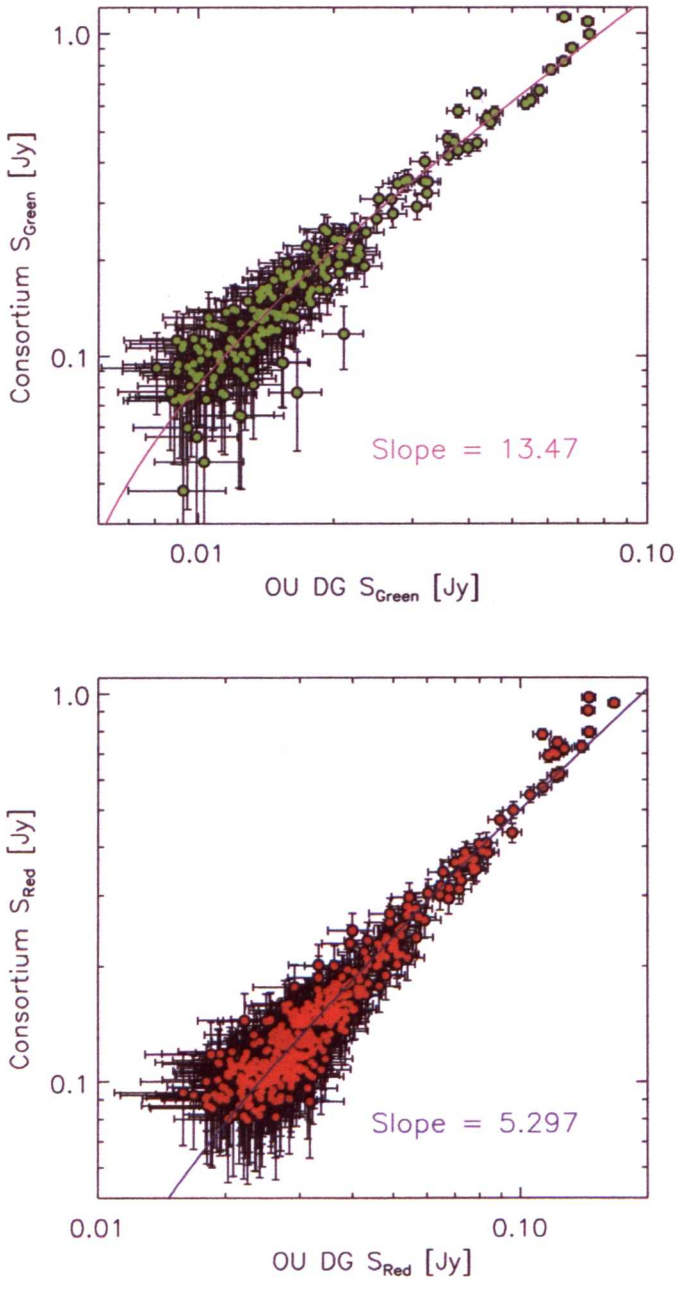

Figure B50: PACS Green (top) and Red (bottom) OU de-glitched flux densities (OU DG S) vs H-ATLAS consortium flux densities (Consortium S). Correction factor of 13.5 and 5.3 for the Green and Red data, respectively, is necessary to recover the full flux densities of the OU data, due to loss of flux at the 1D filtering stage. The bright sources see a less good agreement due to either the MMT de-glitching carried out on the OU data or the different treatment they are given (in comparison to the fainter sources) in the official HIPE pipeline. the curves are lines of linear best fit.

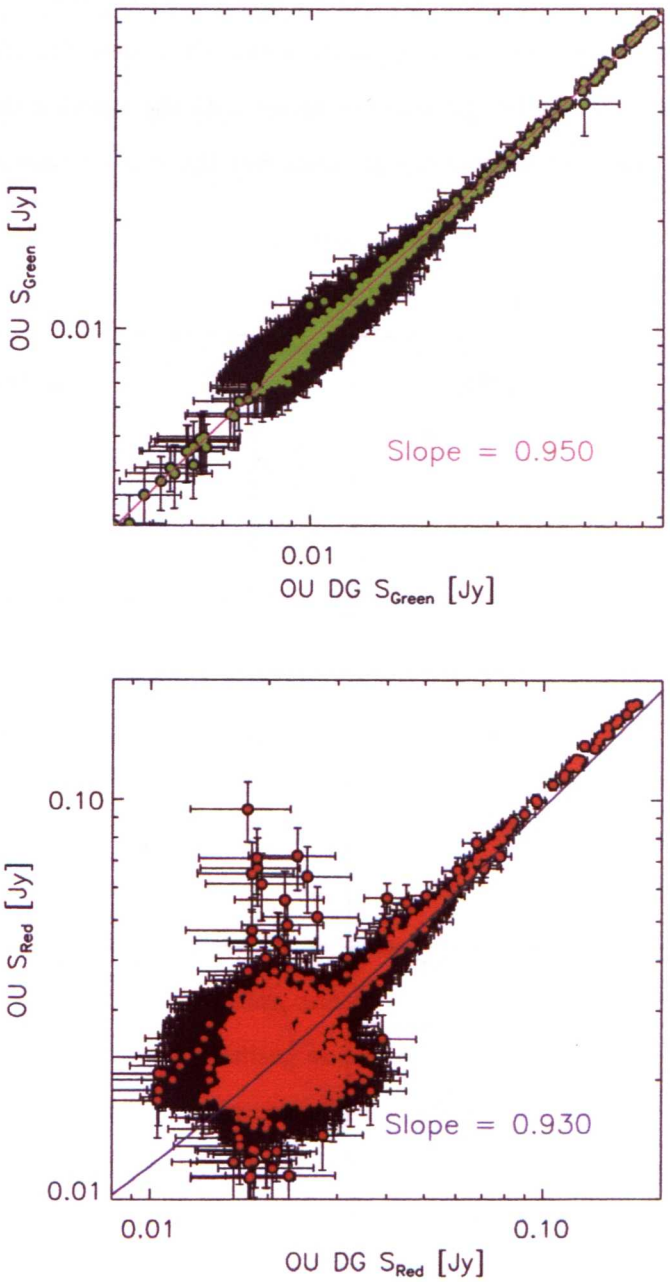

Figure B51: PACS Green (top) and Red (bottom) OU de-glitched flux densities (OU DG S) vs OU flux densities from the data without the HIPE based de-glitching (OU S). The agreement between the flux densities is ≈1, but there is an odd symmetrical scatter seen at the fainter end of the red comparison. This is not seen in the comparison with the H-ATLAS catalouges and therefore may be due to the masking of calibration spikes in the OU data that has no HIPE de-glitching. The de-glitching does not introduce any systematic difference. The curves are lines of linear best fit.

SNR is < 3 as so the peak values were taken for the nearest source. The photometry were added to the best fitting SEDs from Negrello et al. 2010. (figure B52) For ID9, ID11 and ID17 the OU photometry agrees with the previous photometry within the errors. For ID130 the PACS data was previously absent, but the OU photometry agrees with the model within 3σ errors.
For ID81 the upper limit and photometry are high, but this can be explained by the low SNR (< 2).

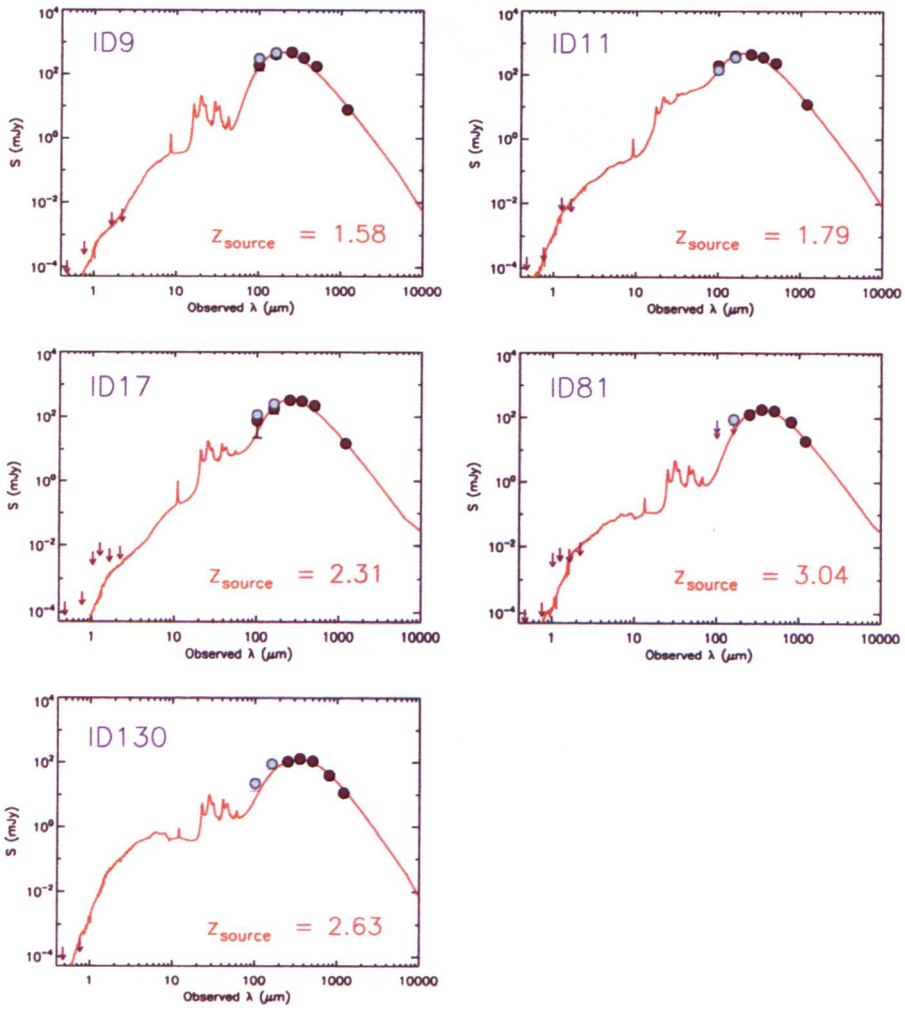

Figure B52: OU PACS photometry (blue points) compared to photometry and the best fit SEDs from Negrello et al. 2010 for the five H-ATLAS SDP gravitational lens background sources. For ID9, ID11 and ID17 the flux densities agree within 1σ and for ID130 there is no comparison, but the new photometry appears to be $\sim$1-3σ away from the SED prediction. For ID81 there are only upper limits for comparison and the 160 μJy data point is below the limit set.

B5.3 P(k) comparison

To conclude the post reduction and post de-glitching comparisons, P(k) were taken for Red 1342187171 [7,1] timeline for the level1 data, the HIPE de-glitched data and the beam-switched sky subtracted data (figure B53). A less negative best fit slope was found for the de-glitched P(k), compared to the level 1 P(k). Ideal 1/f noise has a slope of -1 in Fourier frequency space, therefore suggesting there the 1/f noise is far from idea in the PACS data. After the the beam-switching has been performed the P(k) flattens at lower frequencies, which is expected for white noise. The positive slope that is present after the beam-switched sky subtraction still needs to be understood. Although the de-glitching removes some of the noise dominating the slope of the P(k) it does not give an improved 'knee', that would enable the 1/f noise frequency modes to be isolated are removed. It may be possible to optimise the 1D filtering by examining the P(k) of the filtered results until an optimum result is obtained.

B6 Summary and future work

There are several areas of this data reduction that may benefit from further testing and adaption. Most importantly is the choice of filters, both for the 1D beam-switching kernel size and switch width and the 2D filter size and shape. The investigation performed so far into the beam-switching has shown that flux loss is minimised for a 1D kernel FWHM approximately equal to the estimated FWHM of the data and a beam-switch width twice that size, however this has a negative impact on the resulting noise and leads to enhanced striping in the final images. There may be a suitable compromise to be struck between flux loss and noise reduction, which can then be accounted for during the 2D filtering and flux calibration. Once the timelines are sky-subtracted, the associated source PSF sees a significant change in profile. The FWHM is reduced and negative side lobes are introduced. These changes should be addressed when filtering in 2D, either by using an empirical PSF (which is now easier to model due to the implementation of de-glitching), or by choosing an appropriate shaped PSF rather than the 2D Gaussian that is currently employed e.g. the Vio filter. A second area that requires attention is that of photometry testing. To test the effects of filtering on source flux, artificial sources should be introduced at the 1D level and the resulting photometry after de-glitching and filtering should be compared to the input flux. This process will help to derive a flux calibration

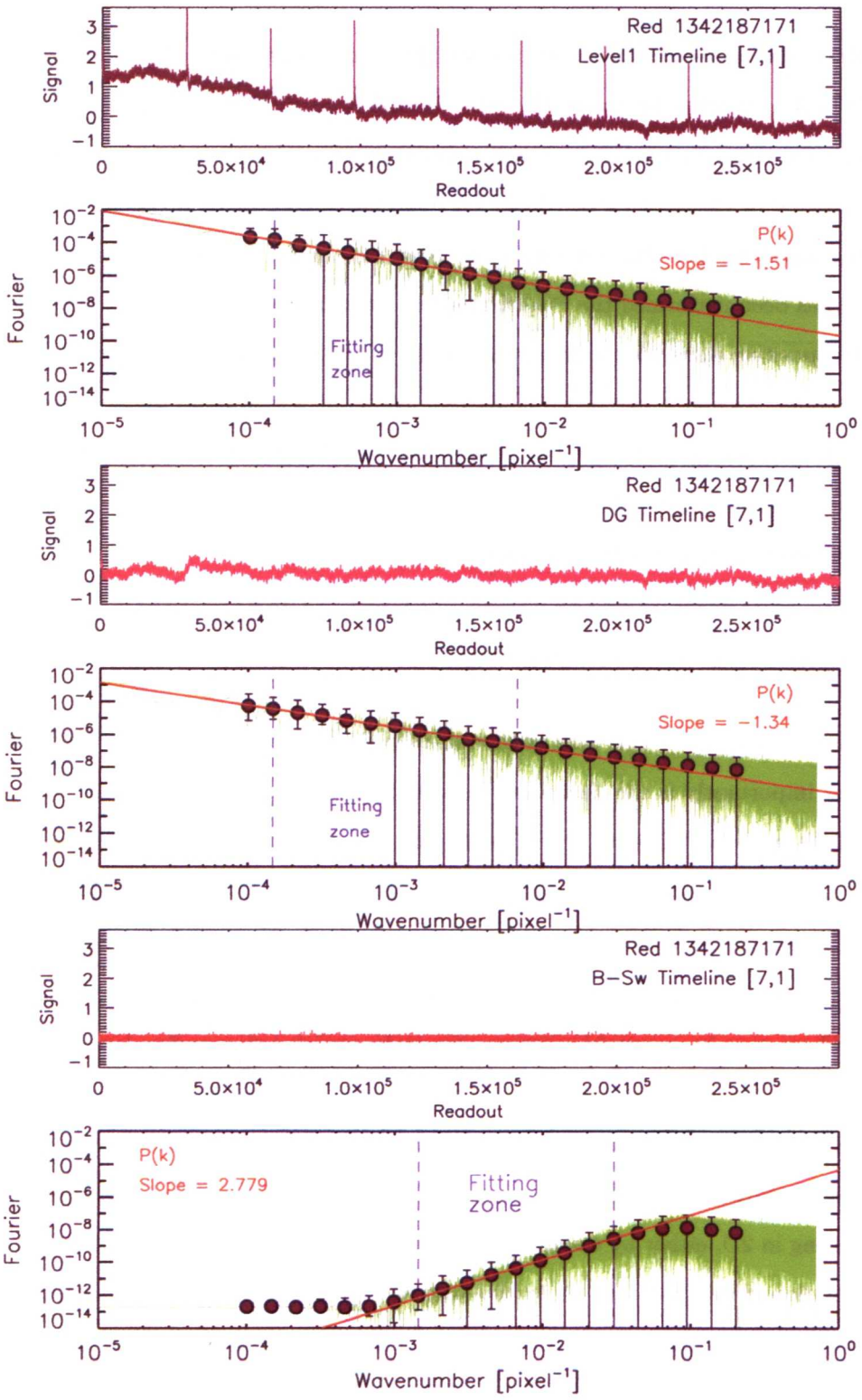

Figure B53: P(k) plots at various stages through the reduction process: for the raw timeline (top pair, note the calibration spikes); after the de-glitching (middle pair) and after the beam-switching (bottom pair). There is an as yet, unexplained slope for the final P(k).

factor, rather than calibrating using the cross-match with the official catalogue, and if necessary a flux dependent calibration factor can be derived that will account for the deficit seen for the brightest sources (possibly due to the application of MMT de-glitching).

All these tasks will be considerable easier to investigate and achieve using the HIPE de-glitched data product.

References

Abazajian, K., et al. 2003, AJ, 126, 2081

Adelman-McCarthy, J. K., et al. 2008, ApJS, 175, 297

Aharonian, F., et al. 2006, Nature, 440, 1018

Alcock, C., et al. 2000, ApJ, 542, 281

Allam, S. S., Tucker, D. L., Lin, H., Diehl, H. T., Annis, J., Buckley-Geer, E. J., & Frieman, J. A. 2007, ApJ, 662, L51

Altieri, B., et al. 2010, A&A, 518, L17+

Aretxaga, I., Hughes, D. H., Chapin, E. L., Gaztañaga, E., Dunlop, J. S., & Ivison, R. J. 2003, Mon. Not. R. Astron. Soc., 342, 759

Auger, M. W., Treu, T., Bolton, A. S., Gavazzi, R., Koopmans, L. V. E., Marshall, P. J., Bundy, K., & Moustakas, L. A. 2009, ApJ, 705, 1099

Aussel, H., Cesarsky, C. J., Elbaz, D., & Starck, J. L. 1999, A&A, 342, 313

Bacon, D. J., Refregier, A. R., & Ellis, R. S. 2000, MNRAS, 318, 625

Baes, M., et al. 2010, A&A, 518, L39+

Bertin, E., & Arnouts, S. 1996, A&AS, 117, 393

Béthermin, M., Dole, H., Beelen, A., & Aussel, H. 2010a, A&A, 512, A78+

Béthermin, M., Dole, H., Lagache, G., Le Borgne, D., & Pénin, A. 2010b, ArXiv e-prints

Blain, A. W. 1996, Mon. Not. R. Astron. Soc., 283, 1340

—. 2002, MNRAS, 330, 219

Blain, A. W., Chapman, S. C., Smail, I., & Ivison, R. 2004, ApJ, 611, 52

Bolton, A. S., Burles, S., Koopmans, L. V. E., Treu, T., Gavazzi, R., Moustakas, L. A., Wayth, R., & Schlegel, D. J. 2008a, ApJ, 682, 964

Bolton, A. S., Burles, S., Koopmans, L. V. E., Treu, T., & Moustakas, L. A. 2006, ApJ, 638, 703

Bolton, A. S., Treu, T., Koopmans, L. V. E., Gavazzi, R., Moustakas, L. A., Burles, S., Schlegel, D. J., & Wayth, R. 2008b, ApJ, 684, 248

Bolzonella, M., Miralles, J., & Pelló, R. 2000, A&A, 363, 476

Bonnarel, F., et al. 2000, A&AS, 143, 33

Borys, C., et al. 2004, MNRAS, 352, 759

Bower, R. G., Lucey, J. R., & Ellis, R. S. 1992, MNRAS, 254, 601

Bradford, C. M., et al. 2004, in Society of Photo-Optical Instrumentation Engineers (SPIE) Conference Series, Vol. 5498, Society of Photo-Optical Instrumentation Engineers (SPIE) Conference Series, ed. C. M. Bradford, P. A. R. Ade, J. E. Aguirre, J. J. Bock, M. Dragovan, L. Duband, L. Earle, J. Glenn, H. Matsuhara, B. J. Naylor, H. T. Nguyen, M. Yun, & J. Zmuidzinas, 257–+

Brammer, G. B., van Dokkum, P. G., & Coppi, P. 2008, ApJ, 686, 1503

Bridle, S. 2008, in A Decade of Dark Energy

Broadhurst, T. 1995, ArXiv Astrophysics e-prints

Broadhurst, T. J., Taylor, A. N., & Peacock, J. A. 1995, ApJ, 438, 49

Brown, T. M., Kimble, R. A., Ferguson, H. C., Gardner, J. P., Collins, N. R., & Hill, R. S. 2000, AJ, 120, 1153

Browne, I. W. A., et al. 2003, MNRAS, 341, 13

Burkert, A. 1993, A&A, 278, 23

Caon, N., Capaccioli, M., & D'Onofrio, M. 1993, MNRAS, 265, 1013

Chae, K. 2003, MNRAS, 346, 746

Chae, K., & Mao, S. 2003, ApJ, 599, L61

Chapman, S. C., Blain, A. W., Smail, I., & Ivison, R. J. 2005, ApJ, 622, 772

Chary, R., & Elbaz, D. 2001, ApJ, 556, 562

Chary, R., & Pope, A. 2010, ArXiv e-prints

Chary, R., et al. 2004, ApJS, 154, 80

Clements, D. L., et al. 2010, A&A, 518, L8+

Coleman, G. D., Wu, C., & Weedman, D. W. 1980, ApJS, 43, 393

Collister, A. A., & Lahav, O. 2004, PASP, 116, 345

Condon, J. J. 1974, ApJ, 188, 279

Coppin, K., et al. 2006, MNRAS, 372, 1621

Cutri, R. M., et al. 2003, 2MASS All Sky Catalog of point sources. (NASA/IPAC Infrared Science Archive)

da Cunha, E., Charlot, S., & Elbaz, D. 2008, Mon. Not. R. Astron. Soc., 388, 1595

da Cunha, E., Eminian, C., Charlot, S., & Blaizot, J. 2010, MNRAS, 403, 1894

Daddi, E., et al. 2009, ApJ, 694, 1517

D'Aloisio, A., & Natarajan, P. 2010, ArXiv e-prints

De Lucia, G., & Blaizot, J. 2007, MNRAS, 375, 2

de Santis, C., Grazian, A., Fontana, A., & Santini, P. 2007, New Astronomy, 12, 271

de Zotti, G., Ricci, R., Mesa, D., Silva, L., Mazzotta, P., Toffolatti, L., & González-Nuevo, J. 2005, A&A, 431, 893

Devlin, M. J., et al. 2009, Nature, 458, 737

Dey, A., et al. 2008, ApJ, 677, 943

Dickinson, M., Giavalisco, M., & GOODS Team. 2003a, in The Mass of Galaxies at Low and High Redshift, ed. R. Bender & A. Renzini, 324–+

Dickinson, M., Papovich, C., Ferguson, H. C., & Budavári, T. 2003b, ApJ, 587, 25

Dole, H., et al. 2006, A&A, 451, 417

Dye, S., et al. 2006, ApJ, 644, 769

Eales, S., Lilly, S., Webb, T., Dunne, L., Gear, W., Clements, D., & Yun, M. 2000, AJ, 120, 2244

Eales, S., et al. 2010, PASP, 122, 499

Ebbels, T., Ellis, R., Kneib, J., Le Borgne, J., Pello, R., Smail, I., & Sanahuja, B. 1998, MNRAS, 295, 75

Edelstein, J., Bowyer, S., & Lampton, M. 2000, ApJ, 539, 187

Efstathiou, A., & Rowan-Robinson, M. 1995, MNRAS, 273, 649

Egami, E. 2010, In preparation

Egami, E., et al. 2010, A&A, 518, L12+

Elbaz, D., Cesarsky, C. J., Chanial, P., Aussel, H., Franceschini, A., Fadda, D., & Chary, R. R. 2002a, A&A, 384, 848

Elbaz, D., Flores, H., Chanial, P., Mirabel, I. F., Sanders, D., Duc, P., Cesarsky, C. J., & Aussel, H. 2002b, A&A, 381, L1

Elbaz, D., et al. 1999, A&A, 351, L37

Elíasdóttir, Á., et al. 2007, ArXiv e-prints

Ellis, R., Santos, M. R., Kneib, J., & Kuijken, K. 2001, ApJ, 560, L119

Faber, S. M., & Jackson, R. E. 1976, Astrophys. J., 204, 668

Fabian, A. C. 2009, ArXiv e-prints

Fassnacht, C. D., Moustakas, L. A., Casertano, S., Ferguson, H. C., Lucas, R. A., & Park, Y. 2004, ApJ, 600, L155

Fazio, G. G., et al. 2004, ApJS, 154, 39

Fioc, M., & Rocca-Volmerange, B. 1997, A&A, 326, 950

Fixsen, D. J., Dwek, E., Mather, J. C., Bennett, C. L., & Shafer, R. A. 1998, ApJ, 508, 123

Franceschini, A., Aussel, H., Cesarsky, C. J., Elbaz, D., & Fadda, D. 2001, A&A, 378, 1

Frayer, D. T., et al. 2011, ApJ, 726, L22+

Gardner, J. P., Brown, T. M., & Ferguson, H. C. 2000, ApJ, 542, L79

Gavazzi, R., Treu, T., Rhodes, J. D., Koopmans, L. V. E., Bolton, A. S., Burles, S., Massey, R. J., & Moustakas, L. A. 2007, ApJ, 667, 176

Geach, J. E., Smail, I., Chapman, S. C., Alexander, D. M., Blain, A. W., Stott, J. P., & Ivison, R. J. 2007, ApJ, 655, L9

Georgantopoulos, I., Akylas, A., Georgakakis, A., & Rowan-Robinson, M. 2009, ArXiv e-prints

Giavalisco, M., et al. 2004, ApJ, 600, L93

Gil de Paz, A., & Madore, B. F. 2002, AJ, 123, 1864

Glenn, J., et al. 2010, ArXiv e-prints

González-Nuevo, J., et al. 2010, A&A, 518, L38+

Gorjian, V., Wright, E. L., & Chary, R. R. 2000, ApJ, 536, 550

Graham, A. W., & Guzmán, R. 2003, AJ, 125, 2936

Grazian, A., et al. 2006, A&A, 449, 951

Griffin, M. J., et al. 2010, A&A, 518, L3+

Gruppioni, C., Lari, C., Pozzi, F., Zamorani, G., Franceschini, A., Oliver, S., Rowan-Robinson, M., & Serjeant, S. 2002, MNRAS, 335, 831

Gruppioni, C., Pozzi, F., Lari, C., Oliver, S., & Rodighiero, G. 2005, ApJ, 618, L9

Guilloteau, S., et al. 1992, A&A, 262, 624

Harris, A. I., et al. 2007, in Astronomical Society of the Pacific Conference Series, Vol. 375, From Z-Machines to ALMA: (Sub)Millimeter Spectroscopy of Galaxies, ed. A. J. Baker, J. Glenn, A. I. Harris, J. G. Mangum, & M. S. Yun , 82–+

Hatsukade, B., et al. 2010, ApJ, 711, 974

Hauser, M. G., & Dwek, E. 2001, ARA&A, 39, 249

Hauser, M. G., et al. 1998, ApJ, 508, 25

Hjorth, J., & Madsen, J. 1995, ApJ, 445, 55

Högbom, J. A. 1974, A&AS, 15, 417

Hogg, D. W. 2001, AJ, 121, 1207

Holland, W. S., Duncan, W., Kelly, B. D., Irwin, K. D., Walton, A. J., Ade, P. A. R., & Robson, E. I. 2003, in Society of Photo-Optical Instrumentation Engineers (SPIE) Conference Series, Vol. 4855, Society of Photo-Optical Instrumentation Engineers (SPIE) Conference Series, ed. T. G. Phillips & J. Zmuidzinas, 1–18

Hopkins, A. M. 2004, ApJ, 615, 209

Hopwood, R., et al. 2010, ApJ, 716, L45

Houck, J. R., Schneider, D. P., Danielson, G. E., Neugebauer, G., Soifer, B. T., Beichman, C. A., & Lonsdale, C. J. 1985, ApJ, 290, L5

Howell, S. B. 1989, PASP, 101, 616

Hubble, E. P. 1936, Realm of the Nebulae (Yale University Press)

Hughes, D. H., et al. 2002, Mon. Not. R. Astron. Soc., 335, 871

Ibar, E., et al. 2010, MNRAS, 409, 38

Ishihara, D., et al. 2010, A&A, 514, A1+

Ivison, R. J., et al. 2010, A&A, 518, L35+

Jackson, N., Bryan, S. E., Mao, S., & Li, C. 2010, MNRAS, 403, 826

Jørgensen, I., Franx, M., Hjorth, J., & van Dokkum, P. G. 1999, MNRAS, 308, 833

Jullo, E., Kneib, J.-P., Limousin, M., Elíasdóttir, Á., Marshall, P. J., & Verdugo, T. 2007, New Journal of Physics, 9, 447

Kassiola, A., & Kovner, I. 1993, ApJ, 417, 450

King, I. R. 1971, PASP, 83, 199

Kneib, J., Mathez, G., Fort, B., Mellier, Y., Soucail, G., & Longaretti, P. 1994, A&A, 286, 701

Kneib, J.-P., Ellis, R. S., Smail, I., Couch, W. J., & Sharples, R. M. 1996, ApJ, 471, 643

Kneib, J. P., Mellier, Y., Pello, R., Miralda-Escude, J., Le Borgne, J., Boehringer, H., & Picat, J. 1995, A&A, 303, 27

Knudsen, K. K., Kneib, J., Richard, J., Petitpas, G., & Egami, E. 2010, ApJ, 709, 210

Knudsen, K. K., van der Werf, P. P., & Kneib, J. 2008, MNRAS, 384, 1611

Knudsen, K. K., et al. 2006, MNRAS, 368, 487

Ko, J., et al. 2009, ApJ, 695, L198

Koopmans, L. V. E., & the CLASS collaboration. 2001, PASP, 18, 179

Koopmans, L. V. E., Treu, T., Bolton, A. S., Burles, S., & Moustakas, L. A. 2006, ApJ, 649, 599

Kovács, A., Chapman, S. C., Dowell, C. D., Blain, A. W., Ivison, R. J., Smail, I., & Phillips, T. G. 2006, ApJ, 650, 592

Kraus, J. D. 1966, Radio astronomy (New York: McGraw-Hill)

Krause, O., Lemke, D., Hofferbert, R., Böhm, A., Klaas, U., Katzer, J., Höller, F., & Salvasohn, M. 2006, in Society of Photo-Optical Instrumentation Engineers (SPIE) Conference Series, Vol. 6273, Society of Photo-Optical Instrumentation Engineers (SPIE) Conference Series

Lacy, M., Rawlings, S., & Serjeant, S. 1998, MNRAS, 299, 1220

Lagache, G., Abergel, A., Boulanger, F., Désert, F. X., & Puget, J. 1999, A&A, 344, 322

Lagache, G., Haffner, L. M., Reynolds, R. J., & Tufte, S. L. 2000, A&A, 354, 247

Lagache, G., Puget, J., & Dole, H. 2005, ARA&A, 43, 727

Lagache, G., et al. 2004, ApJS, 154, 112

LeFloc'h, E., et al. 2009, ApJ, 703, 222

Lilly, S., Eales, S. A., Gear, W. K., Webb, T. M., Bond, J. R., & Dunne, L. 1999, in The Formation of Galactic Bulges, ed. C. M. Carollo, H. C. Ferguson, & R. F. G. Wyse, 26–+

Lonsdale, C. J., Farrah, D., & Smith, H. E. 2006, Ultraluminous Infrared Galaxies (Springer Verlag), 285–+

Lorente, R., Onaka, T., Ita, Y., Ohyama, Y., Tanabé, T., & Pearson, C. P. 2008, AKARI IRC Data User Manual, 1.4 edn.

Low, F. J., & Tucker, W. H. 1968, Physical Review Letters, 21, 1538

Lupu, R. E., et al. 2010, ArXiv e-prints

Madau, P., Ferguson, H. C., Dickinson, M. E., Giavalisco, M., Steidel, C. C., & Fruchter, A. 1996, MNRAS, 283, 1388

Madau, P., & Pozzetti, L. 2000, MNRAS, 312, L9

Makovoz, D., & Khan, I. 2005, in Astronomical Society of the Pacific Conference Series, Vol. 347, Astronomical Data Analysis Software and Systems XIV, ed. P. Shopbell, M. Britton, & R. Ebert, 81–+

Maloney, P. R., et al. 2005, ApJ, 635, 1044

Markwardt, C. B. 2009, in Astronomical Society of the Pacific Conference Series, Vol. 411, Astronomical Society of the Pacific Conference Series, ed. D. A. Bohlender, D. Durand, & P. Dowler, 251–+

Marsden, G., et al. 2009, ApJ, 707, 1729

Marshall, P. J., et al. 2007, ApJ, 671, 1196

McCarthy, J. K., et al. 1998, in Presented at the Society of Photo-Optical Instrumentation Engineers (SPIE) Conference, Vol. 3355, Society of Photo-Optical Instrumentation Engineers (SPIE) Conference Series, ed. S. D'Odorico, 81–92

McKean, J. P., et al. 2007, MNRAS, 378, 109

Mellier, Y. 1999, ARA&A, 37, 127

Mellier, Y., Soucail, G., Fort, B., & Mathez, G. 1988, A&A, 199, 13

Merline, W. J., & Howell, S. B. 1995, Experimental Astronomy, 6, 163

Metcalfe, L., et al. 2003, A&A, 407, 791

Michałowski, M., Hjorth, J., & Watson, D. 2010a, A&A, 514, A67+

Michałowski, M. J., Watson, D., & Hjorth, J. 2010b, ApJ, 712, 942

Miville-Deschênes, M., Lagache, G., & Puget, J. 2002, A&A, 393, 749

Mobasher, B., et al. 2004, ApJ, 600, L167

More, A., McKean, J. P., More, S., Porcas, R. W., Koopmans, L. V. E., & Garrett, M. A. 2009, MNRAS, 394, 174

Mortier, A. M. J., et al. 2005, MNRAS, 363, 563

Murakami, H., et al. 2007, PASJ, 59, 369

Myers, S. T., et al. 2003, MNRAS, 341, 1

Nakagawa, T. 2004, Advances in Space Research, 34, 645

Narayanan, D., et al. 2010, MNRAS, 407, 1701

Natarajan, P., Loeb, A., Kneib, J., & Smail, I. 2002, ApJ, 580, L17

Naylor, B. J., et al. 2003, in Society of Photo-Optical Instrumentation Engineers (SPIE) Conference Series, Vol. 4855, Society of Photo-Optical Instrumentation Engineers (SPIE) Conference Series, ed. T. G. Phillips & J. Zmuidzinas, 239–248

Negrello, M., Magliocchetti, M., Moscardini, L., De Zotti, G., Granato, G. L., & Silva, L. 2004, MNRAS, 352, 493

Negrello, M., Perrotta, F., González-Nuevo, J., Silva, L., de Zotti, G., Granato, G. L., Baccigalupi, C., & Danese, L. 2007, MNRAS, 377, 1557

Negrello, M., et al. 2009, MNRAS, 394, 375

Nesvadba, N. P. H., et al. 2006, ApJ, 650, 661

Oguri, M., et al. 2006, AJ, 132, 999

—. 2008, AJ, 135, 512

Oke, J. B., et al. 1995, Publ. Astron. Soc. Pac., 107, 375

Oliver, S. J., et al. 2010, A&A, 518, L21+

Onaka, T., et al. 2007, PASJ, 59, 401

Ott, S., Science Centre, H., & Space Agency, E. 2010, ArXiv e-prints

Packham, C., et al. 2003, MNRAS, 345, 395

Papovich, C., et al. 2004, ApJS, 154, 70

Paraficz, D., & Hjorth, J. 2010, ApJ, 712, 1378

Pascale, E., et al. 2010, ArXiv e-prints

Patanchon, G., et al. 2009, ApJ, 707, 1750

Pearson, C. 2005, MNRAS, 358, 1417

—. 2010, In preparation

Pearson, C. P., et al. 2007, Advances in Space Research, 40, 605

Peng, C. Y., Ho, L. C., Impey, C. D., & Rix, H. 2002, AJ, 124, 266

Penzias, A. A., & Wilson, R. W. 1965, ApJ, 142, 419

Perrotta, F., Magliocchetti, M., Baccigalupi, C., Bartelmann, M., De Zotti, G., Granato, G. L., Silva, L., & Danese, L. 2003, Mon. Not. R. Astron. Soc., 338, 623

Pilbratt, G. L., et al. 2010, A&A, 518, L1+

Poglitsch, A., et al. 2010, A&A, 518, L2+

Polletta, M., et al. 2007, ApJ, 663, 81

Pozzetti, L., & Mannucci, F. 2000, MNRAS, 317, L17

Press, W. H., Teukolsky, S. A., Vetterling, W. T., & Flannery, B. P. 1992, Numerical recipes in FORTRAN. The art of scientific computing (Cambridge: University Press, 2nd ed.)

Puget, J.-L., Abergel, A., Bernard, J.-P., Boulanger, F., Burton, W. B., Desert, F.-X., & Hartmann, D. 1996, A&A, 308, L5+

Ratnatunga, K. U., Ostrander, E. J., Griffiths, R. E., & Im, M. 1995, ApJ, 453, L5+

Reimers, D., Hagen, H., Baade, R., Lopez, S., & Tytler, D. 2002, A&A, 382, L26

Renault, C., Barrau, A., Lagache, G., & Puget, J.-L. 2001, A&A, 371, 771

Retzlaff, J., Rosati, P., Dickinson, M., Vandame, B., Rité, C., Nonino, M., Cesarsky, C., & GOODS Team. 2010, A&A, 511, A50+

Richard, J., Kneib, J., Limousin, M., Edge, A., & Jullo, E. 2010, MNRAS, 402, L44

Rigby, E. E., et al. 2010, ArXiv e-prints

Rodighiero, G., Lari, C., Fadda, D., Franceschini, A., Elbaz, D., & Cesarsky, C. 2004, A&A, 427, 773

Rodighiero, G., et al. 2010, A&A, 515, A8+

Roeser, H., & Meisenheimer, K. 1991, A&A, 252, 458

Rowan-Robinson, M. 2009, MNRAS, 394, 117

Rowan-Robinson, M., et al. 1991, Nature, 351, 719

Rush, B., Malkan, M. A., & Spinoglio, L. 1993, ApJS, 89, 1

Sánchez, S. F., Cardiel, N., Verheijen, M. A. W., Pedraz, S., & Covone, G. 2007, MNRAS, 376, 125

Santini, P., et al. 2010, A&A, 518, L154+

Savage, R. S., & Oliver, S. 2005, ArXiv Astrophysics e-prints

Schechter, P. L., & Moore, C. B. 1993, AJ, 105, 1

Schneider, D. P., et al. 2000, AJ, 120, 2183

—. 2005, AJ, 130, 367

Schroedter, M. 2005, ApJ, 628, 617

Serjeant, S., & Harrison, D. 2005, Mon. Not. R. Astron. Soc., 356, 192

Serjeant, S., et al. 2000, MNRAS, 316, 768

—. 2003, MNRAS, 344, 887

—. 2008, MNRAS, 386, 1907

—. 2010a, A&A, 518, L7+

—. 2010b, A&A, 514, A10+

Sersic, J. L. 1968, Atlas de galaxias australes (Cordoba, Argentina: Observatorio Astronomico)

Silva, L., Granato, G. L., Bressan, A., & Danese, L. 1998, ApJ, 509, 103

Smail, I., Ivison, R. J., & Blain, A. W. 1997, ApJ, 490, L5+

Smail, I., Ivison, R. J., Blain, A. W., & Kneib, J. 2002, MNRAS, 331, 495

Smail, I., Kuntschner, H., Kodama, T., Smith, G. P., Packham, C., Fruchter, A. S., & Hook, R. N. 2001a, MNRAS, 323, 839

—. 2001b, VizieR Online Data Catalog, 732, 30839

Soucail, G., Fort, B., Mellier, Y., & Picat, J. P. 1987, A&A, 172, L14

Starck, J., & Murtagh, F. 1998, PASP, 110, 193

Stark, D. P., Ellis, R. S., Richard, J., Kneib, J., Smith, G. P., & Santos, M. R. 2007, ApJ, 663, 10

Stecker, F. W., & de Jager, O. C. 1997, ApJ, 476, 712

Stetson, P. B. 1987, PASP, 99, 191

—. 2000, DAOPHOT2 user's manual, Herzberg Institute of Astrophysics, 5071 West Saanich Road, Victoria, British Coumbia V8X 4M6

Suyu, S. H., & Halkola, A. 2010, ArXiv e-prints

Takagi, T., Arimoto, N., & Hanami, H. 2003, MNRAS, 340, 813

Takagi, T., & Pearson, C. P. 2005, MNRAS, 357, 165

Takata, T., Sekiguchi, K., Smail, I., Chapman, S. C., Geach, J. E., Swinbank, A. M., Blain, A., & Ivison, R. J. 2006, ApJ, 651, 713

Teplitz, H. I., Charmandaris, V., Chary, R., Colbert, J. W., Armus, L., & Weedman, D. 2005, ApJ, 634, 128

Thompson, M. A., et al. 2010, A&A, 518, L134+

Thompson, R. I. 2003, ApJ, 596, 748

Treu, T. 2010, ARA&A, 48, 87

Treu, T., Koopmans, L. V., Bolton, A. S., Burles, S., & Moustakas, L. A. 2006, ApJ, 640, 662

Väisänen, P., et al. 2002, MNRAS, 337, 1043

van den Bergh, S. 2009, ApJ, 694, L120

Vieira, J. D., et al. 2010, ApJ, 719, 763

Vio, R., Tenorio, L., & Wamsteker, W. 2002, A&A, 391, 789

Wada, T., et al. 2007, PASJ, 59, 515

Walsh, D., Carswell, R. F., & Weymann, R. J. 1979, Nature, 279, 381

Wambsganss, J. 1998, Living Reviews in Relativity, 1, 12

Wardlow, J. L., et al. 2010, ArXiv e-prints

Weiß, A., et al. 2009, ApJ, 707, 1201

Wittman, D. M., Tyson, J. A., Kirkman, D., Dell'Antonio, I., & Bernstein, G. 2000, Nature, 405, 143

Wolf, C., et al. 2004, A&A, 421, 913

Wright, E. L. 2001, ApJ, 553, 538

—. 2004, New Astron. Rev., 48, 465

Wuyts, S., Labbé, I., Schreiber, N. M. F., Franx, M., Rudnick, G., Brammer, G. B., & van Dokkum, P. G. 2008, ApJ, 682, 985

Yamamura, I., Makiuti, S., Ikeda, N., Fukuda, Y., Oyabu, S., Koga, T., & White, G. J. 2010, VizieR Online Data Catalog, 2298, 0

York, T., Jackson, N., Browne, I. W. A., Wucknitz, O., & Skelton, J. E. 2005, MNRAS, 357, 124

Zavagno, A., et al. 2010, A&A, 518, L101+

Ziegler, B. L., Bower, R. G., Smail, I., Davies, R. L., & Lee, D. 2001, MNRAS, 325, 1571